Neuroimaging Diagnosis for Alzheimer's Disease and Other Dementias

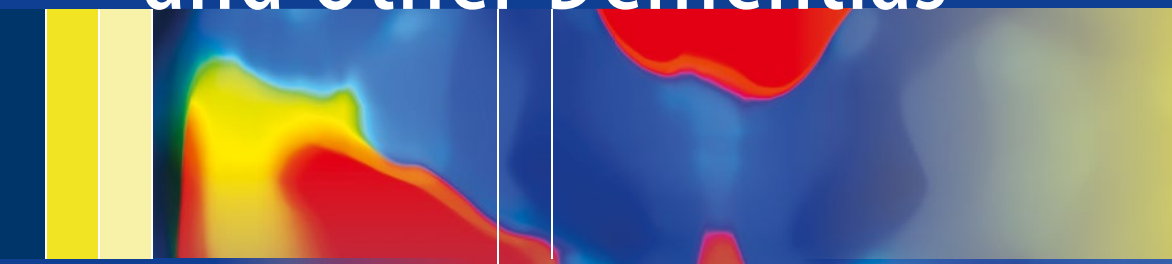

Hiroshi Matsuda
Takashi Asada
Aya Midori Tokumaru
Editors

Springer

Neuroimaging Diagnosis for Alzheimer's Disease and Other Dementias

Hiroshi Matsuda • Takashi Asada
Aya Midori Tokumaru
Editors

Neuroimaging Diagnosis for Alzheimer's Disease and Other Dementias

Springer

Editors
Hiroshi Matsuda
Integrative Brain Imaging Center
National Center of Neurology & Psychiatry
Kodaira
Tokyo
Japan

Takashi Asada
Department of Psychiatry
Institute of Clinical Medicine
University of Tsukuba
Tsukuba
Ibaraki
Japan

Aya Midori Tokumaru
Department of Diagnostic Radiology
Tokyo Metropolitan Geriatric Hospital
and Institute of Gerontology
Tokyo
Japan

ISBN 978-4-431-55132-4 ISBN 978-4-431-55133-1 (eBook)
DOI 10.1007/978-4-431-55133-1

Library of Congress Control Number: 2017951313

Printed on acid-free paper

This Springer imprint is published by Springer Nature
The registered company is Springer Japan KK
The registered company address is: Chiyoda First Bldg. East, 3-8-1 Nishi-Kanda, Chiyoda-ku, Tokyo 101-0065, Japan

Preface

Nowhere is the serious social problem of dementia more acute than in Japan, where an estimated one fourth of elderly persons already have or show signs of developing it. The prevalence of dementia has increased over the past few decades, either because of greater awareness and more accurate diagnosis, or because increased longevity has created a larger population of the elderly, the age group most commonly affected. More aging will develop from now on, and so it is predicted that 7 million elderly persons will be demented by 2025 in Japan.

Although the diagnosis of dementia is still largely a clinical one, based on the history and disease course, neuroimaging has dramatically changed our ability to accurately diagnose it. The role of neuroimaging in dementia nowadays extends beyond its traditional role of excluding neurosurgical lesions. Neuroimaging in dementia is recommended by most clinical guidelines. Moreover new neuroimaging methods facilitate diagnosis of most of the neurodegenerative conditions after symptom onset and show promise for diagnosis even in very early or presymptomatic phases of some diseases.

Neuroimaging also provides useful information in clinical trials of dementia. As the need to develop a successful disease-modifying treatment for Alzheimer's disease, which accounts for more than one half of dementia cases, becomes more urgent, imaging is increasingly used in therapeutic trials. Treatments for Alzheimer's disease and related disorders are currently limited to those that provide only modest symptomatic benefit. Disease-modifying therapies are urgently needed, especially those that would delay the onset of clinical decline. An effective treatment that delays symptom onset has been estimated to potentially reduce predicted dementia prevalence and healthcare costs. A large number of candidate disease-modifying therapies are under development; the studies that will be assessing these therapies are increasingly incorporating a range of imaging and other biomarkers to better understand their effects and to show evidence of disease slowing. This evidence is particularly important for guiding decisions about which therapies to take forward into large and expensive late-phase trials. Imaging endpoints provide possible benefits to clinical trials in dementia. They provide a means of assessing potential disease-modifying effects and differentiating these from symptomatic benefits that do not affect underlying pathological progression. Many imaging biomarkers have been shown to correlate with disease severity, as well as predict future progression in subjects yet to show clinical symptoms. The quantitative nature of the imaging

biomarkers often has far less variability than the primary cognitive and functional endpoints, and thus will require smaller sample sizes to be powered to show a statistically significant effect. These quantitative endpoints are objective measures where the data can be saved for further re-analysis.

Under these conditions, all clinicians and researchers who are involved in neuroimaging for dementia should decide which patients to scan, when imaging patients is most useful, which modality to use, how to handle imaging data from many institutions, and which analytical tool to use. This book describes the latest modalities such as tau and amyloid PET imaging for the diagnosis of Alzheimer's disease and other dementias, and also provides information on handling and analyzing imaging data that is not found in other books. In addition, it introduces routine imaging studies in the management of dementia in Japan. This edition comprises contributions from leading Japanese experts in their respective fields. We are very happy that our book is to be published by one of the premier publishers in the scientific field. This guarantees a high quality of reproduction allowing for the inclusion of many color figures, which is essential in the field of functional neuroimaging. We are encouraged by the enthusiastic response from contributors from all over Japan who have made this endeavor successful.

Finally we would like to thank Ms. Suzuki and Ms. Kambara from Springer Japan KK for their continuous help and support during the development of this book. We sincerely hope that this book will become a key tool not only for all physicians in radiology, nuclear medicine, neurology, psychiatry, geriatrics, and neurosurgery, but also for all professionals working to understand or treat dementia. In addition, this edition may be of interest and importance for industry, as neuroimaging is becoming more and more important in today's aging population. This book may serve as a guide towards the present use of neuroimaging in dementia and as a catalyst for future research.

Tokyo, Japan — Hiroshi Matsuda
Tsukuba, Japan — Takashi Asada
Tokyo, Japan — Aya Midori Tokumaru

Contents

Epidemiology of Dementia in Japan

1

Takashi Asada

Abstract

The survey of early-onset dementia was done in five prefectures and two cities in all parts of Japan from 2006 to 2008. The estimated number of patients per 100,000 in the 18–64-year-old population was 47.6 (95% confidence interval (CI): 45.5–49.7). The estimated patient number in all of Japan was calculated to be 37,800 (95% CI: 36,100–39,400). As a result, we found that vascular dementia (VaD) was the most common illness causing dementia, followed by Alzheimer's disease (AD), posttraumatic syndrome, and then frontotemporal degeneration.

The prevalence of late-onset dementia was surveyed with in ten areas in all parts of Japan from 2009 to 2012. From the results, the estimated national prevalence was 15%, with a standard error of 0.0136 and 95% CI of 0.12, 0.17. The number of people with dementia in all of Japan was estimated to be about 4.62 million out of a population of 30.79 million people (definite value) aged 65 years and older as of October 1, 2012. The number had probably reached 50 million by the end of 2014.

For the immediate future, both the prevalence and the total number of dementia patients are expected to rise steadily with the increase in the mean life expectancy.

Keywords

Prevalence • Early-onset dementia • Late-onset dementia

T. Asada
Department of Psychiatry, University of Tsukuba,
1-1-1 Tennodaia, Tsukuba, Ibaraki 305-8575, Japan
e-mail: tasada@md.tsukuba.ac.jp

H. Matsuda et al. (eds.), *Neuroimaging Diagnosis for Alzheimer's Disease and Other Dementias*, DOI 10.1007/978-4-431-55133-1_1

1.1 Introduction

Japan is not the only country with an aging population. In Asia, for example, China is aging at a rate that surpasses Japan, with a current elderly population of about 12% which is predicted to reach 20% within 10 years. In the future, aging populations and the resulting growth in the number of people with dementia will become a major problem not only in China but also in South Korea, India, and the entire Asian region. The problem of dementia is also inevitable in Western countries, which were the first to experience aging populations.

Today, societies are aging and longevity is increasing on a global scale; therefore, dealing with dementia is not simply a medical issue but a fundamental policy-making challenge for each country. In November 2014, the G7 Dementia Summit was held in Japan, and knowledge on dementia care and prevention was presented and shared.

This article looks at the epidemiology of dementia and describes the number of patients and future trends in both early-onset (EOD) and late-onset dementia (LOD).

1.2 EOD

1.2.1 Definition

EOD is a popular term. Formally, dementia that first occurs between the ages of 18 and 44 is called juvenile dementia, while dementia that first occurs between the ages of 45 and 64 is called presenile dementia [1]. The upper limit, however, is taken to be 60 years in some cases and 65 years in others.

1.2.2 Epidemiology

(1) Number of patients

No data on the epidemiological status of early-onset dementia (EOD) in Japan existed until recently. The first nationwide epidemiological survey in Japan was the "Research on the present status of early onset dementia" (project leader: Naomichi Ichinowatari) [1]. The survey was conducted in 1996 in all of Aomori, Gunma, and Tottori Prefectures, plus the cities of Kitakyushu and Hachioji. The survey was done in two stages: the first was a screening, and the second was a more detailed examination. From the results, the number of EOD patients in all Japan was estimated to between 25,613 and 37,434.

We conducted an epidemiological survey on EOD in five prefectures and two cities in all parts of Japan from 2006 to 2008 [2, 3]. The purpose was to calculate the prevalence of EOD, defined as "people under the age of 65 years both at the

time of onset and the time of the survey." The survey areas were Kumamoto, Ehime, Toyama, Gunma, and Ibaraki [3] Prefectures, Kohoku Ward in the city of Yokohama, and all of Tokushima City. The survey was done following the same procedures in all areas. In each area, questionnaires were sent in two stages to all centers and institutions that were thought to be associated with medical care or public health and welfare for dementia. Responses were then collected and analyzed.

The mean inverse number of the product of the response rate in the first and second surveys was 1.49 (1.23–1.74). Based on the obtained data, the estimated number of patients per 100,000 in the 18–64-year-old population was 47.6 (95% confidence interval (CI): 45.5–49.7). The number of men was 57.9, greater than that of women (36.7). The estimated patient number in all of Japan was calculated to be 37,800 (95% CI: 36,100–39,400). As shown in Fig. 1.1, the global prevalence of dementia in those aged 65 or older is thought to double every 5 years, but this survey showed that this doubling phenomenon is seen from the 1930s.

Oddly, the response rate was exactly the same in two surveys in Japan [1, 2]. It is also worth noting that the estimated number of patients was the same. This is because while EOD is said to be increasing in recent years, the obtained results show that it is in fact nearly the same. Estimates from these two surveys are similar to previously reported results from various countries [4–12] (Table 1.1).

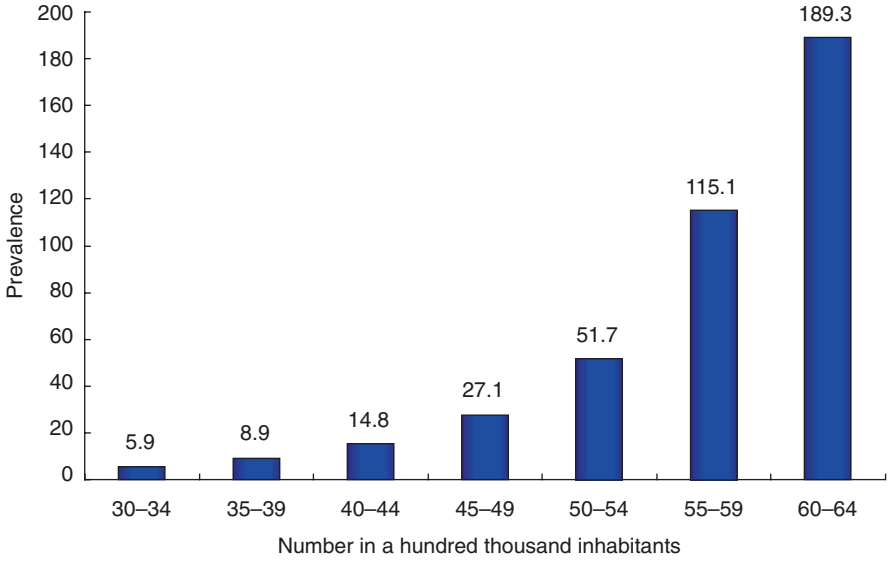

Fig. 1.1 Prevalence of early-onset dementia in terms of 5-year age strata

Table 1.1 Comparison of prevalence of dementia per 100,000 in the 30–64 year age group among studies

Authors	Year	Country	Place	Age range	Population at risk	n	Prevalence	Target
Mölsä et al. [4]	1982	Finland	Turku	45–54		10	51.0	All dementia
				55–64		24	144.0	
Sulkava et al. [5]	1985	Finland		30–64	6120	2	32.7	Severe dementia
Schoenberg et al. [6]	1985	USA	Mississippi	45–64	5489	1	18.2	Severe dementia
Kokmen et al. [7]	1989	USA	Rochester	45–49		2	77.0	All dementia
				50–54		1	40.0	
				55–59		2	86.0	
				60–64		5	249.0	
Newens et al. [8]	1993	UK	Northern Health Region	45–64	655,800	227	34.6	AD
Ohshiroa et al. [9]	1994	Japan	Tottori	40–64	209,621	100	81.4	All dementia
Ichinowatari et al. [1]	1997	Japan	Five catchment areas	18–64	3,729,706	1203	48.1	All dementia
Ratnavalli et al. [10]	2002	UK	London	45–64	326,019	59	81.0	All dementia
Harvey et al. [11]	2003	UK		30–64	240,766	130	54.0	All dementia
Rosso et al. [12]	2003	Netherlands	Zuid-Holland	30–59	1,435,769	21	1.5	FTLD
Ikejima et al. [3]	2014	Japan	Five catchment areas	18–64	9,370,651	2059	47.6	All dementia

AD Alzheimer disease, *VaD* vascular dementia, *FTLD* frontotemporal lobar degeneration

1.2.3 Illnesses Causing Dementia

Summarizing reports from Western countries and Japan, Alzheimer's disease (AD) is shown to be the most common form of dementia in a large majority of reports. Next is vascular dementia (VaD) or frontotemporal dementia, including Pick's disease; these conditions account for about half as many cases as AD. They are followed by dementia with Lewy bodies (DLB) or Parkinson's disease with dementia (PDD). Since these diseases have become widely known fairly recently, the possibility cannot be ruled out that they were previously underestimated.

In a previous survey [13], we found that VaD was the most common illness causing dementia, followed by AD, posttraumatic syndrome, and then frontotemporal degeneration. The fact that the prevalence of stroke was high in men under the age of 65 years both at the time of onset and the time of the survey is thought to be important as background for the unexpected result that VaD was the most common causative illness. The cause of cerebrovascular disease is also important. In Japan, cerebrovascular disease in old age has been decreasing in recent years. Central to that condition is multiple infarctions and lacunar infarctions, which are to some degree preventable. Incidentally, major cerebral infarction, cerebral hemorrhage, and subdural hemorrhage are common in cerebrovascular disease that is a cause of EOD. There are no reports that these conditions are decreasing in people under the age of 65 years at the time of onset in Japan.

In the 1996 study by Ichinowatari [1] VaD was found to be the most common of the illnesses causing dementia, followed by AD. It is also important that VaD was the leading cause in both of Ichinowatari's and our surveys. This is not seen in reports from other countries, and it may be the major feature of EOD in Japan. In particular, there were 1.6 times more men than women with dementia caused by VaD in this study and twice as more in the earlier study (Fig. 1.2).

1.3 LOD

1.3.1 Past Findings in Japan

The epidemiological situation of LOD in Japan in recent years is not well understood for the following reasons: survey methods vary, surveys are small, and there is no history of surveys conducted with the same method at the same time on a national scale.

Figure 1.1 shows the prevalence of dementia in terms of age strata, which has been said to be the greatest common measure. The prevalence of dementia in people aged 65–69 years is 1.5% but is thought to double every 5 years after that, reaching 27% at age of 85. Past estimates of the prevalence of dementia in the elderly population aged 65 years and older put it at around 10% in 2011. Shimokata [14] estimated that the number of dementia patients will increase together with the rapid increase in the elderly population in the future, reaching 3.25 million people in 2020.

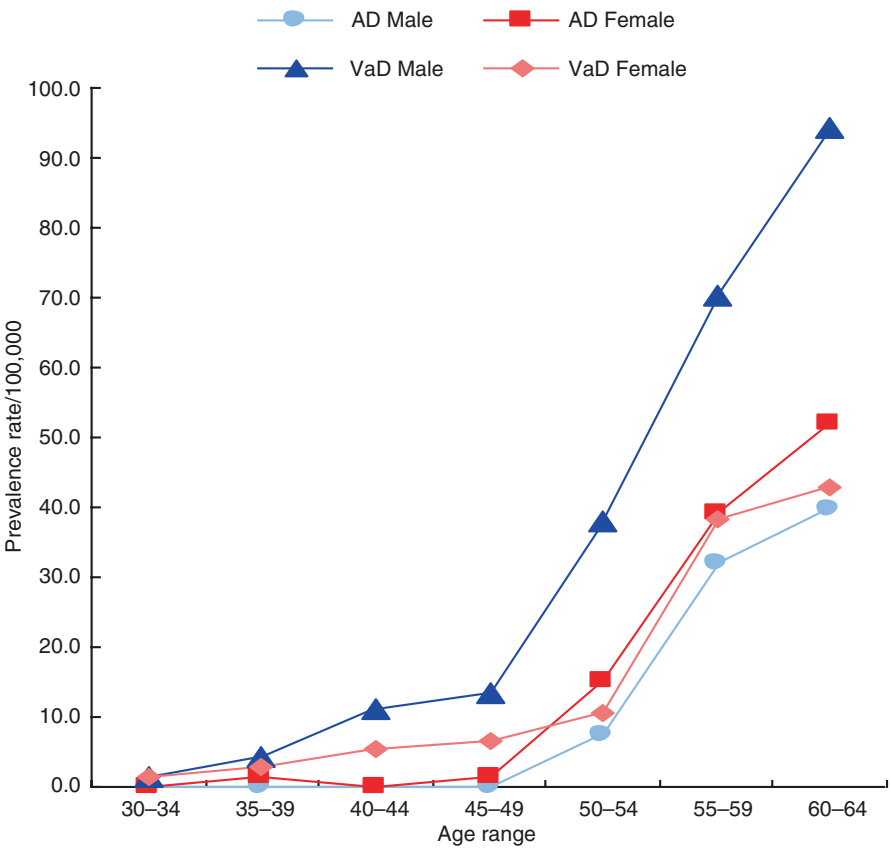

Fig. 1.2 Comparison of the prevalence of AD and VaD between men and women

1.3.2 The Most Recent National Survey in Japan

The prevalence of dementia was surveyed with a standardized method in ten areas in all parts of Japan from 2009 to 2012 [15]. The survey was carried out in the following seven regions from October 1, 2009 to September 30, 2010: Kurihara, Miyagi Prefecture; Tone, Ibaraki Prefecture; Joetsu, Niigata Prefecture; Obu, Aichi Prefecture; Ama, Shimane Prefecture; Imari, Saga Prefecture; and Kitsuki, Oita Prefecture. From 2011, it was carried out in Tsukuba, Ibaraki Prefecture; Hisayama, Fukuoka Prefecture; and Omuta, Fukuoka Prefecture for the purpose of understanding the actual situation in urban areas (Fig. 1.3).

In stage 1 of the survey, investigators spoke with family members during a home visit and conducted interviews with the patient at the home or interview site. In stage 2, doctors conducted interviews, and in stage 3, MRIs were obtained and blood tests were performed. Tests used in the Alzheimer's Disease Neuroimaging Initiative, the current global standard, were adopted for assessment of all cases.

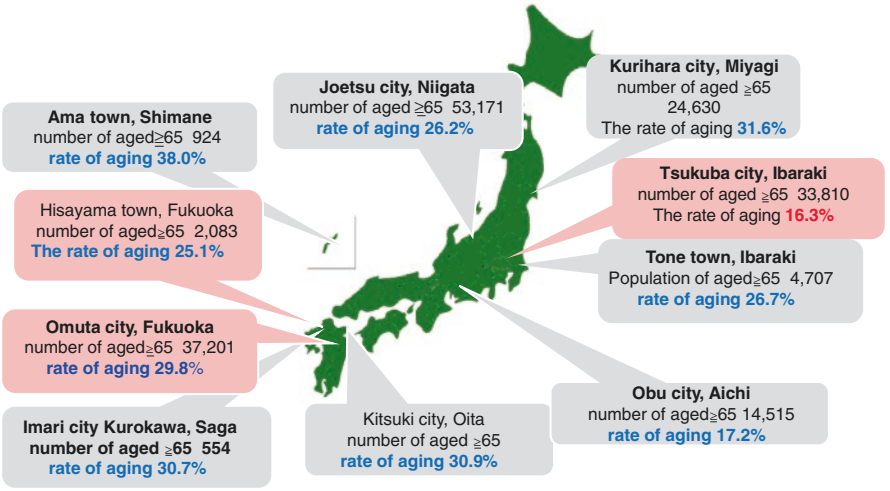

Fig. 1.3 Study sites of nationwide survey for dementia prevalence

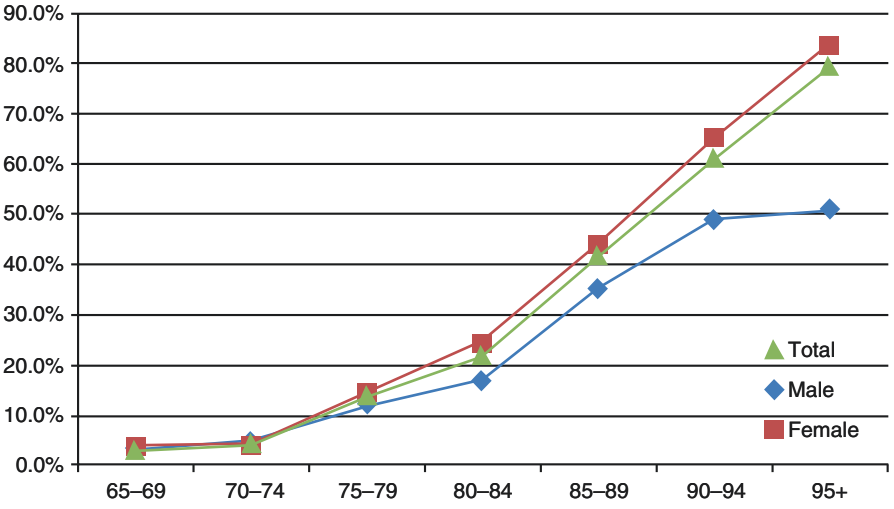

Fig. 1.4 Prevalence of dementia in terms of 5-year age strata

In estimating prevalence, data on 7825 subjects and 5386 participants from eight regions were used. From the results, the estimated national prevalence was 15%, with a standard error of 0.0136 and 95% CI of 0.12, 0.17. The number of people with dementia in all of Japan was estimated to be about 4.62 million out of a population of 30.79 million people (definite value) aged 65 years and older as of October 1, 2012 [15]. The number had probably reached 50 million by the end of 2014. The prevalence of dementia gained from the data shown in terms of 5-year age strata is shown in Fig. 1.4.

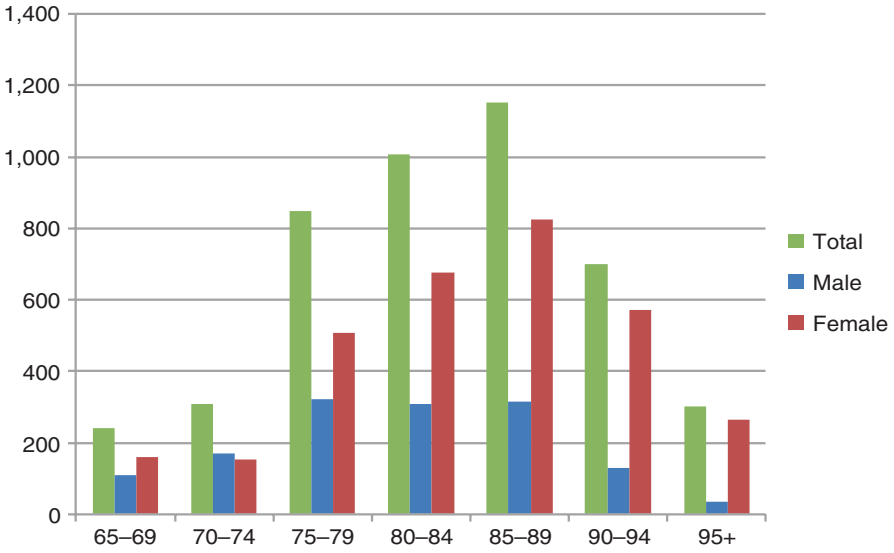

Fig. 1.5 Number of demented elderly in terms of 5-year age strata

One may wonder why the prevalence has so clearly exceeded predictions. Crucial to the answer is thought to be the increase in the mean life expectancy in Japan. As has been well known for some time, aging is the largest risk factor for dementia. The risk of dementia is known to double every 5 years after the age of 65. In 1994, the mean life expectancy for Japanese was 77 years for men and 83 for women. After 20 years, it increased to 80 and 87 years, respectively. This is thought to have led to a great increase in the prevalence of dementia.

The number of people with dementia is shown in 5-year age cohorts (Fig. 1.5). This shows that the greatest number of patients is concentrated in the 80s. Here, they account for about half of the number of people with dementia in Japan. By sex, the number of male patients does not increase after the age of 75. Among women, however, the number increases steadily from this age. Carrying this to its logical conclusion, it may not be an overstatement to say that the problem of dementia in Japan is a problem of women in their 80s. Why does such a difference between the sexes exist? The most important thing is thought to be the 7-year age gap in mean life expectancy between men, at 80 years, and women at 87 years. That is because, as mentioned above, the risk of dementia doubles every 5 years after the age of 65. A 7-year age difference is thus equal to about a threefold difference in risk.

Regarding illnesses of causing dementia, Alzheimer's disease (AD) is shown to be the most common form of dementia, followed by vascular dementia (VaD), and DLB or PDD (Fig. 1.6).

The standardized prevalence of mild cognitive impairment is estimated to be about 13% [15]. Thus, the number of elderly people thought to be in a precursor state for dementia is shown to be roughly equal to the number with dementia.

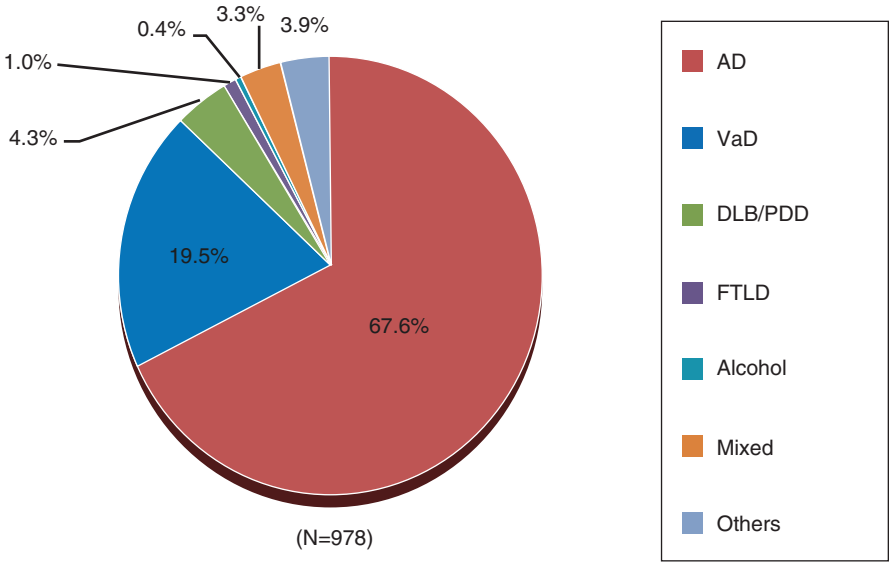

Fig. 1.6 Proportion of illnesses causing dementia

For the immediate future, both the prevalence and the total number of dementia patients are expected to rise steadily with the increase in the mean life expectancy of Japanese. It is truly coming to be that "there is no calling time" for dementia.

References

1. Ichinowatari N. Health Science Research Grants. Study on the early onset dementia. Annual report for the 8th fiscal year of Heisei, 1997 (in Japanese).
2. Asada T. Health and Labor Science Research Grants. Comprehensive Research on Aging and Health. Study on the actual condition of the individuals with early onset dementia and providing the infrastructure for them. Annual report for the 20th fiscal year of Heisei, 2009 (in Japanese).
3. Ikejima C, Ikeda M, Hashimoto M, Ogawa Y, Tanimukai S, Kashibayashi T, Miyanaga K, Yonemura K, Kakuma T, Murotani K, Asada T. Multicenter population-based study on the prevalence of early onset dementia in Japan: vascular dementia as its prominent cause. Psychiatry Clin Neurosci. 2014;68(3):216–24.
4. Mölsä PK, Marttila RJ, Rinne UK. Epidemiology of dementia in a Finnish population. Acta Neurol Scand. 1982;65:541–52.
5. Sulkava R, Wikström J, Aromaa A, et al. Prevalence of severe dementia in Finland. Neurology. 1985;35:1025–9.
6. Schoenberg BS, Anderson DW, Haerer AF. Severe dementia. Prevalence and clinical features in a biracial US population. Arch Neurol. 1985;42:740–3.
7. Kokmen E, Beard CM, Offord KP, et al. Prevalence of medically diagnosed dementia in a defined United States population: Rochester, Minnesota, January 1, 1975. Neurology. 1989;39(6):773.
8. Newens AJ, Forster DP, Kay DW, et al. Clinically diagnosed presenile dementia of the Alzheimer type in the Northern Health Region: ascertainment, prevalence, incidence and survival. Psychol Med. 1993;23:631–44.

9. Ohshiro H, Kurozawa Y, Iwai N, et al. Estimated prevalence of presenile dementia in Tottori prefecture. Nihon Koshu Eisei Zasshi. 1994;41:424–7. (in Japanese)
10. Ratnavalli E, Brayne C, Dawson K, et al. The prevalence of frontotemporal dementia. Neurology. 2002;58:1615–21.
11. Harvey RJ, Skelton-Robinson M, Rossor MN. The prevalence and causes of dementia in people under the age of 65 years. J Neurol Neurosurg Psychiatry. 2003;74(9):1206.
12. Rosso SM, Landweer EJ, Houterman M, et al. Medical and environmental risk factors for sporadic frontotemporal dementia: a retrospective case-control study. J Neurol Neurosurg Psychiatry. 2003;74:1574–6.
13. Ikejima C, Yasuno F, Mizukami K, et al. Prevalence and causes of early-onset dementia in Japan: a population-based study. Stroke. 2009;40:2709–14.
14. Shimokata H. Epidemiological statistics of dementia in Japan. Nihon Rinsho. 2004;62(Suppl 4):121–6. (in Japanese)
15. Asada T. Health and Labor Science Research Grants. Research on Dementia. Prevalence of dementia in the urban areas of Japan and development of treatment of the daily life disability associated with dementia. Report of comprehensive research for the 23rd to 24th fiscal year of Heisei, 2013 (in Japanese).

Diagnostic Criteria for Alzheimer's Disease

2

Tetsuaki Arai

Abstract

Recent advances in biomarkers and genetic studies have indicated that the pathophysiological process of Alzheimer's disease (AD) takes place many years before the onset of dementia. Based on these findings, the diagnostic criteria for AD established in 1984 have recently been updated by the National Institute on Aging/Alzheimer's Association (NIA-AA) incorporating biomarkers into it. The expert workgroup proposed three phases of AD progression over time—AD dementia, mild cognitive impairment due to AD, and preclinical AD. The American Psychiatric Association has published the fifth edition of the *Diagnostic and Statistical Manual of Mental Disorders*, in which dementia has been renamed a major neurocognitive disorder, and a concept of mild neurocognitive disorder has been introduced. These new guidelines are expected to improve clinical diagnosis and to help establish new therapeutic intervention for AD in the future.

Keywords

Biomarker • Tau • Amyloid • Imaging

T. Arai, MD, PhD
Department of Neuropsychiatry, Division of Clinical Medicine, Faculty of Medicine, University of Tsukuba, 1-1-1 Tennoudai, Tsukuba, Ibaraki 305-8575, Japan
e-mail: 4632tetsu@md.tsukuba.ac.jp

H. Matsuda et al. (eds.), *Neuroimaging Diagnosis for Alzheimer's Disease and Other Dementias*, DOI 10.1007/978-4-431-55133-1_2

2.1 Introduction

The clinical diagnosis of Alzheimer's disease (AD) had traditionally been based on the criteria of the National Institute of Neurological and Communicative Disorders and Stroke–Alzheimer's Disease and Related Disorders Association (NINCDS-ADRDA) established in 1984 [1] or the fourth edition of the *Diagnostic and Statistical Manual of Mental Disorders* (DSM-IV) [2]. When applied by expert clinicians, these criteria have an 80% positive predictive value for the accurate clinical diagnosis of AD when compared with postmortem examination.

Recent advances in biomarker studies have led to a reconsideration of the time course of AD. These include decreased amyloid β protein (Aβ) and increased tau in CSF, abnormal tracer retention on amyloid PET imaging, decreased FDG uptake on PET, and atrophy on MRI, all of which take place many years prior to the onset of dementia in AD. These findings suggest that the pathophysiological process of AD begins many years before the onset of dementia. On the basis of these data, AD can be reconceptualized as a progressive disorder that advances from pathological changes in the brain with no accompanying cognitive deficits, to a state of mild cognitive impairment (MCI) with biomarker abnormalities indicative of AD, to dementia stages of AD (Fig. 2.1) [3].

Based on these advances in research findings, in 2011, the criteria of NINCDS-ADRDA have been updated by the National Institute on Aging/Alzheimer's Association (NIA-AA) in the United States [3–6]. The aim of the new guidelines was to improve clinical diagnosis and establish research priority for the future. Then, in 2013, the American Psychiatric Association published DSM-5, in which

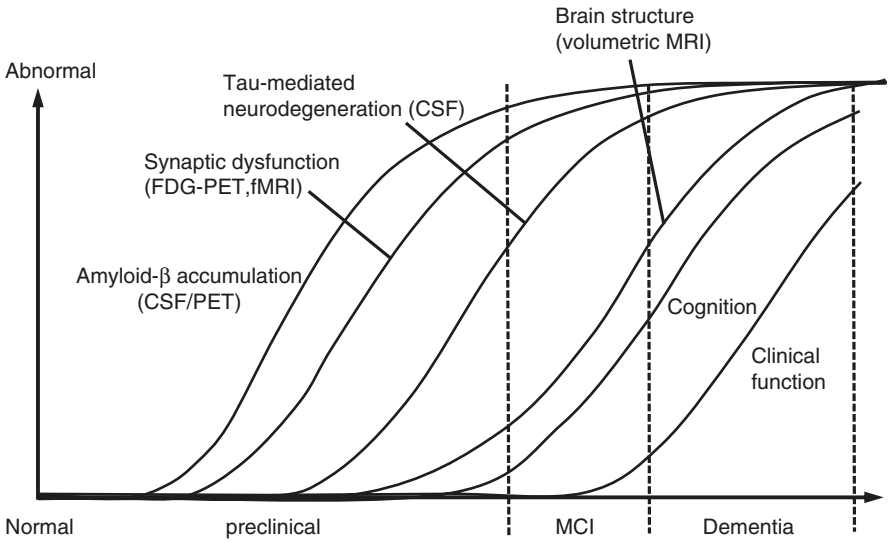

Fig. 2.1 Hypothetical model of dynamic biomarkers and clinical disease stage of AD. Modified from Sperling et al. [5]

dementia has been renamed "major neurocognitive disorder," and a concept of "mild neurocognitive disorder" has been introduced [7]. The aim of this reclassification includes reducing stigma associated with dementia and providing the diagnostic guideline into line with current clinical practice.

2.2 The National Institute on Aging/Alzheimer's Association (NIA-AA) Criteria

The NIA-AA diagnostic guidelines for AD were designed to reflect recent research which indicates that the pathophysiological process of AD takes place many years before cognitive decline or behavioral disturbance are noticeable [6]. The workgroup proposed three phases of AD progression over time—AD dementia, MCI due to AD, and preclinical AD. The core clinical criteria of the recommendations regarding AD dementia and MCI due to AD are intended to guide diagnosis in the clinical setting. However, the recommendations of preclinical AD are solely intended for research purpose and do not have any clinical implications at this time.

2.2.1 AD Dementia

The workgroup first proposed (1) criteria for all-cause dementia (Table 2.1) and then (2) criteria for AD dementia [4]. AD dementia involves memory, thinking, and behavioral symptoms that impair a person's ability to function in daily life. The expert workgroup emphasized that memory impairment may not always be the most central characteristic of a diagnosis of AD and that biomarkers may be increasingly used to help improve diagnostic certainty, especially for research purposes.

The following terminology for classifying individuals with dementia caused by AD was proposed: (1) probable AD dementia, (2) possible AD dementia, and (3)

Table 2.1 Criteria for all-cause dementia

1. Interference with the ability to function at work or at usual activities
2. A decline from previous levels of functioning and performing
3. Not explained by delirium or major psychiatric disorder
4. Cognitive impairment is detected through a combination of history-taking and cognitive assessment
5. The cognitive or behavioral impairment involves a minimum of two domains:
a. Impaired ability to acquire and remember new information
b. Impaired reasoning and handling of complex tasks and poor judgment
c. Impaired visuospatial abilities
d. Impaired language functions (speaking, reading, writing)
e. Changes in personality, behavior, or comportment

Modified from McKhann et al. [4]

Table 2.2 Probable AD dementia: core clinical criteria

1. Meets criteria for all-cause dementia
2. Insidious onset: symptoms that have a gradual onset over month to years
3. Clear-cut history of worsening of cognition by report or observation
4. Initial cognitive deficits are evident and most prominent in one of the following categories:
a. Amnestic presentation: impairment in learning and recall of recently learned information
b. Nonamnestic presentations:
• Language presentation: the most prominent deficits are in word-finding
• Visuospatial presentation: the most prominent deficits are in spatial cognition
• Executive: the most prominent deficits are impaired reasoning, judgment, and problem solving
5. Diagnosis of AD should not be applied when there is evidence of another dementing illness

Modified from McKhann et al. [4]

probable or possible AD dementia with evidence of the AD pathophysiological process. The first two were intended for use in all clinical settings. The third was intended for research purposes.

Probable AD dementia is diagnosed when the person meets all the core clinical criteria (Table 2.2). In persons who meet the core clinical criteria for probable AD dementia, documented cognitive decline increases the certainty that the condition represents an active, evolving pathologic process, but it does not specifically increase the certainty that the process is that of AD pathophysiology. Probable AD dementia with documented decline is defined as follows: evidence of progressive cognitive decline on subsequent evaluations based on information from informants and cognitive testing in the context of either formal neuropsychological evaluation or standardized mental status examinations. Probable AD dementia in a carrier of a causative AD genetic mutation is also defined as evidence of a causative genetic mutation (in APP, PSEN1, or PSEN2), which increases the certainty that the condition is caused by AD pathology.

Possible AD dementia is diagnosed when there is atypical course or etiologically mixed presentation. Atypical course has a sudden onset of cognitive impairment or demonstrates insufficient historical detail or objective cognitive documentation of progressive decline. Etiologically mixed presentation has evidence of (a) concomitant cerebrovascular disease, defined by a history of stroke temporally related to the onset or worsening of cognitive impairment, or the presence of multiple or extensive infarcts or severe white matter hyperintensity burden; (b) features of dementia with Lewy bodies other than the dementia itself; or (c) evidence for another neurological disease or a non-neurological medical comorbidity or medication use that could have a substantial effect on cognition.

Probable or possible AD dementia with evidence of the AD pathophysiological process is diagnosed when there is biomarker evidence to increase the certainty that the dementia is due to AD (Table 2.3). The biomarkers are divided into two major categories: (1) the biomarkers of Aβ accumulation, which are abnormal tracer retention on amyloid PET imaging and low CSF $A\beta_{42}$, and (2) the biomarkers of neuronal

Table 2.3 AD dementia criteria incorporating biomarkers

Diagnostic category	Aβ (PET or CSF)	Neuronal degeneration (CSF tau, FDG-PET, structural MRI)
	Unavailable or indeterminate	Positive
Probable AD dementia with evidence of AD pathophysiological process	Positive	Unavailable or indeterminate
	Positive	Positive
Possible AD dementia (atypical clinical presentation) with evidence of AD pathophysiological process	Positive	Positive
Dementia—unlikely due to AD	Negative	Negative

Modified from McKhann et al. [4]
AD Alzheimer's disease, *Aβ* amyloid-beta, *PET* positron emission tomography, *CSF* cerebrospinal fluid, *FDG* fluorodeoxyglucose, *MRI* magnetic resonance imaging

degeneration or injury, which are elevated CSF tau (both total and phosphorylated tau), decreased FDG uptake on PET in a specific topographic pattern involving temporoparietal cortex, and atrophy on structural MRI in a specific topographic pattern involving medial, basal, and lateral temporal lobe and medial and lateral parietal cortices [6]. Probable AD dementia with evidence of the AD pathophysiological process is diagnosed when the persons meet the core clinical criteria for probable AD dementia with biomarker evidence. If one of these biomarker categories is positive, the biomarker probability of AD etiology rises to intermediate, and both categories must be positive for the highest probability. The lowest probability is present if both categories are negative. Possible AD dementia with evidence of the AD pathophysiological process is the category for persons who meet clinical criteria for a non-AD dementia but who either have biomarker evidence of AD pathophysiological process or meet the neuropathological criteria for AD.

2.2.2 MCI Due to AD

The workgroup developed the following two sets of criteria for the symptomatic predementia phase of AD, which was referred to as MCI due to AD: (1) core clinical criteria (Table 2.4) that could be used by healthcare providers without access to advanced imaging techniques or CSF analysis and (2) research criteria that could be used in clinical research settings, including clinical trials [3]. The second set of criteria incorporate the use of biomarkers based on imaging and cerebrospinal fluid measures [3].

Based on these new criteria, diagnosing MCI is divided into two steps. First, criteria are presented for the clinical and cognitive syndrome of MCI (Table 2.4), and second, criteria are presented regarding the etiology of the MCI syndrome being consistent with AD (Table 2.5) [8].

Table 2.4 Core clinical criteria for MCI

1. Concern regarding a change in cognition
2. Impairment in one or more cognitive domains
(e.g., memory, executive function, attention, language, visuospatial skills)
3. Preservation of independence in functional abilities
4. Not demented

Modified from Albert et al. [3]

Table 2.5 MCI criteria incorporating biomarkers

Diagnostic category	Aβ (PET or CSF)	Neuronal degeneration (CSF tau, FDG-PET, structural MRI)
MCI due to AD—intermediate likelihood	Positive	Untested
	Untested	Positive
MCI due to AD—high likelihood	Positive	Positive
MCI—unlikely due to AD	Negative	Negative

Modified from Albert et al. [3]
MCI mild cognitive impairment, *AD* Alzheimer's disease, *Aβ* amyloid-beta peptide, *PET* positron emission tomography, *CSF* cerebrospinal fluid, *FDG* fluorodeoxyglucose, *MRI* magnetic resonance imaging

Depending on the presence and nature of the biomarker findings, MCI is finally classified into four levels:

1. MCI—core clinical criteria is diagnosed when the person meets all the core clinical criteria.
2. MCI due to AD—intermediate likelihood is diagnosed when the person meets all the core clinical criteria in addition to some biomarker evidence in one of the two biomarker categories (Aβ accumulation or neuronal degeneration).
3. MCI due to AD—high likelihood is diagnosed when the person meets all the core clinical criteria in addition to biomarker evidence in both of the categories.
4. MCI—unlikely due to AD is diagnosed if both categories are negative.

2.2.3 Preclinical AD

Preclinical AD involves the detection of changes in biomarkers that indicate the very earliest signs of AD in the brain, before any cognitive or behavioral symptoms are noticeable. The recently proposed biomarker model parallels the hypothetical pathophysiological sequence of AD and is particularly useful for tracking the preclinical stage of AD (Fig. 2.1) [5].

Based on this model, the workgroup proposed a three-stage framework for preclinical AD:

Stage 1—when there is biomarker evidence of Aβ accumulation with elevated tracer retention on PET amyloid imaging and/or low $A\beta_{42}$ in CSF, but no biomarker evidence of neurodegeneration or no cognitive and/or behavioral symptomatology.

Stage 2—when there is biomarker evidence of Aβ accumulation in the brain and one or more markers of neurodegeneration, but no cognitive or behavioral symptoms. The markers of neurodegeneration are (1) elevated CSF tau or phospho-tau, (2) hypometabolism in an AD-like pattern on FDG-PET, and (3) cortical thinning in specific anatomic distribution on volumetric MRI.

Stage 3—when there is biomarker evidence of both Aβ accumulation and neurodegeneration in the brain and evidence of subtle cognitive decline. The person in this stage may show evidence of decline from their own baseline, even if they still perform within the normal range on standard cognitive measures.

2.3 Diagnostic and Statistical Manual of Mental Disorders, Fifth Edition (DSM-5) Criteria

Although the NIA-AA diagnostic guidelines have a primary focus on future research directions, DSM-5 focuses mainly on clinical diagnosis. In DSM-5, the two terms are newly introduced: major neurocognitive disorder (NCD) as an alternative term for dementia and mild NCD which is equivalent to MCI [7]. DSM-5 provides diagnostic criteria for both major NCD and mild NCD, followed by diagnostic criteria for the different causes of NCD.

To diagnose NCDs, evidence of significant cognitive decline from a previous level of performance in one or more cognitive domain (complex attention, executive function, learning and memory, language, perceptual motor, or social cognition) is needed. The cognitive decline should interfere with independence in everyday activities. The cognitive deficits must not be due to delirium or another mental disorder.

To diagnose NCDs due to AD, the criteria should be met for major or mild NCD with insidious onset and gradual progression of impairment in one or more cognitive domains (for major NCD, at least two domains must be impaired). NCDs due to AD can be defined as either probable or possible (Table 2.6).

Table 2.6 Major or mild neurocognitive disorder due to AD

1. Meets criteria for major or mild neurocognitive disorder (NCD)
2. Insidious onset and gradual progression in one or more cognitive domains
3. For major NCD:
Probable AD is diagnosed if either of the following is present; otherwise, possible AD is diagnosed
1. Evidence of a causative AD genetic mutation
2. All three of the following are present:
a. Decline in memory and learning and at least one other cognitive domain
b. Steadily progressive, gradual decline in cognition, without extended plateaus
c. No evidence of mixed etiology
4. For mild NCD:
Probable AD is diagnosed if there is evidence of a causative AD genetic mutation
Possible AD is diagnosed if there is no evidence of a causative AD genetic mutation, and all three of the following are present:
a. Decline in memory and learning
b. Steadily progressive, gradual decline in cognition, without extended plateaus
c. No evidence of mixed etiology
5. The disturbance is not better explained by cerebrovascular disease, another neurodegenerative disease, the effects of substance, or another mental, neurological, or systemic disorder

Modified from American Psychiatric Association [7]

Conclusion

The new criteria can provide a strategy to the clinician to diagnose AD dementia and MCI due to AD with more clarity, although most biomarkers are only used in research studies at this time. Advancing research on biomarkers, neuropsychological assessments, and genetic studies will provide new information with which to revise the criteria and enhance their utility. These approaches will lead to establish new therapeutic intervention for AD in the future.

References

1. McKhann G, Drachman D, Folstein M, Katzman R, Price D, Stadlan EM. Clinical diagnosis of Alzheimer's disease: report of the NINCDS-ADRDA Work Group under the auspices of Department of Health and Human Services Task Force on Alzheimer's Disease. Neurology. 1984;34(7):939–44.
2. America Psychiatric Association. Diagnostic and statistical manual of mental disorders (IV-TR), 4th ed.—text revised. Washington, DC: American Psychiatric Publishing; 2000.
3. Albert MS, DeKosky ST, Dickson D, Dubois B, Feldman HH, Fox NC, Gamst A, Holtzman DM, Jagust WJ, Petersen RC, Snyder PJ, Carrillo MC, Thies B, Phelps CH. The diagnosis of mild cognitive impairment due to Alzheimer's disease: recommendations from the National Institute on Aging-Alzheimer's Association workgroups on diagnostic guidelines for Alzheimer's disease. Alzheimers Dement. 2011;7(3):270–9. doi:10.1016/j.jalz.2011.03.008.

4. McKhann GM, Knopman DS, Chertkow H, Hyman BT, Jack CR Jr, Kawas CH, Klunk WE, Koroshetz WJ, Manly JJ, Mayeux R, Mohs RC, Morris JC, Rossor MN, Scheltens P, Carrillo MC, Thies B, Weintraub S, Phelps CH. The diagnosis of dementia due to Alzheimer's disease: recommendations from the National Institute on Aging-Alzheimer's Association workgroups on diagnostic guidelines for Alzheimer's disease. Alzheimers Dement. 2011;7(3):263–9. doi:10.1016/j.jalz.2011.03.005.
5. Sperling RA, Aisen PS, Beckett LA, Bennett DA, Craft S, Fagan AM, Iwatsubo T, Jack CR Jr, Kaye J, Montine TJ, Park DC, Reiman EM, Rowe CC, Siemers E, Stern Y, Yaffe K, Carrillo MC, Thies B, Morrison-Bogorad M, Wagster MV, Phelps CH. Toward defining the preclinical stages of Alzheimer's disease: recommendations from the National Institute on Aging-Alzheimer's Association workgroups on diagnostic guidelines for Alzheimer's disease. Alzheimers Dement. 2011;7(3):280–92. doi:10.1016/j.jalz.2011.03.003.
6. Jack CR Jr, Albert MS, Knopman DS, McKhann GM, Sperling RA, Carrillo MC, Thies B, Phelps CH. Introduction to the recommendations from the National Institute on Aging-Alzheimer's Association workgroups on diagnostic guidelines for Alzheimer's disease. Alzheimers Dement. 2011;7(3):257–62. doi:10.1016/j.jalz.2011.03.004.
7. America Psychiatric Association. Diagnostic and statistical manual of mental disorders. 5th ed. Washington, DC: American Psychiatric Publishing; 2013.
8. Mendiratta P, Wei JY. Diagnosing Alzheimer's disease: update for the primary care clinician. J Ark Med Soc. 2014;110(8):160–3.

Structural Neuroimaging in Alzheimer's Disease

3

Hiroshi Matsuda and Etsuko Imabayashi

Abstract

MRI-based evaluation of brain atrophy is regarded as a valid method to assess the disease state and progression of Alzheimer's disease (AD). As an auxiliary measure for visual inspection, manual volumetry has been historically performed for the detection of hippocampal atrophy, which is one of the core biomarkers in AD. Recently freely available volumetric software such as FreeSurfer has made it possible to quantify gray matter in the human brain in a more automated fashion. However these tools cannot be used routinely, since they are time-consuming, requiring more than several hours. At present, voxel-based morphometry (VBM) is easily applicable to the routine clinical procedure with a much shorter execution time of several minutes. The importance of the VBM approach is that it is not biased to one particular structure and facilitates an even-handed and comprehensive assessment of anatomical differences throughout the brain. Stand-alone VBM software running on Windows, voxel-based specific regional analysis system for AD (VSRAD), has been widely used in the clinical practice of AD diagnosis in Japan. A VBM technique may be also feasible using X-ray CT data with more homogeneity and less distortion than MRI.

Keywords

MRI • X-ray CT • Voxel-based morphometry • VSRAD • Alzheimer's disease

H. Matsuda (✉) • E. Imabayashi
Integrative Brain Imaging Center, National Center of Neurology and Psychiatry,
4-1-1 Ogawahigashi-cho, Kodaira, Tokyo 187-8551, Japan
e-mail: matsudah@ncnp.go.jp

H. Matsuda et al. (eds.), *Neuroimaging Diagnosis for Alzheimer's Disease and Other Dementias*, DOI 10.1007/978-4-431-55133-1_3

3.1 Introduction

Studies of brain morphometry using magnetic resonance imaging (MRI) have been carried out by many researchers as the resolution of an anatomical scan of a whole brain increases with shorter acquisition time. MRI-based evaluation of atrophy is regarded as a valid method to assess the disease state and progression in Alzheimer's disease (AD) [1]. However, differences in the shape and neuroanatomical configuration of individual brains may cause overlooking of structural alterations by visual inspection. Moreover visual inspection can hardly evaluate slight cross-sectional and longitudinal changes of atrophy in AD. To overcome these drawbacks of visual inspection, manual volumetry has been historically performed for the detection of hippocampal atrophy, which is one of the core biomarkers in the revised National Institute on Aging-Alzheimer's Association diagnostic criteria for AD [2]. The hippocampal atrophy rate is currently being used as a secondary outcome parameter in a number of clinical trials with candidate disease modifiers. Although manual outlining by an expert human rater is a validated procedure used to estimate hippocampal atrophy, it might give rise to undesired variations in volumetric measures [3]. To minimize these variations by human raters, an international effort to harmonize existing protocols for manual volumetry of hippocampus has been recently made [4]. Nevertheless manual volumetry is still time-consuming, precluding its becoming a routine procedure for clinical practice. On the other hand, over the last decade, surface-based morphometry tools have made it possible to quantify gray matter in the human brain in a more automated fashion. Software packages such as FreeSurfer [5] (http://surfer.nmr.mgh.harvard.edu/) provide measurements of cortical and subcortical gray matter features based on MRI data. This surface-based morphometry can measure not only volume but also cortical thickness. Using this technique, we recently revealed that poor episodic memory and depressive state in patients with mild cognitive impairment were associated with thinner cortices in the left entorhinal region and in the anterior medial temporal lobe and gyrus adjacent to the amygdala, respectively [6]. Moreover a recent advance in MRI analysis, Automatic Segmentation Hippocampal Subfields (ASHS) [7] (https://sites.google.com/site/hipposubfields/), has made it possible to automatically measure hippocampal subfields and adjacent cortical subregions (Fig. 3.1). However these software tools have not become routinely used either, since the execution time of the volumetric workflow required for a single MRI analysis ranges from 10 to 30 h. At present voxel-based morphometry (VBM) is easily applicable to the routine clinical procedure for AD diagnosis, although the VBM does not provide absolute volume measures but only statistical indices. The importance of the VBM approach [8] is that it is not biased to one particular structure and gives an even-handed and comprehensive assessment of anatomical differences throughout the brain [9].

This chapter describes common VBM techniques using MRI incorporated in statistical parametric mapping (SPM) software (http://www.fil.ion.ucl.ac.uk/spm/) running on Matlab platform and its application to normal aging and AD. Then a new VBM technique using X-ray computed tomography (CT) is proposed as a substitute for MRI. Finally newly developed stand-alone VBM software running on Windows is described in detail as an adjunct to the clinical assessment of AD.

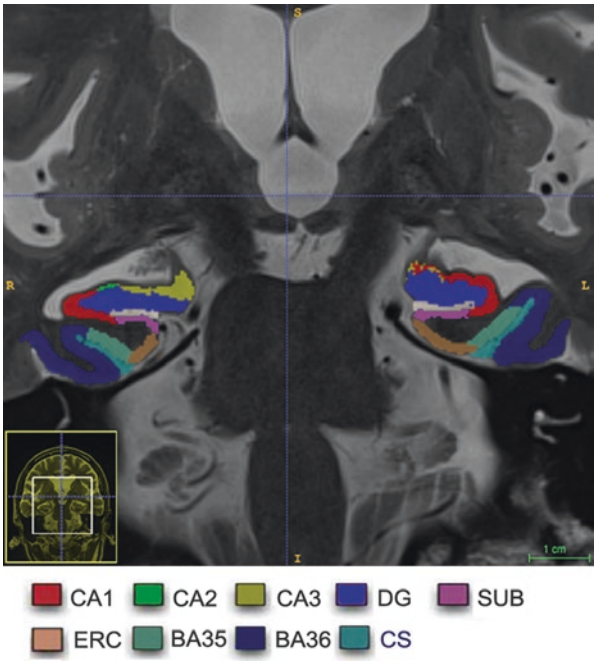

Fig. 3.1 Subfield segmentation from high-resolution T2-weighted image. Automatic volumetry is possible in hippocampal subfields and adjacent cortical subregions. *CA* cornu ammonis, *DG* dentate gyrus, *SUB* subiculum, *ERC* entorhinal cortex, *BA*35/36 Brodmann area 35/36 (which together form the perirenal cortex), *CS* collateral sulcus

3.2 VBM

3.2.1 VBM Using MRI

MRI data for VBM are acquired as a three-dimensional volumetric T1-weighted image, which has a thin thickness of 1–1.5 mm without interslice gap. The image matrix is usually 256 × 256. VBM of MRI data comprises segmentation into gray matter, white matter, and cerebrospinal fluid (CSF) partitions, anatomical standardization of all the images to the same stereotactic space using linear affine transformation, and further nonlinear warping, smoothing, and finally a statistical analysis. The output from the method is a statistical parametric map.

3.2.1.1 Optimized VBM

This method has been developed to remove areas of missegmented nongray matter voxels by the introduction of additional preprocessing steps to exclude nonbrain voxels prior to anatomical standardization and subsequent segmentation [10, 11]. Initial segmentation involves segmentation of the original structural MR images in native space into gray and white matter images, followed by a series of fully automated morphological operations to remove unconnected nonbrain voxels in skull and dural venous sinus from the segmented images. The resulting images are extracted gray and white matter partitions in native space. The extracted segmented gray/white matter images are standardized to the gray/white matter templates, thereby preventing

any contribution of nonbrain voxels and affording optimal anatomical standardization of gray/white matter. To facilitate an optimal segmentation, the optimized standardization parameters are reapplied to the original, whole-brain structural images in native space. The optimally standardized whole-brain structural images in stereotactic space are then segmented into gray and white matter and CSF partitions and subject to a second extraction of standardized segmented gray/white matter images. The brain extraction step is repeated at this stage because some nonbrain voxels from scalp, skull, or venous sinuses in the optimally normalized whole-brain images can still remain outside the brain margins on segmented gray/white matter images.

As a result of nonlinear spatial normalization based on discrete cosine transforms, the volumes of certain brain regions may increase, whereas others may shrink. In order to preserve the volume of a particular tissue within a voxel, a further processing step is incorporated. This involves multiplying (or modulating) voxel values in the segmented images by the Jacobian determinants derived from the anatomical standardization step. In effect, analyses of modulated and unmodulated data try to identify regional differences in the absolute amount (volume) of gray matter, whereas analysis of unmodulated data tests for and in the concentration of gray matter, respectively. Finally, each optimally standardized, segmented, modulated image is smoothed by convolving with an isotropic Gaussian kernel with 12-mm full width at half maximum (FWHM). The smoothing step helps to compensate for the inexact nature of the anatomical standardization. Moreover it has the effect of more normally distributing the data, increasing the validity of parametric statistical tests.

3.2.1.2 VBM Using SPM8 Plus Diffeomorphic Anatomical Registration Using Exponentiated Lie Algebra (DARTEL)

DARTEL incorporated in SPM8 is an implemented algorithm for diffeomorphic image registration [12]. It has been formulated to include an option for estimating inverse consistent deformations. This nonlinear registration is considered a local optimization problem, which is solved using a Levenberg–Marquardt strategy. A constant Eulerian velocity framework is used, which allows a rapid scaling and squaring method to be used in the computations. This technique improves intersubject registration. VBM8 toolbox (http://dbm.neuro.uni-jena.de/vbm8/) is available for VBM using SPM8 plus DARTEL for both cross-sectional and longitudinal studies.

In the SPM8 plus DARTEL procedure, T1-weighted images were classified into gray matter, white matter, and CSF using the segmentation routine implemented in SPM8, which gives both the native space versions and DARTEL imported versions of the tissues. SPM8 and VBM8 toolbox provides better segmentation accuracy and reliability than FMRIB's Software Library and FreeSurfer software programs [13]. The DARTEL imported versions of gray and white matter were used to generate the flow fields (which encode the shapes) and a series of template images by running "DARTEL (create templates)" routine. During this step, DARTEL increases the accuracy of intersubject alignment by modeling the shape of each brain using millions of parameters. DARTEL works by aligning gray matter among the images while simultaneously aligning white matter. This is achieved by generating increasingly crisp average

template data, to which the data are iteratively aligned. The flow fields and final template image created in the previous step are used to generate smoothed (8-mm FWHM), modulated, spatially normalized, and Jacobian scaled gray and white matter images resliced to isotropic voxel size in Montreal Neurological Institute space. DARTEL provides better registration accuracy than other widely used nonlinear deformation algorithms including optimized VBM [14].

3.2.1.3 VBM in Normal Aging

Studying the distribution and time course of alterations that occur in the normal brain with aging is important for understanding the mechanisms underlying these changes and for better characterization of neurological disorders whose risk increases with advancing age. The advent of VBM techniques of MRI structural data has facilitated a sensitive detection of regional patterns of gray matter and white matter volume changes. Most studies have employed a cross-sectional design in which correlations of volume and age at specific time points are used to make inferences about how the aging process affects the brain structure over time. However cross-sectional studies inevitably have some degree of overlap of regional volume changes between normal aging and AD [15]. Large longitudinal VBM studies involving the acquisition of serial MRI measurements over time are desirable in the same subject samples [16].

Numerous VBM investigations have been conducted on gray matter volume changes with advancing age (Fig. 3.2). Most cortical regions prominently in the frontal and insular areas have been reported to show a linear negative association between volume and age [10, 17–24]. In contrast, many reports have found preservation of gray matter volume in specific structures such as the amygdala, hippocampus, and thalamus [10, 18, 20, 23, 24]. Relative preservation of these subcortical limbic or paralimbic regions is consistent with the functional importance of the thalamo-limbic circuits in sensory integration, arousal, emotion, and memory. This preservation in areas with early maturation may lend credence to the contention that later-maturing cortical regions are more vulnerable to age-related morphologic changes. These age-related features may be already present during earlier stages of adulthood. During non-elderly life prefrontal areas showed linear volume reduction with advancing age, while the medial temporal region showed volume preservation [24]. Cortical gray matter volume showed an age-related reduction even during adolescence [25].

Throughout adulthood, white matter volumes also showed a linear negative association with advancing age in the anterior thalamic radiation, internal capsule, cerebral peduncle, cerebellum, and external capsule [26] (Fig. 3.2). In contrast, nonlinear relationships between white matter volume and age were found in the superior longitudinal fascicle and superior corona radiata. This nonlinear inverted U-shaped relationship with age, slightly increasing during adulthood, is consistent with the notion of an ongoing maturation of the white matter beyond adolescence, reaching its peak in the fourth decade.

In a longitudinal study of an interval of 2.5 years during adolescence, a significant increase in white matter was found in the frontal white matter bilaterally connected via the body of the corpus callosum [25]. In this context, it must be remembered that

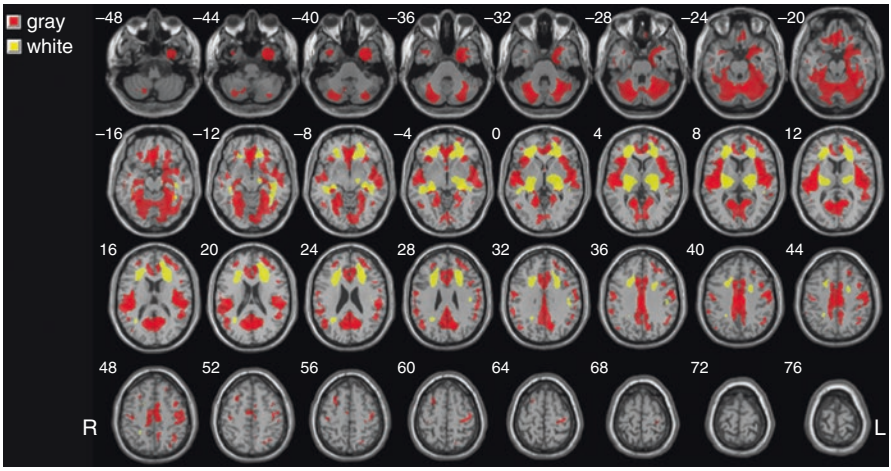

Fig. 3.2 Age-related atrophy in gray and white matter in healthy controls. VBM analysis for 93 healthy volunteers aged from 38 to 85 years showed significant negative correlation of gray and white matter volume with advancing age most prominently in insula and frontal cortex (*red*) and thalamic radiation and deep frontal white matter (*yellow*), respectively

dehydration may induce a significant widespread loss of white matter volume in the temporoparietal areas [27]. Consequently, VBM studies investigating white matter changes should consider controlling subjects' hydration state to avoid the potential confounder of differences in hydration.

As mentioned before, the morphology of cortical gray matter is assessed using not only VBM but also cortical thickness measures. How gray matter changes identified using voxel-based cortical thickness measures compare with local gray matter volume changes identified using VBM was investigated [28]. VBM and voxel-based cortical thickness measures yield overall consistent results when investigating healthy aging, but voxel-based cortical thickness provides a more sensitive measure of the age-associated decline in gray matter compared with VBM. Voxel-based cortical thickness specifically measures cortical thickness, while VBM provides a mixed measure of gray matter including cortical surface area or cortical folding as well as cortical thickness.

3.2.1.4 VBM in AD

Structural MRI measurements of brain atrophy are promising biomarkers for tracking disease progression in patients with AD. Progression of atrophy matches the stereotypical pattern of an increase in neurofibrillary tangles described by the Braak staging scheme [29]. Six stages are reported in the development of neurofibrillary tangles. Stages I and II involve the transentorhinal region which is situated along the lateral border of the entorhinal cortex and mediates between the entorhinal allocortex and temporal neocortex. The entorhinal region is located between the hippocampus and transentorhinal region, spreading over both the ambient gyrus and anterior portions of the parahippocampal gyrus. The brain change remains below the

threshold associated with clinical symptoms. Stages III and IV show severe involvement of both the entorhinal and transentorhinal regions accompanied by mild changes in the hippocampus and the virtual absence of changes in the neocortical regions. The clinical assessment of many individuals at these stages notes an impairment of cognitive functions. Stages V and VI show involvement of the neocortical association areas. These stages correspond to the conventionally used criteria for neuropathologic confirmation of the clinical diagnosis of AD. Many researchers have demonstrated progression of atrophy in AD corresponding to these Braak stages using VBM [30–40]. In the Alzheimer's Disease Neuroimaging Initiative (ADNI) study [41], VBM showed strong associations between composite scores of memory generated from ADNI's neuropsychological battery and gray matter atrophy in the medial and lateral temporal lobes and between composite scores of executive functions and gray matter atrophy in the parietal and temporal lobes.

Antemortem VBM studies [42] in demented patients with AD pathology revealed three subtypes based on the distribution of neurofibrillary tangles: typical AD, hippocampal-sparing AD, and limbic-predominant AD. Compared with typical AD, hippocampal-sparing AD has more neurofibrillary tangles and atrophy in the cortex and fewer in the hippocampus, with the opposite pattern seen in limbic-predominant AD. Age at onset differed between the subtypes, with the youngest ages recorded in the group with hippocampal-sparing AD and oldest in the group with limbic-predominant AD. This difference well explains why patients with early-onset AD have atypical clinical syndromes associated with widespread involvement of the association cortex. Topographical differences in gray matter involvement between early- and late-onset AD have also been reported by several investigators [43–45].

White matter changes have been reported to be less marked than gray matter ones in AD. A meta-analysis of VBM studies of white matter volume alterations in AD revealed significant volume reductions in the left parahippocampal gyrus extending to the temporal white matter, the right temporal white matter extending to the parahippocampal gyrus, and posterior corpus callosum [46]. These white matter volume reductions are close to the structures of memory formation including the hippocampus, amygdala, and entorhinal cortex. The mechanism underlying white matter atrophy in AD remains unclear. According to one argument, gray matter degeneration results in white matter atrophy through demyelination because these regions contain efferent connections of both the hippocampus and amygdala. Another argument states that a white matter deficit contributes to the development of cortical pathology in AD. White matter damage in AD results in cortico-cortical and/or cortico-subcortical disconnection of cognitive networks and thus contributes to cognitive impairment in AD patients.

3.2.2 VBM Using X-Ray CT

Basically, in diagnostic strategies for dementias, X-ray CT is used for screening major structural brain changes resulting from hemorrhage, tumor, edema, or other organic diseases. Nowadays, MRI is used mainly for this purpose, though

X-ray CT is still more widely available and has some advantages over MRI in economy, time, and spatial resolution. Brain X-ray CT images are more homogeneous and show less distortion than MR images, even though they are scanned with different machines or protocols. Furthermore, recently, X-ray CT data are available from a routine study obtained with hybrid machines: single photon emission computed tomography (SPECT)/CT or positron emission tomography (PET)/CT.

X-ray CT was developed by an English electrical engineer Godfrey Hounsfield in 1967. His name is immortalized in the Hounsfield unit (HU), the definition of the scale for measurement of radiodensity. The degree of HU of air and water is defined as −1000 and 0 HU, respectively, and the proportional scaling is applied to X-ray attenuation. Though the tissue differentiation ability in X-ray CT is inferior to that of MRI, it is 2–4 HU, representing a more than 10% difference between gray and white matter [47]. This difference is possibly used to segment gray and white matter in brain X-ray CT images and enables VBM.

3.2.2.1 Scan Parameter

For X-ray CT data acquisition, from the radiation protection point of view, the radiation dose should be kept as low as reasonably achievable. The usual brain X-ray CT dose used in clinical radiology is sufficient for segmentation, though the low-dose X-ray CT used for PET/CT or SPECT/CT is not. Example parameters are as follows: in the helical scanning mode, 1.0-sec gantry rotation time, 130 kV, 150–240 mAsec, 0.5:1 beam pitch, 3-mm table feed per gantry rotation, and 6 × 2 mm detector configuration. The images were reconstructed at 3-mm thickness with filtered back projection, a display field of view of 25 cm, and a reconstruction matrix size of 512 × 512. Image quality and thin slice thickness are important. Finally image voxel size is adjusted to approximately 2 mm for segmentation. Accordingly, though the x- and y-axis resolution is adequate, z-axis should be interleaved. Examples of images suitable and unsuitable for segmentation are shown in Fig. 3.3.

3.2.2.2 Image Preprocessing and Segmentation

Before using the segmentation function in SPM12, Image J (http://rsb.info.nih.gov/ij) was used to preprocess the X-ray CT images. This software was used to trim the edges of the head and to rescale the voxel sizes equivalent to the tissue probability maps in SPM12, approximately 2 × 2 × 2 mm. Extraction of gray and white matter was performed using the segmentation module of SPM12. “Extremely heavy regularization” was selected for the bias regularization item, “no correction” was chosen for bias FWHM, “nonparametric” was selected for the number of Gaussians for every tissue probability map, and a shorter sampling distance of “2” was set for the sampling distance. Figure 3.4 is a sample image of the result from segmentation applied to a CT image as compared with MRI. Segmented gray matter images from X-ray CT were anatomically standardized and then smoothed with isotropic

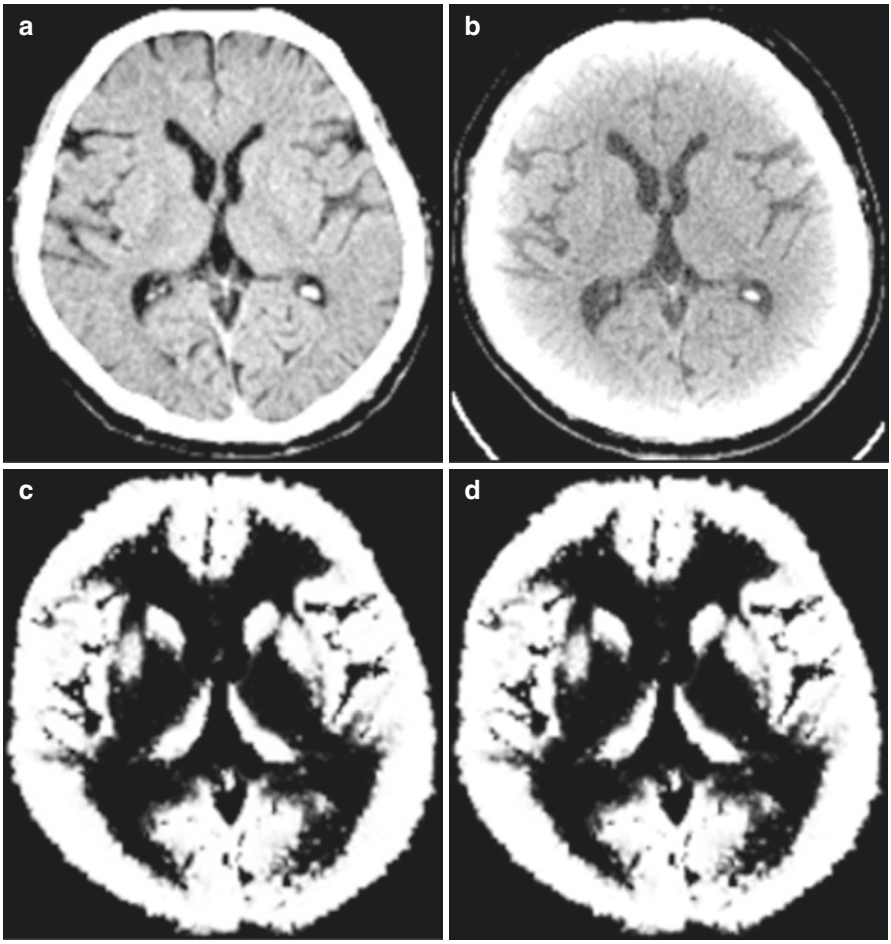

Fig. 3.3 X-ray CT images which are suitable (**a**) and unsuitable (**b**) for segmentation. Both images are obtained from the same subject with different parameters. Scanning parameters in image (**a**) are described as an example; in the helical scanning mode, 1.0-s gantry rotation time, 130 kV, 150–240 mAsec, 0.5:1 beam pitch, 3-mm table feed per gantry rotation, and 6 × 2 mm detector configuration. (**c**) Cortical image segmented from (**a**). (**d**) Cortical image segmented from (**b**). Image quality in (**d**) is not adequate for VBM

Gaussian kernel to use the partial volume effect to create a spectrum of gray matter intensities. The gray matter densities are equivalent to the weighted average of gray voxels located in the volume fixed by the smoothing kernel; therefore, regional intensities can be taken as being equivalent to gray matter volumes for MRI [8, 30]. Voxel-based analysis can be applied to these images.

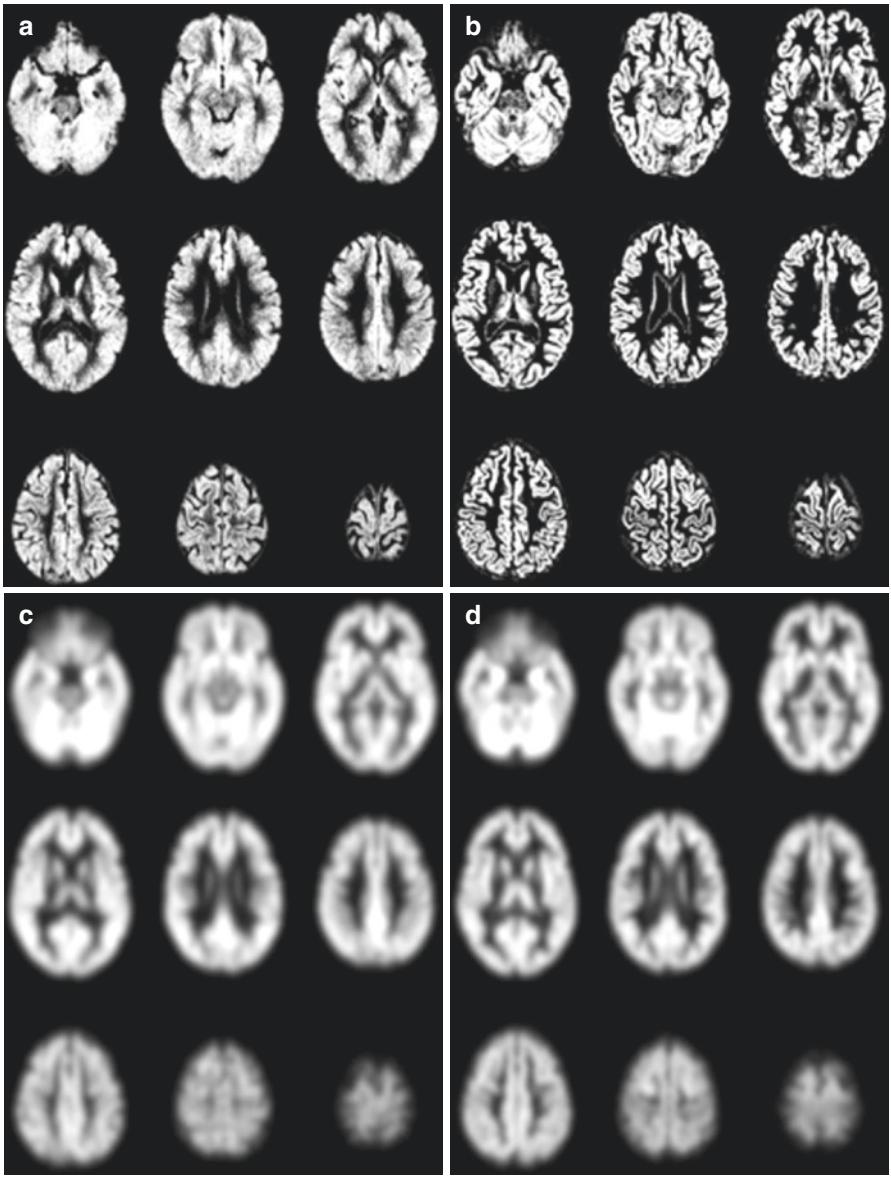

Fig. 3.4 Cortical images segmented from X-ray CT (**a**) and MRI (**b**), and smoothed images with isotropic Gaussian kernel (**c** and **d**, respectively) from the same subject. Smoothed images show fundamental similarity of distribution of the gray matter in CT and MRI

3.2.2.3 Atrophied Areas in AD Using X-Ray CT-VBM

Figure 3.5 shows the CT-based VBM result from a comparison between ^{11}C-PiB-positive AD subjects and ^{11}C-PiB-negative cognitively normal controls. With the CT-based VBM, AD subjects showed a significant decrease of gray matter volume

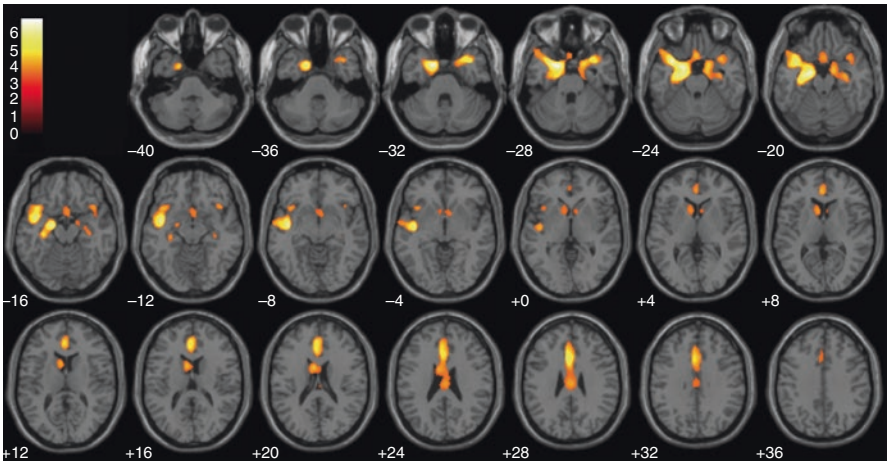

Fig. 3.5 Result from the comparison of 14 AD patients (8 females and 6 males, 66.7 ± 8.37 y.o.) and 14 age-matched cognitively normal controls (CN) (5 females and 9 males, 65.3 ± 4.73 y.o.). Group analysis of gray matter volume between the AD patients and cognitive normal controls was performed with a spatial extent threshold of 341 continuous voxels. Main effects used whole-brain analyses with threshold at voxel level of $p < 0.001$ and cluster false discovery rate <0.05 for the multiple comparison corrections

in the bilateral entorhinal cortex, hippocampus, anterior cingulate gyrus, temporopolar area, and head of the caudate, compared to a cognitively normal group. In a comparison between two VBM procedures in our study [48], though in MR-based VBM, the AD group showed a significant decrease of gray matter volume in a more concentrated small area, the bilateral hippocampus and left entorhinal cortex to the cognitively normal controls, while significant atrophy in the left entorhinal cortex at Brodmann area 28 was observed both with CT-based and MR-based VBM. Atrophy in the caudate head, anterior cingulate, and temporal pole was observed using only CT-VBM in this study. These areas are reportedly associated with AD pathology, with both amyloid deposition and neurofibrillary changes observed in them [49]. Atrophy in the temporal pole and anterior cingulate has been reported by some MRI-based VBM. Furthermore, Madsen et al. [50] showed a reduction of caudate volume in patients with mild cognitive impairment (MCI) and a further reduction in AD patients. Inhomogeneity, distortion, or some other artifact might make these findings difficult to detect in MR-based VBM.

3.2.2.4 Pursuit of the Clinical Findings

The Z-score analysis – the number of standard deviations by which a patient's voxel value differs from the normal mean value as described in the next section – is useful to analyze a single individual's data against a normal database obtained from many control subjects. Figure 3.6 shows the results of Z-score analysis comparing one ^{11}C-PiB-positive AD patient with a normal database. This normal database was constructed with gray matter extracted from 14 cognitively normal subjects' CT images. Blue color in the bilateral medial temporal regions shows a more than 2 standard

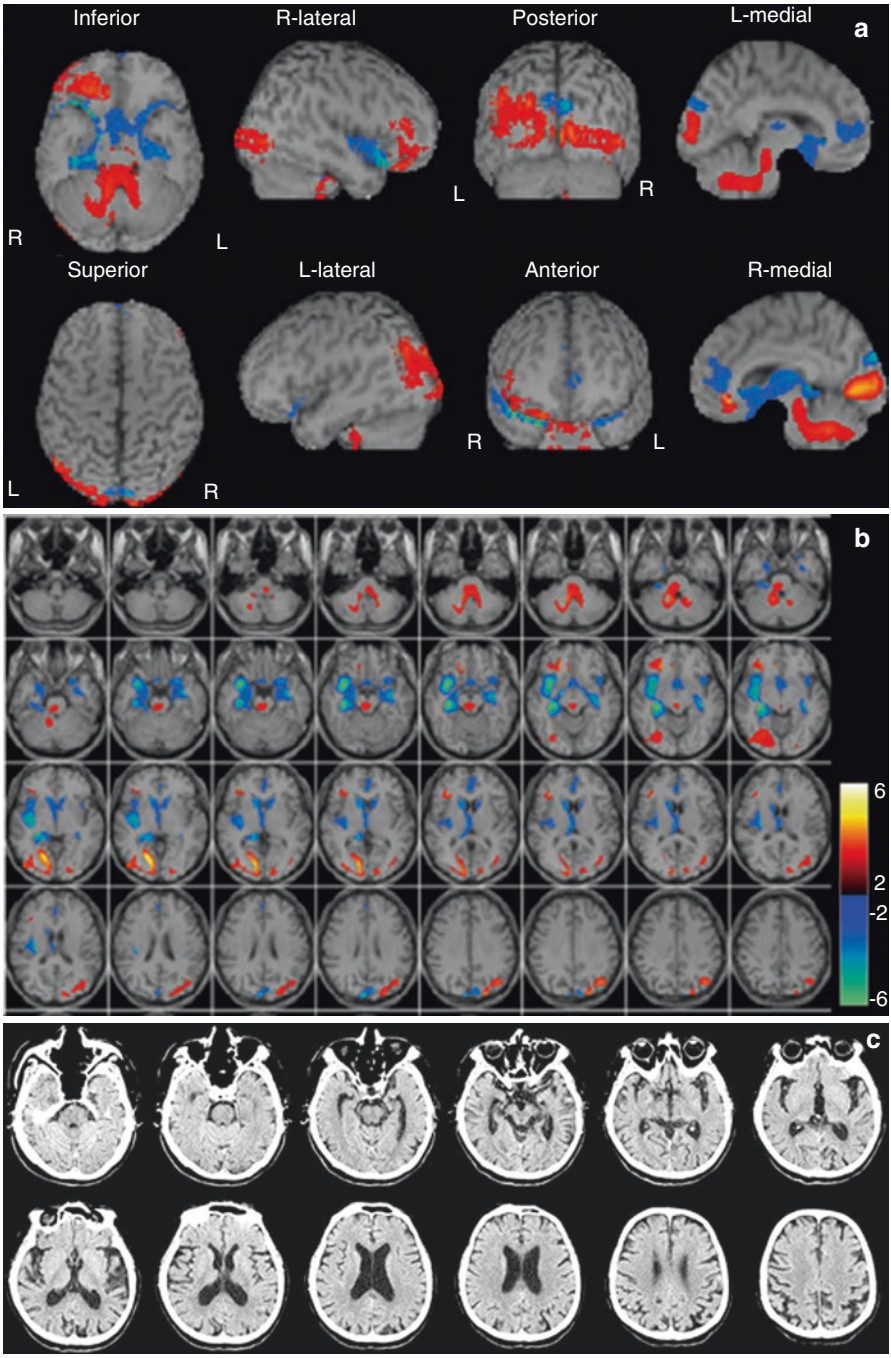

Fig. 3.6 Z-score image of one ^{11}C-PiB-positive AD patient superimposed on MRI template. (**a**) Rendering image, (**b**) transaxial images, and (**c**) original X-ray CT image. Significant atrophy more than 2SD in medial temporal area, temporal pole, and bilateral caudate head is detected

deviation reduction of the gray matter volume in this AD patient. This result shows that to some extent, it may be feasible to replace MR-based VBM with CT-based VBM to diagnose AD.

Furthermore, with this procedure, because of homogeneity and ubiquity, regardless of institution or machine, a normal database could be held in common without interinstitutional collection.

3.3 Voxel-Based Specific Regional Analysis System for Alzheimer's Disease (VSRAD)

VBM approach has been reported to show higher accuracy in discriminating AD and controls than VOI-based analysis [51]. To facilitate VBM approach in an individual subject, a stand-alone software program running on Windows for VBM analysis based on SPM8 plus DARTEL was developed to discriminate a patient from healthy controls [52] (Fig. 3.7). First, MRI data were anatomically standardized with only 12-parameter affine transformation to the SPM template so as to correct for differences in brain size. Then MR images were segmented into gray matter, white matter, and CSF images by unified tissue segmentation procedure after image intensity nonuniformity correction. These linearly transformed and segmented

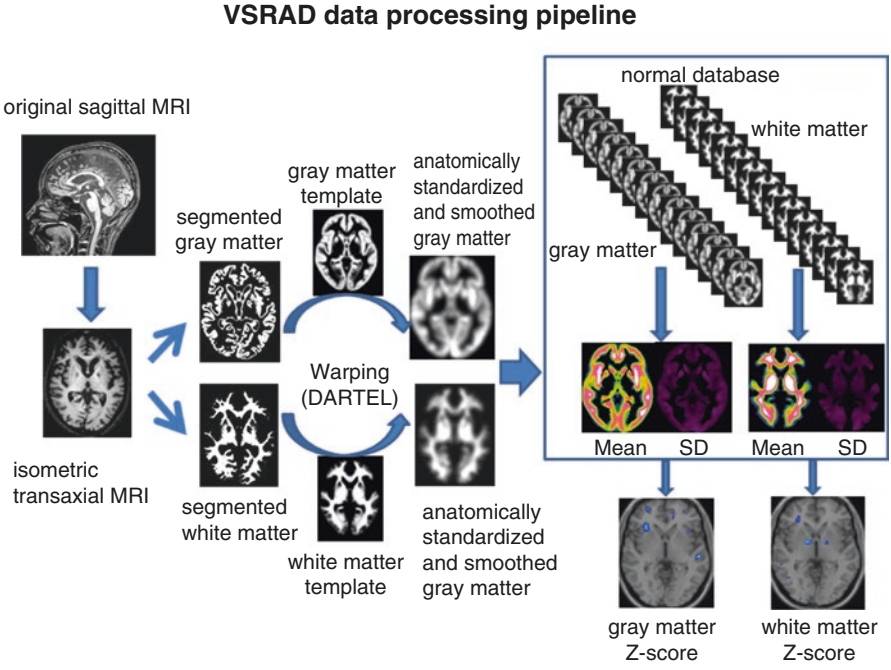

Fig. 3.7 Data processing pipeline for stand-alone VBM software, VSRAD. Comparison of patient's MRI with MRI normal database yields *color*-coded Z-score maps of both gray matter and white matter using VBM analysis based on SPM8 plus DARTEL

images were nonlinearly transformed by DARTEL procedures and then modulated to the customized template for DARTEL followed by smoothing using an 8-mm FWHM kernel. Each processed segmented image was compared to the mean and standard deviation of gray matter or white matter images of 80 healthy volunteers using voxel-by-voxel Z-score analysis with and without voxel normalization to global mean intensities (global normalization), Z-score = ([control mean]-[individual value])/(control standard deviation). These Z-score maps were displayed by overlay on tomographic sections and surface rendering of the standardized brain. Inversed warping also makes it possible to display Z-score maps on the tomographic sections of the individual brain. This program registered the target volume of interest (VOI) in medial temporal structures defined by group comparison of patients with early AD and healthy controls. This software program takes approximately 9 min for all procedures using a 64-bit personal computer with Intel® Core™ i7 CPU, 3.33 GHz, 6 gigabyte memory.

Four indicators for characterizing atrophy in the target VOI and in the whole brain were determined. The first is the severity of atrophy obtained from the averaged positive Z-score in the target VOI. The second is the extent of a region showing significant atrophy in the target VOI, that is, the percentage rate of the coordinates with a Z value exceeding the threshold value of 2 in the target VOI. The third is the extent of a region showing significant atrophy in the whole brain, that is, the percentage rate of the coordinates with a Z value exceeding the threshold value of 2 in the whole brain. These three indicators of severity and extent for the target VOI and extent for the whole brain are useful for the early diagnosis (Fig. 3.8) and

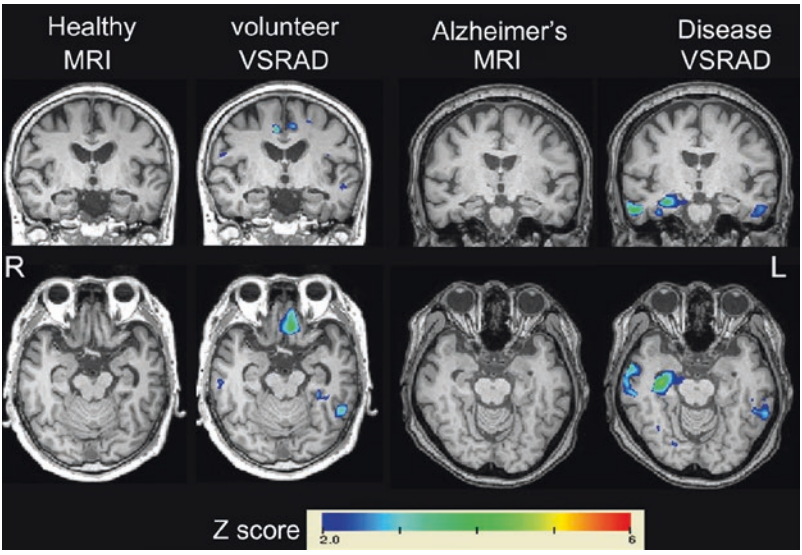

Fig. 3.8 Utility of VSRAD for differentiation between aged healthy volunteer and AD patient. Although visual inspection of MRI cannot differentiate healthy volunteer (a man aged 79 years) and AD patient (a woman aged 68 years), VSRAD can detect significant atrophy in the right medial and lateral temporal areas as displayed by a Z-score color map

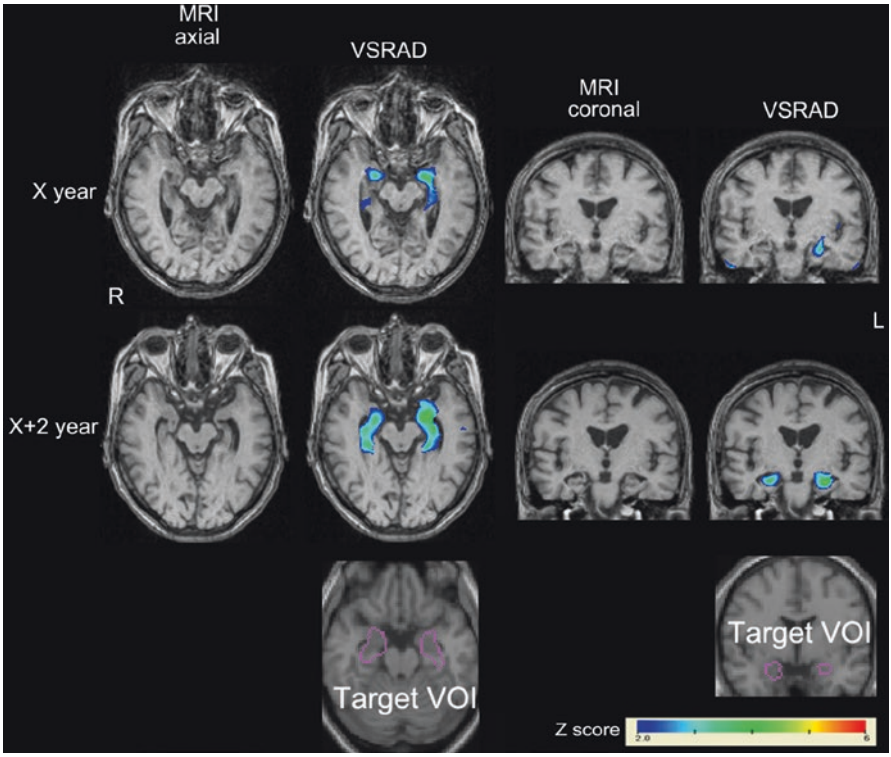

Fig. 3.9 Longitudinal VBM analysis using VSRAD in a patient with AD. VSRAD demonstrates progressive atrophy in left-side dominant gray matter atrophy in medial temporal areas during a 2-year period in a woman with AD aged 65 years at onset. MMSE score decreased from 25 to 20 during this period. The severity of atrophy in the target VOI (medial temporal areas as circumscribed by a *purple line*), the extent of a region showing significant atrophy in the target VOI, the extent of a region showing significant atrophy in the whole brain, and the ratio of the extent of a region showing significant atrophy in the target VOI to the extent of a region showing significant atrophy in the whole brain are 1.9, 44.3%, 2.5%, and 17.6 at X year and 2.8, 82.1%, 2.7%, and 34.7 at X + 2 years, respectively

longitudinal evaluation of AD (Fig. 3.9). The fourth is the ratio of the extent of a region showing significant atrophy in the target VOI to the extent of a region showing significant atrophy in the whole brain. This ratio may be useful for differentiation of AD from other neuropsychiatric diseases manifesting dementia.

Conclusion

Atrophy rates of whole-brain and medial temporal structures are sensitive markers of neurodegeneration and are increasingly being used as outcome measures in trials of potentially disease-modifying therapies in AD. Recent progress has been made on brain volumetry using MRI. Absolute volume measures are automatically possible even in hippocampal subfields. Stand-alone VBM software, VSRAD, has been applied to routine clinical procedure for AD diagnosis in

Japan. A VBM technique may be also feasible using X-ray CT data with more homogeneity and less distortion than MRI. The utility of VBM will be increased hereafter as adjuncts to clinical assessment in the diagnosis and monitoring of progression of AD.

References

1. Frisoni GB, Fox NC, Jack CR Jr, et al. The clinical use of structural MRI in Alzheimer disease. Nat Rev Neurol. 2010;6:67–77.
2. Jack CR, Barkhof F, Bernstein MA, et al. Steps to standardization and validation of hippocampal volumetry as a biomarker in clinical trials and diagnostic criterion for Alzheimer's disease. Alzheimers Dement. 2011;7:474–85.
3. Geuze E, Vermetten E, Bremner JD. MR-based in vivo hippocampal volumetrics: 1. Review of methodologies currently employed. Mol Psychiatry. 2005;10:147–59.
4. Frisoni GB, Jack CR, Bocchetta M, et al. The EADC-ADNI harmonized protocol for manual hippocampal segmentation on magnetic resonance: evidence of validity. Alzheimers Dement. 2014;11(2):111–25. doi:10.1016/j.jalz.2014.05.1756.
5. Fischl B, Salat DH, Busa E, et al. Whole brain segmentation: automated labeling of neuroanatomical structures in the human brain. Neuron. 2002;33:341–55.
6. Fujishima M, Maikusa N, Nakamura K, et al. Mild cognitive impairment, poor episodic memory, and late-life depression are associated with cerebral cortical thinning and increased white matter hyperintensities. Front Aging Neurosci. 2014;6:306.
7. Yushkevich PA, Pluta JB, Wang H, et al. Automated volumetry and regional thickness analysis of hippocampal subfields and medial temporal cortical structures in mild cognitive impairment. Hum Brain Mapp. 2015;36:258–87.
8. Ashburner J, Friston KJ. Voxel-based morphometry--the methods. NeuroImage. 2000;11:805–21.
9. Ashburner J, Friston KJ. Why voxel-based morphometry should be used. NeuroImage. 2001;14:1238–43.
10. Good CD, Johnsrude IS, Ashburner J, et al. A voxel-based morphometric study of ageing in 465 normal adult human brains. NeuroImage. 2001;14:21–36.
11. Karas GB, Burton EJ, Rombouts SA, et al. A comprehensive study of gray matter loss in patients with Alzheimer's disease using optimized voxel-based morphometry. NeuroImage. 2003;18:895–907.
12. Ashburner J. A fast diffeomorphic image registration algorithm. NeuroImage. 2007;38:95–113.
13. Eggert LD, Sommer J, Jansen A, et al. Accuracy and reliability of automated gray matter segmentation pathways on real and simulated structural magnetic resonance images of the human brain. PLoS One. 2012;7:e45081.
14. Klein A, Andersson J, Ardekani BA, et al. Evaluation of 14 nonlinear deformation algorithms applied to human brain MRI registration. NeuroImage. 2009;46:786–802.
15. Raji CA, Lopez OL, Kuller LH, et al. Age, Alzheimer disease, and brain structure. Neurology. 2009;73:1899–905.
16. Raz N, Lindenberger U, Rodrigue KM, et al. Regional brain changes in aging healthy adults: general trends, individual differences and modifiers. Cereb Cortex. 2005;15:1676–89.
17. Resnick SM, Pham DL, Kraut MA, et al. Longitudinal magnetic resonance imaging studies of older adults: a shrinking brain. J Neurosci. 2003;23:3295–301.
18. Matsuda H, Ohnishi T, Asada T, et al. Correction for partial-volume effects on brain perfusion SPECT in healthy men. J Nucl Med. 2003;44:1243–52.
19. Tisserand DJ, van Boxtel MP, Pruessner JC, et al. A voxel-based morphometric study to determine individual differences in gray matter density associated with age and cognitive change over time. Cereb Cortex. 2004;14:966–73.

20. Grieve SM, Clark CR, Williams LM, et al. Preservation of limbic and paralimbic structures in aging. Hum Brain Mapp. 2005;25:391–401.
21. Smith CD, Chebrolu H, Wekstein DR, et al. Age and gender effects on human brain anatomy: a voxel-based morphometric study in healthy elderly. Neurobiol Aging. 2007;28:1075–87.
22. Curiati PK, Tamashiro JH, Squarzoni P, et al. Brain structural variability due to aging and gender in cognitively healthy Elders: results from the Sao Paulo Ageing and Health study. AJNR Am J Neuroradiol. 2009;30:1850–6.
23. Kalpouzos G, Chételat G, Baron JC, et al. Voxel-based mapping of brain gray matter volume and glucose metabolism profiles in normal aging. Neurobiol Aging. 2009;30:112–24.
24. Terribilli D, Schaufelberger MS, Duran FL, et al. Age-related gray matter volume changes in the brain during non-elderly adulthood. Neurobiol Aging. 2011;32:354–68.
25. Giorgio A, Watkins KE, Chadwick M, et al. Longitudinal changes in grey and white matter during adolescence. NeuroImage. 2010;49:94–103.
26. Giorgio A, Santelli L, Tomassini V, et al. Age-related changes in grey and white matter structure throughout adulthood. NeuroImage. 2010;51:943–51.
27. Streitbürger DP, Möller HE, Tittgemeyer M, et al. Investigating structural brain changes of dehydration using voxel-based morphometry. PLoS One. 2012;7:e44195.
28. Hutton C, Draganski B, Ashburner J, et al. A comparison between voxel-based cortical thickness and voxel-based morphometry in normal aging. NeuroImage. 2009;48:371–80.
29. Braak H, Braak E. Staging of Alzheimer's disease-related neurofibrillary changes. Neurobiol Aging. 1995;16:271–8.
30. Ohnishi T, Matsuda H, Tabira T, et al. Changes in brain morphology in Alzheimer disease and normal aging: is Alzheimer disease an exaggerated aging process? AJNR Am J Neuroradiol. 2001;22:1680–5.
31. Matsuda H, Kitayama N, Ohnishi T, et al. Longitudinal evaluation of both morphologic and functional changes in the same individuals with Alzheimer's disease. J Nucl Med. 2002;43:304–11.
32. Chetelat G, Desgranges B, de la Sayette V, et al. Dissociating atrophy and hypometabolism impact on episodic memory in mild cognitive impairment. Brain. 2003;126:1955–67.
33. Rémy F, Mirrashed F, Campbell B, et al. Verbal episodic memory impairment in Alzheimer's disease: a combined structural and functional MRI study. NeuroImage. 2005;25:253–66.
34. Hirata Y, Matsuda H, Nemoto K, et al. Voxel-based morphometry to discriminate early Alzheimer's disease from controls. Neurosci Lett. 2005;382:269–74.
35. Di Paola M, Macaluso E, Carlesimo GA, et al. Episodic memory impairment in patients with Alzheimer's disease is correlated with entorhinal cortex atrophy. A voxel-based morphometry study. J Neurol. 2007;254:774–81.
36. Hämäläinen A, Pihlajamäki M, Tanila H, et al. Increased fMRI responses during encoding in mild cognitive impairment. Neurobiol Aging. 2007;28:1889–903.
37. Leube DT, Weis S, Freymann K, et al. Neural correlates of verbal episodic memory in patients with MCI and Alzheimer's disease--a VBM study. Int J Geriatr Psychiatry. 2008;23:1114–8.
38. Schmidt-Wilcke T, Poljansky S, Hierlmeier S, et al. Memory performance correlates with gray matter density in the ento−/perirhinal cortex and posterior hippocampus in patients with mild cognitive impairment and healthy controls--a voxel based morphometry study. NeuroImage. 2009;47:1914–20.
39. Goto M, Abe O, Miyati T, et al. Entorhinal cortex volume measured with 3T MRI is positively correlated with the Wechsler Memory Scale-Revised logical/verbal memory score for healthy subjects. Neuroradiology. 2011;53:617–22.
40. Chételat G, Villemagne VL, Pike KE, et al. Independent contribution of temporal beta-amyloid deposition to memory decline in the pre-dementia phase of Alzheimer's disease. Brain. 2011;134:798–807.
41. Nho K, Risacher SL, Crane PK, et al. Voxel and surface-based topography of memory and executive deficits in mild cognitive impairment and Alzheimer's disease. Brain Imaging Behav. 2012;6:551–67.

42. Whitwell JL, Dickson DW, Murray ME, et al. Neuroimaging correlates of pathologically defined subtypes of Alzheimer's disease: a case-control study. Lancet Neurol. 2012;11:868–77.
43. Ishii K, Kawachi T, Sasaki H, et al. Voxel-based morphometric comparison between early- and late-onset mild Alzheimer's disease and assessment of diagnostic performance of z score images. AJNR Am J Neuroradiol. 2005;26:333–40.
44. Matsunari I, Samuraki M, Chen WP, et al. Comparison of ^{18}F-FDG PET and optimized voxel-based morphometry for detection of Alzheimer's disease: aging effect on diagnostic performance. J Nucl Med. 2007;48:1961–70.
45. Frisoni GB, Pievani M, Testa C, et al. The topography of grey matter involvement in early and late onset Alzheimer's disease. Brain. 2007;130:720–30.
46. Li J, Pan P, Huang R, et al. A meta-analysis of voxel-based morphometry studies of white matter volume alterations in Alzheimer's disease. Neurosci Biobehav Rev. 2012;36:757–63.
47. Yamamura H, Kaga S, Kaneda K, et al. Head computed tomographic measurement as an early predictor of outcome in hypoxic-ischemic brain damage patients treated with hypothermia therapy. Scand J Trauma Resusc Emerg Med. 2013;21:37.
48. Imabayashi E, Matsuda H, Tabira T, et al. Comparison between brain CT and MRI for voxel-based morphometry of Alzheimer's disease. Brain Behav. 2013;3:487–93.
49. Braak H, Braak E. Neuropathological stageing of Alzheimer-related changes. Acta Neuropathol. 1991;82(4):239–59.
50. Madsen SK, Ho AJ, Hua X, et al. 3D maps localize caudate nucleus atrophy in 400 Alzheimer's disease, mild cognitive impairment, and healthy elderly subjects. Neurobiol Aging. 2010;31:1312–25.
51. Testa C, Laakso MP, Sabattoli F, et al. A comparison between the accuracy of voxel-based morphometry and hippocampal volumetry in Alzheimer's disease. J Magn Reson Imaging. 2004;19:274–82.
52. Matsuda H, Mizumura S, Nemoto K, et al. Automatic voxel-based morphometry of structural MRI by SPM8 plus diffeomorphic anatomic registration through exponentiated lie algebra improves the diagnosis of probable Alzheimer Disease. AJNR Am J Neuroradiol. 2012;33:1109–14.

MRI Diagnosis in Other Dementias

4

Aya M. Tokumaru, Yuko Saito, Shigeo Murayama, and Keita Sakurai

Abstract

The role of neuroradiologists in the diagnosis of dementia is to identify the wide range of disorders causing dementia through diagnostic imaging in patients clinically exhibiting cognitive impairments, and provide information that directly contributes to their treatment, care, and nursing to clinical workers. The diseases included in dementia are diverse and include degenerative dementia, cerebrovascular dementia, idiopathic normal pressure hydrocephalus, metabolic disorders, poisoning, encephalitis, and encephalopathy, and the diagnostic process markedly differs according to the disease. It is important to diagnose diseases that can be cured and to evaluate images independently of the clinical diagnosis. Images need to be evaluated from multiple viewpoints by taking clinical information from the patient, physicians at clinical departments, local doctors, nurses, care staff, and family as well as information obtained by multiple modalities into consideration.

One aspect of dementia is the long duration of disease. We are now focusing on how to diagnose dementia early and correctly through the application of advanced medical technologies; however, for this to succeed, efforts by all of

A.M. Tokumaru (✉) • K. Sakurai
Department of Diagnostic Radiology, Tokyo Metropolitan Geriatric Hospital and Institute of Gerontology, 35-2 Sakae-cho, Itabashi-ku, Tokyo 173-0015, Japan
e-mail: aya.tokumaru01@gmail.com

Y. Saito
Department of Pathology and Laboratory Medicine, National Center Hospital for Neurology and Psychiatry, 4-1-1 Ogawa-Cho Kodaira-City, Tokyo 187-8551, Japan

S. Murayama
Department of Neurology and Neuropathology (the Brain Bank for Aging Research), Tokyo Metropolitan Medical Center of Gerontology, Tokyo Metropolitan Geriatric Hospital and Institute of Gerontology, 35-2 Sakae-cho, Itabashi-ku, Tokyo 173-0015, Japan

H. Matsuda et al. (eds.), *Neuroimaging Diagnosis for Alzheimer's Disease and Other Dementias*, DOI 10.1007/978-4-431-55133-1_4

society for an early diagnosis are necessary rather than "making premature judgments about disorders and diagnosing them accordingly." Furthermore, diagnostic imaging is often difficult to perform when examining patients with a long clinical course or in an advanced stage due to problems unique to older people. Encounters with patients with Alzheimer's disease (AD) complicated by cerebrovascular disease (CVD) and Lewy body disease (DLB) are not rare in clinical practice.

We herein presented the imaging findings of senile tauopathy as an important disease causing dementia, and discussed topics regarding a wide variety of diseases causing dementia in which imaging findings are key for a differential diagnosis.

Keywords
Senile tauopathy • Dementia with grains (DG) • Amyloid angiopathy

4.1 Senile Tauopathy

Senile tauopathy is a group of neurodegenerative diseases that cause neuropathy due to the accumulation of tau protein in neurons and glia cells and develop into dementia [1–6]. Tau protein is a kind of microtubule-binding protein that has been classified into 3-repeat and 4-repeat tau isoforms according to the number of binding sites with microtubules. Major tauopathies are dementia with grains (DG), Senile dementia of the neurofibrillary tangle type (SD-NFT), progressive supranuclear palsy (PSP), and corticobasal degeneration (CBD/CBS), globular glial tauopathies (GGT) in which 4-repeat tau primarily accumulates, and Pick disease, in which 3-repeat tau primarily accumulates (Table 4.1).

Of the 1,212 patients (689 males and 523 females aged 31–104 years) examined by serial autopsy between August 1999 and May 2012 at the Brain Bank in the Tokyo Metropolitan Medical Center of Gerontology and Institute of Gerontology, AD was observed in 19%, DG and NFTD which are senile tauopathies were observed in 18% each, followed by DLB in the group with neurodegenerative dementia with a clinical dementia ratio (CDR) of 0.5. Furthermore, dementia with senile tauopathy in the background including that present as a complication was detected in the majority (57%) of patients (Fig. 4.1) [4, 5]. Among those with a CDR of 1 or higher, the diagnosis was AD in 35% and DLB in 19%, while senile

Table 4.1 Senile tauopathy

1. Dementia with grains: DG
2. Senile dementia of the neurofibrillary tangle type (SD-NFT)
3. Progressive supranuclear palsy: PSP
4. Corticobasal degeneration: CBS
5. Pick disease
6. Diffuse neurofibrillary tangle with calcification: DNTC
7. Globular glial tauopathies: GGT

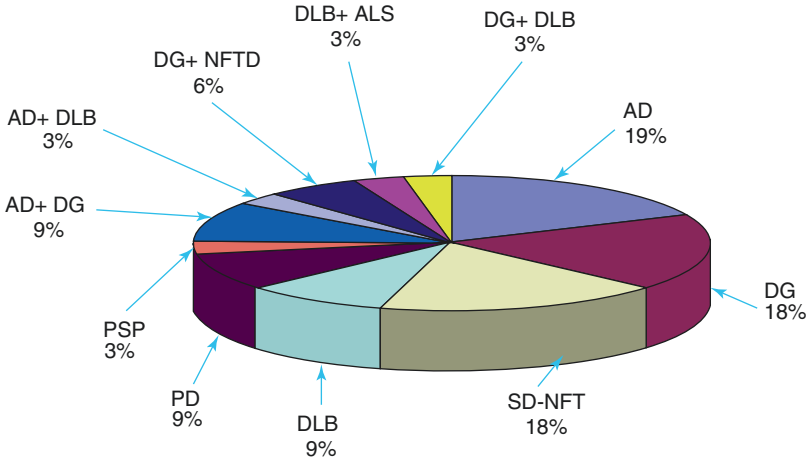

Fig. 4.1 CDR = 0.5 Background pathology of degenerative dementia. *AD* Alzheimer's disease, *DG* Dementia with grains, *SD-NFT* Senile dementia of the neurofibrillary tangle type, *DLB* dementia with Lewy body, *PD* Parkinson's disease, *PSP* Progressive supranuclear palsy, *ALS* Amyotrophic lateral sclerosis. (From [5] with permission)

tauopathy including that exhibiting complex pathological features was noted in 33%. These findings indicated that senile tauopathy is important as the background pathology of dementia in older people and needs to be considered in clinical and imaging diagnoses.

4.2 Dementia with Grains

4.2.1 Disease Concept

Dementia with grains (DG) is a late-onset dementia morphologically characterized by the presence of abundant spindle-shaped argyrophilic grains in neuronal processes and coiled bodies in oligodendrocytes proposed by Braak and Saito et al. [1–4]. It is an important disease to be considered, in addition to AD and DLB, as a causative disorder for senile dementia (Table 4.1, Fig. 4.1). Neuropathologically, the disease is characterized by the deposition of argyrophilic grains, which are granules that are stained by the Gallyas–Braak silver impregnation method. Deposits first appear in the ambient gyrus, and pathological changes gradually spread to the cortex of the frontal and temporal lobes. Neuropathological staging of the disease into I–III according to the area of pathological changes has been proposed by Saito et al., with dementia occurring in stage III [4]. Figure 4.2 shows the progression of pathological changes in DG. The affected region is close to the areas in which early pathological changes have been reported to appear in AD and, with progression of the disease, overlaps the areas affected in AD.

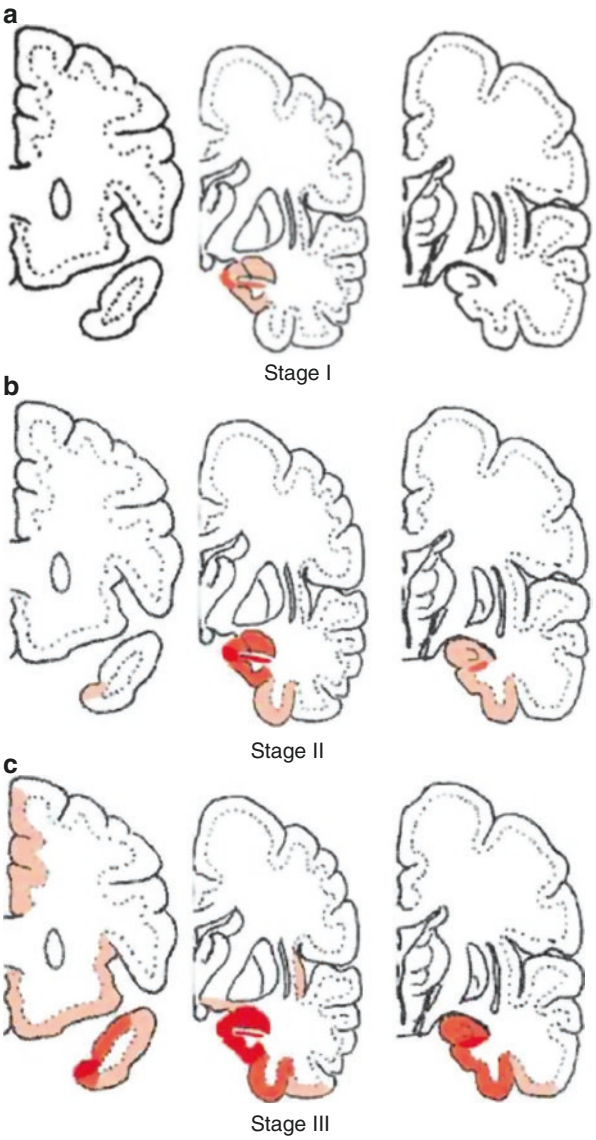

Fig. 4.2 Neuropathological staging of DG [2]. The topographical distribution of argyrophilic grains (AGs) in each grain stage. Three coronal sections through the genu of corpus callosum, the mammillary body, and the lateral geniculate body. Stage I: AGs are localized to the ambient gyrus, the anterior CA1 of hippocampus, the anterior entorhinal area, and the amygdala. Stage II: AGs are more apparent in the medial temporal pole, in the posterior subiculum, and the entorhinal and transentorhinal cortex. Stage III: AGs involve the anterior cingulate gyrus, septum, accumbens, gyri recti, insular cortex, and hypothalamus in addition to the medial temporal lobe. It is highly probable that the pathology in argyrophilic grain stage III contributed to cognitive decline. (From [2] with permission)

4.2.2 Problems with a Clinical Diagnosis

Clinical diagnostic criteria for dementia with grains (DG) have not yet been established. Therefore, DG is diagnosed as diseases with another background pathology including vascular dementia and AD in many patients. The establishment of clinical diagnostic criteria based on the background pathology is considered to lead to appropriate treatments, care, and nursing [4–7].

An analysis of the history of DG definitively diagnosed with neuropathological evidence indicates the following as characteristics of the disease: (1) slow progression, (2) symptoms suggestive of frontotemporal dementia such as personality changes, irritability, and poor personal contact, (3) forgetfulness as a frequent initial symptom, and (4) the older age of patients than those with other degenerative dementias [5–7]. The frequent complications of DG by diseases including AD, SD-NFT, and vascular dementia in older individuals also make its clinical diagnosis difficult. Therefore, although clinical diagnostic criteria for DG are difficult to formulate, their establishment by relating clinical, imaging, and pathological findings in this important disease, which was recognized due to neuropathological evidence, is an urgent requirement.

The development of radical treatments for AD such as Aβ-vaccine therapy based on the amyloid cascade hypothesis, tau targeting drug, and the development of secretase inhibitors further increases the necessity of an accurate diagnosis of mild cognitive impairment (MCI), which is attracting attention as a precursor of AD. Radical treatments for AD are not expected to be effective for DG without β-amyloid deposition, and an accurate diagnosis in the stage of MCI or even earlier is essential. The clinical symptoms of DG overlap those described in the international diagnostic criteria for AD, and difficulties are also associated with their morphological differentiation. The development of evaluation methods that integrate neuroimaging findings as objective data in addition to clinical and neuropsychiatric diagnoses is awaited.

4.2.3 MRI Findings in DG

In typical DG, MRI shows atrophy near the ambient gyrus and uncus [5, 6] (Figs. 4.2, 4.3, 4.4, and 4.5). Asymmetric atrophy is shown in many cases of DG; however, there are also some cases that the difference between right and left is not clear. By the progress of the stage of dementia, atrophic area progresses extensively toward the temporal and frontal lobe widely.

The structures of the medial temporal lobe near the parahippocampal gyrus, such as the entorhinal cortex and ambient gyrus, in which the earliest changes occur, need to be examined in MRI of the early stage of AD and DG; however, these structures are extremely small, and a visual evaluation of atrophy in such small structures is difficult. MRI has many advantages, the greatest of which are its non-invasiveness and repeatability. Since objectivity is insufficient by visual

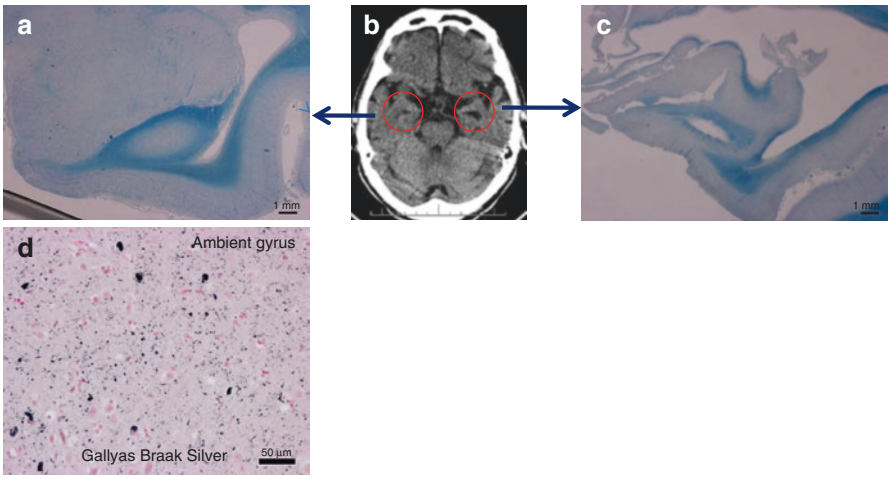

Fig. 4.3 90s male, CDR = 1 Dementia case. [5] (**a**) (right side medial temporal lobe): Microscopic specimen (KB stain) shows no obvious atrophy. (**b**) Brain CT shows dilatation of left interior horn of the lateral ventricle suggesting atrophy of the medial temporal lobes including the ambient and parahippocampal gyri (**c**) (left side medial temporal lobe): Microscopic specimen (KB stain) shows atrophy in the amygdala, anterior side of hippocampus, ambient gyrus to entorhinal cortex. (**d**) A large number of Gallyas–Braak argyrophilic grains exist in the left medial temporal lobe especially in the ambient gyrus. (From [5] with permission)

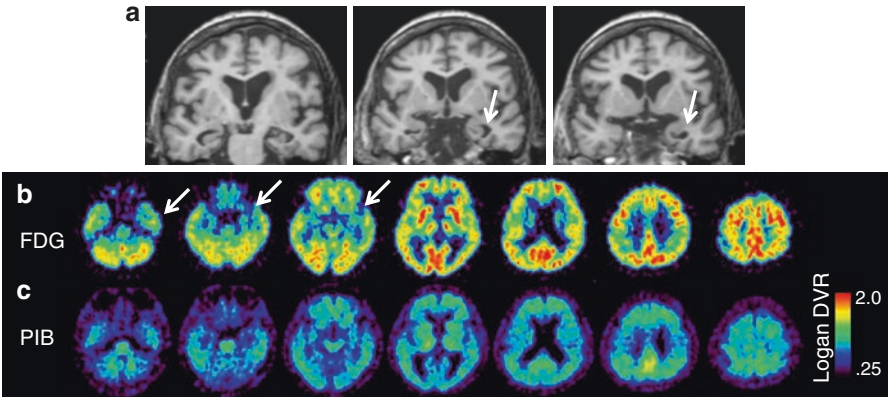

Fig. 4.4 70s female. (**a**) MRI 3D T1-weighted image shows dilatation of left inferior horn of the lateral ventricle (*white arrows*) suggesting left dominant atrophy of anteromedial temporal lobe. (**b**) FDG-PET shows left dominant decrease of glucose metabolism in the frontotemporal lobe (*white arrows*). (**c**) 11C PIB-PET study was negative suggesting no accumulation of Aβ in this patient. (From [5] with permission) Courtesy of Dr. Kenji Ishii

evaluations alone, a statistical image analysis was recently introduced to overcome this limitation. In the diagnosis of dementia, the usefulness of objective evaluations of the gray matter volume determined by voxel-based morphometry (VBM) as a statistical image analysis technique has also been reported. In the future, problems such as the differentiation of DG from other degenerative dementias including AD

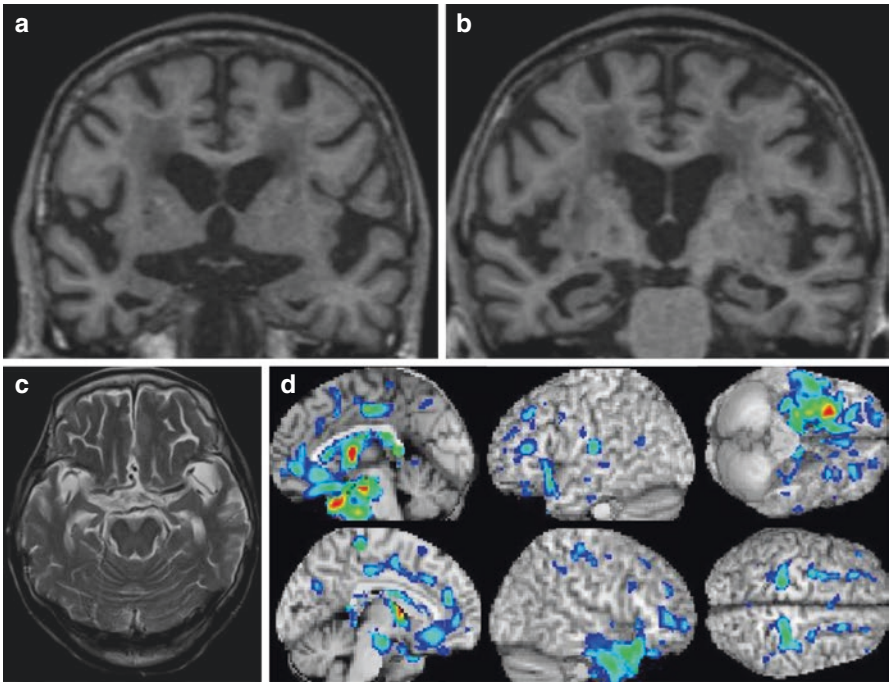

Fig. 4.5 Dementia with grains, MRI of an 80-year-old female patient with pathologically proven dementia with grains. She had a six-year history of cognitive impairment with an antemortem diagnosis of Alzheimer's disease. (**a**, **b**) Coronal three-dimensional (3D) T1-weighted images reveal the right dominant asymmetric atrophy of the medial temporal lobes including the ambient and parahippocampal gyri. (**c**) Additionally, T2-weighted image reveals right dominant bilateral atrophy of the amygdala. (**d**) Voxel-based morphometry on Voxel-based Specific Regional analysis system for Alzheimer's disease (VSRAD) software can objectively display this right dominant asymmetric atrophy of the temporal lobes and limbic system

by a statistical assessment of ambient gyrus atrophy, which is an initial pathological change in DG, in patients with a confirmed background pathology, the setting of a region of interest for the extraction of DG, and the development of software for the differentiation of DG from AD need to be addressed. In the patient shown in Fig. 4.2, neuropathological findings show clear asymmetry in atrophy of the medial temporal lobe, reflecting CT findings. A large number of Gallyas–Braak argyrophilic grains exist in this site, and the diagnosis was confirmed to be DG. However, the ambient gyrus, which shows deposits of argyrophilic grains and atrophy in the early stage of the disease, is very close to the entorhinal cortex, which is atrophied in an early stage of AD, and the degree of atrophy may also be asymmetric in AD, making differentiation difficult.

An evaluation using multiple modalities in combination, particularly amyloid imaging using PIB [8, 9] which is considered to reflect the accumulation of β-amyloid, is regarded as a useful tool for differentiating between AD and DG. In the patient shown in Fig. 4.4, atrophy of the parahippocampal gyrus was clear, whereas the accumulation of PIB was absent; therefore, it was necessary to suspect a pathological condition different from AD. If, with the progression of a clinical assessment

of PET preparations including PIB for the labeling of β-amyloid proteins, which constitute a core pathological feature of AD, reflection of the amyloid accumulation process in images becomes clear, expectations for the use of amyloid imaging to monitor treatment and care as well as early diagnoses will grow. Furthermore, the development of PET preparations that specifically label phosphorylated tau is in progress, and the possibility of a specific diagnosis of tauopathy is broadening.

While this remains controversial, a characteristic of DG observed on FDG-PET is reduced glucose metabolism on the medial temporal lobe. The area that shows this change is relatively limited, and metabolism in the lateral temporal lobe and parietal lobe is typically intact relative to the disease stage. In AD, pathological changes first appear in the posterior cingulate gyrus and precuneus and then spread to the parietal, lateral, and medial temporal and frontal lobes in typical cases. Furthermore, the pattern of progression may differ from that of the decline in metabolism.

On brain perfusion SPECT, a typical pattern in AD is also decreases starting in the parietal lobe and temporal association cortex that spread to the frontal association cortex. The usefulness of brain perfusion SPECT for the diagnosis of DG has not been established; however, a decrease in cerebral blood flow is observed in the medial temporal lobe, and the spread of areas with reduced blood flow are limited for the disease stage. The techniques of a statistical image analysis have been adopted in brain perfusion SPECT without relying on visual evaluations or the highly arbitrary setting of the region of interest. In three-dimensional stereotactic surface projection (3D-SSP), the results of analyses are projected on the brain surface. Using the easy Z-score Imaging System developed by Matsuda et al., 3-D images of a brain phantom are obtained with SPECT systems at various facilities, differences among the systems are corrected, and a database of normal images is shared among facilities [10–12].

4.3 Senile Dementia of The Neurofibrillary Tangle Type (SD-NFT)

4.3.1 Disease Concept

SD-NFT is a new type of dementia proposed by Yamada et al. on the basis of recent neuropathological findings [13–16]. It is an important disease to be considered, in addition to AD and DLB, as a causative disorder of senile dementia (Table 4.1). Neuropathologically, the disease is characterized by the deposition of numerous NFT in the parahippocampal region with the absence or scarcity of senile plaque.

It was proposed that SD-NFT be termed primary age-related tauopathy (PART) in 2014 [17], but an opposing argument was put forward in 2015 that PART is just a subtype of AD [18]. Establishment of its disease concept by accumulating knowledge in various aspects of neuropathology, biochemistry, neuroimaging, and clinical diagnosis is desired. To clarify the disease concept of SD-NFT, knowledge based on the currently established background pathology is described in this report.

4.3.2 Clinical Diagnosis

The clinical characteristics are as follows: (1) it develops with memory disturbance at an elderly age, (2) shows slow progression, (3) atrophy of the hippocampal region is observed, but diffuse cerebral atrophy is mild, and (4) it can be differentiated from Alzheimer's disease and other degenerative dementias [13–15].

4.3.3 MRI Findings

There is no well-organized report on the characteristics of imaging diagnosis, but it is important to accumulate slowly progressing dementia cases in the advanced elderly, taking the possibility of differentiation from Alzheimer's disease and argyrophilic grain dementia into consideration [19], to develop fundamental therapeutic agents, appropriately proceed with clinical trials, and plan precise treatment, care, and nursing plans.

Figure 4.6 shows a female in her 90s who developed dementia with forgetfulness in her 80s, and dementia relatively slowly progressed. An MR image with an MMSE score of 23 at 6 years after the onset is presented. Amygdala atrophy with laterality, such as that observed in DG, could not be confirmed, but atrophy extending to the posterior hippocampus was suggested by visual examination and voxel-based morphometry on Voxel-based Specific Regional analysis system for Alzheimer's disease (VSRAD) software [20]. Uptake was negative on amyloid imaging, based on which SD-NFT was considered.

In SD-NFT, neurofibrillary tangles are widely observed in the parahippocampal gyrus and hippocampus and accompanied by neuronal loss and gliosis. Morphological changes correspond to these neuropathological changes, and

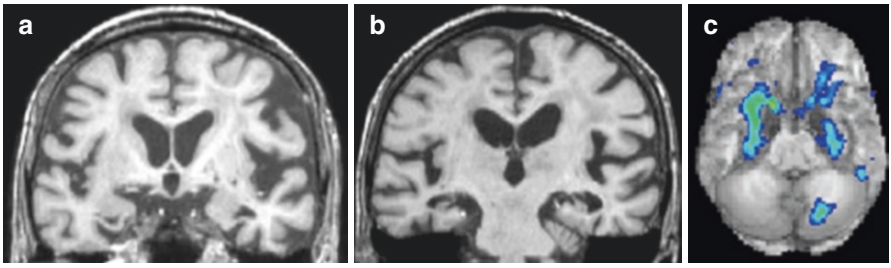

Fig. 4.6 Senile dementia of the neurofibrillary tangle type (tangle only dementia): SD-NFT. MRI of an 80-year-old female in her 90s who developed dementia with forgetfulness in her 80s, and dementia relatively slowly progressed. An MR image with an MMSE score of 23 at 6 years after the onset is presented. (**a**, **b**) Coronal three-dimensional (3D) T1-weighted images reveal atrophy of the hippocampus. Severe amygdala atrophy with laterality, such as that observed in DG, could not be confirmed. (From [79] with permission). (**c**) Voxel-based morphometry on Voxel-based Specific Regional analysis system for Alzheimer's disease (VSRAD) software can objectively display atrophy of the hippocampus extending to the posterior hippocampus

atrophy of the parahippocampal gyrus and hippocampal region is observed [13–15]. These morphological changes require differentiation from AD and DG. Atrophy extending to the posterior hippocampus is observed in SD-NFT, in contrast to DG in which atrophy starts in the ambient gyrus and is noticeable on the ventral side of the medial temporal lobe.

Progression of whole-brain atrophy with the disease stage is clear in AD, whereas extensive cerebral cortical atrophy in SD-NFT has been suggested to be mild. When the progression of cognitive disorder is very mild despite morphological atrophy progressing, it is necessary to consider the differentiation of SD-NFT and DG. Since atrophy extending to the posterior hippocampus is present from an early stage, unlike DG, differentiation from AD by visual assessment of MRI alone is difficult at present. The grade of whole-brain atrophy following the disease stage is suggested to be milder than that in AD.

There is no organized report on cerebral blood flow SPECT. Cases showing reduced blood flow localized in the medial temporal lobe and those showing a pattern similar to that observed in Alzheimer's disease have been suggested. Negativity on amyloid imaging using PIB, which reflects Aβ accumulation, and the development and application of a PET preparation specifically labeling phosphorylated tau may expand the possibility of the specific diagnosis of tauopathy and become a useful tool to differentiate between AD and DG and SD-NFT. Accurate early diagnosis is essential for early and preclinical diagnoses and clinical trials of fundamental therapeutic agents, for which the preparation of diagnostic criteria by accumulating background pathology-based clinical and imaging courses and findings is urgently needed [14, 15].

Although it is hard to say that the evaluation has been established, the characteristic of argyrophilic grain dementia on FDG-PET is reduced glucose metabolism in the medial temporal lobe. It is relatively localized, and metabolism is retained in the lateral temporal lobe and parietal lobe compared with the disease stage progression. SD-NFT has also been suggested to show a tendency similar to DG or be difficult to differentiate from AD in some cases. The accumulation of background pathology-based findings is necessary. The presence of a concomitant pathology of AD, DG, or DLB in SF-NFT has also been reported [4, 16]. It is necessary to be aware of the presence of a complex background pathology at a high rate in advanced elderly patients with dementia.

4.4 Progressive Supranuclear Palsy

4.4.1 Disease Concept

Progressive supranuclear palsy (PSP) is a neurodegenerative disease established as a disease entity by Steel et al., who reported 9 patients including autopsied cases in 1964 [21]. It is a type of tauopathy that exhibits atrophy of the midbrain and superior cerebellar peduncle, depigmentation of the substantia nigra and coeruleus nucleus, and pathological changes in wide areas including the globus pallidus,

subthalamic nucleus, and dentate nucleus of the cerebellum, and is histologically characterized by tufted astrocytes.

4.4.2 Clinical Profile

The disease occurs after the age of 40, progresses slowly, and is characterized by supranuclear vertical gaze palsy, frequent falling due to impaired postural maintenance, Parkinsonism, and gait disorders from early after its onset [22].

In studies investigating clinical symptoms of PSP definitely diagnosed pathologically, clinical symptoms suggesting dementia were noted at a high rate, such as changes in personality/frontal sign, psychological symptoms, and memory impairment/cognitive disorder, being present in 33, 18, and 32%, respectively, showing that PSP is an important background disease of cognitive impairment [23, 24]. Since head injury caused by falling affects the prognosis, and an accurate imaging-based diagnosis directly facilitates precise assistance, nursing, and medical care.

Clinical and pathological diversities of PSP have recently been clarified. Classic PSP showing a clinical course of early postural instability, falls, and supranuclear gaze palsy, so-called Richardson's syndrome (PSP-RS) reported by Richardson et al. [21], accounts for about 50% of all cases. In addition, the presence of PSP-subtypes showing diverse clinical and pathological spectra [25], such as PSP-parkinsonism (PSP-P) difficult to differentiate from Parkinson's disease (PD), pure akinesia, PSP-pure akinesia with gate freezing (PSP-PAGF) preceded by gate freezing, PSP-primary non-fluent aphasia (PSP-PNFA) developing non-fluent aphasia, PSP-corticobasal syndrome (PSP-CBS) developing asymmetric cortical symptoms, and rare cases of PSP with cerebellar ataxia (PSP-C) in which cerebellar symptoms precede, has been clarified, and imaging findings reflect each subtype.

Clinicopathologically, the pathology of PSP overlaps with those of AD, PD, and DLB, and it is difficult to make clinical and neuroimaging diagnoses of patients with these complications. The suggestion of the presence of an overlapping background pathology while carefully observing changes in the medical history and imaging findings of individual cases is an important role of neuroradiologists.

4.4.3 MRI Findings

4.4.3.1 PSP-RS

Structural MRI findings are useful to diagnose PSP-RS. Examination of the sagittal view is essential, and the characteristic midbrain atrophy with relative preservation of the pons on a sagittal image, termed a "hummingbird sign" or "penguin-silhouette sign," is the most important finding [26, 27] (Figs. 4.7 and 4.8). The axial image also reflects midbrain atrophy, and reduction of the anteroposterior diameter of the midbrain at the superior colliculi level is observed referred as "Morning glory sign" or "Mickey Mouse sign" (Fig. 4.7) [28].

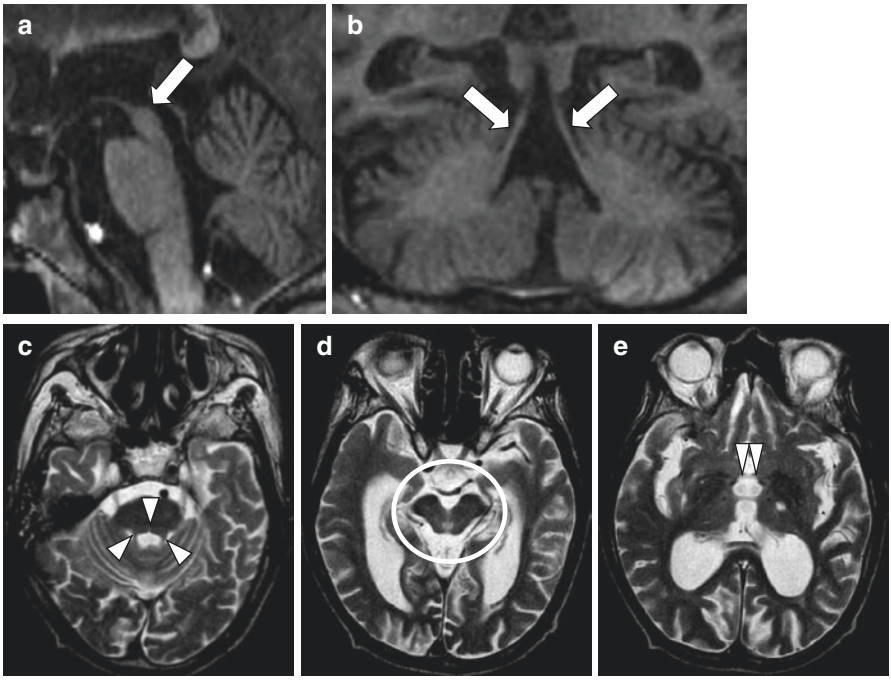

Fig. 4.7 PSP-RS. 80s male. Pathologically proven PSP (PSP-RS). (**a**, **b**) Eight years after symptoms onset, reconstructed sagittal and oblique coronal three-dimensional (3D) T1-weighted images (T1WI) reveal the severe atrophy of the midbrain tegmentum and superior cerebellar peduncles (*arrows*). This characteristic shape of the brainstem including the small midbrain with a concave profile and large pons indicative of "hummingbird sign" or "penguin-silhouette sign" is a typical imaging finding of PSP. (**c**–**e**) The atrophy of the pontine tegmentum, bilateral superior cerebellar peduncles (**c**, *arrowheads*), the reduced anteroposterior midbrain diameter referred as "Mickey mouse sign" (**d**, *circle*), and thalami, and dilatation of the third ventricles (**e**, *double arrowhead*), which are also typical imaging findings, are apparent on axial T2-weighted images (T2WI). Small round high signal intensity in the left thalamus indicates an old infarction

Atrophy of the superior cerebellar peduncle reflects secondary changes of the efferent pathway caused by degeneration of the dentate nucleus of the cerebellum, and it has a high diagnostic value (Figs. 4.7 and 4.8) [29]. In addition, dilatation of the 3rd and 4th ventricles and atrophy of the pontine tegmentum, anterior cingulate gyrus, and medial frontal lobe may also contribute to making a diagnosis [30]. A high intensity may be observed in the globus pallidus, periaqueductal region, and superior cerebellar peduncle on T2-weighted imaging (Fig. 4.8) [31]. These atrophic changes can be objectively evaluated using area measurement with a medial sagittal view and voxel-based morphometry (VBM). Regarding VBM, in addition to the midbrain tegmentum, atrophy of the frontal lobe including the region near the precentral gyrus, caudate nucleus, thalamus, and cerebellum has been reported [32–35]. However, neuroradiologists should understand that even PSP-RS may not exhibit midbrain atrophy in the early disease process (Fig. 4.9).

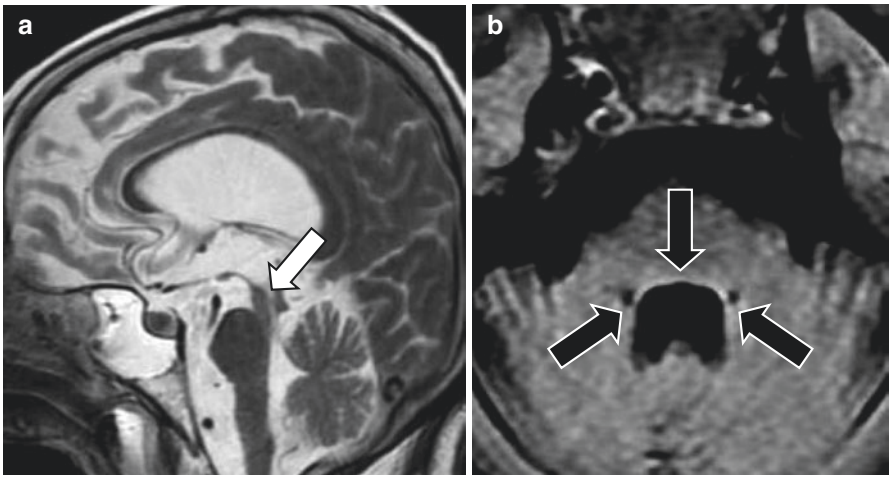

Fig. 4.8 PSP-RS. 70s female. Pathologically proven PSP (PSP-RS). (**a**) Nine years after symptoms onset, in addition to the typical midbrain atrophy (*arrow*), sagittal T2WI reveals the atrophy of the corpus callosum and dilatation of frontal sulcus suggestive of the frontal lobe atrophy. (**b**) Subtle high signal intensity of the superior cerebellar peduncles and brainstem tegmentum on fluid attenuated inversion recovery (FLAIR) images (*arrowheads*) is also a characteristic finding of PSP. (Courtesy of Dr. Fuji Yokoi, Narita Memorial Hospital, Meiyokai Medical Corporation)

Fig. 4.9 PSP-RS. 60s female. Pathologically proven PSP (PSP-RS). In contrast to advanced stage patients of Figs. 4.7 and 4.8, sagittal T2WI performed 2 years after symptoms onset does not exhibit the typical atrophy of the midbrain tegmentum and corpus callosum

Regarding evaluation of the microstructural changes based on water diffusivity using diffusion tensor imaging (DTI), it has been reported that differentiations not only between PSP and other parkinsonism but also between PSP-RS and PSP-P are necessary [36]. Greater importance is attached to the superior

cerebellar peduncle in evaluation using DTI as well as conventional morphological imaging [37, 38].

Susceptibility weighted imaging (SWI) is a technique with a long echo time high-resolution fully flow-compensated 3D GRE sequence, which has higher sensitivity to the brain mineralization, including iron depositions and blood products, than conventional T2*-weighted imaging [39, 40]. Additionally, this sequence can create better anatomic images in which the basal ganglia structures are easily visible. Previous studies utilizing SWI have reported that the iron deposition in the red nucleus is useful to differentiate PSP from other parkinsonian syndromes [41, 42].

4.4.3.2 PSP-Subtypes

Milder atrophy of the midbrain and superior cerebellar peduncle in PSP-subtypes than in PSP-RS has been reported, to which attention should be paid when making a diagnosis. To make a correct diagnosis of these subtypes, radiologists should focus on the different regions, including the globus pallidus, frontal lobe, and cerebral peduncle, other than the midbrain [42]. Evaluations of the atrophied regions by disease types using statistical imaging analysis, such as VBM analysis, may be accumulated in the future [34, 42–47].

4.4.3.3 PSP-P

PSP-P is the second most frequent subtype following PSP-RS, accounting for 20–35% of PSP variant cases. The patients with PSP-P had less severe tau pathology than those with PSP-RS, although the pattern of distribution between both groups was similar: the subthalamic nucleus and substantia nigra were the regions that were most severely affected. Although the substantia nigra is severely affected in PSP-P, the clinical features that distinguish PSP-P from PSP-RS, including tremor and moderate levo-dopa responsiveness, might be due to less severe depletion of dopamine in the extranigral midbrain in PSP-P [25, 48]. Its response to levo-dopa may be favorable in the early stage in some cases, but the disease stage progresses more rapidly compared with PD. Ophthalmoplegia and postural instability appear and the response to levo-dopa becomes poor as the disease stage progresses. Compared with typical PSP-RS, the degree of midbrain atrophy is less severe in this subtype (Fig. 4.10). Another important point is that atrophy of the superior cerebellar peduncles is less severe in PSP-P patients. Therefore, only the pons/midbrain ratio is useful to distinguish PSP-P from PD patients, but with a relatively lower diagnostic accuracy (sensitivity = 60%, specificity = 96%, accuracy = 86%) [49]. In reports on quantitative analysis, midbrain atrophy is not as noticeable as that in PSP-RS, and atrophy of the midbrain, superior cerebellar peduncle, thalamus, and frontal white matter was also reported to be milder than that in PSP-RS [34].

4.4.3.4 PSP-PAGF

PSP-PAGF is characterized by early difficulties in initiating gait and freezing during walking, writing, and speaking, without rigidity, tremor, cognitive impairment, or eye movement abnormality during the first 5 years of the disease. Levo-dopa is not effective. No characteristic finding is observed on visual inspection [50]. However,

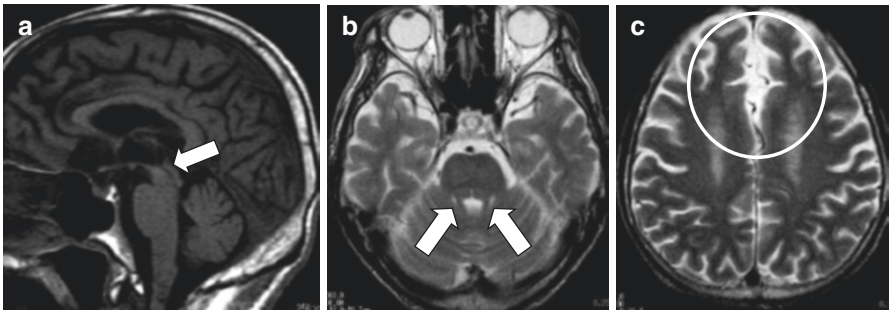

Fig. 4.10 PSP-P. 90s male. Pathologically proven PSP-P. (**a**, **b**) Compared with typical PSP-RS cases, there are no obvious atrophic changes of the midbrain tegmentum (**a**: *arrow*), and superior cerebellar peduncles (**b**: *arrows*) on sagittal and axial image. (**c**) T2WI reveals atrophy in the anterior cingulate gyrus (*circle*)

T2 prolongation of the globus pallidus can be the diagnostic clue in this subtype [51] (Fig. 4.11). On VBM analysis, atrophy of the thalamus, globus pallidus, frontal, inferior parietal, temporal lobes, and limbic lobes including the hippocampal region and anterior cingulate gyrus, compared with normal controls has been reported [52] (Fig. 4.11). It is necessary to accumulate cases to investigate morphological differences from those of PSP-RS and other PSP-subtypes and associations with clinical findings and the background pathology.

4.4.3.5 PSP-PNFA

There is a rare subtype of PSP which causes marked progressive speech and language dysfunction as a progressive non-fluent aphasia. PNFA is known as a disease type of frontotemporal lobar degeneration (FTLD), and PSP may be present as a background pathology in some cases. Accurate diagnosis of the pathology is also needed with regard to care and nursing, such as the necessity of considering the risk of falls due to background PSP. Predominant frontal lobe atrophy, particularly on the left side, in PSP-PNFA has been reported, and atrophy of the ipsilateral cerebral peduncle is also observed [53–55] (Fig. 4.13).

Midbrain atrophy is not as noticeable as that in PSP-RS, but it is atrophied compared with normal controls, and the disease may be diagnosed based on this. On VBM analysis, it has been reported that the main cortical regions with atrophy were the premotor and supplemental motor areas in cases of apraxia of speech, and the anterior periSylvian area in PNFA cases [54, 56] (Figs. 4.12 and 4.13). The accumulation of analyses connecting the clinical, pathological, and imaging findings is desired.

4.4.4 Differential Diagnosis

Midbrain tegmentum atrophy in the median sagittal view on MRI is an important finding based on which PSP may be diagnosed. However, PSP is not the only

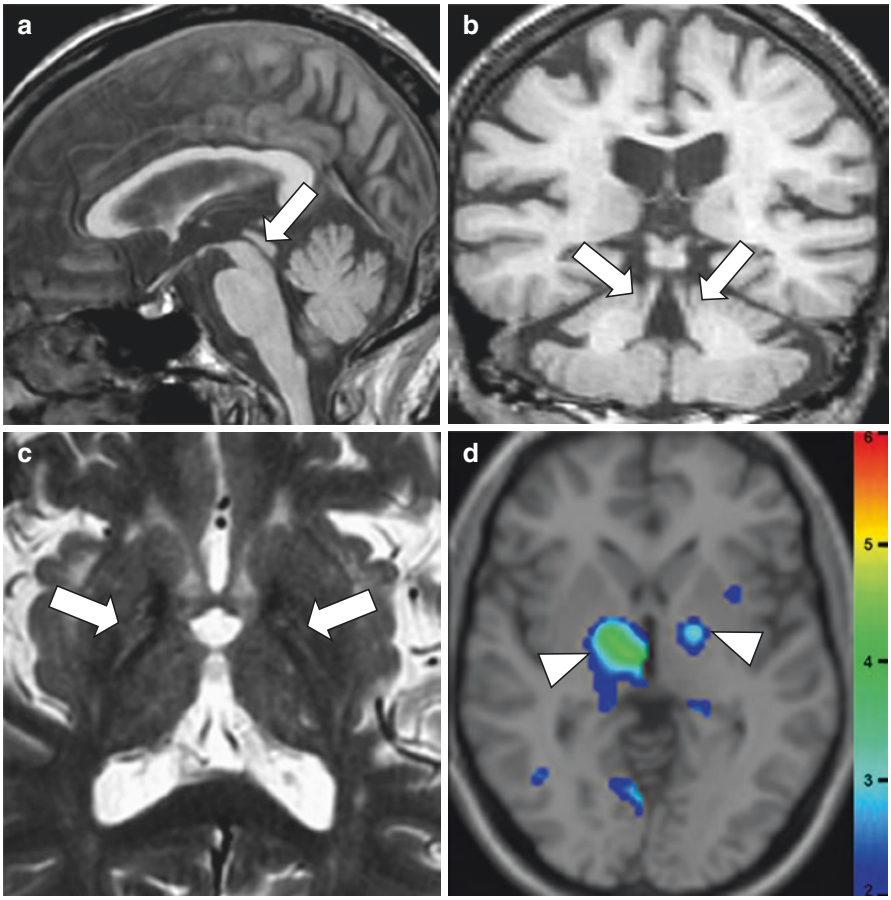

Fig. 4.11 PSP-PAGF. 80s female. Pathologically proven PSP (PSP-PAGF). (**a**, **b**) Compared with typical PSP-RS cases, there are no obvious atrophic changes of the midbrain tegmentum (**a**: *arrow*), corpus callosum and superior cerebellar peduncles (**b**: *arrows*) on sagittal and reconstructed oblique coronal 3DT1WIs. (**c**) On the other hand, T2WI reveals right dominant bilateral triangle-shaped high signal intensities of the globus pallidus (*arrows*). (**d**) Of note, voxel-based morphometry (VBM) on Voxel-based Specific Regional analysis system for Alzheimer's disease (VSRAD) software can objectively display right dominant bilateral atrophy of the globus pallidus and right thalamus (*arrowheads*), which are prediction sites of pathological changes in PSP patients. The degree of atrophy is represented using Z-scores on the rainbow scale color bar

disease causing midbrain tegmentum atrophy, and corticobasal degeneration (CBD) is the most important disease to be differentiated. In CBD, cortical atrophy with laterality and laterality of accompanying cerebral peduncle atrophy are observed, but differentiation is difficult because laterality is also observed in PSP-PNFA and

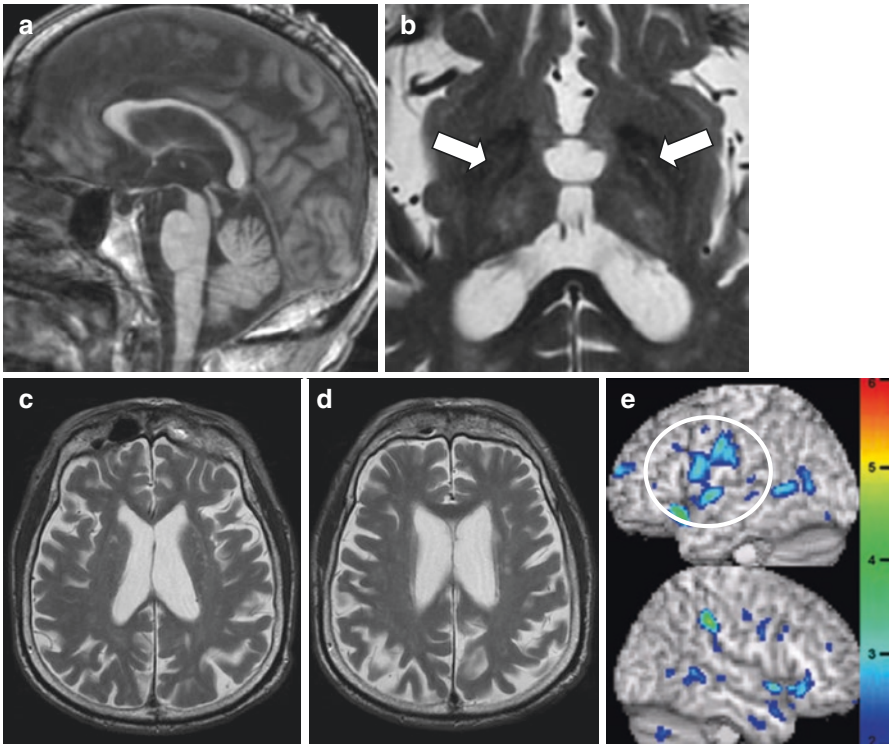

Fig. 4.12 PSP-PNFA. 80s male. Pathologically proven PSP (PSP-PNFA). (**a**) The degree of the midbrain atrophy is relatively mild on sagittal 3DT1WI. (**b**):T2WI reveals bilateral club-shaped high signal intensity of the globus pallidus (*arrows*). (**c**–**e**) Although it is difficult to evaluate the left dominant frontal atrophy on visual inspection of T2WIs (**c**, **d**), VBM on VSRAD software can display the left dominant frontal gray and white matter atrophy. 3D render views emphasize the left frontal lobe gray matter atrophy, especially in the Broca's area (**e**, *circle*)

PSP-CBS. It is known that pathological changes in the white matter are marked in CBD compared with those in PSP, which is useful to differentiate the disease in many cases, and evaluation using VBM has been reported, in addition to visual examination. Machado–Joseph disease and dentatorubral-pallidoluysian atrophy, which are forms of autosomal dominant spinocerebellar ataxias, can also exhibit the atrophy of the midbrain and superior cerebellar peduncle. Midbrain atrophy may also develop in idiopathic normal pressure hydrocephalus (i-NPH). Tight high convexity, medial subarachnoid spaces, and enlarged Sylvian fissures with ventriculomegaly can be defined as disproportionately enlarged subarachnoid-space hydrocephalus (DESH), which is a characteristic of iNPH. Patients with DESH can exhibit midbrain atrophy indistinguishable from that of PSP.

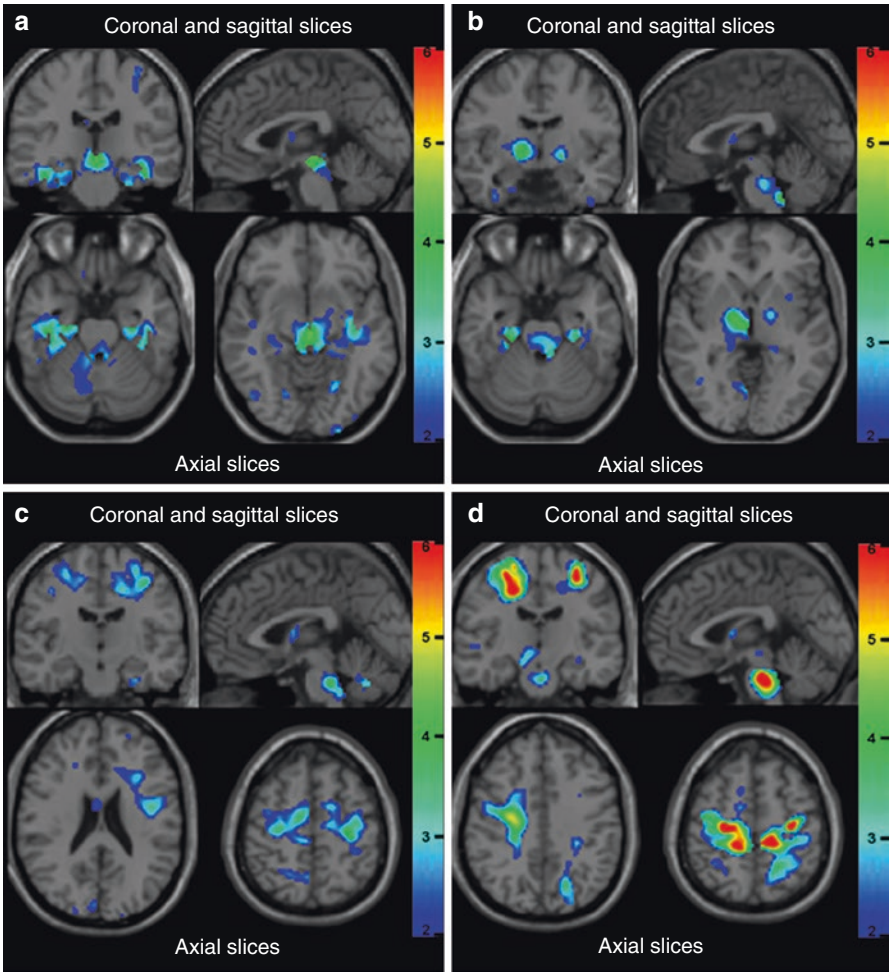

Fig. 4.13 Axial views of VBM result in pathologically proven PSP-RS (**a**), PSP-PAGF (**b**), PSP-PNFA (**c**), and PSP-CBS (**d**) patients. VBM analyses can reveal the characteristic white matter atrophy of PSP clinical subtypes indicative of the midbrain and superior cerebellar peduncles of PSP-RS, globus pallidus of PSP-PAGF, left frontal lobe including the inferior frontal gyrus of PSP-PNFA, and asymmetric frontoparietal lobes around the central sulcus of PSP-CBS. Additionally, most subtypes reveal the atrophy of the pontine tegmentum

4.5 Corticobasal Degeneration and Corticobasal Syndrome

4.5.1 Disease Concept

Corticobasal degeneration (CBD) is a progressive neurodegenerative disorder first described by Rebeiz et al. [57] and characterized by progressive, asymmetric, cortical dysfunction (e.g., apraxia, alien limb sign, cortical sensory loss, and myoclonus), and

extrapyramidal dysfunctions (e.g., akinesia, dystonia) [57]. As a pathologic diagnosis, CBD is characterized by widespread deposition of hyperphosphorylated 4-repeat tau in neurons and glia in specific topographic areas [58]. When first described, CBD was considered a distinct clinicopathologic entity, however, CBD has much clinicopathological heterogeneity [59–61], the term corticobasal syndrome (CBS) has been used as a clinical diagnosis, and CBD is used to refer to the pathological diagnosis [59, 60].

CBS can be the clinical syndrome of a host of different background pathologies, including corticobasal degeneration (CBS-CBD), progressive supranuclear palsy (CBS-PSP), Alzheimer's disease (CBS-AD), and frontotemporal lobar degeneration (CBS-FTLD).

4.5.2 Clinical Diagnosis

Definition and standardization of clinical diagnostic criteria for CBD are critical as potential development of curative therapeutic drugs for tauopathies. Current criteria for the clinical diagnosis of pathologically confirmed CBD no longer reflect the expanding understanding of this disease and its clinicopathological correlations. An international consortium of behavioral neurology, neuropsychology, and movement disorders specialists developed new criteria based on consensus and a systemic literature review [62]. Combined with consensus, four CBD phenotypes emerged: corticobasal syndrome (CBS), frontal behavioral-spatial syndrome (FBS), non-fluent/agrammatic variant of primary progressive aphasia (naPPA), and progressive supranuclear palsy syndrome (PSPS). They propose two sets of criteria: more specific clinical research criteria for probable CBD (diagnostic criteria excluding background pathology other than cr-CBD) and broader criteria for possible CBD (p-CBD) that has less specificity for CBD pathology while representing other tau-based pathology [62].

Previous clinical criteria excluded "early dementia" to increase diagnostic specificity, but dementia is now recognized as an important clinical feature in many cases of CBD [63–65].

4.5.3 MRI Findings

Although neuroimaging is not described in the latest diagnostic criteria described above, these criteria will need continued revisions as understanding of CBD and as neuroimaging studies advance, and are validated for distinguishing different phenotypes and diagnoses.

At present, there are two main roles of MRI in diagnosing CBD. The first role is clarification of MRI findings useful for cr-CBD, for which tenacious investigation connecting the clinical findings-imaging-background pathology is necessary. Previous MRI studies have reported distinct neuroimaging findings of pathologically diagnosed CBD, including asymmetric atrophy in the cerebral cortex and peduncle with dominance contralateral to the more clinically affected side, atrophy of the midbrain tegmentum and corpus callosum, and abnormal T2 prolongation in the subcortical white matter [55, 66] (Figs. 4.14 and 4.15). At sites where MRI

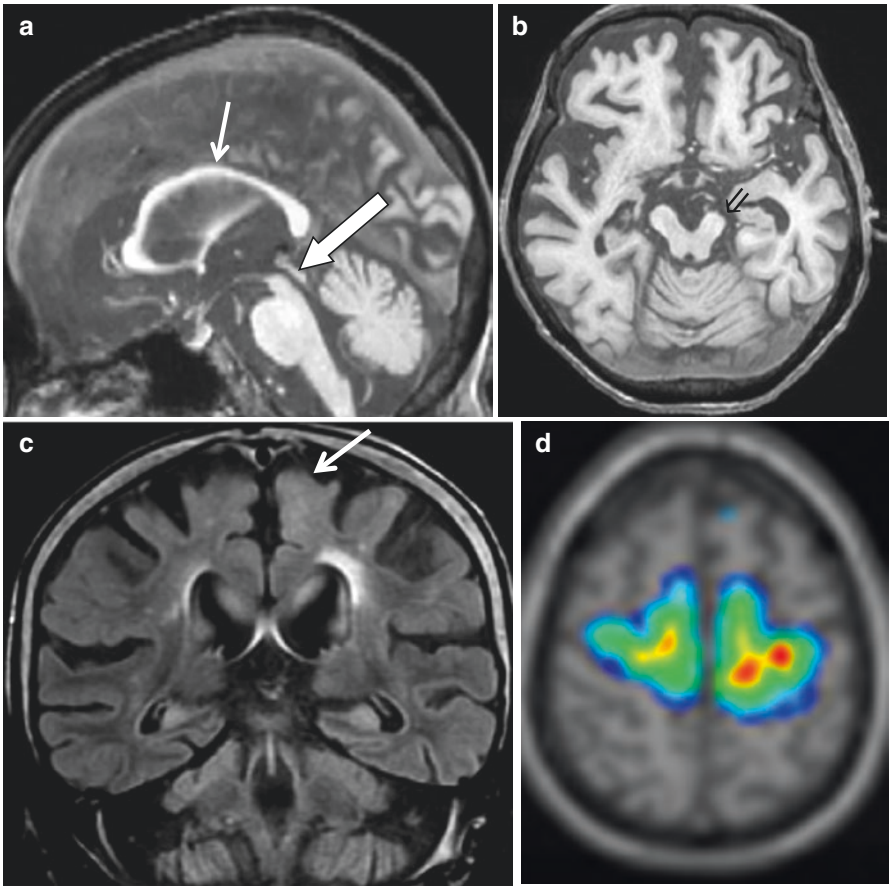

Fig. 4.14 80s female. CBD. (**a**) Sagittal T1-weighted image shows severe atrophy of midbrain (*bold arrow*) and thinning of corpus callosum (*arrow*). (**b**) T1-weighted axial image shows left dominant atrophy of cerebral peduncle (*arrow*). (**c**) FLAIR coronal image shows hyperintensity in the subcortical white matter (*arrow*). (**d**) Axial views of VBM reveal left dominant white matter atrophy

showed white matter lesions, although neuropathological examination revealed some secondary degeneration, tauopathy in the white matter, particularly the subcortical white matter, was clearly evident [66] (Fig. 4.14). Visually, the grade of changes in the intensity of the white matter varies among cases from widely extending to unclear changes. Atrophy of the midbrain tegmentum is present in both CBD and PSP, reflecting the pathology, and their differentiation may be difficult clinically or on imaging in some cases, but white matter degeneration impairing U-fibers is pathologically severer in CBD than PSP, and changes in the intensity of the white matter may serve as a point of differentiation. However, its judgment by visual evaluation alone may be difficult, for which the usefulness of objective evaluation

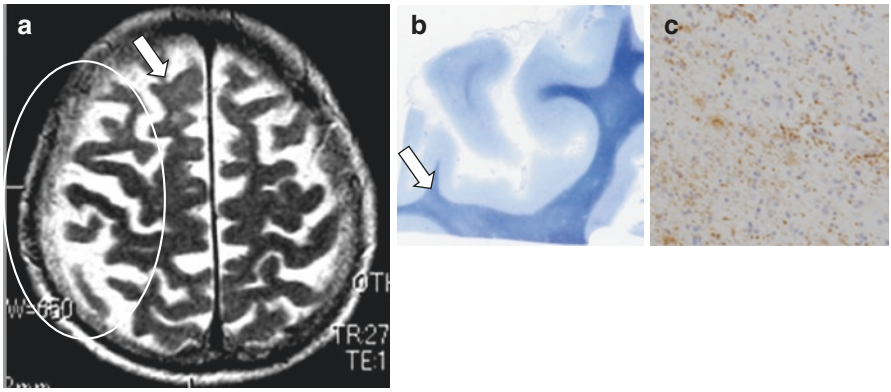

Fig. 4.15 Pathologically proven CBD:80s female. (**a**) Axial T2-weighted image shows right dominant atorophy (*circle*)and subcortical hyperintensity in the right frontal lobe (*arrow*). (**b**) In a microscopic specimen, myelin sheath staining is decreased in the white matter (*arrow*). (**c**) There is positive staining for antiphosphorylated tau antibody on AT8 staining, which is compatible with the primary changes in CBD

by Voxel-based morphometry (VBM) analysis has been reported. VBM analysis using SPM8 plus DARTEL demonstrated the diagnostic value of significant atrophy in the bilateral frontal subcortical WM for diagnosing CBS [67]. Thus, the VBM approach can be useful for discriminating between CBS and PSP-RS. However, considering the broad clinical spectrum of CBD, more pathologically proven cases of CBD are required to establish the diagnostic value of WM volume reduction on VBM analysis. It is difficult to differentiate CBD from PSP-CBS, PSP-PNFA even using VBM analysis of WM volume reduction.

The second role of MRI is differentiation of diseases with background pathology included in p-CBD other than CBD [68, 69]. Although there are diverse pathological backgrounds, lesions in the cortex of the frontal and parietal lobes and regions involved in- and output are present in common, suggesting that clinical symptoms are determined by localization of the lesions, but not by background pathology of the lesions, i.e., apraxia and cortical sensory loss may be due to lesions in the parietal lobe and alien limb signs may be due to lesions in the frontal or parietal lobe. It is essential to realize that AD, FTLD, PSP, and Creutzfeldt-Jakob disease (CJD) are present as the background pathology of CBS. In CJD, a high intensity in the cortex on diffusion-weighted MRI is the characteristic, and MRI performed at an appropriate timing is useful for exclusion diagnosis. There are still only a few reports on comparison between pathologically diagnosed CBS and images, VBM analysis has been reported. Imaging patterns of atrophy in CBS vary according to pathologic diagnosis. Widespread atrophy points toward a pathologic diagnosis of FTLD-TDP or AD, with frontotemporal atrophy suggesting FTLD-TDP and temporoparietal atrophy suggesting AD. On the contrary, more focal atrophy predominantly involving the premotor and supplemental motor area suggests CBD or PSP pathology. These atrophy patterns in CBS are promising but require prospective validation prior to inclusion in diagnostic criteria.

Diffusion tensor imaging (DTI) measures the translational movement of water molecules in biologic tissues. It measures fractional anisotropy (FA), an index of white matter coherence and axonal packing, and apparent diffusion coefficient average (ADC ave), an index of the average magnitude of the rate of diffusion within each voxel. DTI has a possibility to sharply detect different distributions of microstructural tissue damage, and its usefulness for differentiation between PS and CBD has been reported.

Detections of atrophy on MRI and microstructure damage on DTI are expected to serve as biomarkers which may correspond to the molecular pathology [70]. To attempt treatment targeting βamyloid, tau, and TDP-43, accumulation of investigations connecting clinical-neuroimaging-pathology is necessary to play a specific role as objective criteria.

4.6 Hippocampal Sclerosis of Aging

4.6.1 Disease Concept

Hippocampal sclerosis of aging (HS-Aging) is a relatively common neuropathological finding characterized by cell loss, gliosis, and atrophy in the hippocampus that is not explained by AD [71–79]. HS-Aging pathology is observed in up to 20% of individuals over the age of 85 years [73, 77]. The presence of HS-Aging pathology is associated with cognitive impairment [72–76]. HS-Aging is known as a complication of AD, DLB, and FTLD, but, independently from these pathologies, pathological reports of HS-Aging, in which neuronal loss and gliosis are detected in the CA1 area of the hippocampus and subiculum, have recently been accumulating [71–79]. A high frequency of the TAR DNA-binding protein 43 (TDP-43) pathology has also been reported, but investigation of its association with clinical and imaging findings is insufficient [71, 73, 76]. While investigation is proceeding from the viewpoint that it is an independent neurodegenerative disease, changes accompanying posticteric encephalopathy, hypoxic-ischemic encephalopathy, encephalitis, and vascular disorder, or superimposition of these are also assumed, and its pathology may be diverse.

HS-Aging is present in the background pathology at a relatively high frequency in the elderly. Its importance as a factor of dementia has been clarified by investigation of the background pathology; however, establishment of consensus guidelines for clinical diagnosis is needed, for which development of objective biomarkers including neuroimaging is an urgent task.

4.6.2 Neuroimaging

Only a few studies on neuroimaging based on the background pathology of HS-Aging have been reported [71, 76, 77], but MRI is expected to be an important tool as a biomarker to diagnose HS-Aging clinically. To acquire images of the hippocampus, observation of the coronal view vertical to the long axis of the

hippocampus is necessary. The sagittal plane was acquired, and the coronal section vertical to the hippocampus was set. The basic sequences of evaluation of hippocampal sclerosis are fast spin echo T2-weight imaging, and fluid attenuated inversion recovery (FLAIR).

The MRI findings of hippocampal sclerosis are atrophy and a high intensity on T2-weighted imaging and FLAIR (Figs. 4.16, 4.17, and 4.18). It develops on the unilateral side in many cases, but there are bilateral cases. Differentiation from AD is essential because hippocampal atrophy is observed. When clinical progress of dementia is slow despite a clear high intensity and atrophy being detected on T2-weighted imaging and FLAIR of the hippocampal formation, the possibility of hippocampal sclerosis with relatively preserved verbal fluency despite impaired word list delayed recall performance (which is informative because the former relies more on neocortical function and the latter on brain function referent more directly to the hippocampal formation) is considered [75]. Clinically, many cases were diagnosed as AD or clinically diagnosed as FTLD [73–78], but improvement of the sensitivity and specificity of differential diagnosis by further accumulating definite pathologically diagnosed cases is necessary.

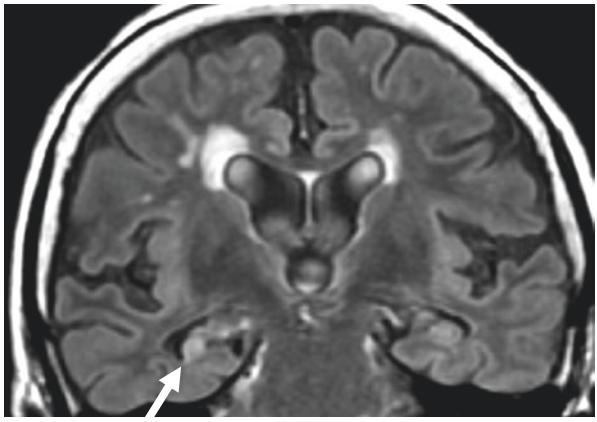

Fig. 4.16 70s female, memory disturbance. On the coronal view of FLAIR, local atrophy and a high intensity of the right hippocampus were clear, suggesting hippocampal sclerosis

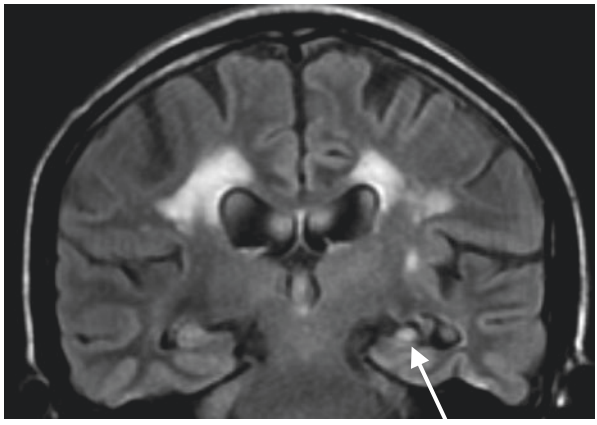

Fig. 4.17 70s male with dementia without marked progression for 12 years. He had past history of epilepsy. Left-side dominant local atrophy of the hippocampus and an increased intensity on FLAIR were clear (*arrow*). Left-side dominant hippocampal sclerosis was suggested

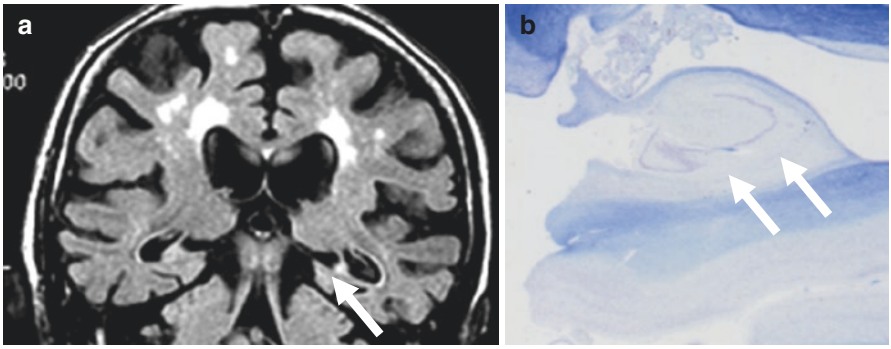

Fig. 4.18 80s male. (**a**) Left hippocampal atrophy and an increased intensity were noted in the coronal view on FLAIR (*arrow*). Morphologically, differentiation of hippocampal sclerosis was necessary. (**b**) The background pathology was neuronal loss in the left hippocampus CA1-2 (*arrows*), corresponding to hippocampal sclerosis. Accumulation of TDP-43 was also noted

The severity of dementia may be different due to the presence of hippocampal sclerosis on the right or left side. Attention should be paid to whether or not hippocampal sclerosis is located in the dominant hemisphere of the patient.

Atrophy and an abnormal intensity of the hippocampus suggest hippocampal sclerosis, but at present, attention should be paid to the possible heterogeneity of its background pathology, and attitude to diagnose along the clinical course of individual cases is essential.

In studies on HS-Aging, dementia is the main symptom and the frequency of epilepsy is low. Based on experience of the elderly at an emergency site, when the morphology suggests hippocampal sclerosis, similarly to early-onset cases, careful investigation of a past medical history of epilepsy, present illness, infection, vascular disorder, a past medical history of trauma, and the course may be significant to prepare a treatment plan [79–81]. Epilepsy symptoms may be recognized as dementia in elderly patients because many seizure episodes are non-convulsive, making diagnosis difficult in some cases. In this aging society, rapid elevation of the incidence of epilepsy in the elderly aged 70 years or older should be kept in mind [80, 81]. Attention should be paid to whether or not cases showing hippocampal sclerosis on MRI are included in the case group.

It has been reported that TDP-43 was negative on brain sections from younger individuals after hippocampectomy due to seizures, who had pathologically confirmed hippocampal sclerosis, but further accumulation of cases is necessary to investigate differences and overlapping between HS-Aging with foreground dementia in the elderly and early-onset hippocampal sclerosis manifesting epilepsy as a clinical symptom.

Although HS-Aging pathology may be associated with heterogeneous underlying causes linked previously to vascular factors, AD, and FTLD, there is a need to better understand the implications of pathologic observation [73–76].

4.6.3 Differential Diagnosis

Alzheimer's disease, dementia with grains should be included in clinical and imaging differential diagnoses. For neuroimaging, reliably diagnosing encephalitis (Fig. 4.19), posticteric encephalopathy (Fig. 4.20), hypoxic-ischemic encephalopathy, and cerebral infarction during the course is also important.

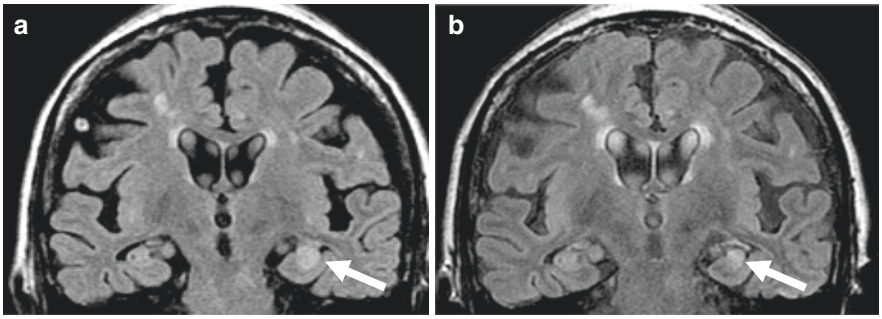

Fig. 4.19 70s female with suspected non-herpetic limbic encephalitis (NHLE). (**a**) Coronal FLAIR image shows left hippocampal swelling and high intensity at the onset of NHLE and the increased intensity prolonged on FLAIR (*arrow*). (**b**) 11 months later of onset, coronal FLAIR image shows hippocampal atrophy with hyperintensity (*arrow*). The clinical course was clearly followed and imaging findings were also followed as the course of NHLE. However, if the first examination was performed at 11 months after the onset when the MMSE score was 24 showing mild cognitive dysfunction, how do radiologists consider these findings? They may include hippocampal sclerosis in differentiation, and at the same time, careful consideration of the course after inflammation and convulsion and the course of ischemia would be necessary. (From [79] with permission)

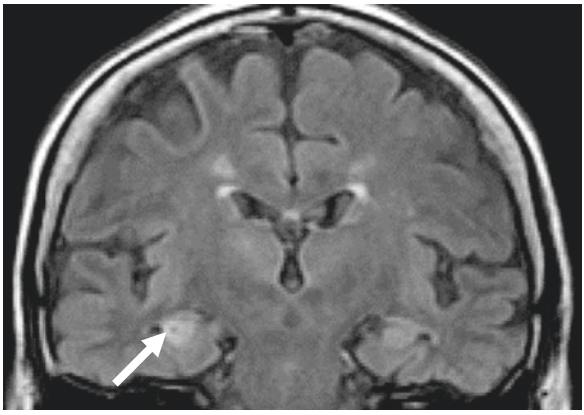

Fig. 4.20 80s female. Coronal FLAIR image was taken a 10 days after convulsive attack. This image shows high intensity in the right hippocampus probably due to posticteric encephalitis. (From [79] with permission)

4.7 Idiopathic Normal Pressure Hydrocephalus (iNPH)

4.7.1 Disease Concept

Normal pressure hydrocephalus (NPH) is well known as a treatable cause of dementia in elderly, and is characterized by the classical clinical triad of gait disturbance, dementia, and urinary incontinence [82–84]. NPH can be classified into idiopathic NPH (iNPH) and secondary NPH (See Table 4.2). International guidelines and Japanese guidelines for the diagnosis and management of iNPH have been published [82–89]. The etiology and pathomechanism of iNPH remain unknown. Clinical improvement by ventricle-peritoneal (VP) and lumbo-peritoneal (LP) shunts based on appropriate diagnostic criteria can be expected, and neuroimaging providing objective information plays a major role.

4.7.2 MRI Findings of iNPH

Table 4.3 shows the points of the diagnostic criteria for iNPH proposed in 2011 [86]. MRI plays an important role in making a diagnosis, and acquisition of the coronal and sagittal images, in addition to the transverse image, is recommended. There are 3 main findings of iNPH on MRI, as follows (Figs. 4.21, 4.22, and 4.23): (1) Ventricular dilatation: Evans index (determined by the largest diameter of the frontal horns divided by the diameter of the internal skull, on the same

Table 4.2 Classification of normal pressure hydrocephalus

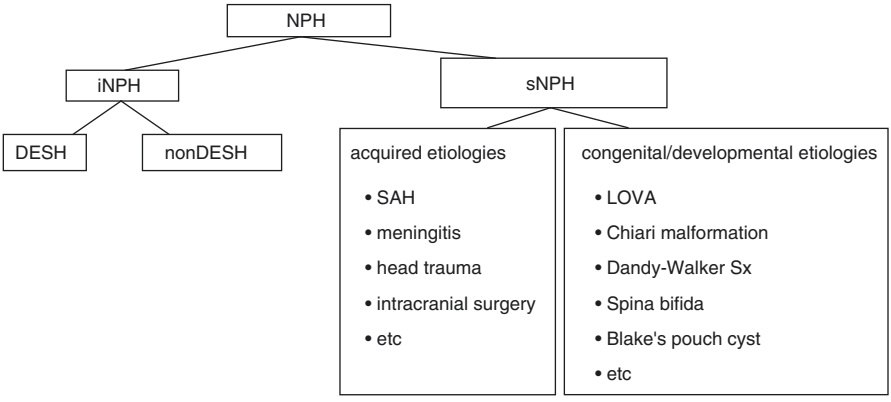

DESH: disproportionately enlarged subarachnoid-space hydrocephalus
SAH: subarachnoid hemorrhage
LOVA: long-standing overtventriculomegaly in adults
iNPH: idiopathic NPH
sNPH: secondary NPH

Table 4.3 Diagnostic criteria for idiopathic normal pressure hydrocephalus (iNPH) in these revised guidelines

1. Possible iNPH: meets all of the following five features:
(1) Individuals who develop the symptoms in their 60s or older
(2) More than one of the clinical triad: gait disturbance, cognitive impairment, and urinary incontinence
(3) Ventricular dilatation (Evans index > 0.3)
(4) Above-mentioned clinical symptoms cannot be completely explained by other neurological or non-neurological diseases
(5) Preceding diseases possibly causing ventricular dilatation are not obvious, including subarachnoid hemorrhage, meningitis, head injury. congenital hydrocephalus, and aqueductal stenosis
Possible iNPH supportive features
(a) Small stride, shuffle, instability during walking, and increase of instability on turning
(b) Symptoms progress slowly; however, sometimes an undulating course, including temporal discontinuation of development and exacerbation, is observed
(c) Gait disturbance is the most prevalent feature, followed by cognitive impairment and urinary incontinence
(d) Cognitive impairment is detected on cognitive tests
(e) Sylvian fissures and basal cistern are usually enlarged
(f) Other neurological diseases, including Parkinson's disease, Alzheimer's disease, and cerebrovascular diseases, may coexist; however, all such disease should be mild
(g) Periventricular changes are not essential
(h) Measurement of CBF is useful for differentiation from other dementias
Possible iNPH with MRI support
Possible iNPH with MRI support indicates the condition fulfilling the requirements for possible iNPH, where MRI shows narrowing of the sulci and subarachnoid spaces over the high convexity/midline surface (DESH). This class of diagnosis can be used in circumstances where a CSF examination is not available, for example, in a population-based cohort study
2. Probable iNPH: meets all of the following three features:
(1) Meets the requirements for possible iNPH
(2) CSF pressure of 200mm H2O or less and normal CSF content
(3) One of the following three investigational features:
(a) Neuroimaging features of narrowing of the sulci and subarachnoid spaces over the high convexity/midline surface(DESH) under the presence of gait disturbance
(b) Improvement of symptoms after CSF tap test
(c) Improvement of symptoms after CSF drainage test
3. Definite iNPH
Improvement of symptoms after the shunt procedure

**CBF* cerebral blood flow, *CSF* cerebrospinal fluid, *DESH* disproportionately enlarged subarachnoid-space hydrocephalus, *MRI* magnetic resonance imaging
From [86]

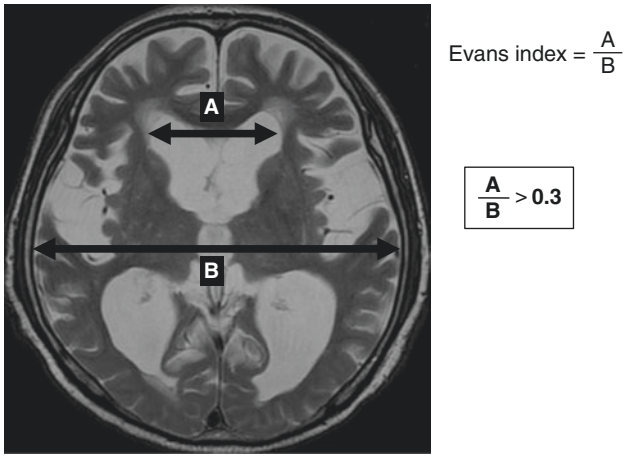

Fig. 4.21 Evans index = A/B. A/B ≥ 0.3. **A** = the largest diameter of the frontal horns. **B** = the diameter of the internal skull, on the same plane. (Courtesy of Dr. Mori Harushi, Department of Radiology, The University of Tokyo)

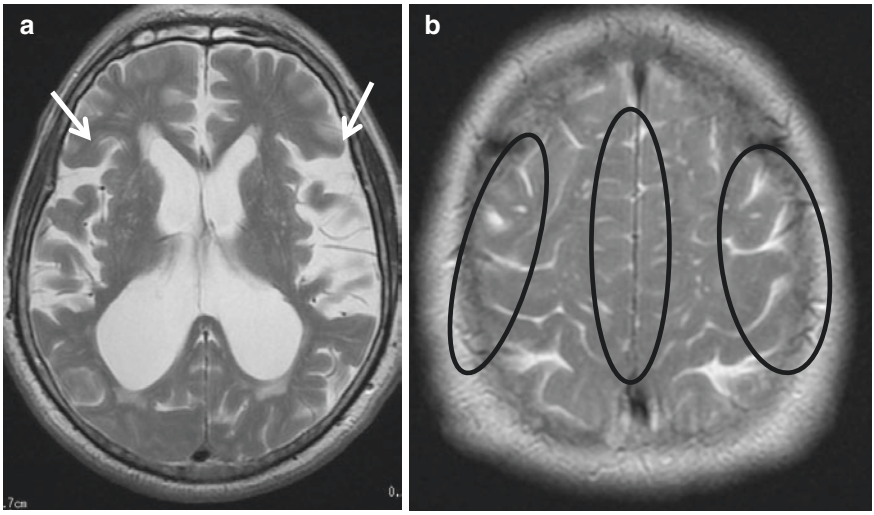

Fig. 4.22 DESH 80s male. He had gait disturbance, urinary incontinence, and cognitive impairment. (**a**) Axial T2-weighted image shows ventricular enlargement and Sylvian fissure (*arrow*) (**b**) Axial T2-weighted image shows tightened high convexity/midline CSF space (*circles*). (Courtesy of Dr. Mori Harushi, Department of Radiology, The University of Tokyo)

plane) >0.3 (Fig. 4.21) [85, 90, 91], (2) enlargement of Sylvian fissure, and (3) basal cistern tightened high convexity/midline CSF space. A pathological state meeting all these conditions and reflecting disproportional distribution of CSF between the superior and inferior subarachnoid spaces is termed disproportionately enlarged subarachnoid-space hydrocephalus (DESH), and many cases of iNPH show this morphology [90–92]. Sylvian fissure dilatation is less likely to be observed in NPH, other than iNPH. DESH is characterized by tight high

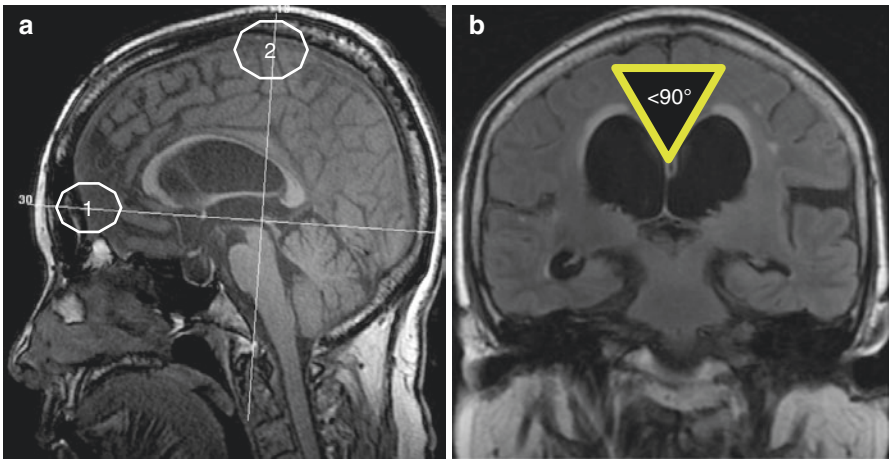

Fig. 4.23 CA (callosal angle): 60s female with gait disturbance. (**a**) 1 = the anteroposterior commissure line. 2 = coronal plane just on the posterior commissure perpendicular to the anteroposterior commissure line. (**b**) CA is under 90° in the coronal plane just on the posterior commissure. (Courtesy of Dr. Mori Harushi, Department of Radiology, The University of Tokyo)

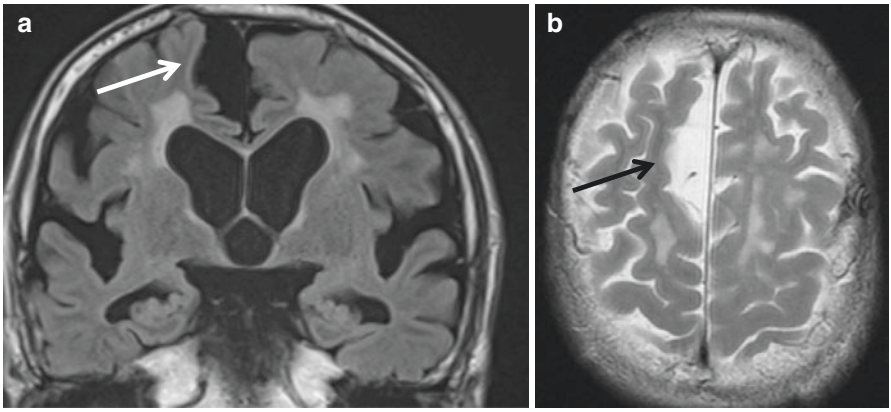

Fig. 4.24 80s M, iNPH. He had cognitive decline and gait disturbance. His background pathology did not show any degenerative diseases. (**a**) FLAIR coronal image shows dilatation of lateral ventricle and Sylvian fissure. (**b**) Axial T2-weighted image shows tightened CSF space in the posterior medial side of high convexity. Local cerebral sulcus dilatation is observed in (**a** and **b**) (*arrows*)

convexity and medial subarachnoid space, but local cerebral sulcus dilatation is often observed (Fig. 4.24).

Reference findings include dilatation of the anterior cingulate sulci [92, 93] and narrowing of the corpus callosal angle (CA) [94] (Fig. 4.23). CA represents the angle formed by the corpus callosum on the posterior commissure perpendicular to the anteroposterior commissure line (AC-PC line) on coronal MRI (Fig. 4.23). It has been reported that when the angle is 90° or smaller, the angle is useful for

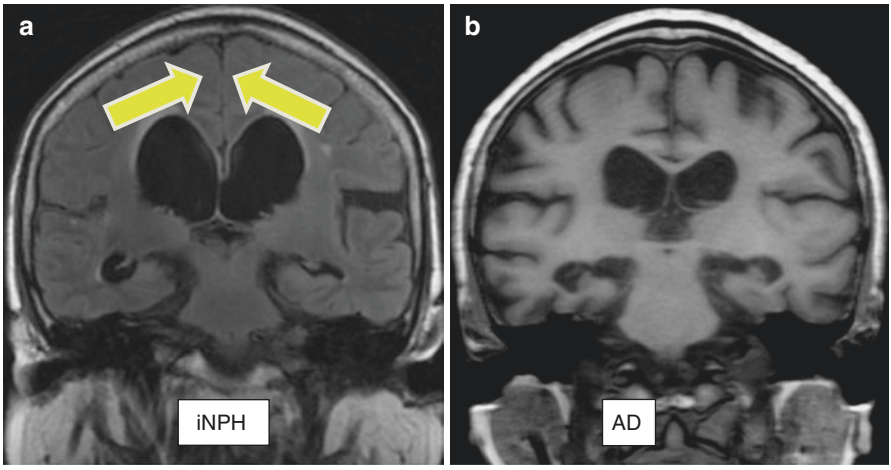

Fig. 4.25 Differential diagnosis between iNPH and AD. (**a**, **b**) Ventricular enlargement is observed in both iNPH and AD, but the tightened high convexity/midline CSF space is clear and the callosal angle is 90° or smaller in iNPH (**a**), whereas it is unclear in AD (**b**). (Courtesy of Dr. Mori H, Department of Radiology, The University of Tokyo)

differentiation between normal aging and AD at an accuracy of 93%, sensitivity of 97%, and specificity of 88% [91]. Many iNPH cases are not accompanied by periventricular hyperintensity (PVH), and currently, the presence or absence of PVH does not contribute to the differentiation of iNPH.

iNPH cases are mixed with cases of ventricular enlargement dilatation showing no DESH finding, and these are termed non-DESH-type iNPH. Some cases are not accompanied by clinical symptoms despite typical DESH findings being observed on MRI. These are considered at high risk of progressing to iNPH, and termed asymptomatic ventriculomegaly with features of iNPH on MRI (AVIM) [95]. Differentiation between DESH and AVIM on MRI is difficult, and it is judged in consideration of clinical symptoms, but it is necessary to call attention to how the follow-up of clinical and MRI findings is essential.

4.7.3 Differential Diagnosis

(1) The incidence of iNPH is high in the elderly. The disease is accompanied by cognitive impairment, it may be treatable, and its differentiation from Alzheimer's disease (AD) and Parkinson's disease (PD) is important. Since the DESH findings were proposed, the accuracy of diagnosing iNPH by MRI improved, but it should be noted that iNPH is frequently complicated by AD, PD, and cerebrovascular disease (CVD) in elderly patients, and the disease is difficult to diagnose by MRI alone. Figures 4.25 and 4.26 show the differentiation points between AD and iNPH on MRI. Ventricular enlargement is observed in both iNPH and AD, but the tightened

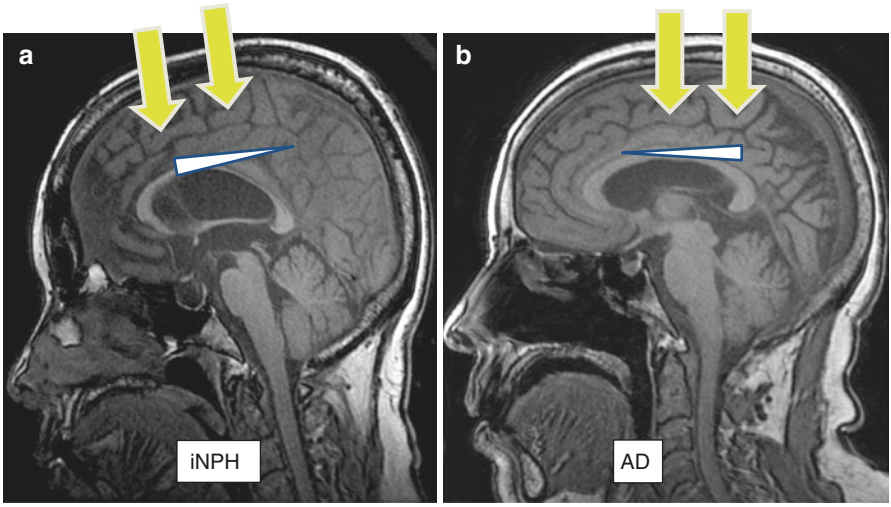

Fig. 4.26 Differential diagnosis between iNPH and AD. (**a**, **b**) Cingulate sulcus dilatation is detected in the anterior region in iNPH (**a**), but it is dominant in the posterior region in AD (**b**). (Courtesy of Dr. Mori H, Department of Radiology, The University of Tokyo)

high convexity/midline CSF space is clear and the callosal angle is 90° or smaller in iNPH, whereas it is unclear in AD. In addition, cingulate sulcus dilatation is detected in the anterior region in iNPH, but it is dominant in the posterior region in AD.

Yamashita et al. have been reported recently that the VBM-based CSF space analysis can accurately detect disproportionate changes in the CSF space and differentiate iNPH patients from those with AD or PD and healthy elderlies, for which usefulness is expected [96]. In addition to contributing to early and differential diagnoses, the VBM-based CSF space analysis can be used to predict the onset of diseases and to monitor morphological changes between responders and nonresponders to shunt operations. To apply the VBM-based CSF space analysis as a useful tool and lead it to future multicenter trials, further cross-validation studies are needed.

Midbrain atrophy may also develop in iNPH, and attention should be paid to differentiation of and complication by progressive supranuclear palsy (PSP) and corticobasal degeneration (CBD).

(2) Secondary normal pressure hydrocephalus (sNPH)

sNPH is induced by acquired etiologies, such as subarachnoid hemorrhage (SAH) and meningitis. If the presence of its past medical history is confirmed, the diagnosis can be made without a doubt. Morphologically, ventriculomegaly and a tightened CSF space are observed compared with those in iNPH, but the Sylvian fissure dilatation is mild in many cases.

(3) Long-standing overt ventriculomegaly in adults (LOVA) [97]

In LOVA, ventriculomegaly persists for a prolonged period from infancy. It results in hydrocephalus inducing urinary incontinence and cognitive impairment

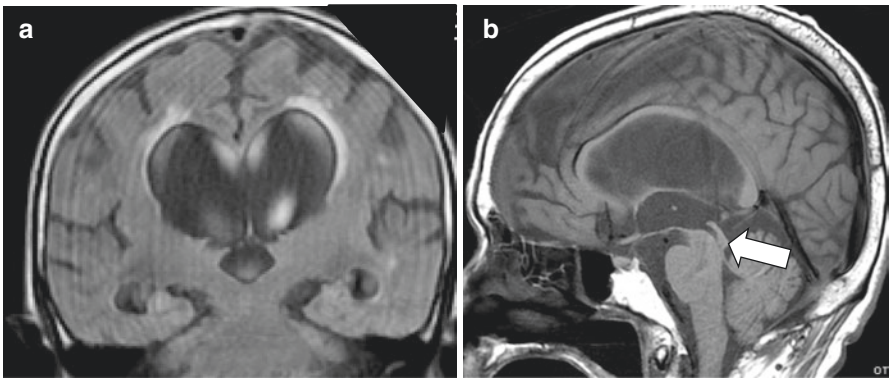

Fig. 4.27 LOVA: 80s M. He had long-standing gait disturbance and easy to fall. (**a**) There are marked ventriculomegaly without dilatation of Sylvian fissures. (**b**) There shows stenosis of caudal aqueduct of midbrain (*arrow*)

in adults, and aqueductal stenosis is considered to be the cause (Fig. 4.27) [97]. Long-term ventriculomegaly may be accompanied by sella turcica expansion and destruction. Its incidence is high in the young population, from teens to 60s, compared with that of iNPH. Ventriculomegaly and tightened CSF space are extensively observed, but no Sylvian fissure dilatation is observed (Fig. 4.27).

4.7.4 Pathophysiology of CSF Dynamics Remains Unknown

The current CSF movement is based on the hypothesis proposed by Dandy and Blackfan [98] and Cushing et al. in the early twentieth century, i.e., there is unidirectional flow in which CSF is produced at the site of the choroid plexus and absorbed in the pacchionian granulations.

Dandy et al. proposed the CSF bulk flow theory: Hydrocephalus is caused by imbalance between CSF formation and absorption. In contrast to the bulk flow theory, Greiz et al. proposed the "hydrodynamic theory" [99]: Chronic hydrocephalus is due to decreased intracranial compliance, causing restricted arterial pulsations and increased capillary pulsations.

However, explanation of the pathology of DESH is difficult with either theory, and at present, the cause of iNPH is unclear. Recently, Yamada et al. investigated CSF movement using the time-spatial labeling inversion pulse (SLIP) technique [100]. According to them, pulsatile CSF flow was observed up to the Sylvian fissure, but no CSF pulsatile flow continuous from the Sylvian fissure to the cerebral convexity was observed, and CSF movement is not limited to steady-state unidirectional flow, suggesting that the previous common wisdom of CSF movement may be changed by the new MR technique.

4.8 Vascular Dementia

4.8.1 Disease Concept

Vascular dementia (VaD) is one of the most common causes of age-associated dementia. In addition, cerebrovascular disease (CVD) may worsen the dementia of neurodegenerative diseases, for example, Alzheimer's disease (AD), Parkinson's disease (PD), Lewy body disease (DLB), etc.

There is a diversity in the cause and pathology of VaD, and clinical symptoms and courses are also diverse. When CVD develops, dementia develops at the same time. The causal relationship between these is very clear in some cases, but various pathologies are present in others, such as that dementia progresses during the course of repeated cerebrovascular disorder, small vascular lesions modify dementia, and cortical microinfarcts cause dementia. There are also several clinical diagnostic criteria [101, 102]. This report describes points to remember of imaging diagnosis based on the National Institute of Neurological Disorders and Stroke (NINDS)–Association Internationale pour la Recheche et l'Enseignement en Neurosciences (AIREN) diagnostic criteria including brain imaging, and introduces diverse imaging findings of cortical microinfarcts, cerebral autosomal dominant arteriopathy with subcortical infarcts and leukoencephalopathy (CADASIL), and cerebral amyloid angiopathy.

4.8.2 MRI Diagnosis

4.8.2.1 Multi-Infarct Dementia

Multiple large complete infarcts, usually from large-vessel occlusions involving cortical and subcortical areas, resulting in a clinical syndrome of dementia.

4.8.2.2 Strategic Single-Infarct Dementia

The cognitive impairment resulting from small, localized ischemic damage in functionally important cortical and subcortical areas is well defined [101, 103–106].

Regions in which cognitive decline-inducing strategic infarcts occur are shown in Table 4.4 [101, 103–106]. The Papez circuit is a series of neural circuits starting

Table 4.4 The areas causing strategic infarct dementia [101, 103–106]

1. Angular gyrus
2. Basal forebrain
3. Thalamus
4. Head of the caudate nucleus
5. Hippocampus
6. Fornix
7. Corpus callosum
8. Papex circuit

from the hippocampal formation to the fornix, mammillary body, mammillothalamic tract (Vicq d'Azyr bundle), anterior thalamic nucleus, cingulum, entorhinal cortex, and returns to the hippocampal formation, and cerebrovascular disorder impairing the Papez circuit is involved in cognitive decline because the circuit is closely involved in the memory.

Paramedian thalamic infarction occurs on the bilateral sides in many cases, and bilateral paramedian thalamic lesions are often accompanied by rostral midbrain lesions, producing a mesencephalothalamic syndrome of which a triad of symptoms are altered mental status, vertical gaze palsy, and amnesia. The paramedian thalamic area is perfused by the thalamoperforating artery branching from the P1 segment of the posterior cerebral artery (PCA), but there is an anatomic variant termed the artery of Percheron (AOP) branching from the PCA as a single dominant thalamoperforating artery, and many bilateral paramedian thalamic infarcts are caused by obstruction of the AOP [105]. Figure 4.28 shows a male patient in his 50s in whom cognitive decline occurred after sudden development of vertical eye movement. Infarcts were detected in the bilateral paramedian thalami and midbrain.

Figure 4.29 shows a male patient in his 60s with amnesic cognitive dysfunction accompanying infarction of the subcallosal artery territory (ScA) which branches from the anterior communicating artery (A-com). High-intensity lesions were detected in the bilateral anterior commissures and columns of the fornix on diffusion-weighted imaging and FLAIR (Fig. 4.29). Stroke in the vascular territory of the ScA leads to a characteristic imaging and clinical pattern. Ischemia involves the anterior columns of the fornix and the genu of the corpus callosum, and patients present with Korsakoff's syndrome including cognitive disturbances. These regions should also be noted in those involved in cognitive decline after surgery for A-com aneurysm [106].

Figure 4.30 shows a female patient in her 70s in whom secondary degeneration of the mammillo-thalamic tract occurred after infarction of the left anteromedial thalamus and the ipsilateral mammillary body atrophied, this was the responsible lesion for her memory disturbance.

4.8.2.3 Small Vessel Disease with Dementia

Lesions caused by small vessel disease may be cortical or subcortical: the latter include lacunes and white matter lesions frequently observed in the brains of elderly people. Lesions in the multiple basal ganglia and white matter lacunes are caused by obstruction of the perforating and medullary arteries. Binswanger's disease (BD) is characterized clinically by pseudobulbar signs, behavioral changes, memory disturbances, psychomotor retardation, and other subcortical features such as gait disturbances, urinary incontinence, and parkinsonian signs. BD is also termed subcortical arteriosclerotic encephalopathy and forms diffuse ischemic lesions extensively in the cerebral white matter. High-intensities are extensively observed in the white matter on T2-weighted imaging and FLAIR on MRI, and complications by multiple lacunes and small hemorrhages are frequently observed (Fig. 4.31). In BD, in elderly hypertensive patients (particularly, nocturnal hypertension) who survived

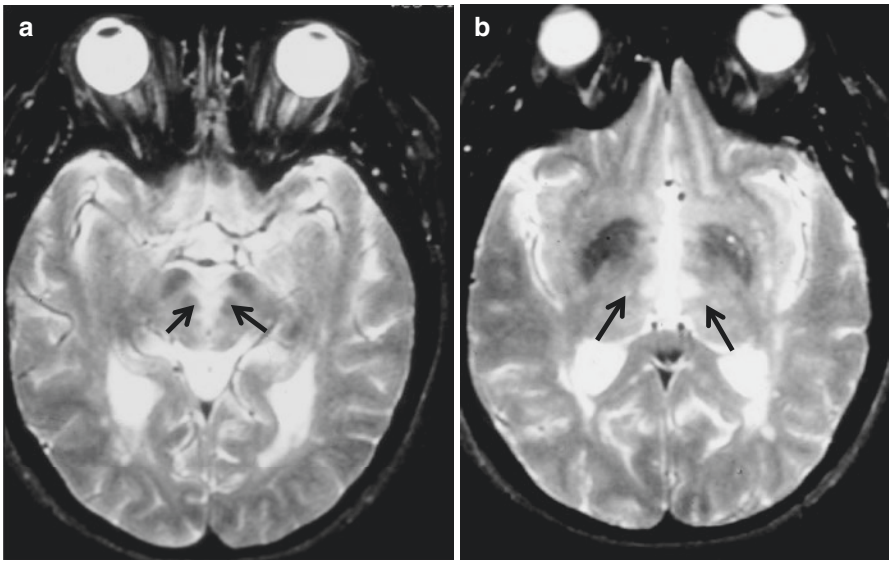

Fig. 4.28 Male patient in his 50s in whom vertical eye movement suddenly occurred. (**a**, **b**) T2-weighted transverse image shows infarcts in the bilateral paramedian thalami and midbrain (*arrows*). (From Tokumaru A et al.: Neuro-Ophthalmology Japan. Vol. 15(3) with permission)

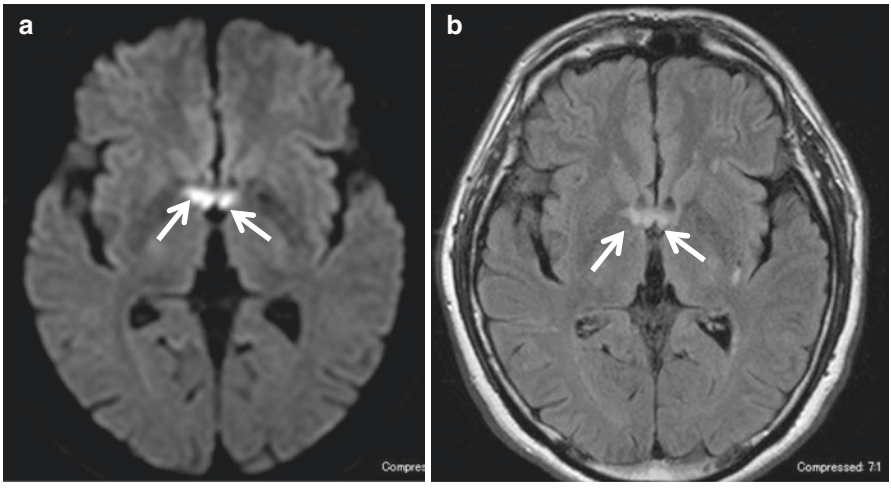

Fig. 4.29 60s M: Amnesia and cognitive disorder suddenly developed several days earlier. (**a**, **b**) Amnesia and cognitive disorder (strategic infarct) accompanying infarction of the bilateral columns of the fornix and anterior commissure (region perfused by the subcallosal artery)

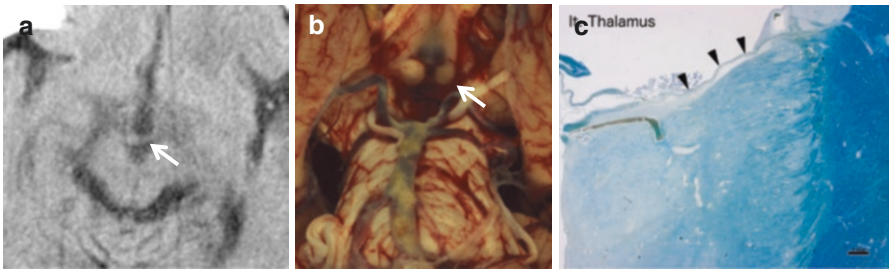

Fig. 4.30 70s female: Memory disturbance. (**a**, **b**) Axial CT image shows atrophy of left mammillary body (*arrow)*. Macrospecimen represents atrophy of left mammillary body (*arrow*). (**c**) KB stain shows left medial thalamic infarct. After the development of left thalamic infarction (*arrowheads*), mammillary body atrophy occurred due to secondary degeneration of the mammillothalamic tract. (From Tokumaru A et al.: Japanisch-Deutsche Medizinische Berichte. Vol. 52(4) with permission)

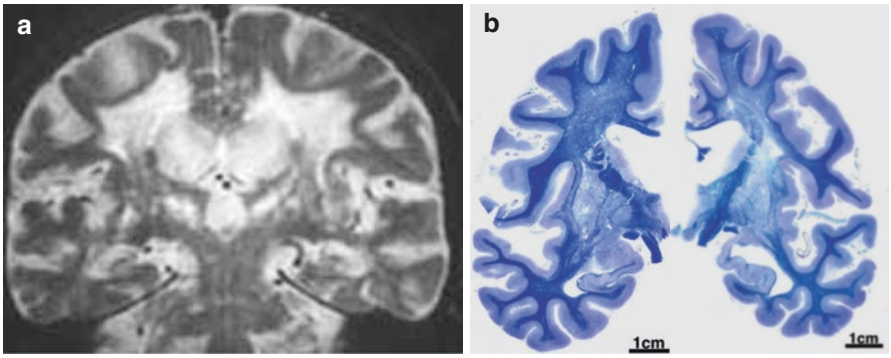

Fig. 4.31 Binswanger's disease. (**a**) On coronal T2-weighted imaging, diffuse high-intensities in the white matter, multiple small infarcts in the bilateral thalamic and basal ganglias, and microbleeding were observed. (**b**) On myelin sheath staining, myelin sheath sustainability decreased corresponding to the high-intensities on T2WI, but U-fibers were relatively retained. Multiple small infarcts and microbleeding were scattered in the basal ganglia and thalamus

arteriosclerosis-induced large vascular obstruction and large cardiac vascular events, progression of cerebral hypertensive small vessel disease and chronic hypoperfusion generate lacunes and white matter lesions mainly in the frontal lobe in which the arterial and venous densities are embryologically low [107–109]. In BD, not only ischemia in the region perfused by the medullary artery but also watershed ischemia with the lenticulostriate and medullary arteries and perforating branch of the insular cortex are important causes. In this context, prevention of not only hypertensive small vessel disease but also chronic hypoperfusion is included in the treatment strategy.

4.8.2.4 Cortical Microinfarcts and Cognitive Decline

The involvement of cortical microinfarcts in cognitive impairment has recently been attracting attention from clinical, imaging, and pathological aspects [110, 111]. Reportedly, microinfarcts microscopically observed in the cerebral cortex are involved in cognitive decline. It has been reported that microinfarcts can be detected by carefully observing FLAIR, and cortical microinfarcts can be more clearly visualized using double inversion recovery (DIR) and 3-dimensional fluid attenuated inversion recovery (3D-FLAIR) on 3-Tesla MRI [111]. Mechanisms by which microinfarcts relate to dementia and cognition are currently unknown. Half of those with microinfarcts did not have macroscopic infarcts; in addition, the microinfarct effects were independent of other common pathologies. Association with cerebral amyloid angiopathy and the possibility of artery-to-artery embolic infarcts are considered, for which it may be essential to clearly visualize cortical microinfarcts on MRI and build up investigations of correspondences with clinical and pathological findings and risk factors [110, 111]

Figure 4.32 shows a female patient in her 80s with progressive cognitive impairment examined by MRI. Parietal lobe atrophy was clearly observed on T2-weighted imaging (Fig. 4.32a). When the FLAIR image was closely observed, small high-intensities were scattered in the cortex (Fig. 4.32a), and the presence of microcortical infarcts in this region was also pathologically confirmed (Fig. 4.32c), suggesting that these modified dementia of this patient. No other degenerative disease, such as Alzheimer's disease, was confirmed in this patient.

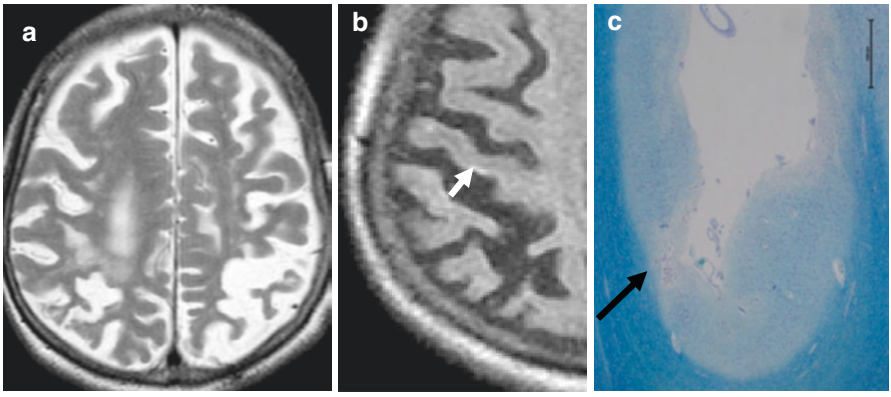

Fig. 4.32 80s female. Cortical microinfarct with progressive cognitive impairment. Parietal lobe atrophy was clearly observed on T2-weighted imaging (**a**). When the FLAIR image was closely observed, small high-intensities were scattered in the cortex (**b**), and the presence of microcortical infarcts in this region was also pathologically confirmed (**c**), suggesting that these modified dementia of this patient. No other degenerative disease, such as Alzheimer's disease, was confirmed in this patient

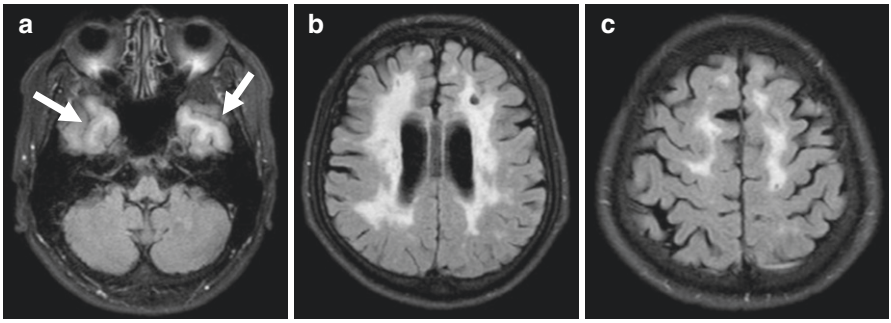

Fig. 4.33 CADASIL. 40s male with genetically proven CADASIL. He had a five-year history of memory disturbance, personality change, and hypertension. Gradually, he was suffered from deterioration of cognitive impairment and other symptoms including left-side hemiparesis. (**a**–**c**) Axial FLAIR images reveal characteristic abnormal findings including multiple white matter hyperintensities including anterior temporal pole (**a**: *arrows*), periventricular and deep white matter, and frontal deep white matter hypointensities suggestive of chronic ischemic changes and small infarctions. Courtesy of Dr. Keita Sakurai. A case of Medical College of Nagoya City University

4.8.2.5 Cerebral Autosomal Dominant Arteriopathy with Subcortical Infarcts and Leukoencephalopathy

Cerebral autosomal dominant arteriopathy with subcortical infarcts and leukoencephalopathy (CADASIL) is a representative autosomal dominant inheritance cerebral small vessel disease (responsible gene: NOTCH3). Lacuna infarction repeats without a risk factor of cerebrovascular disorder from a young age, and cerebral white matter lesions aggravate and lead to progressive dementia. On MRI, multiple lacuna infarcts were detected on T2-weighted imaging, and diffuse high-intensities were observed in the white matter on FLAIR. Lesions in the bilateral symmetric subcortical white matters in the temporal pole were characteristic to this patient (Fig. 4.33) [112]. Symmetric high-intensity lesions in the external capsule were also characteristic, but these may also be observed in Binswanger's disease [113].

Relative diseases of CADASIL include autosomal recessive inheritance (responsible gene: HTRA1) cerebral arteriopathy with subcortical infarcts and leukoencephalopathy (CARASIL). The disease concept has been established in Japan, and many cases were reported from Japan. Clinically, it is accompanied by early-onset baldness, spondylosis deformans, and progressive dementia, and the imaging findings are similar to those of CADASIL.

4.8.2.6 Hypoperfusion

Cognitive decline may result from global brain ischemia, and this may be caused by systemic circulatory disorders such as profound hypotension, obstruction of the major arteries, and high-grade stenosis. Figure 4.34 shows a male patient in his 70s with slowly progressive dementia. Atrophy progressed including the limbic system on MRI over 6 years, and no degenerative dementia, such as Alzheimer's disease, was observed in its background pathology. Severe stenosis of the bilateral internal

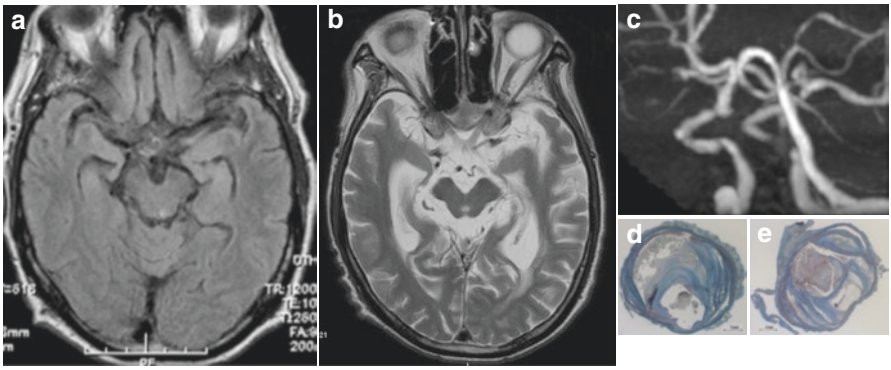

Fig. 4.34 Hypoperfusion. (**a**) FLAIR transverse image at 72 years old. (**b**) After 6 years, progression of atrophy including the limbic system was distinct, and cognitive decline aggravated during this period. (**c**) On MRA, high-grade stenosis of the bilateral internal carotid arteries was detected. (**d**, **e**) Pathologically, no degenerative dementia was detected, and only high-grade stenosis of the bilateral internal carotid arteries was confirmed

carotid arteries was confirmed, showing that hypoperfusion was likely to be involved in the progression of cognitive impairment and atrophy in this patient.

4.8.2.7 Hemorrhagic Dementia

Hemorrhagic lesions, including chronic subdural hematoma, sequelae of subarachnoid hemorrhage, and cerebral hematoma may produce vascular dementia. Cerebral amyloid angiopathy (CAA) is a common small vessel disease of the brain, characterized by the progressive deposition of amyloid-β (Aβ) in the walls of small to medium sized arteries (up to about 2 mm in diameter), arterioles and capillaries in the cerebral cortex and overlying leptomeninges, preferentially affect occipital regions for unclear reasons. In contrast with amyloid plaques found in Alzheimer's disease (AD), which are predominantly composed of the 42 amino acid residue fragment, the vascular amyloid in CAA is mostly composed of the more soluble 40 amino acid fragment, suggesting different pathophysiological mechanisms for pathological deposition [114]. When symptomatic, intracerebral hemorrhage (ICH) in the elderly is the most well-known manifestation of CAA (Fig. 4.35). In addition to typical acute cortical–subcortical ICH, CAA leads to various types of vascular lesions including chronic ICHs, microbleeds (MBs) (Figs. 4.36 and 4.37), subarachnoid hemorrhage (SAH), superficial siderosis (SS) (Fig. 4.38), microinfarction, CAA-related leukoencephalopathy [40, 115–117]. It is necessary for radiologists and clinicians to understand the wide spectrum of CAA-related imaging findings [40]. A prospective study conducted in Rotterdam showed that 5 or more microbleeds on T2*-weighted imaging are involved in cognitive decline excluding memory [118].

In addition to hemorrhagic complications, a syndrome of perivascular inflammation and leukoencephalopathy has been reported associated with CAA [119]. Pathologically, CAA-related inflammation reveals vascular amyloid deposition accompanied by perivascular, intramural, and/or transmural inflammatory changes

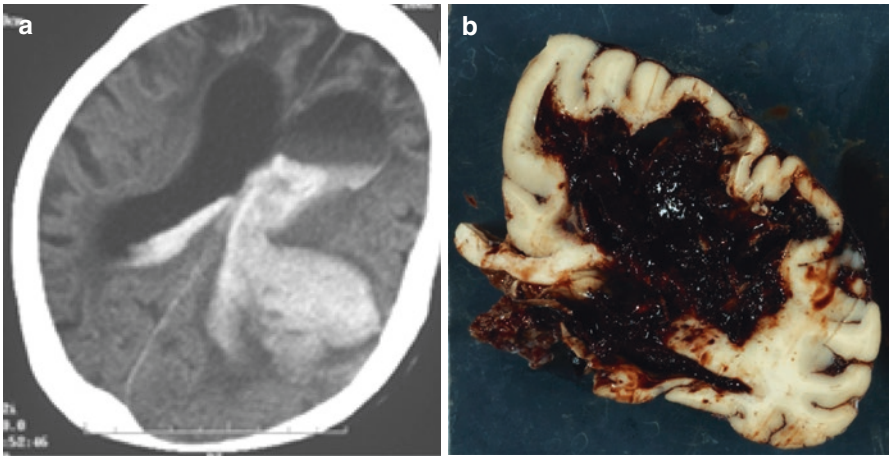

Fig. 4.35 CAA-related subcortical hemorrhage. Fetal CAA-related ICH with associated massive ventricular hemorrhage in a 92-year-old woman. (**a**) A CT scan revealed large left-sided parietal subcortical ICH extending into the left lateral ventricle. (**b**) A huge subcortical and intraventricular hematoma was identified on a macroscopic specimen at autopsy [117]

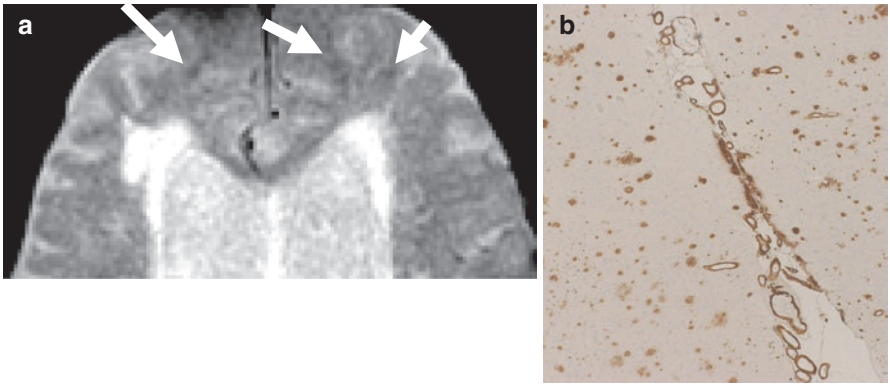

Fig. 4.36 70s male. Pathologically proven CAA-related microbleeds. Pathologically proved subcortical MBs with CAA. (**a**) An axial GRE T2*-weighted image showed multiple cortical–subcortical hypointense foci suggestive of CAA-related microbleeds (*arrows*). (**b**) A histopathological section of frontal lobe. Amyloid beta immunoreactive deposits were present in the leptomeningeal and cortical vessel walls of the frontal lobe

[120]. The white matter lesion is characterized by large confluent asymmetric areas of abnormal intensity extending to the subcortical white matter and occasionally the overlying cortical gray matter (Fig. 4.39). Compared with CT, these lesions are depicted more clearly on MRI, especially on the FLAIR sequence. These lesions involved one or more cortical territories, distributed approximately equally across the frontal, parietal, temporal, and occipital lobes without evident preferential laterality [121]. DWI and ADC maps can add further information suggestive of vasogenic

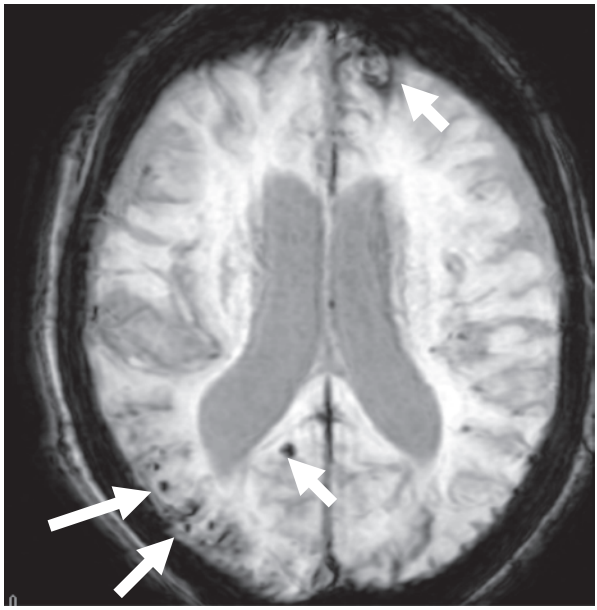

Fig. 4.37 80s F with memory disturbance. CAA-related microbleeds and subcortical hemorrhage. 3D T2* image showed multiple microbleeds in the right occipital lobe (*arrows*). Subcortical hemorrhage was also shown in the left frontal lobe (*arrowhead*)

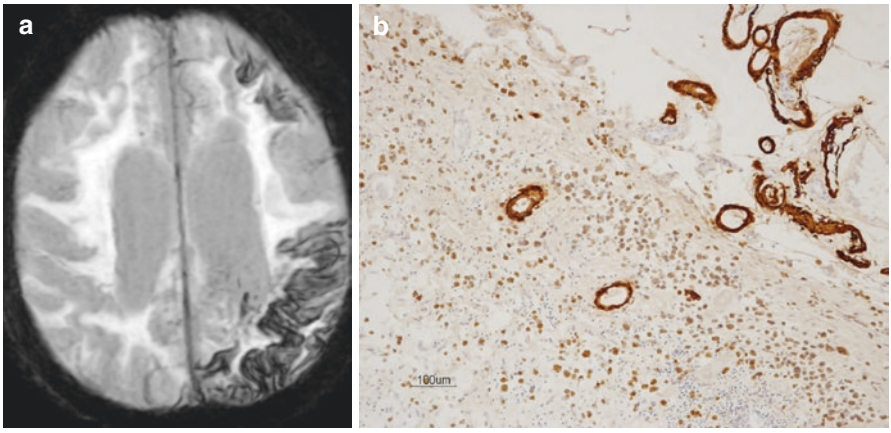

Fig. 4.38 90s M. Pathologically proven CAA-related superficial siderosis. (**a**) 3D T2*-weighted image demonstrated gyriform low signals along the left cerebral sulci. (**b**) Severe amyloid beta immunoreactive deposits were present in the leptomeningeal and cortical vessel walls of the parietal lobe (immunohistochemistry raised against monoclonal antibody Aβ 11–28) [117]

edema (Fig. 4.39). Because various pathologic conditions could manifest as multiple white matter lesions, the essential step in the diagnosis of CAA-related inflammation is the recognition of CAA. In other words, GRE (gradient echo) sequences including susceptibility weighted image (SWI) and principles of echo shifting with a train of observations (PRESTO) images which enable recognition of CAA-related MBs are fundamental to diagnose CAA-related inflammation noninvasively.

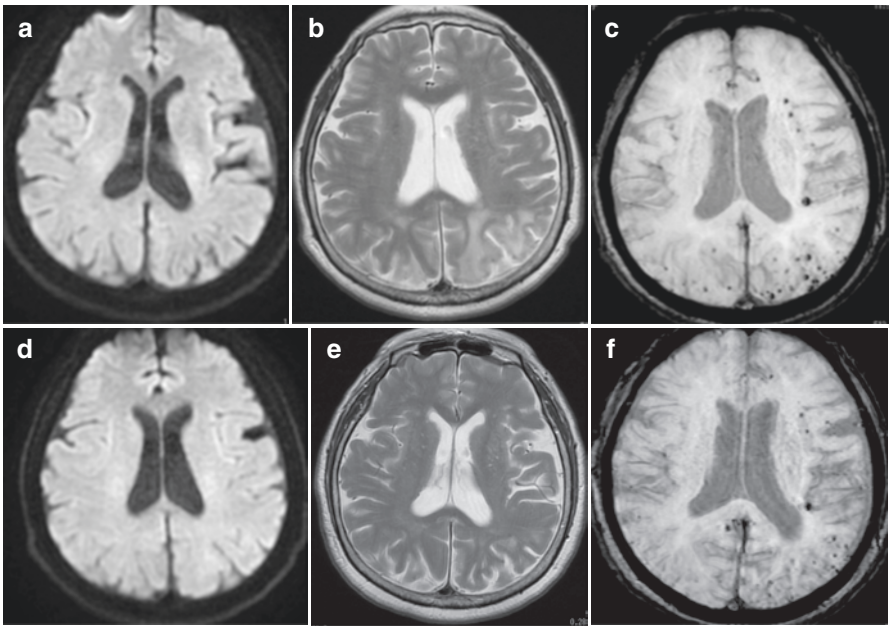

Fig. 4.39 70s F. CAA-related inflammation. CAA-related inflammation, MBs, and microinfarctions in a 70s female. (**a**) An axial DWI showed no obvious abnormal intensity. (**b**) Axial T2-weighted image showed confluent asymmetric hyper-intense lesions, which involved left dominant occipitoparietal cortices (*arrow*). Vasogenic edema was suggested. (**c**) 3D T2*-weighted image showed multiple MBs. (**d**–**f**) Seven months after a course of intravenous steroid therapy, an improvement in the white matter lesions was identified on a T2-weighted image (**e**, *arrow*). MBs in the left occipital regions decrease in number (**f**)

The apparent response of some patients to immunosuppressive/steroid therapy suggests that this disorder represents a treatable form of CAA, highlighting the importance of reaching this diagnosis in practice (Fig. 4.39).

VaD involves diverse pathologies, and making careful imaging diagnoses corresponding to individual cases is important. With progress in MRI technology, making visual diagnoses of cortical microinfarcts and diverse pathologies of the CAA became possible. Clarification of the causes of the individual pathologies by accumulating and analyzing imaging findings, clinical courses, and pathological findings is needed.

4.9 Treatable and Reversible Dementias

There are many reversible cases of dementia, and many of them show a rapidly progressing course for which a concept of rapidly progressive dementia has been proposed. Neuroimaging including MRI is useful for differentiation of dementia

which progresses in the acute to subacute phase and it plays an important role in differentiation of treatable and reversible dementias. This report reviews diseases for which MRI is useful for differentiation centering on treatable and reversible dementias.

Firstly, diseases causing rapidly progressive dementia edited by Mori et al. based on reports by Cummings et al. and Picchini et al. are shown in Table 4.5 [122–124]. (Vascular dementia is overviewed in 4.8.)

4.9.1 Infection

Central nervous system infections include those showing an acute course accompanied by fever and those in which cognitive decline and psychological symptoms slowly and progressively aggravate.

4.9.1.1 Sporadic Creutzfeldt-Jacob Disease (sCJD)

Creutzfeldt-Jacob disease was initially described as a disease group with neuropathological characteristics by German neuropathologists, Creutzfeldt and Jacob, in the early 1920s, and now, abnormal prion protein proposed by Prusiner of the USA who was awarded the Nobel Prize in Physiology or Medicine is widely accepted as its pathogen. Abnormal prion protein accumulates in the brain and impairs nerve cells, causing degeneration and necrosis of nerve cells and inducing the disease. It is classified into sporadic, hereditary, and infectious (bovine spongiform encephalopathy (variant), iatrogenic, and kuru) cases accounting for 80, 10, and 10% of cases, respectively.

sCJD is a prion disease characterized by spongiosis of the brain and abnormal prion protein accumulation. The cause of its development is unclear, but it is classified into six types (MM1, MM2, MV1, MV2, VV1, and VV2) based on the polymorphism of PrP gene codon 129 (methionine (M), valine (V)) and protease-resistant Western blot pattern. MM1 and MV1 cause rapidly progressive dementia, and myoclonus and periodic synchronous discharge (PSD) on electroencephalography are detected. There are characteristic imaging findings and these play an important role in deciding on the diagnosis. Since myoclonus, which is a clinical characteristic, occurs, control of body movement is often difficult in examinations, but it is desirable to suspect this disease in an early phase and perform MRI at an appropriate time-point. Diffusion-weighted imaging is the most useful for the early phase (Fig. 4.40) [125, 126]. A high intensity is detected along the cortex, and high-intensities are also detected in the thalamus and basal ganglia depending on the stage (Fig. 4.41). Unlike lesions of cerebral infarction, abnormal intensities on diffusion-weighted imaging protract for long time in Creutzfeldt-Jacob disease. In addition to the significance of these findings, diffusion-weighted imaging can be repeatedly performed without hesitation in patients with difficulty in controlling body movement because it employs high-speed acquisition, and this is an important advantage for course observation of this disease. On diffusion-weighted imaging, high-intensities are detected in the cortex, basal ganglia, and thalamus in an early

Table 4.5 Rapid progressive dementia [122–124]

VINDICATE!!!+P
*Vascular
Multiple cerebral infarctions
Strategic infarct
Microcortical infarct
Dural arterio-venous fistula
Dural thrombosis
Superficial siderosis
Carotid artery occlusion
*Infection
Creuzfeldt-Jacob disease
Viral infection
HIV encephalitis, AIDS, Herpes encephalitis
Limbic encephalitis, Japanese-B encephalitis
Progressive multifocal leukoencephalitis
Subacute sclerosing panencehpalitis
Brain abscess
Tuberculosis (Tb), fungi, toxoplasma, Parasites etc
Whipple disease
Mycotic meningitis (Cryptococcus, Candida, Aspergillus)
Tb meningitis
Lyme disease, neurosyphilis
*Neoplasm
Brain tumors (meningioma, glioma, malignant lymphoma)
Intravascular lymphomatosis
Cartinomatous meningitis
*Degeneratibe/metabolic
AD, DLB, PD with dementia, FTLD
Huntington disease
Senile tauopathy (PSP, CBD, GGT, Pick disease, NFTD, DG)
Multiple systemic atrophy (MSA), Adrenoleukodystrophy
Cerebral Amyloid Angiopathy
Neurodegeneration with brain iron accumulation: NBIA
*Pantothenate kinase-associated neurodegeneration*PKAN (Halllervorden-Spatz disease)
*Neuroferritinopathy
*Aceruloplasminemia etc
Hyperammonemic encephalopathy
Wilson disease
Uremia, Hemodialysis
Osmotic demyelination syndrome
Reversible posterior leukoencephalopathy syndrome (RPLS)
Hypoglycemic encephalopathy

Table 4.5 (continued)

Hypoxic ischemic encephalopathy
Wernicke encephalopathy (Thiamine deficiency)
Subacute combined degeneration of the spinal cord (Vitamine B12 deficiency)
Marchiafava-Bignami disease
Hepatic encephalopathy
*Intoxication
• Drugs which directly act on the central nervous system: Antipsychotics, hypnotics, sedatives, antianxiety drugs, antidepressants, antiepileptic drugs
• Anticholinergic action: Antiparkinsonian drugs, anticholinergic drugs for digestive diseases, drugs for urologic diseases (therapeutic drugs for overactive bladder), antiasthmatic drugs
• Antihistaminic action: Antiallergic agents, H2 receptor antagonistic drugs for digestive diseases
• Others: Adrenocortical steroid, sedatives (opioids, NSAIDs), drugs for circulatory diseases (antihypertensive drugs, antiarrhythmic drugs, diuretics, digitalis), antitumor drugs, antibiotics, antiviral agents
Chronic alcoholism
Heavy metals (mercury, lead, arsenic, thallium, manganese)
Poisonous and deleterious substances (trichloroethylene, toluene, carbon bisulfide, organic phosphorus)
Intermittent carbon monoxide poisoning
*Autoimmune
Autoimmune-mediated encephalitis/encephalopathy (paraneoplastic syndrome inducing limbic encephalitis/encephalopathy, anti-NMDA receptor encephalitis, anti-VGKC complex antibody-associated encephalitis [anti-LGI1 antibody encephalitis/anti-Casper2 antibody encephalitis])
Hashimoto encephalopathy (anti-NAE antibody limbic encephalitis)
lgG4-related diseases
Anti-phospholipid antibody syndrome
Systemic lupus erythematosus (SLE)
Neuro-Behcet disease
Sjögren syndrome
Rheumatoid arthritis
Vasculitis syndrome (aortic vasculitis syndrome, temporal arteritis, polyarteritis nodosa, granulomatosis with polyangiitis, microscopic polyangiitis)
Primary angiitis of the central nervous system (PACNS)
Multiple sclerosis (MS)
Acute disseminated encephalomyelitis (ADEM)
Neurosarcoidosis
Cogan's disease
*Trauma
Brain injury
Chronic subdural hematoma
*Endocrinopathy

(continued)

Table 4.5 (continued)

Chronic hypoadrenocorticism (Addison's disease)
Elderly-onset isolated ACTH deficiency
Panhypopituitarism
Hypothyroidism (myxedema)
Hyperthyroidism
Hypoparathyroidism
Hyperparathyroidism
Cushing's disease/Cushing's syndrome
*!atrogenic
Excess electroconvulsive therapy
Drug administration
*!diopathic
Idiopathic Normal Pressure Hydrocphelus
Aqueductal stenosis
Epilepsy (convulsive, non-convulsive)
Physical disease (Respiratory failure, arrhythmia, severe anemia, polycytemia)
Sleep disorder (Sleep apnea syndrome)
*!nheritance
CADASIL, CARASIL, falimiar CJD, Gerstmann-Straűssler-Scheinker syndrome

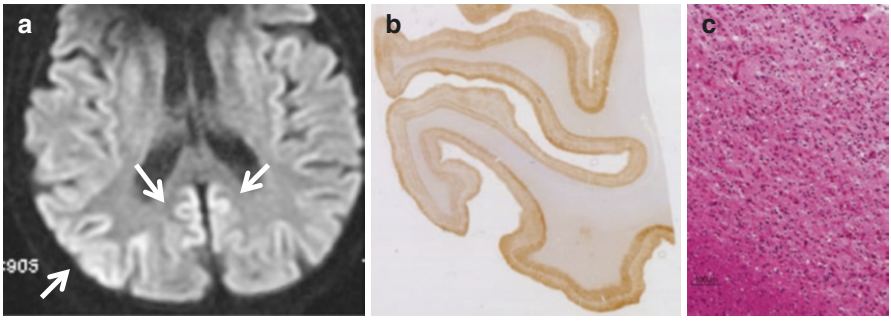

Fig. 4.40 80s F. CJD (Type MM1). Her initial symptom was visual disturbance with rapidly progressive cognitive disorder. (**a**) Diffusion-weighted image (DWI) shows high intensity in the bilateral occipital, temporal cortex (*arrow*). (**b**) Prion deposition in the cortex (*brown color*) is shown. (**c**) In the visual cortex, spongy changes are shown which is compatible with high intensity on DWI

phase, and high-intensities also appear in these regions on T2-weighted imaging and FLAIR. The abnormal intensity of the cortex may be localized, and laterality is clear in many cases [125, 127], whereas basal ganglia and thalamic lesions are bilaterally observed in many cases. Whole-brain atrophy rapidly occurs following changes in the intensity, and cortical thinning becomes marked. Sporadic

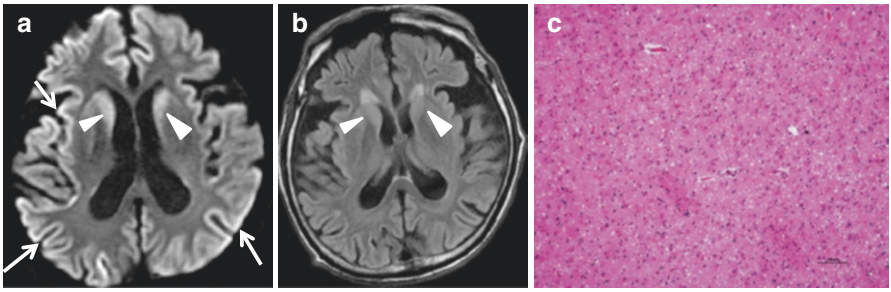

Fig. 4.41 70 M. CJD type MM1.Rapidly progressive dementia. (**a**) DWI shows high intensity along the bilateral cortices (*arrow*). Symmetrical high intensity is also shown in the caudate nucleus (*arrowhead*). (**b**) On FLAIR, faint high intensity is suspected in the caudate nuclei (*arrowhead*). (**c**) Spongy change is shown in the caudate nucleus

Creutzfeldt-Jacob disease was previously classified based on clinical symptoms and localization of imaging findings, but currently it is classified based on abnormal prion protein positivity. However, it may not necessarily be easy to diagnose it on the first examination, and it should be mentioned that some cases develop with visual disturbance [128]. Heidenhain-type Creutzfeldt-Jacob disease is known to develop with visual disturbance, and an abnormal intensity is detected in the occipital lobe corresponding to the clinical symptoms.

In bovine spongiform encephalopathy-associated variant Creutzfeldt-Jacob disease, a high intensity in the pulvinar is typical (pulvinar sign) [129, 130]. Lesions showing a high intensity on diffusion-weighted imaging to be differentiated include hypoglycemic, post-convulsive, and hypoxic-ischemic encephalopathies.

4.9.1.2 HIV-Associated Neurocognitive Dysfunction/Disorders

Regarding rapidly progressive dementia in the young, it is important to firstly differentiate HIV-associated neurocognitive dysfunction/disorders (HANDs) in addition to neuro-syphilis.

The term HANDs has been used to describe the spectrum of neurocognitive dysfunction/disorders associated with HIV infection. Despite entering the era of combination antiretroviral therapy (CART), HANDs remains prevalent, however, less severe forms of HANDs now predominate. Attention should be paid to that clinical symptoms are modified by treatment course, and cognitive disorder may rapidly aggravate at the time of turning to virus-negative and immune reconstitution [131–134].

Knowledge of the neuroimaging findings associated with HANDs, as well as the impact of the treatment on them, is important in treatment strategy.

As shown in Figs. 4.41 and 4.42 40s M HIV encephalopathy, atrophy is noticeable compared with the age, and nonspecific pale high-intensities are observed in the deep cerebral white matter on MRI T2-weighted imaging and FLAIR. U-fibers are retained in many cases, and changes in the intensity are not noticeable on

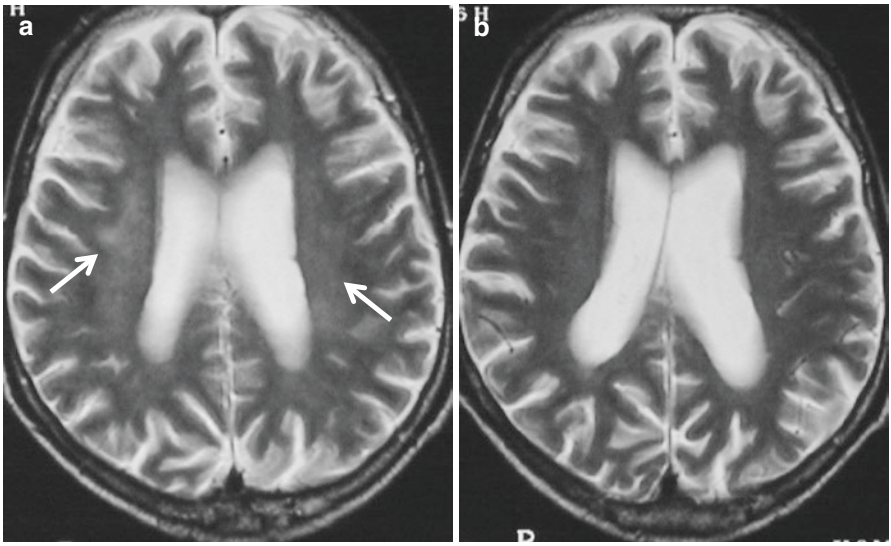

Fig. 4.42 40s M. HIV encephalopathy. (**a**) Atrophy is noticeable compared with his age. Mild hyperintensities are shown in the bilateral deep white matter before HAART therapy (*arrow*). (**b**) After HAART therapy, hyperintensities in the white matter disappear on T2-weighted image. (Courtesy of Prof. Terada H, Sakura Medical Center of Toho University). (From Jpn J Clin Radiol. 2008;53:743–760 (in Japanese) with permission)

T1-weighted imaging in many cases [133]. HIV encephalopathy does not result in mass effect or enhancement. If either of these findings is present, another diagnosis must be considered [133]. Diffusion tensor imaging depicts abnormalities in mean diffusivity and fractional anisotropy in the subcortical white mater, even when the white mater appears normal on conventional T1- and T2-weighted images [133, 135].

4.9.1.3 Neuro-Syphilis

Neuro-syphilis is a sexually transmitted disease caused by Treponema pallidum infection of the central nervous system, and diverse imaging findings are observed depending on the stage and pathology including meningeal vasculitis, gumma, and encephalitis. A resurgence of this entity has seen among the HIV-infected population.

On MRI, diverse findings may be observed, such as contrast enhancement of the meninx, chronic meningeal inflammation-induced hydrocephalus, granuloma formation, abnormal contrast enhancement of the cranial nerves, contrast-enhancing effect on the optic nerve, meninx-derived granuloma formation (gumma), and vasculitis-associated angiostenosis. Regions in which vasculitis-induced cerebral infarction frequently occurs include the basal ganglia (Nissle's endarteritis of the perforating branch) and middle cerebral arterial territory (Heubner's endarteritis). White matter lesions, such as those in the subcortex in the temporal lobe apex and insular gyri, are frequently observed in neuro-syphilis [132, 136] (Fig. 4.43).

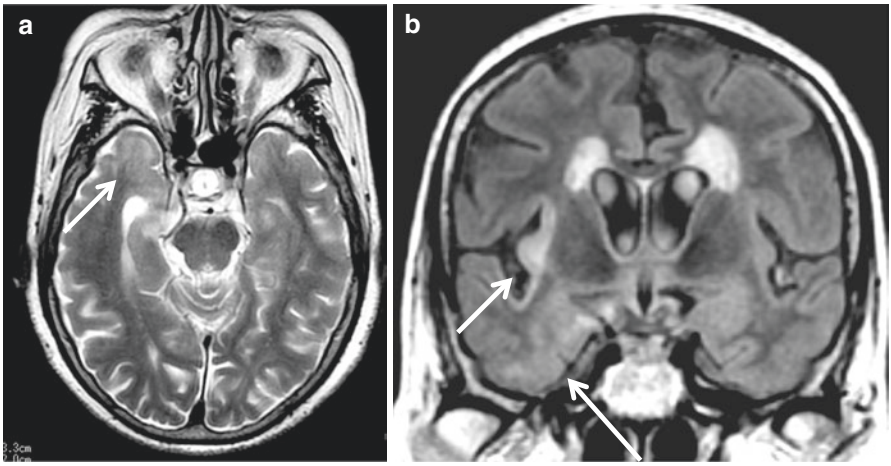

Fig. 4.43 80s F. Neuro-syphilis. Her chief complaint is memory disturbance. (**a**) T2-weighted image shows high intensity in the right dominant temporal white matter (*arrow*). (**b**) FLAIR image shows high-intensity lesions in the right insular cortex (*arrow*), right temporal area (*arrow*)

4.9.1.4 Progressive Multifocal Leukoencephalopathy

Progressive multifocal leukoencephalopathy (PML) is a progressive demyelinating disease caused by oligodendrocyte impairment by John Cunningham (JC) virus reactivated by reduced immunity [137]. HIV infection is important as an underlying disease, but malignant tumors, collagen disease, and post-organ transplantation also increase the risk of PML [138]. It also develops during the monoclonal antibody treatment course for multiple sclerosis. Patients with PML develop cognitive decline, altered mental status. Without appropriate treatment, patients have a progressive downhill course, with death occurring within 1 year of PML in 90% of cases [139].

Early diagnosis and treatment initiation lead to improvement of the vital prognosis and quality of life. Imaging findings vary among the stages, the main lesion is localized in the subcortical white matter, and lesions are laterally asymmetric in many cases. However, since oligodendrocytes are impaired, lesions may also be present in the basal ganglia and thalamus in which oligodendrocytes are present. On MR images, there are typically multifocal, asymmetric areas of T1 and T2 prolongation in the periventricular and subcortical white matter (Fig. 4.44). U-fiber involvement is frequently seen. Mass effect and hemorrhage are unusual [140, 141]. Early and advanced lesions may be mixed in one lesion. Contrast enhancement is normally not noticeable. In one study, 50% of the long-term survivors showed enhancement of PML lesions of MRI [135]. Enhancement has been considered to be related to the patient's ability to mount an inflammatory response; however, in a study of imaging-pathologic correlation, no correlation between enhancement of MRI and inflammation seen in pathologic specimens [140]. Other report suggests that the enhancement results from immune response to viral antigen [142].

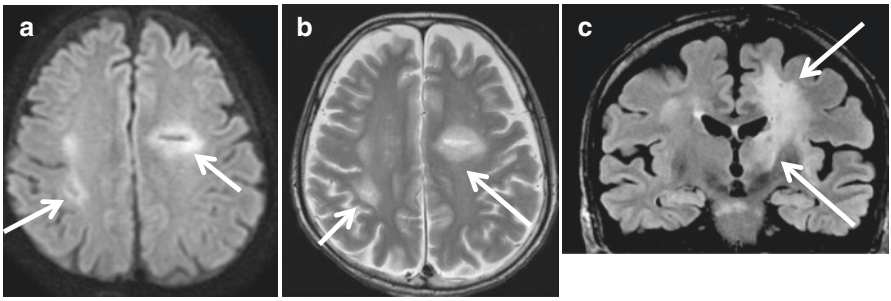

Fig. 4.44 Progressive multifocal leukoencephalopathy (PML). (**a**, **b**) Diffusion-weighted image (DWI) and T2-weighted image (T2WI) shows hyperintensity multifocal lesions in the white matter of both frontal lobes (*arrow*). (**c**) FLAIR image shows diffuse hyperintensity in the left frontal white matter, left basal ganglia devoid of marked swelling or mass effect (*arrow*)

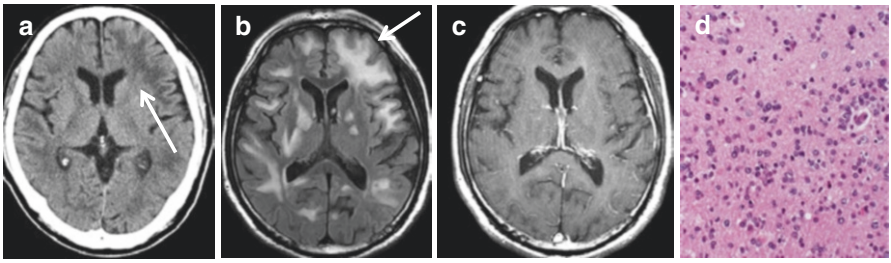

Fig. 4.45 70s M. Lymphomatosis cerebri (diffuse large B cell lymphoma). His chief complaint: Easy to fall, headache. Gradually progressive cognitive decline. (**a**) Axial CT shows low density in the left subcortical white matter. (**b**) FLAIR image shows diffuse high-intensity lesions in the bilateral white matter and basal ganglia associated with left frontal swelling (*arrow*). (**c**) No obvious enhancement is shown on post-contrast T1-weighted image (T1WI). (**d**) Tissue biopsy specimen (H & E stain) shows diffuse invasion of large B cell lymphoma. (From Jpn J Diagn Imaging. 2016;36:72–482 (in Japanese) with permission)

4.10 Other Forms of Dementia

4.10.1 Neoplasm

• A tumorous lesion with cognitive disorder is an initial symptom. It is necessary to accurately diagnose slowly progressive meningioma, gliomatosis cerebri, intravascular B cell lymphomatosis (IVLBL), and lymphomatosis cerebri. Lymphomatosis cerebri is a rare variant of malignant lymphoma, in which clinically progressive dementia and gait unsteadiness develop, and diffuse leukoencephalopathy without contrast enhancement is observed on MRI (Fig. 4.45).

IVLBL is a variant of primary malignant lymphoma of the central nervous system, and intravascular tumorous lymphocyte proliferation causes embolus symptoms. Clinically diverse courses, such as subacutely progressive cognitive dysfunction,

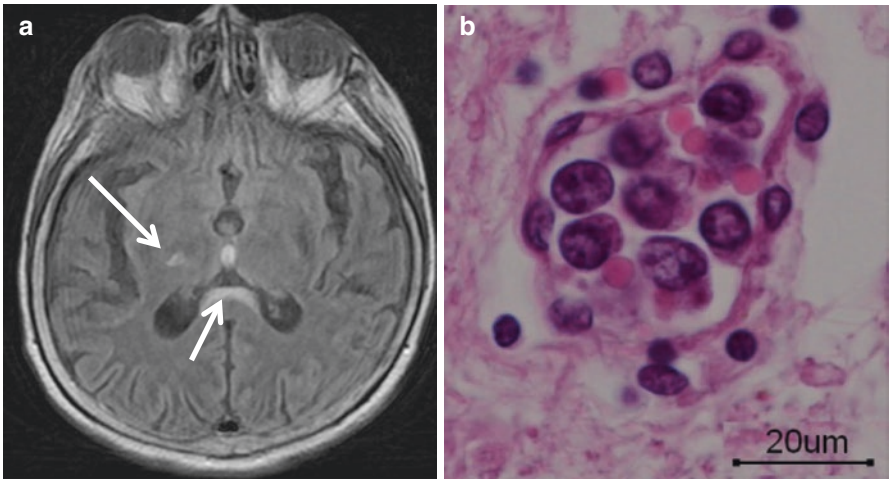

Fig. 4.46 70s M. Intravascular B cell lymphoma. His chief complaint: Rapidly progressive cognitive decline. (**a**) FLAIR image shows high-intensity lesions in the right thalamus and fornix (*arrow*). (**b**) H & E stain. Microscopic specimen in the fornix shows lymphoma cells in the vascular lumen

disturbance of consciousness, and headaches, are observed, and the prognosis is poor with rapid aggravation in many cases. An early diagnosis suspecting the disease is needed. It has recently been reported that the Western form is characterized by central nervous system infiltration and skin symptoms, and the Asian-variant with slight central nervous system and skin symptoms developing into pancytopenia and hepatosplenomegaly. Prostatic acid phosphatase (PAP) is expected to be a tumor marker [143]. It can be diagnosed by bone marrow biopsy because bone marrow infiltration is observed. On the other hand, the usefulness of random skin biopsy, which is simpler than bone marrow biopsy, has been reported [144]. MRI findings are diverse, including multiple variable infarction-like findings inconsistent with regions with arterial supply, nonspecific diffuse white matter lesions (Figs. 4.45 and 4.46), mass-like lesions, and meningeal enhancement. High intensity in the pons requiring differentiation from osmotic myelinolysis, which may be observed on T2-weighted imaging/FLAIR, is suggested to be due to venous congestion [145]. No contrast enhancement is usually observed, but it may be detected when there is extravascular advancement of tumor cells. Once proper diagnosis of IVL is determined by tissue biopsy, complete remission can be achieved by chemotherapy using R-CHOP [146, 147]. Recognition and careful interpretation of the findings on cerebral MR imaging may facilitate early diagnosis and intervention, and improve the prognosis of IVLBL.

4.10.2 Metabolic

Metabolic encephalopathy exhibits characteristic imaging findings due to metabolic abnormalities, and the imaging diagnosis is directly connected to the functional and vital prognoses.

4.10.2.1 Wernicke Encephalopathy (Thiamine Deficiency)

Wernicke encephalopathy occurs due to thiamine deficiency. The causes include chronic alcoholism, malignant tumor, long-term dialysis, long-term intravenous nutrition, anorexia nervosa, hyperemesis gravidarum, stomach surgery, malnutrition during a course of chemotherapy, and severe pancreatitis. On MRI, symmetric high-intensities are observed in the thalamus along the 3rd ventricle, hypothalamus, and region around the aqueduct of the midbrain on T2-weighted imaging and FLAIR (Fig. 4.47). Clinically, it develops as encephalopathy with impaired orientation and eye movement disorders because the eye movement center located at the medial side of the thalamus is impaired. Early thiamine administration may improve clinical and imaging findings (Fig. 4.48). In severe cases accompanied with mammillary body atrophy and necrosis, Korsakoff's syndrome accompanied by memory disturbance, retrograde amnesia, and allolalia develops.

4.10.2.2 Hypoglycemic Encephalopathy

Hypoglycemia can be induced by overuse of insulin or oral hypoglycemic agents, insulinoma, or other conditions such as sepsis, renal, or hepatic failure. Hypoglycemia can cause several neurological symptoms ranging from focal neurological deficits to permanent dysfunction or death. The prognosis of neurological sequelae of hypoglycemic encephalopathy depends on the severity and duration of hypoglycemia. Making an early accurate diagnosis and returning the blood glucose level to the normal range are important to improve the outcome.

If hyper-intense lesions are detected in white matter, such as in the corpus callosum, internal capsule, or corona radiata, and the hyper-intense lesions regress on follow-up images, the patient will likely recover without neurological deficit. Glucose replacement should be administered promptly, targeting euglycemia (Fig. 4.49). However, if lesions are detected with extensive cortical involvement (Fig. 4.50), the outcome will be poor [148–150]. Furthermore, frontal and parietal cortical involvement was correlated with a worse outcome than only white matter

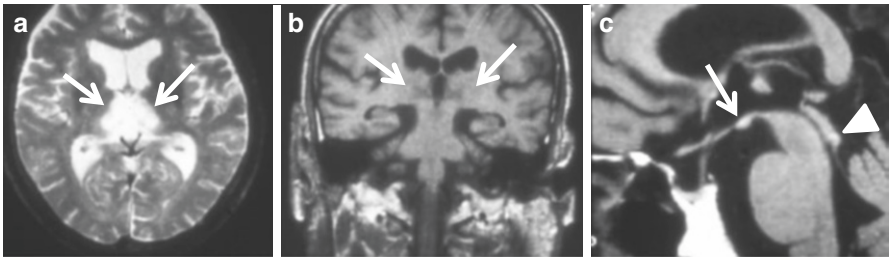

Fig. 4.47 50s M with chronic alcoholism. Wernicke encephalopathy with Korsakoff's syndrome. (**a**) T2-weighted image (T2WI) shows symmetrical hyperintensity in the thalamus along the third ventricle (*arrow*). (**b**) T1-weighted image shows symmetrical low intensity in the medial thalamus (*arrow*). (**c**) Post-contrast T1-weighted image shows enhanced lesions in the mammillary body (*arrow*) and inferior colliculus (*arrowhead*). (From Toyoda K eds. *Maruwakari toukeibu ryouikino gasoushindan* (in Japanese). Tokyo: Gakken Medical Shujunsha, 2015. p. 208–209 with permission)

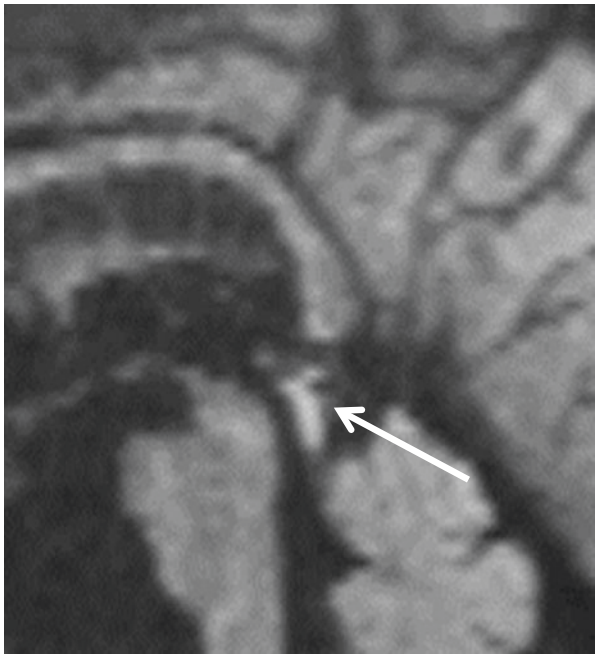

DWI (b=1000)

Fig. 4.48 40s M with thiamine deficiency. Wernicke encephalopathy. On emergency MRI, diffusion-weighted image (DWI) shows hyperintensity in the quadrigeminal plate (*arrow*). His clinical symptom improved after early parenteral thiamine therapy. (From Toyoda K eds. *Maruwakari toukeibu ryouikino gasoushindan* (in Japanese). Tokyo: Gakken Medical Shujunsha, 2015. p. 208–209 with permission)

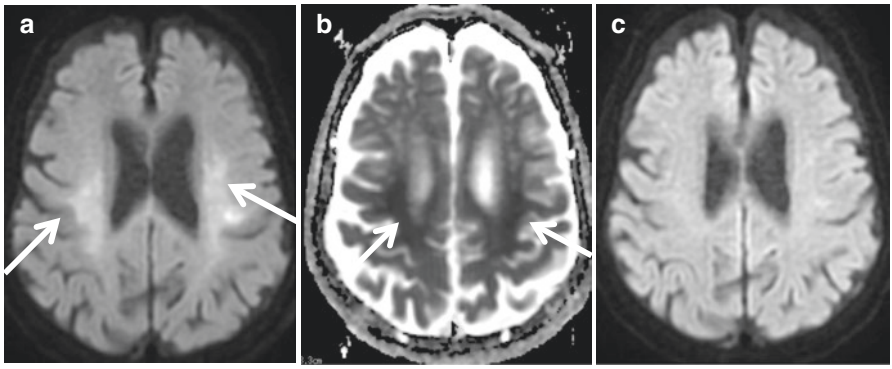

DWI (b=1000)
BS=33

ADC map
BS=33

DWI (b=1000)
After glucose replacement

Fig. 4.49 70s F with consciousness disturbance. Hypoglycemic encephalopathy. (**a**, **b**) Diffusion-weighted image (DWI) shows symmertrical high intensity in the frontal white matter with low intensity on apparent diffusion coefficient (ADC) (*arrow*). (**c**) She recovered after prompt glucose replacement clinically. DWI shows disappearance of abnormal high intensity in the frontal white matter

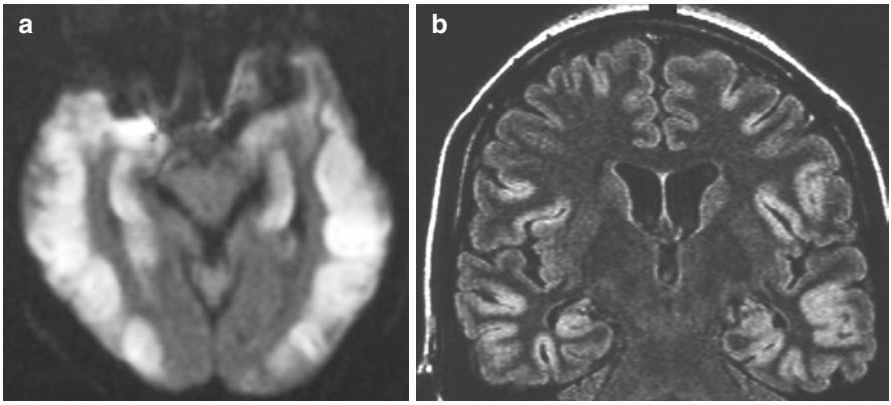

Fig. 4.50 20s F. Hypoglycemic encephalopathy induced by overuse of insulin. (**a**) Diffusion-weighted image (DWI) shows hyperintensity lesion in the bilateral cortices and hippocampus with swelling of cortices. (**b**) 3 week after DWI. FLAIR coronal image shows hyperintensity in the hippocampus with extensive cortical involvement

involvement, but with a better outcome than diffuse cortical involvement or basal ganglia involvement [151].

4.10.3 Posticteric Encephalopathy, Epilepsy, Convulsion

The incidence of epilepsy, including symptomatic (structural/metabolic) epilepsy [152], is high in children and the young, but an increase in initial epilepsy cases in the elderly with progression of the aging society has become a hot topic [153]. It has been reported that the prevalence is almost equivalent in all generations aged 65 years or older, but the incidence increases with aging [153]. Central nervous system diseases developing with aging newly cause structural/metabolic (symptomatic) epilepsy. As the treatment strategies are prepared based on the cause of disease, it is necessary to recognize the differences that depend on the age at imaging diagnosis.

The population is aging worldwide and the incidence of epilepsy rapidly rises at 70 years old or older. The frequent causes of disease are malformation of the cerebral cortex, perinatal disorder, and tumors with a high complication rate in children and the adolescent, whereas neurodegenerative diseases, such as cerebrovascular disorder (30–40%), head injury, Alzheimer's disease, and brain tumors increase with aging. Amyloid angiopathy exhibits diverse imaging findings, such as subcutaneous hemorrhage, subarachnoid hemorrhage, related inflammatory pathology, and microhemorrhage, and these should be taken into consideration as a cause of acute symptomatic seizures and symptomatic (structural/metabolic) epilepsy in the elderly. Disturbance of consciousness, aphasia, paralysis, and dementia may develop at the forefront and delay a diagnosis of epilepsy. The

recurrence rate after the first seizure is higher than that in young patients. Moreover, complications by acute myocardial infarction accompanying status epilepticus and acute coronary insufficiency have been reported, requiring clinical attention different from that for the young. In dementia with background epilepsy, the cognitive disorder may be improved by appropriate treatment with antiepileptic agents.

The first-line diagnostic imaging for epilepsy is MRI, but CT is superior in evaluating calcified lesions. For tumors accompanied with calcification, vascular malformation, or tuberous sclerosis, CT is added.

Regarding the cause of symptomatic epilepsy, when no lesion can be detected by CT, MRI is selected as the emergency examination requested by the emergency department. Differentiation of encephalitis, encephalopathy, intoxication, and encephalopathy after convulsion with background acute systemic disease is important for survival and to prevent the transition to epilepsy.

Hippocampal sclerosis in the elderly was described in 1.4. In symptomatic epilepsy cases, several causes of disease may be present. The presence of other causes of hippocampal sclerosis is termed dual pathology of hippocampal sclerosis, and it is necessary to note several pathologies, especially for complication by hippocampal sclerosis. Status epilepticus may be accompanied by hippocampal swelling and a high intensity on diffusion-weighted imaging, but this cannot be judged as hippocampal sclerosis. However, progressed hippocampal atrophies and cognitive decline develop during follow-up after convulsion in some cases. This is important for follow-up of symptomatic epilepsy.

Encephalopathy after convulsion develops due to local vascular dilatation in the brain accompanying the convulsive seizure, which increases cerebral blood flow, but demands for oxygen and glucose exceed the increase in blood flow. This disease represents brain injury caused by relative lack of oxygen and glucose. It is caused by status epilepticus with convulsions persisting for one hour or longer, and 30 min or longer in many cases of adults and infants, respectively, and its development markedly influences quality of life and functional outcomes. Differentiation of encephalopathy after convulsion from other pathologies causing convulsions, such as limbic encephalitis, hypoglycemic encephalopathy, hypoxic-ischemic encephalopathy, and Creutzfeldt Jakob disease, is often difficult.

Imaging findings include high-intensities accompanied by swelling of the hippocampus, cerebellum, amygdala, thalamus, and cortex on T2-weighted imaging and FLAIR (Fig. 4.51). The presence or absence of high intensity and reduction of ADC in the acute phase on diffusion-weighted imaging are different among cases. Inconsistency with the vascular territory is an important point of differentiation from acute-phase cerebrovascular disorder. An increase in blood flow may be detected by cerebral blood flow SPECT in the acute phase. The presence of transient cases is known, but a high intensity can be detected by T1-weighted imaging when cortical necrosis occurs (Fig. 4.51). The course and pathology of pediatric status epilepticus-type encephalopathy are markedly different from those in adults. A biphasic pattern may be observed in both clinical and imaging findings. MRI findings are diverse depending on the severity and timing, such as that some cases are not accompanied by any cortical lesion, and

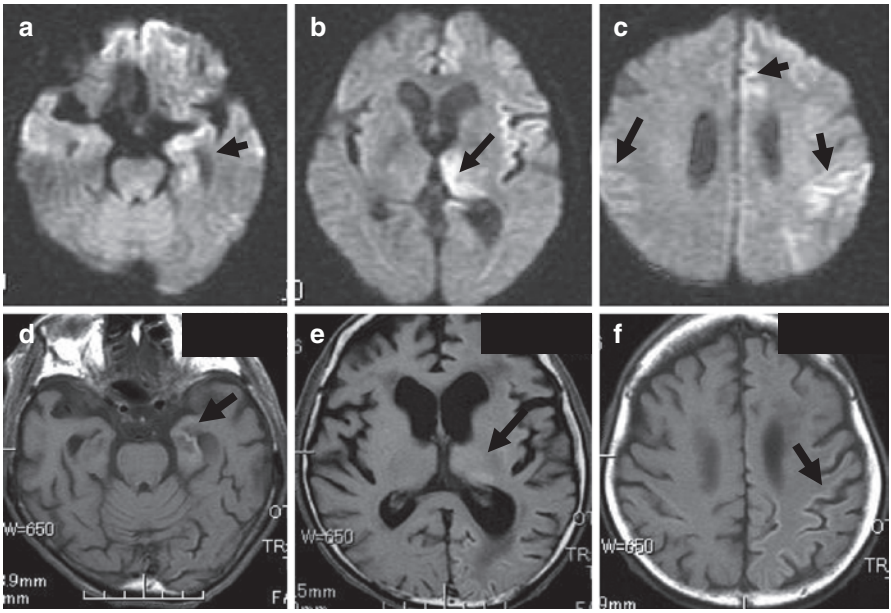

Fig. 4.51 70s F. Posticteric hypoxic encephalopathy. Status epilepticus. (**a**–**c**) Diffusion-weighted image (DWI) shows high-intensity lesion in the left hippocampus, amygdala, thalamus, and cerebral cortex (*arrow*). (**d**–**f**) T1-weighted image (T1WI) shows high intensity in the left hippocampus, thalamus, frontal and parietal cortices representing cortical necrosis (*arrow*). Hosoya T et al. eds. Nou no MRI. (in Japanese). Tokyo: Medical Science International. p. 890 with permission)

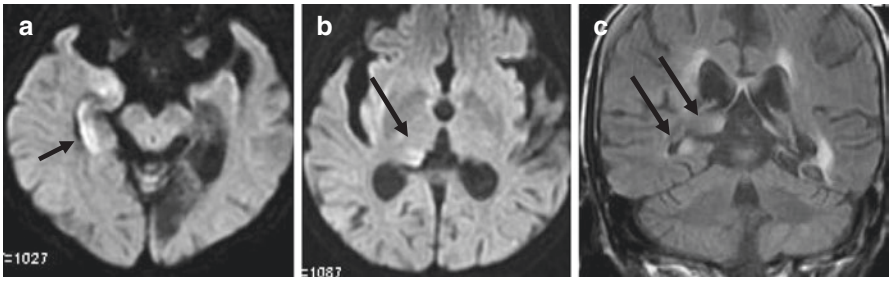

Fig. 4.52 70s female. Memory disturbance after convulsion. MR images acquired when status epilepticus occurred. (**a**–**c**) No extensive abnormality was detected in the cortex, and high-intensities were detected in the right thalamus and hippocampus on diffusion-weighted imaging and FLAIR. After sedation of convulsion, marked cognitive hypo-function, mainly memory defects, was observed compared with before the onset

lesions are localized in the hippocampus in others [154] (Fig. 4.52). It is not rare in the elderly for cognitive disorders to develop in the forefront, while convulsive seizures cannot be clinically observed. Careful interpretation of MRI findings is clinically useful.

4.10.4 Intoxication

As shown in Table 4.5, there are diverse causes of intoxication-associated encephalopathy such as taking medicine aiming at suicide, drug abuse, accidents, occupational exposure, and adverse drug reactions. It is easy to make a diagnosis when the condition of the development can be accurately clarified, but accurate clarification of the condition by an interview is difficult in many cases. Intoxication should be included in differential diagnosis when consciousness is markedly disturbed and cognitive disorder acutely aggravated in healthy young adults, in addition to cases suspected as intoxication based on the condition at the onset time.

Only nonspecific leukoencephalopathy develops in many cases, and making a diagnosis by MRI may be difficult, but specific MRI findings may be observed depending on the causative substance of intoxication. It is important to make an imaging diagnosis while judging the clinical condition and taking clinical information into consideration.

4.10.4.1 Carbon Monoxide (CO) Intoxication

Carbon monoxide is a colorless, odorless gas produced as a by-product of combustion. CO is the leading cause of poisoning injury and death worldwide. Once CO is inhaled, it binds with hemoglobin to form carboxyhemoglobin (COHb) with an affinity 250-times greater than oxygen, which causes reduced oxygen-carrying capacity and decreased release of oxygen to tissues, leading to tissue hypoxia. The initial symptoms of CO exposure when COHb is 15–30% are nonspecific and include headache, dizziness, nausea, fatigue, and impaired manual dexterity. Following resolution of acute symptoms, there may be a lucid interval of 2–40 days before the development of delayed neurological sequelae with diffuse demyelination in the brain, accompanied by lethargy, behavior changes, forgetfulness, memory loss, and parkinsonian features.

On acute MRI, necrosis in the globus pallidus is most commonly observed. Symmetrical hyper-intensity is observed in the globus pallidus on T2-weighted imaging and FLAIR [155]. On the other hand, delayed neurological sequelae develop in some cases in which clinical symptoms re-aggravate after the lucid interval (Fig. 4.53). No abnormality or only mild findings on MRI are observed in the early phase, but high-intensity white matter lesions expand with aggravation of neurological manifestation on T2-weighted imaging and FLAIR, exhibiting diffuse white matter lesions (Figs. 4.53 and 4.54). For CO intoxication cases, periodic follow-up by MRI while paying attention to the course of neurological manifestation is necessary after surviving the acute phase [155–157] (Figs. 4.53 and 4.54).

4.10.5 Autoimmune

Autoimmune encephalitis causes subacute deficits in memory and cognition, often followed by a suppressed level of consciousness. Autoimmune limbic encephalitis may occur as a paraneoplastic phenomenon associated with tumors or may occur in the absence of a neoplasm [158–160]. It is roughly divided into two groups. One is

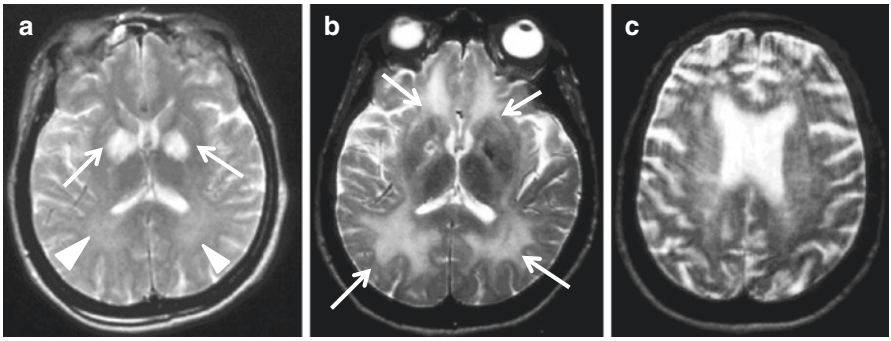

Fig. 4.53 30s F. The course of CO intoxication. (**a**) Symmetric high-intensities are observed in the bilateral globus pallidus in the acute phase of CO intoxication on T2-weighted imaging (T2WI) (*arrow*). A pale high intensity was suspected in the white matter, but it was not clear (*arrowhead*). (**b**) When the consciousness level aggravated after 2 weeks, diffuse high-intensities were present extensively in the bilateral white matter (*arrow*). (**c**) One year later, severe atrophy occurred. Severe cognitive dysfunction and Parkinson's symptoms protracted. (From Aoki S et al. eds. *Yokuwakaru nou MRI* 3rd ed. Tokyo: Gakken Medical Shujunsha. 2012. p. 544–545 with permission)

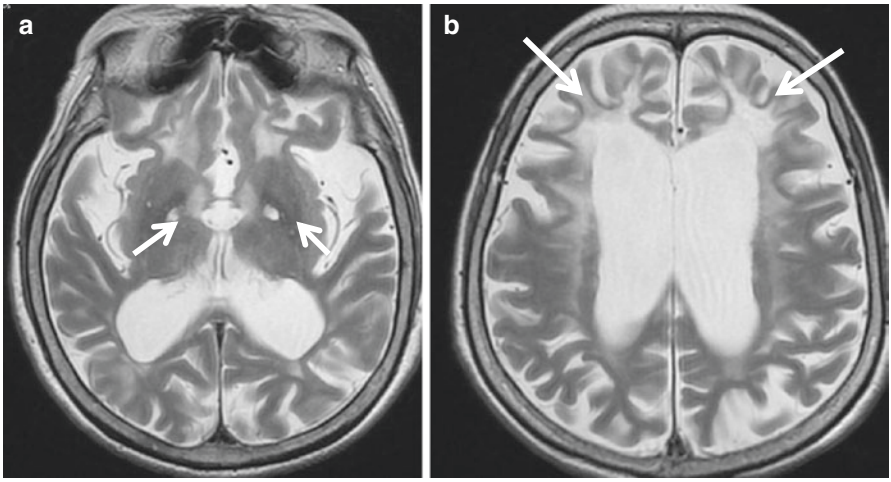

Fig. 4.54 70s F. Chronic phase of CO intoxication. Three years had passed after the onset. Cognitive dysfunction aggravated compared with before onset. (**a**) T2-weighted image (T2WI) shows symmetrical high intensity in the bilateral globus pallidus (*arrow*). (**b**) T2WI shows diffuse high intensity in the frontal lobe-dominant white matter (*arrow*). Atrophy clearly observed in regions with severe white matter lesions

cases with poor prognosis, related to antibodies to intracellular antigens such as anti-Hu, anti-CV2, anti-Ta, anti-Ma2, and anti-Yo [161]. The second group involves auto-antibodies to extracellular epitopes of ion channels, receptors, and other associated proteins such as the Anti-N-methyl-D-aspartate receptor (anti-NMDAR) and

voltage-gated potassium channel complex (VGKC). The tumor associations are variable, and the prognosis tends to be better. Autoimmune testing is extremely important for the proper diagnosis of autoimmune encephalitis. It is important to diagnose tumors associated with autoimmune encephalitis promptly for several reasons. First, treating the relevant tumor is thought to be helpful for treating the autoimmune encephalitis. Second, tumor therapy and therapy for the autoimmune encephalitis may need to be given simultaneously. Third, steroid therapy, such as rituximab or cyclophosphamide, may complicate tumor diagnosis, especially in the case of tumors such as malignant lymphoma.

4.10.5.1 Anti-N-Methyl-D-Aspartate Receptor Encephalitis

Anti-N-methyl-D-aspartate receptor (Anti-NMDAR) encephalitis is a treatment-responsive encephalitis associated with IgG antibodies against the GluN1subunit of the NMDAR [162–166]. The antibodies are detected in the CSF/serum of young women with ovarian teratoma, who typically develop schizophrenia-like psychiatric symptoms, usually preceded by fever, headache, or viral infection-like illness. After reaching the peak of psychosis, most patients develop seizures followed by an unresponsive/catatonic state, decreased level of consciousness, central hypoventilation frequently requiring mechanical ventilation, orofacial-limb dyskinesias, and autonomic symptoms [162–164]. The antibodies were initially found only in young women with teratoma in the ovaries. However, recent studies demonstrate that this disorder can occur even in the absence of teratoma, and even boys and adult men have been affected [165].

MRI studies are often mild, transient, and nonspecific, preferentially seen in T2-weighted imaging/FLAIR, usually involving cortical and subcortical regions of the brain and hippocampus, but sometimes affect the basal ganglia (Fig. 4.55). Brain MRI is usually unremarkable, but focal enhancement or medial temporal lobe abnormalities may be observed. The CSF exhibits nonspecific changes. EEG often

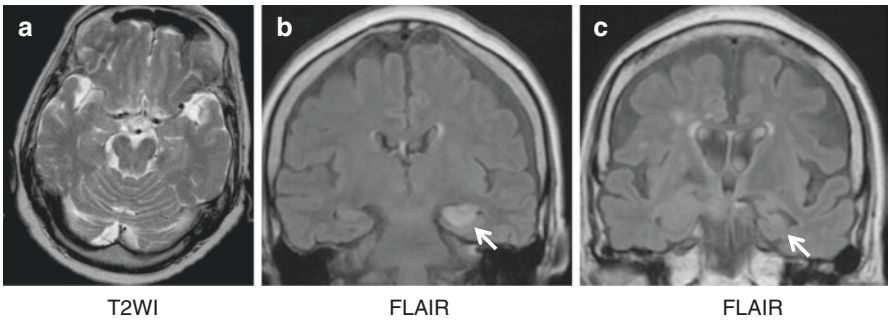

Fig. 4.55 70s F. Anti-NMDAR encephalitis. (**a**) T2-weighted image (T2WI) shows no obvious abnormality when consciousness disturbance and abnormal behavior occurred. (**b**) On MRI performed when consciousness disturbance protracted 2 months after the onset, high intensity with swelling is shown in the left hippocampus on FLAIR (*arrow*). (**c**) One year after the onset. FLAIR shows atrophic change of left hippocampus (*arrow*). Severe consciousness disturbance remitted, but memory deficits protracted

demonstrates diffuse delta slowing without paroxysmal discharges despite frequent bouts of seizures. Although the symptoms are severe, only 35% of the patients have abnormal brain MRI at disease onset, increasing to 50%, when the entire course of the disease is considered [164, 166, 167]. Current studies indicate that patients with anti-NMDAR encephalitis may develop demyelinating disorders as concurrent or independent episodes. Testing for AQP4 and MOG antibodies often helps to recognize these associations. When demyelination-like changes are observed on MRI, it is necessary to consider the presence or absence of complex autoimmune abnormalities [166].

Figure 4.55 shows anti-NMDAR encephalitis in a female in her 70s. No abnormality was identified on MRI when disturbance of consciousness and abnormal behavior occurred. On MRI performed when disturbance of consciousness protracted 2 months after the onset, high intensity and swelling was observed in the left hippocampus on FLAIR. After approximately 1 year, the abnormal intensity in the hippocampus disappeared, but atrophy progressed. Severe disturbance of consciousness remitted, but memory deficits were clear and protracted. No pelvic tumor was observed on abdominal CT.

4.10.5.2 Hashimoto Encephalopathy (Anti-NH2-Terminal of a-Enolase (NAE) Limbic Encephalopathy)

Hashimoto encephalopathy (HE) is associated with autoimmune thyroiditis and is considered to be an autoimmune disorder. HE manifests with a wide range of clinical symptoms including behavioral changes, confusion, and cognitive impairment, which sometimes mimics a prion disease [168–170]. HE may develop although the thyroid function is normal. Measurement of thyroid antibodies and the specific diagnostic marker, anti-NAE antibody, is useful for diagnosis. Most HE patients respond well to steroid therapy [171, 172]. Clinical improvements are also observed with IV immunoglobulin and plasmapheresis. Evidence of vasculitis was obtained by biopsy in some reported cases, but vasculitis was absent in others, demonstrating that the pathology of HE has not been clarified.

MR images are usually unremarkable, but diverse MR findings were also reported (Fig. 4.56). Diffusion-weighted image (DWI) is able to detect small, active ischemic lesions that are not detected by conventional MR imaging [171, 173, 174]. These DWI changes are also seen in CNS vasculitis and improve with treatment. In addition, cerebellar and brain stem lesions, cerebellar atrophy, and nonspecific leukoencephalopathy requiring differentiation from limbic encephalitis, tumors, granuloma, and infections have been reported [175–178].

Although it is difficult to identify HE based on diverse MR findings, consideration and recognition of HE are important for differential diagnosis of subacutely progressing cognitive impairment because some cases are steroid-responsive.

4.10.5.3 Neuropsychiatric Lupus Erythematosus (NPSLE)

SLE is a chronic, relapsing-remitting systemic disease characterized by loss of immune tolerance resulting in auto-antibody production with immune complex deposition. Females are more predisposed, with a female to male ratio that ranges

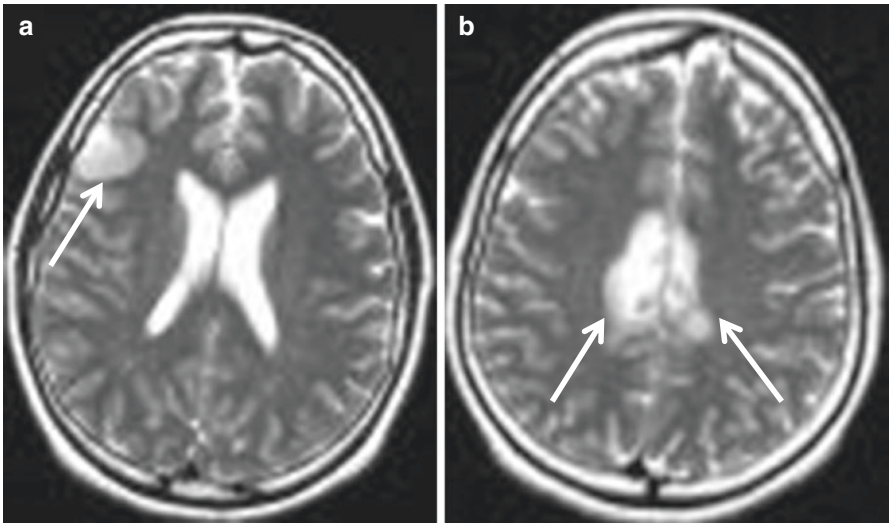

Fig. 4.56 20s F. Hashimoto encephalopathy. (**a**, **b**) T2WI shows multiple high intensity in bilateral frontal cortices (*arrow*). (Courtesy of Dr. Shiraga N. Department of Radiology, Toho University). (From Jpn J Clin Radiol. 2005;50:480–490 (in Japanese) with permission)

from 7:1 to 15:1. Patients with NPSLE have worse outcomes with those with systemic lupus erythematosus. NPSLE has been divided into cerebrovascular disease, cognitive dysfunction, seizures and psychosis, and peripheral nervous system disorders [179–182]. NPSLE should be considered as a potential differential diagnosis for patients with seizures and cognitive decline.

The cause of the disease has not yet been established. Associations with antinuclear antibodies, anti-DNA antibodies, anti-Ro, anti-La, anti-RNP, NMDAR, and antiphospholipid antibodies have been reported, and defective apoptosis, involvement of cytokines, T-cell receptor dysfunction, and leukocyte embolus formed due to complement activation were described. It is considered that the disease develops through the involvement of chromosome 1,1q23-24 and ultraviolet light, crystalline silica, and EB virus infection as environmental factors in the immunologic abnormality-associated diverse pathology in a complex manner [183, 184]. Regarding impairment of the central nervous system, impairment through reactions of lupus antibodies with DNA and the N-methyl-D-aspartate (NMDA) receptor has been reported.

NPSLE exhibits several types of brain lesions including global ischemic changes, parenchymal edema, microhemorrhages, glial hyperplasia, diffuse neuronal/axonal loss, resolved infarction, embolic microthrombi, blood vessel remodeling, acute infarction, acute macrohemorrhages, and resolved intracranial hemorrhages. Lesions due to perivascular inflammatory cell infiltration and vascular wall disorder cause small infarction, small hemorrhage, and perivascular inflammation, as well as subsequent thrombus formation. Lesions suggesting perivascular inflammation observed in the white matter were macular lesions demonstrating a high intensity on

T2-weighted imaging and FLAIR in many reports. Lesions occasionally exhibit contrast enhancement, which may be accompanied by perivascular and meningeal contrast enhancement, hinting at the pathology. Leukoencephalopathy, transverse myelitis, and aseptic meningitis have also been reported [185–191]. Antiphospholipid syndrome (APS) is characterized by antiphospholipid antibodies (aPL). A high incidence of thrombosis in complicated cases has been reported. In general, the size of blood vessels impaired by SLE is the capillaries to small and medium blood vessel levels, but large vessels may be occluded in antiphospholipid syndrome, which should be noted [186, 191–196]. Cytotoxic or vasogenic edema is mixed depending on the stage or activity of lesions. Application of diffusion tensor imaging (DTI) and brain networks to make an early diagnosis of NPSLE, as well as to judge the treatment course and prognosis has recently been reported, and advanced neuroimaging is expected to play a role as an objective biomarker of structural and metabolic abnormalities in the brain in patients with NPSLE who appear normal on conventional MRI [197–200].

Figures 4.57, 4.58, 4.59, and 4.60 show diverse MRI findings of NPSLE, such as hemorrhage and infarction, in cases complicated by APS, arterial stenosis, nonspecific white matter lesions, and limbic encephalitis [201]. Figure 4.61 shows a female SLE patient in her 50s with headache, vomiting, and treatment-resistant skin eruptions. Irregular-shaped lesions demonstrating a heterogeneous low intensity were observed in the left thalamus on T2-weighted MRI. These were accompanied by multinodular contrast enhancement on T1-weighted imaging, and the disease was deep mycosis. The patient had been treated with steroids for SLE for a prolonged period, suggesting opportunistic infection. Many cases had been through a long-term course, which may require consideration of treatment modification.

NPSLE as well as CNS lesions of autoimmune disease, such as CNS sarcoidosis, neuro Behçet's disease, anti-neutrophil cytoplasmic antibodies (ANCA) related angitis, IgG4 related disease, and primary angitis of the central nervous system (PANCS), demonstrates diverse nonspecific findings, and strong statements have

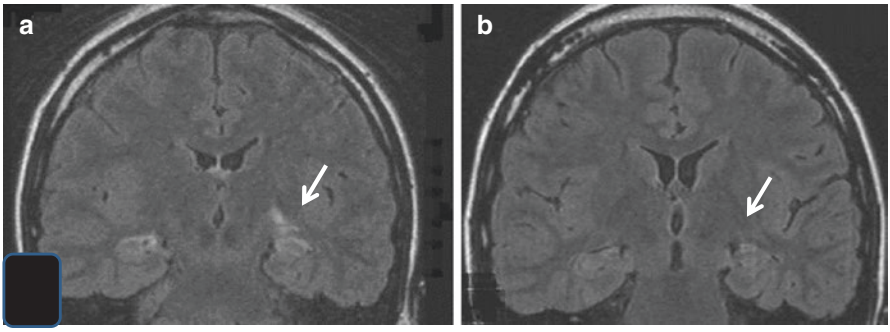

Fig. 4.57 30s F with memory disturbance. NPSLE. (**a**) MRI was acquired when memory disturbance occurred. FLAIR coronal image shows high-intensity lesions in the left lateral thalamus (*arrow*). (**b**) Three weeks after steroid therapy, high signal intensity in the thalamus disappears

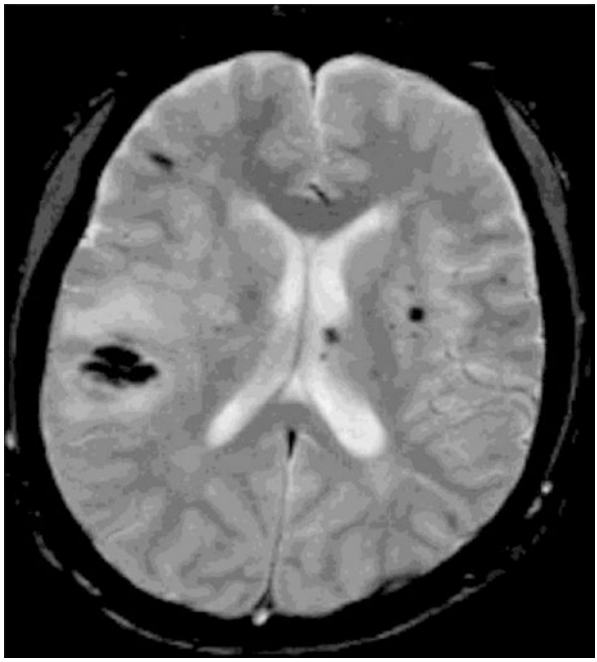

Fig. 4.58 30s F with SLE accompanied by antiphospholipid syndrome. T2*-weighted image shows multiple, heterogeneous low intensity lesions in the right frontal, temporal subcortical region, left thalamus, basal ganglia. (from Aoki S et al. eds. *Yokuwakaru nou MRI* 3rd ed. Tokyo: Gakken Medical Shujunsha. 2012. p. 556–557 with permission)

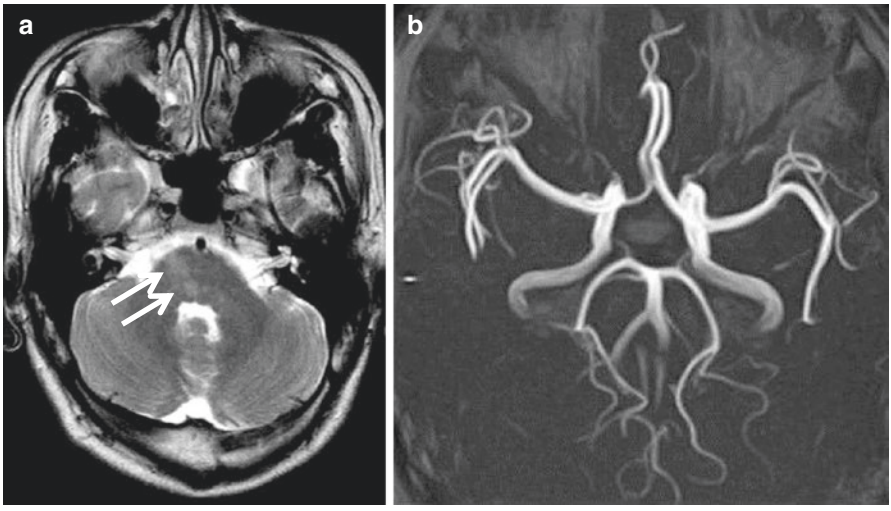

Fig. 4.59 30s F. NPSLE with staggering and diplopia as chief complaints. (**a**, **b**) T2-weighted image (T2WI) shows pale high-intensities in the right pontine base and pontine tegmentum (*arrow*). No obvious abnormality was identified within the range evaluable by MRA at this time-point. (From Aoki S et al. eds. *Yokuwakaru nou MRI* 3rd ed. Tokyo: Gakken Medical Shujunsha. 2012. p. 556–557 with permission)

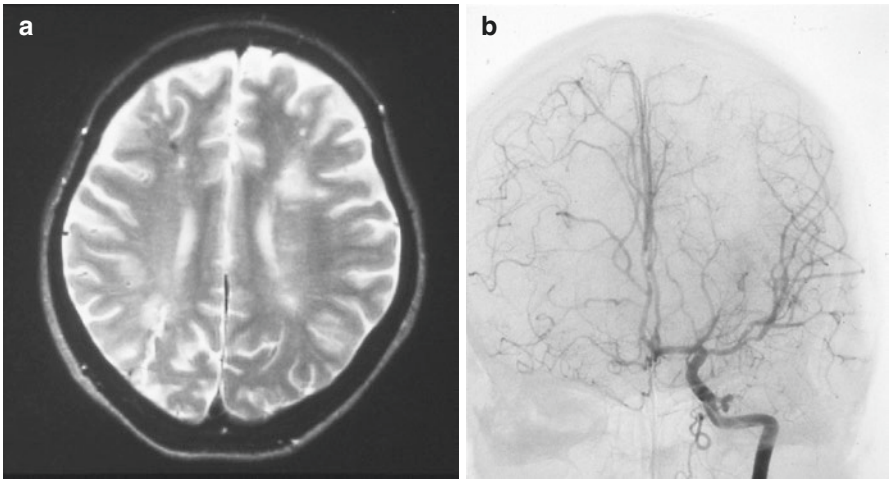

Fig. 4.60 30s F with SLE accompanied by antiphospholipid syndrome. (**a**) T2-weighted image (T2WI) shows several high-intensity lesions in the deep and subcortical white matter, and several low intensity lesions representing multiple small infarcts and microbleeds. (**b**) In the frontal view of left internal carotid arteriography, irregular walls were observed in the left middle cerebral artery

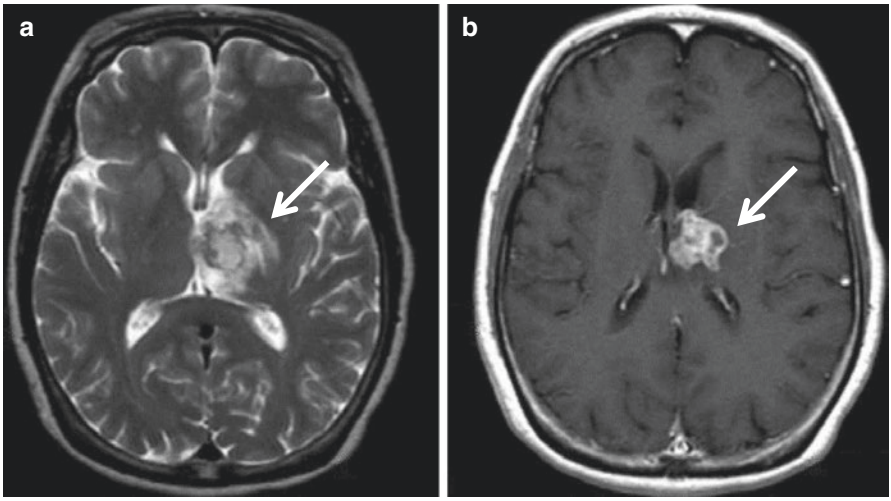

Fig. 4.61 A female SLE patient in her 50s with headache, vomiting, and treatment-resistant skin eruptions. (**a**) T2-weighted image (T2WI) shows irregular-shaped lesions demonstrating a heterogeneous intensity in the left thalamus (*arrow*). (**b**) Post-contrast T1-weighted image shows multinodular contrast enhancement and the disease is deep mycosis. The patient had been treated with steroids for SLE for a prolonged period, suggesting opportunistic infection. Many cases had been through a long-term course, which may require consideration of treatment modification. (From Jpn J Clin Radiol. 2008;53:783–796 (in Japanese) with permission)

been made implying that neuroimaging is useless to diagnose SLE [202]. However, the background pathological findings of SLE are also diverse, and the imaging findings should faithfully reflect the diverse clinical pictures corresponding to the examined stage and pathology of individual cases. Although it is difficult to visualize involvement of different antibodies, such as APS, in the lesions in the brain by micro examination by usual screening methods, objective description on what is happening in the brain, i.e., the diverse and nonspecific findings, in each actual clinical scene without hesitation is the advantage of imaging diagnosis. Studying images and carefully analyzing the findings in each case may be important for routine medical practice.

Distinguishing oneself and others is required for life, and failure of this affects the entire body. The role of imaging diagnosis is to objectively identify lesions induced by this failure and suggest the cause of failure. Faithfully scrutinizing the background of images may be useful for individually diagnosing and treating each patient.

4.11 Other Forms of Dementia

[New pathology for which diffusion-weighted imaging lead to the diagnosis (New Topics)]

4.11.1 Neuronal Intranuclear Hyaline Inclusion Disease

Neuronal intranuclear hyaline inclusion disease (NIHID) is a group of neurodegenerative disorders characterized by the presence of intranuclear inclusions in neuronal cells and neuronal loss in several areas of the nervous system. Only 30 cases have been reported over 35 years after it was initially reported pathologically in 1980, making it a rare neurodegenerative disease [203–206]. However, many cases have been reported since we reported that diffusion-weighted MRI may lead to the diagnosis of NIHID using autopsy-proven cases in 2011 [207]. Based on the reported cases, three clinical subgroups of NIHID, infantile, juvenile, and adult, were proposed [207]. NIHID is a pathological entity, usually diagnosed by post-mortem histological examination. Sporadic and familial cases have been reported, but no genetic abnormality has been identified. Recently, skin biopsy has been reported to be useful for the antemortem diagnosis of NIHID because of nuclear inclusions in adipocytes, fibroblasts, and sweat gland cells in cutaneous tissues [208–211].

Core symptoms in typical adult-form NIHID are memory loss, cognitive declines, and disorientation. Autonomic and peripheral nerve disturbances are also commonly associated symptoms [208–211].

The following characteristic MRI findings may lead to the diagnosis of NIHID: High intensity at the corticomedullary junction on diffusion-weighted imaging (DWI) and leukoencephalopathy with high-intensity areas on T2WI and FLAIR imaging (Fig. 4.62). The high-intensity lesions at the corticomedullary junction

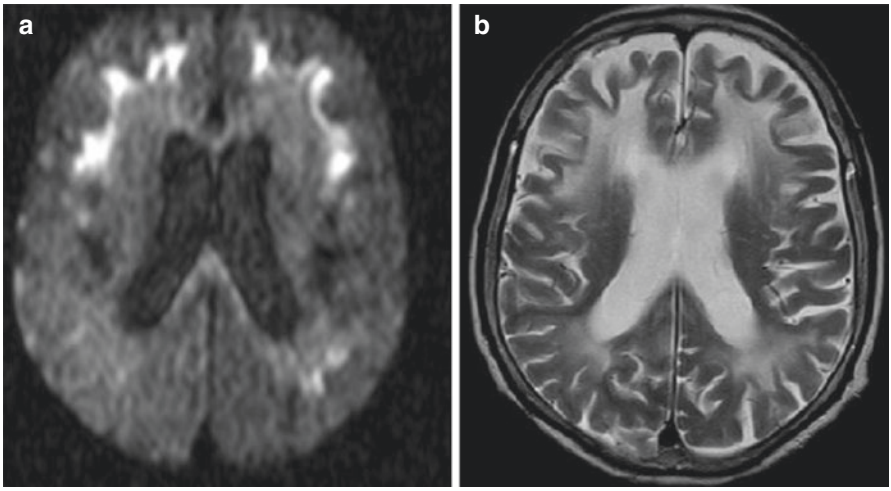

Fig. 4.62 60s F with neuronal intranuclear inclusion disease (NIHID). (**a**) Diffusion-weighted image shows high-intensity lesions in the corticomedullary junctions. (**b**) T2-weighted image shows diffuse high intensity in the subcortical, deep white matter. Brain atrophy is also noted

remain persistent on DWI [208, 211, 212]. Diffuse white mater lesions on T2WI/FLAIR progress and protract. Brain atrophy may progresses with clinical aggravation. Abnormal intensities may be observed in the cerebellum and brain stem. When cortical lesions are produced, careful investigation is necessary as to whether these are primary lesions due to NIID or combined with post-convulsive encephalopathy, other encephalopathy, or encephalitis.

Fragile X-associated tremor/ataxia syndrome (FXTAS) is the most important finding for differential diagnosis pathologically and for imaging diagnosis [213–215].

4.11.2 Hereditary Diffuse Leukoencephalopathy with Spheroids

Hereditary diffuse leukoencephalopathy with spheroids (HDLS) is one of the neurodegenerative diseases with clinical manifestations including dementia, Parkinsonism, seizures, and several other symptoms. Pathological features include formation of axonal spheroids, loss of myelin sheaths, axonal destruction, and gliosis. Recently, colony stimulating factor1 receptor (CSF1R) has been identified as a causative gene for HDLS [216–220].

Characteristic findings leading to the diagnosis of HDLS were observed on MRI and CT. On MRI [210–212], cerebral atrophy and patchy white matter changes, most pronounced in the frontal and frontoparietal area with extension through the posterior limb of the internal capsule into the pyramidal tracts of the brainstem, were observed (Fig. 4.63). On DWI, white matter lesions demonstrated a high intensity and the abnormal intensities tend to protract (Fig. 4.63). Unlike NIHID, white matter lesions are enhanced around the ventricle and deep white matter

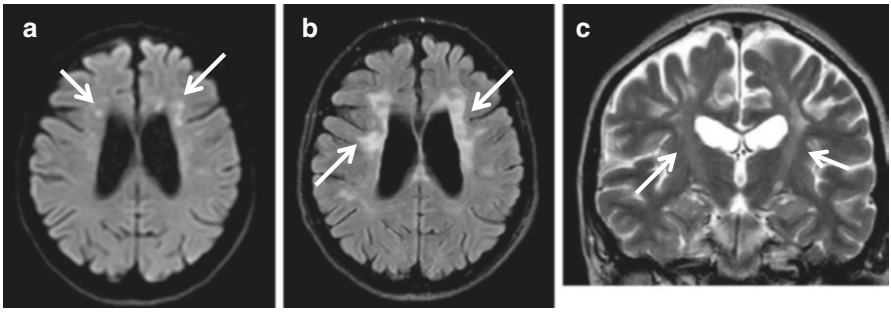

Fig. 4.63 30s F. HDLS (Sequence analysis of CSF1R showed a novel missense mutation Exon 18, Ile794Thr). Her initial symptom is difficulty of writing and speaking. (**a**) Diffusion-weighted image (DWI) shows multiple high-intensity lesions around the lateral ventricle (*arrow*). (**b**) FLAIR image shows diffuse high intensity in the deep white matter with atrophy (*arrow*). (**c**) Coronal T2-weighted image shows high intensity extends to internal capsule (*arrow*). (Medical College of Nagoya City University's case. Courtesy of Dr. Sakurai K)

(Fig. 4.63). Fusion of white matter lesions progresses with disease progression, with which thinning and atrophy of the corpus callosum progresses. On CT, micro calcification of the white matter may occur, which is useful for differentiation of unremarkable leukoencephalopathy.

Acknowledgements I would like to express my gratitude to Dr. Kenji Ishii, Dr. Harushi Mori, Dr. Kazutomi Kanemaru, Dr. Renpei Sengoku, Dr. Junko Fujigasaki, Dr. Hitoshi Terada, Dr. Hiroshi Oba, Dr. Satoshi Matsushima, Dr. Sunao Mizumura, Dr, Fuji Narita, Dr. Keigo Shimoji, and Dr. Kameyama for helpful discussions. I also gratefully acknowledge the work of past and present members of Department of Diagnostic Radiology, Neurology, Psychiatry, Brain Bank of Tokyo Metropolitan Geriatric Hospital and Institute of Gerontology. Without Ms. Asuka Tokumaru and Ms. Makie Kambara's encouragement, this project would not have materialized. This work is supported by a Grant-in-Aid for Scientific Research on Innovative Areas (Comprehensive Brain Science Network) from the Ministry of Education, Culture, Sports, Science and Technology of Japan (221S0003) and Grants-Aid-for Scientific Research(C) KAKENHI.

References

1. Braak H, Braak E. Argyrophilic grains: characteristic pathology of cerebral cortex in cases of adult onset dementia without Alzheimer changes. Neurosci Lett. 1987;76:124–7.
2. Saito Y, Ruberu NN, Sawabe M, et al. Staging of argyrophilic grains: an-age associated tauopathy. J Neuropathol Exp Neurol. 2004;63:911–8.
3. Saito Y, Yamazaki M, Kanazawa I, et al. Severe involvement of the ambient gyrus in a case of dementia with argyrophilic grain disease. J Neurol Sci. 2002;196:71–5.
4. Saito Y, Murayama S. Neuropathology of mild cognitive impairment. Neuropathology. 2007;27:578–84.
5. Tokumaru AM, Saito Y, Murayama S. Dementia with Grains. In: Matsuda H, Asada T, editors. Imaging diagnosis of dementia, 2nd ed. Osaka: Nagai Shoten; 2010. p. 284–293.
6. Adachi T, Satito Y, Hatsuta H, et al. Neuropathologica asymmetry in argyrophilic grain disease. J Neuropathol Exp Neurol. 2010;69:737–44.

7. Murayama S, Saito Y, Adachi T. Degenerative disease, Argyrophilic grain disease. Nippon Rinsho. 2014.03;supple II:46–50.
8. Verhoeff NPLG, Wilson AA, Takeshita S, et al. In-vivo imaging of Alzheimer's disease β-amyloid with [11C] SB-13 PET. Am J Geriatr Psychiatry. 2004;12:584–95.
9. Okamura N, Suemoto T, Shinomitsu T, et al. A novel imaging probe for in vivo detection of neuritic and diffuse amyloid plaques in the brain. J Mol Neurosci. 2004;24:247–55.
10. Matsuda H, Mizumura S, Nagao T, et al. Automatic discrimination between very early Alzheimer disease and controls using an easy X-score imaging system for multicenter brain perfusion single-photon emission tomography. AJNR. 2007;28:731–6.
11. Waragai M, Yamada T, Matuda H. Evaluation of brain perfusion SPECT using an easy Z-score imaging system (eZIS) as an adjunct to early-diagnosis of neurodegenerative diseases. J Neurol Sci. 2007;260:57–64.
12. Waragai M, Mizumura S, Yamada T, et al. Differentiation of early-stage Alzheimer's disease from other types of dementia using brain perfusion single photon emission computed tomography with easy X-score imaging system analysis. Dement Geriatr Cogn Disord. 2008;26:547–55.
13. Yamada M, Itoh Y, Otomo E, et al. Dementia of the Alzheimer type and related demenitas in the aged: DAT subgroups and senile dementia of neurofibrillary tangle type. Neuropathlogy. 1996;16:89–98.
14. Yamada M. Senile dementia of the neurofibrillary tangle type (tangle only dementia); The neuropathological criteria and clinical guidelines for the diagnosis. Neuropathology. 2003;23:311–7.
15. Yamada M, Ito Y. Senile Dementia of the NFT Type (ND-NFT). In Matsuda H, Asada T, editors. Neuroimaging of Dementia, 2nd ed. Osaka: Nagai Shoten; 2010. p.278–283.
16. Ulrich J, Spillantini MG, Goedert M, et al. Abundunt neurofibrillary tangles without senile plaques in a subset of patients with senile dementia. Neurodegeneration. 1992;1:257–64.
17. Crary JF, Trojanowski JQ, Schneider JA, et al. Primary age-related tauopathy (PART): a common patholofy associated with human aging. Acta Neuropathol. 2014;128:755–66.
18. Duyckaerts C, Braak H, Brion J-P, et al. PART is part of Alzheimer disease. Acta Neuropathol. 2015;129:749–56.
19. Saito Y, Tokumaru AM, Kanemaru K, et al. Diagnostic point of senile tauopathy Japanese. J of Geriatric Psychiatry. 2011;22(Suppl 1):36–44.
20. Matsuda H, et al. Automatic voxel-based morphometry of structural MRI by SPM8 puls diffeomorphic anatomic registration through exponentiated lie aglbra improves the diagnosis of probable Alxheimer disease. AJNR. 2012;33:1109–14.
21. Steele JC, Richardson JC, Olszewski J. Progressive supranuclear palsy. A heterogeneous degeneration involving the brain stem, basal ganglia and cerebellum with vertical supranuclear gaze and pseudobulbar palsy, nuchal dystonia and dementia. Arch Neurol. 1964;10:333–59.
22. Litvan I, Mangone CA, McKee A, et al. Natural history of progressive supranuclear palsy (Steele-Richardson-Olszewski syndrome) and clinical predictors of survival: a clinicopathological study. J Neurol Neurosurg Psychiatry. 1996;60:615–20.
23. Josephs KA, Dickson DW. Diagnostic accuracy of progressive supranuclear palsy in the Society for Progressive Supranuclear Palsy brain bank. Mov Disord. 2003;18:1018–26.
24. Donker Kaat L, Boon AJ, Kamphorst W, et al. Frontal presentation in progressive supranuclear palsy. Neurology. 2007;69:723–9.
25. Williams DR, Lees AJ. Progressive supranuclear palsy:clinicopathological concepts and diagnostic challenges. Lancet Neurol. 2009;8:270–9.
26. Kato N, Arai K, Hattori T. Study of the rostral midbrain atrophy in progressive supranuclear palsy. J Neurol Sci. 2003;210:57–60.
27. Oba H, Yagishita A, Terada H, et al. New and reliable MRI diagnosis For progressive supranuclear palsy. Neurology. 2005;64:2050–5.
28. Adachi M, Kawanami T, Ohshima H, et al. Morning glory sign: a particular MR finding in progressive supranuclear palsy. Magn Reson Med Sci. 2004;3:125–32.

29. Paviour DC, Price SL, Stevens JM, et al. Quantitative MRI measurement of superior cerebellar peduncle in progressive supranuclear palsy. Neurology. 2005;64:675–9.
30. Stamelou M, Knake S, Oertel WH, et al. Magnetic resonance imaging in progressive supranuclear palsy. J Neurol. 2011;258:549–58.
31. Kataoka H, Tonomura Y, Taoka T, et al. Signal changes of superior cerebellar peduncle on fluid-attenuated infersion recobery in progressive supranuclear palsy. Parkinsonism Relat Disord. 2008;14:63–5.
32. Shi HC, Zhong JG, Pan PL, et al. Gray matter atrophy in progressive supranuclear palsy: meta-analysis of voxel-based morphometry studies. Neurol Sci. 2013;34:1049–55.
33. Yang J, Shao N, Li J, Shang H. Voxelwise meta-analysis of white matter abnormalities in progressive supranuclear palsy. Neurol Sci. 2014;35:7–14.
34. Josephs KA, Whitwell JL, Dickson DW, et al. Voxel-based morphometry in autopsy proven PSP and CBD. Neurobiol Aging. 2008;29:280–9.
35. Kaasinen V, Kangassalo N, Gardberg M, Iet a. Midbrain-to-pons ratio in autopsy-confirmed progressive supranuclear palsy: replication in an independent cohort. Neurol Sci. 2015;36:1251–3.
36. Agosta F, et al. Diffuision tensor MRI contributes to differentiate Richardson's syndrome from PSP-parkinsonism. Neurobiol Aging. 2012;33:2817–26.
37. Whitewell JL, Master AV, Avula R, et al. Clinical correlates of white matter tract degeneration in progressive supranuclear palsy. Arch Neurol. 2011;68:753–60.
38. Canu E, Agosta F, Baglio F, et al. Diffusion tensor magnetic resonance imaging tractography in progressive supranuclear palsy. Mov Disord. 2011;26:1752–5.
39. Sakurai K, Kawaguchi T, Kawai T, et al. Usefulness of 3D-PRESTO imaging in evaluating putaminal abnormality in parkinsonian variant of multiple system atrophy. Neuroradiology. 2010;52:809–14.
40. Sakurai K, Tokumaru AM, Nakatsuka T, et al. Imaging spectrum of sporadic cerebral amyloid angiopathy: multifaceted features of a single pathological condition. Insights Imaging. 2014;5:375–85.
41. Gupta D, Saini J, Kesavadas C, et al. Utility of susceptibility-weighted MRI in differentiating Parkinson's disease and atypical parkinsonism. Neuroradiology. 2010;52:1087–94.
42. Sakurai K, Tokumaru AM, Shimoji K, et al. Beyond the midbrain atrophy: wide spectrum of structural MRI finding in cases of pathologically proven progressive supranuclear palsy. Neuroradiology. 2017;59(5):431–43.
43. Meijer FJ, van Rumund A, Fasen BA, et al. Susceptibility-weighted imaging improves the diagnostic accuracy of 3T brain MRI in the work-up of parkinsonism. Am J Neuroradiol. 2015;36:454–60.
44. Agosta F, Kostić VS, Galantucci S, et al. The in vivo distribution of brain tissue loss in Richardson's syndrome and PSP-parkinsonism: a VBM-DARTEL study. Eur J Neurosci. 2010;32:640–7.
45. Josephs KA, Eggers SD, Jack CR Jr, et al. Neuroanatomical correlates of the progressive supranuclear palsy corticobasal syndrome hybrid. Eur J Neurol. 2012;19:1440–6.
46. Focke NK, Helms G, Scheewe S, et al. Individual voxel-based subtype prediction can differentiate progressive supranuclear palsy from idiopathic Parkinson syndrome and healthy controls. Hum Brain Mapp. 2011;32:1905–15.
47. Sakurai K, Imabayashi E, Tokumaru AM, et al. The feasibility of white matter volume reduction analysis using SPM8 plus DARTEL for the diagnosis of patients with clinically diagnosed corticobasal syndrome and Richardson's syndrome. Neuroimage Clin. 2014;7:605–10.
48. Williams DR, de Silva R, Paviour DC, et al. Characteristics of two distinct clinical phenotypes in pathologically proven progressive supranuclear palsy: Richardson's syndrome and PSP-parkinsonism. *Brain*. 2005;128:1247–58.
49. Longoni G, Agosta F, Kostić VS, et al. MRI measurements of brainstem structures in patients with Richardson's syndrome, progressive supranuclear palsy-parkinsonism, and Parkinson's disease. Mov Disord. 2011;26:247–55.

50. Matsuo H, Takashima H, Kishikawa M, Kinoshita I, Mori M, Tsujihata M, Nagataki S. Pure akinesia: an atypical manifestation of progressive supranuclear palsy. J Neurol Neurosurg Psychiatry. 1991;54:397–400.
51. Yagishita A, Oda M. Progressive supranuclear palsy: MRI and pathological findings. Neuroradiology. 1996;38:S60–6.
52. Hong JY, Yun HJ, Sunwoo MK, Ham JH, Lee JM, Sohn YH, Lee PH. Comparison of regional brain atrophy and cognitive impairment between pure akinesia with gait freezing and Richardson's syndrome. Front Aging Neurosci. 2015;7:180.
53. Mochizuki A, Ueda Y, Komatsuzaki Y, et al. Progressive supranuclear palsy presenting with primary progressive aphasia--clinicopathological report of an autopsy case. Acta Neuropathol. 2003;105:610–4.
54. Santos-Santos MA, Mandelli ML, Binney RJ, et al. Features of patients with nonfluent/agrammatic primary progressive aphasia with underlying progressive supranuclear palsy pathology or corticobasal degeneration. JAMA Neurol. 2016;73:733–42.
55. Koyama M, Yagishita A, Nakata Y, et al. Imaging of corticobasal degeneration syndrome. Neuroradiology. 2007;49:905–12.
56. Josephs KA, Duffy JR, Strand EA, et al. Clinicopathological and imaging correlates of progressive aphasia and apraxia of speech. Brain. 2006;129(Pt 6):1385–98.
57. Rebeiz JJ, Kolodny EH, Richardson EP Jr. Corticodentatonigral degeneration with neuronal achromasia: a progressive disorder in late adult life. Trans Am Neurol Assoc. 1967;92:23–6.
58. Dickson DW, Bergeron C, Chin SS, et al. Coricobasal degeneration. Brain. 1989;112:1171–92.
59. Boeve BF, Maraganore DM, Parisi JE, et al. Pathologic heterogeneity in clinically diagnosed corticobasal degeneration. Neurology. 1999;53:795–800.
60. Cordato NJ, Halliday GM, McCann H, et al. Corticobasal syndrome with tau pathology. Mov Disord. 2001;16:656–67.
61. Boeve BF, Lang AE, Litvan I. Corticobasal degeneration and its relationship to progressive supranuclear palsy and frontotemporal dementia. Ann Neurol. 2003;54:S15–9.
62. Armstrong MJ, Litvan I, Lang AE, et al. Criteria for the diagnosis of corticobasal degeneration. Neurologyn. 2013;80:496–503.
63. Grimes DA, lang AE, Bergeron CB. Dementia as the most common presentation of cortical-basal ganglionic degeneration. Neurology. 1999;53:1969–74.
64. Murray R, Neumann M, Forman MS, et al. Cognitive and motor assessment in autopsy-proven corticobasal degeneration. Neurology. 2007;68:1274–83.
65. Se L, Rabinovici GD, Mayo MC, et al. Clinicopathological correlations in coricobasal degeneration. Ann Neurol. 2011;70:327–40.
66. Tokumaru AM, Saito Y, Murayma S, et al. Imaging-pathologic correlation in corticobasal degeneration. AJNR. 2009;30:1884–92.
67. Sakurai K, Imabayashi E, Tokumaru AM, et al. The feasibility of white matter volume reduction analysis using plus DARTEL for the diagnosis of patients with clinically diagnosed corticobasal syndrome and Richardson's syndrome. Neuroimage: Clin. 2015;17:605–10.
68. Whitwell JL, Jack CR Jr, Boeve BF, et al. Imaging correlates of pathology in corticobasal syndrome. Neurology. 2010;75:1879–87.
69. Whitwell JL, Jack CR Jr, Parisi JE, et al. Imaging signatures of molecular pathology in behavioral variant frontotemporal demential. J Mol Neurosci: MN. 2011;45:372–8.
70. Erbetta A, Mandelli ML, Savoiardo M, et al. Diffusion tensor imaging shows different topographic involvement of the thalamus in progressive supranuclear palsy and corticobasal degeneration. AJNR. 2009;30:1482–7.
71. Probst A, Taylor KI, Tolnay M. Hippocampal sclerosis dementia; a reapparaisal. Acta Neuropathol. 2007;114:335–45.
72. Ala TA, Geh GO, Frey WH 2nd. Pure hippocampal sclerosis; a rare cause of dementia mimicking Alzheimer's disease. Neurology. 2000;54:843–8.
73. Nelson PT, Schmitt FA, Kin Y, et al. Hippocampal sclerosis in advanced age: clinical and pathological features. Brain. 2011;134:1506–18.

74. Brenowitz WE, Monsell SE, Schmitt FA, et al. Hippocampal sclerosis of aging is a key Alzheimer's disease mimic: clinical-pathologic correlations and comparisons with both Alzheimer's disease and non-tauopthic frontotemporal lobar degeneration. J Alzheimers Dis. 2014;39:691–702.
75. Nelson PT, Smith CD, Abner EL, et al. Hippocampal sclerosis of aging, a prevalent and high-morbidity brain disease. Acta Neuropathol. 2013;126:161–77.
76. Pao WC, Dickson DW, Crook JE, et al. Hippocampal sclerosis in the elderly: genetic and pathologic findings, some mimicking Alzheimer disease clinically. Alzheimer Dis Assoc Disord. 2011;25:364–8.
77. Zarow C, Weiner MW, Ellis WG, Chui HC. Prevalence, laterality, and comorbidity of hippocampal sclerosis in an autopsy sample. Brain Behav. 2012;2:435–42.
78. Schneider JA, Aggarwal NT, Barnes L, et al. The neuropathology of older persons with and without dementia from community versus clinic cohorts. J Alzheimers Dis. 2009;18:691–701.
79. Tokumaru AM. Hippocampal sclerosis dementia (HSD). In: Matuda H, Asada T,. editors. Kouyomu Ninchishou genninn sindnannnotameno nougazou (in Japanese). Tokyo: Personshobop; 2015. p. 272-279
80. Faught E, Richman J, Martin R, et al. Incidence and prevalence of epilepsy among older US Medicare beneficiaries. Neurology. 2012;78:448–53.
81. Leppik IE. Epilepsy in the elderly. Epilepsia. 2006;47(Suppl 1):65–70.
82. Adams RD, Fisher CM, Hakim S, et al. Symptomatic occult hydrocephalus with normal cerebrospinal fluid pressure, a treatable syndrome. N Engl J Med. 1965;273:117–26.
83. Hakim S, Adams RD. The special clinical problem of symptomatic hydrocephalus iwht normal cerebrospinal fluid pressure. J Neurol Sci. 1965;273:307–27.
84. Vassilouthis J. The syndrome normal-pressure hydrocephalu. J Neurosurg. 1984;61:501–9.
85. Ishikawa M, Hashimoto M, Kuwana N, et al. Guidelines for management of idiopathic normal pressure Hydrocephalus, the Japanese Society of Normal Pressure Hydrocephalus. Neurol Med Chir (Tokyo). 2008;48(Suppl):S1–S23.
86. Mori E, Ishikawa M, Kato T, et al. iNPH guideline guidelines for management of idiopathic normal pressure hydrocephalus: second edition. Neurol Med Chir (Tokyo). 2012;52:775–809.
87. Marmarou A, Bergsneider M, Relkin N, Klinge P, Black PM. Development of guidelines for idiopathic normal-pressure hydrocephalus: introduction. Neurosurgery. 2005;57(Suppl):S1–3.
88. Rekin N, Marmarou A, Klinge P, et al. Diagnosing idiopathic normal-pressure hydrocephalus. Neurosurgery. 2005;57(Suppl):S4–16.
89. Evans WA. An encephalographic ratio for estimating ventricular enlargement and cerebral atrophy. Arch Neurol Psychiarty. 1942;47:931–7.
90. Kitagaki H, Mori E, Ishii K, et al. CSF spaces in idiopathic normal pressure hydrocephalus: morphology and volumetry. AJNR. 1998;19:1277–84.
91. Hashimoto M, Ishikawa M, Mori E, et al. Study of INPH on neurological improvement (SINPHONI). Diagnosis of idiopathic normal pressure hydrocephalus is supported by MRI-based scheme: a prospective cohort study. Cerebrospinal Fliuid Res. 2010;7:18.
92. Sasaki M, Honda S, Yuasa T, et al. Narrow CSF space at high convexity and high midline areas in idiopathic normal pressure hydrocephalus detected by axial and coronal MRI. Neuroradiology. 2008;50:117–22.
93. Adachi M, Kawatani T, Oshima F, et al. Upper midbrain profile sign and cingulate sulcus sign: MRI findings on sagittal images in idiopathic normal-pressure hydrocephalus, Alzheimer's disease, and progressive supranuclear palsy. Radiat Med. 2006;24:568–72.
94. Ishii K, Kanda T, Harada A, et al. Clinical impact of the callosal angle in the diagnosis of idiopathic normal pressure hydrocephalus. Eur Radiol. 2008;18:2678–83.
95. Iseki C, Kawanami T, Nagasawa H, et al. Asymtomatic ventriculomegaly with features of iNPH on MRI (AVIM) in the elderly.:a prospective study in a Japanese population. J Neurol Sci. 2009;277:54–7.

96. Yamashita F, Sasaki M, Saito M, et al. Voxel-based morphometry of disproportionate cerebrospinal fluid space distribution for the differential diagnosis of idiopathic normal pressure hydrocephalus. J Neuroimaging. 2014;24:359–65.
97. Oi S, Shimoda M, Shibata M, et al. Pathophysiology of long-standing overt ventriculomegaly in adults. J Neurosurg. 2000;92:933–40.
98. Dandy WE, Blackfan KD. Internal hydrocephalus. An experimental, clinical and pathological study. Am J Dis Child. 1914;8:406–81.
99. Greiz D. Radiological assessment of hydrocephalus: new theories and implications for therapy. Neurosurg Rev. 2004;27:145–65.
100. Yamada S, Miyazaki M, Kanazawa H, et al. Visualization of cerebrospinal fluid movement with spin labeling at MR imaging preliminary results in normal and pathophysiologic conditions. Radiology. 2008;249:644–52.
101. Román GC, Tatemichi TK, Erkinjuntti T, et al. Vascular dementia: diagnostic criteria for research studies report of the NINDS-AIREN International Workshop. Neurology. 1993;43:250–60.
102. Chui HC, Victoroff JI, Margolin W, et al. Criteria for the diagnosis of ischemic vascular dementia proposed by the state of California Alzheimer's Disease Diagnostic and Treatment Centers. Neurology. 1992;42:473–80.
103. Tatemichi TK. How acute brain failure becomes chronis: a view of the mechanisms of dementia related to stroke. Neurology. 1990;40:1652–9.
104. Tatemichi TK, Dresmond DW, Prohovnik I, et al. Confusion and memory loss from capsular genu infarcts: a thalamocortical disconnection syndrome? Neurology. 1992;42:1966–79.
105. Lazzaro NA, Wright B, Castillo M, et al. Artery of Percheron infarction: imaging patterns and clinical spectrum. AJNR. 2010;31:1283–9.
106. Meila D, Sailou G, Kringo T, et al. Subcallosal artery stroke: infarction of the fornix and the genu of the corpus callosum. The importance of the anterior communicating artery complex. Case series and review of the literature. Neuroradiology. 2015;57:41–7.
107. Akiguchi I. Pathophysiology and therapeutic approaches on Binswanger's disease. No To Shinkei. 2006;58:289–97.
108. Akiguchi I, Budka H, Shirakashi Y, et al. MRI features of Binswanger's disease predict prognosis and associated pathology. Ann. Clin. Transl. Neurol. 2014;1(10):813–21.
109. Okudera T, Huang YP, Fukusumi A, et al. Micro-angiographical studies of the medullary venous system of the cerebral hemisphere. Neuropathology. 1999;19:93–111.
110. Arbanitakis Z, Leurgans SE, Barnes LL, et al. Microinfarct pathology, dementia, and cognitive systems. Stroke. 2011;42:722–7.
111. Ii Y, Maeda M, Kida H, et al. In vivo detection of cortical microinfarcts on ultrahigh-field MRI. J Neuroimaging. 2013;23:28–32.
112. Yamamoto Y, et al. Neuropathological correlates of temporal pole white matter hyperintensities in CADASIL. Stroke. 2009;40:204–2011.
113. Tomimoto H, Ohtani R, Wakita H, et al. Small artery dementia in JAPAN: radiological differences between CADASIL, leukoariosis and Binswanger's disease. Dement Geriatr Cog Disord. 2006;21:162–9.
114. Attems J, Lintner F, Jellinger KA. Amyloid beta peptide 1-42 highly correlates with capillary cerebral amyloid angiopathy and Alzheimer disease pathology. Acta Neuropathol. 2004;107:283–91.
115. Charidimou A, Gang Q, Werring DJ. Sporadic cerebral amyloid angiopathy revisited: recent insights into pathophysiology and clinical spectrum. J Neurol Neurosurg Psychiatry. 2012;83:124–37.
116. Chételat G, Villemagne VL, Villain N, Jones G, Ellis KA, Ames D, Martins RN, Masters CL, Rowe CC, AIBL Research Group. Accelerated cortical atrophy in cognitively normal elderly with high β-amyloid deposition. Neurology. 2012;78:477–84.
117. Becker JA, Hedden T, Carmasin J, et al. Amyloid-β associated cortical thinning in clinically normal elderly. Ann Neurol. 2011;69:1032–42.

118. Poels MM, Ikram MA, van der Lugt A, et al. Cerebral microbleeds are associated with worse cognitive function: the Rotterdam scan study. Neurology. 2012;78:326–33.
119. Eng JA, Frosch MP, Choi K, Rebeck GW, Greenberg SM. Clinical manifestations of cerebral amyloid angiopathy-related inflammation. Ann Neurol. 2004;55:250–6.
120. Chung KK, Anderson NE, Hutchinson D, Synek B, Barber PA. Cerebral amyloid angiopathy related inflammation: three case reports and a review. J Neurol Neurosurg Psychiatry. 2011;82:20–6.
121. Kinnecom C, Lev MH, Wendell L, Smith EE, Rosand J, Frosch MP, Greenberg SM. Course of cerebral amyloid angiopathy-related inflammation. Neurology. 2007;68:1411–6.
122. Cummings J, Benson DF, Jr LVS, et al. Reversible dementia. Illustrative cases, definition, and review. JAMA. 1980;243:2434–9.
123. Piccini C, Bracco L, Amaducci L. Treatable and reversible dementias: an update. J Neurol Sci. 1998;153:172–81.
124. Mori H, Kunimatsu S, Sasaki H, et al. Rapidly progressive dementias-Diagnostic process. Clin Imagiol. 2014;30:156–76.
125. Demaerel P, Paert AL, Vanopdenbosch L, et al. Diffusion-weighed magnetic resonance imaging in Creutzfeldt-Jacob disease. Lancet. 1997;349:847–8.
126. Vitali P, Maccagnano E, Caverzasi E, et al. Diffusion-weighted MRI hyperintensity patterns cdifferentiate CJD from other rapid dementias. Neurology. 2011;76:1711–9.
127. Finkenstaedt M, Azudra A, Aerr I, et al. MR imaging of Creutzfeldt-Jacob disease. Radiology. 1996;199:793–8.
128. Nozaki I, Hamaguchi T, Noguchi-Shinohara M, et al. The MM2-cortical form of sporadic Creutzfeldt-Jacob disease presenting with visual disturbance. Neurology. 2006;67:531–3.
129. Zeidler M, Sellar RJ, Collie DA, et al. The pulvinar sign on magnetic resonance imaging in variant Creutzfeldt-Jacob disease. Lancet. 2000;355:1412–8.
130. Collie DA, Summers DM, Sellar RJ, et al. Diagnosing variant Creutzfeld-Jacob disease with the Pulvinar Sign: MR imaging findings in 86 Neuropathologically confirmed cases. AJNR. 2003;24:1560–9.
131. Schouten J, Cinque P, Gisslen M, et al. HIV-1 infection and cognitive impairment in the cART era: a review. AIDS. 2011;25:561–75.
132. Smith AB, Smirniotipoulos JG, Rushing EJ, et al. From the archives of the AFIP: central nervous system infections assoiciated with human immunodeficiency virus infection: radiologic-pathologic correlation. RadioGraphics. 2011;28:2033–58.
133. Masters MC, Acnes BM. Role of neuroimaging in HIV-associated neurocognitive disorders. Semin Neurol. 2014;34:89–102.
134. Saylor D, Dickens AM, Sacktor N, et al. HIV-associated neurocognitive disorder-pathogenesis and prospects for treatment. Nat Rev Neurol. 2016;12:234–48.
135. Filippi CG, Ulug AM, Ryan E, et al. Diffusion tensor imaging of patients with HIV and normal-appearing white matter on MRimages of the brain. AJNR Am J Neuroradiol. 2001;22(2):277–83.
136. Bash S, Hathout GM, Cohen S. Mesiotemporal T2-weighted hyperintensity: neurosyphilis mimicking herpes encephalitis. AJNR Am J Neuroradiol. 2001;22(2):314–6.
137. Hogan TF, Padgett BL, Walker DL, et al. Rapid detection and identification of JC virus and BK virus in human urine by using immunofluorescence microscopy. J Clin Microbiol. 1980;11(2):178–83.
138. Petito CK, Cho ES, Lemann W, et al. Neuropathology of acquired immunodeficiency syndrome (AIDS): an autopsy review. J Neuropathol Exp Neurol. 1986;45(6):635–46.
139. Berger JR, Levy RM, Flomenhoft D, et al. Predictive factors for prolonged survival in acquired immunodeficiency syndrome-associated progressive multifocal leukoencephalopathy. Ann Neurol. 1998;44(3):341–9.
140. Whiteman ML, Post MJ, Berger JR, et al. Progressive multifocal leukoencephalopathy in 47 HIV-seropositive patients: neuroimaging with clinical and pathologic correlation. Radiology. 1993;187(1):233–40.

141. Wheeler AL, Truwit CL, Kleinschmidt-DeMasters BK, et al. Progressive multifocal leukoencephalopathy: contrast enhancement on CT scans and MR images. AJR. 1993;161(5):1049–51.
142. Arbusow V, Strupp M, Pfister HW, et al. Contrast enhancement in progressive multifocal leukoencephalopathy: a predictive factor for long-term survival? J Neurol. 2000;247(4):306–8.
143. Kishi Y, Kami M, Kusumi E, et al. Prostatic acid phosphatase (PAP): a possible diagnostic marker of intravascular large B-cell lymphoma. Haematologica. 2004;89(4):e43–e452.
144. Matsue K, Asada N, Takeuchi M, et al. A clinicopathological study of 13 cases intravascular lymphoma: experience in a single institution over a 9-yr period. Eur J Haematol. 2007;80:236–44.
145. Yamamoto A, Kikuchi Y, Homma K, et al. Characteristics of intravascular large B-cell lymphoma on cerebral MR imaging. AJNR. 2012;33:292–6.
146. Shimada K, Matsue K, Yamamoto K, et al. Retrospective analysis of intravascular large B-cell lymphoma treated with rituximab-containing chemotherapy as reported by the IVL study group in Japan. J Clin Oncol. 2008;26:3189–95.
147. Han K, Haley JC, Carlson K, et al. Regression of cutaneous intravascular lymphoma with rituximab. Cutis. 2003;72:137–40.
148. Finelli PF. Diffusion-weighted MR in hypoglycemic coma. Neurology. 2001;57:933.
149. Aoki T, Sato T, Hasegawa K, et al. Reversible hyperintensity lesion on diffusion-weighted MRI in hypoglycemic coma. Neurology. 2004;27:392–3.
150. Cho SJ, Minn YK, Kwon KH. **S**evere hypoglycemia and vulnerability of the brain. Arch Neurol. 2006;63:138.
151. Kang EG, Jeon SJ, Choi SS, et al. Diffusion MR imaging of hypoglycemic encephalopathy. AJNR. 2010;31:559–64.
152. Berg AT, Berkovic SF, Brodie MJ, et al. Revised terminology and concepts for seizures and epilepsies: report of the ILAE Commission on Classification and Ternimonology. 2005–2009. Epilepsia. 2010;51:676–85.
153. Faught E, Richman J, Martin R, et al. Incidence and prevalence of epilepsy among older U.S. Medicare beneficiaries. Neurology. 2012;78:448–53.
154. Tokumaru AM, Saito Y, Mizuno M, et al. Imaging findings of Posticteric encephalopathy-clinico-radio-pathological correlation. In: Report of Tokyo Metoropolitan Medical Center of Gerontology, 2008 year book.
155. Rahmani M, Bennani M, Benabdelilil M, et al. Neuropsychological and magnetic resonance imaging findings in five patients after carbon monoxide poisoning. Rev Neurol. 2006;162:1240–7.
156. Durak AX, Coskun A, Yikilmaz A, et al. Magnetic resonance imaging findings in chronic carbon monoxide intoxication. Acta Radiol. 2005;46:322–7.
157. Parkinson RB, Hopkins R, Cleavinger HB, et al. White matter hyperintensities and neuropsychological outcome following carbon monoxide poisoning. Neurology. 2002;58:1525–32.
158. Ances BM, Vitaliani R, Taylor RA, et al. Treatment-responsive limbic encephalitis identified by neuropil antibodies: MRI and PETcorrelates. Brain. 2005;128:1764–77.
159. Gultekin SH, Rosenfeld MR, Voltz R, et al. Paraneoplastic limbic encephalitis: neurological symptoms, immunological findings and tumour association in 50 patients. Brain. 2005;123:1481–94.
160. Lucchinetti CF, Kimmel DW, Lennon VA. Paraneoplastic and oncologic profiles of patients seropositive for type 1 antineuronal nuclear autoantibodies. Neurology. 1998;50:652–7.
161. Lancaster E. The diagnosis and treatment of autoimmune encephalitis. J Clin Neurol. 2016;12:1–13.
162. Dalmau J, Gleichman AJ, Hughes EG, et al. Anti-NMDA-receptor encephalitis: case series and analysis of the effects of antibodies. Lancet Neurol. 2008;7:1091–8.
163. Hughes EG, Peng X, Gleichman AJ, et al. Cellular and synaptic mechanisms of anti-NMDA receptor encephalitis. J Neurosci. 2010;30:5866–75.
164. Fine C, Kopp UA, Pajkert A, et al. Structural hippocampal damage following anti-N-Methyl-D-aspartate receptor encephalitis. Biol Psychiatry. 2016;79:727–34.

165. Iizuka T, Sakai F, Ide T, et al. Anti-NMDA receptor encephalitis in Japan: long-term outcome without tumor removal. Neurology. 2008;70:504–11.
166. Titulaer M, Hoftberger R, Iizuka T, et al. Overlapping demyelinating syndromes and anti-NMDA receptor encephalitis. Ann Neurol. 2014;75:411–28.
167. Titulaer MJ, McCracken L, Gabilondo I, et al. Treatment and prognostic factors for long-term outcome in patients with anti-NMDA receptor encephalitis: an observational cohort study. Lancet Neurol. 2013;12:157–65.
168. Seipelt M, Zerr I, Nau R, et al. Hashimoto's encephalitis as a differential diagnosis of Creutzfeldt–Jakob disease. J Neurol Neurosurg Psychiatry. 1999;66:172–6.
169. Song YM, Seo DW, Chang GY. MR findings in Hashimoto encephalopathy. AJNR. 2004;25:807–8.
170. McCabe DJ, Burke T, Connolly S, et al. Amnestic syndrome with bilateral mesial temporal lobe involvement in Hashimoto's encephalopathy. Neurology. 2000;54:737–9.
171. Grommes C, Griffin C, Downes KA, et al. Steroid-responsive encephalopathy associated with autoimmune thyroiditis presenting with diffusion MR imaging changes. AJNR. 2008;29:1550–1.
172. Mahad DJ, Staugaitis S, Ruggieri P, et al. Steroid-responsive encephalopathy associated with autoimmune thyroiditis and primary CNS demyelination. J Neurol Sci. 2005;228:3–5.
173. White ML, Hadley WL, Zhang Y, et al. Analysis of central nervous system vasculitis with diffusion-weighted imaging and apparent diffusion coefficient mapping of the normal-appearing brain. AJNR Am J Neuroradiol. 2007;28:933–7.
174. Moritani T, Hiwatashi A, Shrier DA, et al. CNS vasculitis and vasculopathy: efficacy and usefulness of diffusion-weighted echoplanar MR imaging. Clin Imaging. 2004;28: 261–70.
175. Mouzak A, Agathos P, Vourdeli-Giannakoura E. Subacute cerebellar syndrome and Hashimoto's thyroiditis: association or simple coincidence? Act Neurol Scand. 2002;106: 374–8.
176. Nolte KW, Unbehaun A, Sieker H, et al. Hashimoto encephalopathy: a brainstem vasculitis. Neurology. 2000;54:769.
177. Bohnen N, Parnell K, Harper C. Reversible MRI findings in a patient with Hashimoto's encephalopathy. Neurology. 1997;49:246–7.
178. Shibata N, Yamamoto Y, Sunami N, et al. Isolated angiitis of the CNS associated with Hashimoto's disease. Rinsho Shinkeigaku. 1992;32:191–8.
179. Johnson RT, Richardson EP. The neurological manifestations of systemic lupus erythematosus. Medicine. 1968;47:337–69.
180. O'Connor JF, Musher DM. Central nervous system involvement in systemic lupus erythematosus: a study of 150 cases. Arch Neurol. 1966;14:157–64.
181. Fanouriakis A, Boumpas DT, Bertsias GK. Pathogenesis and treatment of CNS lupus. Curr Opin Rheumatol. 2013;25:577–83.
182. Sibbitt WL Jr, Brooks WM, Kornfeld M, et al. Magnetic resonance imaging and brain histopathology in neuropsychiatric systemic lupus erythematosus. Semin Arthritis Rheum. 2010;40:32–52.
183. Nojima J, Kuratsune H, Suehjisa E, et al. Strong correlation between the prevalence of cerebral infarction and the presence of annti-cardiolipin/β2-glycoprotein I and anti-phosphatidylserine/prothrombin antibodies. Thromb Haemost. 2004;91:867–76.
184. Alexander JJ, Richard JQ. Systemic lupus erythematosus and the brain: what mice are telling us. Neurochem Int. 2007;50:5–11.
185. Fazekas F, Kleinert R, Offenbacher H, et al. **T**he morphologic correlate of incidental punctate white matter hyperintensities on MR images. AJNR. 1991;12:915–21.
186. Harris EN, Gharavi AE, Asherson RA, et al. Cerebral infarction in systemic lupus: association with anticardiolipin antibodies. Clin Exp Rheumatol. 1984;2:47–51.
187. Moritani T, Shrier DA, Numaguchi Y, et al. Diffusion-weighted echo-planar MR imaging of CNS involvenent in systemic lupus erythematosus. Acta Radiol. 2001;8:741–53.

188. Böckle BC, Jara D, Aichhorn K, et al. Cerebral large vessel vasculitis in systemic lupus erythematosus. Lupus. 2014;23:1417–21.
189. Sato S, Nakajima J, Shimura M, et al. Reversible basal ganglia lesions in neuropsychiatric lupus: a report of three pediatric cases. Int J Rheum Dis. 2014;17:274–9.
190. Jeong HW, Her M, Bae JS, et al. Brain MRI in neuropsychiatric lupus: associations with the 1999 ACR case definitions. Rheumatol Int. 2015;35:861–9.
191. Jennings JE, Attwood J, et al. Value of MRI of the brain in patients with systemic lupus erythematosus and neurologic disturbance. Neuroradiology. 2003;46:15–21.
192. Kaichi Y, Kakeda S, Moriya J, et al. Brain MR findings in patients with systemic lupus erythematosus with and without antiphospholipid antivody syndrome. AJNR. 2014;35:100–5.
193. Harris EN, Gharavi AE, Mackworth-Young CG, et al. Lupoid sclerosis: a possible pathogenetic role for antiphospholipid antibodies. Ann Rheum Dis. 1985;44:281–3.
194. Provenzale JM, Barboriak DP, Allen NB, et al. Patients with antiphospholipid antibodies: CT and MRfindings of the brain. AJR. 1996;167:1573–8.
195. Asherson RA, Mercey D, Phillips G, et al. Recurrent stroke and multi-infarct dementia in systemic lupus erythematosus: association with antiphospholipid antibodies. Ann Rheum Dis. 1987;46:605–11.
196. Provenzale JM, Heinz ER, Ortel TL, et al. Antiphospholipid antibodies in patients without systemic lupus erythematosus: neuroradiologic findings. Radiology. 1994;192:531–7.
197. Shastri R, Sha G, Wang P, et al. MR diffusion tractography to identify and characterize microstructural white matter tract changes in systemic lupus erythematosus patients. Acad Radiol. 2016;23:1431–40.
198. Xu X, Hui ES, Mok MY, et al. Sutrucural brain network reorganization in patients with neuropsychiatric systemic lupus erythematosus. AJNR. 2016;38(1):64–70.
199. Shapira-Lichter I, Weinstein M, Lustgarten N, et al. Impaired diffusion tensor imaging findings in the corpus callosum and cingulum may underlie impaired learning and memory abilities in systemic lupus erythematosus. Lupus. 2016;25:1200–8.
200. Hughes M, Sundgren PC, Fan X, et al. Diffusion tensor imaging in patients with acute onset of neuropsychiatric systemic lupus erythematosus: a prospecrive study of apparent diffusion coefficient, fractional anisotrphy values, and eigenvalues in different regions of the brain. Acta Radiol. 2007;48:213–22.
201. Tokumaru AM, Saito Y, Murayama S. Imaging diagnosis for CNS abnormalities in autoimmune disease. Rinsho Houshasen 2005;50:480–90.
202. D'Cruz DP, Khamashta MA, Hughes GR. Systemic lupus erythematosus. Lancet. 2007;369:587–96.
203. Sung JH, Ralirez-Lassepas M, Mastri AR, et al. An unusual degenerative disorder of neurons associated with a novel intranuclear hyaline inclusion (neuronal intranuclear hyaline inclusion disease). A clinicopathological study of a case. J Neuropathol Exp Neurol. 1980;39:107–30.
204. Patel H, Normal MG, Perry TL, et al. Multiple system atrophy with neuronal intranuclear hyaline inclusions. Report of a case and review of the literature. J Neurol Sci. 1985;67:57–65.
205. Funata N, Maeda Y, Koike M, et al. Neuronal intranuclear hyaline inclusion disease: report of a case and review of the literature. Clin Neuropathol. 1990;9:89–96.
206. Takahashi-Fujigasaki J. Neuronal intranuclear hyaline inclusion disease. Neuropathology. 2003;23:351–9.
207. Tokumaru AM, Sakurai K, Imabayashi E, et al. MRI findings of neuronal intranuclear hyaline inclusion disease (NIHID)-Histopathologic correlation. Neuropathology. 2013;33(Suppl):131. (abstract in Japanese)
208. Takahashi-Fujigasaki J, Nakano Y, Uchino A, et al. Adult-onset neuronal intranuclear hyaline inclusion disease in not rare in older adults. Griatr Gerontol Int. 2016;16(Suppl 1):51–6.
209. Sone J, Kitagawa N, Sugawara E, et al. Neuronal intranuclear inclusion disease with leukoencephloopathy diagnosed via skin biopsy. J Neurol Neurosurg Psychiarty. 2014;85:354–6.
210. Sone J, Tanaka F, Koike H, et al. Skin biopsy is useful for the antemortem diagnosis of neuronal intranuclear inclusion disease. Neurology. 2011;76:1372–6.

211. Morimoto S, Hatsuta H, Komiya T, et al. Simultaneous skin-nerve-biopsy and abnormal mitochondorial inclusions in intranuclear hyaline inclusion body disease. J Neurol Sci. 2016;372:447–9.
212. Tokumaru AM. MRI findings of neuronal intranuclear hyaline inclusion body disease. Jpn J Diagn Imaging. 2014;34:10–2.
213. Greco CM, Hagerman RJ, Tassone F, et al. Neuronal intranuclear inclusions in a new cerebellar tremor/ataxia syndrome among fragile X carriers. Brain. 2002;125(Pt 8):1760–71.
214. Greco CM, Berman RF, Martin RM, et al. Neuropathology of fragile X-associated tremor/ataxia syndrome (FXTAS). Brain. 2006;129(Pt 1):243–55.
215. Brunberg JA, Jacquemont S, Hagerman RJ, et al. Fragile X premutation carriers: characteristic MR imaging findings of adult male patients with progressive cerebellar and cognitive dysfunction. AJNR. 2002;23:1757–66.
216. van der Knaap MS, Naidu S, Kleinschmidt-Demasters BK, et al. Autosomal dominant diffuse leukoencephalopathy with neuroaxonal spheroids. Neurology. 2000;54(2):463–8.
217. Freeman SH, Bt H, Sims KB, et al. Adult onset leukodystrophy with neuroaxonal spheroids: clinical, neuroimaging and neuropathologic observations. Brain Pathol. 2009;19:39–47.
218. Kinosita M, Yoshida K, Oyanagi K, et al. Hereditary diffuse leukoencephalopathy with axonal spheroids caused by R782H mutation in CSF1R: Case report. J Neurolo Sci. 2012;318:115–8.
219. Kim EJ, Shin JH, Kim JH, et al. Adult-onset leukoencephalopathy with axonal spheroids and pigmented glia linked CSF1Rmutation: report of four Korean cases. J Neurol Sci. 2015;349:232–8.
220. Sundel C, Van Gerpen JA, Wider C, et al. MRI characteristics and scoring in HDLS due to CSF1R gene mutations. Neurology. 2012;79:566–74.

Diffusion Tensor Imaging in Dementia

5

Toshiaki Taoka

Abstract

While there are huge number of reports in the gray matter changes in Alzheimer's disease (AD), there are also increasing number of reports on white matter changes in the cases of AD due to the development of diffusion tensor methods. This report summarizes the recent knowledge about white matter lesions in Alzheimer's disease.

Keywords

Dementia • White matter • Alzheimer's disease • Diffusion tensor

5.1 Introduction

Pathological changes in Alzheimer's disease include senile plaques, neurofibrillary tangles, neuropil threads, dystrophic neurites containing hyperphosphorylated tau, and loss of neurons, neuropil, and synaptic elements. Atrophy of the entorhinal cortex occurs in the early stage and is followed by atrophy of the hippocampus, amygdaloid body, and border areas of the temporal, occipital, and parietal lobes. Many pathological studies have been conducted about the changes in gray matter in the abovementioned regions. Magnetic resonance imaging (MRI) studies have also

T. Taoka
Department of Radiology, Nagoya University,
65 Tsurumai-cho, Showa-ku, Nagoya, Aichi 466-8550, Japan
e-mail: ttaoka@med.nagoya-u.ac.jp

H. Matsuda et al. (eds.), *Neuroimaging Diagnosis for Alzheimer's Disease and Other Dementias*, DOI 10.1007/978-4-431-55133-1_5

been performed to evaluate the atrophy in the cortex, particularly the parahippocampal gyrus.

On the other hand, studies about changes in the white matter in dementia including Alzheimer's disease began later compared to studies of the gray matter. However, with recent development and increased use of diffusion tensor methods, MRI of the white matter changes in dementia patients is progressing. Because the gray matter changes in Alzheimer's disease have been studied intensely and are well described, changes in white matter tend to be considered changes that are secondary to gray matter changes. White matter fibers communicate with the gray matter of the mesial temporal lobe, and Wallerian degeneration in Alzheimer's disease causes collapse of the neurons. However, whether white matter changes are truly only secondary changes is unknown. In this chapter, the importance of evaluating the white matter in dementia will be discussed.

5.2 Evaluation of the White Matter in Alzheimer's Disease Using Conventional MRI

Pathological changes in white matter reported in Alzheimer's disease include the breakdown of axons or myelin sheaths and gliosis [1, 2]. Progression of these microstructural changes leads to a decrease in the white matter volume or changes in the water content of the white matter, and these changes finally lead to the detectable signal changes on conventional MRI including T1- or T2-weighted images.

Several studies have been published on the changes in white matter in Alzheimer's disease observed with conventional MRI. In a study of 3D T1-weighted imaging, a decrease in the white matter volume was reported in the lower parietal lobe and rostral middle frontal gyrus as well as the parahippocampal gyrus and entorhinal cortex [3]. Several large-scale studies are currently being performed to image Alzheimer's disease including US-ADNI (United States-Alzheimer's Disease Neuroimaging Initiative) and J-ADNI (Japan-Alzheimer's Disease Neuroimaging Initiative). In these studies, conventional MRI is being used to evaluate morphological changes in the brain. These studies have shown that the volume of the area with a high signal in the white matter on T2-weighted images can predict convalescence transfer from normal to mild cognitive impairment (MCI). These findings have been shown in several studies indicating that abnormal white matter signals on images can be used in the prognosis of dementia.

5.3 Techniques for Analyzing Diffusion Tensor Images

5.3.1 Region of Interest (ROI) and Tract-Based Analysis

In contrast to analysis with the abovementioned conventional MRI, which reflects macroscopic changes in the white matter, the diffusion tensor method reflects pathological changes in the tissue microstructure such as collapse of myelin sheaths and

axons. Diffusion tensor imaging is expected to provide information on histopathological changes in the white matter at an earlier stage than conventional images.

A report by Rose et al. in 2000 appears to be the first report to apply the diffusion tensor method in Alzheimer's disease [4]. The report showed that diffusion anisotropy decreases in the ROIs that were placed in the splenium of the corpus callosum, cingulum, and superior longitudinal fasciculus in cases of Alzheimer's disease. Another report used a manually placed ROI and showed decreased *fractional anisotropy* (*FA*) and increased diffusivity in the corpus callosum and the white matter in each cerebral lobe [5].

Manual placing of ROIs for evaluation of white matter degeneration is a simple method for measuring changes in anisotropy or diffusivity. However, this method does not have sufficient anatomical selectivity and tends to suffer from bias among observers and incorrect inclusion of unwanted white matter tracts. Tract-based analysis is a method in which selective measurement of the white matter tract can be done. In this method, tractography of the selected white matter tract is set as a volume of interest, and anisotropy or diffusivity is measured in the volume. In Alzheimer's disease cases, Taoka et al. reported evaluation with tract-based analysis of the uncinate fasciculus, which is a limbic system circuit (Fig. 5.1) [6]. In this report, white matter tracts passing through the temporal stem were identified with diffusion tensor tractography to measure anisotropy and diffusivity. In the Alzheimer's disease cases, decreased FA and increased diffusivity were observed in the limbic system tract including the uncinated fascicles compared with control

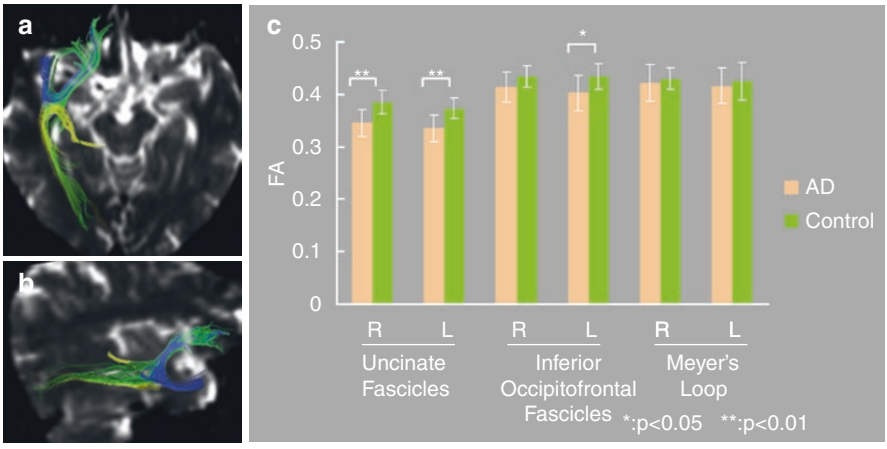

Fig. 5.1 Analysis using the tract-based method. Tractographies were drawn using diffusion-weighted images (EPI imaging: TR/TE, 2300/122 ms; b = 1000 s/mm^2; 6-axis encoding). Tractographies of the inferior occipitofrontal fasciculus (*green*), uncinate fasciculus (*blue*), and Meyer's loop (*yellow*) are shown ((**a**) view from the *bottom*, (**b**) view from the *right*). Comparison of mean fractional anisotropy (FA) between patients with Alzheimer's disease and controls is shown (**c**). The patients with Alzheimer's disease had significantly lower mean FA than the controls on both sides of the uncinate fasciculus and on the left side of the inferior occipitofrontal fasciculus

cases, whereas the optic radiation as an internal control did not show a difference compared to control cases (Fig. 5.1). This tract-based analysis required a shorter computation time compared to voxel-based analysis (described below). Evaluation of an individual case or an individual tract can also be easily performed using the tract-based method. However, the tract-based method has several limitations including interobserver variations, and this method cannot provide information in regions other than the targeted white matter tract. In addition, the FA threshold in making tractography influences the measured value of the anisotropy and diffusivity, and thus, the evaluation must made with uniform conditions [7]. To eliminate the interobserver variation, an automated tractography method (TRActs Constrained by UnderLying Anatomy, (TRACULA)) was developed and published. This method uses prior information on the anatomy of white matter pathways from a set of training subjects and does not constrain the exact spatial location or shape of the pathways but only their trajectory relative to the surrounding anatomical structures. Thus, a set of healthy training subjects can be used to accurately reconstruct the pathways in patients as well as in healthy controls [8].

5.3.2 Voxel-Based Analysis and Tract-Based Spatial Statistics (TBSS) Analysis

Voxel-based morphometry is an analysis method using voxel-wise comparison of the local brain structure between two groups of subjects using spatially normalized high-resolution images from all subjects in the study in the same stereotactic space. The voxel-based method is also applied to diffusion tensor data. Voxel-based analysis of diffusion tensor data is one method for objective analysis of tensor images in which the data for every voxel can be compared with the standard data after conversion to the normalized brain while keeping the local diffusion tensor information. Although this method prevents the variations among observers due to the automatic analysis, the computational load is large, and a long time is needed for computation. In addition, optimal analysis using standard registration algorithms has not been a satisfactory solution to the problem of how to align FA images from multiple subjects in a way that allows valid conclusions.

TBSS is an analysis method that aims to solve these problems using nonlinear registration, followed by projection onto an alignment-invariant white matter tract representation that is called the “mean FA skeleton” [9]. TBSS does not require a hypothesis, and white matter tracts of the whole brain can be analyzed. This technique does not require spatial smoothing, utilizes smaller steps for the comparison between voxels, has little computational complexity, and requires a relatively short computational time (Fig. 5.2). However, care should be taken with interpretation of the result because multiple fiber bundles can be reflected on a single FA skeleton. Histogram analysis is another method for evaluating diffusion tensor data including diffusivity and anisotropy [10]. Histogram analysis can be performed for the whole brain or a partial area and can provide objective information about the distribution

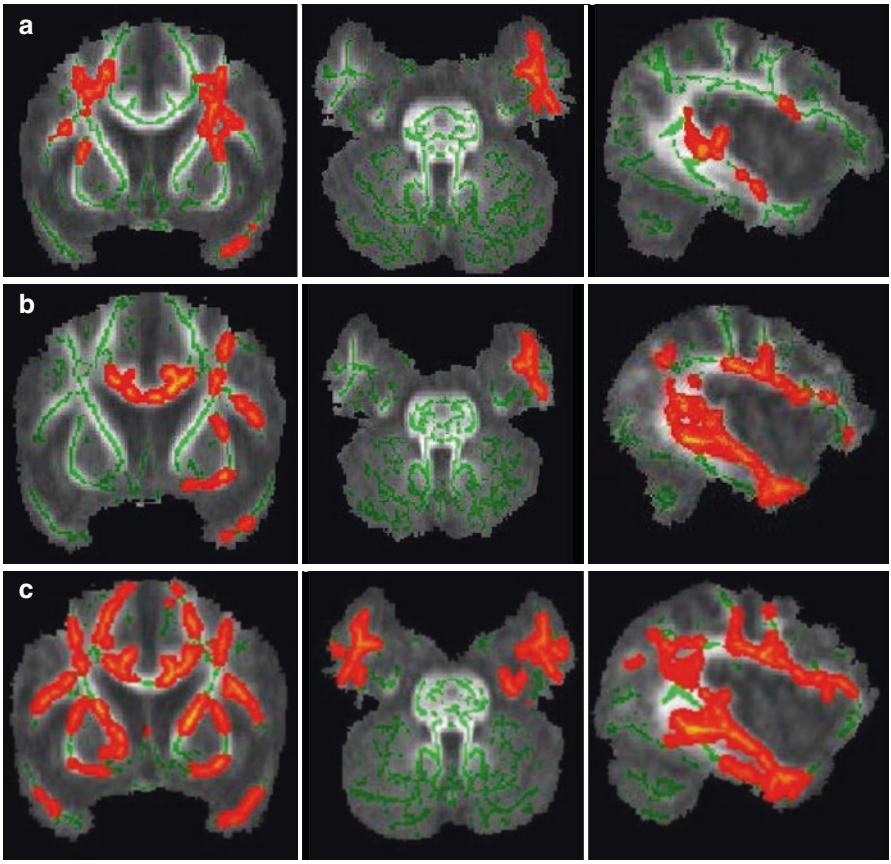

Fig. 5.2 Analysis using tract-based spatial statistics (TBSS). Comparison of Alzheimer's disease cases (mild, moderate, severe) and controls using TBSS analysis. Areas with significantly decreased FA levels ($p < 0.001$) compared with controls are shown in *orange*. Decreases in FA are seen in the left temporal lobe and bilateral frontal lobe in mild cases (**a**). In moderate cases, the corpus callosum and cingulate gyrus also show decreases in FA (**b**). In severe cases, an anisotropic decrease is seen over a wide area (**c**)

profile of the diffusion tensor data. However, a problem with this approach is that the detailed spatial information is lost.

The network-based approach or connectome study is a recently developed analysis method for understanding the function of neural networks in the brain [11]. Connectome studies include structural and functional connectivity, and diffusion tensor studies can provide information about the structural connectivity of all the measurable pathways in the brain. Connectivity is evaluated using graph theory, i.e., the study of "graphs," which are mathematical structures used to model pairwise relationships between objects. Several metric methods can be used to evaluate connectivity or topological properties of the network including

the clustering coefficient, characteristic path length, k-core, or small-worldness. Connectivity studies with diffusion tensor images can provide information on the large-scale connection patterns within the brain and also on the division of the human cortex into distinct areas based on a combination of structural and functional data in the same individual.

5.3.3 Non-Gaussian Distribution Diffusion

The diffusion tensor method is based on the premise that diffusion shows a Gaussian distribution. However, the Gaussian distribution is adapted to only free diffusion in a fluid and is uniform and sufficiently large. Complicated wall structures exist in the human body, and the Gaussian distribution model does not reflect the existence of a large number of compartments and nerve tracts, particularly in the central nervous system. Therefore, instead of a simple Gaussian distribution model, measurement of the probability distribution of a detailed water molecule is necessary. One method is q-space imaging (QSI) [12]. QSI is performed by measurement of a large amount of diffusion encoding and can provide the probability density function of water molecules. The shape of the probability density function curvature is characterized by the mean displacement of water molecules and is calculated from the full width at half height and probability for zero displacement, which is given by the height of the profile at zero displacement (Fig. 5.3). Although QSI is theoretically superior to conventional Gaussian distribution analysis, one limitation of QSI is the long acquisition time due to the large sampling number. The concept of kurtosis is another method to evaluate non-Gaussianity. Kurtosis is a quantity that reflects a gap between the diffusion distribution of a water molecule in vivo and the Gaussian distribution and can be calculated from datasets of relatively few diffusion encoding elements compared to QSI. Thus, a rather short acquisition time is required for kurtosis.

5.4 Reported Studies on White Matter Changes in Alzheimer's Disease Using Various Methods for Analyzing Diffusion Tensor Data

Compared to the large number of imaging studies on gray matter changes in Alzheimer's disease, white matter changes have been explored less frequently with imaging studies. However, several reports evaluating white matter with the diffusion tensor method for dementia cases including Alzheimer's disease have been published. The following studies demonstrate the pathological changes detected with the diffusion tensor method in dementia disorders. Studies using manually located ROIs are still useful for evaluation of white matter changes in dementia cases. A study examined the neuropsychiatric symptoms that occur with MCI and Alzheimer's dementia using manually located ROIs in the fornix, inferior cingulum, posterior cingulum, anterior cingulum, splenium, and cerebral peduncles. *FA* of the anterior

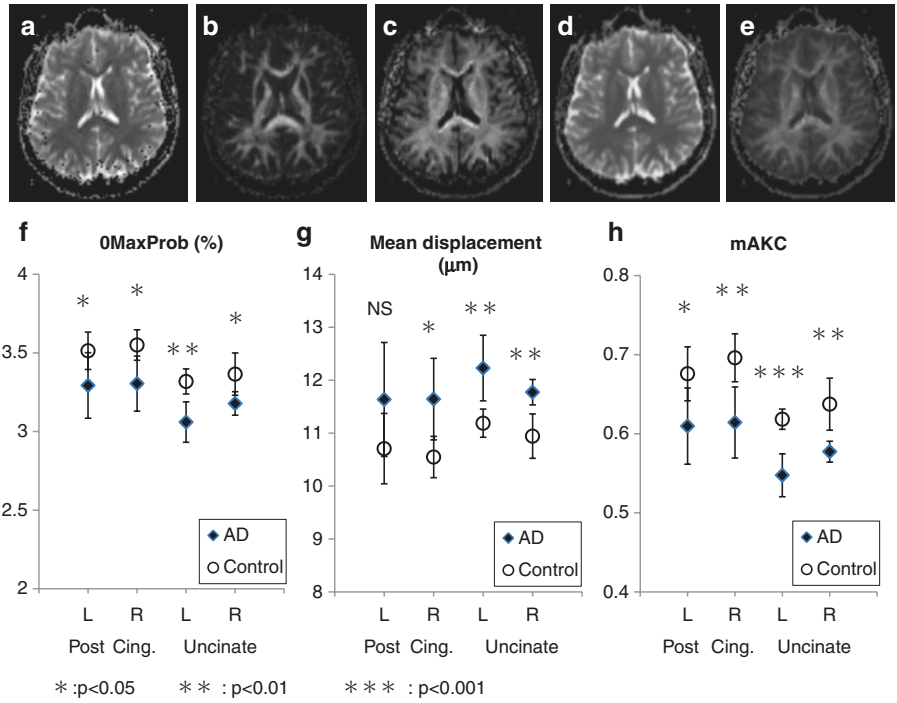

Fig. 5.3 Non-Gaussian diffusion analysis. Images obtained with QSI imaging are shown. In addition to diffusivity (**a**) and FA (**b**) images, which are the coefficients of the diffusion tensor data, zero-displacement probability density (**c**), mean displacement (**d**), and mean kurtosis (**e**) images are provided. Tract-based analysis of QSI for the limbic system including the uncinate and posterior cingulum in cases with Alzheimer's disease compared with controls is shown [34]. Mean 0MaxProb values (**f**) for the uncinate were 3.06% in the *left* and 3.18% in the *right* side in Alzheimer's disease cases. Mean 0MaxProb values for the posterior cingulum were 3.29% in the *left* and 3.31% in the *right* side. These 0MaxProb values were significantly ($p < 0.001$) smaller compared to controls. Mean displacement values for the uncinate were 12.2 μm in the *left* and 11.8 μm in the *right* side in Alzheimer's disease cases. Mean displacement values (**g**) for the posterior cingulum were 11.6 μm in the *left* and 11.6 μm in the *right* side for the Alzheimer's disease cases. These mean displacement values were significantly different ($p < 0.001$) compared to the controls except for the left posterior cingulum. Mean of meal apparent kurtosis coefficient (mAKC) values (**h**) for the uncinate were 0.55 in the *left* and 0.58 in the *right* side in Alzheimer's disease cases. Mean mAKC values for the posterior cingulum were 0.61 in the *left* and 0.61 in the *right* side. These mAKC values were significantly ($p < 0.001$) lower compared to the controls. *NS* not significant

cingulum and fornix regions was most strongly associated with neuropsychiatric symptoms, and low *FA* of the anterior cingulum was associated with increased odds of irritability in participants with mild Alzheimer's disease and MCI [13]. Tract-based analysis is also used as an important tool in analysis of diffusion tensor data in dementia. A multicenter study using automated tractography of the cingulate bundle in Alzheimer's disease was performed in nine centers comprising the

"European DTI Study in Dementia Group" using different magnetic field (1.5 T and 3 T) scanners and different sets of motion proving gradients. Although significant center effects were observed, after adjustment for center and age, the Alzheimer's disease group showed significantly higher diffusivity and lower anisotropy compared with the control group. Thus, diffusion tensor imaging indices of the cingulate bundle as obtained with automated tractography may be useful as a biologically sustained surrogate marker for diagnostic and monitoring purposes in multicenter Alzheimer's disease trials [14]. TBSS has been used in many diffusion tensor studies on dementia. One report demonstrated that TBSS shows that decreases in diffusion anisotropy in the inferior longitudinal fasciculus are more prominent than in the superior longitudinal fasciculus in Alzheimer's disease cases [15]. Another study showed that decreased diffusion anisotropy was seen only in the anterior temporal lobe in Alzheimer's disease compared with the age-matched normal control group [16]. Another report showed a limitation of TBSS. This study compared evaluation using TBSS with atlas-based tractography in Alzheimer's disease cases. Consistent results were obtained for the two methods. However, their atlas-based tractography approach but not TBSS detected a selective anisotropy change in the parietal corpus callosum and left temporal and occipital regions in patients with amnestic MCI compared to controls. This finding indicates that analysis including a higher number of voxels and the tractography-based method may detect the characteristic pattern of anisotropy in the corpus callosum of patients with preclinical Alzheimer's disease when brain atrophy is still modest [17]. Thus, the study showed that skeletonizing diffusion tensor data with TBSS preprocessing may obscure subtle differences in anisotropy.

The network-based approach for diffusion tensor data was also applied in dementia cases. One study examined the relationship between measures of whole-brain white matter connectivity and cognitive performance in patients with early Alzheimer's disease using a network-based approach. The study used diffusion tensor imaging-based tractography to reconstruct the brain network of each individual, followed by graph theoretical analyses. Overall network efficiency was assessed with measures of local and global connectivity and demonstrated that the structural brain network of patients had a reduced local efficiency compared to controls [18].

Recently developed connectivity studies have already been applied for evaluation of Alzheimer's disease using diffusion tensor images. One study analyzed anatomical connectivity based on diffusion-weighted images from patients with Alzheimer's disease, MCI, and healthy elderly persons in whom whole-brain tractography was performed. The data were analyzed based on orientation distribution functions, and connectivity matrices were compiled showing the proportions of detected fibers interconnecting 68 cortical regions. They found widespread network disruptions, because connections are lost in Alzheimer's disease. In Alzheimer's disease cases, the network nodal degree, normalized characteristic path length, and efficiency were decreased, whereas the normalized small-worldness and normalized clustering coefficient were increased [19].

Some studies have been performed using non-Gaussian diffusion MRI. Because QSI requires a longer acquisition time, a diffusion kurtosis study seemed practical.

One such study investigated changes in the brain tissue microstructure of cases with MCI using diffusion kurtosis imaging [20]. They characterized and compared the microstructure in selected brain regions in terms of diffusion kurtosis imaging-derived metrics using analysis of covariance and found that mean and radial kurtoses in the anterior corona radiata were the best individual discriminators of patients with MCI from controls. Their results suggest that non-Gaussian diffusion MRI may be beneficial for assessing microstructural tissue damage at an early stage of MCI and may be useful in developing biomarkers for clinical staging of Alzheimer's disease.

5.5 Early Changes in the White Matter in the Alzheimer's Disease Cases

The studies introduced above showed that white matter lesions do exist in Alzheimer's disease and can be detected with diffusion tensor methods. A comparison study of an Alzheimer's disease high-risk (family history, APOE4 alleles) group and low-risk group using the diffusion tensor method showed that although the entorhinal cortex and hippocampal volumes were equivalent between the two groups, the high-risk group showed decreased microstructural integrity in white matter tracts with direct and secondary connections to the medial temporal lobe [21]. The next question is whether pathological changes in the white matter in Alzheimer's disease are only a secondary change following cortical change. If so, measurement of diffusion tensor data in the white matter is not important for evaluating pathological changes in Alzheimer's disease.

Several studies have shown that the white matter changes in Alzheimer's disease are independent of cortical changes. In a study on regional patterns of white matter tissue changes in cases with Alzheimer's disease using the diffusion tensor method, alterations in diffusion properties were found in several regions in Alzheimer's disease including the parahippocampal white matter, which has direct and secondary connections to the medial temporal lobe. Diffusion tensor changes measured in the parahippocampal white matter were independent of gray matter degeneration as measured with hippocampal volume, demonstrating distinct zones of alterations that may stem from differences in the underlying pathology and potential myelin-specific pathology in the parahippocampal white matter [22]. A study in a healthy aging group was performed using diffusion tensor imaging to determine if microstructural alterations are present in the parahippocampal white matter fibers in cognitively healthy older individuals compared to young individuals. The parahippocampal white matter volume, memory performance, and diffusion tensor imaging indices of the parahippocampal white matter integrity were significant indicators for differentiating the young and old participants. These findings suggest that age-related alterations do occur in the parahippocampal white matter region and may contribute to the normal decline in memory function seen in healthy aging due to decreasing information flow to the hippocampus [23]. A pathological study showed the disappearance of myelin sheaths, axons, and oligodendrocytes and reactive gliosis in the white matter of Alzheimer's disease. In addition, hyaline

membrane degeneration of arterioles was seen. These pathological changes show a distribution that is independent of the distribution of gray matter lesions [24].

Several reports have asked: Which came first, the cortex or the white matter? In cases of MCI, even at a stage in which cortical atrophy is limited to the medial part of the temporal lobe, white matter changes observed with diffusion tensor imaging are not limited to the medial temporal lobe but are spread throughout a wide range in the brain independent of cortical atrophy [25]. A pathological study compared advanced cases of Alzheimer's disease and cases before the onset of symptoms and showed remarkable atrophy in the white matter even though cortical lesions are not yet seen. The report stated that changes in the white matter are peculiar to Alzheimer's disease and include axonal disappearance before cortical changes. One possibility is that white matter changes cause cortical changes [26].

The mechanism of white matter lesions at the molecular level has been examined in Alzheimer's disease. One study indicated that amyloid β is a direct cause of white matter lesions. This group examined sections of the frontal lobe from autopsy-confirmed cases of Alzheimer's disease and assessed the relationship among degenerative large and small vessel disease, parenchymal amyloid β load, and several objective measures of white matter damage including quantification of glial fibrillary acidic protein (GFAP), axonal accumulation of amyloid precursor protein, axon density in superficial and deep white matter, and intensity of myelin staining. No association was found between atherosclerosis or arteriolosclerosis and white matter damage. However, labeling of white matter for GFAP was strongly correlated with the parenchymal amyloid β load and with amyloid precursor protein accumulation. These findings suggest that the severity of frontal white matter damage in Alzheimer's disease is closely related to parenchymal amyloid β load and that in most cases, the contribution of degenerative vascular disease is relatively minor [27]. More specifically, amyloid β 1-40 and amyloid β 25-35 have been reported to cause cell death of oligodendrocytes in a dose-dependent manner [28]. An additional hypothesis has been proposed in which tau protein participates as an axonal obstacle [29].

5.6 Diffusion Tensor Studies on Other Diseases That Cause Dementia

The earliest study using the diffusion tensor method to examine a disease that causes dementia appears to be on cerebral autosomal dominant arteriopathy with subcortical infarcts and leukoencephalopathy in 1999 [30]. This study showed that even in areas that do not show abnormal signals on T2-weighted diffusion tensor images, elevation of the diffusivity and decreased *FA* is seen, suggesting possible injury to neural cells or myelin structures.

Several studies have examined white matter changes in cases of frontotemporal lobar degeneration using the diffusion tensor method. In a study of a semantic dementia case, although diffusion tensor parameter changes were predominantly seen on the ventral side of the left temporal lobe, uncinate fascicles in particular

showed a large contribution to the changes observed with the diffusion tensor method [31]. In a study on primary progressive aphasia, which is a clinical syndrome that encompasses three major phenotypes (nonfluent/agrammatic, semantic, and logopenic), each variant showed different patterns of altered diffusion tensor metrics [32]. These diffusion tensor studies indicated that nonfluent patients showed the greatest changes in *FA* and radial and mean diffusivities, semantic variant patients had severe changes in all metrics, and logopenic patients had the least white matter damage mainly involving diffusivity with *FA* altered only in the temporoparietal component of the dorsal pathway. A study using diffusion tensor imaging in an infectious disease that causes dementia has also been performed. The study performed histogram analysis of the whole brain regarding cognitive impairment in conjunction with human immunodeficiency virus, in which the peak in the diffusion anisotropic histogram was reduced compared with a control [33].

References

1. Warren JD, Schott JM, Fox NC, et al. Brain biopsy in dementia. Brain. 2005;128(Pt 9):2016–25.
2. Terada S, Ishizu H, Yokota O, et al. An autopsy case of hereditary diffuse leukoencephalopathy with spheroids, clinically suspected of Alzheimer's disease. Acta Neuropathol. 2004;108(6):538–45.
3. Salat DH, Greve DN, Pacheco JL, et al. Regional white matter volume differences in nondemented aging and Alzheimer's disease. NeuroImage. 2009;44(4):1247–58.
4. Rose SE, Chen F, Chalk JB, et al. Loss of connectivity in Alzheimer's disease: an evaluation of white matter tract integrity with colour coded MR diffusion tensor imaging. J Neurol Neurosurg Psychiatry. 2000;69(4):528–30.
5. Head D, Buckner RL, Shimony JS, et al. Differential vulnerability of anterior white matter in nondemented aging with minimal acceleration in dementia of the Alzheimer type: evidence from diffusion tensor imaging. Cereb Cortex. 2004;14(4):410–23.
6. Taoka T, Iwasaki S, Sakamoto M, et al. Diffusion anisotropy and diffusivity of white matter tracts within the temporal stem in Alzheimer disease: evaluation of the "tract of interest" by diffusion tensor tractography. AJNR Am J Neuroradiol. 2006;27(5):1040–5.
7. Taoka T, Morikawa M, Akashi T, et al. Fractional anisotropy – threshold dependence in tract-based diffusion tensor analysis: evaluation of the uncinate fasciculus in Alzheimer disease. AJNR Am J Neuroradiol. 2009;30(9):1700–3.
8. Yendiki A, Panneck P, Srinivasan P, et al. Automated probabilistic reconstruction of white-matter pathways in health and disease using an atlas of the underlying anatomy. Front Neuroinform. 2011;5:23.
9. Smith SM, Jenkinson M, Johansen-Berg H, et al. Tract-based spatial statistics: voxelwise analysis of multi-subject diffusion data. NeuroImage. 2006;31(4):1487–505.
10. Kin T, Hirano M, Taoka T, et al. Global and region-specific analyses of apparent diffusion coefficient in dentatorubral-pallidoluysian atrophy. AJNR Am J Neuroradiol. 2006;27(7):1463–6.
11. Sporns O, Tononi G, Kotter R. The human connectome: a structural description of the human brain. PLoS Comput Biol. 2005;1(4):e42.
12. Hori M, Fukunaga I, Masutani Y, et al. Visualizing non-Gaussian diffusion: clinical application of q-space imaging and diffusional kurtosis imaging of the brain and spine. Magn Reson Med Sci. 2012;11(4):221–33.
13. Tighe SK, Oishi K, Mori S, et al. Diffusion tensor imaging of neuropsychiatric symptoms in mild cognitive impairment and Alzheimer's dementia. J Neuropsychiatry Clin Neurosci. 2012;24(4):484–8.

14. Fischer FU, Scheurich A, Wegrzyn M, et al. Automated tractography of the cingulate bundle in Alzheimer's disease: a multicenter DTI study. J Magn Reson Imaging. 2012;36(1):84–91.
15. Damoiseaux JS, Smith SM, Witter MP, et al. White matter tract integrity in aging and Alzheimer's disease. Hum Brain Mapp. 2009;30(4):1051–9.
16. Stricker NH, Schweinsburg BC, Delano-Wood L, et al. Decreased white matter integrity in late-myelinating fiber pathways in Alzheimer's disease supports retrogenesis. NeuroImage. 2009;45(1):10–6.
17. Preti MG, Baglio F, Lagana MM, et al. Assessing corpus callosum changes in Alzheimer's disease: comparison between tract-based spatial statistics and atlas-based tractography. PLoS One. 2012;7(4):e35856.
18. Reijmer YD, Leemans A, Caeyenberghs K, et al. Disruption of cerebral networks and cognitive impairment in Alzheimer disease. Neurology. 2013;80(15):1370–7.
19. Daianu M, Jahanshad N, Nir TM, et al. Breakdown of brain connectivity between normal aging and Alzheimer's disease: a structural k-core network analysis. Brain Connect. 2013;3(4):407–22.
20. Falangola MF, Jensen JH, Tabesh A, et al. Non-Gaussian diffusion MRI assessment of brain microstructure in mild cognitive impairment and Alzheimer's disease. Magn Reson Imaging. 2013;31(6):840–6.
21. Gold BT, Powell DK, Andersen AH, Smith CD. Alterations in multiple measures of white matter integrity in normal women at high risk for Alzheimer's disease. NeuroImage. 2010;52(4):1487–94.
22. Salat DH, Tuch DS, van der Kouwe AJ, et al. White matter pathology isolates the hippocampal formation in Alzheimer's disease. Neurobiol Aging. 2010;31(2):244–56.
23. Rogalski E, Stebbins GT, Barnes CA, et al. Age-related changes in parahippocampal white matter integrity: a diffusion tensor imaging study. Neuropsychologia. 2012;50(8):1759–65.
24. Brun A, Englund E. A white matter disorder in dementia of the Alzheimer type: a pathoanatomical study. Ann Neurol. 1986;19(3):253–62.
25. Agosta F, Pievani M, Sala S, et al. White matter damage in Alzheimer disease and its relationship to gray matter atrophy. Radiology. 2011;258(3):853–63.
26. de la Monte SM. Quantitation of cerebral atrophy in preclinical and end-stage Alzheimer's disease. Ann Neurol. 1989;25(5):450–9.
27. Chalmers K, Wilcock G, Love S. Contributors to white matter damage in the frontal lobe in Alzheimer's disease. Neuropathol Appl Neurobiol. 2005;31(6):623–31.
28. Xu J, Chen S, Ahmed SH, et al. Amyloid-beta peptides are cytotoxic to oligodendrocytes. J Neurosci. 2001;21(1):RC118.
29. Alonso AC, Zaidi T, Grundke-Iqbal I, Iqbal K. Role of abnormally phosphorylated tau in the breakdown of microtubules in Alzheimer disease. Proc Natl Acad Sci U S A. 1994;91(12):5562–6.
30. Chabriat H, Pappata S, Poupon C, et al. Clinical severity in CADASIL related to ultrastructural damage in white matter: in vivo study with diffusion tensor MRI. Stroke. 1999;30(12):2637–43.
31. Acosta-Cabronero J, Patterson K, Fryer TD, et al. Atrophy, hypometabolism and white matter abnormalities in semantic dementia tell a coherent story. Brain. 2011;134(Pt 7):2025–35.
32. Galantucci S, Tartaglia MC, Wilson SM, et al. White matter damage in primary progressive aphasias: a diffusion tensor tractography study. Brain. 2011;134(Pt 10):3011–29.
33. Ragin AB, Storey P, Cohen BA, Epstein LG, Edelman RR. Whole brain diffusion tensor imaging in HIV-associated cognitive impairment. AJNR Am J Neuroradiol. 2004;25(2):195–200.
34. Taoka T, Sakamoto M, Akashi T. q-space imaging in the clinical cases with Alzheimer disease: analysis of fibers in the limbic system. In: Proceedings of the 20th annual meeting of ISMRM; 2012. p. 983.

Arterial Spin Labeling in Dementia

6

Takashi Yoshiura

Abstract

Arterial spin labeling (ASL) is a type of MR perfusion imaging which utilizes magnetically labeled arterial blood as an intrinsic tracer. Because ASL involves no radioactive tracers or contrast administration, it is considered to be completely noninvasive. Moreover, ASL theoretically allows for quantitative measurement of regional cerebral blood flow (rCBF). However, ASL suffers from technical limitations including low signal-to-noise ratio and high sensitivity to arterial transit time inhomogeneity. A variety of ASL pulse sequences have been proposed, which are categorized into pulsed ASL and continuous ASL sequences. Maps of rCBF obtained with ASL are typically analyzed quantitatively, often using image statistical methods. Typical ASL findings of Alzheimer's disease include hypoperfusion in the cortical areas of the posterior cingulate and precuneus as well as the temporoparietal association cortex. Several studies have shown that ASL has high diagnostic performance in discriminating patients with Alzheimer's disease and healthy elderly subjects, although its clinical roles in diagnosing dementia have not been established.

Keywords

Arterial spin labeling • ASL • Perfusion

T. Yoshiura
Department of Radiology, Graduate School of Medical and Dental Sciences, Kagoshima University, 8-35-1 Sakuragaoka, Kagoshima 890-8544, Japan
e-mail: yoshiura@m3.kufm.kagoshima-u.ac.jp

H. Matsuda et al. (eds.), *Neuroimaging Diagnosis for Alzheimer's Disease and Other Dementias*, DOI 10.1007/978-4-431-55133-1_6

6.1 Introduction

Since the 1980s, various techniques of MRI-based brain perfusion-weighted imaging techniques have been proposed. Today, the most widely available is the dynamic susceptibility contrast (DSC) technique, in which a bolus of paramagnetic contrast agent is intravenously injected [1]. With a strong susceptibility effect from the paramagnetic agent, this method provides a high contrast-to-noise ratio at both 1.5 T and 3 T, providing primarily regional blood volume. While the DSC method is very popular in imaging of brain tumors and acute ischemia, its application in dementia has been limited due to the necessity of contrast administration. Arterial spin labeling (ASL) is a type of MR perfusion imaging which involves no contrast administration. Due to its noninvasiveness, it has been attracting much attention in dementia imaging.

ASL was first proposed by Williams and Detre in 1992 [2, 3]. In ASL, magnetically "labeled" arterial blood is used as an intrinsic tracer. Labeling of arterial blood is achieved by inversion pulse, which inverts the magnetization of the spins in the blood, at the upstream location. Images of the brain are obtained when the arterial blood including the inverted spins flows in the brain tissue. These images are called "labeled images," since they include labeled arterial blood. During the same imaging session, images without effective labeling, which are called "control images," are also obtained. Simple subtraction of the two images (control images–labeled images) is used to cancel out the signals from the static brain tissues, thereby yielding a perfusion-related signal from the labeled arterial blood (Fig. 6.1). The signal intensity of the perfusion-related signal accounts for only a few percentage points of the total signal intensity. To increase the ratio of the perfusion-related signal to the noise, typically 30–50 sets of control and labeled scans are repeated, resulting in an imaging time of 4–5 min. For some time, the problem of the low signal-to-noise ratio hampered the clinical use of ASL. However, the recent spread of clinical 3 T MR systems, which theoretically doubles the signal-to-noise ratio compared to 1.5 T systems, has made the clinical use of ASL feasible.

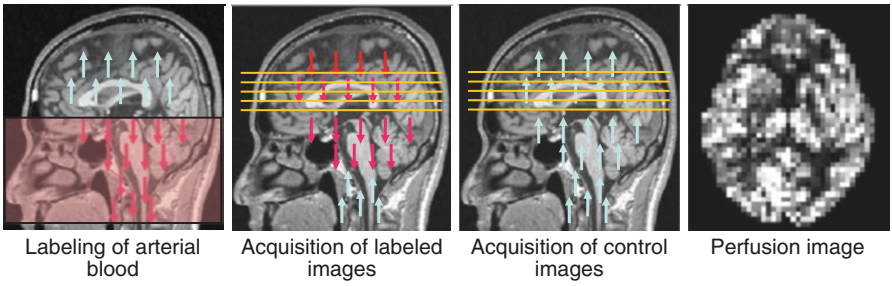

Fig. 6.1 Schematic description of ASL perfusion imaging. Labeled images are obtained when labeled arterial blood with inverted magnetization reaches the brain tissue in the imaging plane, while control images are obtained without effective labeling of blood. Perfusion-related signals can be obtained by subtracting the labeled images from the control images

6.2 Quantification of Regional Cerebral Blood Flow

Theoretically, ASL enables us to quantify regional cerebral blood flow (rCBF) [4]. In this quantification, the length of time after labeling needs to be taken into account, since inverted spins in the arterial blood will return to the steady state with a time constant of T1, which is approximately 1.4 s at 1.5 T. After a post-labeling delay much longer than the blood T1, the effect of inverted magnetization would be rapidly diminished. Higher magnetic field strength has advantages over conventional field strength in ASL not only due to its improved intrinsic signal-to-noise ratio but also its prolonged T1 of blood (approximately 1.6 s at 3 T), which in turn results in more durable inverted arterial blood spins as an intrinsic tracer.

Figure 6.2 shows a typical rCBF maps obtained using ASL. Previous studies have demonstrated that quantitative in vivo measurement of rCBF by ASL is feasible in healthy subjects, based on a comparison of this approach with the gold standard method of positron emission tomography (PET) using ^{15}O-labeled tracers [5, 6]. ASL rCBF measurement is prone to failure in subjects with pathological conditions, especially those with steno-occlusive lesions of major cerebral arteries [7]. Major arterial steno-occlusive lesions result in a delayed arrival of the labeled blood at the brain tissue due to both lowered perfusion pressure and blood supply via collateral circulation. The transit time for the labeled blood to reach the imaging plane is called the

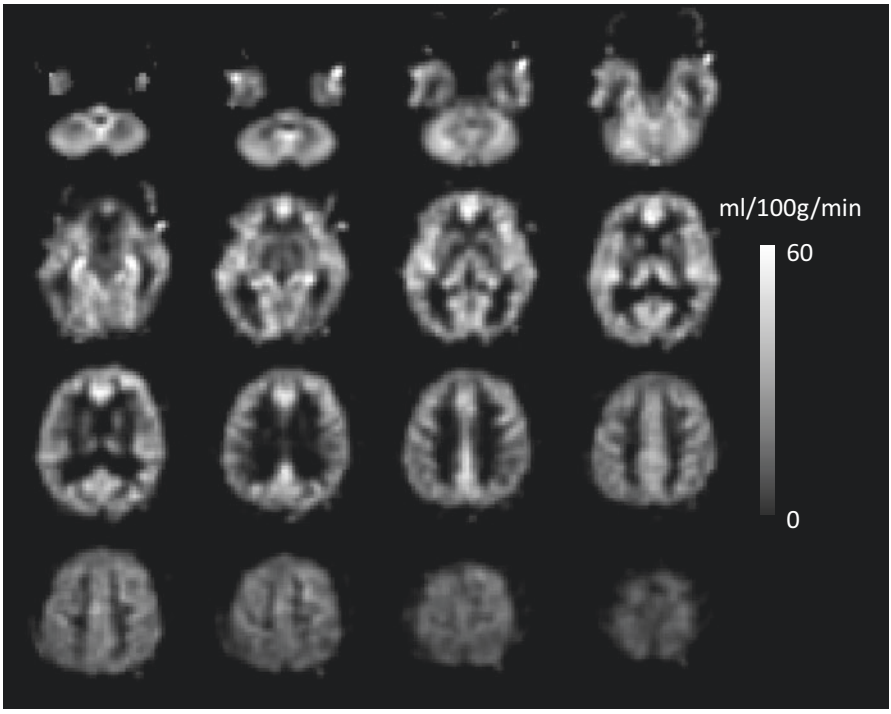

Fig. 6.2 rCBF maps of a healthy subject

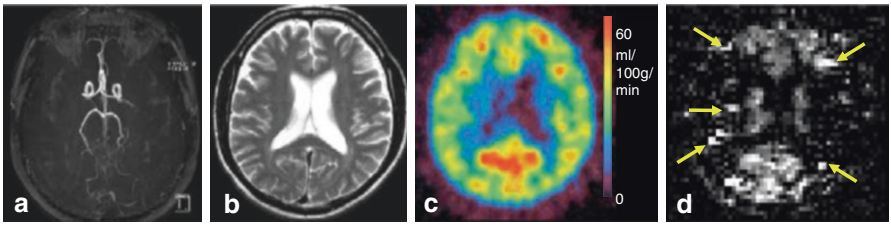

Fig. 6.3 Effect of ATT prolongation on ASL images. A patient with bilateral middle cerebral artery occlusion on MR angiography (**a**) but without obvious infarction on a T2-weighted image (**b**) underwent pulsed ASL imaging and ^{15}O PET. PET (**c**) reveals preserved blood flow, presumably due to collateral blood supply. In the ASL image (**d**), a complete deficit of blood flow is observed in the bilateral middle cerebral artery territories, likely due to ATT prolongation. Spotty hyperperfused areas (*arrows*) are seen in the periphery of the perfusion deficits, indicating labeled blood in the arteries

arterial transit time (ATT). The prolonged ATT can profoundly affect the accuracy in rCBF measurement. In ASL, the labeled arterial blood must reach the brain tissue before a labeled image can be obtained. To meet this requirement, the labeled images are obtained after a certain post-labeling delay. Since the post-labeling delay cannot be much longer than the T1 of the arterial blood, the typical delay setting for clinical 3 T scanners ranges from 1.5 to 2 s. These post-labeling times are long enough for healthy young individuals in whom ATT is relatively short. However, in patients with steno-occlusive lesions in the major cerebral arteries, in whom ATT will be much longer, a post-labeling delay of 1.5–2 s would be inadequate. Consequently, the labeled images are scanned before the labeled blood reaches the brain tissue, which in turn results in underestimation of rCBF. Under these conditions, the labeled blood stays in the arterial vessels at the time of imaging. This labeled blood within the arteries can create spotty areas of high blood flow in the final blood flow maps, and these artifactual hyperperfused areas may coexist with the underestimated rCBF, completely degrading the rCBF mapping. Figure 6.3 shows a typical example. To minimize the effect of residual intra-arterial-labeled blood, ASL pulse sequences are often implemented with crusher gradients, which selectively attenuate signals from flowing blood [8]. The normal range of ATT is known to be longer in the elderly population. Since dementia is a geriatric disease, it should be noted that underestimation of rCBF due to prolonged ATT can occur among healthy elderly individuals, especially in the vascular border zones [9], where ATT is always longer than the other regions (Fig. 6.4).

In clinical imaging, ASL measurement can be deteriorated by several other factors. Patients with cognitive disorders often find it difficult to stay still during the scan. As ASL rCBF measurement includes subtraction between the labeled and control images, the patients' head motion can seriously degrade the rCBF measurement. Magnetic field inhomogeneity due to air-filled paranasal sinuses and mastoid air cells, skull base bones, or implanted metallic devices may result in failure of ASL, especially when echo planar imaging sequence is employed. A metallic stent in the neck where labeling inversion pulses are applied can also cause problems.

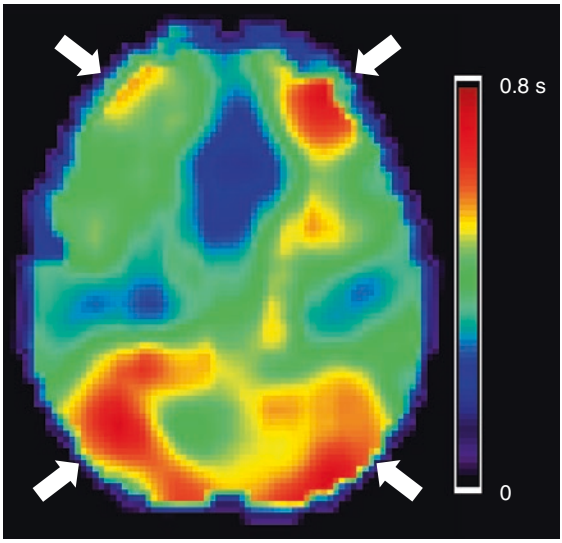

Fig. 6.4 ATT map of a healthy subject. Note that ATT is prolonged in the bilateral border zones (*arrows*)

The reproducibility of ASL rCBF measurement has been demonstrated using healthy volunteers [10–12], but it has not been fully established in clinical settings.

6.3 ASL Pulse Sequences

There are two distinct types of ASL pulse sequences, pulsed ASL (PASL) and continuous ASL (CASL). In PASL, labeling of arterial blood is carried out in short duration over a relatively thick labeling slab, whereas in CASL a continuous labeling pulse is applied over a thinner labeling slab. Compared to CASL, PCASL is easier to implement in clinical MR scanners. However, PASL sequences generally suffer from lower SNR and higher sensitivity to ATT prolongation. To mitigate the latter issue, sophisticated PASL sequences with multiple inversion time sampling have been proposed [13, 14]. On the other hand, the longer labeling in CASL results in a larger number of labeled spins, thereby improving the signal-to-noise ratio in rCBF measurement. Moreover, CASL has an advantage over PCASL in terms of its lower sensitivity to ATT prolongation. However, due to the longer labeling pulse, CASL tends to deposit higher amounts of energy, often exceeding the regulatory limit on the specific absorption rate. This issue of CASL has been solved by using a series of short labeling pulses in a scheme called pseudo-continuous ASL or pulsed continuous ASL (PCASL) [15, 16]. PCASL has been combined with 2-D and 3-D acquisition and is fastly becoming the standard ASL method [17].

6.4 Analysis of ASL rCBF Maps

Imaging of rCBF during the resting state is known to be useful in diagnosing neurodegenerative dementias such as Alzheimer's disease. It is conceivable that rCBF parallels the functional activity of the neural tissue. Thus a deficit in rCBF could reflect a functional failure representing either a degeneration of local brain tissue or its transneuronal effects in remote regions. The rCBF in dementia has been evaluated using nuclear medicine techniques such as PET utilizing ^{15}O-labeled water and single-photon emission tomography (SPECT). In clinical practice, SPECT has been the most widely available modality (see Chap. 11: Brain perfusion SPECT in Alzheimer's disease). Although SPECT is an established technique, ASL has several key advantages over SPECT. Most importantly, ASL does not use radiation or contrast administration and is completely noninvasive. In addition, ASL is superior to SPECT in terms of spatial resolution. Finally, ASL can be easily incorporated into a clinical MR imaging protocol, thereby allowing simultaneous morphological evaluation. This could lead to improved cost-effectiveness.

With these theoretical strengths in mind, researchers have investigated the feasibility of using ASL in the diagnosis of dementia, especially Alzheimer's disease [18, 19]. The rCBF maps obtained with ASL can be evaluated both qualitatively and quantitatively. Quantitative evaluation is popular among the research community, since it provides more objective information. In the past reports, ASL rCBF maps have been analyzed with almost the same technique as used for SPECT rCBF maps. The quantitative analysis of ASL rCBF maps may include statistical methods, such as statistical parametric mapping (SPM). In these analyses, the rCBF map of each individual patient is normalized according to a common template of a standard anatomical space (a predefined "average brain") so that the rCBF of different individuals can be compared on a voxel-by-voxel basis. Alternatively, mean rCBF values are measured in anatomically labeled brain regions on each patient's native rCBF map using region-of-interest (ROI) templates defined in the standard space which are subsequently warped according to the native space.

Since ASL theoretically allows for quantitative rCBF measurement, it is possible that analysis of absolute rCBF maps is meaningful. However, rCBF values are often normalized, especially for the diagnosis of dementia. Normalization of rCBF could effectively eliminate variations in absolute rCBF measurement, which may originate from both physiological variability of global CBF and scaling error in absolute rCBF measurement. The normalization results are critically dependent on the choice of reference region: the reference regions should be among those least affected by the disease. In the past literature, localized reference regions such as the sensorimotor (or motor) and calcarine cortices were used.

ASL has better spatial resolution than SPECT. Nevertheless, it is still not high enough to clearly separate the white matter (WM), cortical gray matter (GM), and surrounding cerebrospinal fluid (CSF), and thus a substantial partial volume effect (PVE) in voxels involving the cortical GM is unavoidable. Many dementing diseases are associated with cortical volume loss, which can result in a decreased GM volume fraction in an imaging voxel. This in turn results in underestimation of the

CBF of local GM. Correction for the PVE has been often implemented in the generation of rCBF maps in which corresponding high-resolution 3D anatomical MR images, which can distinguish the three compartments, are coregistered to the rCBF maps and used as a reference [20].

6.5 ASL of Alzheimer's Disease and Other Dementias

Previous nuclear medicine studies reported that the hypoperfusion related to Alzheimer's disease typically involves several brain regions, including the posterior cingulate gyrus and precuneus, as well as the association cortex in the parietal and temporal lobes [21, 22]. Perfusion abnormality on ASL is seen in essentially the same brain regions as those on PET and SPECT [19, 20, 23–25] (Fig. 6.5), as shown in a few previous studies that compared ASL hypoperfusion with results of PET studies using the same subjects for validation [26–28].

The hippocampus is one of the brain regions that are affected by Alzheimer's disease in its early stage. Previous ASL studies have shown an unexpected increase in PVE-corrected rCBF in the hippocampus of patients with early Alzheimer's disease [29], which was attributed to the reorganization of local neuronal tissue, although this finding is still controversial.

Several studies have evaluated the diagnostic performance of ASL in Alzheimer's disease [23, 24, 30, 31]. These studies have shown that ASL can discriminate between patients with Alzheimer's disease and age-matched healthy subjects with relatively high accuracy, demonstrating the clinical feasibility of ASL as a tool for screening. Nevertheless, the diagnostic value of ASL in dementia has not been established. This is due not only to the small size of the patient populations in these studies but also to the divergent methodologies: they used different magnetic field strengths (1.5 T vs. 3 T), different ASL pulse sequences, and different methods of image analysis. Future studies with consistent methodologies are needed.

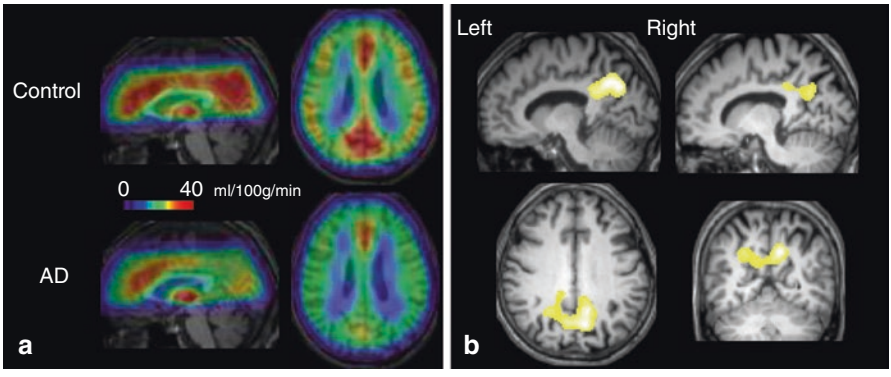

Fig. 6.5 Averaged ASL rCBF maps of healthy elderly subjects (n = 23) and patients with Alzheimer's disease (n = 20) (**a**). Note the rCBF reduction in patients, especially in the posterior cingulate gyrus and precuneus. The SPM analysis (**b**) reveals significant rCBF reduction ($p < 0.001$, uncorrected for multiple comparisons)

Mild cognitive impairment (MCI) includes a prodromal stage of Alzheimer's disease. Discrimination of patients with MCI from healthy subjects using ASL appears to be more challenging than detection of Alzheimer's disease, since the decrease in rCBF is more subtle [20, 25]. A previous study attempted to predict the conversion from MCI into Alzheimer's disease based on ASL findings and found that hypoperfusion in several regions in the right cerebral hemisphere was predictive of subsequent conversion [32].

ASL may also be useful for differential diagnosis of dementia. Alzheimer's disease and frontotemporal lobar degeneration displayed distinct spatial patterns of hypoperfusion on ASL rCBF maps [33, 34], suggesting that ASL is useful in distinguishing the two diseases.

As mentioned earlier, ASL can be obtained simultaneously with morphological imaging in the clinical protocol for dementia. It has been hypothesized that the combination of ASL rCBF measurement and morphological assessment would increase the diagnostic accuracy for dementia compared to either approach used singly. This hypothesis has been supported by a few studies [30, 35], although it is still controversial. Thus the relative roles of ASL and MR morphological assessment are subject to future research.

Conclusion

ASL is an emerging MR-based perfusion imaging technique which is most characterized by its noninvasiveness and convenience. Previous studies have found that it is a promising tool for diagnosing dementia, but further studies will be needed to establish its clinical values.

References

1. Rosen BR, Belliveau JW, Aronen HJ, et al. Susceptibility contrast imaging of cerebral blood volume: human experience. Magn Reson Med. 1991;22:293–9.
2. Williams DS, Detre JA, Leigh JS, Koretsky AP. Magnetic resonance imaging of perfusion using spin inversion of arterial water. Proc Natl Acad Sci U S A. 1992;89:212–6.
3. Detre JA, Leigh JS, Williams DS, Koretsky AP. Perfusion imaging. Magn Reson Med. 1992;23:37–45.
4. Buxton RB, Frank LR, Wong EC, Siewert B, Warach S, Edelman RR. A general kinetic model for quantitative perfusion imaging with arterial spin labeling. Magn Reson Med. 1998;40:383–96.
5. Ye FQ, Berman KF, Ellmore T, et al. H(2)(15)O PET validation of steady-state arterial spin tagging cerebral blood flow measurements in humans. Magn Reson Med. 2000;44:450–6.
6. Heijtel DF, Mutsaerts HJ, Bakker E, et al. Accuracy and precision of pseudo-continuous arterial spin labeling perfusion during baseline and hypercapnia: a head-to-head comparison with ^{15}O H_2O positron emission tomography. NeuroImage. 2014;92:182–92.
7. Kimura H, Kado H, Koshimoto Y, Tsuchida T, Yonekura Y, Itoh H. Multislice continuous arterial spin-labeled perfusion MRI in patients with chronic occlusive cerebrovascular disease: a correlative study with CO2 PET validation. J Magn Reson Imaging. 2005;22:189–98.
8. Ye FQ, Mattay VS, Jezzard P, et al. Correction for vascular artifacts in cerebral blood flow values measured by using arterial spin tagging techniques. Magn Reson Med. 1997;37:226–35.

9. Hendrikse J, Petersen ET, van Laar PJ, Golay X. Cerebral border zones between distal end branches of intracranial arteries: MR imaging. Radiology. 2008;246:572–80.
10. Jahng G-H, Song E, Zhu X-P, Matson GB, Weiner MW, Schuff N. Human brain: reliability and reproducibility of pulsed arterial spin-labeling perfusion MR imaging. Radiology. 2005;234:909–16.
11. Petersen ET, Mouridsen K, Golay X, et al. The QUASAR reproducibility study, part II: results from a multi-center arterial spin labeling test-retest study. NeuroImage. 2010;49:104–13.
12. Chen Y, Wang DJJ, Detre JA. Test-retest reliability of arterial spin labeling with common strategies. J Magn Reson Imaging. 2011;33:940–9.
13. Günther M, Bock M, Schad LR. Arterial spin labeling in combination with a look-locker sampling strategy: inflow turbo-sampling EPI-FAIR (ITS-FAIR). Magn Reson Med. 2001;46:974–84.
14. Petersen ET, Lim T, Golay X. Model-free arterial spin labeling quantification approach for perfusion MRI. Magn Reson Med. 2006;55:219–32.
15. Dai W, Garcia D, de Bazelaire C, Alsop DC. Continuous flow-driven inversion for arterial spin labeling using pulsed radio frequency and gradient fields. Magn Reson Med. 2008;60:1488–97.
16. WC W, Fernandez-Seara M, Detre JA, Wehrli FW, Wang J. A theoretical and experimental investigation of the tagging efficiency of pseudocontinuous arterial spin labeling. Magn Reson Med. 2007;58:1020–7.
17. Alsop DC, Detre JA, Golay X, et al. Recommended implementation of arterial spin-labeled perfusion MRI for clinical applications: A consensus of the ISMRM perfusion study group and the European consortium for ASL in dementia. Magn Reson Med. 2014;73(1):102–16. doi:10.1002/mrm.25197.
18. Sandson TA, O'Connor M, Sperling RA, et al. Noninvasive perfusion MRI in Alzheimer's disease: a preliminary report. Neurology. 1996;47:1339–42.
19. Alsop DC, Detre JA, Grossman M. Assessment of cerebral blood flow in Alzheimer's disease by spin-labeled magnetic resonance imaging. Ann Neurol. 2000;47:93–100.
20. Johnson NA, Jahng G-H, Welner MW, et al. Pattern of cerebral hypoperfusion in Alzheimer disease and mild cognitive impairment measured with arterial spin-labeling MR imaging: initial experience. Radiology. 2005;234:851–9.
21. Kogure D, Matsuda H, Ohnishi T, et al. Longitudinal evaluation of early Alzheimer's disease using brain perfusion SPECT. J Nucl Med. 2000;41:1155–62.
22. Ishii K, Sasaki M, Yamaji S, Sakamoto S, Kitagaki H, Mori E. Demonstration of decreased posterior cingulate perfusion in mild Alzheimer's disease by means of $H_2{}^{15}O$ positron emission tomography. Eur J Nucl Med. 1997;24:670–3.
23. Asllani I, Habeck C, Scarmeas N, Borogovac A, Brown TR, Stern Y. Multivariate and univariate analysis of continuous arterial spin labeling perfusion MRI in Alzheimer's disease. J Cereb Blood Flow Metab. 2008;28:725–36.
24. Yoshiura T, Hiwatashi A, Noguchi T, et al. Arterial spin labelling at 3-T MR imaging for detection of individuals with Alzheimer's disease. Eur Radiol. 2009;19:2819–25.
25. Binnewijzend MA, Kuijer JP, Benedictus MR, et al. Cerebral blood flow measured with 3D pseudocontinuous arterial spin-labeling MR imaging in Alzheimer disease and mild cognitive impairment: a marker for disease severity. Radiology. 2013;267:221–30.
26. Xu G, Rowley HA, Wu G, et al. Reliability and precision of pseudo-continuous arterial spin labeling perfusion MRI on 3.0 T and comparison with 15O-water PET in elderly subjects at risk for Alzheimer's disease. NMR Biomed. 2010;23:286–93.
27. Chen Y, Wolk DA, Reddin JS, et al. Voxel-based comparison of arterial spin-labeled perfusion MRI and FDG-PET in Alzheimer disease. Neurology. 2011;77:1977–85.
28. Musiek ES, Chen Y, Korczykowski M, et al. Direct comparison of fluorodeoxyglucose positron emission tomography and arterial spin labeling magnetic resonance imaging in Alzheimer's disease. Alzheimers Dement. 2012;8:51–9.
29. Alsop DC, Casement M, de Bazelaire C, Fong T, Press DZ. Hippocampal hyperperfusion in Alzheimer's disease. NeuroImage. 2008;42:1267–74.

30. Mak HK, Qian W, Ng KS, et al. Combination of MRI hippocampal volumetry and arterial spin labeling MR perfusion at 3-Tesla improves the efficacy in discriminating Alzheimer's disease from cognitively normal elderly adults. J Alzheimers Dis. 2014;41:749–58.
31. Bron EE, Steketee RM, Houston GC, et al. Alzheimer's disease neuroimaging initiative. Diagnostic classification of arterial spin labeling and structural MRI in presenile early stage dementia. Hum Brain Mapp. 2014;35:4916–31.
32. Chao LL, Buckley ST, Kornak J, et al. ASL perfusion MRI predicts cognitive decline and conversion from MCI to dementia. Alzheimer Dis Assoc Disorder. 2010;24:19–27.
33. Du AT, Jahng GH, Hayasaka S, et al. Hypoperfusion in frontotemporal dementia and Alzheimer disease by arterial spin labeling MRI. Neurology. 2006;67:1215–20.
34. WT H, Wang Z, Lee VM, Trojanowski JQ, Detre JA, Grossman M. Distinct cerebral perfusion patterns in FLD and AD. Neurology. 2010;75:881–8.
35. Dashjamts T, Yoshiura T, Hiwatashi A, et al. Simultaneous arterial spin labeling cerebral blood flow and morphological assessments for detection of Alzheimer's disease. Acad Radiol. 2011;18:1492–9.

Proton Magnetic Resonance Spectroscopy for Dementia

7

Akihiko Shiino

Abstract

Proton magnetic resonance spectroscopy (MRS) can be used to investigate metabolite changes and shows potential for clinical study and diagnosis of degenerative disorders such as mild cognitive impairment (MCI), Alzheimer's disease (AD), dementia with Lewy bodies (DLB), and frontotemporal dementia (FTD). The common features of those degenerative disorders include a decrease in the concentration of NAA or in the NAA/Cr ratio and increase in the concentration of mIns or in the mIns/Cr ratio. Moreover, these findings tend to be regionally specific to the diseases, for example, to the hippocampus and the posterior cingulate and precuneal cortices in cases of AD, to the occipital lobe in cases of DLB, and to the frontal lobe in cases of FTD. Therefore MRS has potential clinical utility to differentiate those disorders. However, this approach may not be thoroughly established due to the inherent difficulty of quantitative measurement of metabolites, and therefore its utility is still limited to the local institutional level. In this section, we first briefly introduce the basic theory and principal methodologies of MRS, which may be useful to cultivate a better understanding of targeting for clinicians and neuroscientists, and then discuss the clinical uses of MRS in dementia by reviewing the literature.

Keywords

Magnetic resonance spectroscopy • Dementia • Alzheimer's disease • Mild cognitive impairment • Chemical shift

A. Shiino
Division of Biomedical MR Science, Molecular Neuroscience Research Center, Shiga University of Medical Science, Seta Tsukinowa-cyo, Otsu, Shiga 520-2192, Japan
e-mail: shiino@belle.shiga-med.ac.jp

H. Matsuda et al. (eds.), *Neuroimaging Diagnosis for Alzheimer's Disease and Other Dementias*, DOI 10.1007/978-4-431-55133-1_7

7.1 Introduction

Magnetic resonance spectroscopy (MRS) allows noninvasive in vivo measurement of certain metabolites, with a detection threshold of approximately 0.5–1.0 mM. In 1992, Klunk et al. [1] reported that magnitude of decrease of N-acetylaspartate (NAA) correlated with the number of senile plaques and neurofibrillary tangles in postmortem brain samples from Alzheimer's disease (AD) patients. Soon after, the first report on the use of in vivo MRS was published by Shiino et al. [2] showing that the NAA to creatine + phosphocreatine (Cr) ratio was more than 30% lower in demented patients. In addition to decreased NAA levels, Miller et al. reported elevated myoinositol (mIns)-to-Cr ratios in AD patients [3]. At present, NAA is thought to be a marker of neuronal integrity, and an increased level of mIns is thought to indicate some glial response. The findings of decreased NAA and elevated mIns in patients with AD or mild cognitive impairment (MCI) have largely been confirmed in several studies, even in the early stage of the disease. The clinical use of MRS for investigation of patients with cognitive impairment, however, may not be thoroughly established due to inherent difficulty in quantitative measurement of metabolites or multifarious settings of acquisition parameters including the sequence used, voxel size and location, TR/TE setting, and post-processing methods. There are no standardized referable values to which all results can be compared. Therefore the power of MR spectroscopy is still limited to the local institutional level and lacks evidence from large clinical trials. This chapter firstly introduces a brief basic theory and principal methodologies of single-voxel proton MRS, which may be useful to cultivate a better understanding of targeting for clinicians and neuroscientists, and secondly this chapter discusses the clinical uses of MRS in dementia by reviewing the literature.

7.2 Basic Principals of Magnetic Resonance Spectroscopy

MRS has been used to investigate brain neurochemistry. The basic physical principles of proton (^{1}H) MRS are the same as those of MR imaging and can be done with conventional MR imaging machines. MRS is also applicable to other nuclei such as carbon (^{13}C) and phosphorus (^{31}P), as shown in Table 7.1. Since resonance frequency (Larmor frequency, ω_0) varies among nuclei, additional hardware is generally needed for MRS of those nuclei.

The difference between MRS and MRI is that MRS detects the different chemical components within tissues, whereas MRI shows the anatomical architecture. The targeted nuclei have slightly different resonance frequencies due to interactions via the electrons, which induce small magnetic field change μ_e around the nuclei (Fig. 7.1). Because of these small local magnetic field differences, the resonance frequencies of the nuclei will shift known as the "chemical shift." The information produced by MRS is displayed graphically as a spectrum with a chemical shift

Table 7.1 Nuclei commonly used for MRS in vivo

Nucleus	Name	Spin	Frequency (B_0 = 1.5 T)	Inherent sensitivity	Natural abundance (%)
^{1}H	Proton	1/2	63.87	1	99.99
^{7}Li	Lithium	3/2	24.81	0.272	92.58
^{13}C	Carbon	1/2	16.06	0.0159	1.11
^{19}F	Fluorine	1/2	60.08	0.833	100.00
^{23}Na	Sodium	1/2	16.89	0.0925	100.00
^{31}P	Phosphorous	1/2	25.85	0.0663	100.00
^{35}Cl	Chloride	3/2	6.26	0.0047	75.53
^{39}K	Potassium	3/2	2.98	0.00051	93.08

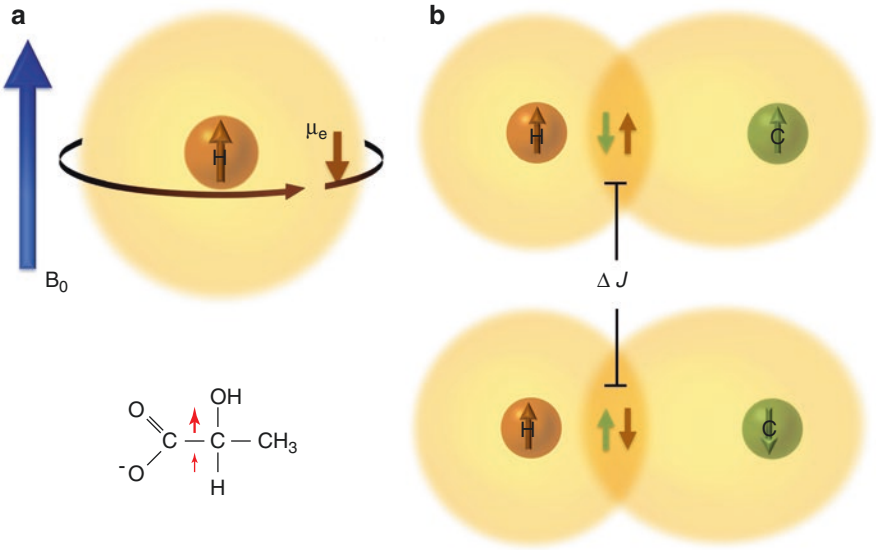

Fig. 7.1 Chemical shift and *J*-coupling. (**a**) Since electrons are negatively charged, the electron cloud shielding a nucleus induces an opposing small magnetic moment μ_e to the applied field. As a result, the nucleus experiences a slightly different magnetic field ($B_0 - \mu_e$), which causes a slight shift of resonance frequency: $B = B_0(1 - \mu_e)$. The oxygen atoms shift the electron density away from the protons leading to reduced electronic shielding; therefore the resonance frequency of the proton nucleus shifts higher. (**b**) The proton resonance is split into a doublet due to scalar coupling with the carbon in which the energy level repeatedly switches between high- and low-spin state. This effect is called *spin-spin coupling* or *J-coupling*

(horizontal) axis in parts per million (ppm) and a signal amplitude (vertical) axis enabling identification of chemical components. Since each signal amplitude or area is proportional to each particular metabolite concentration, one can measure relative or absolute values of concentrations of chemicals.

7.2.1 Chemical Shift

In practice, chemical shift is not expressed in absolute units (such as hertz). This is because the value of chemical shift depends on the applied magnetic field strength; that is, if the magnetic field B_0 is doubled, then the absolute value of the chemical shift will be doubled. Therefore, the chemical shift is measured in relative terms as follows:

$$\text{Chemical shift} = \left(B_{\text{sample}} - B_{\text{reference}}\right) / B_0 = \left(\omega_{\text{sample}} - \omega_{\text{reference}}\right) / \omega_0$$

In proton MRS, tetramethylsilane (TMS), $Si(CH_3)_4$, is traditionally used as universal standard for chemical shift calibration. For example, if the obtained value of the chemical shift between the main peak of *N*-acetylaspartate ($-CH_3$) and TMS ($\omega_{\text{NAA}} - \omega_{\text{TMS}}$) is measured by 1.5 T scanner as 128 Hz, then the chemical shift will be presented as 128/64,000,000 Hz = 2 ppm. Here, the number of 64,000,000 (64 MHz) is the center resonance frequency (ω_0) of protons at 1.5 T. In case of the resonance frequency of the proton in water, the peak appears at 4.7 ppm.

7.2.2 *J*-Coupling and Splitting Pattern

The actual local magnetic field encounters an indirect interaction of neighboring magnetic nuclei (spin-spin splitting) causing perturbation of the electron distribution and splitting of NMR signals. This phenomenon, known as spin-spin coupling or *J*-coupling, provides detailed information on identities of spin-possessing nuclei in a molecule. *J*-coupling can occur between any species of nuclei with spin, in homonuclear (e.g., ^1H–^1H) and heteronuclear (e.g., ^1H–^{13}C) interactions (Fig. 7.1). Peak splitting from *J*-coupling shows the same actual frequency values, whatever the externally applied magnetic field strength, so its value is expressed in "Hz" and not in "ppm." When a species of nucleus is coupled to n equivalent nuclei, its signal splits into an $n + 1$ multiplet, with component amplitude ratios following Pascal's triangle: singlet 1; doublet 1:1; triplet 1:2:1; quartet 1:3:3:1; quintet 1:4:6:4:1; etc. Coupling with additional spin-possessing nuclei causes additional splitting of each component of the multiplet, for example, producing a doublet of doublets.

In lactate (CH_3–CH(OH)–COOH), for example, the methyl groups (CH_3) at 1.31 ppm interact with the methine groups (CH) at 4.10 ppm, and the methyl nucleus signal is split into two equal peaks (a doublet) separated by 6.93 Hz. *J*-coupling also causes phase evolutions that cause peak and baseline distortions that vary with echo time and field strength [4]. This phenomenon is well known as the observation that the lactate doublet has inverted doublet peaks for TE ≈ 143 ms (Fig. 7.2). Since the overlapping within individual metabolites and between other metabolites due to *J*-coupling cancels each other by dephasing effect at longer echo times, metabolites such as γ-aminobutyric acid glutamate and glutamine are hard to measure using long echo times (TE > 50 ms) with in vivo proton spectroscopy [4].

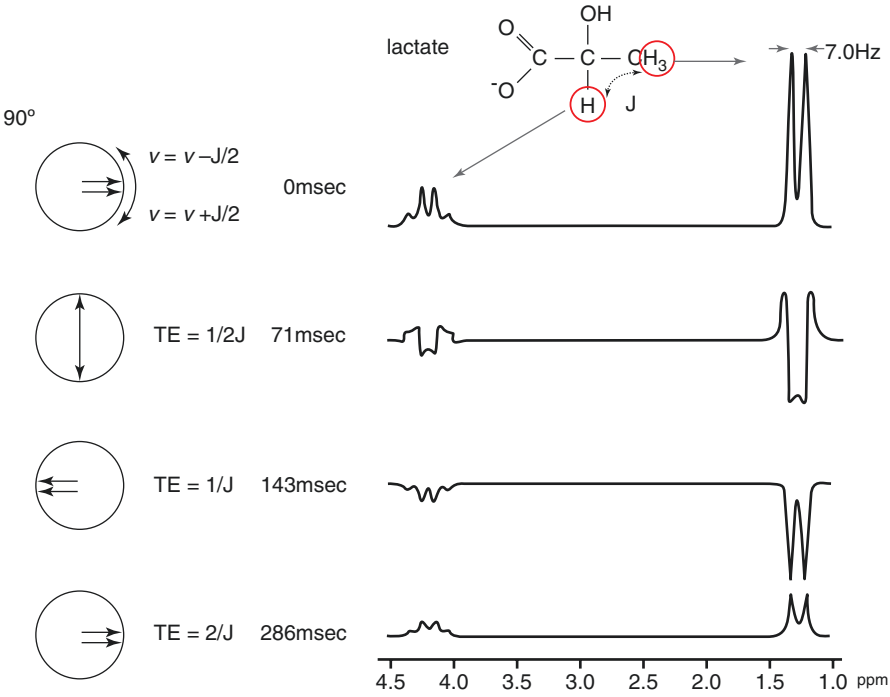

Fig. 7.2 MR spectrum of lactate showing different phase modulations caused by *J*-evolution for different echo times. The proton signal from the methyl group (CH_3) is split into a doublet by the proton of the methine group (CH). On the other hand, the proton signal from the methine group (CH) is split into a quartet with a signal ratio of 1:3:3:1 by the three protons of the methyl group (CH_3). In coupled spin systems, the amplitude and phase of the resonance are modulated and suffer large signal attenuation during T2 decay

7.3 Metabolites Seen by Proton MRS in the Brain

At high magnetic fields of 7 T and above, at least 18 metabolites can be identified noninvasively by MRS [5, 6]. In clinical MR scanners at 1.5 T, the metabolites distinguishable in proton MRS are limited to several metabolites such as choline-containing compounds, creatine + phosphocreatine, glutamine + glutamate, myoinositol, and *N*-acetylaspartate + *N*-acetylaspartylglutamate (NAAG). γ-Aminobutyric acid (GABA) can be measured too by a spectral editing method like MEGA-PRESS in a clinical MR machine at 3.0 T [7].

7.3.1 *N*-Acetylaspartate (NAA)

NAA is an amino acid present in the brain in high concentrations, second in amount to glutamic acid. Interestingly, NAA is found only in the central and peripheral nervous systems and is thought to reflect neuronal density and dysfunction. The

NAA concentrations in the brains of mammals and birds are especially high (up to 10 mM), while in the brains of amphibians, reptiles, and invertebrates, it is much lower [8, 9]. The NAA concentration in the peripheral nervous system and the retina is about 10–20% that of the levels in the central nervous system [10–12]. NAA shows a conspicuous singlet peak at 2.02 from the *N*-acetyl (CH3–CO–NH–) moiety in vivo MRS and has attracted intense interesting from researchers, but little is known about its metabolism and functions. Several functions have been suggested to explain the presence and amount of NAA in the nervous system, including the following:

1. NAA works as an osmoregulator/molecular water pump, removing metabolic water from neurons [13].
2. It is an immediate precursor for NAAG synthesis.
3. It shuttles acetate into oligodendrocytes for myelin synthesis.
4. It is a storage and transport form of acetyl-coenzyme A (acetyl-CoA) in the nervous system that lacks substantial glycogen reserves [14]. Acetyl-CoA cannot cross cell membranes, so it must be converted to citrate in the Krebs cycle for transport to the cytoplasm. NAA may function as an exportable molecule carrying both acetate and aspartate.

NAA is synthesized from L-aspartate and acetyl-CoA by the enzyme aspartate N-aspartate transferase (Asp-NAT) in an oxygen- and ADP-dependent manner. The synthesis increased with age within the first few years of life, and plateaus from age 2 to 20 years, depending on the brain region [15, 16]. In the adult brain, NAA synthesis occurs almost only in neurons [17]. NAA synthesis is coupled to glucose metabolism, and the metabolic relationships can be shown in the following equation [18, 19].

$$40\mathrm{Glc} + 240\mathrm{O}_2 = 240\mathrm{CO}_2 + 240\mathrm{H}_2\mathrm{O} + 1440\mathrm{ATP} + 1\mathrm{NAA} + 0.1\mathrm{NAAG}$$

The time required for NAA synthesis is comparable to that for the brain glycogen synthesis from glucose in the awake rat [20], which takes about 10–14 h [21, 22], and much slower than the synthesis of glutamate, around 1–2 h [23–25]. Furthermore, the NAA synthesis rate in the human brain is in the same range as that found in rat cortex [22]. Therefore, the estimated complete turnover of NAA from glucose is thought to be very slow, taking approximately 70 h [21]. Asp-NAT has not been identified molecularly due to the difficulty of purification, but a recent study indicates that *N*-acetyltransferase 8-like protein (NAT8L) is a strong candidate for Asp-NAT [14, 26]. It has long been believed that NAA is synthesized within mitochondria, but NAT8L is localized to the membrane of endoplasmic reticulum [27]. Glutamate acts as a substrate for NAT8L, with a 50 times lower affinity, and shows competitive inhibition of the aspartate incorporation into NAA [26].

NAA is released to extracellular fluid space and taken up by glial cells via sodium-dependent dicarboxylate (NaDC3) transporters [28]. In oligodendrocytes, NAA is hydrolyzed by aspartoacylase (ASPA) to aspartate and acetate [18], and that acetate is used in lipid synthesis [29] (Fig. 7.3). Deficiency of ASPA causes leukodystrophy, which appears as spongy degeneration of the white matter that is known as Canavan disease [30]. In this case, MRS shows a high concentration of NAA

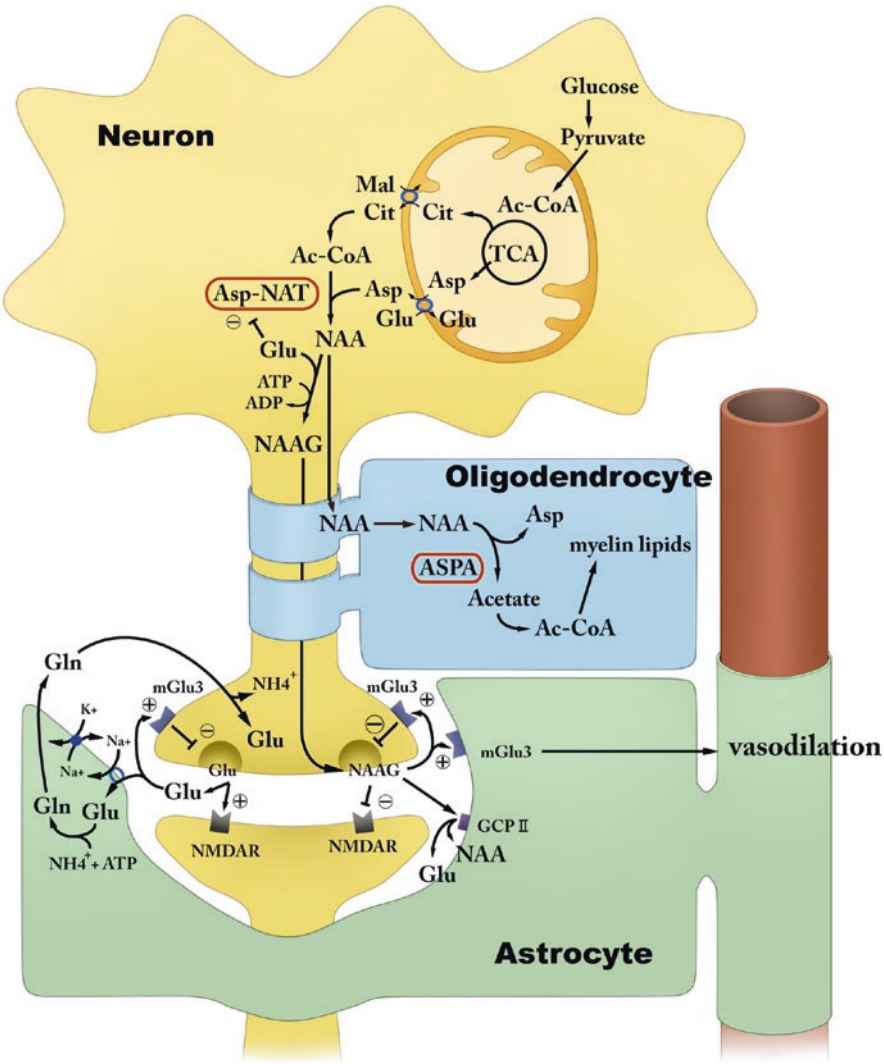

Fig. 7.3 *N*-Acetylaspartate (NAA) and *N*-acetylaspartylglutamate (NAAG) metabolism and function of the brain. Aspartate (Asp) is synthesized in the mitochondria and exported by neuronal AGC1 ARALAR. NAA is synthesized from acetyl-coenzyme A (Ac-CoA) and Asp by aspartate-*N*-acetyltransferase (Asp-NAT), now thought to be a membrane-bound microsomal enzyme. Ac-CoA arises from citrate (Cit) through ATP citrate lyase and is transported into cytoplasm from mitochondria through the citrate carrier. The NAA transporter NaDC3 is primarily expressed in astrocytes and oligodendrocytes and transports NAA into these cells in a Na^+-coupled manner. NAA carries Ac-CoA from neurons to oligodendrocytes for synthesis of myelin lipid. Aspartoacylase (ASPA) cleaves NAA giving rise to acetate and Asp. NAAG is synthesized by NAAG synthetase (NAAGS) in an ATP-dependent reaction. NAAG is released from presynaptic terminals as a neurotransmitter. Released NAAG is degraded into NAA and glutamate extracellularly by GCP-II. NAAG also binds to mGluR3 on presynaptic membranes and inhibits release of neurotransmitters, including glutamate and GABA. NAAG activates mGluR3 on astrocytes, initiating astrocyte Ca^{2+} waves responsible for astrocyte-astrocyte and astrocyte-vascular system signaling and induction of vasodilation and consequent hyperemia in locally activated neurons

which is fairly specific to this disease. Interestingly, there was one reported case of NAA and NAAG deficiency in the brain, possibly due to lack of Asp-NAT [26], and the patient suffered lack of expressive speech, truncal ataxia, seizures, mental retardation, and microcephaly [31–33].

7.3.2 *N*-Acetylaspartylglutamate (NAAG)

NAAG is the most abundant dipeptide of the brain and is synthesized by NAAG synthetase catalyzing the ATP-dependent condensation of NAA and glutamate [34]. Absolute measurement of NAAG has shown that its concentrations in the brain are approximately 0.6–1.5 mM in gray matter and 1.5–2.7 mM in white matter. NAAG is released together with glutamate during neuronal depolarization. NAAG activates metabotropic glutamate receptor mGluR3 [35], localized on presynaptic site of neuron terminal and on astrocyte. The presynaptic mGluR3 receptors inhibit release of neurotransmitters, including glutamate and GABA [36–40]. NAAG also acts on NMDAR as a partial antagonist. These negative modulatory effects of NAAG must be important in synaptic plasticity and also in neuronal protection against excessive glutamate release. NAAG activates mGluR3 on astrocytes, initiating astrocyte Ca^{2+} waves responsible for astrocyte-astrocyte and astrocyte-vascular system signaling and induction of vasodilation and consequent hyperemia in locally activated neurons [19]. As NAAG is a signal molecule specifically targeting the astrocytic mGluR3 receptor, its triggering of brain-activation-related focal BOLD response is thought to be stronger than that of glutamate [41] (Fig. 7.3).

NAAG is hydrolyzed into NAA and glutamate by glutamate carboxypeptidase type II (GCP-II) which is also known as prostate-specific membrane antigen (PSMA) or folate hydrolase 1 (FOLH1), and the products are transported into astrocytes and oligodendrocytes. GCP-II inhibitors have been shown to reduce brain glutamate resulting in neuronal protection in preclinical models of stroke, amyotrophic lateral sclerosis, and neuropathic pain [42].

7.3.3 Creatine and Phosphocreatine (Cr)

Creatine and phosphocreatine (PCr) are abundant in metabolically active tissues such as the muscle, heart, and brain. PCr anaerobically donates a phosphate group to ADP to form ATP via creatine kinase during the first few seconds following an intense muscular or neuronal effort, by the well-known pathway as follows:

$$\mathrm{PCr} + \mathrm{ADP} = \mathrm{ATP} + \mathrm{Creatine}$$

Creatine kinase is highly concentrated in the cerebellum, choroid plexus, and hippocampal granular and pyramidal cells [43]. In postmortem examination, brain-type creatine kinase levels were found to be decreased in the patients with AD, especially in the temporal, cingulate, and occipital cortices [44]. Creatine is biosynthesized endogenously by two sequential steps. The first step is guanidinoacetate

synthesis from arginine by L-arginine/glycine amidinotransferase (AGAT) expressed mostly in the kidneys, and the second step is creatine synthesis from guanidinoacetate by guanidinoacetate methyltransferase (GAMT), expressed mostly in the liver. Creatine is imported through the blood-brain barrier by a specific transporter, SLC6A8, also called creatine transporter (CRT), expressed in the microcapillary endothelial cells. CRT is widely expressed in the adult mammalian brain, particularly in regions related to limbic functions [45–47]. In general, half of creatine stores originate from endogenous synthesis, while the other half is supplied from food. However in the brain, CRT is scarce in astrocytes, particularly in their feet lining microcapillary endothelial cells [48]. Thus the transport of creatine from blood to brain seems to be relatively insufficient [49, 50], and the brain depends more on its own creatine synthesis through AGAT and GAMT expression than on external supply from blood [51, 52]. Both AGAT and GAMT are found in all types of brain cells but rarely together in any one cell [48, 53–55], so guanidinoacetate must be moving from cells holding AGAT to cells holding GAMT [52]. However, guanidinoacetate is not transported without CRT, so in case of CRT deficiency, even with AGAT and GAMT expression in the CNS, MRS finds little or no Cr (creatine and PCr) in the brain [56]. GAMT is expressed strongly in oligodendrocytes, moderately in astrocytes, and very weakly in neurons [55], suggesting that the final step of creatine synthesis in the brain predominates in glial cells.

In proton MRS, the singlet peaks at 3.07 and 3.96 ppm arise from the methyl and methylene protons of creatine and PCr, respectively. The resonances of creatine and PCr are very close, but the methylene resonance of creatine at 3.931 ppm and PCr at 3.930 ppm can be separated into two components at magnetic fields of 7.0 T and higher. Total creatine (Cr) level seems to be fairly stable with time unless there is some severe disease, which is why Cr is usually reliable as an internal standard. However, the Cr signal may increase or decrease in disease.

7.3.4 Choline-Containing Compounds (Cho)

There are several types of phospholipids, including phosphatidylcholine (PC), phosphatidylethanolamine (PE), phosphatidylserine (PS), sphingomyelin, phosphatidylinositol, and cardiolipin. Of these, only PS carries a net negative charge. Newly synthesized lipids are incorporated into the plasma membrane, where PC ends up mainly on the external surface, whereas the aminophospholipids, PS and PE, end up mostly on the cytoplasmic [57]. In most eukaryotic membranes, PC and PE make up some 60–85% of the phospholipid fraction, but the relative amounts of other phospholipids vary between species and between cell types [58]. The major pathway of biosynthesis of PC and PE is the cytidine diphosphate (CDP)-choline and CDP-ethanolamine pathway, known as the “Kennedy” pathway (Fig. 7.4). PE is converted to PC by phosphatidylethanolamine *N*-methyltransferase (PEMT), which occurs mostly in the liver in mammals. Phospholipids are hydrolyzed by phospholipases. PC is catabolized into lyso-PC by phospholipase A or into glycerophosphocholine (GPC) by phospholipase

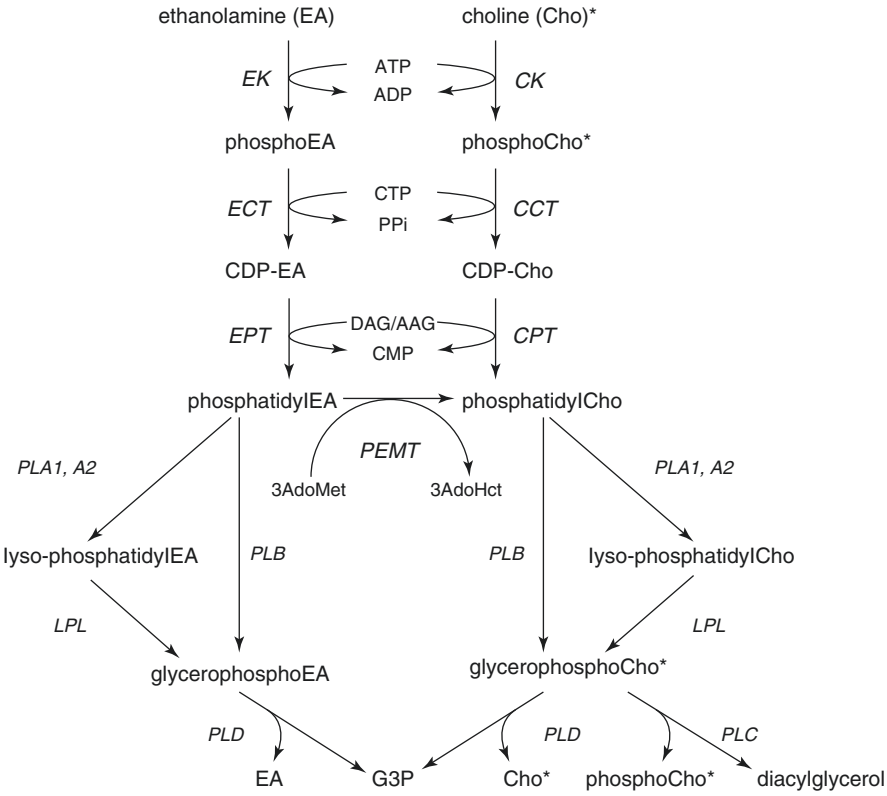

Fig. 7.4 Pathways of glycerophospholipid biosynthesis and catabolism. The glycerophospholipid is synthesized by three enzymatic steps. First, choline kinase (CK) catalyzes the phosphorylation of choline with ATP to form phosphocholine. The second step is the synthesis of high-energy donor CDP-choline, which is rate-limiting of the pathway. This step is catabolized by the phosphocholine cytidylyltransferase (CCT) to synthesize CDP-choline from phosphocholine and CTP. The final step is the synthesis of phosphatidylcholine, which is catabolized by the cholinephosphotransferase (CPT) using CDP-choline and a lipid anchor such as diacylglycerol (DAG) or alkylacylglycerol (AAG) to form phosphatidylcholine [172]. The synthesis of water-soluble glycerophosphocholine (GPC) could involve sequential activity of a phospholipase A (PLA) and a lysophospholipase (LPL) or, alternatively, activity of a single phospholipase B (PLB). GPC is then degraded by hydrolysis to glycerol-3-phosphate (G3P) and choline, catalyzed by phospholipase D (PLD). The synthesis and catabolism of phosphatidylethanolamine is similar to the process of phosphatidylcholine. The MRS-visible choline-containing compounds (*) usually present in cytosol as choline, phosphocholine, and GPC. GPC is produced by cell membrane breakdown, but phosphocholine is produced both in catabolic and anabolic process. *EK* ethanolamine kinase, *ECT* phosphoethanolamine cytidylyltransferase, *EPT* ethanolaminephosphotransferase, *PEMT* phosphatidylethanolamine N-methyltransferase

B. Lyso-PC is rapidly converted to GPC by lysophospholipase (LPL). GPC is then catalyzed into free choline and glycerol-3-phosphate (G3P) by choline phosphodiesterase or phospholipase D (PLD) (Fig. 7.4).

Most of the choline in the brain is located in cell membranes, bound as phospholipids, and this immobile choline is invisible by MRS. Therefore, the Cho peak of MRS reflects water-soluble forms of choline such as phosphorylcholine and GPC. The contribution of free choline seems to be very little because its concentration is usually under detection limit of MRS. The concentration of the total amount of these MRS-visible choline-containing compounds in human brain tissue is approximately 1–2 mM [59–61]. Choline, phosphorylcholine, and GPC show a strong singlet resonance at 3.22 ppm from protons of trimethyl moieties ($-N(CH_3)_3$) at 3.2 ppm, whereby small differences can be observed between 3.5 and 4.3 ppm in multiplet resonances from the remaining CH_2 protons. The concentration of PE in human brain is approximately 0.5–1.0 mN [62], and it can be detected by MRS, as it shows multiplet resonances around 3.1–3.2 and 3.8–4.0 ppm. Possible overlap of resonances from ethanolamine, mIns, glucose, and taurine should be taken into account when using short echo MRS.

The Cho peak is considered as a marker of cellular density and membrane turnover. Elevated Cho signals have been found in tumors, in active demyelination sites, and in inflammation. There is a report that the Cho peak is increased in AD, and in patients with amnestic type MCI (aMCI) who progress to AD, but decreased in patients with aMCI who remain stable [63]. It has also been shown that a higher Cho/Cr ratio in the white matter is associated with an increased risk of developing AD within 4 years [64]. It is reported that soluble Aβ oligomers can open cell channels, letting calcium ions into the cell leading to mitochondrial dysfunction, inflammation, and even cell death [65, 66]. Low concentrations of soluble $A\beta_{1-40}$ or $A\beta_{1-42}$ peptide induce calcium-dependent release of arachidonic acid via inducing PLA_2 activation in a calcium-independent manner [67].

7.3.5 Myoinositol (mIns)

Myoinositol is a major osmolyte released from brain cells, mainly from astrocytes, and also serves as the precursor to phosphatidylinositols. Phosphatidylinositol 4,5-bisphosphate (PIP_2) is the source of the inositol 1,4,5-triphosphate (IP_3), which is a second messenger in signal transduction and lipid signaling. Inositol is a cyclic sugar alcohol consisting of six-carbon rings with six NMR detectable protons and exists in nine possible stereoisomers, of which mIns is the most abundant in human tissue, representing about 90% of total inositol content. The concentration in the brain is normally 4–8 mM, sufficient for MRS sensitivity. NMR of mIns shows a doublet of doublets centered at 3.52 ppm from ^{1}CH and ^{3}CH protons and a triplet at 3.61 ppm from ^{4}CH and ^{6}CH protons. In practice, these proton peaks are seen as a singlet at about 3.57 ppm at 1.5 T. The proton resonances from ^{4}CH and ^{6}CH partially overlap with the glutamate and glutamine multiplet peaks. Since the T2 relaxation time of the ^{4}CH and ^{6}CH protons is short due to their strong coupling, mIns can only be detected at short echo times. The second most concentrated isomer is scyllo-inositol (0.2 mM), which possesses six symmetric protons and evokes a singlet at 3.34 ppm.

Myoinositol is obtained from food and by de novo synthesis. Synthesis and breakdown occur predominantly in the kidneys, so both neurons and glia need to take it in via transporters, sodium/myoinositol cotransporter SMIT1 and SMIT2 and H+/myoinositol cotransporter HMIT. SMIT is expressed in the kidneys and in the brain [68, 69] and is found in both neural and non-neural cells [70]. It is well known that the upregulation of SMIT1 and SMIT2 occurs under hyperosmotic conditions [71–75], whereas no such osmoregulatory function has been reported for HMIT in mammals. SMIT activity is increased by extracellular alkalization, although under physiological conditions, this effect is small. HMIT is activated by extracellular acidification and is close to inactive at pH 7.5 or higher [76]. Since the activity of HMIT is regulated by pH, mIns uptake may induced at any site of low extracellular pH caused by synapse activation or activated glial cells around the synapse [76]. However, the buffering system in the brain is very complicated, and little is known about HMIT. There are many conflicting findings on HMIT, for example, that it is predominately expressed in astrocytes [76] or specifically in neurons [77] and is localized on cell surfaces [78] or in intra-cytosolic membranes [77, 79, 80] and regulating intracellular signaling.

There are several clinical reports of decreased or increased mIns levels of the brain when measured by MRS. It is known that neurodegenerative disorders such as AD, Huntington's disease [81], and spinocerebellar ataxia [82] show increased level of mIns in the affected brain areas. People with Down syndrome show significantly increased mIns concentrations in their parietal [83] and hippocampal [84] regions before neuronal degeneration becomes apparent [85]. Interestingly, the human SMIT gene is located in q22.1 on chromosome 21, and inability to downregulate expression of three copies of the osmoregulatory gene could result in increased flux of mIns [86]. Chronic hyponatremia may cause reduction in mIns [87]; and conversely, chronic hypernatremia increases brain mIns concentration [88]. Ammonia is normally converted to urea in the liver, but in cases of chronic liver dysfunction, accumulated ammonia in the brain is detoxified in astrocytes by conversion to glutamine because of the lack of the urea cycle in the brain. This may increase intracellular osmolarity, and astrocytes may compensate by releasing mIns [89]. Lithium treatment may reduce mIns levels in bipolar patients [90, 91]. Valproate causes 20% reduction of mIns level in mouse frontal cortex [92]. These drugs may inhibit monophosphatase, an enzyme required for inositol recycling and de novo synthesis [93]. However, the proportion of mIns participating the phosphatidylinositol second messenger cycle system appears to be low to affect total brain mIns signal.

Whereas mIns has long been seen as a marker of glial cell proliferation, based on the fact that higher mIns levels are found in cultured astrocytes than in neurons in vitro [94, 95], the true mechanisms of increase or decrease of its concentration remain largely unclear. Brain mIns levels may not always correlate with other molecular markers of gliosis [96–98]. It should be noted that high concentrations of mIns are observed in some types of cultured neurons [99, 100] and that mIns is actively taken up into most types of mature brain cells, including neurons and glia [70]. Therefore the assumption that mIns is a specific glial maker should be treated with caution.

7.3.6 Glutamine and Glutamate (Glx)

In mammalian brains, glutamate is both the main excitatory neurotransmitter and the direct precursor of the inhibitory neurotransmitter γ-aminobutyric acid (GABA). The concentration of glutamate of the brain is about 6–12 mM, with a significant difference between gray and white matter. Under steady-state conditions, two thirds of the glucose oxidation in astrocytes is used for de novo synthesis of glutamate [101], and most astrocytic glutamate is converted to glutamine that is transferred into glutamatergic neurons, completing the glutamate-glutamine cycle. The uptake of synaptic glutamate provides up to 80% of the substrate for glutamine synthesis [102]. Since glutamate transport by excitatory amino acid transporter (EAAT) is coupled to and driven by cotransport of sodium, proton, and potassium ions, any increase in rate of the cycle is matched by increased energy consumption. In this model of glutamate metabolism, glutamate metabolism in the brain is compartmentalized into two pools: a larger neuronal pool comprising about 80% of total glutamate, metabolized with relatively slower turnover time, and a smaller astrocytic pool comprising about 20% of total glutamate, which is rapidly converted to glutamine [103].

NMR of glutamate shows a doublet of doublets centered at 3.75 ppm from the single ^{2}CH methine proton, while the resonances from the other four protons appear as multiplets between 2.04 and 2.35 ppm. Glutamine and glutamate are structurally similar, and their resonances overlap each other. The ^{2}CH methine proton of glutamine shows triplet peak at 3.75 ppm, while the multiplets peaks from the methylene protons are closely resonated between 2.12 and 2.46 ppm. Glutamine has also two amide protons at 6.82 and 7.73 ppm. Unfortunately it is difficult to distinguish between glutamate and glutamine by MRS at low magnetic field strength, so the total amount of glutamate and glutamine is often summed up as Glx. There are minor contributions from glutathione and GABA to this combined signal. Since the concentration of glutamine is almost the same as that of glutamate in the brain [104, 105], the glutamine signal is the major confounder of glutamate quantification. The strong coupling of protons also causes different appearances of spectrum at different echo times and different magnetic field strengths. These factors make their observation and quantification difficult with MRS, although the sum of glutamine and glutamate (Glx) can be quantified with high accuracy. Since the glutamine and glutamate levels can change in opposite directions, the total amount of these metabolites tends to be stable. Most clinical MRS studies can measure only this combined amount, resulting in a reduced sensitivity of Glx as a disease marker. Moreover, about 21% of the total glutamate of the brain is thought to be located in intracellular compartments, in which NMR hardly detects it [106].

7.4 Spectrum Analyses

The area under a peak is proportional to both the number of nuclei per molecule of a metabolite resonating at that frequency and the metabolite concentration to which the nuclei belong. Therefore, quantitative measurement can be done either from the

amplitude of the first data point of the time domain signal, that is, free induction decay (FID), or from the determination of peak areas in the frequency domain after Fourier transformation of FID. Reliable metabolite quantification by MRS is still challenging. One important factor causing systematic error is the baseline correction. The baseline in any MR spectrum is much affected by field inhomogeneities, tissue heterogeneities, and patient movements, all of which may distort the line shape. There have been various proposals to correct these unwanted distortions during signal processing [107–112]. For accurate quantification in short echo MRS of the brain, correction must be made for the contribution of macromolecules to the baseline [113, 114].

A number of advanced techniques based on mathematical models have been developed for analyses of MR spectra. Time domain methods are grossly divided into "black-box" and interactive model methods. HSVD and HSLVD are commonly used black-box methods, so as VARPRO and AMARES are well-known interactive methods. Frequency domain methods can be also divided into nonparametric and parametric methods. Nonparametric quantification is performed by simple integration of the areas under the peaks of interest, but this method cannot disentangle overlapping peaks, and its accuracy is highly dependent on proper phase correction, which is far from trivial [115]. The parametric methods are based on a model function to fit the spectrum represented by LCModel.

VARPRO is a basic program for time domain analysis that uses a simple Osborne's Levenberg-Marquardt algorithm for local optimization. It has been replaced by AMARES, which allows accurate and efficient parameter estimation of MRS signals, using a sophisticated nonlinear fitting in the time domain with prior knowledge about the signal parameters, the model function (Lorentzian, Gaussian, Voigt model), and the type of signal (FID or echo). These methods cannot remove nuisance peaks such as macromolecules, lipids, unsuppressed water, and other unknown signals.

Two other programs, AQSES [109] and QUEST [116], make use of a metabolite basis set, which can be built up from simulated spectra from quantum mechanics such as NMR-SCOPE [117] or GAMMA [118] or from in vitro spectra [119]. AQSES [109] is a program that has been especially developed for short echo MRS. In its framework, VARPRO is modified to enable prior knowledge of upper and lower bounds on the nonlinear parameters, equal phase corrections for each metabolite, and optimize the nonlinear least squares problem. AQSES is freely available as Java open-source software AQSES GUI [109, 118], as a measurement system in the Matlab® graphical user interface SPID [120], and as a plug-in in the jMRUI software package (version 4.1) [121].

The jMRUI software [122] runs in either the time or the frequency domain, using signal processing algorithms such as VARPRO, HLSVD, and AMARES [123]. Basis spectrum fitting in jMRUI is performed by the Quantum ESTimation (QUEST) [116] algorithm, which fits the data to a basis set in the time domain. Both AMARES and QUEST enable handling of macromolecule signals and spectral baselines in a number of ways by truncation or down-weighting of the initial points in FID. jMRUI can also use basic methods such as HSVD or HSLVD that can be applied to remove a residual water signal as preconditioning.

LCModel (Linear Combination of Model) is widely used commercial software [124] that uses frequency domain fitting by a linear combination of individual peak profiles of metabolites. The complexities of metabolite spectra become an advantage for this program, since overlaid peaks from different metabolites can be separated from the information at the peaks of other metabolites. This software is fully automatic (noninteractive) and operator independent, so it is highly suitable for studies across centers. LCModel uses a nearly model-free lineshape function and presumes neither a Lorentzian nor a Gaussian lineshape model. It uses the water signal as an internal reference and integrates with the basis set contained in the software, acquired from the standard phantom. It uses the Levenberg-Marquardt nonlinear fitting algorithm and gives some error assessments of the Cramér-Rao type or the like. Mosconi et al. [125] recently compared those four measurement methods (LCModel, AMARES, QUEST, and AQSES) to see whether they produced different statistical results and found that LCModel worked best in their simulation.

7.5 Quality Control

Reliability of fit can be estimated by Cramér-Rao lower bounds (CRLB) [126]. CRLB gives the minimal possible variance on a fit parameter, so any peak measurement with this value over 20% is usually judged as unreliable. MRS is highly sensitive to inhomogeneities in the magnetic field, so shimming is an important procedure for spectral quality. Shimming reduces field inhomogeneity reading to improve water suppression, signal-to-noise ratio (SNR), and spectral resolution. Since SNR is directly reflected in the CRLB that is more directly linked to confidence limits, CRLB seems to be a better parameter by which to judge the quality of quantified data than mere statements of SNR. Linewidth is defined as the full-width at half-maximum (FWHM) peak height in the frequency domain and also reflected in the CRLB indirectly. Broad linewidth means poor spectral resolution that is critical for model fitting. One should note that CRLB indicates only the quality of the spectral fit and does not necessarily reflect the quality of the original data. CRLB is calculated on the assumption that the fitting model and prior knowledge are correct and that systematic errors are not reflected. Possible sources of systematic error are inaccurate T1 and T2 values for each metabolite, incorrect prior knowledge, difficulties in reference-setting and calibration, ROI position or size, structural mixture of GM/WM/CSF, outer volume signal contamination, and operational mistakes [127]. Fit residual is the difference between the measured signal and the model fit, and ideally this should be flat or only white noise if the model fitting is perfect. Fit residual is usually checked by visual inspection, but numerical estimation has been worked out [128]. In LCModel, residues are used as noise level of SNR. Kreis [127] recommended the following acceptance criteria for MR spectral data as follows: FWHM <0.1 ppm (6.4 Hz at 1.5 T, 12.8 Hz at 3 T), CRLB $\leqq$ 50%, the fitting residual should not contain unexplained features, and the spectra should not contain artifacts. From our experience, it is better to set CRLB acceptance criteria as <15% for clinical use regarding possible dementia.

7.6 Acquisition Parameters and Sequences for MRS

The range of echo time (TE) in brain MRS varies from 18 ms to 288 ms, affecting signal peak height and shape depending on the spin-spin relaxation time (T2) and *J*-coupling of each metabolite. Since diphase and signal loss of protons occurs more rapidly in metabolites with short T2 than long T2, the height of metabolite peaks will change with TE in MRS. For example, in case of the relation between Cr and NAA, since the T2 of Cr is significantly shorter than that of NAA, the peak ratio of NAA/Cr becomes larger in the spectrum obtained from long TE than short TE. Since the T2 relaxation times for Glx and mIns are very short, the peaks of these metabolites cannot be detected at long echo times (Fig. 7.5). This is more obvious in Cho/Cr ratio because T2 for Cho is longer than that for NAA. The T2 values of the metabolites also differ depending on the environment, even in the difference between gray and

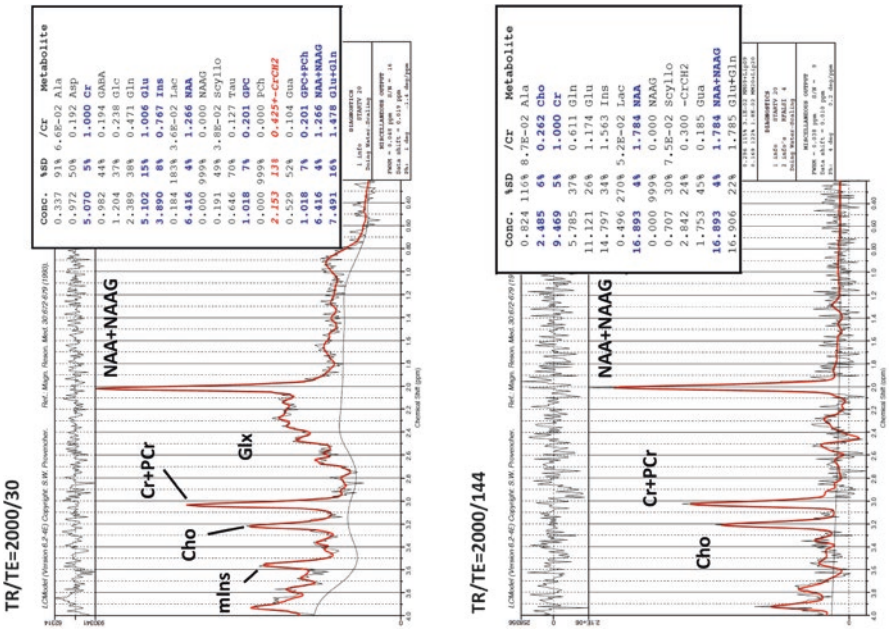

Fig. 7.5 MR spectra of posterior cingulate cortices obtained from normal elderly volunteer. The peak ratio of NAA + NAAG/Cr is 1.266 at echo time = 30 ms, whereas it is 1.784 at echo time = 144. LCModel calculates each metabolite concentration by using tissue water as an internal standard. It should be noted that the default of LCModel for T2 correction of water (T2 = 80 ms) is set at TE = 30 ms, i.e., exp.(−TE/T2) = exp.(−30/80). Therefore if researchers use any TE other than 30 ms, the concentration value of LCModel must be corrected. If TE = 144, then the metabolite concentrations (TE = 144) = (values of LCModel) × exp.(−144/80)/exp.(−30/80) = (values of LCModel) × 0.243. For about NAA + NAAG, it should be 16.893 × 0.243 = 4.105 mM that is too low when compared to the value of 6.416 mM obtained from the results at TE = 30 ms. This is because of the effects of T2 relaxation of NAA and NAAG in vivo, which are uncertain and might differ in each individual. Therefore it is better to use long TR and short TE for quantitative measurement of metabolites to minimize the uncertain effect of T1 and T2 relaxation of the metabolites in vivo

white matter. Longer echo time is sometimes used for lactate identification. Lactate and lipid resonances are overlaid together, but the lipid resonances may decay fully in case of long echo times that facilitate identification of the lactate peak.

Theoretically, metabolite signals are more affected by uncertain T2 when using long TE than short TE that will cause errors in absolute quantification (Fig. 7.5). Therefore using shorter TE seems to be more profitable for absolute quantification. The other advantage of using short TE is to gain higher signal intensity and to enable detection of metabolites with short T2 such as mIns, glutamate, glutamine, GABA, scyllo-inositol, and lipids. On the other hand, this may cause unwanted distortion of the spectrum baseline and superimposition of peaks from metabolites that may lead to errors in both absolute and relative metabolite quantitation. At short TE, multiple resonance peaks between 2.05 and 2.45 ppm from glutamine, glutamate, and GABA partially overlap the NAA peak at 2.01 ppm. Since the information contained in the short TE and long TE spectra are actually complementary, it may be desirable to use short and long TE sequences as far as permitted by total scanning time, patient tolerance, and cost.

There are two major sequences for volume localization in single-volume MRS: stimulated echo acquisition mode (STEAM) and point-resolved spectroscopy (PRESS). STEAM offers advantages for using MRS of very short TE and more effective water suppression than PRESS because the pulses of water suppression can be applied prior to the first slice selective pulse and during the *TM* phase [129]. The advantages of PRESS are that it gives double the signal intensity given by STEAM, it is less disturbed by motion and by diffusion, and it does not suffer from multiple-quantum effects. STEAM has a tendency to acquire a volume larger than the chosen VOI, whereas PRESS has the opposite tendency [130].

The methods for absolute quantification of metabolites are summarized elsewhere [131]. In brief, there are three main methods: internal water reference, external reference, and electrical reference. In the method using internal water reference, the signal from unsuppressed tissue water from the same VOI for MRS is used as internal standard. Researchers need to correct the results by %CSF of the VOI and by T1 and T2 relaxation times of each metabolite and water. The inaccuracy of the method is caused by uncertain tissue water content, uncertain T1 and T2 relaxation times of each metabolite, receiver gain instability, and compartmentation such as gray and white matter in the VOI.

7.7 Clinical Application of MRS for Dementia

Many kinds of disorders cause dementia including neurodegenerative disease, vascular or small vessel disease, brain trauma, hydrocephalus, inflammatory diseases, and metabolic disorders. Of these, neurodegenerative diseases represented by Alzheimer's disease (AD), dementia with Lewy bodies (DLB), and frontotemporal dementia (FTD) are frequently encountered. Recent studies have been disclosing the causes of neurodegenerative dementia at molecular levels, and disease classification is becoming better understood in terms of pathogenesis (Table 7.2).

Table 7.2 Classification of degenerative dementias

Pathology	Disease	Tau	Parkinsonism
Amyloid β	AD	4R + 3R(n)	–
α-Synuclein	DLB	4R + 3R(n)[a]	++
Tau	SD-NFT	4R + 3R(n)	–
	AGD	4R(n,g)	–
	PSP	4R(n,g)	+
	CBD	4R(n,g)	+
	FTDP-17	3R,3R + 4R,4R	+
	Pick	3R(n,g)	–
TDP-43	FTLD-U (PPA, SD)		–
	FTLD-MND(ALS)		–

AD Alzheimer's disease, *DLB* dementia with Lewy bodies, *SD-NFT* senile dementia of the neurofibrillary tangle type, *AGD* argyrophilic grain disease, *PSP* progressive supranuclear palsy, *CBD* corticobasal degeneration, *FTDP-17* frontotemporal dementia with parkinsonism linked to chromosome 17, *Pick* Pick's disease, *FTLD-U* frontotemporal lobar degeneration with ubiquitin, *FTLD-MND* frontotemporal lobar degeneration with motor neuron disease, *PPA* primary progressive aphasia, *SD* semantic dementia, *ALS* amyotrophic lateral sclerosis

4R and 3R indicate 4-repeat tau and 3-repeat tau, respectively. "n" and "g" indicate tau-rerated degeneration of neurons and glia, respectively

[a]In case of multiple system atrophy (MSA), *α*-synucleinopathy occurs both in oligodendrocytes and neurons

The common features seen by MRS in those degenerative disorders are decreased concentrations of NAA or NAA/Cr ratio and increased concentration of mIns or mIns/Cr ratio. Moreover, these findings show a tendency to region specificity, for example, to the hippocampus and the posterior cingulate and precuneal cortices (PCC) in cases of AD, to the occipital lobes of DLB, and to the frontal lobes in case of FTD. Therefore MRS has potential clinical utility to differentiate those disorders. However, searching for such regional distribution anomalies of metabolites may not make MRS the optimal choice in this context, even if using multi-voxel technique. There are many other examinations that can be more adequate for differential diagnosis, such as FDG PET, CBF SPECT, and MRI morphometry. Moreover, new techniques of molecular image targeting pathognomonic biomarkers have been developed, for example, Pittsburg Compound-B (PiB) PET for beta amyloid, PBB3 PET for tau, imaging of dopamine transporter (DAT) or metaiodobenzylguanidine (MIBG) for DLB, and PK11195 PET for microglia. Molecular imaging with target-specific ligands is a promising approach to the early diagnosis of dementia and the evaluation of anti-dementia therapy. Given such alternative diagnostic tools, how can MRS be best exploited for clinical diagnosis of dementia? There is no clear consensus on this. However, there are several clues from previous studies. Firstly, NAA decrease and mIns increase can be identified by MRS before morphometrical change becomes significant. Secondly, MRS provides additional information to clinicians, which improves diagnostic accuracy (Fig. 7.6). MRS is noninvasive, without use of radioactive agents, and is uniquely

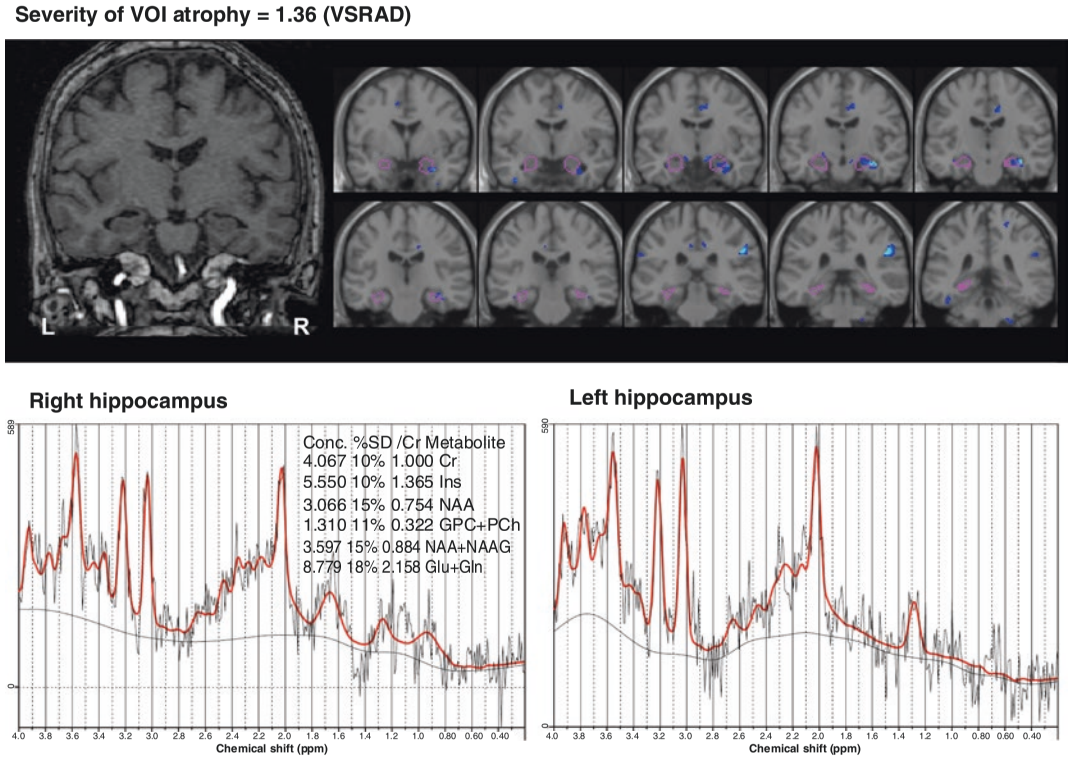

Fig. 7.6 Illustrative case of Alzheimer's disease. A 56-year-old female visited our hospital with her family having a complaint of memory disturbance. She had come to ask the same questions repeatedly following her retirement at 1 year before. At screening, her MMSE score was 28, and CBF SPECT did not show any remarkable abnormality. The hippocampal volume estimated by VSRAD showed slight atrophy (z score = 1.36), which was equivocal as to diagnosis. However, her verbal recognition score in the WMS-R was under 50, and her logical memory II score was 0, indicating deep cognitive impairment. MRS showed significant decrease of NAA + NAAG concentration under 2SD (our institutional range [151]) in her right and left hippocampi and posterior cingulate gyrus. She had no parkinsonian symptoms, and MIBG SPECT showed normal appearance of the heart-to-mediastinum uptake ratio (H/M ratio)

able to provide information on cerebral metabolites that may reflect neuronal or glial activity or transmission. Moreover, MRI and MRS can share the examination time, which is cost-effective and expeditious.

7.7.1 Age-Related Change

Findings on the brain metabolites changes related to normal aging have been inconsistent. Brooks et al. reported that the absolute concentration of NAA decreased significantly with age ($r = -0.42$) with an overall decrease of 12% between the third and seventh decades, whereas any decrease of the concentrations of Cr and Cho was not significant [132]. However, some recent papers showed rather different results. In one study revised from their previous study [133] by adding correction of transverse relaxation time and percentage of cerebrospinal fluid of the voxels centered in the frontal gray and white matter, parietal gray matter, and basal ganglia, the concentration of NAA and Cho showed no significant age-related change, but Cr concentration was significantly increased when measuring frontal white matter [134]. This paper also showed the significant age-related declines in glutamate, especially in the parietal gray matter and basal ganglia [134]. Similar results were reported measuring spectrum of the centrum semiovale, which showed that Cr concentration increased with age ($r = 0.495$, $p < 0.001$), whereas there were no age-related changes in NAA, Cho, and mIns [135]. Another paper [136] showed significant decrease in NAA concentration ($r = -0.36$, $p = 0.007$) and increase in mIns concentration ($r = 0.37$, $p = 0.007$) in the supraventricular white matter. The Cr and Cho concentrations were unchanged with age, but Glx showed U-shaped change with higher concentrations in the young and old subjects [136].

In summary, the age-related changes of metabolite concentrations are not entirely clear, but there seems to be some increase of Cr with age and possible decrease of NAA. Any increase in Cr and mIns may reflect glial cell responses to aging. Researchers need to be aware that metabolite ratios such as the decreased ratio of NAA/Cr that is frequently observed in AD patients do not necessarily mean NAA decrement.

7.7.2 Application to Alzheimer's Disease

Decreased NAA or NAA/Cr ratio has been observed in patients with AD and MCI in medial temporal, posterior cingulate, and parietal cortices. The magnitude of decline has been found to be approximately 10–15% across these brain regions. Several MRS studies have also found an increase in mIns levels by 15–20% in the brain of AD patients. The combination of NAA and mIns measurement may improve the accuracy of discriminating AD patients from normal subjects [137–140]. Decrease of NAA/Cr ratios and increase of mIns/Cr ratios in the PCC correlate with the pathologic severity of AD [141]. NAA/Cr in the medial temporal lobe has been found correlated with Mini-Mental State Examination (MMSE) scores [142]. The

NAA/mIns ratio has also been shown to correlate with MMSE scores and may even be predictive of MMSE decline 12 months later [143]. In a recent study of pathologically confirmed AD patients, reduction of NAA/Cr ratio in the PCC was significantly related to both reduced synaptic vesicle immunoreactivity and accumulation of early intracellular and neuritic hyperphosphorylated tau pathology. Furthermore, elevated mIns/Cr and lower NAA/mIns ratios were found to be related to the accumulation of amyloid-β pathology [144].

The results of MRS studies to distinguish AD patients from normal subjects vary depending on the acquisition parameters of MRS, VOI setting on anatomical regions, measuring single or multi-voxels, and choice of relative or absolute measurements. However, many studies support the clinical usability of MRS as an adjunct diagnostic tool. The overall sensitivity and specificity from the literature for discrimination between AD and normal elderly were 64–94.1% and 72.7–92.3%, respectively. Since the results from these studies have not been validated, the reported values might be somewhat lenient. There is one study showing the results of cross-validation [145]: this study measured hippocampal metabolites in 30 AD and 36 control subjects and compared those findings to the results of MRI-based volumetric analysis. The sensitivity and specificity of MRS alone were 76% and 83%, respectively, somewhat less effective than structural analysis with 93% sensitivity and 86% specificity for the same cohort. Combining the modalities, however, improved the results to 97% sensitivity and 94% specificity. Several other reports confirm the benefits of combining MRS and volumetric MRI for AD diagnosis [140, 146–149]. In a study comparing the diagnostic accuracies of hippocampal volumetry, MRS and diffusion-weighted imaging for discriminating between MCI, AD, and normal elderly subjects [146], the most sensitive tool for distinguishing MCI (79%) and AD (86%) from controls was hippocampal volumetry when specificity was fixed at 80%. For discriminating between AD and MCI, the most sensitive tool was NAA/Cr (67%) measured by MRS of the PCC. Moreover, a combination of these three methods showed better diagnostic sensitivity than any single method for discriminating either AD or MCI from normal. A study of PCC measurement in 25 AD patients, 10 aMCI, and 33 normal volunteers showed an increase of 5.5% for aMCI and of 11.1% for AD in specificity and an increase of 3.7% for aMCI and of 5% for AD in diagnostic accuracy when MRS measures were conjoined with behavioral-functional scales, with a 100% specificity and diagnostic accuracy for distinguishing normal from AD groups [150].

VOI location is also important in clinical use of MRS. There have been many researchers and many variations of VOI settings, and most researches have selected one or a combination of the parietal cortex, PCC, and hippocampus for VOI, those regions being usually involved in AD pathology. Zhu et al. [140] compared 14 AD patients to 22 cognitively normal subjects using short spin-echo (25 ms) MRS imaging (MRSI) with lipid signal nulling by slice selective inversion recovery. AD patients had increased mIns concentrations and mIns/Cr ratios primarily in their parietal gray matter, whereas frontal gray and white matter were spared. In a study of MRSI with long echo time (135 ms) comparing 56 AD patients to 54 cognitively normal subjects [149], NAA concentration was less in AD patients than in healthy

subjects by 21% ($p < 0.0001$) in the medial temporal lobe and by 13–18% ($p < 0.003$) in parietal lobe gray matter but was not changed in gray and white matter of the frontal lobe. MRS of the hippocampus is technically difficult due to its small volume, irregular shape, and location proximity to the skull base or air sinuses which are likely to induce local magnetic field inhomogeneities due to susceptibility difference. However, recently MRS technology has been improving to allow accurate measurements in such regions, and selection of thinner VOIs can reduce susceptibility effects. In a study of single-voxel MRS targeting eight locations of PCC, hippocampus, occipital gray matter, and frontal and parietal white matter in 70 AD patients, 47 aMCI patients, and 52 elderly control subjects, decrease in NAA concentration or increase in mIns concentration was more significant in the hippocampus than in the other regions in both AD and aMCI patients [151].

7.7.3 Application to Mild Cognitive Impairment

MCI is frequently seen as a prodromal stage of dementia and has been a focus for trials to prevent or delay progression to AD. The annual conversion rate of amnestic MCI (aMCI) to AD was approximately 10–15% [152] or 44–64% conversion rate within just 2 years of initial observation [153–155]. However, some aMCI patients do not progress, while some improve over time [156, 157]. In a recent meta-analysis study [158], the adjusted annual conversion rates from MCI to dementia, AD, and VaD were 9.6%, 8.1%, and 1.9%, respectively, diagnosed in specialist centers, and the cumulative proportions who progressed to dementia, to AD, and to VaD were 39.2%, 33.6%, and 6.2%, respectively, which was a low conversion rate than previously thought. This is because MCI is a syndrome representing very heterogeneous disease etiologies. Whereas many MCI patients show AD-type pathology, a substantial number also have non-AD pathology of which cerebrovascular disease is the most common etiology [159]. Therefore an effective test for predicting conversion from MCI to AD would be valuable.

MR spectrum profiles in aMCI patients are generally similar to but milder than those in AD patients [146, 151, 160, 161]. Fortunately a meta-analysis has been done, giving an overview of MRS results (Table 7.3) [162]. As expected, NAA/Cr ratio and NAA concentration were reduced in the PCC and hippocampus of aMCI patients. Effect size was more prominent in NAA concentration than in NAA/Cr ratio. Heterogeneity between studies was lower in NAA concentration ($I^2 = 0.98\%$) than in NAA/Cr ratio ($I^2 = 79.71\%$) when measured in the PCC. The concentration of mIns was increased in PCC, but it was not significant in the hippocampus. It should be noted that the absolute measurements of NAA and mIns in the PCC show significant difference between MCI and normal controls with small variance. Interestingly, Cr concentration is significantly reduced in the hippocampus, but not in the PCC, which may affect the dissociating results of mIns/Cr ratio between the PCC and the hippocampus.

Low concentrations of Cho and Cr in the hippocampus may reflect sparse cellularity or low cellular metabolism in that region. This may be explained by the facts

Table 7.3 Results of the meta-analysis of MCI patients [162]

VOI location	Metabolites	*k*	*n*	ES	CI		*p*	I^2 (%)
Posterior cingulate	**NAA/Cr**	14	798	−0.58	−0.92	−0.24	0.00	79.71
	mIns/Cr	13	774	0.26	−0.04	0.57	0.09	75.25
	Cho/Cr	12	734	0.27	0.00	0.55	0.05	66.71
	NAA/mIns	7	445	−0.76	−1.44	−0.09	0.03	89.83
	NAA	6	383	−0.63	−0.84	−0.42	0.00	0.98
	mIns	6	374	0.39	0.18	0.60	0.00	0
	Cho	6	374	0.09	−0.12	0.30	0.41	6.79
	Cr	5	280	−0.21	−0.45	0.02	0.08	0
Hippocampus	**NAA/Cr**	9	450	−0.43	−0.76	0.09	0.01	59.07
	mIns/Cr	6	218	0.60	0.12	1.09	0.02	63.95
	Cho/Cr	5	182	−0.19	−0.48	0.11	0.21	0
	NAA	5	377	−0.60	−1.03	−0.17	0.01	66.22
	mIns	5	377	−0.03	−0.23	0.31	0.88	21.03
	Cho	5	377	−0.42	−0.70	−0.15	0.00	24.29
	Cr	5	377	−0.40	−0.62	−0.18	0.00	0

k number of studies, *n* total sample size, *ES* effect size for Hedges' g, *CI* confidence intervals, *p* *p*-value, I^2 (%) the percentage of variance in a meta-analysis that is attributable to study heterogeneity (higher value indicates more heterogeneity)
NAA *N*-acetylaspartate + *N*-acetylaspartylglutamate, *mIns* myoinositol, *Cho* choline-containing compounds, *Cr* creatine + phosphocreatine. Minus sign in ES column indicates decrease in MCI compared to controls
Bold characters indicate results significant at $p < 0.05$

that tau pathology generally proceeds earlier in the hippocampus earlier than in the PCC and neuronal loss in the hippocampus must progress substantially to reduce Cho and Cr in MCI patients.

Several longitudinal studies have described differences between converters and non-converters among aMCI patients. The most consistent finding is that converters have lower NAA concentrations and/or lower NAA/Cr ratios than non-converters in several brain regions including the PCC [163, 164], occipital gray matter [164, 165], temporoparietal gray matter [166], and paratrigonal white matter [167]. Unlike those studies, two other studies failed to find baseline differences in metabolites between converters and non-converters [63, 168]. Both these studies measured metabolites in the PCC. One showed that the future decline in cognitive function among MCI patients was predicted by measurement of absolute quantification of NAA and Cr concentrations [168]. The other study later proposed additionally that NAA/Cr ratio measurement improves the prediction of conversion when added to hippocampal volume measurement [169].

A study of 53 aMCI patients followed for a mean period of 3 years [165] examined by 1.5 T MR scanner using PRESS sequence (TR/TE = 2500/30) demonstrated that the ratio of NAA/Cr in the left occipital cortex predicted progression to dementia at 100% sensitivity and 46% specificity, with an area under the receiver operating characteristic (ROC) curve of 0.69 when thresholding the ratio at or below 1.61. In the

hippocampus, a mIns/Cr ratio higher than 1.04 predicted conversion with 66.7% sensitivity and 72% specificity, with an area under the curve of 0.66. The same author [164] later reported the results of a study of 78 aMCI patients with a mean follow-up period of 2 years. An NAA/Cr ratio equal to or lower than 1.43 in the PCC predicted conversion to AD with 74.1% sensitivity and 83.7% specificity, with an area under the curve of 0.84. In the left medial occipital lobe, the predictive value was somewhat lower, with 85.2% sensitivity and 61.4% specificity, and an area under the curve was 0.8. In another study, of a cohort of 119 consecutive aMCI patients followed for a mean period of 29 months [163] examined by 1.5 T MR machine using PRESS sequence (TR/TE = 2500/30), MRS of the PCC predicted conversion from aMCI to probable AD with 82% sensitivity and 72% specificity, based on an NAA/Cr ratio less than 1.40. Similarly, a mIns/NAA ratio in the PCC higher than 0.47 predicted conversion with 79% sensitivity and 67% specificity, with an area under the curve of 0.77. MRS in the left occipital cortex predicted conversion from aMCI to AD with 78% sensitivity and 69% specificity, with an area under the curve of 0.79 using a NAA/Cr threshold less than 1.57. In a study of 41 aMCI patients and 35 cognitively unimpaired controls with a relatively short follow-up period of 1 year [170], examined by 1.5 T MR scanner using PRESS sequence (TR/TE = 1500/35), the NAA/Cr ratio in the left hippocampus was significantly lower in aMCI patients than in controls ($p = 0.008$), but there were no differences in metabolite ratios at baseline between aMCI converters and stable subjects. A mIns/Cr ratio of 0.349 or more in the right parietal lobe predicted progression of disease with 70% sensitivity and 85% specificity. Unfortunately there are no studies reporting absolute values of metabolites.

One interesting project sought surrogate markers for development of MCI using quantitative MRI and MRS markers [171]. Subjects were recruited from cognitively normal 1156 subjects in the population-based Mayo Clinic Study and underwent MRI and MRS examinations. MRS focused on the PCC, and volumes of hippocampus and white matter hyperintensity were measured automatically. After a median follow-up of 2.8 years, 214 subjects had progressed to MCI or dementia. In multivariable modeling, only decreased hippocampal volume and NAA/mIns in the PCC were independent predictors of MCI, with hazard ratio of 1.8 and 1.4, respectively.

To summarize, MRS shows promising results for predicting conversion from MCI to AD, but it is not currently proven by measuring absolute values. The use of absolute quantification, rather than metabolite ratios, may improve the reliability of MRS for this purpose. For earlier diagnosis of MCI, MRS of the hippocampus and entorhinal cortex may be preferable, but MRS of these regions is technically more difficult because of small volumes, field inhomogeneities due to air sinuses, and the presence of cerebrospinal fluid.

7.7.4 Limits on Progress

The technical/procedural aspects of proton MRS have improved with time, but clinical applications have not kept pace. There are as yet insufficient MRS data on the significance of metabolite changes found with various pathological processes. Also,

lack of consensus on standard procedures for MRS complicates the interpretation of results, especially for the purposes of multicenter analysis, which in turn creates difficulty for clinical application of MRS to dementia diagnosis.

References

1. Klunk WE, Panchalingam K, Moossy J, McClure RJ, Pettegrew JW. N-acetyl-L-aspartate and other amino acid metabolites in Alzheimer's disease brain: a preliminary proton nuclear magnetic resonance study. Neurology. 1992;42(8):1578–85.
2. Shiino A, Matsuda M, Morikawa S, Inubushi T, Akiguchi I, Handa J. Proton magnetic resonance spectroscopy with dementia. Surg Neurol. 1993;39(2):143–7.
3. Miller BL, Moats RA, Shonk T, Ernst T, Woolley S, Ross BD. Alzheimer disease: depiction of increased cerebral myo-inositol with proton MR spectroscopy. Radiology. 1993;187(2):433–7. doi:10.1148/radiology.187.2.8475286.
4. Drost DJ, Riddle WR, Clarke GD, Group AMT. Proton magnetic resonance spectroscopy in the brain: report of AAPM MR Task Group #9. Med Phys. 2002;29(9):2177–97.
5. Mekle R, Mlynarik V, Gambarota G, Hergt M, Krueger G, Gruetter R. MR spectroscopy of the human brain with enhanced signal intensity at ultrashort echo times on a clinical platform at 3T and 7T. Magn Reson Med. 2009;61(6):1279–85. doi:10.1002/mrm.21961.
6. Duarte JM, Lei H, Mlynarik V, Gruetter R. The neurochemical profile quantified by in vivo 1H NMR spectroscopy. NeuroImage. 2012;61(2):342–62. doi:10.1016/j.neuroimage.2011.12.038.
7. O'Gorman RL, Michels L, Edden RA, Murdoch JB, Martin E. In vivo detection of GABA and glutamate with MEGA-PRESS: reproducibility and gender effects. J Magn Reson Imaging. 2011;33(5):1262–7. doi:10.1002/jmri.22520.
8. Birken DL, Oldendorf WH. N-acetyl-L-aspartic acid: a literature review of a compound prominent in 1H-NMR spectroscopic studies of brain. Neurosci Biobehav Rev. 1989;13(1):23–31.
9. Burri R, Bigler P, Straehl P, Posse S, Colombo JP, Herschkowitz N. Brain development: 1H magnetic resonance spectroscopy of rat brain extracts compared with chromatographic methods. Neurochem Res. 1990;15(10):1009–16.
10. Nadler JV, Cooper JR. N-acetyl-L-aspartic acid content of human neural tumours and bovine peripheral nervous tissues. J Neurochem. 1972;19(2):313–9.
11. Miyake M, Kakimoto Y, Sorimachi M. A gas chromatographic method for the determination of N-acetyl-L-aspartic acid, N-acetyl-alpha-aspartylglutamic acid and beta-citryl-L-glutamic acid and their distributions in the brain and other organs of various species of animals. J Neurochem. 1981;36(3):804–10.
12. Ory-Lavollee L, Blakely RD, Coyle JT. Neurochemical and immunocytochemical studies on the distribution of N-acetyl-aspartylglutamate and N-acetyl-aspartate in rat spinal cord and some peripheral nervous tissues. J Neurochem. 1987;48(3):895–9.
13. Baslow MH, Hrabe J, Guilfoyle DN. Dynamic relationship between neurostimulation and N-acetylaspartate metabolism in the human visual cortex: evidence that NAA functions as a molecular water pump during visual stimulation. J Mol Neurosci. 2007;32(3):235–45.
14. Ariyannur PS, Moffett JR, Manickam P, Pattabiraman N, Arun P, Nitta A, Nabeshima T, Madhavarao CN, Namboodiri AM. Methamphetamine-induced neuronal protein NAT8L is the NAA biosynthetic enzyme: implications for specialized acetyl coenzyme A metabolism in the CNS. Brain Res. 2010;1335:1–13. doi:10.1016/j.brainres.2010.04.008.
15. Kreis R, Hofmann L, Kuhlmann B, Boesch C, Bossi E, Huppi PS. Brain metabolite composition during early human brain development as measured by quantitative in vivo 1H magnetic resonance spectroscopy. Magn Reson Med. 2002;48(6):949–58. doi:10.1002/mrm.10304.
16. Pouwels PJ, Brockmann K, Kruse B, Wilken B, Wick M, Hanefeld F, Frahm J. Regional age dependence of human brain metabolites from infancy to adulthood as detected by quantitative localized proton MRS. Pediatr Res. 1999;46(4):474–85. doi:10.1203/00006450-199910000-00019.

17. Urenjak J, Williams SR, Gadian DG, Noble M. Specific expression of N-acetylaspartate in neurons, oligodendrocyte-type-2 astrocyte progenitors, and immature oligodendrocytes in vitro. J Neurochem. 1992;59(1):55–61.
18. Baslow MH. N-acetylaspartate in the vertebrate brain: metabolism and function. Neurochem Res. 2003;28(6):941–53.
19. Baslow MH. N-acetylaspartate and N-acetylaspartylglutamate. In: Lajtha A, Oja S, Schousboe A, Saransaari P, editors. Handbook of neurochemistry and molecular neurobiology: amino acids and peptides in the nervous system. New York: Springer; 2007. p. 305–46.
20. Choi IY, Gruetter R. In vivo 13C NMR assessment of brain glycogen concentration and turnover in the awake rat. Neurochem Int. 2003;43(4-5):317–22.
21. Choi IY, Gruetter R. Dynamic or inert metabolism? Turnover of N-acetyl aspartate and glutathione from D-[1-13C]glucose in the rat brain in vivo. J Neurochem. 2004;91(4):778–87. doi:10.1111/j.1471-4159.2004.02716.x.
22. Moreno A, Ross BD, Bluml S. Direct determination of the N-acetyl-L-aspartate synthesis rate in the human brain by (13)C MRS and [1-(13)C]glucose infusion. J Neurochem. 2001;77(1):347–50.
23. Hyder F, Chase JR, Behar KL, Mason GF, Siddeek M, Rothman DL, Shulman RG. Increased tricarboxylic acid cycle flux in rat brain during forepaw stimulation detected with 1H[13C] NMR. Proc Natl Acad Sci U S A. 1996;93(15):7612–7.
24. Pfeuffer J, Tkac I, Choi IY, Merkle H, Ugurbil K, Garwood M, Gruetter R. Localized in vivo 1H NMR detection of neurotransmitter labeling in rat brain during infusion of [1-13C] D-glucose. Magn Reson Med. 1999;41(6):1077–83.
25. Pfeuffer J, Tkac I, Provencher SW, Gruetter R. Toward an in vivo neurochemical profile: quantification of 18 metabolites in short-echo-time (1)H NMR spectra of the rat brain. J Magn Reson. 1999;141(1):104–20. doi:10.1006/jmre.1999.1895.
26. Wiame E, Tyteca D, Pierrot N, Collard F, Amyere M, Noel G, Desmedt J, Nassogne MC, Vikkula M, Octave JN, Vincent MF, Courtoy PJ, Boltshauser E, van Schaftingen E. Molecular identification of aspartate N-acetyltransferase and its mutation in hypoacetylaspartia. Biochem J. 2010;425(1):127–36. doi:10.1042/BJ20091024.
27. Tahay G, Wiame E, Tyteca D, Courtoy PJ, Van Schaftingen E. Determinants of the enzymatic activity and the subcellular localization of aspartate N-acetyltransferase. Biochem J. 2012;441(1):105–12. doi:10.1042/BJ20111179.
28. Huang W, Wang H, Kekuda R, Fei YJ, Friedrich A, Wang J, Conway SJ, Cameron RS, Leibach FH, Ganapathy V. Transport of N-acetylaspartate by the Na(+)-dependent high-affinity dicarboxylate transporter NaDC3 and its relevance to the expression of the transporter in the brain. J Pharmacol Exp Ther. 2000;295(1):392–403.
29. Burri R, Steffen C, Herschkowitz N. N-acetyl-L-aspartate is a major source of acetyl groups for lipid synthesis during rat brain development. Dev Neurosci. 1991;13(6):403–11.
30. Namboodiri AM, Peethambaran A, Mathew R, Sambhu PA, Hershfield J, Moffett JR, Madhavarao CN. Canavan disease and the role of N-acetylaspartate in myelin synthesis. Mol Cell Endocrinol. 2006;252(1-2):216–23. doi:10.1016/j.mce.2006.03.016.
31. Martin E, Capone A, Schneider J, Hennig J, Thiel T. Absence of N-acetylaspartate in the human brain: impact on neurospectroscopy? Ann Neurol. 2001;49(4):518–21.
32. Boltshauser E, Schmitt B, Wevers RA, Engelke U, Burlina AB, Burlina AP. Follow-up of a child with hypoacetylaspartia. Neuropediatrics. 2004;35(4):255–8. doi:10.1055/s-2004-821036.
33. Burlina AP, Schmitt B, Engelke U, Wevers RA, Burlina AB, Boltshauser E. Hypoacetylaspartia: clinical and biochemical follow-up of a patient. Adv Exp Med Biol. 2006;576:283–287. discussion 361-283. doi:10.1007/0-387-30172-0_20.
34. Becker I, Lodder J, Gieselmann V, Eckhardt M. Molecular characterization of N-acetylaspartylglutamate synthetase. J Biol Chem. 2010;285(38):29156–64. doi:10.1074/jbc.M110.111765.
35. Wroblewska B, Santi MR, Neale JH. N-acetylaspartylglutamate activates cyclic AMP-coupled metabotropic glutamate receptors in cerebellar astrocytes. Glia. 1998;24(2):172–9.

36. Wroblewska B, Wroblewski JT, Saab OH, Neale JH. N-acetylaspartylglutamate inhibits forskolin-stimulated cyclic AMP levels via a metabotropic glutamate receptor in cultured cerebellar granule cells. J Neurochem. 1993;61(3):943–8.
37. Hayashi Y, Momiyama A, Takahashi T, Ohishi H, Ogawa-Meguro R, Shigemoto R, Mizuno N, Nakanishi S. Role of a metabotropic glutamate receptor in synaptic modulation in the accessory olfactory bulb. Nature. 1993;366(6456):687–90. doi:10.1038/366687a0.
38. Sanchez-Prieto J, Budd DC, Herrero I, Vazquez E, Nicholls DG. Presynaptic receptors and the control of glutamate exocytosis. Trends Neurosci. 1996;19(6):235–9.
39. Wroblewska B, Wegorzewska IN, Bzdega T, Olszewski RT, Neale JH. Differential negative coupling of type 3 metabotropic glutamate receptor to cyclic GMP levels in neurons and astrocytes. J Neurochem. 2006;96(4):1071–7. doi:10.1111/j.1471-4159.2005.03569.x.
40. Cartmell J, Schoepp DD. Regulation of neurotransmitter release by metabotropic glutamate receptors. J Neurochem. 2000;75(3):889–907.
41. Gafurov B, Urazaev AK, Grossfeld RM, Lieberman EM. N-acetylaspartylglutamate (NAAG) is the probable mediator of axon-to-glia signaling in the crayfish medial giant nerve fiber. Neuroscience. 2001;106(1):227–35.
42. Mesters JR, Barinka C, Li W, Tsukamoto T, Majer P, Slusher BS, Konvalinka J, Hilgenfeld R. Structure of glutamate carboxypeptidase II, a drug target in neuronal damage and prostate cancer. EMBO J. 2006;25(6):1375–84. doi:10.1038/sj.emboj.7600969.
43. Kaldis P, Hemmer W, Zanolla E, Holtzman D, Wallimann T. 'Hot spots' of creatine kinase localization in brain: cerebellum, hippocampus and choroid plexus. Dev Neurosci. 1996;18(5-6):542–54.
44. Aksenova MV, Burbaeva GS, Kandror KV, Kapkov DV, Stepanov AS. The decreased level of casein kinase 2 in brain cortex of schizophrenic and Alzheimer's disease patients. FEBS Lett. 1991;279(1):55–7.
45. Happe HK, Murrin LC. In situ hybridization analysis of CHOT1, a creatine transporter, in the rat central nervous system. J Comp Neurol. 1995;351(1):94–103. doi:10.1002/cne.903510109.
46. Saltarelli MD, Bauman AL, Moore KR, Bradley CC, Blakely RD. Expression of the rat brain creatine transporter in situ and in transfected HeLa cells. Dev Neurosci. 1996;18(5–6):524–34.
47. Schloss P, Mayser W, Betz H. The putative rat choline transporter CHOT1 transports creatine and is highly expressed in neural and muscle-rich tissues. Biochem Biophys Res Commun. 1994;198(2):637–45. doi:10.1006/bbrc.1994.1093.
48. Braissant O, Henry H, Loup M, Eilers B, Bachmann C. Endogenous synthesis and transport of creatine in the rat brain: an in situ hybridization study. Brain Res Mol Brain Res. 2001;86(1-2):193–201.
49. Ohtsuki S, Tachikawa M, Takanaga H, Shimizu H, Watanabe M, Hosoya K, Terasaki T. The blood-brain barrier creatine transporter is a major pathway for supplying creatine to the brain. J Cereb Blood Flow Metab. 2002;22(11):1327–35. doi:10.1097/00004647-200211000-00006.
50. Perasso L, Cupello A, Lunardi GL, Principato C, Gandolfo C, Balestrino M. Kinetics of creatine in blood and brain after intraperitoneal injection in the rat. Brain Res. 2003;974(1-2):37–42.
51. Braissant O, Bachmann C, Henry H. Expression and function of AGAT, GAMT and CT1 in the mammalian brain. Subcell Biochem. 2007;46:67–81.
52. Braissant O, Henry H. AGAT, GAMT and SLC6A8 distribution in the central nervous system, in relation to creatine deficiency syndromes: a review. J Inherit Metab Dis. 2008;31(2):230–9. doi:10.1007/s10545-008-0826-9.
53. Nakashima T, Tomi M, Tachikawa M, Watanabe M, Terasaki T, Hosoya K. Evidence for creatine biosynthesis in Muller glia. Glia. 2005;52(1):47–52. doi:10.1002/glia.20222.
54. Schmidt A, Marescau B, Boehm EA, Renema WK, Peco R, Das A, Steinfeld R, Chan S, Wallis J, Davidoff M, Ullrich K, Waldschutz R, Heerschap A, De Deyn PP, Neubauer S, Isbrandt D. Severely altered guanidino compound levels, disturbed body weight homeostasis and impaired fertility in a mouse model of guanidinoacetate N-methyltransferase (GAMT) deficiency. Hum Mol Genet. 2004;13(9):905–21. doi:10.1093/hmg/ddh112.

55. Tachikawa M, Fukaya M, Terasaki T, Ohtsuki S, Watanabe M. Distinct cellular expressions of creatine synthetic enzyme GAMT and creatine kinases uCK-Mi and CK-B suggest a novel neuron-glial relationship for brain energy homeostasis. Eur J Neurosci. 2004;20(1):144–60. doi:10.1111/j.1460-9568.2004.03478.x.
56. Salomons GS, van Dooren SJ, Verhoeven NM, Cecil KM, Ball WS, Degrauw TJ, Jakobs C. X-linked creatine-transporter gene (SLC6A8) defect: a new creatine-deficiency syndrome. Am J Hum Genet. 2001;68(6):1497–500. doi:10.1086/320595.
57. Zwaal RF, Comfurius P, Bevers EM. Surface exposure of phosphatidylserine in pathological cells. Cell Mol Life Sci. 2005;62(9):971–88. doi:10.1007/s00018-005-4527-3.
58. Naudi A, Jove M, Ayala V, Cabre R, Portero-Otin M, Pamplona R. Non-enzymatic modification of aminophospholipids by carbonyl-amine reactions. Int J Mol Sci. 2013;14(2):3285–313. doi:10.3390/ijms14023285.
59. Pouwels PJ, Frahm J. Regional metabolite concentrations in human brain as determined by quantitative localized proton MRS. Magn Reson Med. 1998;39(1):53–60.
60. Tan J, Bluml S, Hoang T, Dubowitz D, Mevenkamp G, Ross B. Lack of effect of oral choline supplement on the concentrations of choline metabolites in human brain. Magn Reson Med. 1998;39(6):1005–10.
61. Wang Y, Li SJ. Differentiation of metabolic concentrations between gray matter and white matter of human brain by in vivo 1H magnetic resonance spectroscopy. Magn Reson Med. 1998;39(1):28–33.
62. Bluml S, Seymour KJ, Ross BD. Developmental changes in choline- and ethanolamine-containing compounds measured with proton-decoupled (31)P MRS in in vivo human brain. Magn Reson Med. 1999;42(4):643–54.
63. Kantarci K, Weigand SD, Petersen RC, Boeve BF, Knopman DS, Gunter J, Reyes D, Shiung M, O'Brien PC, Smith GE, Ivnik RJ, Tangalos EG, Jack CR Jr. Longitudinal 1H MRS changes in mild cognitive impairment and Alzheimer's disease. Neurobiol Aging. 2007;28(9):1330–9. doi:10.1016/j.neurobiolaging.2006.06.018.
64. DeKosky ST, Ikonomovic MD, Styren SD, Beckett L, Wisniewski S, Bennett DA, Cochran EJ, Kordower JH, Mufson EJ. Upregulation of choline acetyltransferase activity in hippocampus and frontal cortex of elderly subjects with mild cognitive impairment. Ann Neurol. 2002;51(2):145–55.
65. Ballard C, Gauthier S, Corbett A, Brayne C, Aarsland D, Jones E. Alzheimer's disease. Lancet. 2011;377(9770):1019–31. doi:10.1016/S0140-6736(10)61349-9.
66. Zhang YW, Thompson R, Zhang H, Xu H. APP processing in Alzheimer's disease. Mol Brain. 2011;4:3. doi:10.1186/1756-6606-4-3.
67. Gentile MT, Reccia MG, Sorrentino PP, Vitale E, Sorrentino G, Puca AA, Colucci-D'Amato L. Role of cytosolic calcium-dependent phospholipase A2 in Alzheimer's disease pathogenesis. Mol Neurobiol. 2012;45(3):596–604. doi:10.1007/s12035-012-8279-4.
68. Kwon HM, Yamauchi A, Uchida S, Preston AS, Garcia-Perez A, Burg MB, Handler JS. Cloning of the cDNa for a Na+/myo-inositol cotransporter, a hypertonicity stress protein. J Biol Chem. 1992;267(9):6297–301.
69. Paredes A, McManus M, Kwon HM, Strange K. Osmoregulation of Na(+)-inositol cotransporter activity and mRNA levels in brain glial cells. Am J Phys. 1992;263(6 Pt 1):C1282–8.
70. Fisher SK, Novak JE, Agranoff BW. Inositol and higher inositol phosphates in neural tissues: homeostasis, metabolism and functional significance. J Neurochem. 2002;82(4):736–54.
71. Bissonnette P, Lahjouji K, Coady MJ, Lapointe JY. Effects of hyperosmolarity on the Na+-myo-inositol cotransporter SMIT2 stably transfected in the Madin-Darby canine kidney cell line. Am J Physiol Cell Physiol. 2008;295(3):C791–9. doi:10.1152/ajpcell.00390.2007.
72. Ibsen L, Strange K. In situ localization and osmotic regulation of the Na(+)-myo-inositol cotransporter in rat brain. Am J Phys. 1996;271(4 Pt 2):F877–85.
73. Isaacks RE, Bender AS, Kim CY, Prieto NM, Norenberg MD. Osmotic regulation of myo-inositol uptake in primary astrocyte cultures. Neurochem Res. 1994;19(3):331–8.

74. Klaus F, Palmada M, Lindner R, Laufer J, Jeyaraj S, Lang F, Boehmer C. Up-regulation of hypertonicity-activated myo-inositol transporter SMIT1 by the cell volume-sensitive protein kinase SGK1. J Physiol. 2008;586(6):1539–47. doi:10.1113/jphysiol.2007.146191.
75. Wiese TJ, Dunlap JA, Conner CE, Grzybowski JA, Lowe WL Jr, Yorek MA. Osmotic regulation of Na-myo-inositol cotransporter mRNA level and activity in endothelial and neural cells. Am J Phys. 1996;270(4 Pt 1):C990–7.
76. Uldry M, Ibberson M, Horisberger JD, Chatton JY, Riederer BM, Thorens B. Identification of a mammalian H(+)-myo-inositol symporter expressed predominantly in the brain. EMBO J. 2001;20(16):4467–77. doi:10.1093/emboj/20.16.4467.
77. Di Daniel E, Mok MH, Mead E, Mutinelli C, Zambello E, Caberlotto LL, Pell TJ, Langmead CJ, Shah AJ, Duddy G, Kew JN, Maycox PR. Evaluation of expression and function of the H+/myo-inositol transporter HMIT. BMC Cell Biol. 2009;10:54. doi:10.1186/1471-2121-10-54.
78. Uldry M, Steiner P, Zurich MG, Beguin P, Hirling H, Dolci W, Thorens B. Regulated exocytosis of an H+/myo-inositol symporter at synapses and growth cones. EMBO J. 2004;23(3):531–40. doi:10.1038/sj.emboj.7600072.
79. Augustin R. The protein family of glucose transport facilitators: it's not only about glucose after all. IUBMB Life. 2010;62(5):315–33. doi:10.1002/iub.315.
80. Fu H, Li B, Hertz L, Peng L. Contributions in astrocytes of SMIT1/2 and HMIT to myo-inositol uptake at different concentrations and pH. Neurochem Int. 2012;61(2):187–94. doi:10.1016/j.neuint.2012.04.010.
81. Sturrock A, Laule C, Decolongon J, Dar Santos R, Coleman AJ, Creighton S, Bechtel N, Reilmann R, Hayden MR, Tabrizi SJ, Mackay AL, Leavitt BR. Magnetic resonance spectroscopy biomarkers in premanifest and early Huntington disease. Neurology. 2010;75(19):1702–10. doi:10.1212/WNL.0b013e3181fc27e4.
82. Oz G, Hutter D, Tkac I, Clark HB, Gross MD, Jiang H, Eberly LE, Bushara KO, Gomez CM. Neurochemical alterations in spinocerebellar ataxia type 1 and their correlations with clinical status. Mov Disord. 2010;25(9):1253–61. doi:10.1002/mds.23067.
83. Huang W, Alexander GE, Daly EM, Shetty HU, Krasuski JS, Rapoport SI, Schapiro MB. High brain myo-inositol levels in the predementia phase of Alzheimer's disease in adults with Down's syndrome: a 1H MRS study. Am J Psychiatry. 1999;156(12):1879–86.
84. Beacher F, Simmons A, Daly E, Prasher V, Adams C, Margallo-Lana ML, Morris R, Lovestone S, Murphy K, Murphy DG. Hippocampal myo-inositol and cognitive ability in adults with Down syndrome: an in vivo proton magnetic resonance spectroscopy study. Arch Gen Psychiatry. 2005;62(12):1360–5. doi:10.1001/archpsyc.62.12.1360.
85. Lamar M, Foy CM, Beacher F, Daly E, Poppe M, Archer N, Prasher V, Murphy KC, Morris RG, Simmons A, Lovestone S, Murphy DG. Down syndrome with and without dementia: an in vivo proton magnetic resonance spectroscopy study with implications for Alzheimer's disease. NeuroImage. 2011;57(1):63–8. doi:10.1016/j.neuroimage.2011.03.073.
86. Berry GT, Mallee JJ, Kwon HM, Rim JS, Mulla WR, Muenke M, Spinner NB. The human osmoregulatory Na+/myo-inositol cotransporter gene (SLC5A3): molecular cloning and localization to chromosome 21. Genomics. 1995;25(2):507–13.
87. Videen JS, Michaelis T, Pinto P, Ross BD. Human cerebral osmolytes during chronic hyponatremia. A proton magnetic resonance spectroscopy study. J Clin Invest. 1995;95(2):788–93. doi:10.1172/JCI117728.
88. Lien YH, Shapiro JI, Chan L. Effects of hypernatremia on organic brain osmoles. J Clin Invest. 1990;85(5):1427–35. doi:10.1172/JCI114587.
89. Brusilow SW, Koehler RC, Traystman RJ, Cooper AJ. Astrocyte glutamine synthetase: importance in hyperammonemic syndromes and potential target for therapy. Neurotherapeutics. 2010;7(4):452–70. doi:10.1016/j.nurt.2010.05.015.
90. Davanzo P, Thomas MA, Yue K, Oshiro T, Belin T, Strober M, McCracken J. Decreased anterior cingulate myo-inositol/creatine spectroscopy resonance with lithium treatment in children with bipolar disorder. Neuropsychopharmacology. 2001;24(4):359–69. doi:10.1016/S0893-133X(00)00207-4.

91. Moore GJ, Bebchuk JM, Parrish JK, Faulk MW, Arfken CL, Strahl-Bevacqua J, Manji HK. Temporal dissociation between lithium-induced changes in frontal lobe myo-inositol and clinical response in manic-depressive illness. Am J Psychiatry. 1999;156(12):1902–8.
92. Shaltiel G, Shamir A, Shapiro J, Ding D, Dalton E, Bialer M, Harwood AJ, Belmaker RH, Greenberg ML, Agam G. Valproate decreases inositol biosynthesis. Biol Psychiatry. 2004;56(11):868–74. doi:10.1016/j.biopsych.2004.08.027.
93. Williams RS, Harwood AJ. Lithium therapy and signal transduction. Trends Pharmacol Sci. 2000;21(2):61–4.
94. Brand A, Richter-Landsberg C, Leibfritz D. Multinuclear NMR studies on the energy metabolism of glial and neuronal cells. Dev Neurosci. 1993;15(3-5):289–98.
95. Glanville NT, Byers DM, Cook HW, Spence MW, Palmer FB. Differences in the metabolism of inositol and phosphoinositides by cultured cells of neuronal and glial origin. Biochim Biophys Acta. 1989;1004(2):169–79.
96. Duarte JM, Carvalho RA, Cunha RA, Gruetter R. Caffeine consumption attenuates neurochemical modifications in the hippocampus of streptozotocin-induced diabetic rats. J Neurochem. 2009;111(2):368–79. doi:10.1111/j.1471-4159.2009.06349.x.
97. Kim JP, Lentz MR, Westmoreland SV, Greco JB, Ratai EM, Halpern E, Lackner AA, Masliah E, Gonzalez RG. Relationships between astrogliosis and 1H MR spectroscopic measures of brain choline/creatine and myo-inositol/creatine in a primate model. AJNR Am J Neuroradiol. 2005;26(4):752–9.
98. Kunz N, Camm EJ, Somm E, Lodygensky G, Darbre S, Aubert ML, Huppi PS, Sizonenko SV, Gruetter R. Developmental and metabolic brain alterations in rats exposed to bisphenol A during gestation and lactation. Int J Dev Neurosci. 2011;29(1):37–43. doi:10.1016/j.ijdevneu.2010.09.009.
99. Godfrey DA, Hallcher LM, Laird MH, Matschinsky FM, Sherman WR. Distribution of myo-inositol in the cat cochlear nucleus. J Neurochem. 1982;38(4):939–47.
100. Sherman WR, Packman PM, Laird MH, Boshans RL. Measurement of myo-inositol in single cells and defined areas of the nervous system by selected ion monitoring. Anal Biochem. 1977;78(1):119–31.
101. Hertz L, Peng L, Dienel GA. Energy metabolism in astrocytes: high rate of oxidative metabolism and spatiotemporal dependence on glycolysis/glycogenolysis. J Cereb Blood Flow Metab. 2007;27(2):219–49. doi:10.1038/sj.jcbfm.9600343.
102. Shen J, Petersen KF, Behar KL, Brown P, Nixon TW, Mason GF, Petroff OA, Shulman GI, Shulman RG, Rothman DL. Determination of the rate of the glutamate/glutamine cycle in the human brain by in vivo 13C NMR. Proc Natl Acad Sci U S A. 1999;96(14):8235–40.
103. Waagepetersen HS, Sonnewald U, Schousboe A. Glutamine, glutamate, and GABA: metabolic aspects. In: Lajtha A, Oja S, Schousboe A, Saransaari P, editors. Handbook of neurochemistry and molecular neurobiology: amino acids and peptides in the nervous system. New York: Springer; 2007. p. 1–21.
104. Govindaraju V, Young K, Maudsley AA. Proton NMR chemical shifts and coupling constants for brain metabolites. NMR Biomed. 2000;13(3):129–53.
105. Jensen JE, Licata SC, Ongur D, Friedman SD, Prescot AP, Henry ME, Renshaw PF. Quantification of J-resolved proton spectra in two-dimensions with LCModel using GAMMA-simulated basis sets at 4 Tesla. NMR Biomed. 2009;22(7):762–9. doi:10.1002/nbm.1390.
106. Kauppinen RA, Williams SR. Nondestructive detection of glutamate by 1H nuclear magnetic resonance spectroscopy in cortical brain slices from the guinea pig: evidence for changes in detectability during severe anoxic insults. J Neurochem. 1991;57(4):1136–44.
107. Bartha R, Drost DJ, Menon RS, Williamson PC. Spectroscopic lineshape correction by QUECC: combined QUALITY deconvolution and eddy current correction. Magn Reson Med. 2000;44(4):641–5.
108. Dong Z, Peterson BS. Spectral resolution amelioration by deconvolution (SPREAD) in MR spectroscopic imaging. J Magn Reson Imaging. 2009;29(6):1395–405. doi:10.1002/jmri.21784.

109. Poullet JB, Sima DM, Simonetti AW, De Neuter B, Vanhamme L, Lemmerling P, Van Huffel S. An automated quantitation of short echo time MRS spectra in an open source software environment: AQSES. NMR Biomed. 2007;20(5):493–504. doi:10.1002/nbm.1112.
110. Provencher SW. Automatic quantitation of localized in vivo 1H spectra with LCModel. NMR Biomed. 2001;14(4):260–4.
111. Slotboom J, Boesch C, Kreis R. Versatile frequency domain fitting using time domain models and prior knowledge. Magn Reson Med. 1998;39(6):899–911.
112. Sima DM, Osorio-Garcia MI, Poullet J-B, Suvichakorn A, Antoine J-P, Van Huffel S, van Ormondt D. Lineshape estimation for MRS signals: self-deconvolution revisited. Meas Sci Technol. 2009;20(10):104031. doi:10.1088/0957-0233/20/10/104031.
113. Cudalbu C, Mlynarik V, Gruetter R. Handling macromolecule signals in the quantification of the neurochemical profile. J Alzheimer's Dis. 2012;31(Suppl 3):S101–15. doi:10.3233/JAD-2012-120100.
114. Seeger U, Klose U, Mader I, Grodd W, Nagele T. Parameterized evaluation of macromolecules and lipids in proton MR spectroscopy of brain diseases. Magn Reson Med. 2003;49(1):19–28. doi:10.1002/mrm.10332.
115. Vanhamme L, Sundin T, Van Hecke P, Van Huffel S, Pintelon R. Frequency-selective quantification of biomedical magnetic resonance spectroscopy data. J Magn Reson. 2000;143(1):1–16. doi:10.1006/jmre.1999.1960.
116. Ratiney H, Sdika M, Coenradie Y, Cavassila S, van Ormondt D, Graveron-Demilly D. Time-domain semi-parametric estimation based on a metabolite basis set. NMR Biomed. 2005;18(1):1–13. doi:10.1002/nbm.895.
117. Smith SA, Levante TO, Meier BH, Ernst RR. Computer simulations in magnetic resonance. An object oriented programming approach. J Magn Reson A. 1994;106(1):75–105. doi:10.1006/jmra.1994.1008.
118. De Neuter B, Luts J, Vanhamme L, Lemmerling P, Van Huffel S. Java-based framework for processing and displaying short-echo-time magnetic resonance spectroscopy signals. Comput Methods Prog Biomed. 2007;85(2):129–37. doi:10.1016/j.cmpb.2006.09.005.
119. Poullet JB, Sima DM, Van Huffel S. MRS signal quantitation: a review of time- and frequency-domain methods. J Magn Reson. 2008;195(2):134–44. doi:10.1016/j.jmr.2008.09.005.
120. Poullet JB, Pintelon R, Van Huffel S. A new FIR filter technique for solvent suppression in MRS signals. J Magn Reson. 2009;196(1):61–73. doi:10.1016/j.jmr.2008.10.011.
121. Stefan D, Di Cesare F, Andrasescu A, Popa E, Lazariev A, Vescovo E, Strbak O, Williams S, Starcuk Z, Cabanas M, van Ormondt D, Graveron-Demilly D. Quantitation of magnetic resonance spectroscopy signals: the jMRUI software package. Meas Sci Technol. 2009;20(10):104035. doi:10.1088/0957-0233/20/10/104035.
122. Naressi A, Couturier C, Devos JM, Janssen M, Mangeat C, de Beer R, Graveron-Demilly D. Java-based graphical user interface for the MRUI quantitation package. MAGMA. 2001;12(2-3):141–52.
123. Vanhamme L, van den Boogaart A, Van Huffel S. Improved method for accurate and efficient quantification of MRS data with use of prior knowledge. J Magn Reson. 1997;129(1):35–43.
124. Provencher SW. Estimation of metabolite concentrations from localized in vivo proton NMR spectra. Magn Reson Med. 1993;30(6):672–9.
125. Mosconi E, Sima DM, Osorio Garcia MI, Fontanella M, Fiorini S, Van Huffel S, Marzola P. Different quantification algorithms may lead to different results: a comparison using proton MRS lipid signals. NMR Biomed. 2014;27(4):431–43. doi:10.1002/nbm.3079.
126. Cavassila S, Deval S, Huegen C, van Ormondt D, Graveron-Demilly D. Cramer-Rao bounds: an evaluation tool for quantitation. NMR Biomed. 2001;14(4):278–83.
127. Kreis R. Issues of spectral quality in clinical 1H-magnetic resonance spectroscopy and a gallery of artifacts. NMR Biomed. 2004;17(6):361–81. doi:10.1002/nbm.891.
128. Osorio-Garcia MI. Quantification of magnetic resonance spectroscopy signals with lineshape estimation. J Chemom. 2011;25(4):183–92. doi:10.1002/cem. 1353.

129. Moonen CT, von Kienlin M, van Zijl PC, Cohen J, Gillen J, Daly P, Wolf G. Comparison of single-shot localization methods (STEAM and PRESS) for in vivo proton NMR spectroscopy. NMR Biomed. 1989;2(5-6):201–8.
130. Kwock L. Clinical proton magnetic resonance spectroscopy: basic principles. In: Mukherji SK, editor. Clinical applications of MR spectroscopy. New York: Wiley-Liss; 1998. p. 1–31.
131. Jansen JF, Backes WH, Nicolay K, Kooi ME. 1H MR spectroscopy of the brain: absolute quantification of metabolites. Radiology. 2006;240(2):318–32. doi:10.1148/radiol.2402050314.
132. Brooks JC, Roberts N, Kemp GJ, Gosney MA, Lye M, Whitehouse GH. A proton magnetic resonance spectroscopy study of age-related changes in frontal lobe metabolite concentrations. Cereb Cortex. 2001;11(7):598–605.
133. Sailasuta N, Ernst T, Chang L. Regional variations and the effects of age and gender on glutamate concentrations in the human brain. Magn Reson Imaging. 2008;26(5):667–75. doi:10.1016/j.mri.2007.06.007.
134. Chang L, Jiang CS, Ernst T. Effects of age and sex on brain glutamate and other metabolites. Magn Reson Imaging. 2009;27(1):142–5. doi:10.1016/j.mri.2008.06.002.
135. Charlton RA, McIntyre DJ, Howe FA, Morris RG, Markus HS. The relationship between white matter brain metabolites and cognition in normal aging: the GENIE study. Brain Res. 2007;1164:108–16. doi:10.1016/j.brainres.2007.06.027.
136. Raininko R, Mattsson P. Metabolite concentrations in supraventricular white matter from teenage to early old age: a short echo time 1H magnetic resonance spectroscopy (MRS) study. Acta Radiol. 2010;51(3):309–15. doi:10.3109/02841850903476564.
137. Kantarci K, Weigand SD, Przybelski SA, Preboske GM, Pankratz VS, Vemuri P, Senjem ML, Murphy MC, Gunter JL, Machulda MM, Ivnik RJ, Roberts RO, Boeve BF, Rocca WA, Knopman DS, Petersen RC, Jack CR Jr. MRI and MRS predictors of mild cognitive impairment in a population-based sample. Neurology. 2013;81(2):126–33. doi:10.1212/WNL.0b013e31829a3329.
138. Parnetti L, Tarducci R, Presciutti O, Lowenthal DT, Pippi M, Palumbo B, Gobbi G, Pelliccioli GP, Senin U. Proton magnetic resonance spectroscopy can differentiate Alzheimer's disease from normal aging. Mech Ageing Dev. 1997;97(1):9–14.
139. Rose SE, de Zubicaray GI, Wang D, Galloway GJ, Chalk JB, Eagle SC, Semple J, Doddrell DM. A 1H MRS study of probable Alzheimer's disease and normal aging: implications for longitudinal monitoring of dementia progression. Magn Reson Imaging. 1999;17(2):291–9.
140. Zhu X, Schuff N, Kornak J, Soher B, Yaffe K, Kramer JH, Ezekiel F, Miller BL, Jagust WJ, Weiner MW. Effects of Alzheimer disease on fronto-parietal brain N-acetyl aspartate and myo-inositol using magnetic resonance spectroscopic imaging. Alzheimer Dis Assoc Disord. 2006;20(2):77–85. doi:10.1097/01.wad.0000213809.12553.fc.
141. Kantarci K, Knopman DS, Dickson DW, Parisi JE, Whitwell JL, Weigand SD, Josephs KA, Boeve BF, Petersen RC, Jack CR Jr. Alzheimer disease: postmortem neuropathologic correlates of antemortem 1H MR spectroscopy metabolite measurements. Radiology. 2008;248(1):210–20. doi:10.1148/radiol.2481071590.
142. Jessen F, Block W, Traber F, Keller E, Flacke S, Lamerichs R, Schild HH, Heun R. Decrease of N-acetylaspartate in the MTL correlates with cognitive decline of AD patients. Neurology. 2001;57(5):930–2.
143. Doraiswamy PM, Steffens DC, Pitchumoni S, Tabrizi S. Early recognition of Alzheimer's disease: what is consensual? What is controversial? What is practical? J Clin Psychiatry. 1998;59(Suppl 13):6–18.
144. Murray ME, Przybelski SA, Lesnick TG, Liesinger AM, Spychalla A, Zhang B, Gunter JL, Parisi JE, Boeve BF, Knopman DS, Petersen RC, Jack CR Jr, Dickson DW, Kantarci K. Early Alzheimer's disease neuropathology detected by proton MR spectroscopy. J Neurosci. 2014;34(49):16247–55. doi:10.1523/JNEUROSCI.2027-14.2014.
145. Westman E, Wahlund LO, Foy C, Poppe M, Cooper A, Murphy D, Spenger C, Lovestone S, Simmons A. Combining MRI and MRS to distinguish between Alzheimer's disease and healthy controls. J Alzheimer's Dis. 2010;22(1):171–81. doi:10.3233/JAD-2010-100168.

146. Kantarci K, Xu Y, Shiung MM, O'Brien PC, Cha RH, Smith GE, Ivnik RJ, Boeve BF, Edland SD, Kokmen E, Tangalos EG, Petersen RC, Jack CR Jr. Comparative diagnostic utility of different MR modalities in mild cognitive impairment and Alzheimer's disease. Dement Geriatr Cogn Disord. 2002;14(4):198–207. doi: 66021
147. MacKay S, Ezekiel F, Di Sclafani V, Meyerhoff DJ, Gerson J, Norman D, Fein G, Weiner MW. Alzheimer disease and subcortical ischemic vascular dementia: evaluation by combining MR imaging segmentation and H-1 MR spectroscopic imaging. Radiology. 1996;198(2):537–45. doi:10.1148/radiology.198.2.8596863.
148. Martinez-Bisbal MC, Arana E, Marti-Bonmati L, Molla E, Celda B. Cognitive impairment: classification by 1H magnetic resonance spectroscopy. Eur J Neurol. 2004;11(3):187–93.
149. Schuff N, Capizzano AA, AT D, Amend DL, O'Neill J, Norman D, Kramer J, Jagust W, Miller B, Wolkowitz OM, Yaffe K, Weiner MW. Selective reduction of N-acetylaspartate in medial temporal and parietal lobes in AD. Neurology. 2002;58(6):928–35.
150. Silveira de Souza A, de Oliveira-Souza R, Moll J, Tovar-Moll F, Andreiuolo PA, Bottino CM. Contribution of 1H spectroscopy to a brief cognitive-functional test battery for the diagnosis of mild Alzheimer's disease. Dement Geriatr Cogn Disord. 2011;32(5):351–61. doi:10.1159/000334656.
151. Watanabe T, Shiino A, Akiguchi I. Absolute quantification in proton magnetic resonance spectroscopy is useful to differentiate amnesic mild cognitive impairment from Alzheimer's disease and healthy aging. Dement Geriatr Cogn Disord. 2010;30(1):71–7. doi:10.1159/000318750.
152. Petersen RC, Doody R, Kurz A, Mohs RC, Morris JC, Rabins PV, Ritchie K, Rossor M, Thal L, Winblad B. Current concepts in mild cognitive impairment. Arch Neurol. 2001;58(12):1985–92.
153. Flicker C, Ferris SH, Reisberg B. Mild cognitive impairment in the elderly: predictors of dementia. Neurology. 1991;41(7):1006–9.
154. Geslani DM, Tierney MC, Herrmann N, Szalai JP. Mild cognitive impairment: an operational definition and its conversion rate to Alzheimer's disease. Dement Geriatr Cogn Disord. 2005;19(5-6):383–9. doi:10.1159/000084709.
155. Luis CA, Barker WW, Loewenstein DA, Crum TA, Rogaeva E, Kawarai T, St George-Hyslop P, Duara R. Conversion to dementia among two groups with cognitive impairment. A preliminary report. Dement Geriatr Cogn Disord. 2004;18(3-4):307–13. doi:10.1159/000080124.
156. Wolf H, Grunwald M, Ecke GM, Zedlick D, Bettin S, Dannenberg C, Dietrich J, Eschrich K, Arendt T, Gertz HJ. The prognosis of mild cognitive impairment in the elderly. J Neural Transm Suppl. 1998;54:31–50.
157. Ingles JL, Fisk JD, Merry HR, Rockwood K. Five-year outcomes for dementia defined solely by neuropsychological test performance. Neuroepidemiology. 2003;22(3):172–8. doi:69891
158. Mitchell AJ, Shiri-Feshki M. Rate of progression of mild cognitive impairment to dementia--meta-analysis of 41 robust inception cohort studies. Acta Psychiatr Scand. 2009;119(4):252–65. doi:10.1111/j.1600-0447.2008.01326.x.
159. Markesbery WR. Neuropathologic alterations in mild cognitive impairment: a review. J Alzheimer's Dis. 2010;19(1):221–8. doi:10.3233/JAD-2010-1220.
160. Chao LL, Schuff N, Kramer JH, AT D, Capizzano AA, O'Neill J, Wolkowitz OM, Jagust WJ, Chui HC, Miller BL, Yaffe K, Weiner MW. Reduced medial temporal lobe N-acetylaspartate in cognitively impaired but nondemented patients. Neurology. 2005;64(2):282–9. doi:10.1212/01.WNL.0000149638.45635.FF.
161. Kantarci K, Jack CR Jr, Xu YC, Campeau NG, O'Brien PC, Smith GE, Ivnik RJ, Boeve BF, Kokmen E, Tangalos EG, Petersen RC. Regional metabolic patterns in mild cognitive impairment and Alzheimer's disease: a 1H MRS study. Neurology. 2000;55(2):210–7.
162. Tumati S, Martens S, Aleman A. Magnetic resonance spectroscopy in mild cognitive impairment: systematic review and meta-analysis. Neurosci Biobehav Rev. 2013;37(10 Pt 2):2571–86. doi:10.1016/j.neubiorev.2013.08.004.
163. Fayed N, Davila J, Oliveros A, Castillo J, Medrano JJ. Utility of different MR modalities in mild cognitive impairment and its use as a predictor of conversion to probable dementia. Acad Radiol. 2008;15(9):1089–98. doi:10.1016/j.acra.2008.04.008.

164. Modrego PJ, Fayed N, Sarasa M. Magnetic resonance spectroscopy in the prediction of early conversion from amnestic mild cognitive impairment to dementia: a prospective cohort study. BMJ Open. 2011;1(1):e000007. doi:10.1136/bmjopen-2010-000007.
165. Modrego PJ, Fayed N, Pina MA. Conversion from mild cognitive impairment to probable Alzheimer's disease predicted by brain magnetic resonance spectroscopy. Am J Psychiatry. 2005;162(4):667–75. doi:10.1176/appi.ajp.162.4.667.
166. Rami L, Gomez-Anson B, Sanchez-Valle R, Bosch B, Monte GC, Llado A, Molinuevo JL. Longitudinal study of amnesic patients at high risk for Alzheimer's disease: clinical, neuropsychological and magnetic resonance spectroscopy features. Dement Geriatr Cogn Disord. 2007;24(5):402–10. doi:10.1159/000109750.
167. Metastasio A, Rinaldi P, Tarducci R, Mariani E, Feliziani FT, Cherubini A, Pelliccioli GP, Gobbi G, Senin U, Mecocci P. Conversion of MCI to dementia: role of proton magnetic resonance spectroscopy. Neurobiol Aging. 2006;27(7):926–32. doi:10.1016/j.neurobiolaging.2005.05.002.
168. Pilatus U, Lais C, Rochmont Adu M, Kratzsch T, Frolich L, Maurer K, Zanella FE, Lanfermann H, Pantel J. Conversion to dementia in mild cognitive impairment is associated with decline of N-actylaspartate and creatine as revealed by magnetic resonance spectroscopy. Psychiatry Res. 2009;173(1):1–7. doi:10.1016/j.pscychresns.2008.07.015.
169. Kantarci K, Weigand SD, Przybelski SA, Shiung MM, Whitwell JL, Negash S, Knopman DS, Boeve BF, O'Brien PC, Petersen RC, Jack CR Jr. Risk of dementia in MCI: combined effect of cerebrovascular disease, volumetric MRI, and 1H MRS. Neurology. 2009;72(17):1519–25. doi:10.1212/WNL.0b013e3181a2e864.
170. Targosz-Gajniak MG, Siuda JS, Wicher MM, Banasik TJ, Bujak MA, Augusciak-Duma AM, Opala G. Magnetic resonance spectroscopy as a predictor of conversion of mild cognitive impairment to dementia. J Neurol Sci. 2013;335(1-2):58–63. doi:10.1016/j.jns.2013.08.023.
171. Kantarci K. Magnetic resonance spectroscopy in common dementias. Neuroimaging Clin N Am. 2013;23(3):393–406. doi:10.1016/j.nic.2012.10.004.
172. Gibellini F, Smith TK. The Kennedy pathway – De novo synthesis of phosphatidylethanolamine and phosphatidylcholine. IUBMB Life. 2010;62(6):414–28. doi:10.1002/iub.337.

Toward Clinical Application of Resting-State Functional Magnetic Resonance Imaging to Dementia

8

Yousuke Ogata and Takashi Hanakawa

Abstract

Functional magnetic resonance imaging (fMRI) has been widely used to assess brain activity in many fields including cognitive neuroscience and clinical medicine. Typically, fMRI requires a participant to perform a task of the investigator's interest during MRI acquisition. In this chapter, we introduce an emerging variant of the fMRI technique, resting-state fMRI (rs-fMRI), or resting-state functional connectivity MRI (rsfcMRI), in which a participant is only required to lie quietly within an MRI scanner. That is, rs-fMRI/rsfcMRI does not impose a demanding task on a participant. This property is potentially advantageous for the application of rs-fMRI/rsfcMRI to patients with neuropsychiatric disorders, including dementia, who might have difficulty performing tasks. We discuss the potential of rs-fMRI/rsfcMRI for the diagnosis of dementia and for understanding the mechanism underlying its clinical symptoms, taking into consideration that rs-fMRI/rsfcMRI functional connectivity analysis is increasingly used to identify subtle brain network changes caused by the pathophysiology of dementia.

Keywords

Resting-state functional connectivity MRI • Functional MRI • Functional connectivity • Default mode network

Y. Ogata • T. Hanakawa (✉)
Department of Advanced Neuroimaging, Integrative Brain Imaging Center, National Center of Neurology and Psychiatry, 4-1-1 Ogawa-Higashi, Kodaira, Tokyo 187-8551, Japan
e-mail: hanakawa@ncnp.go.jp

H. Matsuda et al. (eds.), *Neuroimaging Diagnosis for Alzheimer's Disease and Other Dementias*, DOI 10.1007/978-4-431-55133-1_8

8.1 Introduction

Functional magnetic resonance imaging (fMRI) has been widely used to assess brain activity in many fields including cognitive neuroscience and clinical medicine. Typically, fMRI requires a participant to perform a task of the investigator's' interest during MRI acquisition. Here, we introduce an emerging variant of the fMRI technique, resting-state fMRI (rs-fMRI), or resting-state functional connectivity MRI (rsfcMRI), in which a participant is only required to lie quietly within an MRI scanner. That is, rs-fMRI/rsfcMRI does not impose a demanding task on a participant. This property is potentially advantageous to the application of rs-fMRI/rsfcMRI to patients with neuropsychiatric disorders who might have difficulty performing tasks.

8.2 Principles of Functional MRI

Increases in local neuronal activity are associated with increases in regional blood flow [1]. This relationship is a consequence of a complex sequence of cellular, metabolic, and vascular processes, collectivity called neurovascular coupling. In particular, changes in oxygenation, blood flow, and blood volume are called hemodynamic changes. Hemodynamic changes induced by local neuronal and synaptic activity result in changes in MRI signal intensity. One MRI sequence, T2*-weighted MRI, is sensitive to the inhomogeneity of magnetic fields, which can be induced by changes in paramagnetic deoxyhemoglobin and diamagnetic oxyhemoglobin within red blood cells. These changes in deoxyhemoglobin and oxyhemoglobin result from oxygen consumption, which is secondary to aerobic metabolism in producing adenosine triphosphate, supporting local neuronal and synaptic activity. This T2* MRI signal change using deoxyhemoglobin as an internal contrast medium has been called the "blood-oxygen level-dependent (BOLD) effect" [2].

More precisely, demands of aerobic metabolism result in oxygen extraction from oxyhemoglobin, producing deoxyhemoglobin. This should at least temporarily increase the concentration of deoxyhemoglobin, which would reduce magnetic inhomogeneity and shorten T2*. Currently, however, we usually observe the phenomenon that deoxyhemoglobin is rather diluted because of the excessive inflow of oxygenated arterial blood flow. Dilution of deoxygenated hemoglobin stabilizes the local magnetic field and prolongs T2*. This effect results in increases in T2* MRI signals, which are now widely used as a surrogate marker of neural/synaptic activity. The advantages of this BOLD MRI technique include noninvasive measurements of human brain functions with a superior spatial resolution and a fine temporal resolution over other noninvasive brain mapping methods.

Since BOLD fMRI has made the measurement of brain function possible, many researchers have succeeded in visualizing task-related brain activity by comparing BOLD signals across experimental conditions such as sensory stimulus presentation, cognitive or motor performance, and resting state. This conventional type of fMRI is called "task fMRI." The aim of a task fMRI is often the functional localization of a

brain function related to the task of interest. More recently, various analyses have been applied to clarify the relationship between the activities of remote brain regions, that is, the functional binding of brain areas and their modulation across conditions (functional/effective connectivity). For example, a functional connectivity analysis looks at the simple correlation of task-related activity between remote brain areas; a psychophysiological interaction analysis examines the modulation of inter-areal correlation (i.e., functional connectivity) by stimulus or task conditions; the Granger causality analysis analyzes the time series correlation of activity between brain regions; and dynamic causal modeling models the transmission and causation of distributed dynamic systems modulated by external or contextual inputs. Basically, these analyses have been used to clarify the magnitude differences in brain activity across task conditions (task-related activity), the correlation of task-related activity between remote brain areas (functional connectivity), or the modulation of functional connectivity by task conditions (effective connectivity). Although the application of these task-related fMRIs to healthy participants is relatively easy, it is often difficult to apply them to patients with psychiatric and neurological disorders, particularly because they are likely to have difficulty performing demanding cognitive or motor tasks.

8.3 Resting-State Functional (Connectivity) MRI

8.3.1 Principles of Resting-State Functional (Connectivity) MRI

Here, we introduce the emerging methodology of rs-fMRI/rsfcMRI, because this technique is expected to break the limit of conventional task fMRI and to greatly expand the possibilities of the clinical application of BOLD fMRI. rs-fMRI/rsfcMRI is made possible by just acquiring continuous BOLD contrast images at rest; participants do not need to perform a motor/cognitive task or to pay attention to a stimulus presentation. To assess functional connectivity, rs-fMRI/rsfcMRI extracts low-frequency fluctuations from the BOLD fMRI time series taken at rest and then identifies a set of brain regions that shows a correlation between the BOLD signal time course in those fluctuations. This interregional correlation of low-frequency fluctuations is thought to reflect the state of functional connectivity between remote brain regions. Hereafter, we first explore the theoretical and analytical background of rs-fMRI/rsfcMRI, and then outline the potential applicability of rs-fMRI/rsfcMRI to the diagnosis of dementia.

Biswal and colleagues were the first to introduce the concept of rs-fMRI/rsfcMRI [3]. They focused on the BOLD signal time series of the motor cortex in both hemispheres and showed a high correlation of signal fluctuations between the bilateral motor cortices. This correlation in signal fluctuations was particularly obvious in low-frequency domains in the range of 0.08–0.1 Hz. In addition, they explored regions showing the BOLD signal time course correlated with that of the left motor cortex and found activity almost identical to the activity during a bilateral finger-tapping task.

This report was an epoch-making study, which suggested that resting-state BOLD signals contained information about the network architecture between brain areas. However, skepticism about this claim existed because the low-frequency domains of the BOLD signal time course include various types of physiological noise caused by respiration and pulsation. It took a while until the concept of rs-fMRI/rsfcMRI was widely accepted, when later studies showed that functional connectivity information contained in low-frequency BOLD fluctuations was separable from those derived from physiological noise [4, 5].

8.3.2 Default Mode Network (DMN)

In cognitive task fMRI and positron emission tomography (PET) experiments, it has long been known that some brain areas show decreases of the BOLD signal/blood flow (i.e., deactivation), irrespective of the type of cognitive task. Such "universal deactivation" is often seen in the medial frontal area, medial and lateral parietal areas, and inferior temporal area. Conventionally, this phenomenon was thought to reflect redistribution of cerebral blood flow (i.e., intercerebral steel phenomenon) rather than a change in neural activity. Raichle et al. first claimed that these changes of blood flow did not result from the intercerebral steel phenomenon but from increases in neuronal activity in these regions during rest compared with during cognitive task performance [6]. They used PET imaging to measure the oxygen uptake rate, the ratio of oxygen metabolism, and the cerebral blood flow, in participants during a cognitive task and also at rest with the eyes closed. As a result, parts of the brain regions showed increases in the oxygen uptake rate during the task whereas the same regions showed a decrease in the oxygen uptake rate during the eyes-closed rest condition. Here, a decrease in the oxygen uptake rate indicates an increase in local neural activity, and its increase indicates a reduction in local neural activity. Hence, these findings meant that in the areas with increases in blood flow during the eyes-closed rest, neuronal activity was actually increased, arguing against the interpretation of the intercerebral steel phenomenon. From these results, Raichle et al. proposed the hypothesis that the brain areas activated at rest, such as the medial frontal area, medial and lateral parietal areas, and inferior temporal area, may represent the "default mode" of the brain. They coined the term of "default mode network (DMN)" corresponding to the network consisting of the areas above. Later discovery of the DMN as a part of the resting-state network (RSN) has led to the explosion of rs-fMRI/rsfcMRI research in the field. The encounter of the two originally independent concepts, the principle of rsfcMRI by Biswal and the DMN by Raichle, has provided a strong driving force to propel rsfcMRI research toward clinical applications of rs-fMRI/rsfcMRI to dementia.

In addition to the DMN, Beckmann and colleagues used rs-fMRI/rsfcMRI and identified various RSNs such as the medial and lateral visual networks, auditory network, sensory motor network, visuospatial network, executive control network, and left and right dorsal attention networks. Nodes in each RSN show an interregional correlation of the temporal dynamics of the BOLD signal, which is the reason why rsfcMRI is able to assess functional connectivity in those RSNs (Fig. 8.1) [4].

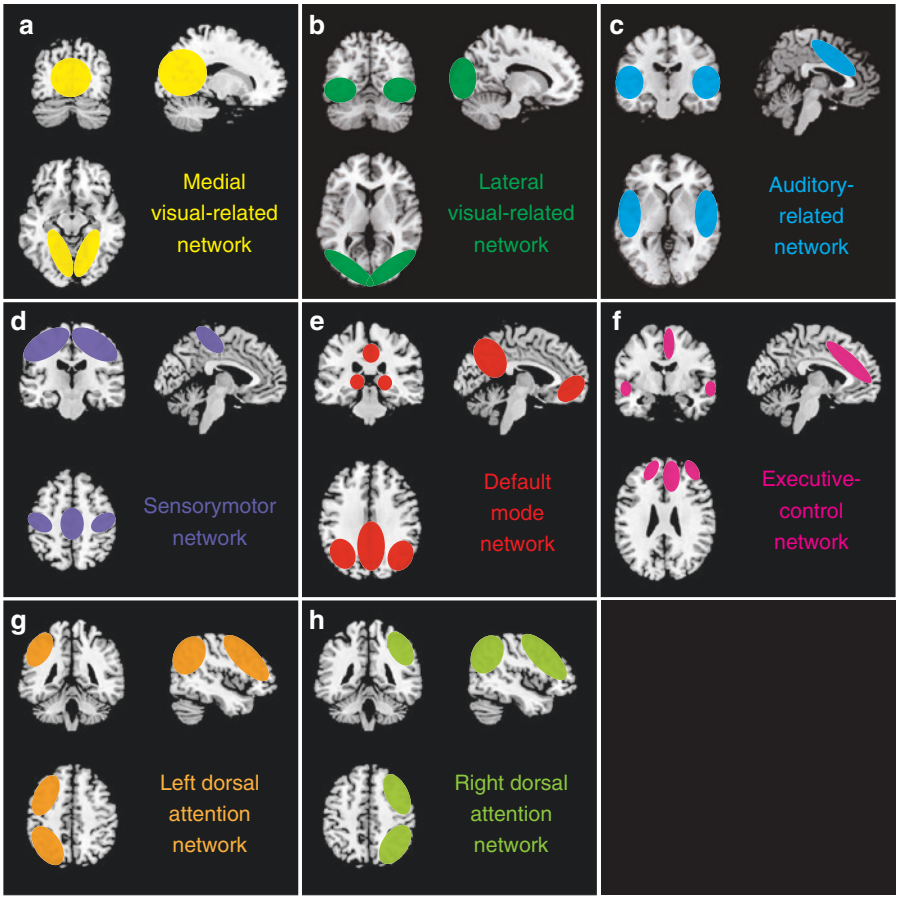

Fig. 8.1 Schema of resting-state networks. (**a**) medial visual-related network, (**b**) lateral visual-related network, (**c**) auditory-related network, (**d**) sensorimotor network, (**e**) default mode network, (**f**) executive control network, (**g**, **h**) left and right dorsal attention network

Because rsfcMRI allows a noninvasive evaluation of those global brain network functions in healthy people and patients, many rsfcMRI studies have been deployed in recent years.

8.3.3 Measurement of rs-fMRI/rsfcMRI

The advantages of rs-fMRI/rsfcMRI include user friendliness and ease of implementation. Experimenters do not have to design complex tasks or to set up a stimulus presentation and response recording systems. Participants do not have to exhaust themselves by working on difficult or nonsensical (at least to them) tasks. It is relatively easy to add rs-fMRI/rsfcMRI to clinical routines of MRI examination as long as echo planar imaging (EPI) is available on the scanner.

To acquire EPIs for rs-fMRI/rsfcMRI, time to repetition (TR) is often set to about 2–3 s to cover the whole brain (Table 8.1). This temporal resolution is satisfactory for rs-fMRI/rsfcMRI because the chronological change of RSN BOLD signals primarily exists in a low-frequency domain ranging from ~0.08 to 0.1 Hz. To date, most rs-fMRI/rsfcMRI studies use a total acquisition time ranging from 5 to 10 min, corresponding to 150–300 EPI volumes. This is consistent with a previous report suggesting that the RSN can be reliably detected with assessment for several minutes [26]. In a large-scale cohort project on Alzheimer's disease (AD) in the USA, the Alzheimer's Disease Neuroimaging Initiative 2 (ADNI2), the rs-fMRI/rsfcMRI protocol uses a TR of 3 s, and a total acquisition time of 7 min (140 EPI volumes). For total acquisition time, however, Birn et al. [27] recently examined the test–retest reliability and similarity of RSNs across sessions. This study has shown that the reliability and similarity of functional connectivity can be improved by increasing the scan lengths from 5 min up to 13 min. However, this finding might

Table 8.1 Summary of the acquisition parameters in previous rsfcMRI studies

Author	Year	Subject	Static magnetic field (T)	Acquired volumes	TR (ms)	TE (ms)	Resolution (mm)
Jafri [7]	2008	Schizophrenia	3.0	168	1860	27	3.75 × 3.75 × 4
Vincent(Data1) [8]	2008	Healthy	3.0	110	3013	25	4 × 4 × 4
Vincent(Data2) [8]	2008	Healthy	3.0	66	5000	30	2 × 2 × 2
Vincent(Data3) [8]	2008	Healthy	3.0	76	5000	30	2 × 2 × 2
Uddin [9]	2009	Healthy	3.0	197	2000	25	3 × 3 × 3
Grigg [10]	2010	Healthy	3.0	170	2000	30	3.125 × 3.125 × 5
Sakoglu [11]	2010	Schizophrenia	3.0	249	1500	27	3.75 × 3.75 × 4
Allen [12]	2011	Healthy	3.0	152	2000	29	3.75 × 3.75 × 4.55
Arbabshirani [13]	2012	Healthy	3.0	200	1500	27	3.75 × 3.75 × 4
Bastin [14]	2012	Healthy	3.0	250	2130	40	3.4 × 3.4 × 4
Koch [15]	2012	MCI	3.0	120	3000	30	3 × 3 × 4
Li [16]	2013	AD	3.0	250	2000	30	4 × 4 × 6
Segall [17]	2012	Healthy	3.0	152	2000	29	3.75 × 3.75 × 4.55
Wang [18]	2012	Healthy	3.0	240	2000	31	3.125 × 3.125 × 3.2
Zuo [19]	2012	healthy	3.0	240	2000	27	3.44 × 3.44 × 4
Damoiseux [20]	2006	Healthy	1.5	200	2850	60	3.3 × 3.3 × 3.3
Wang [21]	2006	AD	1.5	170	2000	60	3.75 × 3.75 × 7
Sorg [22]	2007	MCI, AD	1.5	80	3000	50	3.125 × 3.125 × 4.4
Kelly [23]	2010	Healthy	1.5	180	2000	35	3.5 × 3.5 × 5
Adriaanse [24]	2012	AD	1.5	200	2850	60	3.3 × 3.3 × 3.3
Zarei [25]	2012	AD	1.5	200	2850	60	3 × 3 × 3

TR time to repetition, *TE* echo time, *MCI* mild cognitive impairment, *AD* Alzheimer's disease

have resulted from both increases in scanning time and in the number of volumes. To test this, they assessed the effects of the total number of volumes by comparing results from two data sets with the same total scanning time but with a different number of EPI volumes. In practice, they excluded half the time points by sampling every second image from the first data set and created the half-volume second data set. The results showed that the benefit of increased reliability was found for the increase in the number of volumes as well as the increase in the length of time [27]. According to this result, it seems better to acquire as large a number of volumes as possible with a shortened TR. Currently, our group uses a 10-min scanning protocol with a TR of 2.5 s.

It is important to note that there are many possible states of "resting." In rs-fMRI/rsfcMRI studies, a participant is usually instructed to stay relaxed in a comfortable position within a scanner, and not to think about anything particular or to imagine specific figures or scenes. However, a substantial variability exists across studies as to whether a participant is asked to close their eyes, open their eyes, or fixate on a visual target. However, there is a problem: the functional connectivity pattern may differ between the eyes-open condition and the eyes-closed condition [28]. To date, there is no rule of thumb to judge which condition is ideal for a particular rs-fMRI/rsfcMRI study. Yet one thing is certain: a single condition with either the eyes closed or the eyes open (with or without a fixation target) should be used consistently throughout a single study. In addition, some studies have suggested that RSNs, especially the visual network, may show variation related to the stage of sleep [29]. Currently, our group uses a visual fixation condition with the eyes open to prevent them from falling asleep completely and also to reduce head movement during scanning. This is because we believe that these factors should be controlled as much as possible to reduce possible confounding factors between individuals.

Moreover, a newly developed multimodal imaging technique has been applied for the simultaneous measurement of rs-fMRI/rsfcMRI with near-infrared spectroscopy or with the electroencephalogram [30].

8.3.4 Analysis of rs-fMRI/rsfcMRI

Many analytic methods have been proposed for rs-fMRI/rsfcMRI as they showcase the recent development of neuroimaging. rs-fMRI/rsfcMRI can be analyzed with software packages that have been used for the analysis of task-related fMRI such as statistical parametric mapping (http://www.fil.ion.ucl.ac.uk/spm/doc/), FSL (http://fsl.fmrib.ox.ac.uk/fsl/fslwiki/), and AFNI (http://afni.nimh.nih.gov/afni/), especially with implementation of extension programs such as the Data Processing Assistant for Resting-State fMRI (DPARSF; http://rfmri.org/DPARSF), the conn toolbox (http://web.mit.edu/swg/software.htm [31]), and the Group ICA of fMRI Toolbox (GIFT; http://mialab.mrn.org/software/).

An analysis method focusing on resting-state fluctuations of regional activity is called amplitude of low-frequency fluctuations (ALFF) or fractional ALFF (fALFF). ALFF is defined as the total power within the frequency range between 0.01 and

0.1 Hz in a given voxel; thus, ALFF retrieves local information about the amplitude of low-frequency fluctuations [32]. However, these low-frequency components often contain physiological noise resulting from respiration and pulsation. To overcome this limitation, Zuo and colleagues have proposed fALFF, which is calculated as the power of fluctuations within the low-frequency range (0.01–0.1 Hz) divided by the total power of fluctuations in the entire frequency range. Similar to ALFF, fALFF can index spontaneous brain activity within regions [33, 34]. For example, ALFF and fALFF can test whether two groups may differ in resting-state low-frequency fluctuations in each voxel or region of interest (ROI).

A majority of rs-fMRI/rsfcMRI studies deal with functional connectivity. RsfcMRI analyses explore the correlation of a low-frequency fluctuation of BOLD signals between regions. One of the simplest approaches is to test the correlation of low-frequency fluctuations of BOLD signals between a pair of ROIs. Another typical approach is a seed-to-voxel functional connectivity analysis, or seed-to-voxel analysis for short, adopted by Biswal and colleagues in their original paper [3]. By definition, a seed-to-voxel analysis uses an a priori ROI as the *seed region* and then tests the correlation of low-frequency fluctuations between the seed region and all other voxels in the brain. Seed-to-voxel analysis can explore all the voxels in the whole brain that have a significant correlational relationship with the seed region, yielding a functional connectivity map (Fig. 8.2). Because seed-to-voxel analysis is statistically straightforward and provides comprehensible results, it has become a popular technique. Despite the possibility of clear-cut results being provided, the technique has the major drawback of requiring a priori selection of a seed region. In other words, among the major techniques available for rs-fMRI/rsfcMRI analysis, seed-based analysis is the most explicitly model-based or hypothesis-driven approach derived from traditional fMRI analysis. At the other extreme, independent component analysis (ICA) is a method for multivariate "exploratory" search in which a set of regions or networks having coherent BOLD signal fluctuations can be detected without an a priori model. ICA is a typical model-free analysis in contrast to the model-based functional connectivity analysis requiring an a priori ROI. ICA is originally a method developed for the estimation of a signal source or blind source separation; it is used to decompose an observed signal into a set of independent signal components, by hypothesizing that the observed signal is a linear sum of distinct components from different sources. In ICA of fMRI data, observed, spatially distributed time series BOLD signals are hypothesized as a linear mixture of spatially independent maps, each of which has certain temporal dynamics (signal time course). Thus, ICA of rsfcMRI data identifies RSNs as spatially independent components and creates maps of RSNs accompanied with information about the temporal signal variations of each RSN (Fig. 8.3). An advantage of ICA is that it does not require a priori assumptions about the seed regions or functional connectivity networks. Further, ICA can separate signals that do not reflect neural activity: various types of noise resulting from body movement and physiological noise from respiration and pulsation typically seen in the white matter and cerebrospinal fluid space. Thus, ICA can be used as a filter to remove these noise components. Despite

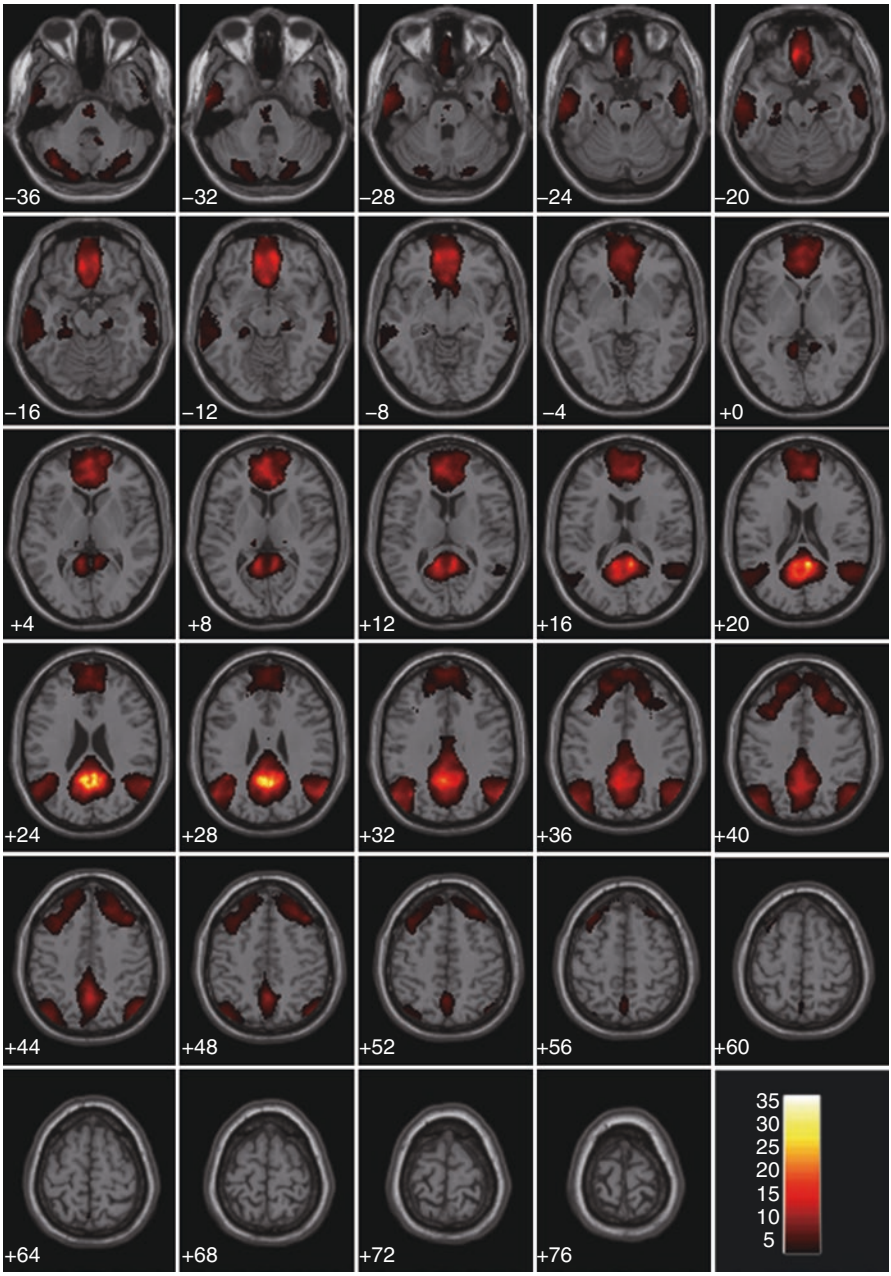

Fig. 8.2 Example of a seed-based analysis with seed ROI at the posterior cingulate cortex/precuneus in the healthy participants group. A significant correlation is observed in the medial part of the frontal lobe, lateral parietal lobe and the lateral inferior temporal gyrus as the default-mode network. The color bar indicates the correlation coefficient

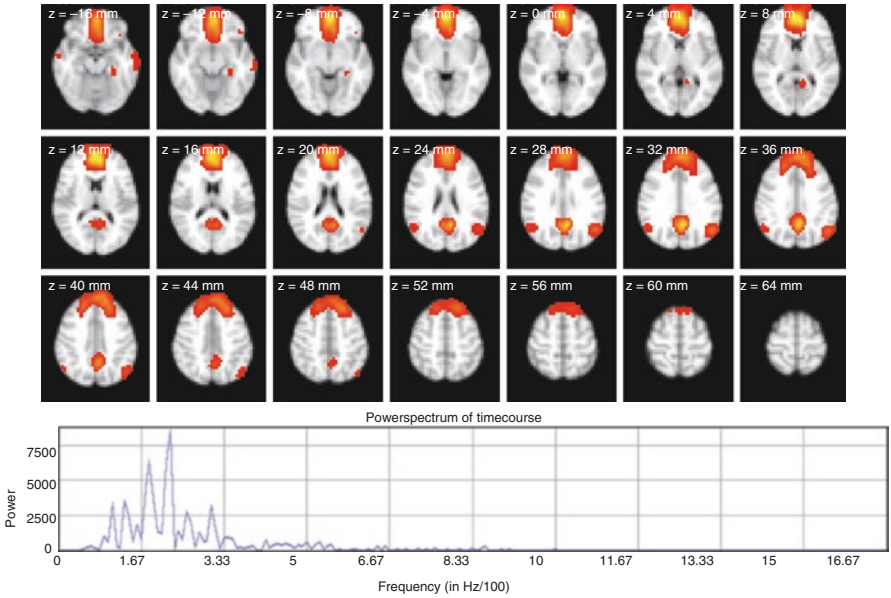

Fig. 8.3 Example of a default mode network identified by an independent component analysis. Because the peak of the power spectrum is observed from 0.02 to 0.03 Hz, we can interpret that this BOLD signal time course has low-frequency oscillation

these merits, a substantial challenge in ICA analysis resides in how to interpret the decomposed ICA components, because ICA-derived spatial maps do not have inherent physiological meanings. Traditionally, the interpretation rested completely upon researchers' eyes classifying the components into valuable and garbage. In this regard, frequency power analysis of the time course of ICA components often helps, because physiologically meaningful RSNs should have a frequency component between 0.08 and 0.1 Hz. For example, the component including most of the frequency-spectrum power above 0.1 Hz shows a "spotty" noise pattern with small clusters of voxels diffusely spread over the brain or ventricle [23]. Also, head motion-related ICA maps typically show a spike-like rapid change of time course. Therefore, motion-related ICA components are predominantly in a high-frequency range of the spectrum. More recently, a template matching method has been employed to match an ICA component from individuals to a single set of component maps representing typical RSNs [35].

Multivariate pattern analysis (MVPA) has significantly progressed the analysis of neuroimaging data in various ways. MVPA first selects a set of brain activity from multiple voxels or a correlation matrix derived from multiple pairs of ROIs, assuming that the selected multivariate data set ("a feature") best characterizes a class or a label of interest. In the case of rsfcMRI, a feature from each individual is typically a correlation matrix derived from several ROIs or from an extensive ROI set covering the entire brain (e.g., automated anatomical labeling); a class may be defined at a level of stimulus (e.g., an orientation of a line), task condition

(e.g., movement A or B), or population (diseased or healthy). A pattern discriminant algorithm is then applied to the correlation matrices to find a hyperplane or criteria that can best discriminate categories within the class. A discriminant algorithm, or a classifier, is often implemented by a form of supervised machine learning such as a support vector machine. After the classifier learns the criteria that best separates a multivariate pattern according to the input data, the capabilities of the classifier might be tested by applying it to a new functional connectivity data set. MVPA is expected to contribute to assisting in clinical diagnosis, provided that it can obtain high classification accuracy. Currently, rsfcMRI-based MVPA classification typically achieves accuracy of about 60–80% (50% chance level) [7, 36, 37]; further improvement would be required for really helpful clinical utility.

Graph theory is one of the most recent network analysis methods and has been introduced to rsfcMRI analysis. Graph theory analysis assumes functional connectivity as a "graph" that consists of a set of objects ("node") corresponding to ROIs and directed or nondirected links ("edge") connecting the objects. A graph characterizes the relationship or state of binding between nodes, namely, brain regions in the case of rsfcMRI analysis. Graph theory analysis provides useful summary information about otherwise complicated relationships between multiple nodes: the small-worldness, the modularity, and the transmission efficiency. Furthermore, graph theory is used to decode the interaction between functional connectivity networks [38].

It is also important to develop analytic methods for multimodal recordings of resting-state brain activity. For example, Omata and colleagues used empirical mode decomposition to classify temporal dynamics of electroencephalogram alpha oscillations at rest into different patterns and then associated each component with rs-fMRI data [30].

8.3.5 rsfcMRI for Diagnosis of Dementia

Recently, abnormal functional connectivity has been reported in various neuropsychiatric diseases such as schizophrenia, depression, and dementia. Particularly, a number of rs-fMRI/rsfcMRI studies have been conducted in AD.

Greicius and colleagues first applied rsfcMRI combined with ICA to AD and healthy control groups. They identified the spatial pattern of the DMN with ICA and then retrieved the BOLD signal time course from the DMN. Then, they performed a correlation analysis of the signal time series typical of the DMN with each individual's rsfcMRI data. As a result, AD patients showed a weak correlation with the typical DMN fluctuation pattern in the posterior cingulate cortex, the hippocampus, and the entorhinal cortex. This finding suggested that, in comparison with healthy participants, patients with AD had reduced functional connectivity in the DMN and medial temporal regions, which play an important role in the process of episodic memory [39]. This seminal report has shown that rs-fMRI/rsfcMRI has the potential to provide a useful biomarker for detecting network abnormalities signifying dementia.

Since then, many studies have followed the study by Greicius and colleagues and have tested the feasibility of rs-fMRI/rsfcMRI in the clinical diagnosis of

neuropsychiatric disorders. Many are interested in network abnormalities of the DMN as a hallmark of AD. As described above, the DMN is one of the RSNs and comprises the medial prefrontal area, posterior cingulate cortex-medial parietal area (precuneus), and the lateral parietal area, in which neural activity is higher at rest than during task engagement. AD transgenic mice show abnormal connectivity in the murine DMN including the human homologs of the posterior cingulate cortex/precuneus to the retrosplenial cortex after age-related deposition of beta-amyloid [40]. Additionally, patients with AD show abnormal functional connectivity of the hippocampus with important hubs of the DMN including the medial prefrontal cortex-ventral anterior cingulate cortex and the posterior cingulate cortex [21]. Zhang and colleagues classified patients with AD into mild, moderate, and severe groups according to the Clinical Dementia Rating (CDR) and the Mini-Mental State Examination (MMSE). When they performed seed-based rsfcMRI analysis using the posterior cingulate cortex as a seed, patients with more severe AD showed a greater reduction in DMN connectivity between the medial prefrontal cortex and the posterior cingulate cortex [41].

Evidence indicates that AD patients may also have abnormal connectivity in other RSNs and also across different RSNs. Patients with amnestic mild cognitive impairment, probably a prodromal phase of AD, show decreased connectivity in the DMN, the hippocampus-posterior cingulate network, and also the attentional network [22]. Brier and colleagues performed seed-based analysis of rs-fMRI/rsfcMRI in a cohort of 510 cases subdivided into normal (CDR of 0), very mild AD (CDR of 0–0.5), and mild AD. They analyzed not only the DMN but also the dorsal attention RSN, executive control RSN, salience RSN, and sensorimotor RSN. The results revealed abnormal intra-RSN connectivity as well as reduced across-RSN connectivity inversely correlated with CDR [42]. Zarei and colleagues classified the hippocampus into three subregions (head, body, and tail) according to its functional connectivity to other brain areas. The head, body, and tail of the hippocampus were strongly connected with the prefrontal cortex, posterior cingulate cortex, and thalamus, respectively. Then, they performed seed-based analysis to compare the connectivity of those hippocampal subnetworks between patients with AD and healthy older patients. The results revealed that there was a correlation between patients with AD who had increased prefrontal-hippocampal head connectivity and reduced posterior cingulate-hippocampal body connectivity and changes in MMSE scores [25, 42].

A famous biomarker of AD is the deposition of beta-amyloid in the brain, and such amyloid deposition can be detected with PET imaging. Interestingly, the posterior cingulate cortex and precuneus, hubs of the DMN, often show the deposition of beta-amyloid with PET imaging. The deposition of beta-amyloid does not always mean cognitive decline. For instance, task-related fMRI activity during a memory task is normal in older participants with amyloid deposition but with normal memory functions [43]. This finding indicates that AD is characterized by abnormal connectivity between the DMN and mesial temporal memory network in addition to the deposition of beta-amyloid. Put differently, the detection of both beta amyloid deposition and DMN abnormality may serve as a specific biomarker of AD. It is then tempting to test whether rs-fMRI/rsfcMRI combined with amyloid PET may provide a better biomarker of predicting AD than the one provided by each technique alone.

In fact, rs-fMRI/rsfcMRI has been applied to cognitively normal or very mildly impaired pre-clinical AD as judged by amyloid PET [44]. Hedden and colleagues prescribed both rs-fMRI/rsfcMRI and PET with Pittsburgh compound B for older participants without clear cognitive decline. Participants with amyloid deposition had decreased DMN connectivity between the medial prefrontal cortex and posterior cingulate cortex and also between bilateral lateral parietal areas as compared with participants without amyloid deposition [43]. Consistent with this, Sheline and coworkers found that older people without cognitive decline had reduced connectivity of the posterior cingulate cortex with the hippocampus, parahippocampus, primary visual areas, and anterior cingulate cortex where amyloid deposition was identified [45]. Oh and colleagues took this one step further [46]. They used gray matter volumetric analysis of structural MRI in combination with amyloid PET and rs-fMRI/rsfcMRI. First, the analysis revealed that in the older population, increased amyloid deposition was correlated with the reduction in gray matter volume in the left inferior frontal gyrus. Second, the reduction of the gray matter volume of the posterior cingulate cortex was exclusively observed in participants with amyloid deposition there. Third, seed-based analysis of rsfcMRI showed that the left inferior frontal gyrus and the posterior cingulate cortex belonged to different RSNs. Last, abnormality of the left inferior frontal RNS was correlated with a reduction in working memory performance, whereas that of the posterior cingulate RNS was not. Taken together, a comprehensive workup with amyloid PET, structural MRI, and rs-fMRI/rsfcMRI likely provides invaluable information about the pathophysiology of preclinical AD.

As discussed, rsfcMRI is expected to assist in the clinical diagnosis of neuropsychiatric disorders. This may be achieved by combining multivariate information from rsfcMRI and pattern classification algorithms such as support vector machine to find a subtle difference between individuals. Such an approach is especially important in neuropsychiatric disorders without established biomarkers for a definite diagnosis such as mood disorders [37], schizophrenia [36], and autism [47]. Furthermore, Koch and coworkers have indicated the feasibility of rsfcMRI for the diagnosis of AD. They retrieved a seed (posterior cingulate cortex)-based feature and also an ICA-based feature from rsfcMRI data, and attempted to classify between AD and healthy older participants. They compared classification performance among the seed-based feature, ICA-based feature, and the combined seed- and ICA-based feature. The classification performance was 64% and 71% when they were based on either the seed- or ICA-based feature, respectively; however, the combined seed- and ICA-based feature achieved a classification performance of 97% [15]. This study has hinted on the usefulness of an rsfcMRI-based classification for the diagnosis of AD. Nevertheless, Koch and coworkers also reported that they were not able to classify between participants with and those without the ApoE4 allele, a risk factor of AD, suggesting a limitation of the current method [15].

We have argued for the feasibility of rs-fMRI/rsfcMRI for assisting in the early diagnosis of AD. It does not seem too difficult to implement rs-fMRI/rsfcMRI into clinical practice because of the convenience of the technique and the low burden to both patients and clinical practitioners. In combination with large imaging data projects such as ADNI, we foresee an explosion of rs-fMRI/rsfcMRI research and the clinical application of rs-fMRI/rsfcMRI to dementia.

References

1. Roy CS, Sherrington CS. On the regulation of the blood-supply of the brain. J Physiol. 1890;11(1–2):85–108.
2. Ogawa S, Lee TM, Kay AR, Tank DW. Brain magnetic resonance imaging with contrast dependent on blood oxygenation. Proc Natl Acad Sci U S A. 1990;87(24):9868–72.
3. Biswal B, Yetkin FZ, Haughton VM, Hyde JS. Functional connectivity in the motor cortex of resting human brain using echo-planar MRI. Magn Reson Med. 1995;34(4):537–41.
4. Beckmann CF, DeLuca M, Devlin JT, Smith SM. Investigations into resting-state connectivity using independent component analysis. Philos Trans R Soc B-Biol Sci. 2005;360(1457):1001–13. doi:10.1098/rstb.2005.1634.
5. Birn RM, Murphy K, Bandettini PA. The effect of respiration variations on independent component analysis results of resting state functional connectivity. Hum Brain Mapp. 2008;29(7):740–50. doi:10.1002/hbm.20577.
6. Raichle ME, MacLeod AM, Snyder AZ, Powers WJ, Gusnard DA, Shulman GL. A default mode of brain function. Proc Natl Acad Sci U S A. 2001;98(2):676–82.
7. Jafri MJ, Calhoun VD. Functional classification of schizophrenia using feed forward neural networks. Conf Proc IEEE Eng Med Biol Soc. 2006;(Suppl):6631–4.
8. Vincent JL, Kahn I, Snyder AZ, Raichle ME, Buckner RL. Evidence for a frontoparietal control system revealed by intrinsic functional connectivity. J Neurophysiol. 2008;100(6):3328–42. doi:10.1152/jn.90355.2008.
9. Uddin LQ, Kelly AMC, Biswal BB, Castellanos FX, Milham MP. Functional connectivity of default mode network components: correlation, anticorrelation, and causality. Hum Brain Mapp. 2009;30(2):625–37. doi:10.1002/hbm.20531.
10. Grigg O, Grady CL. The default network and processing of personally relevant information: converging evidence from task-related modulations and functional connectivity. Neuropsychologia. 2010;48(13):3815–23. doi:10.1016/j.neuropsychologia.2010.09.007.
11. Sakoglu U, Pearlson GD, Kiehl KA, Wang YM, Michael AM, Calhoun VD. A method for evaluating dynamic functional network connectivity and task-modulation: application to schizophrenia. MAGMA. 2010;23(5–6):351–66. doi:10.1007/s10334-010-0197-8.
12. Allen EA, Erhardt EB, Damaraju E, Gruner W, Segall JM, Silva RF, Havlicek M, Rachakonda S, Fries J, Kalyanam R, Michael AM, Caprihan A, Turner JA, Eichele T, Adelsheim S, Bryan AD, Bustillo J, Clark VP, Feldstein Ewing SW, Filbey F, Ford CC, Hutchison K, Jung RE, Kiehl KA, Kodituwakku P, Komesu YM, Mayer AR, Pearlson GD, Phillips JP, Sadek JR, Stevens M, Teuscher U, Thoma RJ, Calhoun VD. A baseline for the multivariate comparison of resting-state networks. Front Syst Neurosci. 2011;5:2. doi:10.3389/fnsys.2011.00002.
13. Arbabshirani MR, Havlicek M, Kiehl KA, Pearlson GD, Calhoun VD. Functional network connectivity during rest and task conditions: a comparative study. Hum Brain Mapp. 2012;34(11):2959–71. doi:10.1002/hbm.22118.
14. Bastin C, Yakushev I, Bahri MA, Fellgiebel A, Eustache F, Landeau B, Scheurich A, Feyers D, Collette F, Chetelat G, Salmon E. Cognitive reserve impacts on inter-individual variability in resting-state cerebral metabolism in normal aging. NeuroImage. 2012;63(2):713–22. doi:10.1016/j.neuroimage.2012.06.074.
15. Koch W, Teipel S, Mueller S, Benninghoff J, Wagner M, Bokde ALW, Hampel H, Coates U, Reiser M, Meindl T. Diagnostic power of default mode network resting state fMRI in the detection of Alzheimer's disease. Neurobiol Aging. 2012;33(3):466–78. doi:10.1016/j.neurobiolaging.2010.04.013.
16. Li R, Wu X, Chen K, Fleisher AS, Reiman EM, Yao L. Alterations of directional connectivity among resting-state networks in Alzheimer disease. AJNR Am J Neuroradiol. 2013;34(2):340–5. doi:10.3174/ajnr.A3197.
17. Segall JM, Allen EA, Jung RE, Erhardt EB, Arja SK, Kiehl K, Calhoun VD. Correspondence between structure and function in the human brain at rest. Front Neuroinform. 2012;6:10. doi:10.3389/fninf.2012.00010.

18. Wang Z, Liu J, Zhong N, Qin Y, Zhou H, Li K. Changes in the brain intrinsic organization in both on-task state and post-task resting state. NeuroImage. 2012;62(1):394–407. doi:10.1016/j.neuroimage.2012.04.051.
19. Zou Q, Ross TJ, Gu H, Geng X, Zuo XN, Hong LE, Gao JH, Stein EA, Zang YF, Yang Y. Intrinsic resting-state activity predicts working memory brain activation and behavioral performance. Hum Brain Mapp. 2013;34(12):3204–15. doi:10.1002/hbm.22136.
20. Damoiseaux JS, Rombouts S, Barkhof F, Scheltens P, Stam CJ, Smith SM, Beckmann CF. Consistent resting-state networks across healthy subjects. Proc Natl Acad Sci U S A. 2006;103(37):13848–53. doi:10.1073/pnas.0601417103.
21. Wang L, Zang Y, He Y, Liang M, Zhang X, Tian L, Wu T, Jiang T, Li K. Changes in hippocampal connectivity in the early stages of Alzheimer's disease: evidence from resting state fMRI. NeuroImage. 2006;31(2):496–504. doi:10.1016/j.neuroimage.2005.12.033.
22. Sorg C, Riedl V, Muehlau M, Calhoun VD, Eichele T, Laeer L, Drzezga A, Foerstl H, Kurz A, Zimmer C, Wohlschlaeger AM. Selective changes of resting-state networks in individuals at risk for Alzheimer's disease. Proc Natl Acad Sci U S A. 2007;104(47):18760–5. doi:10.1073/pnas.0708803104.
23. Kelly RE, Alexopoulos GS, Wang ZS, Gunning FM, Murphy CF, Morimoto SS, Kanellopoulos D, Jia ZR, Lim KO, Hoptman MJ. Visual inspection of independent components: defining a procedure for artifact removal from fMRI data. J Neurosci Methods. 2010;189(2):233–45. doi:10.1016/j.jneumeth.2010.03.028.
24. Adriaanse SM, Sanz-Arigita EJ, Binnewijzend MA, Ossenkoppele R, Tolboom N, van Assema DM, Wink AM, Boellaard R, Yaqub M, Windhorst AD. Amyloid and its association with default network integrity in Alzheimer's disease. Hum Brain Mapp. 2012;35(3):779–91.
25. Zarei M, Beckmann CF, Binnewijzend MA, Schoonheim MM, Oghabian MA, Sanz-Arigita EJ, Scheltens P, Matthews PM, Barkhof F. Functional segmentation of the hippocampus in the healthy human brain and in Alzheimer's disease. NeuroImage. 2012;66:28–35.
26. Van Dijk KRA, Hedden T, Venkataraman A, Evans KC, Lazar SW, Buckner RL. Intrinsic functional connectivity as a tool for human connectomics: theory, properties, and optimization. J Neurophysiol. 2010;103(1):297–321. doi:10.1152/jn.00783.2009.
27. Birn RM, Molloy EK, Patriat R, Parker T, Meier TB, Kirk GR, Nair VA, Meyerand ME, Prabhakaran V. The effect of scan length on the reliability of resting-state fMRI connectivity estimates. NeuroImage. 2013;83:550–8. doi:10.1016/j.neuroimage.2013.05.099.
28. Patriat R, Molloy EK, Meier TB, Kirk GR, Nair VA, Meyerand ME, Prabhakaran V, Birn RM. The effect of resting condition on resting-state fMRI reliability and consistency: a comparison between resting with eyes open, closed, and fixated. NeuroImage. 2013;78:463–73. doi:10.1016/j.neuroimage.2013.04.013.
29. Samann PG, Wehrle R, Hoehn D, Spoormaker VI, Peters H, Tully C, Holsboer F, Czisch M. Development of the brain's default mode network from wakefulness to slow wave sleep. Cereb Cortex. 2011;21(9):2082–93. doi:10.1093/cercor/bhq295.
30. Omata K, Hanakawa T, Morimoto M, Honda M. Spontaneous slow fluctuation of EEG alpha rhythm reflects activity in deep-brain structures: a simultaneous EEG-fMRI study. PLoS One. 2013;8(6):12. doi:10.1371/journal.pone.0066869.
31. Whitfield-Gabrieli S, Nieto-Castanon A. Conn: a functional connectivity toolbox for correlated and anticorrelated brain networks. Brain Connect. 2012;2(3):125–41. doi:10.1089/brain.2012.0073.
32. Zang Y-F, He Y, Zhu C-Z, Cao Q-J, Sui M-Q, Liang M, Tian L-X, Jiang T-Z, Wang Y-F. Altered baseline brain activity in children with ADHD revealed by resting-state functional MRI. Brain and Development. 2007;29(2):83–91. doi:10.1016/j.braindev.2006.07.002.
33. Yan CG, Liu DQ, He Y, Zou QH, Zhu CZ, Zuo XN, Long XY, Zang YF. Spontaneous brain activity in the default mode network is sensitive to different resting-state conditions with limited cognitive load. PLoS One. 2009;4(5):11. doi:10.1371/journal.pone.0005743.
34. Zou Q-H, Zhu C-Z, Yang Y, Zuo X-N, Long X-Y, Cao Q-J, Wang Y-F, Zang Y-F. An improved approach to detection of amplitude of low-frequency fluctuation (ALFF) for resting-

state fMRI: fractional ALFF. J Neurosci Methods. 2008;172(1):137–41. doi:10.1016/j.jneumeth.2008.04.012.
35. Salimi-Khorshidi G, Douaud G, Beckmann CF, Glasser MF, Griffanti L, Smith SM. Automatic denoising of functional MM data: combining independent component analysis and hierarchical fusion of classifiers. NeuroImage. 2014;90:449–68. doi:10.1016/j.neuroimage.2013.11.046.
36. Arbabshirani MR, Kiehl KA, Pearlson GD, Calhoun VD. Classification of schizophrenia patients based on resting-state functional network connectivity. Front Neurosci. 2013;7:16. doi:10.3389/fnins.2013.00133.
37. Craddock RC, Holtzheimer PE III, Hu XP, Mayberg HS. Disease state prediction from resting state functional connectivity. Magn Reson Med. 2009;62(6):1619–28. doi:10.1002/mrm.22159.
38. Supekar K, Menon V, Rubin D, Musen M, Greicius MD. Network analysis of intrinsic functional brain connectivity in Alzheimer's disease. PLoS Comput Biol. 2008;4(6):11. doi:10.1371/journal.pcbi.1000100.
39. Greicius MD, Srivastava G, Reiss AL, Menon V. Default-mode network activity distinguishes Alzheimer's disease from healthy aging: evidence from functional MRI. Proc Natl Acad Sci U S A. 2004;101(13):4637–42. doi:10.1073/pnas.0308627101.
40. Bero AW, Bauer AQ, Stewart FR, White BR, Cirrito JR, Raichle ME, Culver JP, Holtzman DM. Bidirectional relationship between functional connectivity and amyloid-beta deposition in mouse brain. J Neurosci. 2012;32(13):4334–40. doi:10.1523/Jneurosci.5845-11.2012.
41. Zhang H-Y, Wang S-J, Liu B, Ma Z-L, Yang M, Zhang Z-J, Teng G-J. Resting brain connectivity: changes during the progress of alzheimer disease. Radiology. 2010;256(2):598–606.
42. Brier MR, Thomas JB, Snyder AZ, Benzinger TL, Zhang D, Raichle ME, Holtzman DM, Morris JC, Ances BM. Loss of intranetwork and internetwork resting state functional connections with Alzheimer's disease progression. J Neurosci. 2012;32(26):8890–9. doi:10.1523/jneurosci.5698-11.2012.
43. Sperling RA, LaViolette PS, O'Keefe K, O'Brien J, Rentz DM, Pihlajamaki M, Marshall G, Hyman BT, Selkoe DJ, Hedden T. Amyloid deposition is associated with impaired default network function in older persons without dementia. Neuron. 2009;63(2):178.
44. Sheline YI, Raichle ME. Resting state functional connectivity in preclinical Alzheimer's disease. Biol Psychiatry. 2013;74(5):340–7. doi:10.1016/J.Biopsych.2012.11.028.
45. Sheline YI, Raichle ME, Snyder AZ, Morris JC, Head D, Wang SZ, Mintun MA. Amyloid plaques disrupt resting state default mode network connectivity in cognitively normal elderly. Biol Psychiatry. 2010;67(6):584–7. doi:10.1016/J.Biopsych.2009.08.024.
46. Oh H, Mormino EC, Madison C, Hayenga A, Smiljic A, Jagust WJ. Beta-amyloid affects frontal and posterior brain networks in normal aging. NeuroImage. 2011;54(3):1887–95. doi:10.1016/j.neuroimage.2010.10.027.
47. Iidaka T. Resting state functional magnetic resonance imaging and neural network classified autism and control. Cortex. 2015;63:55–67. doi:10.1016/j.cortex.2014.08.011.

FDG-PET in Alzheimer's Disease

9

Yoshitaka Inui, Kengo Ito, and Takashi Kato

Abstract

^{18}F-2-fluoro-2-deoxy-D-glucose (^{18}F-FDG) is a tracer that can objectively evaluate neuronal activity in the brain and has been widely used in the research and diagnosis of Alzheimer's disease (AD). The clinical diagnostic criteria for AD were revised in 2011. Along with magnetic resonance imaging, FDG-positron emission tomography (PET) has been shown to be an important research criteria as an objective biomarker for neuronal injury.

Typical FDG-PET findings in AD include reduced glucose metabolism in the parietotemporal association cortex, precuneus, and posterior cingulate. FDG-PET plays an important role in visually and quantitatively perceiving these types of findings; consequently, the certainty of the clinical diagnosis of AD can be improved, and differentiating between AD and non-Alzheimer's dementia is also possible. Furthermore, FDG-PET may be used as a biomarker for early diagnosis of AD, at the mild cognitive impairment (MCI) or preclinical stages, in order to start medical or non-pharmacologic treatment and, subsequently, as a biomarker to determine treatment effects. This chapter focuses on previously collected evidence about the efficacy and practicality of FDG-PET in the diagnosis of AD.

Y. Inui (✉)
Department of Clinical and Experimental Neuroimaging,
National Center for Geriatrics and Gerontology, Aichi, Japan

Department of Radiology, Fujita Health University School of Medicine,
Toyoake, Aichi, Japan
e-mail: yinui@ncgg.go.jp

K. Ito • T. Kato
Department of Clinical and Experimental Neuroimaging,
National Center for Geriatrics and Gerontology, Aichi, Japan

H. Matsuda et al. (eds.), *Neuroimaging Diagnosis for Alzheimer's Disease and Other Dementias*, DOI 10.1007/978-4-431-55133-1_9

Keywords
^{18}F-FDG-PET • Alzheimer's disease • Mild cognitive impairment • Cerebral glucose metabolism

9.1 Introduction

^{18}F-FDG is a chemical compound similar to glucose that can pass through the blood-brain barrier by means of carrier-mediated transport, specifically, glucose transporter type 1 (GLUT1), to enter the brain and undergo phosphorylation by hexokinase, an enzyme in the glycolytic pathway. Unlike glucose, however, ^{18}F-FDG is not degraded by isomerase and reverse phosphorylation is rare; hence, metabolism is "trapped" at this point and ^{18}F-FDG builds up in cells [1].

Localized brain glucose metabolism reacts to functional activity and density of synapse in the area through neuron-glia metabolic coupling [2] and exhibits a strong correlation with neuronal activity [3, 4]. This is because biologically, the brain's only source of energy is glucose, whereas ATP, which facilitates the glycolytic pathway and the tricarboxylic acid cycle, is mainly used for neuronal activity in the brain. This explains the superiority of the PET scan, which uses ^{18}F-FDG in objectively evaluating neuronal activity in the brain.

When diagnosing AD, computed tomography (CT) and magnetic resonance imaging (MRI) have been necessary for the exclusion of treatable dementia such as normal pressure hydrocephalus and chronic subdural hematoma and for evaluation of cerebrovascular diseases. In the diagnosis of AD, single photon emission CT (SPECT) and PET scans, which evaluate cerebral blood flow and metabolism, respectively, have earned their status as ancillary methods to increase diagnostic certainty. However, due to an increase in the need for early diagnosis and advances in amyloid imaging, the role of imaging diagnosis in AD is changing dramatically. Currently, the Alzheimer's Disease Neuroimaging Initiative (ADNI; http://www.adni-info.org) is advancing globally; it is a large-scale, comprehensive clinical research initiative which aims to standardize early diagnosis of AD internationally. This study involves repeated biomarker testing, such as brain volume measurement with MRI, brain glucose metabolism imaging, amyloid imaging with PET, and measurement of cerebrospinal fluid Aβ and tau, to make early diagnosis of AD and verify the efficacy of treatment and pathophysiological status; the goal is to establish a standard evaluation system for AD, and many of these research results have been published [5]. Among such activities, clinical diagnostic criteria have been revised from the previous National Institute of Neurological and Communicative Disorders and Stroke/Alzheimer's Disease and Related Disorders Association (NINCDS-ADRDA) [6] in 2011 through the working groups of the National Institute of Aging and Alzheimer's Association [7]. In the new criteria, MCI due to AD and preclinical stage of AD were suggested [8, 9]. In all of the disease phases, FDG-PET, along with MRI, has been included in important research criteria as a biomarker that objectively shows neuronal injury.

9.2 ^{18}F-FDG-PET Findings in the Healthy Brain and in AD

FDG uptake in the cerebral cortex, cerebellar cortex, and central gray matter of healthy people is high because there is a clear correlation between gray matter density and glucose metabolism. In the cerebral cortex, accumulation is especially high in the occipital lobe, posterior cingulate, and precuneus. Accumulation of FDG in the striatum and thalamus is equivalent to that in the cerebral cortex.

Typical FDG-PET findings in AD include hypometabolism in the parietotemporal association cortex, posterior cingulate, and precuneus (Fig. 9.1). In many cases, hypometabolism in the frontal cortex becomes clear in the progression period [10–12]. On the other hand, accumulation in the primary sensorimotor cortex, primary visual cortex, basal nuclei, and thalamus tends to remain the same even when the disease progresses. Almost identical findings can be seen on cerebral blood flow SPECT, but these findings are generally clearer with PET than SPECT because the spatial resolution and the quantitativity of PET are superior to SPECT. FDG-PET is superior in terms of diagnostic accuracy for dementia, including AD, especially in its early stages [13, 14]. Atrophy of the hippocampus and parahippocampus is found from the early stages of AD, but the reduction in glucose metabolism corresponding to atrophy is not always detected [15]. There are also known discrepancies depending on the age of onset. In presenile onset AD, the typical AD glucose metabolism pattern is often centered in the parietotemporal association cortex, whereas in senile onset AD, glucose metabolism tends to be reduced in the limbic system and in the frontal lobe, with cases of relatively weak reduction in the parietotemporal association area, posterior cingulate, and precuneus [16, 17]. Furthermore, there are individual differences in the progression of reduced glucose metabolism in each case of AD, and there is no fixed degree of spread or reduction and no fixed speed of progression.

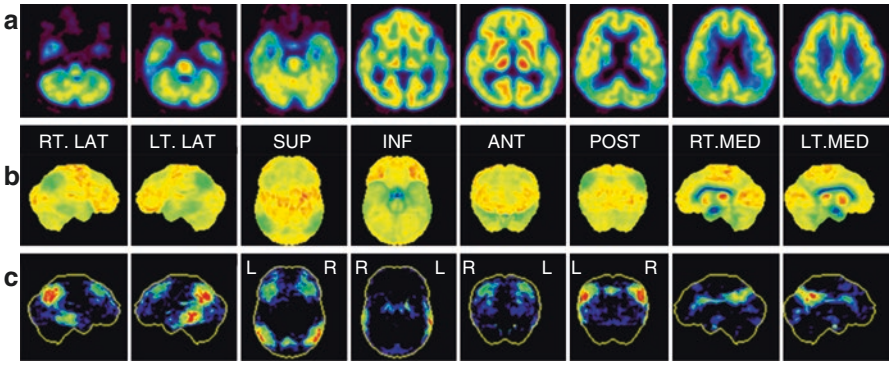

Fig. 9.1 Representative FDG-PET images of AD patient. (**a**) Tomography, (**b**) 3D-SSP, and (**c**) 3D-SSP Z-score images show hypometabolism in the parietotemporal association cortex, posterior cingulate, and precuneus

Reduction in glucose metabolism in the posterior cingulate and precuneus is considered to be an early diagnostic clue for AD [18], because this area lies inside the brain, visual assessment of subtle reductions in metabolism on PET cross-section images is not easy. This may be overcome by the use of statistical image analysis methods, such as the widely used 3D-stereotactic surface projection (3D-SSP) [19] and statistical parametric mapping (SPM) [20]. These are tools which can easily evaluate all the cerebral regions by comparing individual case images with normal database. 3D-SSP applies a z-score mapping to areas with reduced or increased glucose metabolism. Not only does this simplify the assessment of medial side of the brain, it also offers high reproducibility and detection of slight changes.

Many reports have examined the diagnostic ability of FDG-PET on cases that had been diagnosed with AD according to clinical diagnostic criteria such as NINCDS-ADRDA and DSM-IV [19, 21–42]. Reported sensitivity and specificity vary widely, but according to a meta-analysis, the sensitivity and specificity of FDG-PET are 90% and 89%, respectively, demonstrating FDG-PET's superiority over biomarkers such as cerebrospinal fluid Aβ42 and tau, cerebral blood flow SPECT, and MRI [43]. Furthermore, analysis of the literature published after the year 2000 revealed the extremely high diagnostic ability offered by FDG-PET, with 96% sensitivity and 90% specificity. This improvement in diagnostic ability is thought to be due to the use of improved PET devices or improved interpretational skills of observers [44]. However, the best that FDG-PET can do is differentiating between patients with AD and healthy subjects: it must be noted that it does not incorporate histopathological evidence, and clinical diagnosis is the current gold standard.

9.3 Differentiation between Alzheimer's and Non-Alzheimer's Dementia

About half of the patients with dementia have AD, but there are also various cases of non-AD dementia, such as dementia with Lewy bodies (DLB), frontotemporal dementia (FTD), and vascular dementia (VaD), which must be differentiated from AD. Differentiating between non-AD dementia and AD is important for deciding on the treatment approach, estimating future symptoms, and determining prognosis. There are also a number of reports about differentiation between AD and non-AD dementia with FDG-PET [26, 27, 29, 38, 45–52], but according to a meta-analysis, the sensitivity and specificity of FDG-PET are 93% and 70%, respectively; the specificity is somewhat low [43]. Even if only reports with histopathological confirmation are selected, specificity still tends to be low [48, 50–52]. Among non-AD dementia cases, there are many instances of false positive FDG-PET scans which show hypometabolic patterns similar to those seen in AD.

The frequency of DLB is high among non-AD dementia cases. Differential diagnosis of DLB and AD is important for accurate prognostication and appropriate treatment; however, it is not easy because there is clinically overlapping symptoms and hypometabolism observed in DLB is similar to that observed in AD (Fig. 9.2). In addition to a decline in glucose metabolism that is similar to that found in AD,

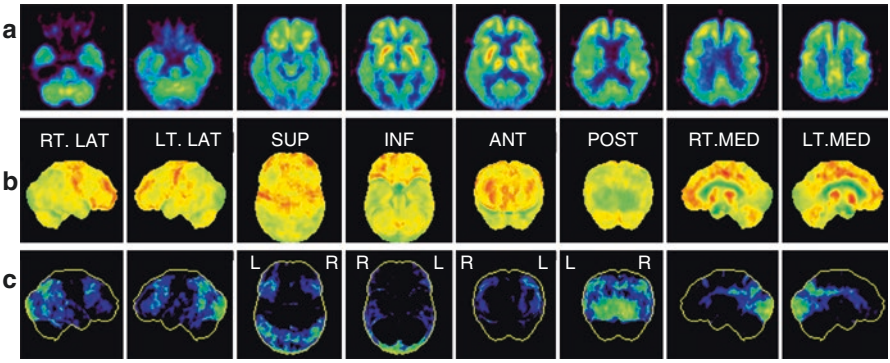

Fig. 9.2 Representative FDG-PET images of DLB patient. (**a**) Tomography, (**b**) 3D-SSP, and (**c**) 3D-SSP Z-score images show hypometabolism in the occipital lobe, parietotemporal association cortex, posterior cingulate, and precuneus

hypometabolism in the occipital lobe including visual cortex is characteristic of DLB. Low uptake in occipital lobe on SPECT and/or PET is one of the supportive features suggested as a clinical diagnostic criterion for DLB [53], although specificity is not high [45–47]. Also, regarding differentiation between AD and FTD, which are covered by the US Medicare system insurance, FDG-PET has been shown to have 99% sensitivity and 65% specificity in a study of a large number of cases [38]. In reports confirmed by histopathological diagnosis, sensitivity was high at 97% and specificity was 71% [48]. These results suggest that it is not uncommon for DLB and FTD to be diagnosed as AD.

9.4 FDG-PET for Mild Cognitive Impairment

MCI was proposed and revised by Petersen et al. as a summary of cognitive function status expressing normal and dementia statuses [54]. Subtypes include amnestic type and non-amnestic type; single-domain types, in which disability forms in the single higher brain function area; and multi-domain type, in which the disability manifests in many areas. The cause of MCI is heterogeneous and involves a number of conditions; besides AD, degenerating dementia, such as DLB and FTD; cerebrovascular disease, including VaD; and psychiatric conditions, such as depression and external injury-type changes; and normal aging [54, 55]. Among these, amnestic-type MCI patients convert to AD at a rate of about 12–15% per year [54]. If disease-modifying treatment is developed in the future, the MCI stage would be considered to be the appropriate period to begin treatment, so there is an especially high necessity for early diagnosis at this stage. Early diagnosis at the MCI stage using FDG-PET allows prediction of conversion from MCI to AD. In past reports with 1–2-year follow-up periods, the accuracy of predicting conversion from MCI to AD was high, at 80% or greater [56–58], and in a meta-analysis conducted by Yuan et al., sensitivity and specificity both tended to be high, at 88.8% and 84.9%, respectively [59].

However, recent reports using ADNI data suggested low diagnostic ability, with a sensitivity of 57% and a specificity of 67% [60]. This lack of consistency in diagnostic ability may be due to differences in backgrounds of the registered MCI groups, discrepancies in analysis or evaluation methods, or differences in follow-up periods.

In Japan, a prospective multicenter study targeting amnestic MCI, the Study on Diagnosis of early Alzheimer's disease-Japan, SEAD-J, was conducted; this report contains the results of 3-yr. observations of progress [61]. According to this study, the diagnostic ability of FDG-PET using visual evaluation has a sensitivity of 98%, specificity of 41%, and an accurate diagnosis rate of 71%. This trend coincides with the results of a similar multicenter study using cerebral blood flow SPECT, the Japan Cooperative SPECT Study on Assessment of Mild Impairment of Cognitive Function, J-COSMIC [62], but the overall diagnostic ability of FGD-PET is higher. In the SEAD-J extension, which included a 5-year follow-up of SEAD-J cases, there were cases of MCI that converted to AD in the fourth or fifth year (Fig. 9.3); hence, it may be possible that the low specificity is caused by being a slow converter. Compared with slow converters, rapid converters have clear tendencies for AD-type changes on baseline images (Fig. 9.3). In fact, on assessments by mathematical indicators using AD t-sum, diagnostic ability was highest at 2 years when sensitivity was 70%, specificity was 90%, and accuracy was 83%, whereas at 3 years, sensitivity was 60%, specificity was 91%, and accuracy was 77% [61]. These results indicate that if there is no

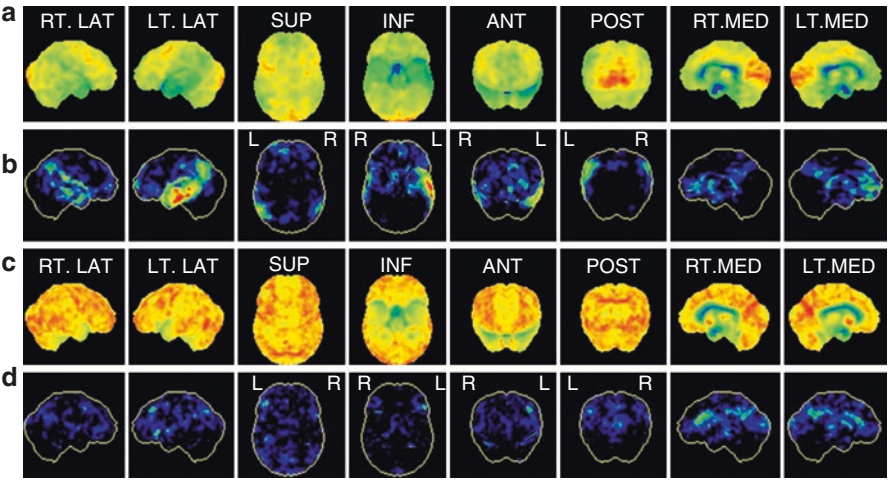

Fig. 9.3 3D-SSP images of MCI patients converted to AD. *Top*: Baseline image of rapid converter during a visit in the second year of follow-up. (**a**) 3D-SSP image, (**b**) 3D-SSP Z-score image. Glucose metabolism decreased in the parietotemporal association cortex, posterior cingulate, and precuneus mainly on the left side. *Bottom*: Baseline image of slow converter during a visit in the fifth year of follow-up. (**c**) 3D-SSP image, (**d**) 3D-SSP Z-score image. Glucose metabolism decreased in the parietotemporal association cortex, posterior cingulate, and precuneus. Rapid converter exhibited clearer AD changes at baseline than slow converter

hypometabolism that suggests AD, the probability of conversion from MCI to AD is low and that selecting cases with clear-cut AD changes using semi-quantitative indicators could make it possible to select rapid converters up to the second year.

In addition to FDG-PET evaluation, concomitant use of the ApoE genotype has been reported to improve accuracy [56, 57]. In any case, in MCI research, histopathological confirmation of the diagnosis is difficult, and results are based on clinical diagnosis using follow-up examinations.

9.5 Preclinical Stage FDG-PET

There are a limited number of reports on the use of FDG-PET in the asymptomatic preclinical stage. In the middle age and older groups at high risk for AD due to family history and positive ApoE ε4, hypometabolism of the parietotemporal association cortex has been reported [63, 64]; this abnormality is also seen in their 20s and 30s [65]. In asymptomatic middle aged and older cases with positive ApoE ε4, parietotemporal association cortex and posterior cingulate glucose metabolism declines at an annual rate of 2% [66]. In elderly cases with normal cognitive function progressing to MCI within 3 years of observation, abnormalities were found in the hippocampus, suggesting that abnormal glucose metabolism may start in this area [67]. It is difficult to predict progression to MCI or AD on an individual level because changes in the association cortex and inner part of the temporal lobe during the preclinical stage are normally extremely subtle; but in cases of preventive intervention for asymptomatic cases, FDG-PET may determine efficacy of medical and non-pharmacologic treatment.

In recent years, a substantial number of cognitively normal, elderly individuals without proven deposition of Aβ on amyloid imaging were reported to have at least one significant marker of neurodegeneration including FDG metabolism [68–70]. Cases like these are placed in a separate category from preclinical AD and are designated as "suspected non-AD pathology, SNAP." It may be affected by the presence of conditions such as cerebrovascular disease, tauopathy, or synucleinopathy, but further verification is required.

References

1. Hertz E, Dienel GA. Energy metabolism in the brain. In: Dwyer DS, editor. Glucose metabolism in the brain. International review of neurobiology, vol. 51. San Diego, CA: Academic; 2002. p. 2–102.
2. Magistretti PJ. Role of glutamate in neuron-glia metabolic coupling. Am J Clin Nutr. 2009;90(3):875S–80S.
3. Sokoloff L. Relation between physiological function and energy metabolism in the central nervous system. J Neurochem. 1977;29(1):13–26.
4. Liu X, Erikson C, Brun A. Cortical synaptic changes and gliosis in normal aging, Alzheimer's disease and frontal lobe degeneration. Dementia. 1996;7(3):128–34.

5. Weiner MW, Veitch DP, Aisen PS, et al. The Alzheimer's disease neuroimaging initiative: a review of papers published since its inception. Alzheimers Dement. 2013;9(5):111–94.
6. McKhann G, Drachman D, Folstein M, et al. Clinical diagnosis of Alzheimer's disease: report of the NINCDS-ADRDA work group under the auspices of Department of Health and Human Services Task Force on Alzheimer's disease. Neurology. 1984;34(7):939–44.
7. McKhann GM, Knopman DS, Chertkow H, et al. The diagnosis of dementia due to Alzheimer's disease: recommendations from the National Institute on Aging-Alzheimer's association workgroups on diagnostic guidelines for Alzheimer's disease. Alzheimers Dement. 2011;7(3):263–9.
8. Albert MS, DeKosky ST, Dickson D, et al. The diagnosis of mild cognitive impairment due to Alzheimer's disease: recommendations from the National Institute on Aging-Alzheimer's association workgroups on diagnostic guidelines for Alzheimer's disease. Alzheimers Dement. 2011;7(3):270–9.
9. Sperling RA, Aisen PS, Beckett LA, et al. Toward defining th preclinical stages of Alzheimer's disease: recommendations from the National Institute on Aging-Alzheimer's association workgroups on diagnostic guidelines for Alzheimer's disease. Alzheimers Dement. 2011;7(3):280–92.
10. Minoshima S, Foster NL, Kuhl DE. Posterior cingulate cortex in Alzheimer's disease. Lancet. 1994;344(8926):895.
11. Friedland RP, Brun A, Budinger TF. Pathological and positron emission tomographic correlations in Alzheimer's disease [letter]. Lancet. 1985;1(8422):228.
12. Mielke R, Schroder R, Fink GR, et al. Regional cerebral glucose metabolism and postmortem pathology in Alzheimer's disease. Acta Neuropathol. 1996;91(2):174–9.
13. Herholz K, Schopphoff H, Schmidt M, et al. Direct comparison of spatially normalized PET and SPECT scans in Alzheimer's disease. J Nucl Med. 2002;43(1):21–6.
14. Silverman DH. Brain ^{18}F-FDG PET in the diagnosis of neurodegenerative dementias: comparison with perfusion SPECT and with clinical evaluations lacking nuclear imaging*. J Nucl Med. 2004;45(4):594–607.
15. Ishii K, Sasaki M, Yamaji S, et al. Relatively preserved hippocampal glucose metabolism in mild Alzheimer's disease. Dement Geriatr Cogn Disord. 1998;9(6):317–22.
16. Mielke R, Herholz K, Grond M, et al. Differences of regional cerebral glucose metabolism between presenile and senile dementia of Alzheimer type. Neurobiol Aging. 1992;13(1):93–8.
17. Sakamoto S, Ishii K, Sasaki M, et al. Differences in cerebral metabolic impairment between early and late onset types of Alzheimer's disease. J Neurol Sci. 2002;200(1–2):27–32.
18. Minoshima S, Giordani B, Berent S, et al. Metabolic reduction in the posterior cingulate cortex in very early Alzheimer's disease. Ann Neurol. 1997;42(1):85–94.
19. Minoshima S, Frey KA, Koeppe RA, et al. A diagnostic approach in Alzheimer's disease using three-dimensional stereotactic surface projections of fluorine-18-FDG PET. J Nucl Med. 1995;36(7):1238–48.
20. Friston KJ, Ashburner J, Kiebel SJ, Nichols TE, Penny WD, editors. Statistical parametric mapping: the analysis of functional brain images. San Diego, CA: Academic; 2007.
21. Fazekas F, Alavi A, Chawluk JB, et al. Comparison of CT, MR, and PET in Alzheimer's dementia and normal aging. J Nucl Med. 1989;30(10):1607–15.
22. Kippenhan JS, Barker WW, Pascal S, et al. Evaluation of a neural-network classifier for PET scans of normal and Alzheimer's disease subjects. J Nucl Med. 1992;33(8):1459–67.
23. Azari NP, Pettigrew KD, Schapiro MB, et al. Early detection of Alzheimer's disease: a statistical approach using positron emission tomographic data. J Cereb Blood Flow Metab. 1993;13(3):438–47.
24. Burdette JH, Minoshima S, Vander Borght T, et al. Alzheimer disease: improved visual interpretation of PET images by using three-dimensional stereotaxic surface projections. Radiology. 1996;198(3):837–43.
25. Scheurich A, Muller MJ, Siessmeier T, et al. Validating the DemTect with 18-fluoro-2-deoxyglucose positron emission tomography as a sensitive neuropsychological screening test for early Alzheimer disease in patients of a memory clinic. Dement Geriatr Cogn Disord. 2005;20(5):271–7.

26. Duara R, Barker W, Loewenstein D, et al. Sensitivity and specificity of positron emission tomography and magnetic resonance imaging studies in Alzheimer's disease and multi-infarct dementia. Eur Neurol. 1989;29(3):9–15.
27. Herholz K, Adams R, Kessler J, et al. Criteria for the diagnosis of Alzheimer's disease with positron emission tomography. Dementia. 1990;1:156–64.
28. Herholz K, Perani D, Salmon E, et al. Comparability of FDG PET studies in probable Alzheimer's disease. J Nucl Med. 1993;34(9):1460–6.
29. Szelies B, Mielke R, Herholz K, et al. Quantitative topographical EEG compared to FDG PET for classification of vascular and degenerative dementia. Electroencephalogr Clin Neurophysiol. 1994;91(2):131–9.
30. Mielke R, Pietrzyk U, Jacobs A, et al. HMPAO SPET and FDG PET in Alzheimer's disease and vascular dementia: comparison of perfusion and metabolic pattern. Eur J Nucl Med. 1994;21(10):1052–60.
31. Ohyama M, Senda M, Mishina M, et al. Semi-automatic ROI placement system for analysis of brain PET images based on elastic model: application to diagnosis of Alzheimer's disease. Keio J Med. 2000;49.1:A105–6.
32. Mosconi L, Tsui WH, De Santi S, et al. Reduced hippocampal metabolism in MCI and AD: automated FDG-PET image analysis. Neurology. 2005;64(11):1860–7.
33. von Borczyskowski D, Wilke F, Martin B, et al. Evaluation of a new expert system for fully automated detection of the Alzheimer's dementia pattern in FDG PET. Nucl Med Commun. 2006;27(9):739–43.
34. Kawachi T, Ishii K, Sakamoto S, et al. Comparison of the diagnostic performance of FDG-PET and VBM-MRI in very mild Alzheimer's disease. Eur J Nucl Med Mol Imaging. 2006;33(7):801–9.
35. Ishii K, Kono AK, Sasaki H, et al. Fully automatic diagnostic system for early- and late-onset mild Alzheimer's disease using FDG PET and 3D-SSP. Eur J Nucl Med Mol Imaging. 2006;33(5):575–83.
36. Ng S, Villemagne VL, Berlangieri S, et al. Visual assessment versus quantitative assessment of 11C-PIB PET and 18F-FDG PET for detection of Alzheimer's disease. J Nucl Med. 2007;48(4):547–52.
37. Matsunari I, Samuraki M, Chen WP, et al. Comparison of 18F-FDG PET and optimized voxel-based morphometry for detection of Alzheimer's disease: aging effect on diagnostic performance. J Nucl Med. 2007;48(12):1961–70.
38. Mosconi L, Tsui WH, Herholz K, et al. Multicenter standardized 18F-FDG PET diagnosis of mild cognitive impairment, Alzheimer's disease, and other dementias. J Nucl Med. 2008;49(3):390–8.
39. Haense C, Herholz K, Jagust WJ, et al. Performance of FDG PET for detection of Alzheimer's disease in two independent multicentre samples (NEST-DD and ADNI). Dement Geriatr Cogn Disord. 2009;28(3):259–66.
40. McMurtray AM, Licht E, Yeo T, et al. Positron emission tomography facilitates diagnosis of early-onset Alzheimer's disease. Eur Neurol. 2008;59(1–2):31–7.
41. Habeck C, Foster NL, Perneczky R, et al. Multivariate and univariate neuroimaging biomarkers of Alzheimer's disease. NeuroImage. 2008;40(4):1503–15.
42. Chen K, Ayutyanont N, Langbaum JB, et al. Characterizing Alzheimer's disease using a hypometabolic convergence index. NeuroImage. 2011;56(1):52–60.
43. Bloudek LM, Spackman DE, Blankenburg M, et al. Review and meta-analysis of biomarkers and diagnostic imaging in Alzheimer's disease. J Alzheimers Dis. 2011;26(4):627–45.
44. Bohnen NI, Djang DS, Herholz K, et al. Effectiveness and safety of 18F-FDG PET in the evaluation of dementia: a review of the recent literature. J Nucl Med. 2012;53(1):59–71.
45. Ishii K, Imamura T, Sasaki M, et al. Regional cerebral glucose metabolism in dementia with Lewy bodies and Alzheimer's disease. Neurology. 1998;51(1):125–30.
46. Higuchi M, Tashiro M, Arai H, et al. Glucose hypometabolism and neuropathological correlates in brains of dementia with Lewy bodies. Exp Neurol. 2000;62(2):247–56.
47. Kono AK, Ishii K, Sofue K, et al. Fully automatic differential diagnosis system for dementia with Lewy bodies and Alzheimer's disease using FDG-PET and 3D-SSP. Eur J Nucl Med Mol Imaging. 2007;34(9):1490–7.

48. Foster NL, Heidebrink JL, Clark CM, et al. FDG-PET improves accuracy in distinguishing frontotemporal dementia and Alzheimer's disease. Brain. 2007;130(Pt 10):2616–35.
49. Salmon E, Sadzot B, Maquet P, et al. Differential diagnosis of Alzheimer's disease with PET. J Nucl Med. 1994;35(3):391–8.
50. Hoffman JM, Welsh-Bohmer KA, Hanson M, et al. FDG PET imaging in patients with pathologically verified dementia. J Nucl Med. 2000;41(11):1920–8.
51. Silverman DH, Small GW, Chang CY, et al. Positron emission tomography in evaluation of dementia: regional brain metabolism and long-term outcome. JAMA. 2001;286(17):2120–7.
52. Jagust W, Reed B, Mungas D, et al. What does fluorodeoxyglucose PET imaging add to a clinical diagnosis of dementia? Neurology. 2007;69(9):871–7.
53. McKeith IG, Dickson DW, Lowe J, et al. Consortium on DLB. Diagnosis and management of dementia with Lewy bodies. Neurology. 2005;65:1–10.
54. Petersen RC. Mild cognitive impairment as a diagnostic entity. J Intern Med. 2004;256(3):183–94.
55. Petersen RC, Morris JC. Mild cognitive impairment as a clinical entity and treatment target. Arch Neurol. 2005;62(7):1160–3.
56. Mosconi L, Perani D, Sorbi S, et al. MCI conversion to dementia and the APOE genotype: a prediction study with FDG-PET. Neurology. 2004;63(12):2332–40.
57. Drzezga A, Grimmer T, Riemenschneider M, et al. Prediction of individual clinical outcome in MCI by means of genetic assessment and (18)F-FDG PET. J Nucl Med. 2005;46(10):1625–32.
58. Anchisi D, Borroni B, Franceschi M, et al. Heterogeneity of brain glucose metabolism in mild cognitive impairment and clinical progression to Alzheimer disease. Arch Neurol. 2005;62(11):1728–33.
59. Yuan Y, ZX G, Wei WS. Fluorodeoxyglucose-positron-emission tomography, single-photon emission tomography, and structural MR imaging for prediction of rapid conversion to Alzheimer disease in patients with mild cognitive impairment: a meta-analysis. Am J Neuroradiol. 2009;30:404–10.
60. Herholz K, Westwood S, Haense C, et al. Evaluation of a calibrated (18)F-FDG PET score as a biomarker for progression in Alzheimer disease and mild cognitive impairment. J Nucl Med. 2011;52(8):1218–26.
61. Ito K, Fukuyama H, Senda M, et al. Prediction of outcomes in MCI by using ^{18}F-FDG-PET: a multicenter study. J Alzheimers Dis. 2014;45(2):543–52.
62. Ito K, Mori E, Fukuyama H, et al. Prediction of outcomes in MCI with (123)I-IMP-CBF SPECT: a multicenter prospective cohort study. Ann Nucl Med. 2013;27(10):898–906.
63. Small GW, Mazziotta JC, Collins MT, et al. Apolipoprotein E type 4 allele and cerebral glucose metabolism in relatives at risk for familial Alzheimer disease. JAMA. 1995;273(12):942–7.
64. Reiman EM, Caselli RJ, Yun LS, et al. Preclinical evidence of Alzheimer's disease in persons homozygous for the e4 allele for apolipoprotein E. N Engl J Med. 1996;334(12):752–8.
65. Reiman EM, Chen K, Alexander GE, et al. Functional brain abnormalities in young adults at genetic risk for late-onset Alzheimer's dementia. Proc Natl Acad Sci U S A. 2004;101(1):284–9.
66. Small GW, Ercoli LM, Silverman DH, et al. Cerebral metabolic and cognitive decline in persons at genetic risk for Alzheimer's disease. Proc Natl Acad Sci U S A. 2000;97(11):6037–42.
67. de Leon MJ, Convit A, Wolf OT, et al. Prediction of cognitive decline in normal elderly subjects with 2-F-18-fluoro-2-deoxy-D-glucose positron-emission tomography (FDG-PET). Proc Natl Acad Sci U S A. 2001;98(19):10966–71.
68. Jack CR Jr, Knopman DS, Weigand SD, et al. An operational approach to National Institute on Aging-Alzheimer's association criteria for preclinical Alzheimer disease. Ann Neurol. 2012;71(6):765–75.
69. Knopman DS, Jack CR Jr, Wiste HJ, et al. Brain injury biomarkers are not dependent on β-amyloid in normal elderly. Ann Neurol. 2013;73(4):472–80.
70. Wirth M, Villeneuve S, Haase CM, et al. Associations between Alzheimer disease biomarkers, neurodegeneration, and cognition in cognitively normal older people. JAMA Neurol. 2013;70(12):1512–9.

Tau PET in Neurodegenerative Diseases Manifesting Dementia

10

Nobuyuki Okamura, Ryuichi Harada, Shozo Furumoto, and Yukitsuka Kudo

Abstract

Noninvasive imaging of tau pathology can contribute to the early and differential diagnosis of neurodegenerative diseases and evaluating the efficacy of disease-specific therapies. For in vivo imaging of tau protein deposits in the human brain, PET tracers should exhibit high binding affinity to the β-pleated sheet structure of PHF-tau, high binding selectivity to tau over amyloid-β, and high blood-brain barrier permeability. Several tau PET tracers have been developed and tested in humans. Recent tau PET studies have demonstrated a high amount of tracer retention in sites that have a predilection for the cortical deposition of tau protein aggregates in patients with Alzheimer's disease (AD). The amount of tracer retention is closely associated with dementia severity and neurodegeneration. Therefore, tau PET is expected to be useful for tracking disease progression, assessing disease severity, and accurately predicting dementia prognosis. In this chapter, we will discuss recent progress in the development of tau-selective PET tracers and clinical PET studies using these tracers.

N. Okamura (✉)
Department of Pharmacology, Tohoku University School of Medicine,
2-1 Seiryo-machi, Aoba-ku, Sendai, Miyagi 980-8575, Japan

Division of Neuro-imaging, Institute of Development, Aging and Cancer, Tohoku University, Sendai, Miyagi, Japan
e-mail: nookamura@med.tohoku.ac.jp

R. Harada • Y. Kudo
Division of Neuro-imaging, Institute of Development, Aging and Cancer, Tohoku University, Sendai, Miyagi, Japan

S. Furumoto
Frontier Research Institute for Interdisciplinary Science, Tohoku University, Sendai, Miyagi, Japan

H. Matsuda et al. (eds.), *Neuroimaging Diagnosis for Alzheimer's Disease and Other Dementias*, DOI 10.1007/978-4-431-55133-1_10

Keywords
Tau proteins • Neurofibrillary tangles • Positron-emission tomography • Imaging • Alzheimer's disease

10.1 Introduction

Alzheimer's disease (AD) is the most common cause of dementia, accounting for more than half of patients with dementia in Japan, followed by vascular dementia, dementia with Lewy bodies, and frontotemporal dementia. The two major neuropathological hallmarks in AD are senile plaques (SPs) and neurofibrillary tangles (NFTs), which are composed of amyloid-β (Aβ) and hyperphosphorylated tau protein, respectively. Although there are distinctive diagnostic criteria for the clinical diagnosis of these diseases, the differential diagnosis of these diseases is sometimes challenging, because there is substantial overlap in clinical phenotypes of these diseases. Postmortem studies have also shown a high frequency of mixed pathology in patients with dementia [1], which makes an accurate clinical diagnosis difficult. A definitive diagnosis of AD is based on the neuropathological confirmation of these protein deposits in the brain. It would thus be ideal if both SPs and NFTs in the brain could be visualized noninvasively. Among several imaging technologies, positron-emission tomography (PET) is the most practical method to visualize and quantify these protein depositions because of its advantages of high sensitivity and quantification accuracy. As shown in the previous chapter, marked progress in the development of Aβ imaging tracers has been made in recent years. In contrast, it has been difficult to develop selective tau PET ligands.

10.2 Requirements for a Tau PET Tracer

There are several requirements for tau PET radiotracers. First, the tracer should have a binding affinity for PHF-tau that is sufficient for in vivo imaging. There are several methods to assess the binding ability of radiotracer candidates to PHF-tau. The binding assay using synthetic tau fibrils has been used for the screening of potential tau PET ligands. However, the binding assay using human brain samples is a more reliable method to assess the binding of a candidate compound to PHF-tau, because this method can directly assess the affinity for the native conformation of tau in the patient's brain. Successful amyloid PET tracers exhibit high binding affinities (K_d or K_i < 20 nM) to AD brain homogenates [2–5]. Tau PET ligands should also exhibit similar binding affinity to AD brain homogenates containing a high density of tau fibrils and a low density of Aβ fibrils. The amount of PHF-tau is reported to be far less than that of Aβ in AD neocortex [6]. Therefore, a tau tracer must be highly selective for tau over Aβ. A tracer that exhibits a high affinity to β-sheet structure of Aβ or tau protein fibrils tends to accumulate in the white matter, possibly due to the binding to β-sheet structures contained in myelin [7]. Because

the white matter retention of tracers will interfere with the early detection of mild tau pathology, these tracer signals should be as low as possible.

As is the case for other neuroimaging tracers, tau tracer should show sufficient uptake in the brain immediately after intravenous administration. The blood-brain barrier (BBB) permeability of radiotracers in humans can be estimated from the pharmacokinetic data in mice or rats. Most successful neuroimaging radiotracers exhibit an initial brain uptake above 3–4% of the injected dose (% ID) immediately after intravenous administration in mice [3, 5, 8]. BBB permeability is strongly associated with the lipophilicity of the tracer. Ideally, log P values of the radiotracer should be between 1 and 3 [9]. In addition, radiotracers should be cleared rapidly from the nontarget areas of the brain, because of the short half-life of the positron-emitting radionuclide. An ideal radiotracer should readily enter the brain and selectively bind to its target in the absence of radiolabeled metabolites. Thus, it is important to confirm that the radiolabeled metabolites do not penetrate BBB. ^{18}F-labeled tracer is more convenient for routine clinical use than is ^{11}C-labeled tracer, because the longer half-life of ^{18}F ($T_{1/2}$ = 110 min) allows time for its delivery to many PET facilities. In ^{18}F-labeled ligands, defluorination causes the emission of ^{18}F signals from the skull, which might interfere with visual assessment of tracer distribution in the brain.

10.3 Tau PET Tracers

Screening of chemical compound libraries have been performed by several different groups to identify small molecule compounds fulfilling the above requirements. Recently, different classes of compounds (Fig. 10.1) have been developed as potential candidates as tau PET tracers and applied to exploratory human PET studies.

10.3.1 Naphthylethylidene Derivative

[^{18}F]FDDNP was developed as a nonselective PET tracer for SPs and NFTs in the brain. Autoradiography of AD brain sections has revealed binding of [^{18}F]FDDNP in the temporal and parietal cortices, which matched the immunohistochemistry of Aβ and tau [10]. Clinical PET studies with [^{18}F]FDDNP have revealed regional accumulation of [^{18}F]FDDNP in the SP- and NFT-rich areas of the AD brain [11]. FDDNP retention in the medial temporal lobes of subjects with mild cognitive impairment (MCI) was at levels that are intermediate relative to FDDNP retention levels in patients with AD and normal subjects [12] and contrasts with the bimodal distribution of Aβ-selective PET tracers in patients with MCI [13]. These findings suggest that FDDNP may be useful in tracing the progression of tau pathology in the MCI stage of AD patients. [^{18}F]FDDNP PET has also been applied to the assessment of patients with Down syndrome [14], suspected of chronic traumatic encephalopathy (CTE) cases [15], and patients with progressive supranuclear palsy (PSP) [16]. However, the lack of selectivity of FDDNP to PHF-tau will make it difficult to

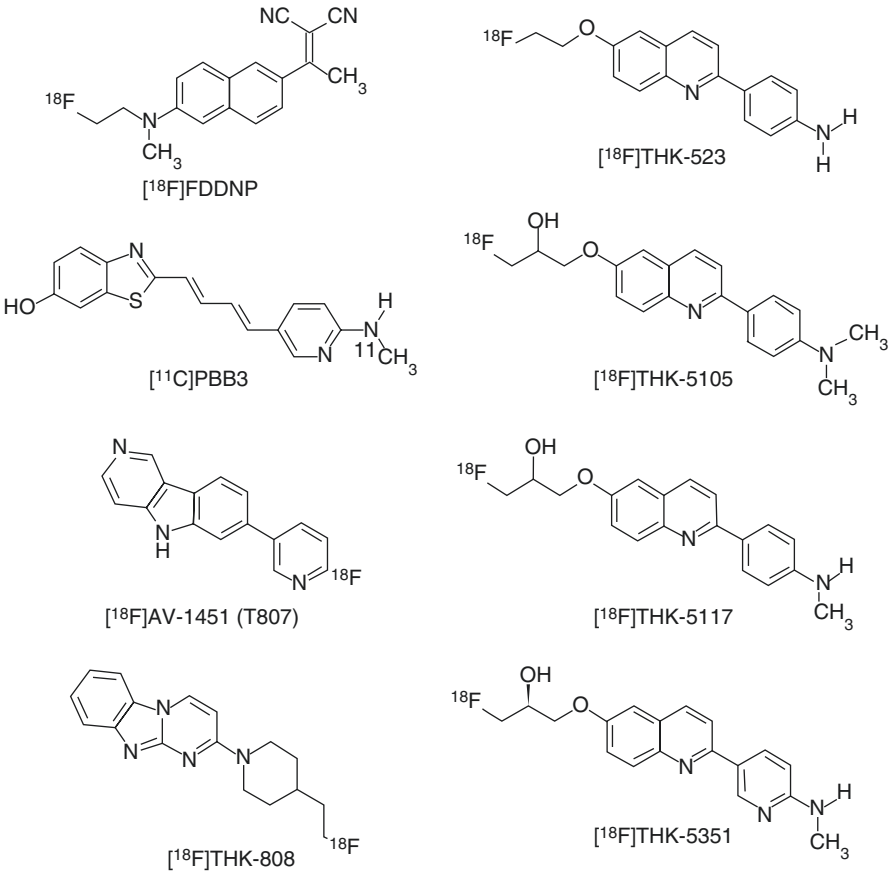

Fig. 10.1 Chemical structures of tau PET radiotracers

interpret the distribution of tau pathology, because the possibility of concomitant tracer binding to Aβ plaques cannot be ruled out.

10.3.2 Phenyl/Pyridinyl-Butadienyl-Benzothiazoles/ Benzothiazolium Derivative

A series of phenyl/pyridinyl-butadienyl-benzothiazoles/benzothiazoliums (PBBs) have been developed as candidates for tau PET tracers [17, 18]. These fluorescent compounds clearly stained NFTs, neuropil threads, and dystrophic neurites in AD brain sections. Intriguingly, these compounds additionally stained various tau inclusions in non-AD tauopathies, such as Pick's disease, PSP, and corticobasal degeneration (CBD). Three hydrophilic compounds (PBB3, PBB4, and PBB5) showed

relatively lower binding affinity to Aβ deposits than did the other lipophilic derivatives. Among them, PBB3 exhibited reasonable biostability and sufficient BBB permeability in mice. A study of [^{11}C]PBB3 PET in PS19 mice has shown successful noninvasive visualization of tau protein deposits in the brain. From these findings, [^{11}C]PBB3 was selected as a final tau PET tracer candidate. An exploratory clinical study has been reported in three healthy controls and three patients with AD [17]. The [^{11}C]PBB3 and amyloid PET tracer [^{11}C]PiB exhibited different patterns of brain retention. Of particular note is that [^{11}C]PBB3 showed preferential accumulation in the medial temporal cortex of patients with AD, where the high density of PHF-tau has been observed in postmortem studies. Furthermore, high [^{11}C]PBB3 accumulation has been observed in the neocortex and subcortical structures of a patient with corticobasal syndrome, suggesting the potential utility of this tracer for in vivo detection of tau lesions in non-AD tauopathies. [^{11}C]PBB3 exhibited minimal nonspecific binding to white matter and brainstem. However, a high density of tracer signals was observed in dural venous sinuses. We expect ongoing multicenter PET studies of [^{11}C]PBB3 and the newly developed ^{18}F-labeled derivative to validate the clinical usefulness of PBB3 derivatives for noninvasive assessment of tau pathology in the human brain.

10.3.3 Benzimidazole Pyrimidine Derivatives

A series of derivatives of benzimidazole pyrimidines have been developed as potential candidates for use as tau tracers. Two promising derivatives, [^{18}F]AV-1451 ([^{18}F]T807) and [^{18}F]T808, have been reported as highly selective tau tracers [19, 20]. Human AD brain sections were used for the assessment of binding selectivity to PHF-tau. An in vitro autoradiography study in AD brain sections has shown the high binding affinity of [^{18}F]AV-1451 to PHF-tau (K_d = 14.6 nM). Furthermore, [^{18}F]AV-1451 binding on AD brain slices co-localizes completely with immunoreactive tau pathology. As mentioned above, the high binding selectivity to tau over Aβ is one of the requirements for a useful tau PET tracer. From the analysis of human brain sections, [^{18}F]AV-1451 showed an estimate 29-fold in vitro binding selectivity to tau over Aβ. A PET study using [^{18}F]AV-1451 conducted in patients with AD and MCI and healthy participants [19]. There was rapid and sufficient tracer distribution in the brain and low white matter retention after intravenous administration of this tracer. Cortical [^{18}F]AV-1451 retention followed the known distribution of PHF-tau in AD brain. Signal-to-background ratio of [^{18}F]AV-1451 was far higher than those of abovementioned tracers. Furthermore, [^{18}F]AV-1451 retention was strongly associated with disease severity. Recent PET studies have suggested the potential usefulness of this tracer for imaging tau lesions in chronic traumatic encephalopathy [21, 22] and non-AD tauopathies.

First-in-man [^{18}F]T808 PET study showed better tracer kinetics than [^{18}F]AV-1451 [23]. However, further clinical evaluation of [^{18}F]T808 was terminated due to substantial defluorination of this tracer in some cases.

10.3.4 Arylquinoline Derivatives

Quinoline and benzimidazole derivatives were discovered to be potential candidates for tau tracer by the screening of a chemical compound library [24]. The quinoline derivative BF-170 showed high binding affinity to synthetic tau protein fibrils and selectively bound to neurofibrillary tangles, neuropil threads, and dystrophic neurites in AD brain sections. Subsequently, the binding selectivity of ^{18}F-labeled BF-170 ([^{18}F]THK-523) was confirmed by the autoradiography of AD brain sections [25, 26]. Following compound optimization, the three ^{18}F-labeled quinoline derivatives ([^{18}F]THK-5105, [^{18}F]THK-5117, and [^{18}F]THK-5351) have been developed and tested in humans [27–29]. Autoradiographic analyses of AD brain sections showed the preferential binding of these tracers to NFTs and neuropil threads, which co-localized with Gallyas-positive and immunoreactive tau protein deposits (Fig. 10.2) [26, 27]. The binding selectivity of THK-5117 to tau over Aβ was estimated to be 30-fold greater. The amount of tracer binding was correlated with the amount of PHF-tau in AD brain homogenates, but it was not correlated with that of Aβ. The biodistribution of ^{18}F-labeled THK compounds was examined in ICR mice. The initial uptake of these tracers in mice (>4% ID/g at 2 min postinjection) meets the prerequisites for useful PET imaging agents described above.

First-in-human PET studies with [^{18}F]THK-5105 and [^{18}F]THK-5117 showed a clear distinction between patients with AD and healthy elderly controls. Partial

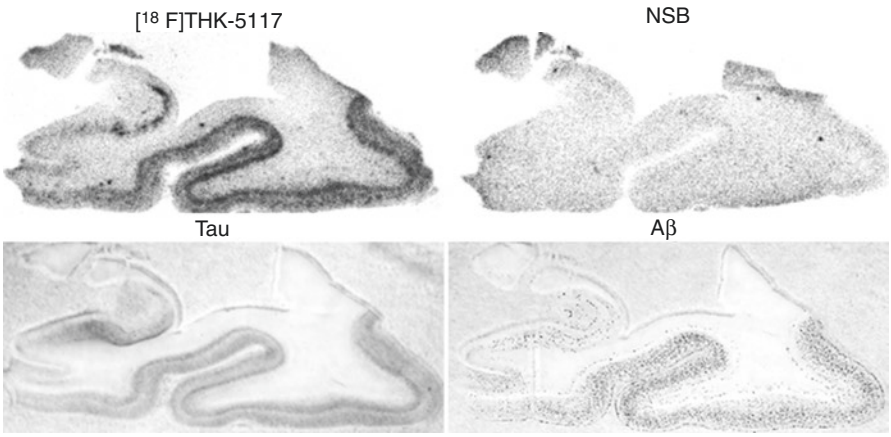

Fig. 10.2 In vitro autoradiography of [^{18}F]THK-5117 in a temporal section from an AD patient, and immunostaining with anti-tau and anti-Aβ antibodies

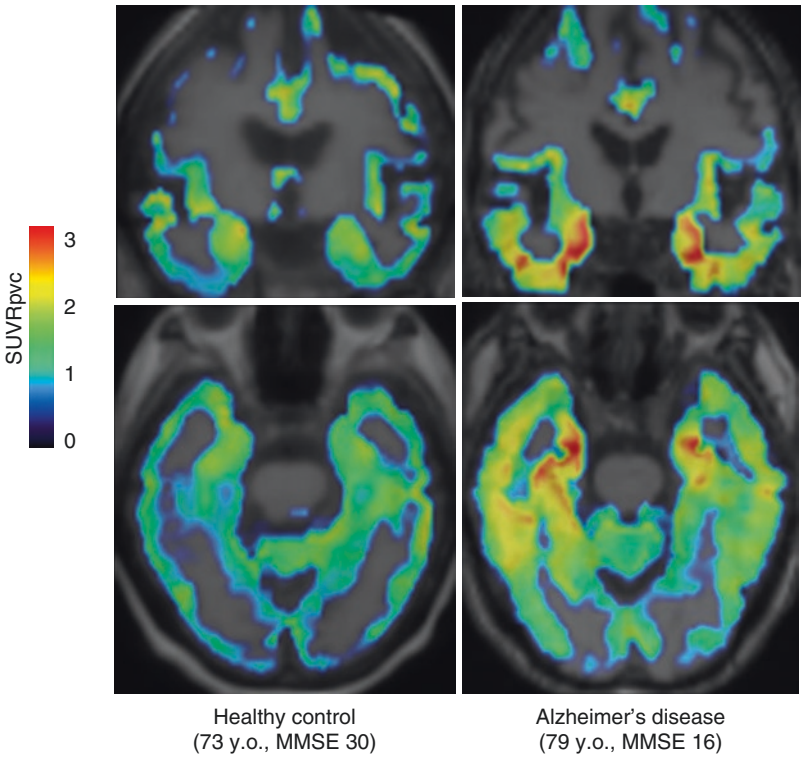

Fig. 10.3 [^{18}F]THK-5117 PET images (after partial volume correction) from 60 to 80 min postinjection in an HC (73 years old, MMSE 30) and in AD patient (79 years old, MMSE 16)

volume corrected [^{18}F]THK-5117 PET images of a healthy control subject (73-year-old man, MMSE score 30) and a patient with AD (79-year-old, MMSE score 16) are shown in Fig. 10.3. Retention of [^{18}F]THK-5117 was observed in the medial temporal cortex of patients with AD, while it was not remarkable in the healthy control subject. [^{18}F]THK-5117 was preferentially accumulated in the temporal and parietal lobe of the AD case, despite diffuse neocortical [^{11}C]PiB retention (Fig. 10.4). In addition, the amount and extent of [^{18}F]THK-5117 retention was associated with the clinical severity of dementia. These results were consistent with findings from postmortem studies showing significant correlations of NFT density with clinical severity of dementia. A new tracer [^{18}F]THK-5351 showed a higher signal-to-noise ratio and lower white matter retention than [^{18}F]THK-5105 and [^{18}F]THK-5117, which will allow clear visual assessment and sensitive detection of tau pathology.

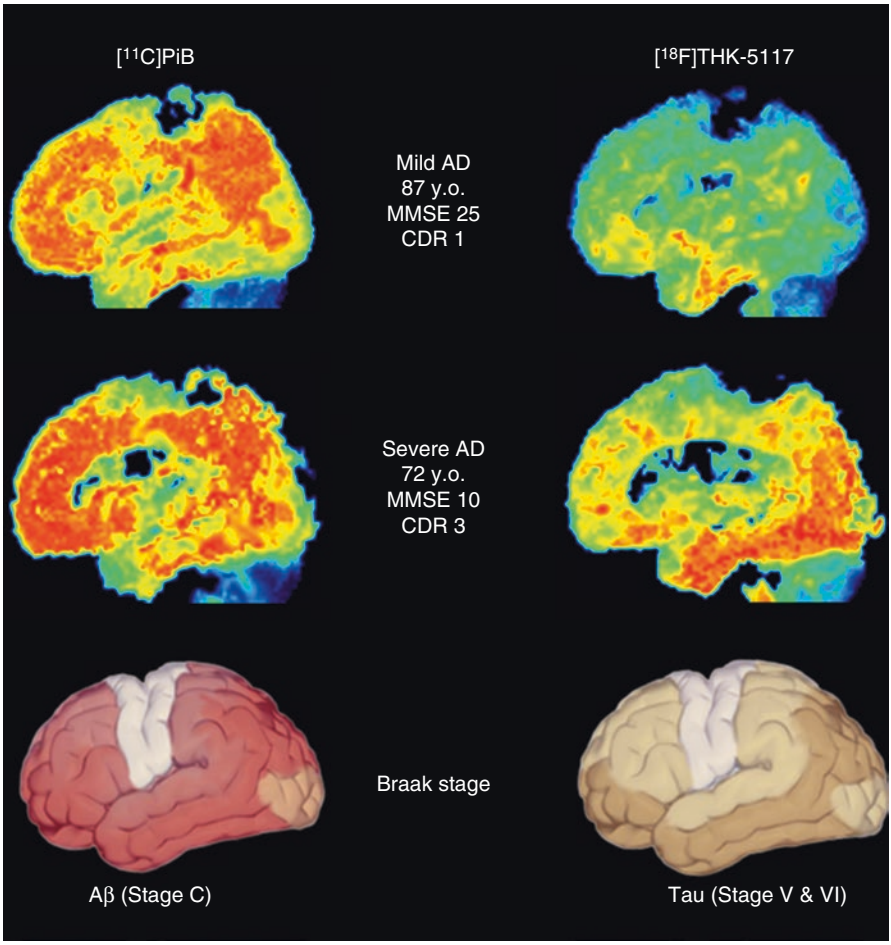

Fig. 10.4 Maximum intensity projection of [^{11}C]PiB and [^{18}F]THK-5117 PET images (after partial volume correction) in mild AD (87 years old, MMSE 25, CDR 1) and severe AD (72 years old, MMSE 10, CDR 3)

10.4 The Role of Tau Imaging

Although AD is the most common tauopathy, many other neurodegenerative diseases are also known to be associated with the pathological aggregation of tau protein in the brain. These neurodegenerative diseases include frontotemporal dementia, PSP, CBD, CTE, argyrophilic grain, disease (AGD) [30], and senile dementia of neurofibrillary tangle type (SDNFT) [31]. Tau lesions in CTE are associated with repeated head trauma and are frequently observed in

military veterans and retired football players [32]. They are considered as high-risk populations for future progression to dementia and depression. Therefore, these populations might also be eligible to participate in preventive intervention using anti-tau drugs. The clinical diagnosis of AGD and SDNFT is generally difficult, because of the similarity of the clinical phenotype of these diseases with that of AD. Using a combination of both amyloid and tau PET imaging, these diseases could be accurately diagnosed in live patients. Recently, individuals with imaging/biomarker evidence of AD-like neurodegeneration—but without β-amyloidosis—have been called "suspected non-Alzheimer's pathophysiology (SNAP)" [33]. Previous studies have shown that more than 20% of cognitively normal individuals and MCI subjects were categorized as SNAP. Although hippocampal atrophy correlates with tau pathology, other pathologies (including ischemia and hippocampal sclerosis) are also known to produce hippocampal atrophy. Tau PET will clarify the contribution of tau pathology to the neurodegenerative process observed in subjects with SNAP.

The diagnosis of AD is complicated by the fact that there is a discrepancy between the clinical phenotype and neuropathological findings. Recent amyloid PET studies have shown that a large amount of SPs is already present in the brain, even in an asymptomatic stage of AD. The pathological Aβ deposition in the brain starts 15–20 years before clinical dementia symptoms appear. A high amyloid burden in elderly people is considered a strong risk factor for future progression to dementia. However, it is hard to predict when these individuals will exhibit dementia using only amyloid PET findings. For the prediction of progression to AD, it is necessary to know the progress of downstream events including tau deposition, inflammation, synaptic failure, and neurodegeneration. The assessment of neurofibrillary pathology using tau PET will support an accurate prediction of prognosis in people who are at high risk of dementia. Furthermore, this technology could be used for the assessment of disease severity in the early stages of AD.

Currently, many therapeutic drugs targeted at Aβ and tau proteins have been developed for the treatment and prevention of AD dementia. For successful treatment by these drugs, it is important to start the clinical trial of these drugs before irreversible neurodegeneration begins. In the clinical trial of the forthcoming anti-tau drugs, tau PET will contribute to the assessment of treatment efficacy and to the establishment of inclusion criteria in the clinical trials of new drugs.

Conclusion

Several tau imaging tracers have been successfully developed for PET imaging. For example, [^{11}C]PBB3, [^{18}F]AV-1451, and [^{18}F]THK-5117 have displayed high binding affinity and selective binding ability to tau protein aggregates. These tracers displayed selective in vivo binding to PHF-tau in the brain and clearly differentiated AD cases from normal populations. Tau PET imaging is expected to facilitate research into the causes, diagnosis, and treatment of neurodegenerative diseases where tau plays a role.

Acknowledgments N. Okamura, S. Furumoto, and Y. Kudo were funded by a grant to study tau PET imaging from GE Healthcare, the SEI (Sumitomo Electric Industries, Ltd.) Group, and the CSR Foundation, as well as by Health and Labor Sciences research grants from the Ministry of Health, Labor, and Welfare of Japan, and a Grant-in-Aid for Exploratory Research (25670524) from the Ministry of Education, Culture, Sports, Science and Technology (MEXT), Japan.

References

1. Villemagne VL, Fodero-Tavoletti MT, Masters CL, Rowe CC. Tau imaging: early progress and future directions. Lancet Neurol. 2015;14(1):114–24. doi:10.1016/S1474-4422(14)70252-2.
2. Ni R, Gillberg PG, Bergfors A, Marutle A, Nordberg A. Amyloid tracers detect multiple binding sites in Alzheimer's disease brain tissue. Brain. 2013;136:2217–27. doi:10.1093/brain/awt142.
3. Choi SR, Golding G, Zhuang Z, Zhang W, Lim N, Hefti F, Benedum TE, Kilbourn MR, Skovronsky D, Kung HF. Preclinical properties of ^{18}F-AV-45: a PET agent for Abeta plaques in the brain. J Nucl Med. 2009;50:1887–94. doi:10.2967/jnumed.109.065284.
4. Klunk WE, Wang Y, Huang GF, Debnath ML, Holt DP, Shao L, Hamilton RL, Ikonomovic MD, DeKosky ST, Mathis CA. The binding of 2-(4′-methylaminophenyl)benzothiazole to postmortem brain homogenates is dominated by the amyloid component. J Neurosci. 2003;23:2086–92.
5. Mathis CA, Wang Y, Holt DP, Huang GF, Debnath ML, Klunk WE. Synthesis and evaluation of 11C-labeled 6-substituted 2-arylbenzothiazoles as amyloid imaging agents. J Med Chem. 2003;46:2740–54. doi:10.1021/jm030026b.
6. Villemagne VL, Furumoto S, Fodero-Tavoletti MT, Harada R, Mulligan RS, Kudo Y, Masters CL, Yanai K, Rowe CC, Okamura N. The challenges of tau imaging. Future Neurol. 2012;7:409–21.
7. Stankoff B, Freeman L, Aigrot MS, Chardain A, Dolle F, Williams A, Galanaud D, Armand L, Lehericy S, Lubetzki C, Zalc B, Bottlaender M. Imaging central nervous system myelin by positron emission tomography in multiple sclerosis using [methyl-(1)(1)C]-2-(4′-methylaminophenyl)-6-hydroxybenzothiazole. Ann Neurol. 2011;69:673–80. doi:10.1002/ana.22320.
8. Snellman A, Rokka J, Lopez-Picon FR, Eskola O, Wilson I, Farrar G, Scheinin M, Solin O, Rinne JO, Haaparanta-Solin M. Pharmacokinetics of [18F]flutemetamol in wild-type rodents and its binding to beta amyloid deposits in a mouse model of Alzheimer's disease. Eur J Nucl Med Mol Imaging. 2012;39:1784–95. doi:10.1007/s00259-012-2178-9.
9. Dischino DD, Welch MJ, Kilbourn MR, Raichle ME. Relationship between lipophilicity and brain extraction of C-11-labeled radiopharmaceuticals. J Nucl Med. 1983;24:1030–8.
10. Agdeppa ED, Kepe V, Liu J, Flores-Torres S, Satyamurthy N, Petric A, Cole GM, Small GW, Huang SC, Barrio JR. Binding characteristics of radiofluorinated 6-dialkylamino-2-naphthylethylidene derivatives as positron emission tomography imaging probes for beta-amyloid plaques in Alzheimer's disease. J Neurosci. 2001;21:RC189.
11. Shoghi-Jadid K, Small GW, Agdeppa ED, Kepe V, Ercoli LM, Siddarth P, Read S, Satyamurthy N, Petric A, Huang SC, Barrio JR. Localization of neurofibrillary tangles and beta-amyloid plaques in the brains of living patients with Alzheimer disease. Am J Geriatr Psychiatry. 2002;10:24–35.
12. Small GW, Kepe V, Ercoli LM, Siddarth P, Bookheimer SY, Miller KJ, Lavretsky H, Burggren AC, Cole GM, Vinters HV, Thompson PM, Huang SC, Satyamurthy N, Phelps ME, Barrio JR. PET of brain amyloid and tau in mild cognitive impairment. N Engl J Med. 2006;355:2652–63. doi:10.1056/NEJMoa054625.
13. Wolk DA, Price JC, Saxton JA, Snitz BE, James JA, Lopez OL, Aizenstein HJ, Cohen AD, Weissfeld LA, Mathis CA, Klunk WE, De-Kosky ST. Amyloid imaging in mild cognitive impairment subtypes. Ann Neurol. 2009;65:557–68. doi:10.1002/ana.21598.

14. Nelson LD, Siddarth P, Kepe V, Scheibel KE, Huang SC, Barrio JR, Small GW. Positron emission tomography of brain beta-amyloid and tau levels in adults with down syndrome. Arch Neurol. 2011;68:768–74. doi:10.1001/archneurol.2011.104.
15. Small GW, Kepe V, Siddarth P, Ercoli LM, Merrill DA, Donoghue N, Bookheimer SY, Martinez J, Omalu B, Bailes J, Barrio JR. PET scanning of brain tau in retired national football league players: preliminary findings. Am J Geriatr Psychiatry. 2013;21:138–44. doi:10.1016/j.jagp.2012.11.019.
16. Kepe V, Bordelon Y, Boxer A, Huang SC, Liu J, Thiede FC, Mazziotta JC, Mendez MF, Donoghue N, Small GW, Barrio JR. PET imaging of neuropathology in tauopathies: progressive supranuclear palsy. J Alzheimers Dis. 2013;36:145–53. doi:10.3233/JAD-130032.
17. Maruyama M, Shimada H, Suhara T, Shinotoh H, Ji B, Maeda J, Zhang MR, Trojanowski JQ, Lee VM, Ono M, Masamoto K, Takano H, Sahara N, Iwata N, Okamura N, Furumoto S, Kudo Y, Chang Q, Saido TC, Takashima A, Lewis J, Jang MK, Aoki I, Ito H, Higuchi M. Imaging of tau pathology in a tauopathy mouse model and in Alzheimer patients compared to normal controls. Neuron. 2013;79:1094–108. doi:10.1016/j.neuron.2013.07.037.
18. Hashimoto H, Kawamura K, Igarashi N, Takei M, Fujishiro T, Aihara Y, Shiomi S, Muto M, Ito T, Furutsuka K, Yamasaki T, Yui J, Xie L, Ono M, Hatori A, Nemoto K, Suhara T, Higuchi M, Zhang MR. Radiosynthesis, photoisomerization, biodistribution, and metabolite analysis of 11C-PBB3 as a clinically useful PET probe for imaging of tau pathology. J Nucl Med. 2014;55:1532–8. doi:10.2967/jnumed.114.139550.
19. Chien DT, Bahri S, Szardenings AK, Walsh JC, Mu F, Su MY, Shankle WR, Elizarov A, Kolb HC. Early clinical PET imaging results with the novel PHF-tau radioligand [F-18]-T807. J Alzheimers Dis. 2013;34:457–68. doi:10.3233/JAD-122059.
20. Xia CF, Arteaga J, Chen G, Gangadharmath U, Gomez LF, Kasi D, Lam C, Liang Q, Liu C, Mocharla VP, Mu F, Sinha A, Su H, Szardenings AK, Walsh JC, Wang E, Yu C, Zhang W, Zhao T, Kolb HC. [^{18}F]T807, a novel tau positron emission tomography imaging agent for Alzheimer's disease. Alzheimers Dement. 2013;9:666–76. doi:10.1016/j.jalz.2012.11.008.
21. Mitsis EM, Riggio S, Kostakoglu L, Dickstein DL, Machac J, Delman B, Goldstein M, Jennings D, D'Antonio E, Martin J, Naidich TP, Aloysi A, Fernandez C, Seibyl J, DeKosky ST, Elder GA, Marek K, Gordon W, Hof PR, Sano M, Gandy S. Tauopathy PET and amyloid PET in the diagnosis of chronic traumatic encephalopathies: studies of a retired NFL player and of a man with FTD and a severe head injury. Transl Psychiatry. 2014;4:e441. doi:10.1038/tp.2014.91.
22. Gandy S, DeKosky ST. [^{18}F]-T807 tauopathy PET imaging in chronic traumatic encephalopathy. F1000Res. 2014;3:229. doi:10.12688/f1000research.5372.1.
23. Chien DT, Szardenings AK, Bahri S, Walsh JC, Mu FR, Xia CF, Shankle WR, Lerner AJ, Su MY, Elizarova A, Kolb HC. Early clinical PET imaging results with the novel PHF-tau radioligand [F18]-T808. J Alzheimers Dis. 2014;38:171–84. doi:10.3233/Jad-130098.
24. Okamura N, Suemoto T, Furumoto S, Suzuki M, Shimadzu H, Akatsu H, Yamamoto T, Fujiwara H, Nemoto M, Maruyama M, Arai H, Yanai K, Sawada T, Kudo Y. Quinoline and benzimidazole derivatives: candidate probes for in vivo imaging of tau pathology in Alzheimer's disease. J Neurosci. 2005;25:10857–62. doi:10.1523/JNEUROSCI.1738-05.2005.
25. Fodero-Tavoletti MT, Okamura N, Furumoto S, Mulligan RS, Connor AR, McLean CA, Cao D, Rigopoulos A, Cartwright GA, O'Keefe G, Gong S, Adlard PA, Barnham KJ, Rowe CC, Masters CL, Kudo Y, Cappai R, Yanai K, Villemagne VL. ^{18}F-THK523: a novel in vivo tau imaging ligand for Alzheimer's disease. Brain. 2011;134:1089–100. doi:10.1093/brain/awr038.
26. Harada R, Okamura N, Furumoto S, Tago T, Maruyama M, Higuchi M, Yoshikawa T, Arai H, Iwata R, Kudo Y, Yanai K. Comparison of the binding characteristics of [^{18}F]THK-523 and other amyloid imaging tracers to Alzheimer's disease pathology. Eur J Nucl Med Mol Imaging. 2013;40:125–32.
27. Okamura N, Furumoto S, Harada R, Tago T, Yoshikawa T, Fodero-Tavoletti M, Mulligan RS, Villemagne VL, Akatsu H, Yamamoto T, Arai H, Iwata R, Yanai K, Kudo Y. Novel

18F-labeled arylquinoline derivatives for noninvasive imaging of tau pathology in Alzheimer disease. J Nucl Med. 2013;54:1420–7. doi:10.2967/jnumed.112.117341.
28. Okamura N, Furumoto S, Fodero-Tavoletti MT, Mulligan RS, Harada R, Yates P, Pejoska S, Kudo Y, Masters CL, Yanai K, Rowe CC, Villemagne VL. Non-invasive assessment of Alzheimer's disease neurofibrillary pathology using ^{18}F-THK5105 PET. Brain. 2014;137:1762–71. doi:10.1093/brain/awu064.
29. Okamura N, Harada R, Furumoto S, Arai H, Yanai K, Kudo Y. Tau PET imaging in Alzheimer's disease. Curr Neurol Neurosci Rep. 2014;14:500. doi:10.1007/s11910-014-0500-6.
30. Saito Y, Ruberu NN, Sawabe M, Arai T, Tanaka N, Kakuta Y, Yamanouchi H, Murayama S. Staging of argyrophilic grains: an age-associated tauopathy. J Neuropathol Exp Neurol. 2004;63:911–8.
31. Yamada M, Itoh Y, Sodeyama N, Suematsu N, Otomo E, Matsushita M, Mizusawa H. Senile dementia of the neurofibrillary tangle type: a comparison with Alzheimer's disease. Dement Geriatr Cogn Disord. 2001;12:117–26.
32. DeKosky ST, Blennow K, Ikonomovic MD, Gandy S. Acute and chronic traumatic encephalopathies: pathogenesis and biomarkers. Nat Rev Neurol. 2013;9:192–200. doi:10.1038/nrneurol.2013.36.
33. Jack CR Jr. PART and SNAP. Acta Neuropathol. 2014;128:773–6. doi:10.1007/s00401-014-1362-3.

Brain Perfusion SPECT in Alzheimer's Disease

11

Kiyotaka Nemoto

Abstract

Over the last decade, research using positron emission tomography (PET) or single photon-emission computed tomography (SPECT) has revealed the distinguishing regional cerebral hypometabolism or hypoperfusion in various neurodegenerative disorders, which is useful for differential diagnosis of diseases. In addition to that, development of statistical analysis of neuroimaging data unveiled the subtle changes which was difficult to notice with visual inspection. SPECT findings of typical AD are characterized with hypoperfusion in (1) parietotemporal association cortex, (2) posterior cingulate gyrus and precuneus, and (3) medial temporal areas. Hypoperfusion in these regions might be a predictor for cognitive decline. With these findings, the neuroimaging examinations have become essential in clinical settings for the purpose of diagnosis of very early Alzheimer's disease (AD) at a prodromal stage, prediction of conversion from mild cognitive impairment (MCI) to AD, or differential diagnosis from other diseases causing dementia.

Keywords

Alzheimer's disease • SPECT • Precuneus • Parietal cortex • Hippocampus

K. Nemoto
Department of Neuropsychiatry, Institute of Clinical Medicine, University of Tsukuba, 1-1-1 Tennodai, Tsukuba, Ibaraki 305-8575, Japan
e-mail: kiyotaka@nemotos.net

H. Matsuda et al. (eds.), *Neuroimaging Diagnosis for Alzheimer's Disease and Other Dementias*, DOI 10.1007/978-4-431-55133-1_11

11.1 Introduction

Over the last decade, the interest toward functional neuroimaging in the field of neurodegenerative disease has gradually increased. Research using positron emission tomography (PET) or single photon-emission computed tomography (SPECT) has revealed the distinguishing regional cerebral hypometabolism or hypoperfusion in various neurodegenerative disorders, which is useful for differential diagnosis of diseases. In addition to that, development of statistical analysis of neuroimaging data unveiled the subtle changes which was difficult to notice with visual inspection. With these findings, the neuroimaging examinations have become essential in clinical settings for the purpose of diagnosis of very early Alzheimer's disease (AD) at a prodromal stage, prediction of conversion from mild cognitive impairment (MCI) to AD, or differential diagnosis from other diseases causing dementia. In this chapter, we first review the neuropathological findings of Alzheimer's disease. Then we go through the SPECT findings of AD with basic knowledge of statistical analysis of SPECT images.

11.2 Neuropathological Legions of Alzheimer's Disease

AD is characterized by two types of lesions: amyloid deposits and neurofibrillary tangles. Amyloid deposits are the extracellular aggregation of Aβ peptide and neurofibrillary tangles composed of intraneuronal bundles of paired helical filaments which are the aggregation of pathologic tau proteins. Both lesions extend progressively to neocortical brain areas during the course of AD. Braak and Braak [1] found that initial changes occur in the transentorhinal region and extend to entorhinal region, Ammon's horn, and neocortex. Delacourte and colleagues [2] further categorized the disease progression in ten stages: transentorhinal cortex, entorhinal, hippocampus, anterior temporal cortex, inferior temporal cortex, medium temporal cortex, polymodal association areas, unimodal areas, primary motor or sensory regions, and all neocortical areas. They also found that the disease could be asymptomatic unless polymodal association areas are affected and that individuals with two polymodal association areas affected by tau pathology showed cognitive impairment. In summary, degeneration occurs initially in limbic regions and extends to neocortices. Clinical symptoms become apparent after the legions affect polymodal association areas.

11.3 Principle of Statistical Mapping

Due to the low spatial resolution, it is not easy to detect subtle hypoperfusion of SPECT images with visual inspection, which results in low intra- and inter-rater reliability [3]. Statistical analysis approach is a way to visualize the hypoperfusion regions plain and clearly. An example is shown in Fig. 11.1. The subject is a

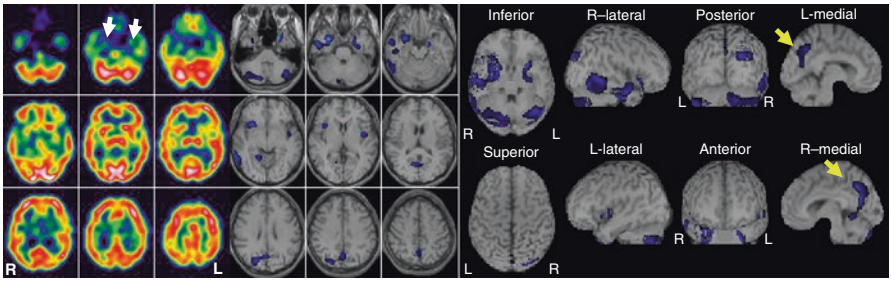

Fig. 11.1 An example of the result of statistical analysis of SPECT image. It is not easy to point out the hypoperfusion regions with visual inspection of SPECT image except for hypoperfusion in medial temporal regions. However, statistical analysis with easy z-score imaging software (eZIS) reveals hypoperfusion in precuneus in addition to hippocampal hypoperfusion. These results are quite persuasive and easy to understand for not only medical staffs but also patients and their families

76-year-old male. One may notice hypoperfusion in bilateral medial temporal regions (arrows in white), but other areas look quite normal with visual inspection. However, statistical analysis reveals hypoperfusion in bilateral precunei (arrow in yellow) in addition to medial temporal regions. These results are quite persuasive and easy to understand for not only medical staffs but also patients and their families. Two software packages are widely used in clinical settings in Japan. One is easy Z-score imaging system (eZIS) developed by Matsuda et al. [4] and the other is three-dimensional stereotactic surface projection (3D-SSP) developed by Minoshima and colleagues [5]. Since both software packages take similar process, here we see the process of eZIS. Note that eZIS employs statistical parametric mapping software (SPM) for normalizing and smoothing of the images.

11.3.1 Preprocessing (Normalizing and Smoothing)

Each individual has a different size and shape of the brain. In order to compare data from several subjects, all the images need to be in the same space. In eZIS which employs SPM, this is accomplished by "normalizing" the images into the space defined by the Montreal Neurological Institute (MNI) template. The detail of normalizing process is described by Ashburner, one of the developers of SPM [6].

Following spatial normalization, the image data would be "smoothed" or blurred. By smoothing, the signal-to-noise ratio is increased. It also ensures that the residual differences are closer to Gaussian and decreases the intersubject registration error. Another reason for smoothing is simplifying the ensuing results, producing fewer regions of significant difference to report [7]. The outline of preprocessing is illustrated in Fig. 11.2.

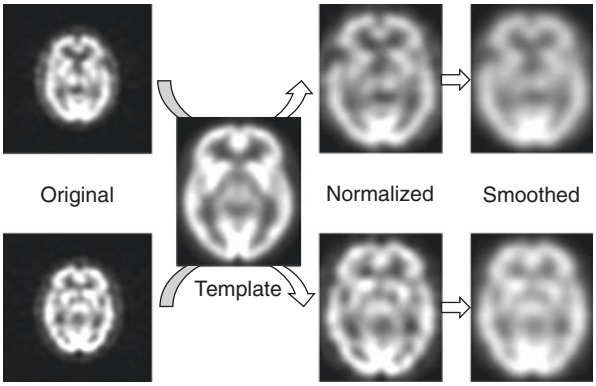

Fig. 11.2 A scheme of preprocessing. In order to compare data from several subjects, data are normalized to the space defined by the Montreal Neurological Institute template. Following spatial normalization, the image data are smoothed to be suited for statistical analysis

11.3.2 Generating Z-Score Images

After preprocessing, intensity of each image is normalized. Note that eZIS takes a different approach from SPM. In SPM, intensity normalization takes a two-step procedure. First, it calculates mean of an image. This averages all of the voxel values (VV) even outside the brain, so we need to threshold the image with certain value. Threshold is calculated by mean divided by 8. Then it calculates global value by averaging the VV above the threshold. Finally global value is set to 50 mL/min/100 g and each VV is adjusted with proportional scaling.

On the other hand, eZIS takes a straightforward procedure. First it applies a brain mask to preprocessed images. Then mean value is calculated with the masked images. Setting global value and adjusting VV is the same as SPM. Figure 11.3 illustrates how mean and VV of a certain voxel will change throughout the procedure. VV of a voxel coordinate [40 30 40] in the preprocessed image is 796.0 and mean VV is 368.8. Note that at this point, mean includes voxels outside the brain. After masking, VV at [40 30 40] remains the same, but the mean changes from 368.8 to 635.1. Now using proportional scaling eZIS sets mean as 50, VV at [40 30 40] will be $796.0 \times \frac{50}{635.1} = 62.7.$ Understanding this procedure is important because sometimes we see apparent hyperperfusion regions in eZIS results. For example, global cerebral blood flow (CBF) of advanced demented patients is generally low such as 30 mL/min/100 g, but the regional CBF in primary sensory motor region is intact such as 45 mL/min/100 g. In this case, after intensity normalization, the adjusted regional CBF in primary somatosensory regions will be $45 \times \frac{50}{30} = 75,$

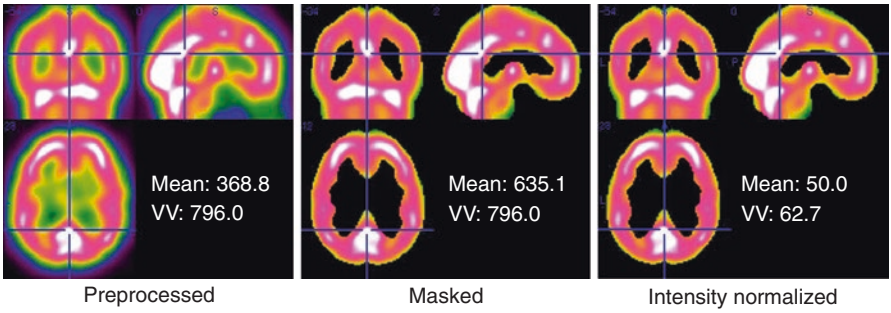

Fig. 11.3 Illustration of how mean and voxel values (VV) of a certain voxel will change by masking and proportional scaling

which will result in remarkable hyperperfusion in this region. In order to prevent misinterpreting the results, it is recommended to check the global CBF regularly.

Following intensity normalization, z-score at each voxel is calculated with the following equation.

$$\text{Z score} = \frac{\text{average of control VV} - \text{subject VV}}{\text{SD of control VV}}$$

Here SD stands for standard deviation. This equation can be rephrased like the following.

$$\text{Subject VV} = \text{average of control VV} - \text{Z score} \times \text{SD of control VV}$$

So if Z-score is 2, one can say that subject's VV in a certain voxel is 2 standard deviation below average of control subjects. This equation also tells us that we need to prepare the mean and standard deviation of control subjects beforehand. Z-score highly depends on the quality of control subjects, so we need to keep in mind that using different control subjects might result in quite a different result.

Z-score images are overlaid on the standard brain as shown in Fig. 11.1. Z-score threshold is an arbitrary set. In Fig. 11.1, z-score = 2 is set as a threshold.

11.4 SPECT Findings in Alzheimer's Disease

SPECT findings of typical AD are characterized by hypoperfusion in (1) the parietotemporal association cortex, (2) posterior cingulate gyrus and precuneus; and (3) medial temporal areas [8]. It is also noteworthy that CBF of primary sensorimotor region is spared until the advanced stage. The yellow arrows in Fig. 11.4 point the characteristic hypoperfusion regions in AD and red arrow points the primary sensorimotor region where CBF is spared.

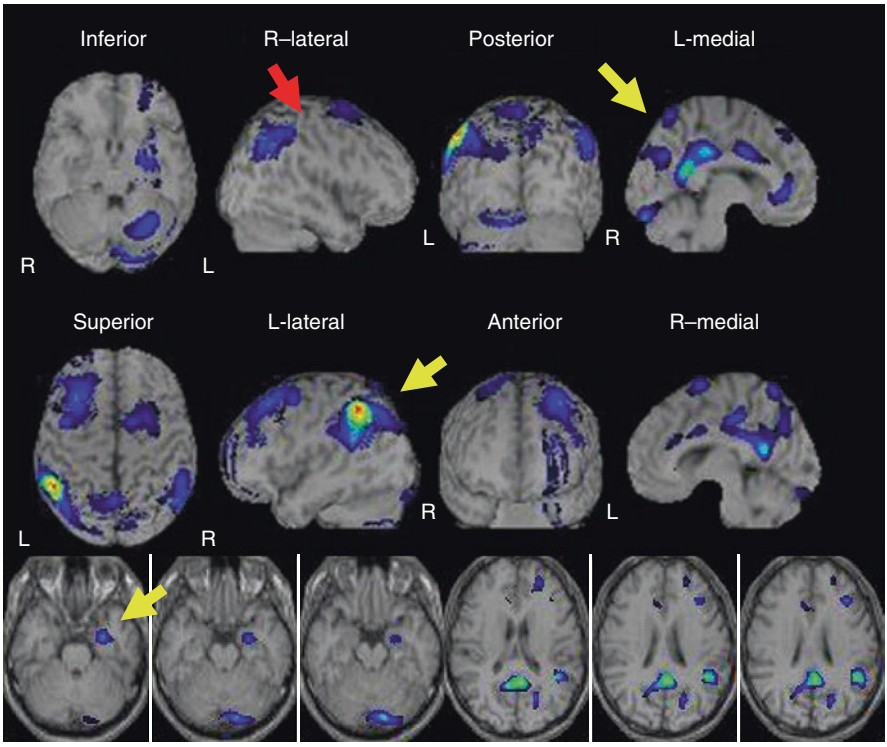

Fig. 11.4 SPECT findings of typical AD are characterized by hypoperfusion in the (1) parietotemporal association cortex, (2) posterior cingulate gyrus and precuneus, and (3) medial temporal areas. Note that CBF of the primary sensorimotor region is spared until the advanced stage. The *yellow arrows* point the characteristic hypoperfusion regions in AD, and the *red arrow* points the primary sensorimotor region where CBF is spared

11.4.1 Parietotemporal Cortex

The parietotemporal cortex is the first cortical region to be affected in AD [8]. Kemp and colleagues reported that early-onset AD patients have greater posterior association cortex involvement than those with late onset [9]. Hypoperfusion regions extend to the frontal lobes except for primary sensorimotor region as the disease progresses.

11.4.2 Posterior Cingulate Gyrus and Precuneus

Hypoperfusion or hypometabolism in the posterior cingulate gyrus (PCG) and precuneus is the very early finding of AD. Indeed, even patients with amnestic MCI patients show hypoperfusion in the region [10]. Though statistical image analysis clearly demonstrates the hypoperfusion in PCG and precuneus, one can notice the

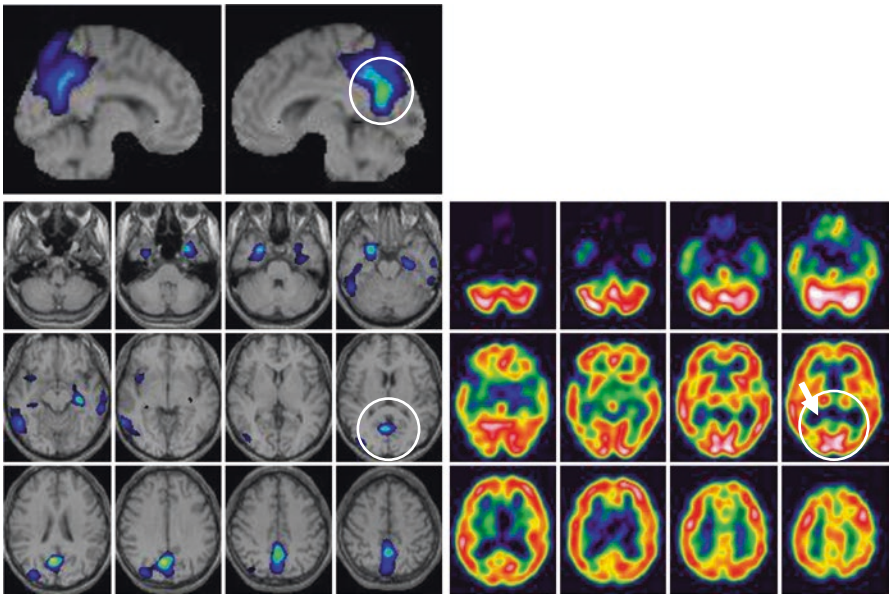

Fig. 11.5 A key to notice hypoperfusion in PCG and precuneus. The *white circle* shows the hypoperfusion in PCG and precuneus. Note the dip in SPECT image shown by white arrow. This dip reflects the hypoperfusion in PCG

hypoperfusion with careful visual inspection. The white circle in Fig. 11.5 shows the hypoperfusion in PCG and precuneus. Note the dip in SPECT image shown by the white arrow. This dip reflects the hypoperfusion in PCG. Small et al. demonstrated that hypometabolism in PCG and precuneus at a presymptomatic stage predicts a future cognitive decline in people with genetic risk of Alzheimer's disease [11]. This shows that hypoperfusion or hypometabolism in PCG and precuneus is recognized well before patients show cognitive impairment.

11.4.3 Medial Temporal Areas

It is well known that AD patients show volume reduction in hippocampal regions from the very early stage [12]. SPECT images, with its lower spatial resolution, are affected by partial volume correction. This means that regional cerebral blood flow (rCBF) in hippocampal regions seems decreased despite true rCBF is not decreased. Indeed, Ishii et al. reported that rCBF at the hippocampus of mild AD patients was intact after partial volume correction [13]. Nonetheless, hypoperfusion in hippocampal regions is clinically useful because it reflects dysfunction in the hippocampus. Figure 11.6 shows hypoperfusion in the hippocampus. With axial view, temporal lobe perfusion of healthy subjects look like "crab claw" (white circle). However, it looks as if medial part of crab claw was lost when the hippocampus perfusion is reduced.

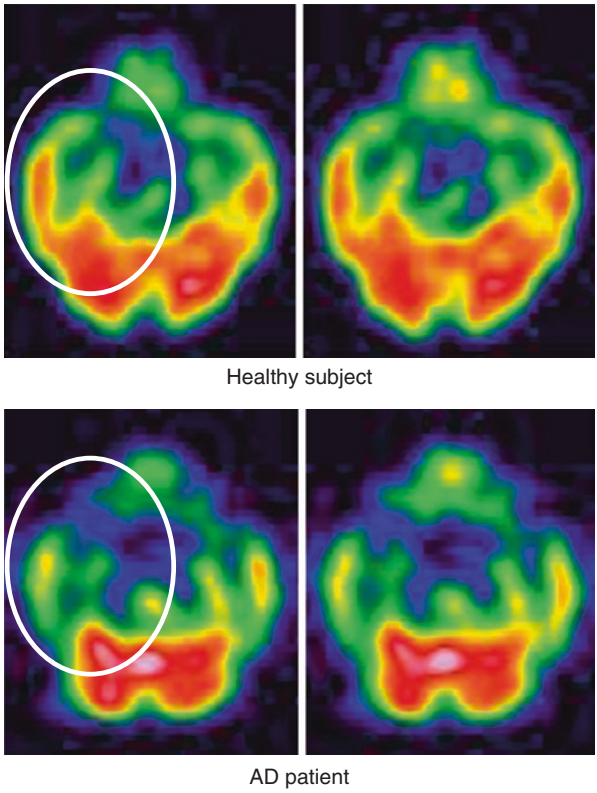

Fig. 11.6 Hypoperfusion in the hippocampus. With axial view, temporal lobe perfusion of healthy subjects looks like a "crab claw" (*white circle*). However, it looks as if the medial part of the crab claw was lost when the hippocampus perfusion is reduced

11.5 Longitudinal SPECT Changes in Alzheimer's Disease

Here we see a 71-year-old male case who was amnestic MCI at an initial visit but developed clinical AD in years. We followed up his SPECT images over 5 years (Fig. 11.7). At an initial visit, his MMSE was 26 and he complained subjective forgetfulness. At this point, SPECT showed hypoperfusion in the PCG and hippocampus. His cognition remained for 2 years. Two years after the initial visit, his MMSE was 25. However, SPECT showed progressive hypoperfusion in PCG and precuneus. From that time on, his cognition declined gradually and MMSE got 21 at 4 years from the first visit. At this time SPECT showed progressive hypoperfusion in the hippocampus. A year later his MMSE declined to 20. Note that his MMSE between initial visit and 2 years later did not change much though his rCBF showed prominent decline in PCG and precuneus. Noticing this in clinical settings is useful because it can be a predictor for cognitive decline. In this respect, just following up MMSE is not enough to predict the disease progression.

As we see in this chapter, SPECT is very useful for the diagnosis and short-term prediction of cognitive decline. If you are not sure about the diagnosis of patients with cognitive decline or want to know the perspective of patients in terms of cognitive decline, considering SPECT might be an asset.

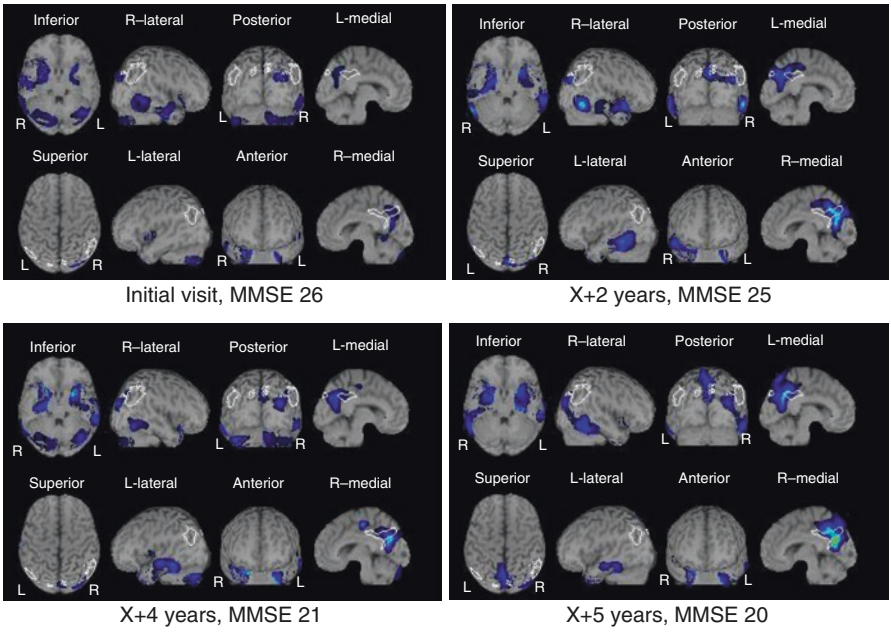

Fig. 11.7 Longitudinal rCBF change of a 71-year-old male who developed clinical AD. Note that progression of hypoperfusion in precuneus preceded the cognitive decline

References

1. Braak H, Braak E. Staging of Alzheimer's disease-related neurofibrillary changes. Neurobiol Aging. 1995;16:271–278.; discussion 278–84. doi:10.1016/0197-4580(95)00021-6.
2. Delacourte A, David JP, Sergeant N, et al. The biochemical pathway of neurofibrillary degeneration in aging and Alzheimer's disease. Neurology. 1999;52:1158–65.
3. Imabayashi E, Matsuda H, Asada T, et al. Superiority of 3-dimensional stereotactic surface projection analysis over visual inspection in discrimination of patients with very early Alzheimer's disease from controls using brain perfusion SPECT. J Nucl Med. 2004;45:1450–7.
4. Matsuda H, Mizumura S, Nagao T, et al. An easy Z-score imaging system for discrimination between very early Alzheimer's disease and controls using brain perfusion SPECT in a multicentre study. Nucl Med Commun. 2007;28:199–205. doi:10.1097/MNM.0b013e328013eb8b.
5. Minoshima S, Frey KA, Koeppe RA, et al. A diagnostic approach in Alzheimer's disease using three-dimensional stereotactic surface projections of fluorine-18-FDG PET. J Nucl Med. 1995;36:1238–48.
6. Ashburner J, Friston KJ. Nonlinear spatial normalization using basis functions. Hum Brain Mapp. 1999;7:254–66.
7. Ashburner J. Computational anatomy with the SPM software. Magn Reson Imaging. 2009;27:1163–74.
8. Kanetaka H, Matsuda H, Asada T, et al. Effects of partial volume correction on discrimination between very early Alzheimer's dementia and controls using brain perfusion SPECT. Eur J Nucl Med Mol Imaging. 2004;31:975–80. doi:10.1007/s00259-004-1491-3.
9. Kemp PM, Holmes C, Hoffmann SM, et al. Alzheimer's disease: differences in technetium-99m HMPAO SPECT scan findings between early onset and late onset dementia. J Neurol Neurosurg Psychiatry. 2003;74:715–9. doi:10.1136/jnnp.74.6.715.

10. Minoshima S, Giordani B, Berent S, et al. Metabolic reduction in the posterior cingulate cortex in very early Alzheimer's disease. Ann Neurol. 1997;42:85–94. doi:10.1002/ana.410420114.
11. Small GW, Ercoli LM, Silverman DH, et al. Cerebral metabolic and cognitive decline in persons at genetic risk for Alzheimer's disease. Proc Natl Acad Sci U S A. 2000;97:6037–42. doi:10.1073/pnas.090106797.
12. Risacher SL, Saykin AJ. Neuroimaging biomarkers of neurodegenerative diseases and dementia. Semin Neurol. 2013;33:386–416. doi:10.1055/s-0033-1359312.
13. Ishii K, Sasaki M, Yamaji S, et al. Paradoxical hippocampus perfusion in mild-to-moderate Alzheimer's disease. J Nucl Med. 1998;39:293–8.

Neuroimaging of Dementia with Lewy Bodies

12

Haruo Hanyu

Abstract

Dementia with Lewy bodies (DLB) is the second most common form of neurodegenerative dementia following Alzheimer's disease (AD). Despite the development of consensus diagnostic criteria, differentiating DLB from other types of dementia, such as AD, can be difficult. Several imaging studies are currently underway to differentiate DLB from other types of dementia. Magnetic resonance imaging of DLB shows preservation of the medial temporal lobe structure and predominant atrophy of subcortical structures, including the substantia innominata and dorsal midbrain, compared with AD. Decreased perfusion in the occipital lobe and relatively increased perfusion in the deep gray matter (striatum and thalamus) on single photon emission CT (SPECT) are shown to be characteristic features of DLB. MIBG myocardial scintigraphy provides a higher sensitivity and higher specificity for diagnosing probable DLB from AD than perfusion SPECT. Dopamine transporter imaging, an available technique in Japan since 2014, shows good diagnostic accuracy for DLB. The international consensus criteria for DLB (2005) incorporate abnormal imaging on dopamine transporter as a supportive feature. As idiopathic REM sleep behavior disorder (iRBD) is considered to be a prodromal stage of alpha-synucleinopathies, the above findings are observed in some patients with iRBD. This review summarizes the applications and findings from neuroimaging studies of DLB and iRBD.

Keywords

Dementia with Lewy bodies • Magnetic resonance imaging • Single photon emission CT • MIBG myocardial scintigraphy • Dopamine transporter imaging • REM sleep behavior disorder

H. Hanyu, MD, PhD
Department of Geriatric Medicine, Tokyo Medical University,
6-7-1 Nishishinjuku, Shinjuku-ku, Tokyo 160-0023, Japan
e-mail: h-hanyu@tokyo-med.ac.jp

H. Matsuda et al. (eds.), *Neuroimaging Diagnosis for Alzheimer's Disease and Other Dementias*, DOI 10.1007/978-4-431-55133-1_12

12.1 Introduction

Dementia with Lewy bodies (DLB) and Parkinson's disease dementia (PDD) are the second most common causes of dementia, exceeded only by Alzheimer's disease (AD), accounting for approximately 15% of all cases at autopsy. DLB (and frequently PDD) is clinically characterized by fluctuating cognition with pronounced variations in alertness, visual hallucinations, and extrapyramidal signs [1]. Other features, such as REM sleep behavior disorder (RBD), delusions, depression, repeated falls, and syncope, are frequently observed. A recent study using comprehensive geriatric assessment demonstrated that DLB has significantly higher frequencies of minor or major problems than AD in several items, including visual function, verbal communication, medication adherence, depression, upper and lower extremity functions, history of falls, urination, and impairment of basic and instrumental activity of daily living (ADL) function [2]. These neurologic and psychotic symptoms and geriatric problems are likely to be associated with poor cognitive and functional outcomes. Indeed, we found that DLB had a greater risk of admission (or death) most commonly because of fall-related injuries and aspiration pneumonia than AD [3]. Therefore, an accurate antemortem diagnosis of DLB is important because there are differences in disease course, treatment, and management between DLB and other types of dementia. However, the diagnosis of DLB is difficult, particularly in the early stages.

Several imaging techniques have emerged as potential means of supporting the clinical diagnosis of various dementias. Magnetic resonance imaging (MRI) and positron emission tomography (PET) or single photon emission CT (SPECT) are currently being employed to differentiate DLB from other types of dementia. In addition, [^{123}I]-metaiodobenzylguanidine (MIBG) myocardial scintigraphy, and dopamine transporter (DAT) imaging are valuable tools to identify DLB patients and to differentiate them from those with other neurodegenerative disorders [4, 5]. DLB and PDD share a similar pattern of neuroimaging studies. In this report, we review several imaging modalities to differentiate DLB from other types of dementia, particularly AD.

12.2 MRI

MRI has shown global and subcortical atrophic changes in DLB [6]. Specifically, qualitative and volumetric MRI studies have shown less medial temporal lobe atrophy in DLB than in AD. These previous findings are consistent with recent findings of voxel-based morphometry studies. These findings are also supported by a prospective MRI study with pathological verification [7]. Using the voxel-based specific regional analysis system for Alzheimer's disease (VSRAD) [8] for MRI, DLB showed significantly smaller z-score for the assessment of hippocampal atrophy than AD (Fig. 12.1). A recent study with manual tracing of hippocampal boundaries and computer-assisted post-processing showed significant tissue

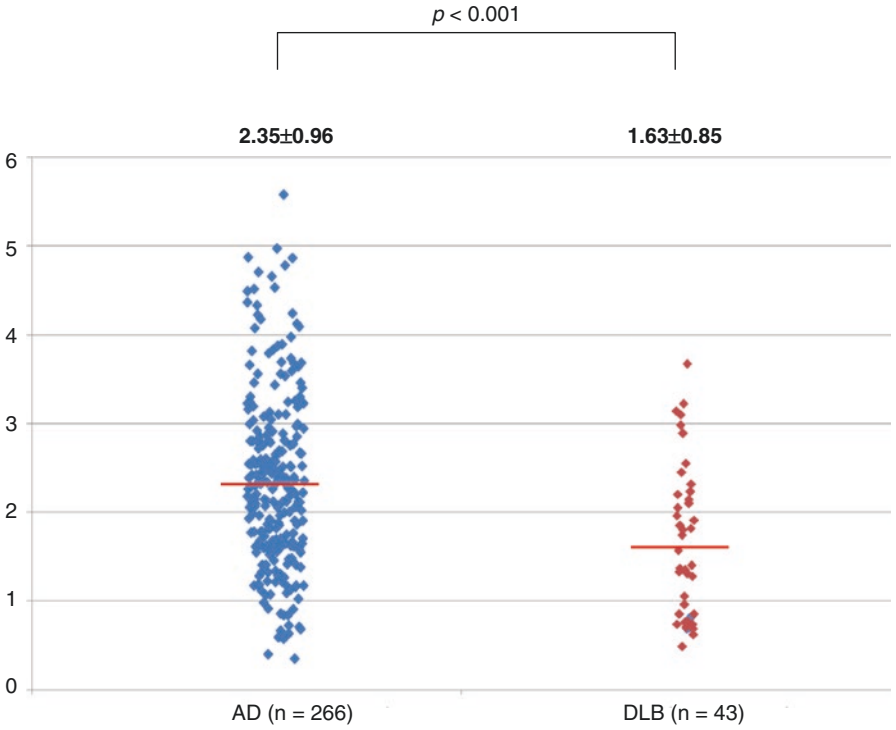

Fig. 12.1 A comparison of z-scores between AD and DLB using VSRAD

loss (10–20%) in the hippocampal subregions of DLB corresponding to the anterior portion of the CA1 field on both sides, along the longitudinal midline in the dorsal aspect within the CA2-3 field, different from the pattern of hippocampal change in AD [9]. We found that the magnetization transfer ratios (MTR) of the hippocampus were significantly higher in DLB than in AD [10]. Pathologic changes in the hippocampus, including loss of neurons, gliosis, demyelination, and axonal loss, may be associated with a decrease in the MTR. These results may reflect underlying histopathological differences with less severe neuronal degeneration in the hippocampus of DLB. Therefore, the relative preservation of the medial temporal lobe structures shows promise as a diagnostic marker in differentiating DLB from AD.

Among subcortical structures, atrophy of the substantia innominata (including the nucleus basalis of Meynert) [11] and dorsal midbrain [12] has been documented in DLB. Atrophy of these structures is supported by the pathological involvement of the areas. Atrophy of the substantia innominata is associated with cholinergic dysfunction in DLB. However, it remains unclear whether these subcortical structural changes are diagnostic markers for the identification of DLB and its differentiation from AD.

12.3 Perfusion SPECT

Perfusion SPECT studies are currently being employed in practice to differentiate between various types of dementia, as this method can reveal perfusion abnormalities that may be characteristic of different types of dementia [13]. Although the neuropathologic and neurochemical bases underlying occipital abnormalities in DLB are not yet clearly understood, functional brain imaging studies using SPECT and PET have revealed that reduced occipital metabolism and perfusion are characteristic features of DLB (Fig. 12.2). Several investigators have indicated the value of functional brain imaging studies in differentiating between DLB and AD, although there are some methodological differences, including patient selection (definite or probable cases), scanning methods (PET versus SPECT), and image analysis (conventional region of interest or statistical image analysis). In a multicenter study examining [^{18}F]fluorodeoxyglucose (FDG) PET measures, the presence of hypometabolism in the occipital lobe discriminated DLB from AD with a sensitivity of 71% and a specificity of 95% [14]. On the other hand, the diagnostic accuracy of SPECT is relatively low, as shown by a sensitivity range of 65–85% and a specificity range of 85–87% [5]. We found that combined MMSE and perfusion SPECT studies achieved a high discrimination between DLB and AD with a sensitivity of 81% and a specificity of 85% [15].

Lim et al. [16] confirmed that occipital hypometabolism and relative preservation of the posterior cingulate gyrus (cingulate island sign) differentiated DLB from AD in patients with a sensitivity of 77% and a specificity of 80%. In addition to occipital hypoperfusion, increased perfusion in the deep gray matter (striatum and thalamus) was shown to be a characteristic feature of DLB, possibly due to compensatory changes to decreased dopaminergic input to the basal ganglia [17] (Fig. 12.3).

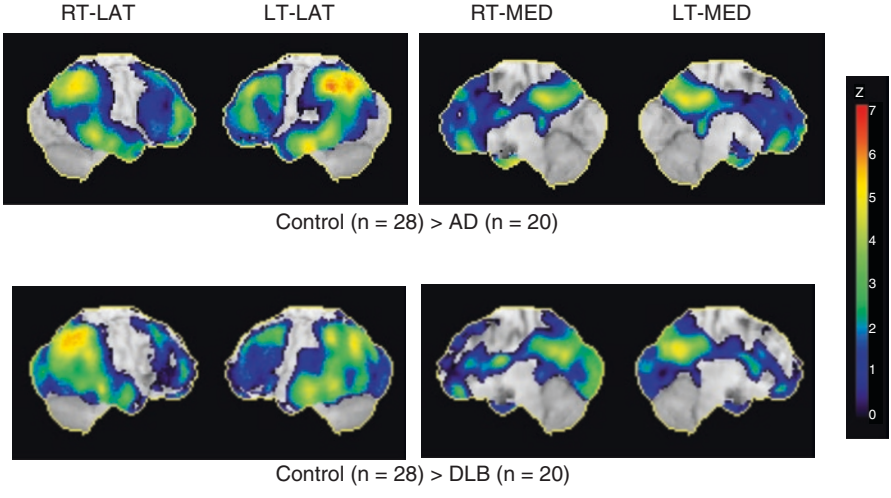

Fig. 12.2 Z-score images of AD and DLB on perfusion SPECT (3D-SSP)

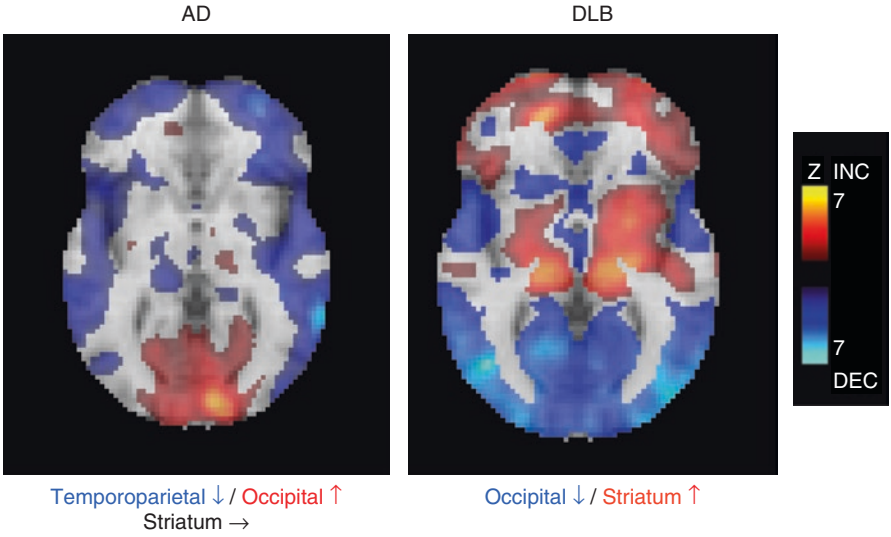

Fig. 12.3 Two-tail views of AD and DLB on perfusion SPECT

These additional alterations on functional brain imaging may enhance the diagnostic accuracy of DLB.

Psychotic symptom clusters in DLB appear to relate to spatially distinct perfusion deficits. Nagahama et al. [18] found that visual hallucinations concord with parietal and occipital association cortices perfusion deficits and delusional misidentifications to perfusion deficits of the limbic-paralimbic structures. Increased thalamic and decreased inferior occipital perfusion may be related to fluctuations in consciousness [19].

12.4 MIBG Myocardial Scintigraphy

MIBG myocardial scintigraphy is a useful, noninvasive technique for estimating local myocardial sympathetic nerve damage not only in primary heart disease but also in synucleinopathies, such as PD, DLB, and REM sleep behavior disorder (RBD) (Fig. 12.4). MIBG scintigraphy has been performed mainly on Japanese cohorts. A number of studies have shown reduced MIBG uptake (heart-to-mediastinum ratio) in DLB patients compared with AD and normal controls. A review from Sinha et al. [5] showed that MIBG myocardial scintigraphy yielded a high sensitivity (range, 83–100%) and a high specificity (range, 82–100%) for diagnosing DLB. MIBG scintigraphy was more sensitive in detecting DLB than occipital hypoperfusion on SPECT [20]. We investigated the role of MIBG scintigraphy in the differential diagnosis of dementia in 96 dementia patients in our Memory Clinic, including 32 with DLB, 9 with PDD, 40 with AD, and 24 with other types of dementia. The overall sensitivity to

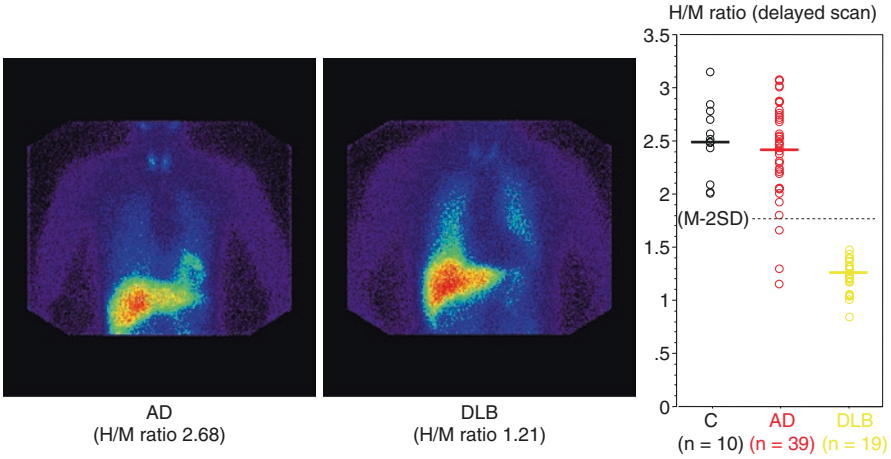

Fig. 12.4 MIBG myocardial scintigraphy

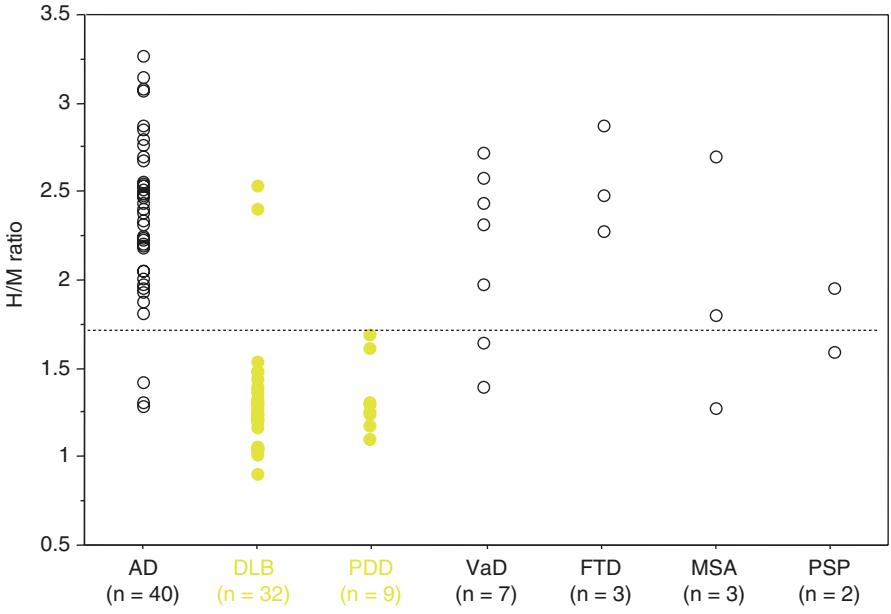

Fig. 12.5 Diagnostic accuracy for DLB and PDD using MIBG myocardial scintigraphy

positively identify patients with Lewy body disease (including DLB and PDD) was 95%, and the specificity to differentiate them from patients with other types of dementia was 87% [21] (Fig. 12.5). There was no correlation between MIBG scintigraphy and disease severity or duration of DLB. Although it is important to note that reduced MIBG uptake has also been reported in patients with

cardiac disorders, diabetes mellitus, and some medications, this technique is also a powerful tool in the differential diagnosis between DLB/PDD and other types of dementia.

12.5 Dopamine Transporter (DAT) Imaging

Imaging with specific SPECT ligands for dopamine transporter (FP-CIT and beta-CIT) provides a marker for presynaptic nigrostriatal degeneration. DAT scan has been clinically available for patients with DLB and PD in Japan since 2014. DAT imaging is abnormal in PD and DLB, reflecting nigrostriatal degeneration, but not in AD, indicating a useful method in the differentiation between DLB and AD. In our preclinical study of DAT imaging, a 4.1 cutoff score of specific binding ratio yielded a sensitivity of 92% and a specificity of 84% for diagnosing probable DLB from AD (Fig. 12.6). A large multicenter study demonstrated a sensitivity and specificity of abnormal DAT scans in diagnosing probable DLB from AD of 78% and 90%, respectively [22]. DAT imaging results were in agreement with autopsy diagnosis in the vast majority of cases (7 of 8 DLB and 12 of 12 non-DLB) and were more precise than clinical diagnosis [23]. FP-CIT SPECT is also reliable in confirming cases of clinically possible DLB, supporting the inclusion of reduced DAT uptake as a suggestive feature of DLB in the International Consensus Criteria [24].

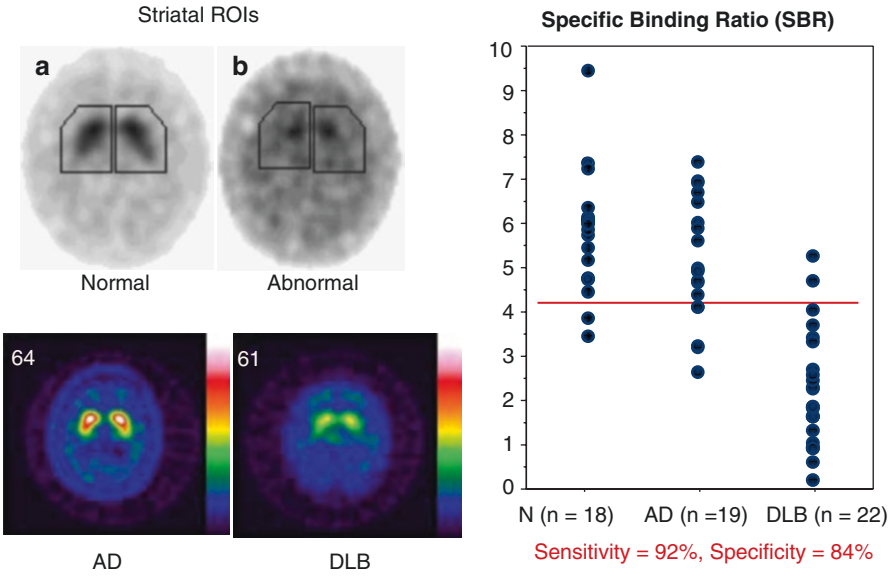

Fig. 12.6 DAT imaging

DAT imaging has demonstrated superior diagnostic accuracy for DLB compared with brain perfusion SPECT and FDG-PET. A recent clinical study has revealed that DAT imaging and MIBG scintigraphy showed similar diagnostic accuracy in differential diagnosis between DLB and other dementias [25]. However, DAT imaging fails to discriminate PD/DLB from other parkinsonian syndromes because reduced striatal dopamine uptake has been shown in progressive supranuclear palsy, multiple system atrophy, and corticobasal syndrome. The impact of concurrent vascular pathology in striatal DAT binding has not yet been determined. Despite the caveat and the limited diagnostic potential to differentiate between different synucleinopathies, the European Federation of Neurological Societies (EFNS) guidelines also recommend the use of DAT scan to differentiate between DLB and AD as the only imaging test to reach the level A category of evidence [26].

12.6 Structural and Functional Changes in Idiopathic RBD (iRBD)

RBD is a type of parasomnia characterized by a loss of normal skeletal muscle atonia during REM sleep and prominent motor activity while dreaming. RBD occurs either as an idiopathic disease or in association with neurodegenerative diseases, particularly alpha-synucleinopathies. Recent studies have demonstrated several neuropsychological impairments in iRBD patients, such as visuospatial construction dysfunction, executive dysfunction, memory disturbance, smell testing abnormalities, reduction of striatal presynaptic dopamine transporters, and reduced MIBG uptake. Since these findings are characteristic features of alpha-synucleinopathies, including PD and DLB, iRBD may be a prodromal stage of alpha-synucleinopathies.

There have been few studies examining structural and functional brain changes in iRBD patients. We investigated structural brain changes using voxel-based MRI morphometry in iRBD patients. Compared with the 18 age-matched controls, 20 iRBD patients had significant gray matter volume reduction in the anterior lobes of the right and left cerebellum, tegmental portion of the pons, and left parahippocampal gyrus [27]. Recently, Scherfler et al. [28] showed significant decreases in fractional anisotropy in the tegmentum of the midbrain and rostral pons and increases in mean diffusivity within the pontine reticular formation in iRBD patients. These studies provide in vivo evidence suggesting that structural lesions of the brain stem are responsible for the occurrence of iRBD. In our SPECT study, a decreased perfusion was shown in the parieto-occipital lobe (precuneus), limbic lobe, and cerebellar hemispheres in iRBD patients, as is commonly observed in patients with alpha-synucleinopathies, including DLB and PDD [29] (Fig. 12.7). In addition, a longitudinal study demonstrated more decreased perfusion in the parieto-occipital lobe in the second SPECT than in the first study in iRBD patients [30], although none of the patients showed any neurological deficits, including extrapyramidal and cerebellar signs, visual hallucinations, or neuropsychological impairments, during the study (Fig. 12.8). Therefore, iRBD may be a progressing neurodegenerative disorder, even though neurological and neuropsychiatric impairments have not been shown.

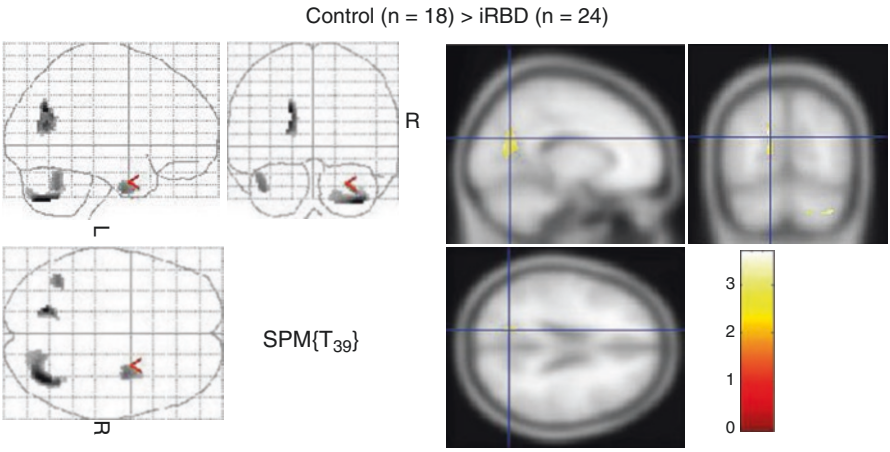

Regions		BA	Z-score	Coordinates		
				x	y	z
Cerebellum	Rt-Posterior lobe	-	3.4	36	-70	-34
	Rt-Anterior lobe	-	2.41	36	-52	-28
	Lt-Posterior lobe	-	2.8	-40	-58	-26
Parietal lobe	Rt-Precuneus	7	2.49	18	-76	39
	Lt-Precuneus	7	3.37	-17	-63	29
Occipital lobe	Lt-Precuneus	31	3.08	-18	-63	20
Limbic lobe	Rt-Uncus	20	2.84	32	-5	-30

Fig. 12.7 SPM analysis of perfusion SPECT in iRBD

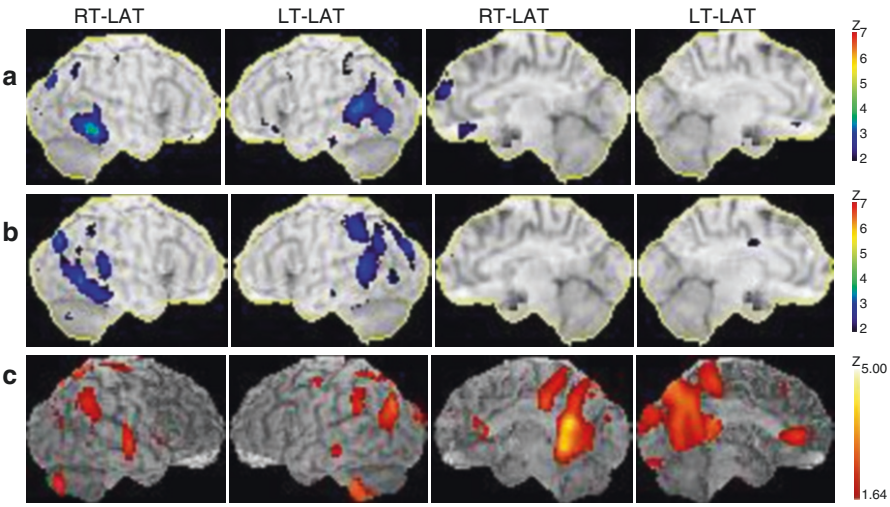

Fig. 12.8 Longitudinal perfusion changes in iRBD. Three-dimensional views of decreased studies showed regional perfusion on first SPECT (**a**) and second SPECT (**b**) of iRBD patients (n = 8, mean age 71 ± 3 years) compared with normal controls (n = 18, mean age 70 ± 8 years). The mean interval was 23 ± 9 months. Three-dimensional views of decreased perfusion on second SPECT compared with first SPECT of iRBD patients (**c**)

Conclusion

On neuroimaging studies, DLB is characterized by (1) preservation of medial temporal lobe structures on MRI, (2) occipital hypoperfusion and relatively striatal hyperperfusion on SPECT, (3) reduced cardiac MIBG uptake, and (4) reduced dopamine transporter in the striatum. These techniques are valuable tools to identify DLB patients and to differentiate DLB from other neurodegenerative disorders such as AD. In the near future, synuclein imaging methods would be available for use in clinical practice, similar to the development of amyloid and tau imagings in AD.

Acknowledgments We are grateful to Maya Vardaman and Associate Professor Edward F. Barroga of the Department of International Medical Communications of Tokyo Medical University for reviewing and editing the manuscript.

References

1. McKeith IG, Dickson DW, Lowe J, et al. Consortium on DLB. Diagnosis and management of dementia with Lewy bodies; third report of the DLB consortium. Neurology. 2005;65:1863–72.
2. Namioka N, Hanyu H, Hatanaka H, et al. Comprehensive geriatric assessment in elderly patients with dementia. Geriatr Gerontl Int Aug. 2014;15(1):27–33.
3. Hanyu H, Sato T, Hirao K, et al. Differences in clinical course between dementia with Lewy bodies and Alzheimer's disease. Eur J Neurol. 2009;16:212–7.
4. Taylor J-P, O'Brien J. Neuroimaging of dementia with Lewy bodies. Neuroimaging Clin N Am. 2012;22:67–81.
5. Sinha N, Firebank M, O'Brien JT. Biomarkers in dementia with Lewy bodies: a review. Int J Geraitr Psychiatry. 2012;27:443–53.
6. Watson R, Blamire AM, O'Brien JT. Magnetic resonance imaging in Lewy body dementias. Dement Geriatr Cogn Disord. 2009;28:493–506.
7. Burton EJ, Barber R, Mukaetova-Ladinska EB, et al. Medial temporal lobe atrophy on MRI differentiate Alzheimer's disease from dementia with Lewy bodies and vascular cognitive impairment: a prospective study with pathological verification of diagnosis. Brain. 2009;132:195–203.
8. Hirata Y, Matsuda H, Nemoto K, et al. Voxel-based morphometry to discriminate early Alzheimer's disease from controls. Neurosci Lett. 2005;382:269–74.
9. Sabattoli F, Boccardi M, Galluzzi S, et al. Hippocampal shape differences in dementia with Lewy bodies. NeuroImage. 2008;41:699–705.
10. Hanyu H, Shimizu S, Tanaka Y, et al. Differences in magnetization transfer ratios of the hippocampus between dementia with Lewy bodies and Alzheimer's disease. Neurosci Lett. 2005;380:166–9.
11. Hanyu H, Shimizu S, Tanaka Y, et al. MR features of the substantia innominata and therapeutic implications in dementias. Neurobiol Aging. 2007;28:548–54.
12. Whitwell JL, Weigand SD, Shiung MM, et al. Focal atrophy in dementia with Lewy bodies on MRI: a distinct pattern from Alzheimer's disease. Brain. 2007;130:708–19.
13. Shimizu S, Hanyu H, Kanetaka H, et al. Differentiation of dementia with Lewy bodies from Alzheimer's disease using brain SPECT. Dement Geriatr Cogn Disord. 2005;20:25–30.
14. Mosconi L, Tsui WH, Herholz K, et al. Multicenter standardized 18F-FDG PET diagnosis of mild cognitive impairment, Alzheimer's disease, and other dementias. J Nucl Med. 2008;49:390–8.

15. Hanyu H, Shimizu S, Hirao K, et al. Differentiation of dementia with Lewy bodies from Alzheimer's disease using mini-mental state examination and brain perfusion SPECT. J Neurol Sci. 2006;250:97–102.
16. Lim SM, Katsifits A, Villemagne VL, et al. The 18F-FDG PET cingulate island sign and comparison to 123I-β-CIT SPECT for diagnosis of dementia with Lewy bodies. J Nucl Med. 2009;50:1638–45.
17. Sato T, Hanyu H, Hirao K, et al. Deep gray matter hyperperfusion with occipital hypoperfusion in dementia with Lewy bodies. Eur J Neurol. 2007;14:1299–301.
18. Nagahama Y, Okina T, Suzuki N, et al. Neural correlates of psychotic symptoms in dementia wit Lewy bodies. Brain. 2010;133:557–67.
19. O'Brien JT, Firbank MJ, Mosimann UP, et al. Changes in perfusion, hallucinations and fluctuations in consciousness in dementia with Lewy bodies. Psychiatry Res. 2005;139:79–88.
20. Hanyu H, Shimizu S, Hirao K, et al. Comparative value of brain perfusion SPECT and [123I] MIBG myocardial scintigraphy in distinguishing between dementia with Lewy bodies and Alzheimer's disease. Eur J Nucl Med Mol Imaging. 2006;33:248–53.
21. Hanyu H, Shimizu S, Hirao K, et al. The role of [^{123}I] MIBG myocardial scintigraphy for the diagnosis of Lewy body disease in patients with dementia in a memory clinic. Dement Geriatr Cogn Disord. 2006;22:379–84.
22. McKeith I, O'Brien J, Walker Z, et al. Sensitivity and specificity of dopamine transporter imaging with 123I-FP-CIT SPECT in dementia with Lewy bodies: a phase III, multicentre study. Lancet Neurol. 2007;6:305–13.
23. Walker Z, Jaros E, Walker RWH, et al. Dementia with Lewy bodies: a comparison of clinical diagnosis, FP-CIT single photon emission computed tomography imaging and autopsy. J Neurol Neurosurg Psychiatry. 2007;78:1176–81.
24. O'Brien JT, McKeith IG, Walker Z, et al. Diagnostic accuracy of 123I-FP-CIT SPECT in possible dementia with Lewy bodies. Br J Psychiatry. 2009;1194:34–9.
25. Treglia G, Cason E, Cortelli P, et al. Iodine-123 metaiodobenzylguanidine scintigraphy and iodine-123 ioflupane single photon emission computed tomography in Lewy body diseases: complementary or alternative techniques? J Neuroimaging. 2014;24:149–54.
26. Hort J, O'Brien JT, Gainotti G, et al. EFNS guidelines for the diagnosis and management of Alzheimer's disease. Eur J Neurol. 2010;17:1236–48.
27. Hanyu H, Inoue Y, Sakurai H, et al. Voxel-based magnetic resonance imaging study of structural brain changes in patients with idiopathic REM sleep behavior disorder. Parkinsonism Relat Disord. 2012;18:136–9.
28. Scherfler C, Frauscher B, Schocke M, et al. White and gray matter abnormalities in idiopathic rapid eye movement sleep behavior disorder: a diffusion-tensor imaging and voxel-based morphometric study. Ann Neurol. 2011;69:400–4007.
29. Hanyu H, Inoue Y, Sakurai H, et al. Regional cerebral blood flow changes in patients with idiopathic REM sleep behavior disorder. Eur J Neurol. 2011;18:784–8.
30. Sakurai H, Hanyu H, Inoue Y, et al. Longitudinal study of regional cerebral blood flow in elderly patients with idiopathic rapid eye movement sleep behavior disorder. Geriatr Gerontol Int. 2014;14:115–20.

Neuroimaging of Frontotemporal Lobe Degeneration

13

Seigo Nakano

Abstract

Frontotemporal dementia (FTD) is a neurodegenerative disease which symptoms are the first signs of illness due to progressive nerve cell loss in the frontal and anterior temporal lobes. It represents the second most frequent form of early-onset dementia. There are three clinical subtypes: behavior variant of frontotemporal dementia (bvFTD), semantic dementia (SD), and progressive nonfluent aphasia. The neuroimagings such as MRI and SPECT help in the diagnosis of FTD on usual clinical aspects in Japan. In this chapter, the typical neuroimagings of FTD are demonstrated in each clinical subtypes.

Keywords

Frontotemporal dementia • Semantic dementia • Progressive nonfluent aphasia • MRI • SPECT

13.1 Introduction

Frontotemporal dementia (FTD) is composed of a spectrum of dementing disorders with degeneration of the frontal lobes, the anterior temporal lobes, or both. The clinical features are the progressive development of behavioral and personality change and/or language impairment. According to the criteria established by Neary et al. [1], FTD is classified into three subtypes: the behavioral variant of FTD (bvFTD), semantic dementia (SD), and progressive nonfluent aphasia (PNFA).

S. Nakano
Center for Treatment, Care and Research of Dementia, Medical Co. LTA,
1-29-1 Honjo, Sumida-ku, Tokyo 130-0004, Japan
e-mail: seigo-nakano@lta-med.com

H. Matsuda et al. (eds.), *Neuroimaging Diagnosis for Alzheimer's Disease and Other Dementias*, DOI 10.1007/978-4-431-55133-1_13

FTD is a common cause of early-onset dementia in individuals younger than 65 years [2]. Population prevalence estimates are in the range of 2–10 per 100,000. Approximately 20–25% of cases of FTD occur in individuals older than 65 years. FTD accounts for about 5% of all cases of dementia in unselected autopsy series. Prevalence estimates of bvFTD and SD are higher among males, and prevalence estimates of PNFA are higher among females [3].

Diagnosis of FTD is demanded in the presence of behavior and language changes. However, those features are the most silent. Therefore, the neuroimaging is useful to define those disorders and identify characteristic patterns of frontotemporal atrophy on structural neuroimages and hypoperfusion on functional neuroimagings on early stages of FTD.

In this chapter, the author demonstrates the characteristic pattern of neuroimages in each subtypes of FTD.

13.2 Neuroimaging Associations with Clinical Subtype

13.2.1 Behavioral Variant Frontotemporal Dementia

The behavioral variant of frontotemporal dementia (bvFTD) is the most common of the FTD. Individuals with bvFTD present with varying degrees of apathy or disinhibition. They may lose interest in socialization, self-care, and personal responsibilities or display socially inappropriate behaviors. Insight is usually impaired, and this often delays medical consultation. Individuals may develop changes in social style and in religious and political beliefs, with repetitive movements, hoarding, changes in eating behavior, and hyperorality. In later stages, loss of sphincter control may occur. Cognitive decline is less prominent, and formal testing may show relatively few deficits in the early stage. Common neurocognitive symptoms are lack of planning and organization, distractibility, and poor judgment. Deficits in executive function, such as poor performance on tests of mental flexibility, abstract reasoning, and response inhibition, are present, but learning and memory are relatively spared, and perceptual motor abilities are almost always preserved in the early stages [4].

The structural neuroimagings show distinct patterns of atrophy, which are in both frontal lobes (especially the medial frontal lobes) and anterior temporal lobes, in bvFTD [5]. MRI is preferred to CT in detecting these findings. However, we should keep in mind that the structural changes are not necessary present in all cases or at very early stages of disease. Follow-up studies are sometimes useful to demonstrate that the frontal and anterior temporal atrophy is progressive [6].

The functional neuroimagings demonstrate cortical hypometabolism and/or hypoperfusion in the predominant frontal or frontotemporal [7, 8], which may be present in the early stages of disease in the absence of structural abnormality [7]. The functional imaging studies using ratings or group-averaged findings suggest that predominant frontal or frontotemporal hypometabolism or hypoperfusion may aid in the differential diagnosis of bvFTD [9–22] (Fig. 13.1a–c).

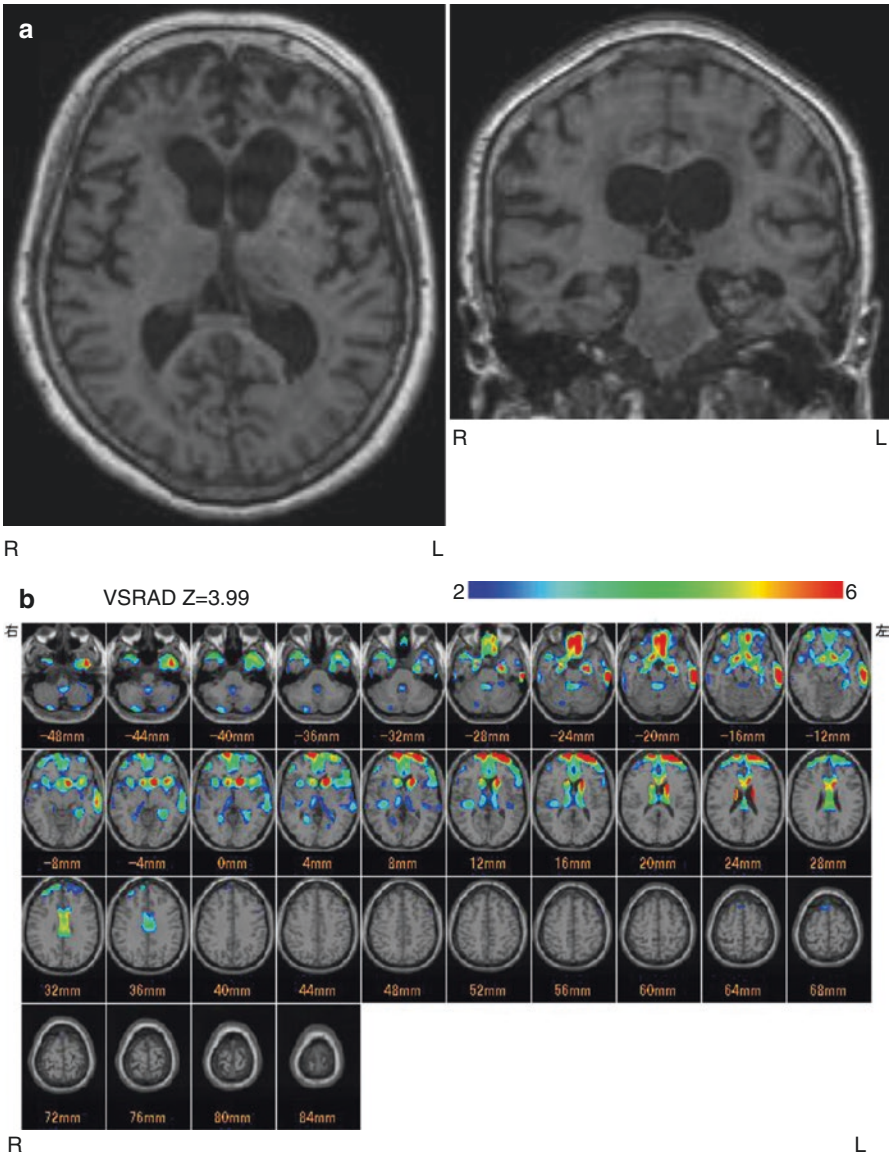

Fig. 13.1 (**a**) MRI (T1) images of bvFTD. The axial (*left*) and coronal (*right*) images demonstrate frontotemporal atrophy. (**b**) The result of VSRAD analysis (normal healthy volunteers vs. bvFTD individual). The colored areas show the regions with atrophy in the bvFTD individual compared with the normal healthy volunteers. (**c**) ^{99m}Tc-ECD SPECT images of bvFTD individual. The axial views demonstrate frontal and anterior temporal hypoperfusion. (**d**) The result of eZIS analysis (normal healthy volunteers vs. bvFTD individual). The colored areas show the regions with hypoperfusion in the bvFTD individual compared with the normal healthy volunteers

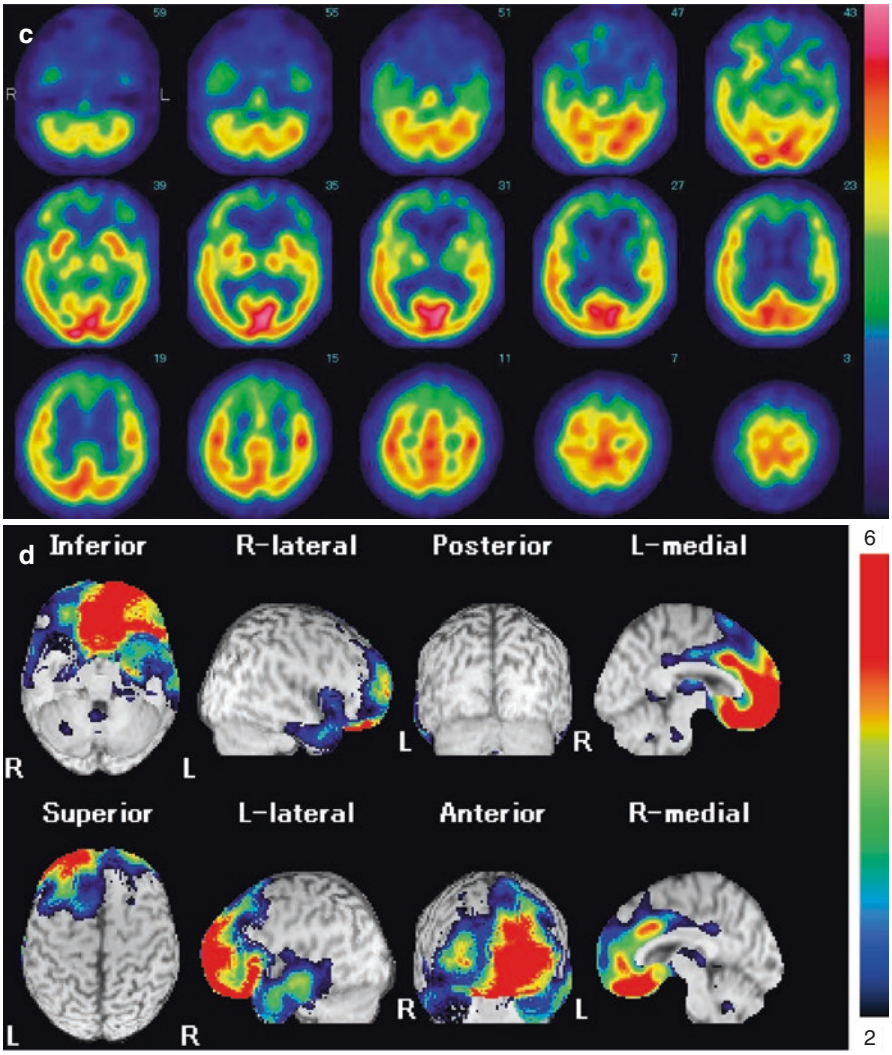

Fig. 13.1 (continued)

13.2.2 Semantic Dementia

Warrington reported three cases with associative agnosia and a fluent-type aphasia characterized by anomia and impaired word comprehension attributed to circumscribed asymmetric atrophy in the anterior temporal lobe, which was considered a selective impairment of semantic memory. Also, this feature was described by Snowden et al. as semantic dementia (SD) [23]. Later, Hodges et al. provided a comprehensive characterization of SD [24]. In 1998, Neary et al. developed diagnosis criteria for SD in relation to frontotemporal lobar degeneration (FTLD) [1].

The diagnosis of SD required a gradually progressive language disorder characterized by fluent, empty, spontaneous speech, loss of word meaning manifested by impaired naming and comprehension, preserved single-word repetition, and preserved ability to read aloud and write down orthographically regular words that are dictated [25]. Instead of the language disorder, individuals with prosopagnosia (impaired recognition of identity of familiar faces) and/or associative agnosia (impaired recognition of object identity) could also be diagnosed as having SD. Other aspects of cognition could be intact or relatively well preserved. Behavioral and personality changes characterized by loss of sympathy and empathy, narrowed preoccupations, and parsimony are included in the supportive diagnostic features, as these changes are considered characteristic of SD and often associated with high diagnostic specificity.

The neuroimaging shows atrophy and hypometabolism and/or hypoperfusion in the middle, inferior, and anterior temporal lobes bilaterally but asymmetrical, with the left side usually being more affected [14] (Fig. 13.2a–c).

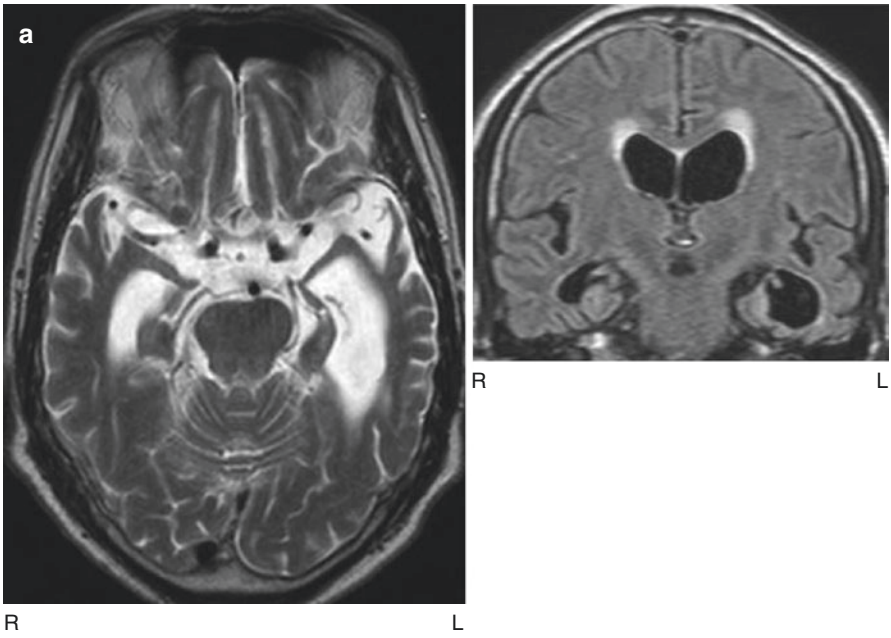

Fig. 13.2 (**a**) MRI (T2: *left*, axial) and (FLAIR: *right*, coronal) images of SD. There is bilateral anterior temporal atrophy disproportionately affecting the left temporal lobe. (**b**) The result of VSRAD analysis (normal healthy volunteers vs. SD individual). The colored areas show the regions with atrophy in the SD individual compared with the normal healthy volunteers. (**c**) ^{99m}Tc-ECD SPECT images of SD individual. The axial views demonstrate bilateral temporal hypoperfusion disproportionately affecting the left temporal lobe. (**d**) The result of eZIS analysis (normal healthy volunteers vs. SD individual). The colored areas show the regions with hypoperfusion in the SD individual compared with the normal healthy volunteers

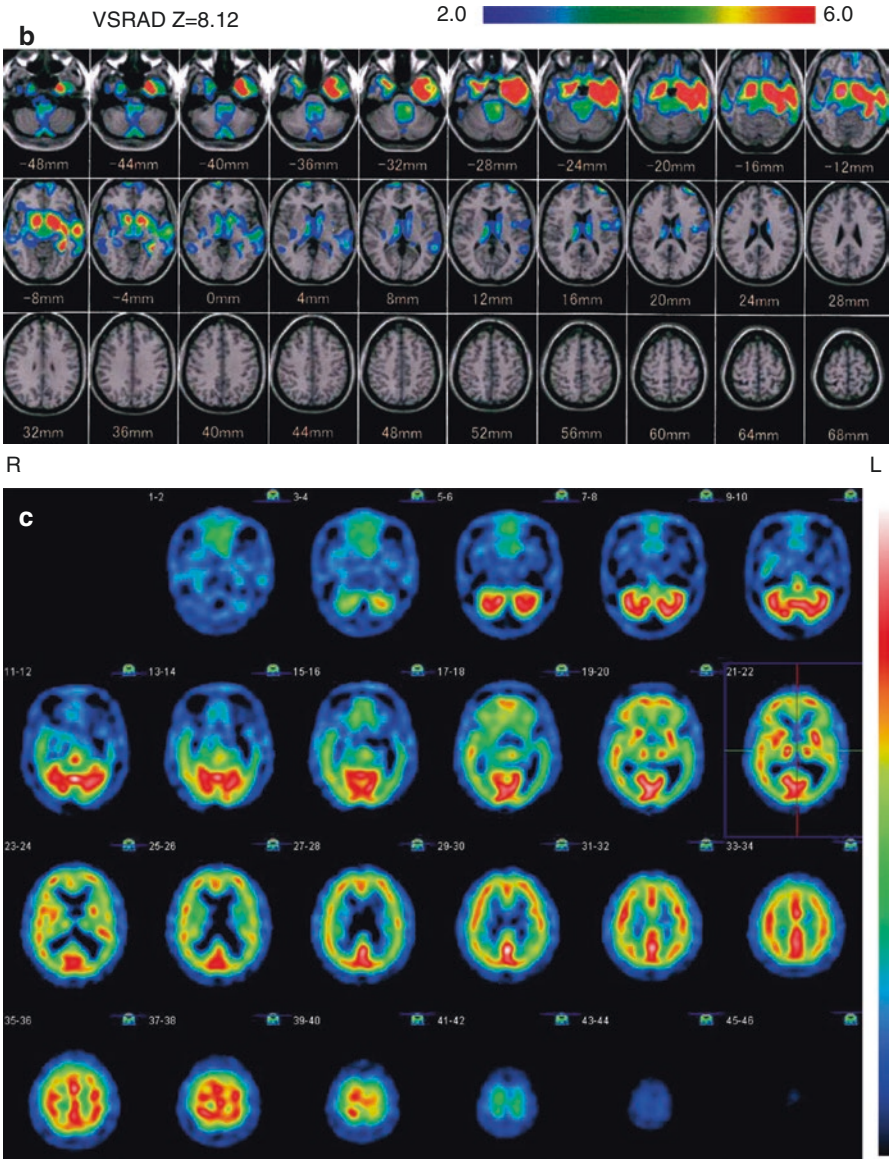

Fig. 13.2 (continued)

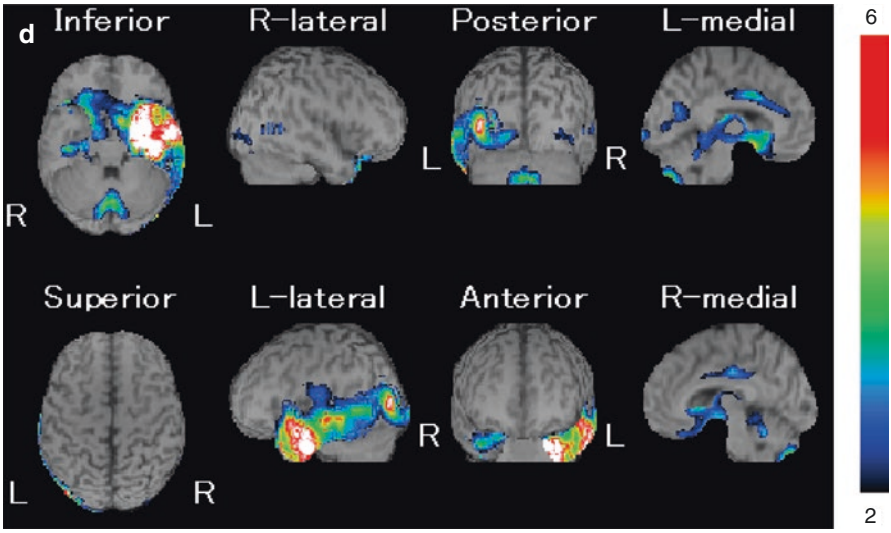

Fig. 13.2 (continued)

13.2.3 Progressive Nonfluent Aphasia

Grossmann et al. reported a different form of progressive language disorder, which was marked by dysfluent and effortful speech, hesitations, and errors in the production of speech sounds, and termed it progressive nonfluent aphasia (PNFA) [26]. In 1998, Neary et al. developed diagnostic criteria for PNFA in relation to FTLD [1].

The diagnosis of PNFA required gradually progressive nonfluent spontaneous speech with at least one of the following symptoms: agrammatism, phonemic paraphasias, or anomia [25]. Other aspects of cognition could be intact or relatively well preserved. Late behavioral changes similar to bvFTD are included as supportive diagnostic features.

The neuroimages show predominantly atrophy and hypometabolism and/or hypoperfusion in the left posterior frontal–insular region [27–29] (Fig. 13.3a–c).

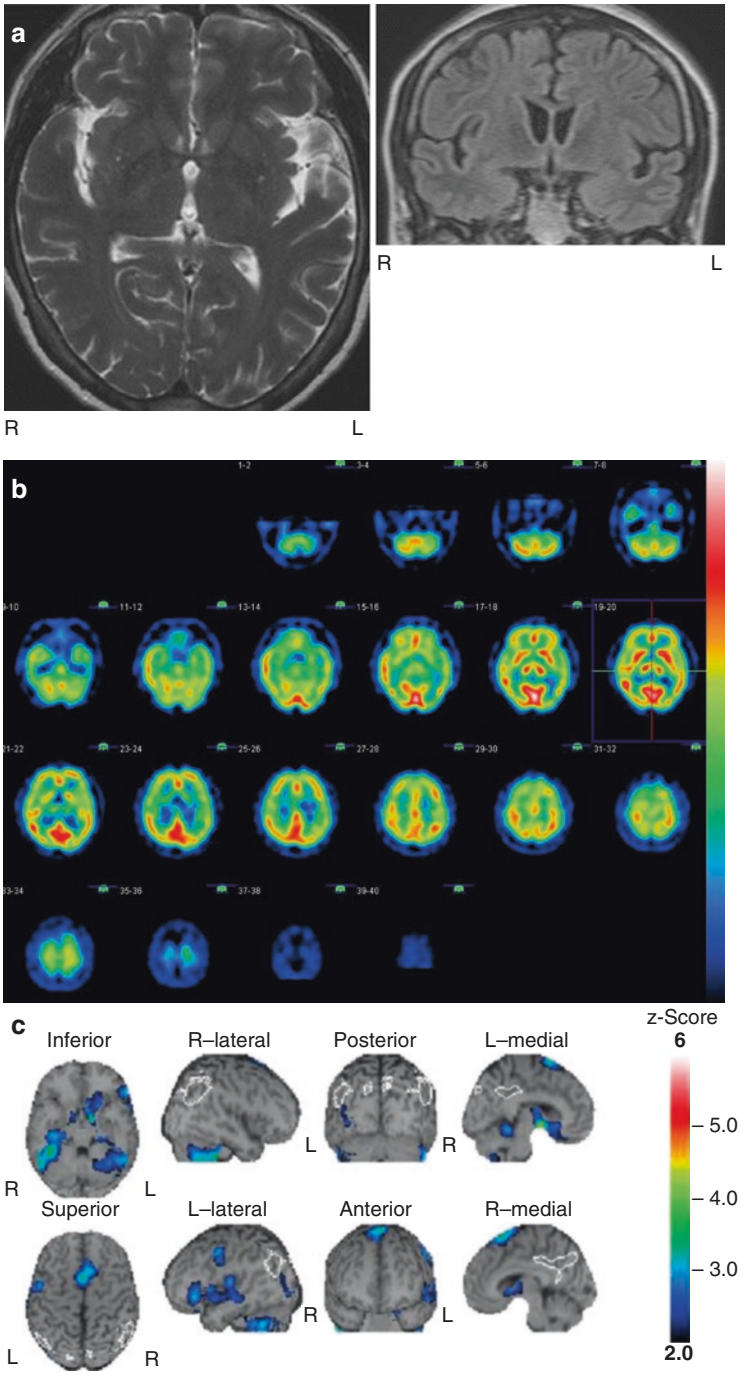

Fig. 13.3 (**a**) MRI (T2: *left*, axial) and (FLAIR: *right*, coronal) images of PNFA. The images demonstrate asymmetric atrophy of the left Sylvian fissure. (**b**) ^{99m}Tc-ECD SPECT images of PNFA individual. The axial views demonstrate asymmetric hypoperfusion in the left posterior frontal–insular. (**c**) The result of eZIS analysis (normal healthy volunteers vs. PNFA individual). The colored areas show the regions with hypoperfusion in the PNFA individual compared with the normal healthy volunteers

References

1. Neary D, Snowden JS, Gustafson L, et al. Frontotemporal lobar degeneration: a consensus on clinical diagnostic criteria. Neurology. 1998;51:1546–54.
2. Ratnavalli E, Brayne C, Dawson K, et al. The prevalence of frontotemporal dementia. Neurology. 2002;58:1615–21.
3. Onyike CU, Diel-Schmid J. The epidemiology of frontotemporal dementia. Int Rev Psychiatr. 2013;25:130–7.
4. Roskovsky K, Hodges JR, Knopman D, et al. Sensitivity of revised diagnostic criteria for the behavior variant of frontotemporal dementia. Brain. 2011;134:2456–77.
5. Rosen HJ, Gorno-Tempini ML, Goldman WP, et al. Patterns of brain atrophy in frontotemporal dementia and semantic dementia. Neurology. 2002;58:198–208.
6. Whitwell JL, Josephs KA. Recent advances in the imaging of frontotemporal dementia. Curr Neurol Neurosci Rep. 2012;12:715–23.
7. Mendez MF, Shapira JS, McMurtray A, et al. Accuracy of the clinical evaluation for frontotemporal dementia. Arch Neurol. 2007;64:830–5.
8. Womack KB, Diaz-Arrastia R, Aizenstein HJ, et al. Temporoparietal hypometabolism in frontotemporal lobar degeneration and associated imaging diagnostic errors. Arch Neurol. 2011;68:329–37.
9. Starkstein SE, Migliorelli R, Teson A, et al. Specificity of changes in cerebral blood in patients with frontal lobe dementia. J Neurol Neurosurg Psychiatry. 1994;57:790–6.
10. Real SL, Miller BL, Mena I, et al. SPECT in dementia: clinical and pathological correlation. J Am Geriatr Soc. 1995;43:1243–7.
11. Charpentier P, Lavenu I, Defebvre L, et al. Alzheimer's disease and frontotemporal dementia are differentiated by discriminant analysis applied to (99m)Tc HmPAO SPECT data. J Neurol Neurosurg Psychiatry. 2000;69:661–3.
12. Sjogren M, Gustafson L, Wikkelso C, et al. Frontotemporal dementia can be distinguished from Alzheimer's disease and subcortical white matter dementia by an anterior-to-posterior rCBF-SPECT ratio. Dementia Geriatr Cogn Dis. 2000;11:275–85.
13. Salmon E, Garraux G, Delbeuck X, et al. Predominant ventromedial frontopolar metabolic impairment in frontotemporal dementia. NeuroImage. 2003;20:435–40.
14. Diehl J, Grimmer T, Drzezga A, et al. Cerebral metabolic patterns at early stages of frontotemporal dementia and semantic dementia. A PET study. Neurobiol Aging. 2004;25:1051–6.
15. Franseschi M, Anchisi D, Pelati O, et al. Glucose metabolism and serotonin receptors in the frontotemporal lobe degeneration. Ann Neurol. 2005;57:216–25.
16. Jeong Y, Cho SS, Park JM, et al. 18F-FDG PET findings in frontotemporal dementia: an SPM analysis of 29 patients. J Nucl Med. 2005;46:233–9.
17. Le Ber I, Guedj E, Gabelle A, et al. Demographic, neurological and behavioral characteristics and brain perfusion SPECT in frontal variant of frontotemporal dementia. Brain. 2006;129:3051–65.
18. Nakano S, Asada T, Yamashita F, et al. Relationship between antisocial behavior and regional cerebral blood flow in frontotemporal dementia. NeuroImage. 2006;32:301–6.
19. Peters F, Perani D, Herholz K, et al. Orbitofrontal dysfunction related to both apathy and disinhibition in frontotemporal dementia. Dement Geriatr Cogn Disord. 2006;21:373–9.
20. Salmon E, Kerrouche N, Herholz K, et al. Decomposition of metabolic brain clusters in the frontal variant of frontotemporal dementia. NeuroImage. 2006;30:871–8.
21. McNeill R, Sare GM, Manoharan M, et al. Accuracy of single-photon emission tomography in differentiating frontotemporal dementia from Alzheimer's disease. J Neurol Neurosurg Psychiatry. 2007;78:350–5.
22. Schroeter ML, Raczka K, Neumann J, et al. Neural networks in frontotemporal dementia-a meta analysis. Neurobiol Aging. 2008;29:418–26.
23. Warrington EK. The selective impairment of semantic memory. QJ Exp Psychol. 1975;27:635–57.

24. Hodges JR, Patterson K, Oxbury S, et al. Semantic dementia. Progressive fluent aphasia with temporal lobe atrophy. Brain. 1992;115:1783–806.
25. Ichimi N, Hashimoto M, Matsusita M, et al. The relationship between primary progressive aphasia and neurodegenerative dementia. East Asian Arch Psychiatry. 2013;23:120–5.
26. Grossman M, Mickanin J, Onishi K, et al. Progressive nonfluent aphasia: language, cognitive and PET measures contrasted with probable Alzheimer's disease. J Cogn Neurosci. 1996;8:135–54.
27. Grono-Tempini ML, Dronkers NF, et al. Cognition and anatomy in three variants of primary progressive aphasia. Ann Neurol. 2004;55:335–46.
28. Whiwell JL, Avula R, Senjem ML, et al. Gray and white matter water diffusion in the syndromic variants of frontotemporal dementia. Neurology. 2010;74:1279–87.
29. Nestor PJ, Graham NL, Fryer TD, et al. Progressive non-fluent aphasia is associated with hypometabolism centred on the left anterior insula. Brain. 2003;126:2406–18.

Neuroimaging Study of Alzheimer's Disease in Volunteer-Based Cohort

14

Miharu Samuraki, Ichiro Matsunari, and Masahito Yamada

Abstract

Neuroimaging techniques such as positron emission tomography (PET) or magnetic resonance imaging (MRI) may provide opportunities to detect AD-related signatures at early or even preclinical stage. We initiated the Ishikawa Brain Imaging Study (IBIS) in 2002 to establish the Japanese standard brain images and to seek imaging biomarkers for clinical and preclinical assessment of AD and other forms of neurodegenerative diseases using PET and MRI. At present, approximately 1400 volunteer subjects and 610 patients with dementia participated in the study. We found that normalcy rate in volunteer-based population decreases significantly as a function of age. Furthermore, neuroimaging biomarkers are affected by factors such as age, but uncertainty still exists as to the effect of ApoE ε4 allele in cognitively normal subjects. Therefore, more work is necessary for better understanding of interaction between genetic or nongenetic factors such as ApoE ε4 allele or aging and neuroimaging biomarkers.

Keywords

MRI • Normal aging • PET • Volunteer-based cohort

M. Samuraki • M. Yamada
Department of Neurology and Neurobiology of Aging, Kanazawa University Graduate School of Medical Sciences, Kanazawa, Ishikawa, Japan

I. Matsunari (✉)
Division of Nuclear Medicine, Department of Radiology, Saitama Medical University Hospital, 38 Morohongo, Moroyama, Irumagun, Saitama 350-0495, Japan
e-mail: m_ichiro@saitama-med.ac.jp

H. Matsuda et al. (eds.), *Neuroimaging Diagnosis for Alzheimer's Disease and Other Dementias*, DOI 10.1007/978-4-431-55133-1_14

14.1 Introduction

Alzheimer's disease (AD) is the leading form of age-related dementia in many countries. Therefore, efforts have been made to develop techniques to detect abnormalities associated with the presence and severity of AD. Neuroimaging techniques such as positron emission tomography (PET) or magnetic resonance imaging (MRI) may provide opportunities to detect AD-related signatures at early or even preclinical stage [1, 2]. In this regard, neuroimaging studies in cognitively normal subjects are important to identify individuals who are likely to develop dementia at later stage. Furthermore, the identification of small disease-related changes in neuroimaging biomarkers such as those seen in AD at early stage requires a carefully prepared normal database (NDB) to be compared to the target subjects on voxel-by-voxel basis. To address these issues, we initiated the Ishikawa Brain Imaging Study (IBIS) [3–6] in 2002, which is the largest single-center PET study aiming at neurodegenerative disease in Japan.

In this chapter, we provide an overview of the IBIS, including study purpose, design, and recruitment process, mainly focusing on cognitively normal subjects. Additionally, we discuss the results obtained so far and some issues related to neuroimaging study of cognitively normal subjects such as normalcy rate.

14.2 Study Description

14.2.1 Study Purpose and Design

The IBIS is a single-center nonrandomized prospective study to establish the Japanese standard brain images and to seek imaging biomarkers for clinical and preclinical assessment of AD and other forms of neurodegenerative diseases using PET and MRI. The study participants have been recruited via newspaper advertisement in Hakui, Japan, or an academic memory disorders clinic at Kanazawa University Hospital (Kanazawa, Japan). Because this is a single-center study, all the imaging procedures have been performed at the Medical and Pharmacological Research Center Foundation (Hakui, Japan) using a single PET (Advance, GE Healthcare, Milwaukee, WI, USA) or MRI (Signa Horizon, GE Healthcare, Milwaukee, WI, USA) system with a homogeneous study protocol.

14.2.2 Examination Procedure

All subjects undergo physical and neuropsychological examinations by neurologists, ^{18}F-fluorodeoxyglucose (FDG) PET, and brain MRI and reply to the

questionnaire for clinical information. Cognitive ability is assessed using the Mini-Mental Status Examination (MMSE). The brain MRI scans (3D-T1, T2, MR angiography) are performed in all subjects on the same day of PET scan. As an option, a subset of subjects also undergo brain amyloid imaging using ^{11}C-Pittsburg compound B (^{11}C-PIB). At present (December 17, 2014), approximately 1400 volunteer subjects and 610 patients with dementia participated in the study.

14.3 Criteria for Normal and Normalcy Rate

Neuroimaging such as PET or structural MRI is considered to be a sensitive and reliable marker of AD-associated abnormalities. This is particularly true when combined with statistical image analysis such as three-dimensional stereotactic surface projections (3D-SSP) [7] or statistical parametric mapping (SPM) [8]. Using statistical approach, images of diseased population are typically compared with those of age-matched cognitively "healthy" normals on voxel-by-voxel basis to identify disease-associated abnormalities. Therefore, recruitment of normals represents a critical issue for the study design and interpretation. In such studies, normal subjects have often been recruited from a pool of volunteer-based population, where the subjects' age varies considerably from study to study depending on study target. To date, however, there have been few studies that focused on the prevalence of normals aiming at neuroimaging in volunteer-based population. We investigated the normalcy rate in such population particularly in relation to age. The criteria to define "normal" were no history of neuropsychological disorders, normal findings on physical and neurological examinations, and normal findings on brain MRI that indicated no asymptomatic cerebral infarctions/hemorrhages/tumors or brain vessel abnormalities on T1-/T2-weighted MRI or MR angiography. Cognitive ability was assessed using the MMSE, and those with an MMSE score of 28 or higher and no clinical evidence of dementia were considered to be normal. We found that even in the voluntary population, there were considerable number of subjects who had abnormalities in neurological examination (Fig. 14.1), a reduced MMSE score (Fig. 14.2), or abnormal findings on MRI (Fig. 14.3). As a result, the overall normalcy rate was not very high, which was particularly true in the elderly subjects (Fig. 14.4). In contrast to the elderly subjects, the normalcy rate in the younger subjects (≤50 years) was relatively high. Thus, normalcy rate in volunteer-based population decreases significantly as a function of age. This should be taken into account when planning a clinical study recruiting volunteers as normal controls.

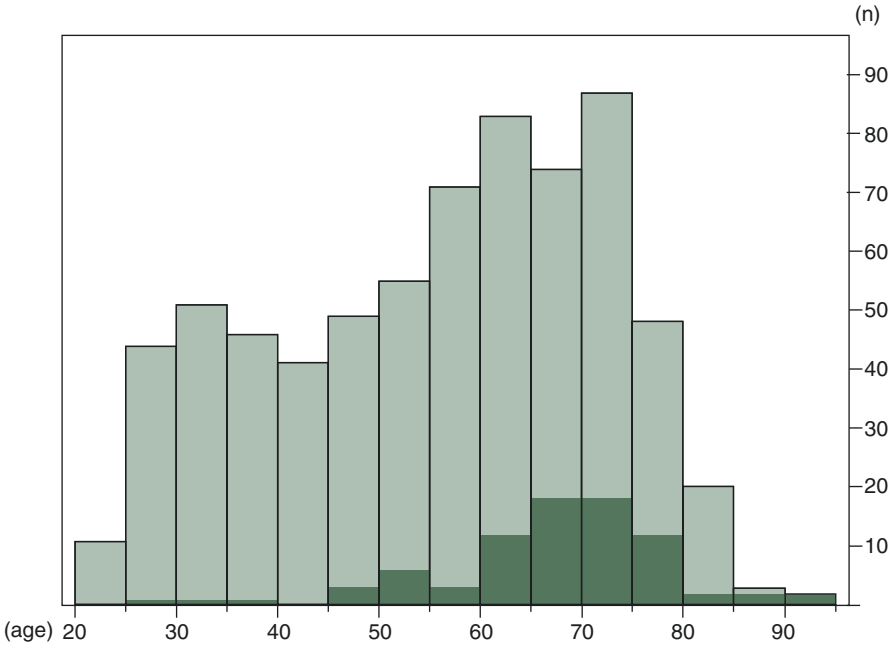

Fig. 14.1 Age distribution of volunteers who revealed neurological abnormalities (e.g., pathological reflex, sensory or motor abnormalities) by physical examination. Of the 685 volunteers (*dark* + *light green*), 81 revealed neurological abnormalities (*dark green*)

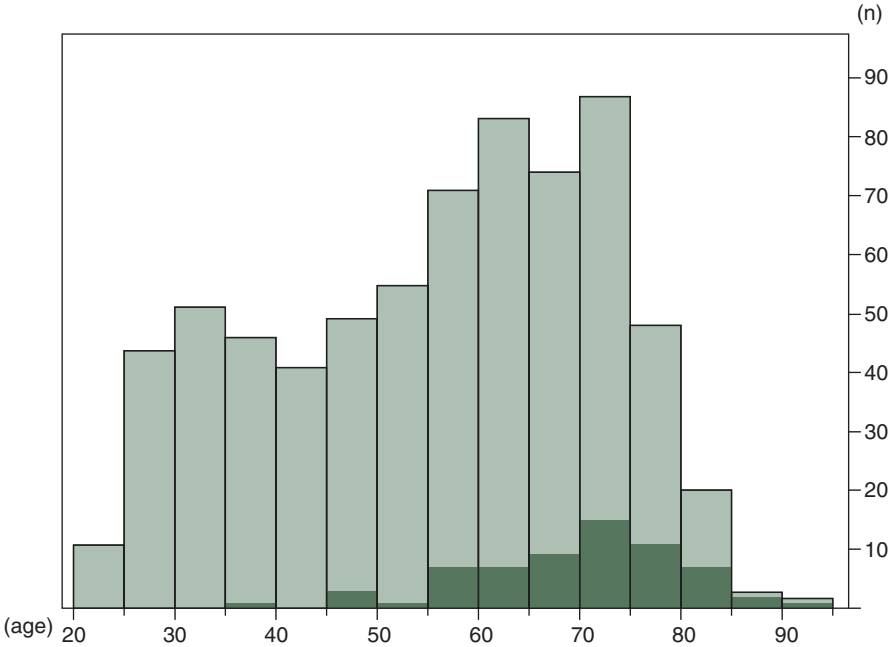

Fig. 14.2 Age distribution of volunteers who had an MMSE score of <28. Of the 685 volunteers (*dark* + *light green*), 54 did not reach an MMSE score of ≥28 (*dark green*)

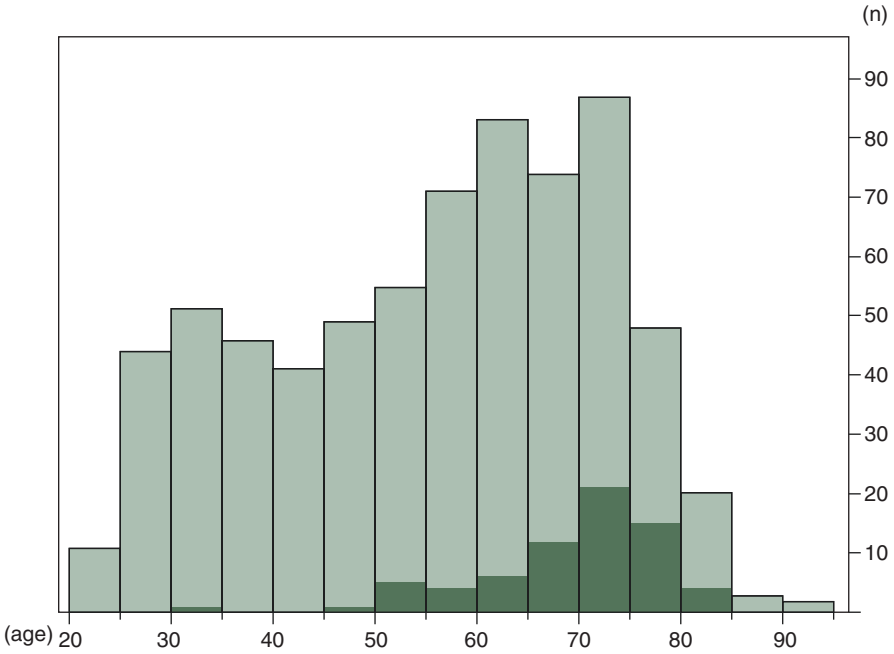

Fig. 14.3 Age distribution of volunteers who revealed asymptomatic abnormalities on brain MRI. Of the 685 volunteers (*dark* + *light green*), 69 showed asymptomatic abnormalities (*dark green*)

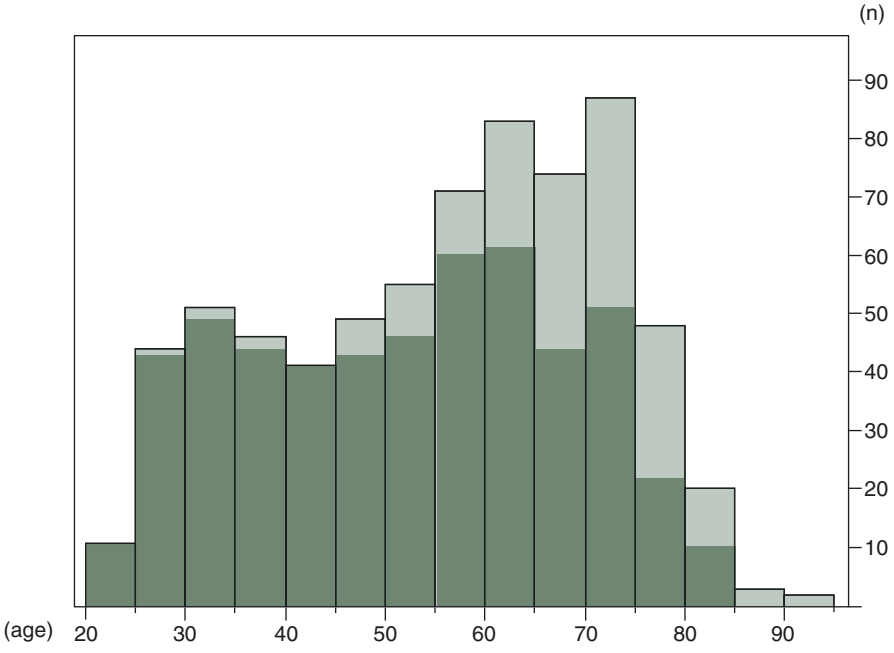

Fig. 14.4 Age distribution of volunteers who were finally considered to be normal. Of the 685 volunteers (*dark* + *light green*), 530 (77%) were finally considered to be normal (*dark green*). The prevalence of normal subjects declined as a function of age, and 53% (85/160) of the elderly subjects (≥70 years) were considered to be normal

14.4 Normal Database Generation

In addition to the aforementioned criteria for normal controls, how NDB is generated represents an important issue because the statistical image analysis depicts differences in images between a patient and NDB on a voxel-by-voxel basis. For example, the sample size for NDB may affect its diagnostic performance. However, there have been few data available that focused on the effect of sample size for NDB on diagnostic performance of PET and MRI using statistical image analysis. In this context, we generated nine NDB sets consisting of 4, 6, 8, 10, 20, 30, 40, 50, and 60 normal subjects to assess the diagnostic performance using these NDBs to distinguish AD patients from normal subjects [9]. We found that small NDBs ($n \leq 10$) yielded poor quality of mean and standard deviation (SD) images as compared with large NDBs ($n \geq 20$) as illustrated in Fig. 14.5 [9], and the area under the receiver operating characteristic (ROC) curves (AUCs) of the large NDBs ($n \geq 20$) did not fall below 0.950, where AUCs of the small NDBs ($n \leq 10$) never exceeded 0.950. Based on the results, we recommend to include at least 20 subjects for generating NDBs.

In addition to appropriate sample size, age and sex matching between a target subject and NDB is regarded as an important factor for NDB generation. We investigated whether the diagnostic performance of FDG PET for AD could be maintained even with age-mismatched and sex-mismatched NDB [10]. In that study, we generated six age-specific NDB sets consisting of participants ranging in age from 20 to 70 years and two sex-specific NDB sets, each consisting of only men or women. We found that there was no significant difference in each z-map and AUC either between

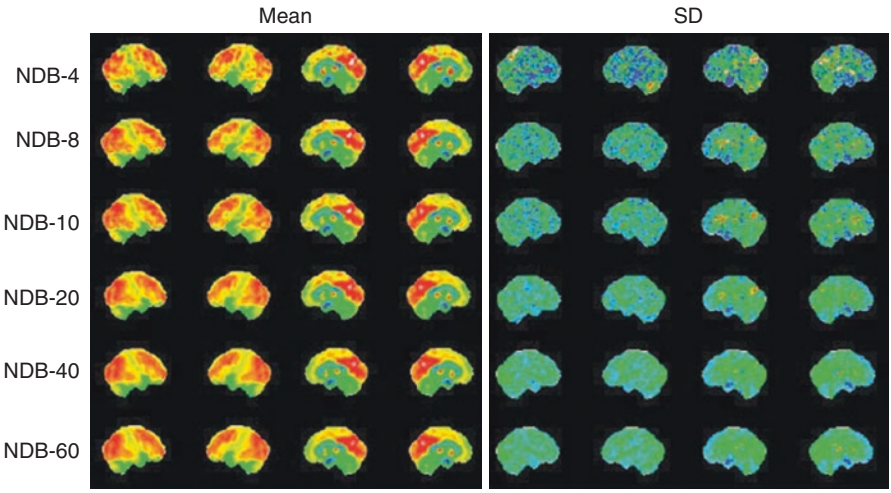

Fig. 14.5 Mean (*left*) and standard deviation (SD) (*right*) images generated from each normal database (NDB). NDB-n indicates normal database sample size. The quality of the mean and SD images of NDB was relatively poor when the sample size for NDB was small ($n \leq 10$); however, both mean and SD image became smoother as the sample size increased. (Adopted from Chen et al. [9])

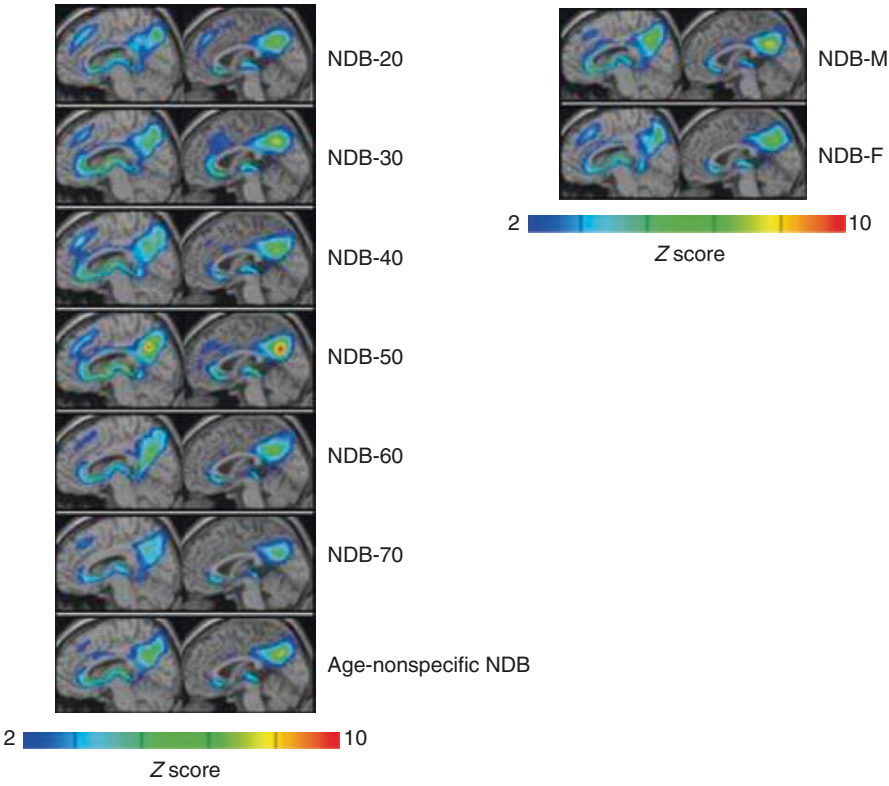

Fig. 14.6 FDG PET *z*-maps of a 59-year-old woman patient with probable Alzheimer's disease. (**a**) *z*-maps generated by each age-related normal database (NDB) set and (**b**) *z*-maps generated by each sex-related NDB set. The *z*-maps of FDG PET do not seem to be so different among the NDB sets. (Adopted from Chen et al. [10])

age-matched and mismatched NDB sets or between sex-matched and mismatched NDB sets, as illustrated in Fig. 14.6. Thus, exact age-matched or sex-matched NDB may not be mandatory for discriminating patients with AD from normal subjects using FDG PET. However, it should be noted that these results are validated only for discrimination of AD from normal controls, and there has been no such a study on MRI. Therefore, we recommend to use age- and sex-matched NDB whenever available to avoid missing any subtle changes between a target subject and NDB.

14.5 Normal Aging on FDG PET

Although the relationship between normal aging and cerebral glucose metabolism has been repeatedly examined using FDG PET, inconsistent results have been reported [11–22]. In our prior study using partial-volume effect (PVE) correction for FDG PET [3], we found that reduction in FDG uptake with advancing age,

detected by FDG PET without PVE correction, could be accounted for largely by an age-related cerebral volume loss in the bilateral perisylvian and medial frontal areas; after PVE correction, the area of age-related FDG decline was confined to fewer regions, including the anterior cingulate and inferior frontal gyrus (Fig. 14.7).

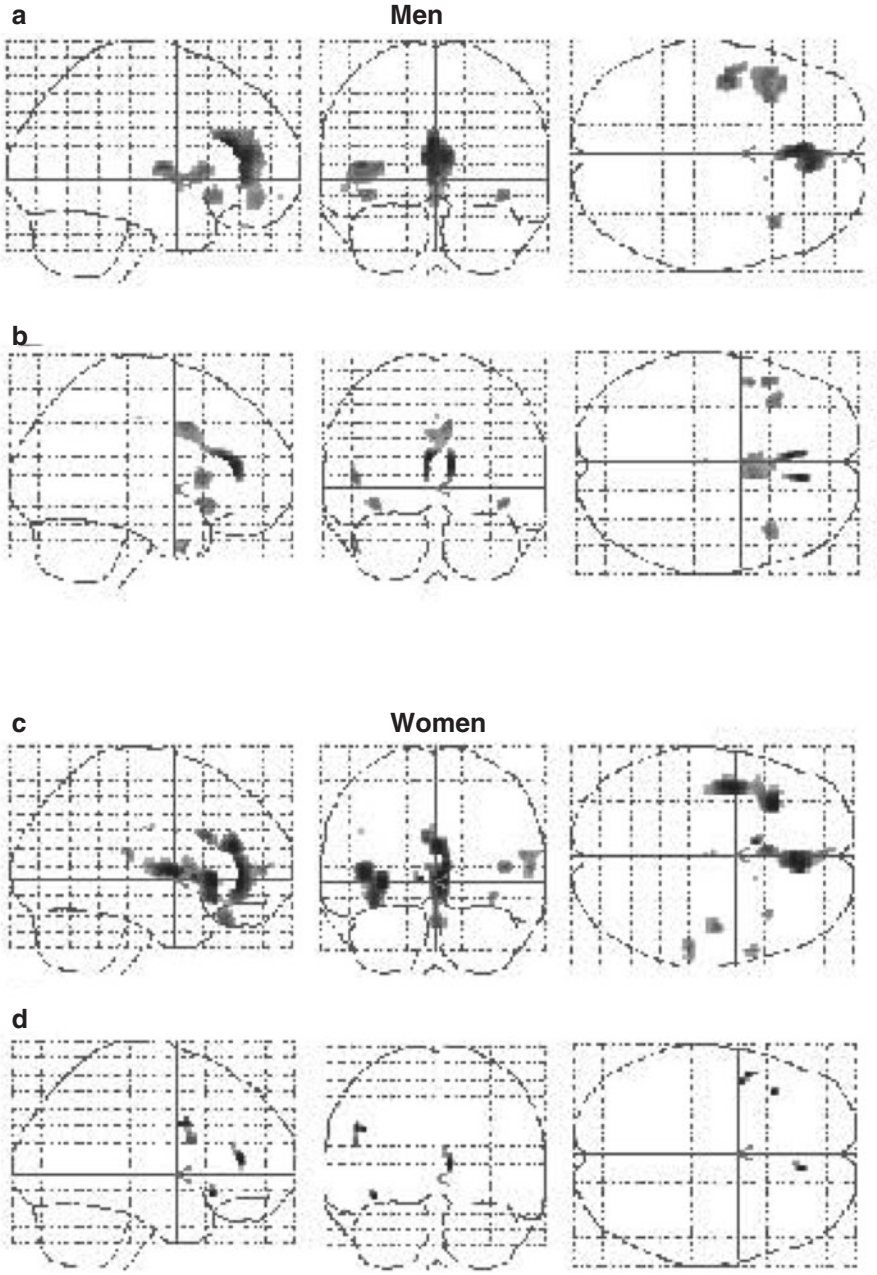

Fig. 14.7 Maximum intensity projections of SPM results for negative correlation of relative FDG activity with advancing age in men and women before (**a**, **c**) and after (**b**, **d**) partial volume effect (PVE) correction. Height threshold <0.001, corrected for multiple comparisons. (Adopted from Yanase et al. [3])

The effect of PVE correction was most significant in the regions showing negative correlations between age and gray matter volumes as assessed by structural MRI and voxel-based morphometry (Fig. 14.8). In a more recent study, however, Knopman et al. [23] observed a modest but significant age-related FDG decline in

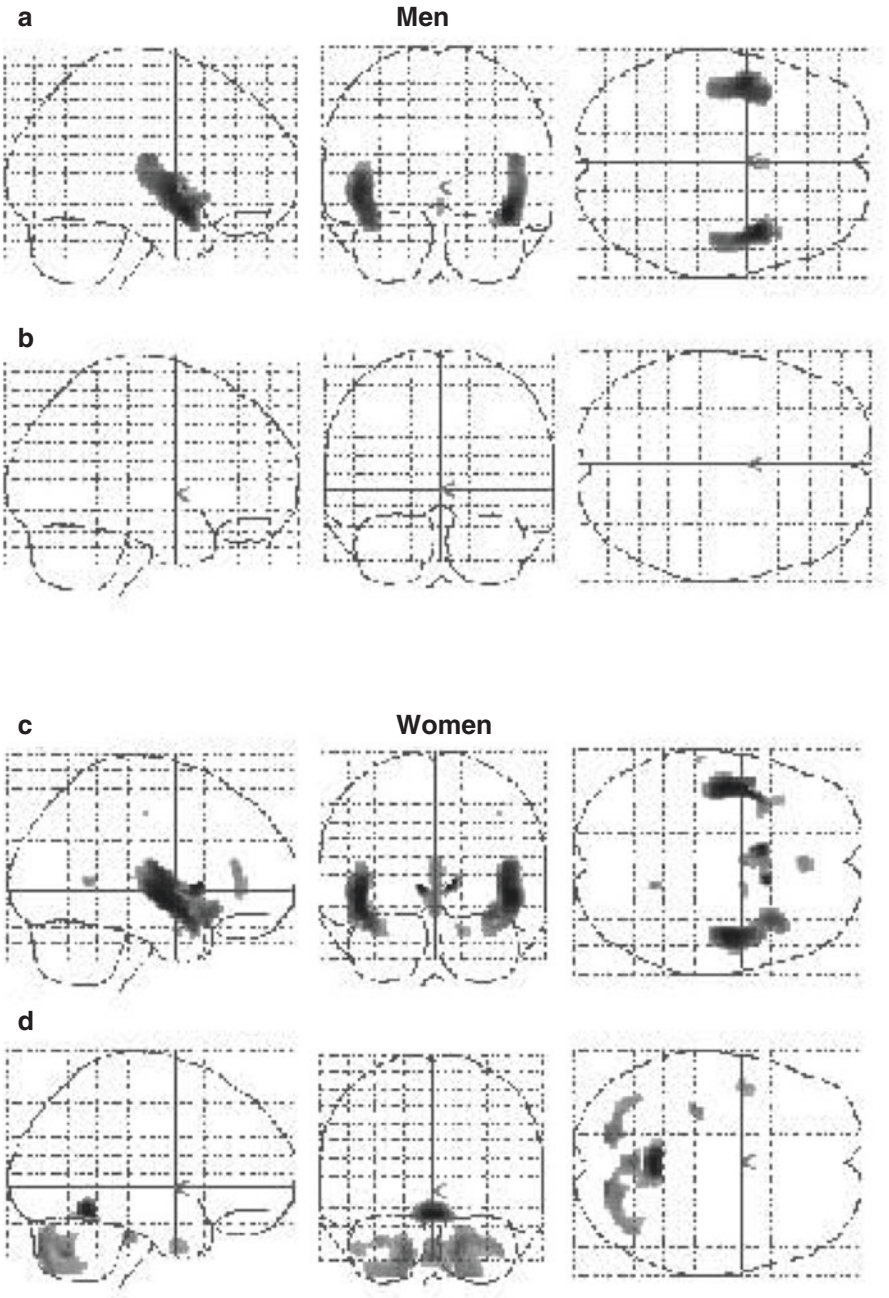

Fig. 14.8 Maximum intensity projections of SPM results for negative (**a**, **c**) and positive (**b**, **d**) correlation of regional gray matter volume with advancing age in men and women. Height threshold <0.001, corrected for multiple comparisons. (Adopted from Yanase et al. [3])

many brain regions, including areas that are known to be affected in AD, such as the posterior cingulate/precuneus, even after correction for atrophy. Thus, more work is necessary for better understanding of interaction between normal aging and brain glucose metabolism.

14.6 Effect of Apolipoprotein E (ApoE) ε4 Allele on Neuroimaging Biomarkers

There is a general agreement that the apolipoprotein E (ApoE) ε4 is a genetic risk factor for developing AD. The ApoE ε4 allele has been associated with glucose metabolic activity impairment in AD-signature regions even in cognitively normal subjects in some studies [24, 25]. As to ApoE ε4-related structural alterations measured by MRI, conflicting results exist as to whether loss of gray matter truly occurs in ε4 carriers [25, 26]. In a study by Reiman et al. [25], the ApoE ε4 homozygotes showed nonsignificant trends for smaller hippocampal volumes, whereas there was a significant decrease of gray matter in e4 homozygous subjects, as compared both to e4 heterozygous subjects and to noncarrier subjects in a study by Lemaitre et al. [26]. In a more recent study by Knopman et al. [23], there was an APOE ε4-associated FDG decline in AD-vulnerable regions, which was independent of amyloid burden, as measured by ^{11}C-PIB PET. In our prior study [5], however, the prevalence of AD-like imaging abnormalities, such as an FDG decline in the posterior cingulate/precuneus or hippocampal atrophy, did not differ among ApoE ε4 carriers with normal cognitive function and noncarriers, as illustrated in Fig. 14.9. Furthermore, the prevalence of FDG PET or MRI abnormalities suggestive of AD in cognitively normal ε4 carriers was rather low and did not differ from that in noncarriers, indicating that the presence of ApoE ε4 allele alone may not be sufficient to induce AD-like imaging abnormalities in the majority of cognitively normal subjects. Although the precise mechanisms explaining for the inconsistent results are unclear, there are several differences between the studies. Firstly, unlike the study by

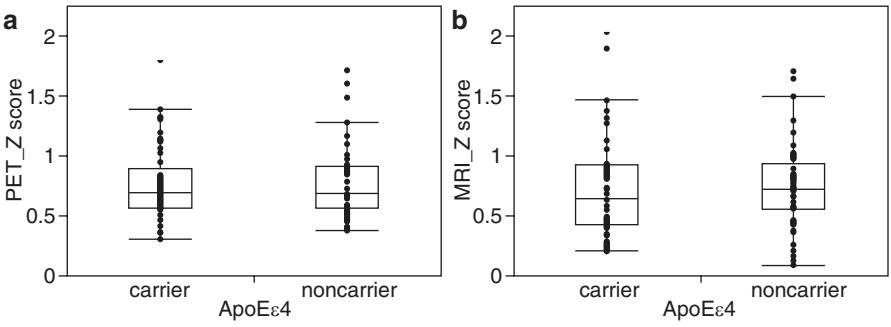

Fig. 14.9 Box-and-whisker plots of mean *z*-score in the AD-specific region of interest (ROI) on FDG PET (**a**) and MR image (**b**) in apolipoprotein E (ApoE) ε4 carrier group and noncarrier group. (Adopted from Samuraki et al. [5])

Knopman et al. [23], we did not use PVE correction for FDG PET, because we expected that uncorrected FDG signal would reflect both metabolism and atrophy due to PVE and therefore may serve as a more sensitive marker of AD-associated changes. This should particularly be the case in individuals with posterior cingulate/precuneus atrophy, which is known to occur in a subset of AD patients [6]. Secondly, our study participants were much younger (mean age: 53.6 years for the ε4 carriers and 53.5 years for the noncarriers) than those (median age: 76 years) in Knopman et al. study [23]; the majority of our participants were 30–60 years old: there were no significant differences between ε4 carriers and noncarriers in that age group in their study [23]. The ApoE ε4-associated FDG decline may be more difficult to detect in such young subjects. These circumstances, alone or in combination, may have contributed to the somewhat discordant observations between the studies. Furthermore, it should be noted that many factors other than ApoE ε4, such as diabetes mellitus, are likely to be involved in the development of AD-like imaging signatures in cognitively normal individuals, which has been demonstrated in a recent study by Roberts et al. [27]. The same study group has also demonstrated that midlife onset of diabetes may affect late-life cognition through loss of brain volume [28]. Thus, it is likely that the effect of ApoE ε4 allele on neuroimaging biomarkers can be modulated by the coexistence of non-ApoE factors, and therefore care should be taken when interpreting the results.

Conclusion

The IBIS is a single-center nonrandomized prospective study to establish the Japanese standard brain images and to seek imaging biomarkers for clinical and preclinical assessment of AD and other forms of neurodegenerative diseases using PET and MRI. The study participants have been recruited via newspaper advertisement or an academic memory disorders clinic. At present, approximately 1400 volunteer subjects and 610 patients with dementia participated in the study. We found that normalcy rate in volunteer-based population decreases significantly as a function of age. Furthermore, neuroimaging biomarkers are affected by factors such as age, but uncertainty still exists as to the effect of ApoE ε4 allele in cognitively normal subjects. Therefore, more work is necessary for better understanding of interaction between genetic or nongenetic factors such as ApoE ε4 allele or aging and neuroimaging biomarkers.

References

1. Jack CR Jr, Holtzman DM. Biomarker modeling of Alzheimer's disease. Neuron. 2013;80(6):1347–58. doi:10.1016/j.neuron.2013.12.003.
2. Weiner MW, Veitch DP, Aisen PS, Beckett LA, Cairns NJ, Green RC, Harvey D, Jack CR, Jagust W, Liu E, Morris JC, Petersen RC, Saykin AJ, Schmidt ME, Shaw L, Shen L, Siuciak JA, Soares H, Toga AW, Trojanowski JQ. The Alzheimer's disease neuroimaging initiative: a review of papers published since its inception. Alzheimers Dement. 2013;9(5):e111–94. doi:10.1016/j.jalz.2013.05.1769.

3. Yanase D, Matsunari I, Yajima K, Chen W, Fujikawa A, Nishimura S, Matsuda H, Yamada M. Brain FDG PET study of normal aging in Japanese: effect of atrophy correction. Eur J Nucl Med Mol Imaging. 2005;32(7):794–805. doi:10.1007/s00259-005-1767-2.
4. Matsunari I, Samuraki M, Chen WP, Yanase D, Takeda N, Ono K, Yoshita M, Matsuda H, Yamada M, Kinuya S. Comparison of 18F-FDG PET and optimized voxel-based morphometry for detection of Alzheimer's disease: aging effect on diagnostic performance. J Nucl Med. 2007;48(12):1961–70. doi:10.2967/jnumed.107.042820.
5. Samuraki M, Matsunari I, Chen WP, Shima K, Yanase D, Takeda N, Matsuda H, Yamada M. Glucose metabolism and gray-matter concentration in apolipoprotein E epsilon4 positive normal subjects. Neurobiol Aging. 2012;33(10):2321–3. doi:10.1016/j.neurobiolaging.2011.11.020.
6. Shima K, Matsunari I, Samuraki M, Chen WP, Yanase D, Noguchi-Shinohara M, Takeda N, Ono K, Yoshita M, Miyazaki Y, Matsuda H, Yamada M. Posterior cingulate atrophy and metabolic decline in early stage Alzheimer's disease. Neurobiol Aging. 2012;33(9):2006–17. doi:10.1016/j.neurobiolaging.2011.07.009.
7. Minoshima S, Koeppe RA, Frey KA, Kuhl DE. Anatomic standardization: linear scaling and nonlinear warping of functional brain images. J Nucl Med. 1994;35(9):1528–37.
8. Friston KJ, Holmes AP, Worsley KJ, Poline JP, Frith CD, Frackowiak RSJ. Statistical parametric maps in functional imaging: a general linear approach. Hum Brain Mapp. 1995;2:189–210.
9. Chen WP, Samuraki M, Yanase D, Shima K, Takeda N, Ono K, Yoshita M, Nishimura S, Yamada M, Matsunari I. Effect of sample size for normal database on diagnostic performance of brain FDG PET for the detection of Alzheimer's disease using automated image analysis. Nucl Med Commun. 2008;29(3):270–6. doi:10.1097/MNM.0b013e3282f3fa76.
10. Chen WP, Samuraki M, Shima K, Yanase D, Takeda N, Miyazaki Y, Ono K, Yoshita M, Nishimura S, Yamada M, Matsunari I. Effect of an age-mismatched and sex-mismatched normal database on the diagnostic performance of ^{18}F-FDG PET for Alzheimer's disease: the Ishikawa brain imaging study. Nucl Med Commun. 2011;32(12):1128–33. doi:10.1097/MNM.0b013e32834b43c2.
11. Kuhl DE, Metter EJ, Riege WH, Phelps ME. Effects of human aging on patterns of local cerebral glucose utilization determined by the [18F]fluorodeoxyglucose method. J Cereb Blood Flow Metab. 1982;2(2):163–71. doi:10.1038/jcbfm.1982.15.
12. Hawkins RA, Mazziotta JC, Phelps ME, Huang SC, Kuhl DE, Carson RE, Metter EJ, Riege WH. Cerebral glucose metabolism as a function of age in man: influence of the rate constants in the fluorodeoxyglucose method. J Cereb Blood Flow Metab. 1983;3(2):250–3. doi:10.1038/jcbfm.1983.34.
13. Duara R, Grady C, Haxby J, Ingvar D, Sokoloff L, Margolin RA, Manning RG, Cutler NR, Rapoport SI. Human brain glucose utilization and cognitive function in relation to age. Ann Neurol. 1984;16(6):703–13.
14. de Leon MJ, George AE, Tomanelli J, Christman D, Kluger A, Miller J, Ferris SH, Fowler J, Brodie JD, van Gelder P, et al. Positron emission tomography studies of normal aging: a replication of PET III and 18-FDG using PET VI and 11-CDG. Neurobiol Aging. 1987;8(4):319–23.
15. Yoshii F, Barker WW, Chang JY, Loewenstein D, Apicella A, Smith D, Boothe T, Ginsberg MD, Pascal S, Duara R. Sensitivity of cerebral glucose metabolism to age, gender, brain volume, brain atrophy, and cerebrovascular risk factors. J Cereb Blood Flow Metab. 1988;8(5):654–61. doi:10.1038/jcbfm.1988.112.
16. Salmon E, Maquet P, Sadzot B, Degueldre C, Lemaire C, Franck G. Decrease of frontal metabolism demonstrated by positron emission tomography in a population of healthy elderly volunteers. Acta Neurol Belg. 1991;91(5):288–95.
17. Muller-Gartner HW, Links JM, Prince JL, Bryan RN, McVeigh E, Leal JP, Davatzikos C, Frost JJ. Measurement of radiotracer concentration in brain gray matter using positron emission tomography: MRI-based correction for partial volume effects. J Cereb Blood Flow Metab. 1992;12(4):571–83. doi:10.1038/jcbfm.1992.81.

18. Loessner A, Alavi A, Lewandrowski KU, Mozley D, Souder E, Gur RE. Regional cerebral function determined by FDG-PET in healthy volunteers: normal patterns and changes with age. J Nucl Med. 1995;36(7):1141–9.
19. Moeller JR, Ishikawa T, Dhawan V, Spetsieris P, Mandel F, Alexander GE, Grady C, Pietrini P, Eidelberg D. The metabolic topography of normal aging. J Cereb Blood Flow Metab. 1996;16(3):385–98. doi:10.1097/00004647-199605000-00005.
20. Petit-Taboue MC, Landeau B, Desson JF, Desgranges B, Baron JC. Effects of healthy aging on the regional cerebral metabolic rate of glucose assessed with statistical parametric mapping. NeuroImage. 1998;7(3):176–84. doi:10.1006/nimg.1997.0318.
21. Ivancevic V, Alavi A, Souder E, Mozley PD, Gur RE, Benard F, Munz DL. Regional cerebral glucose metabolism in healthy volunteers determined by fluordeoxyglucose positron emission tomography: appearance and variance in the transaxial, coronal, and sagittal planes. Clin Nucl Med. 2000;25(8):596–602.
22. Herholz K, Salmon E, Perani D, Baron JC, Holthoff V, Frolich L, Schonknecht P, Ito K, Mielke R, Kalbe E, Zundorf G, Delbeuck X, Pelati O, Anchisi D, Fazio F, Kerrouche N, Desgranges B, Eustache F, Beuthien-Baumann B, Menzel C, Schroder J, Kato T, Arahata Y, Henze M, Heiss WD. Discrimination between Alzheimer dementia and controls by automated analysis of multicenter FDG PET. NeuroImage. 2002;17(1):302–16.
23. Knopman DS, Jack CR Jr, Wiste HJ, Lundt ES, Weigand SD, Vemuri P, Lowe VJ, Kantarci K, Gunter JL, Senjem ML, Mielke MM, Roberts RO, Boeve BF, Petersen RC. 18F-fluorodeoxyglucose positron emission tomography, aging, and apolipoprotein E genotype in cognitively normal persons. Neurobiol Aging. 2014;35(9):2096–106. doi:10.1016/j.neurobiolaging.2014.03.006.
24. Reiman EM, Caselli RJ, Yun LS, Chen K, Bandy D, Minoshima S, Thibodeau SN, Osborne D. Preclinical evidence of Alzheimer's disease in persons homozygous for the epsilon 4 allele for apolipoprotein E. N Engl J Med. 1996;334(12):752–8. doi:10.1056/NEJM199603213341202.
25. Reiman EM, Uecker A, Caselli RJ, Lewis S, Bandy D, de Leon MJ, De Santi S, Convit A, Osborne D, Weaver A, Thibodeau SN. Hippocampal volumes in cognitively normal persons at genetic risk for Alzheimer's disease. Ann Neurol. 1998;44(2):288–91. doi:10.1002/ana.410440226.
26. Lemaitre H, Crivello F, Dufouil C, Grassiot B, Tzourio C, Alperovitch A, Mazoyer B. No epsilon4 gene dose effect on hippocampal atrophy in a large MRI database of healthy elderly subjects. NeuroImage. 2005;24(4):1205–13. doi:10.1016/j.neuroimage.2004.10.016.
27. Roberts RO, Knopman DS, Cha RH, Mielke MM, Pankratz VS, Boeve BF, Kantarci K, Geda YE, Jack CR Jr, Petersen RC, Lowe VJ. Diabetes and elevated hemoglobin A1c levels are associated with brain hypometabolism but not amyloid accumulation. J Nucl Med. 2014;55(5):759–64. doi:10.2967/jnumed.113.132647.
28. Roberts RO, Knopman DS, Przybelski SA, Mielke MM, Kantarci K, Preboske GM, Senjem ML, Pankratz VS, Geda YE, Boeve BF, Ivnik RJ, Rocca WA, Petersen RC, Jack CR Jr. Association of type 2 diabetes with brain atrophy and cognitive impairment. Neurology. 2014;82(13):1132–41. doi:10.1212/WNL.0000000000000269.

Handling of MRI Data in a Multicenter Study

15

Norihide Maikusa

Abstract

A large-scale multisite clinical study to develop surrogate markers which measure directly the essential process of Alzheimer's disease and other dementias has been launched. It aims to develop a way to assess the stages of disease progression objectively and accurately through a variety of examinations including clinical, psychological, imaging, and biochemical ones. These examinations have been performed for several years at generally about 6 month or 1 year intervals. Especially, the methods that delineate the structural changes caused by the disease using brain structural MRI are known to provide objective and reproducible surrogate biomarkers. However, the image quality of MR brain images depends on the scanners and imaging protocols selected. Moreover the reliability of the automated image analysis algorithm depends on the image quality. Therefore it is necessary to use a consistent imaging protocol and scanner for longitudinal analysis. Moreover, several preprocessing steps such as geometrical distortion correction and intensity inhomogeneity correction are needed to improve the reliability of structural analysis.

Keywords

MRI • Multisite study • Quality control • Preprocessing correction

N. Maikusa
Integrative Brain Imaging Center, National Center of Neurology and Psychiatry,
4-1-1 Ogawahigashi-cho, Kodaira, Tokyo 187-8551, Japan
e-mail: maikusa@ncnp.go.jp

H. Matsuda et al. (eds.), *Neuroimaging Diagnosis for Alzheimer's Disease and Other Dementias*, DOI 10.1007/978-4-431-55133-1_15

15.1 Introduction

Precise and accurate qualification of measurement using serial MR images to measure longitudinal structural brain changes is important in understanding the natural progression of neurodegenerative disorders. Large multicenter studies provide a powerful way to understand and treat neurodegenerative dementias as well as Alzheimer's disease. In recent years, multicenter and longitudinal imaging studies have been undertaken all over the world. The Alzheimer's Disease Neuroimaging Initiative (ADNI) is a large-scale multisite clinical study that aims to develop surrogate markers directly shedding light on the essential process of Alzheimer's disease. ADNI included subjects from over 50 sites across the United States and Canada, and its aims include testing the ability of serial magnetic resonance imaging (MRI), positron emission tomography (PET), biological markers, and clinical and neuropsychological assessments to measure progression in mild cognitive impairment (MCI) and early Alzheimer's disease (AD) [1]. Open Access Series of Imaging Studies (OASIS) is a series of magnetic resonance imaging data sets that is publicly available for study and analysis. OASIS contains a cross-sectional collection of 416 subjects aged 18–96 years [2] and a longitudinal collection of 150 subjects aged 60–96 years, all acquired on the same scanner using identical sequences [3]. In the OASIS longitudinal dataset, MRI and neuropsychological and clinical tests were conducted on two more visits, separated by at least 1 year. Subjects were categorized by the Clinical Dementia Rating (CDR) as being cognitively normal or having very mild Alzheimer's disease.

However, the use of images from different sites and/or scanners introduces particular challenges for image analysis algorithms with the potential to lose sensitivity and cause systematic errors [4] because the image quality of MRI brain images depends on the scanners and imaging protocols used. Therefore it is necessary to use a consistent imaging protocol and scanner for the longitudinal analysis. Figure 15.1 shows examples of differences between MR image qualities. Figure 15.1a shows a good quality image, while in Fig. 15.1b a blurring artifact can be seen around the frontal gyrus. Figure 15.1c shows a poor signal-to-noise ratio (SNR) and contrast between gray matter (GM) and white matter (WM). The poor SNR and tissue contrast may degrade the image analysis' reliability and reproducibility interfering with the appreciation of neurodegenerative changes, because many algorithms need to segment GM regions from the brain based on the differential MRI intensity. So quality control that means grading image quality and excluding poor quality is necessary.

Moreover, several preprocessing steps such as geometrical distortion correction and intensity inhomogeneity correction are needed to improve the reliability of structural analysis. Intensity nonuniformity is caused by poor radio frequency coil uniformity, eddy currents, and insufficient sensitivity of the receiving coil. This issue has little impact on the visual diagnosis, but in automatic segmentation techniques, it can significantly degrade the reliability of these results [5]. Geometrical distortion is generated by gradient nonlinearity, nonuniformity of the static magnetic field, and distribution of magnetic susceptibility. The geometric distortions in

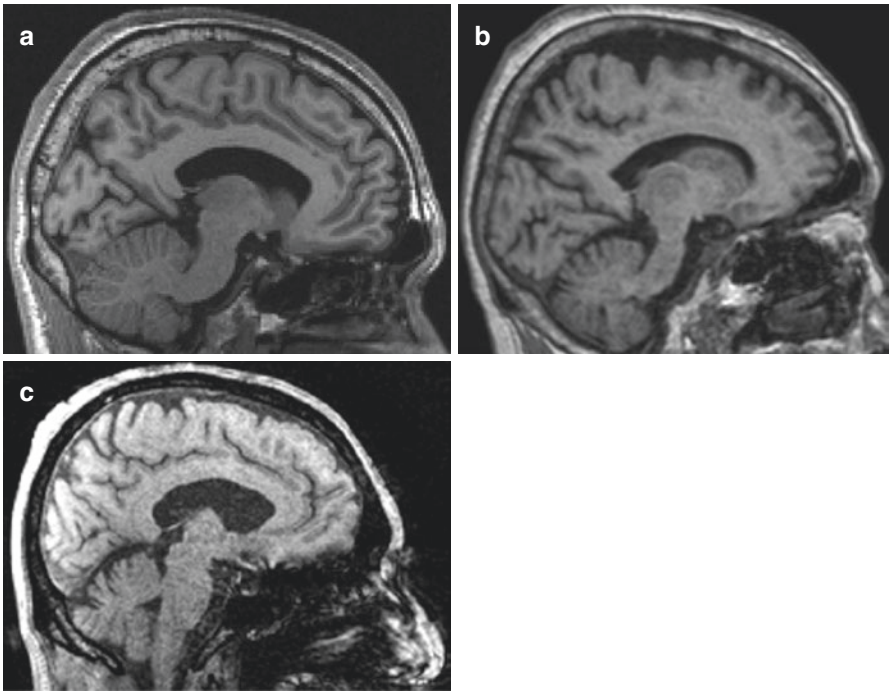

Fig. 15.1 Example of differences between MR image qualities. (**a**) Good quality image, (**b**) blurring artifact around frontal gyrus, (**c**) poor SNR

MR images significantly degrade the reliability and precision of volumetric or morphometric measurements because their property can be changed by MRI manufacturer and time variation. This section introduces intensity nonuniformity correction methods, B1 correction [6] and nonparametric nonuniform intensity normalization [5], and distortion correction methods, Grad-unWarp [7] and phantom-based distortion correction [8].

15.2 Quality Control

It is important to use MRI data obtained with consistent scan parameters and on the same scanner to guarantee the reliability of the image analysis in longitudinal studies. Prior to the study, the site must pass the site qualification. Site qualification includes an examination in which a human volunteer is scanned twice at 1- or 2-week intervals with the study approved sequences loaded by a site local service engineer. The quality control team reviews human scans for the consistent scan parameters and good image quality between two sessions. If the human scan does not pass the review, the quality control team will ask to re-scan the human volunteer. After completely passing the review, the quality control team will provide

site qualification. The quality control team will check whether the scan parameters satisfy certain scan protocols at each scan because image quality is dependent on the scan parameters, for example, field of view (FOV), slice thickness, transmit and receiver coil type, acquisition sequence, and software version (protocol check).

MRI has shown much promise as a biomarker of quantifying AD and other dementia progressions using morphometric or volumetric measurement of the brain atrophy [4]. However, its reliability and reproducibility depend on the image quality. The imaging artifact also affects image quality. So the image quality must be checked and handled to enhance standardization across sites and platforms and the reproducibility of longitudinal image analysis (image quality check).

In this section, we explain how to conduct image quality control. Each scan obtained from multiple imaging centers must be reviewed by the quality control team at the central data center. The quality control team ensures the scan protocol consistency and checks image quality in the acquired images. Moreover, a neuroradiologist checks the image data to identify any clinically significant findings. In the next section, we will describe the details of the consistency, image quality, and clinically significant findings of the checking protocol.

15.2.1 Protocol Check

Most of the clinical image data were contained in digital imaging and communications in medicine (DICOM) format. In 1982, the American College of Radiology (ACR) and the National Electrical Manufacturers Association (NEMA) formed a committee to develop DICOM standards for the interconnection of digital imaging devices [9]. The DICOM files contain information regarding the imaging scanners such as manufacturer name, scanner model name, modality type, and acquisition parameters in the DICOM TAG field. The quality control team checks the imaging parameters and, if not consistent with site notification, then contacts the Clinical Research Coordinator (CRC), technologist and site principal investigator, to notify them of imaging failure and ask for a repeat scan as soon as possible. Table 15.1 shows an example of DICOM TAG for checking the imaging parameters. For some parameters such as repetition time, echo time, field strength, and others, checks in rounded values are permitted. Especially, when the machine manufacturer or model is changed, the reproducibility of the imaging analysis is extremely degraded, and so the quality control team must check the machine change.

15.2.2 Image Quality Check

Numerous artifacts in MR images that are not present in the original imaged object may be caused by improper technical operation of the imaging, while at other times they may be a consequence of natural processes or properties of the human body. Subject motion during the scan generates artifacts by inducing phase errors in the MRI signal. These artifacts can be classified into two types, blurring and ghosting

Table 15.1 DICOM TAG list for checking imaging parameters

DICOM TAG	Description
(0008, 0070)	Manufacturer
(0008, 0080)	Institution name
(0008, 103e)	Series description
(0008, 1090)	Model name
(0018, 0023)	MR acquisition type
(0018, 0050)	Slice thickness
(0018, 0080)	Repetition time
(0018, 0081)	Echo time
(0018, 0082)	Inversion time
(0018, 0083)	Number of averages
(0018, 0087)	Magnetic field strength
(0018, 0088)	Spacing between slices
(0018, 0091)	Echo train length
(0018, 0093)	Percent sampling
(0018, 0094)	Percent phase fov
(0018, 0095)	Pixel bandwidth
(0018, 1000)	Device serial number
(0018, 1020)	Software version
(0018, 1100)	Reconstruction diameter
(0018, 1250)	Receiving coil
(0018, 1310)	Acquisition matrix
(0018, 1312)	Phase encoding direction
(0018, 1314)	Flip angle
(0019, 107e)	Number_of_echoes
(0021, 1057)	Locs_per_slab
(0025, 1007)	Images_in_series
(0028, 0030)	Pixel spacing

artifacts. Blurring artifacts are produced by random movements, mainly in the phase-encode direction. Periodic motion associated with the movement of the lower jaw, eye, and the nasal cavity creates ghosting artifacts. Flow artifacts are caused by blood flow or fluids in the body. Fourier transform from a finite sampled signal causes truncation or gibbs artifacts as parallel lines adjacent to high-contrast borderline. Magnetic susceptibility within the internal magnetization of a tissue also causes artifacts due to interactions with an external magnetic field. Two different magnetic susceptibilities between air and tissues and/or metal and tissues cause local distortions in the magnetic field. Especially metal objects in the subject cause large distortions and significant susceptibility artifacts which result in a loss of signal in the image (metal artifacts). In normal MRI scanning, warp-around (aliasing) artifact occurs when FOV is smaller than an imaging object. The quality control team checks each MR image, and if any image does not have good quality, the quality control team recommends re-scanning. However, if the image quality will not be improved if the scan imaging is repeated, the protocol deviation must be logged or the image data have to be excluded. Checking items will be mentioned below.

15.2.2.1 Checking Gibbs and Blurring Artifacts Within Cerebral Parenchyma or Outside

Glade 0: Not admit obvious blurring within the cerebral parenchyma.
Glade 1: The boundary of the gray and white matter is unclear due to gibbs and blurring.
Glade 2: Not separate gray and white matter, collapse brain sulcus, and clearly identify arc-shaped gibbs artifact.
Glade 3: Admit obvious blurring and ghosting.
If any image acquired from a subject is graded 2 or 3, quality control team will ask your site to re-scan a subject.

15.2.2.2 Checking Ghosting and Flow Artifacts

Glade 0: Not admit ghosting and flow artifacts within the brain parenchyma
Glade 1: Admit ghosting and flow artifacts seen within the brain parenchyma
Glade 2: Admit ghosting and flow artifacts within the brain parenchyma and cannot identify cerebral cortex
Glade 3: Admit severe ghosting and flow artifacts within the brain parenchyma and cannot recognize the outline of the head
If any image acquired from a subject is graded 2 or 3, quality control team will ask your site to re-scan a subject.

15.2.2.3 Checking Metal and Chemical Artifacts

Glade 0: Not admit metal artifacts or chemical shift
Glade 1: Admit metal artifacts or chemical shift
Glade 2: Admit strong metal artifacts and chemical shift
Glade 3: Admit very strong metal artifacts and chemical shift
If any image acquired from a subject is graded 2 or 3, quality control team will ask your site to re-scan a subject.

15.2.2.4 Checking Aliasing (Warp-Around) Artifacts

Glade 0: Not admit aliasing artifacts
Glade 1: Admit aliasing artifacts but not overlap to the whole head
Glade 2: Admit aliasing artifacts and overlap in part of the skull
Glade 3: Admit aliasing artifacts and overlap in some slices of the cerebral parenchyma
Glade 4: Extend to the majority of brain parenchyma
If any image acquired from a subject is graded 2 or 3, quality control team will ask your site to re-scan a subject, and grade 1 should also ideally be re-scanned.

15.2.2.5 Checking Coverage of the Head

Grade 0: Covered whole head
Grade 1: Part of skull lacking
Grade 2: Not covered brain parenchyma
If any image acquired from a subject is graded 1 or 2, it would be desirable to re-scan.

Table 15.2 Examples of clinical findings that affect the imaging

Previous surgery
Hemorrhage
Developmental anomaly
Space-occupying lesion
Atypical atrophy
Hemispheric infarction
Prior head trauma
Metallic artifact
Normal pressure hydrocephalus
Cerebral edema
Others

15.2.3 Clinically Significant Findings Check

Unexpected other degenerative diseases and significant clinical findings affect the imaging analysis to detect the natural progression of a particular disorder. If the subject has any of the significant abnormalities listed in Table 15.2, the MRI data acquired from the subject should be excluded from the statistical imaging analysis data set. Additionally, the subjects should be notified so that they can receive appropriate treatment whenever a significant radiological finding is identified by the neuroradiologist according to the terms of each facility participating in the study.

15.2.4 Preprocessed Intensity Inhomogeneity Correction and Distortion Correction

Nonuniformity receiver coil sensitivity and transmit radio-frequency wave cause intensity inhomogeneity on MR images. Because many image analysis algorithms assume homogeneity of signal intensity within each tissue type, intensity inhomogeneity can reduce the reliability of the analysis method. Moreover, MRI scans often contain geometrical distortions. The most prominent factors of distortion are image gradient nonlinearity, static magnetic field inhomogeneity, and magnetic susceptibility, as typical image reconstruction relies on linear approximation of a magnetic field gradient. A distortion can cause a superficial local volume change, which affects the precision and accuracy of volumetric and morphometric analysis [7]. Some scanner instability such as variation of the static magnetic field strength can introduce changes in the voxel size (a scaling change); it may either mimic or obscure true atrophy changes at longitudinal analysis to detect the rate of brain atrophy [10]. To quantify precisely the rates of brain atrophy, it is important to correct intensity inhomogeneity and distortion including scaling drift. So in this section, two types of intensity correction method, B1 correction and nonparametric nonuniform intensity normalization (N3), and subsequently two distortion correction methods, a theoretical correction method called Grad-unWarp (GW) method and a phantom-based distortion correction method, are introduced.

15.2.4.1 Correction of Intensity Inhomogeneity

B1 Correction

B1 correction employs additional B1 calibration scans to correct the image intensity nonuniformity. In this correction procedure, it is assumed that the body coil has uniform sensitivity. However images scanned by body coil show a poor signal-to-noise ratio. Therefore, the intensity inhomogeneity profile of a head coil can be obtained by dividing the smoothed body coil image by the smoothed surface coil image. The B1-corrected head coil image can be obtained by multiplying the uncorrected image with the estimated intensity inhomogeneity profile [9].

N3 Correction

N3 is independent of pulse sequence and a histogram peak sharpening algorithm without requiring additional B1 calibration scans. N3 will reduce the intensity nonuniformity due at 3 T, and 1.5 T scans also undergo N3 processing to reduce residual intensity nonuniformity. To eliminate the dependence of the field estimate on anatomy, an iterative approach is used to estimate both the multiplicative bias field and the distribution of the true tissue intensities. Preprocessing of MR data using N3 has been shown to substantially improve the accuracy of anatomical analysis techniques such as tissue classification, registration. and cortical surface extraction [10].

The resulting images that were uncorrected and corrected by the B1 correction and N3 correction are shown in Fig. 15.2. In the uncorrected image in Fig. 15.2a, there can be seen an area of high intensity at the fore part of the brain, and by comparing Fig. 15.2b, c, N3 correction is seen to more powerfully correct the intensity distortion than B1 correction.

15.2.4.2 Distortion Correction

Grad-Unwarp Correction

The US-ADNI employs the GW correction method and ADNI phantom-based scaling correction. In GW correction, a set of spherical harmonic coefficients is computed for a particular gradient coil design and can be used to correct the distortion arising from gradient nonlinearity embedded in acquired images. Moreover, ADNI phantom-based linear scaling correction involves reducing the observed geometric drift or voxel size adjustment employing an affine transformation of nine degrees of freedom. The parameters of affine transformation were acquired from design and obtained fiducial points of the ADNI phantom.

Phantom-Based Distortion Correction

Phantom-based distortion correction method is based on image warping using a polynomial function. The method detects fiducial points within a phantom image and calculates warping functions for distortion correction. This method can significantly improve the spatial errors as demonstrated in phantom and human studies. Additionally, the method was significantly better than a distortion correction method based on a description of spherical harmonics, i.e., GW, in improving the distortion

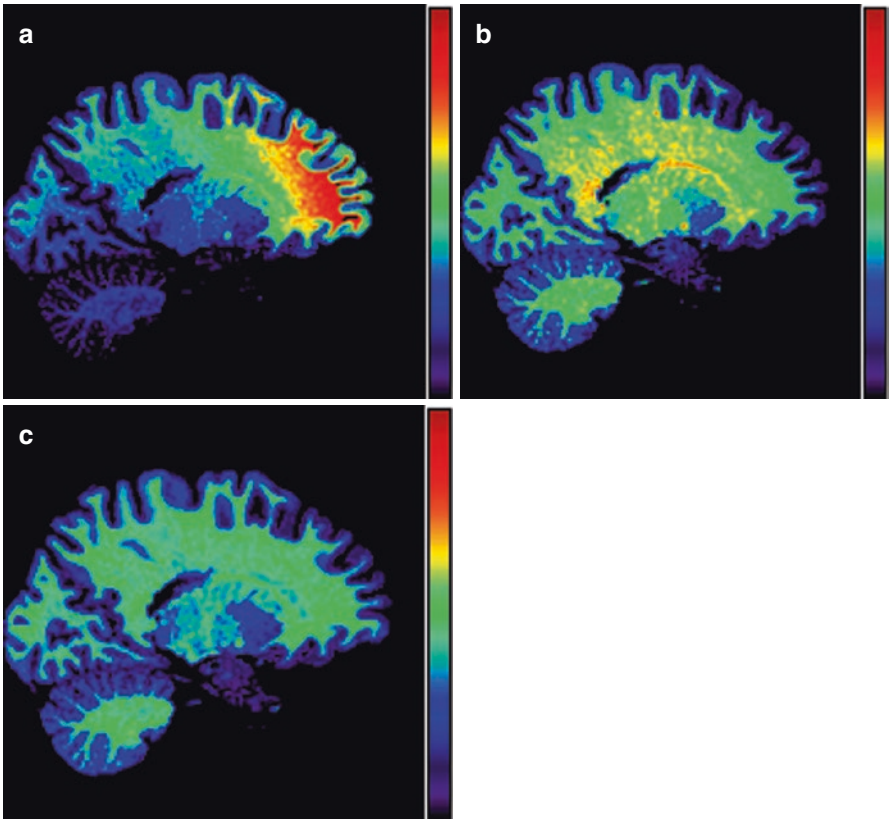

Fig. 15.2 Results of intensity inhomogeneity correction. (**a**) Uncorrected, (**b**) after B1 correction, (**c**) after N3 correction

of root-mean-square errors. The resulting images that were uncorrected and corrected by the phantom-based distortion correction are shown in Fig. 15.3.

Conclusions

Several points promoting high reliability and reproducibility of MRI data in a multicenter longitudinal study were outlined. First, quality control processes included protocol check and image quality check. Protocol check guarantees that consistency and the properties of individual scanners are consistent with the site qualification, and image quality check can exclude inferior quality images with major imaging artifacts that can degrade the reliability of automated image analysis. Unexpected other degenerative disease may also bias the statistical analysis when following the progress of a specific disease. Checking significant clinical findings can be helpful for subjects to obtain optimal treatment as well as enhancement of the statistical power of analysis.

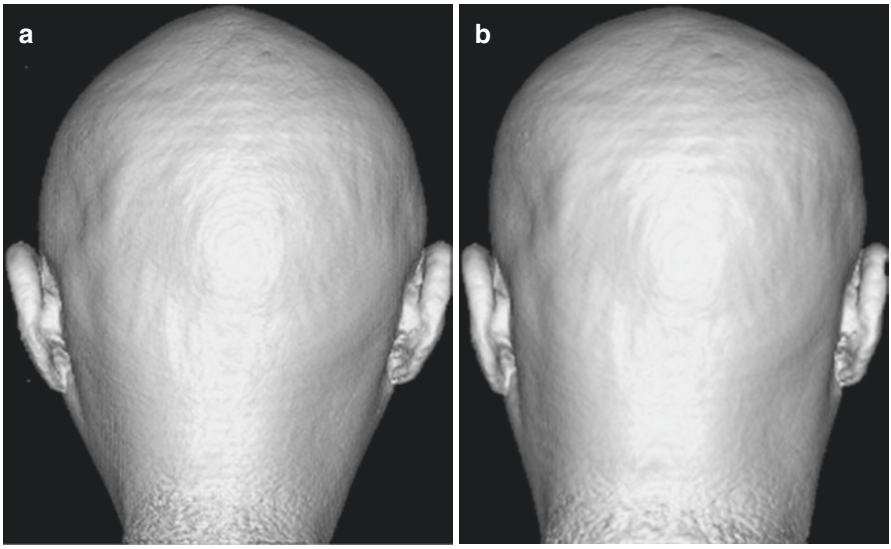

Fig. 15.3 3D head image before and after phantom-based distortion correction. (**a**) Uncorrected, (**b**) after phantom-based distortion correction

Signal intensity inhomogeneity and distortion on MR images also degrade the reliability and reproducibility of MRI data. However several approaches that can correct them have been reported.

Researchers who try to assess disease progression or the therapeutic effect of new drugs should realize that analysis bias can be reduced by adopting an appropriate data handling process.

References

1. Mueller SG, Weiner MW, Thal LJ, Petersen RC, Jack C, Jagust W, Trojanowski JQ, Toga AW, Beckett L. The Alzheimer's disease neuroimaging initiative. Neuroimaging Clin N Am. 2005;15(4):869–77.
2. Marcus DS, Wang TH, Parker J, Csernansky JG, Morris JC, Buckner RL. Open Access series of imaging studies (OASIS): cross-sectional MRI data in young, middle aged, Nondemented, and demented older adults. J Cogn Neurosci. 2007;19:1498–507.
3. Marcus DS, Fotenos AF, Csernansky JG, Morris JC, Buckner RL. Open Access series of imaging studies (OASIS): longitudinal MRI data in Nondemented and demented older adults. J Cogn Neurosci. 2010;22(12):2677–84.
4. Stonnington CM, Tan G, Klöppel S, Chu C, Draganski B, Jack CR, Chen K, Ashburner J, Frackowiak RSJ. Interpreting scan data acquired from multiple scanners: a study with Alzheimer's disease. NeuroImage. 2008;39(3):1180–5.
5. Sled JG, Zijdenbos AP, Evans AC. A nonparametric method for automatic correction of intensity nonuniformity in MRI data. IEEE Trans Med Imaging. 1998;17(1):87–97.
6. Narayana PA, Brey WW, Kulkarni MV, Sievenpiper CL. Compensation for surface coil sensitivity variation in magnetic resonance imaging. Magn Reson Imaging. 1988;6(3):271–4.

7. Janke A, Zhao H, Gowin GJ, Galloway GJ, Doddrell DM. Use of spherical harmonic Deconvolution methods to compensate for nonlinear gradient effects on MRI images. Magnet Reson Med. 2004;52:115–22.
8. Maikusa N, Yamashita F, Tanaka K, Abe O, Kawaguchi A, Kabasawa H, Chiba S, Kasahara A, Kobayashi N, Yuasa T, Sato N, Matsuda H, Iwatsubo T. Improved volumetric measurement of brain structure with a distortion correction procedure using an ADNI phantom. Med Phys. 2013 Jun;40(6):062303.
9. Bidgood WD Jr, Horii SC. Introduction to the ACR-NEMA DICOM standard. Radiographics. 1992 Mar;12(2):345–55.
10. Clarkson MJ, Ourselin S, Nielsen C, Leung KK, Barnes J, Whitwell JL, Gunter JL, Hill DLG, Weiner MW, Jack CR Jr, Fox NC. Comparison of phantom and registration scaling corrections using the ADNI cohort. NeuroImage. 2009;47(4):1506–13.

Standardization and Quality Control of Brain PET Data in a Multicenter Study

16

Michio Senda

Abstract

PET data depends on the PET camera model and the detailed methods of PET scanning including subject preparation, injected activity, accumulation time, scan time, and reconstruction parameters. In a multicenter study, data quality tends to be heterogeneous because participating PET centers have various PET camera models with variable experience in brain PET. Therefore standardization of the PET imaging protocol is essential, and the physical image quality should be harmonized between different camera models based on phantom tests. Japanese Society of Nuclear Medicine (JSNM) has issued the standard PET imaging protocols and determined phantom test criteria to standardize and harmonize brain FDG-PET and amyloid imaging. JSNM has further launched a site qualification program that qualifies PET centers and their cameras for their capability of high-quality standardized PET imaging based on phantom data and site visit. This program can be used to select or qualify PET centers and cameras in a multicenter project before initiation of the study. In such a multicenter study, each PET data should be checked for protocol compliance and data quality by PET QC Core before being forwarded to data interpretation and analysis.

Keywords

Quality control (QC) • Harmonization • Japanese Society of Nuclear Medicine Phantom • J-ADNI

M. Senda
Division of Molecular Imaging, Institute of Biomedical Research and Innovation, 2-2 Minatojima-Minamimachi, Chuo-ku, Kobe, Hyogo 650-0047, Japan
e-mail: senda@fbri.org

H. Matsuda et al. (eds.), *Neuroimaging Diagnosis for Alzheimer's Disease and Other Dementias*, DOI 10.1007/978-4-431-55133-1_16

16.1 Method Dependency is a Challenge

Positron emission tomography (PET) is a nuclear medicine technique, in which a radioactive drug labelled with a positron-emitting radionuclide (PET drug) is injected into a subject and the radioactivity distribution is imaged and measured with a PET camera (including a PET/CT unit). Because the PET drug distributes and accumulates in the brain according to its characteristics, e.g., reflecting blood flow, metabolism, receptor, transmitter, enzyme activity, amyloid-beta and tau deposition, etc., and that analysis of PET data provides quantified measurement of those physiological processes, PET is indispensable in research and diagnosis of various brain disorders including Alzheimer's disease (AD).

However, PET data thus obtained depend on the PET camera model and the detailed methods of the PET scanning including subject preparation, injected activity, accumulation time, scanning time, and reconstruction parameters. This makes it a challenge to acquire reliable data in a multicenter clinical study, in which subjects are recruited, scanned, and evaluated in a number of PET centers, based on an identical protocol. If the PET data quality is variable across centers, the diagnostic capability may also be variable. This is a serious issue because multicenter setting is essential for obtaining evidence of efficacy of a new PET diagnostic as well as for evaluation of the effect of a new therapeutic using PET. To make PET a universal tool for research and patient management, details of the PET scanning methods should be standardized and harmonized between different PET cameras, and the data should be quality controlled.

16.2 Factors Affecting PET Drug Distribution

16.2.1 Accumulation Time

The brain uptake of the PET drug and the radioactivity distribution within the brain depend not only on the pathophysiological state of the subject brain but also the interval between the injection of the PET drug and the start of data acquisition. This interval, which is called accumulation time or uptake time, should be standardized based on the characteristics of the PET drug.

16.2.2 Subject Condition

In case of PET drugs reflecting neuronal activity, such as FDG that accumulate according to glucose metabolism, the distribution is further affected by resting or stimulated condition of the subjects, such as motor, visual, and auditory stimuli. Therefore, controlling the subject condition is important for obtaining brain FDG-PET images of good reproducibility.

16.3 Factors Affecting PET Image Quality

16.3.1 Resolution and Noise

Image quality is another key issue (Fig. 16.1). Image resolution and image noise are two major factors of image quality that affect diagnostic capability. Visual detection of an abnormally high- or low-uptake area depends both on the contrast of the lesion against the background and on the background noise. Image resolution and noise also affect quantitative capability, because quantitative accuracy is influenced by partial volume effect (PVE; spill-in and spill-out) due to limited resolution and that precision is determined by image noise. The image noise mainly comes from statistical uncertainty of radionuclide decay (gamma-ray emission) and can be reduced if a large amount of counts are collected in the scan (thus called statistical noise) or, alternatively, if the images are smoothed at the cost of resolution. As a matter of fact, a trade-off exists between image resolution and image noise.

16.3.2 Injection Activity and Scan Time

Each PET camera model has its own intrinsic sensitivity and resolution. While newer models in general have better intrinsic performance, old cameras are still in use. A PET camera of lower intrinsic sensitivity needs larger injection activity and/or longer scan time to collect sufficient gamma-ray counts to generate images of sufficiently low statistical noise. It should be noted, however, that a limitation exists to the injected activity due to radiation exposure on the subject. Too much injected activity also degrades the image because higher count rate increases random counts

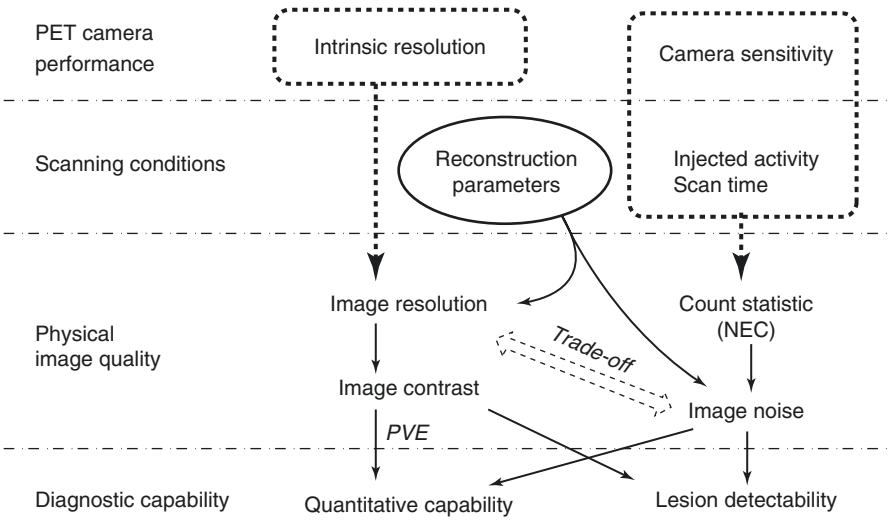

Fig. 16.1 Relationship between method of PET scanning and image quality and their possible effects on diagnostic capability. *NEC* noise equivalent count, *PVE* partial volume effect

and count loss and would only increase noise. Noise equivalent count (NEC), which is the count corrected for random and scatter, is often used instead of crude count to assess "effective" count.

16.3.3 Reconstruction Parameters

The reconstruction parameters, which are the parameters used for generating PET images in the computer after the subject is scanned, together with the post-filter, determine the trade-off between the image resolution and image noise. Iterative reconstruction algorithm called ordered subset expectation maximization (OSEM) and its modifications are often used for the reconstruction process, in which the number of subsets and the number of iterations are the two parameters to be determined by the investigator. By changing the reconstruction parameters, images of various resolution and noise are generated from the identical acquired data (Fig. 16.2). In principle, larger number of subsets or larger number of iterations generates an image of higher resolution but with larger noise.

16.3.4 Harmonization Between Cameras

In a multicenter study using various PET camera models, it is essential to determine appropriate scanning conditions for each PET camera model, especially scan time and reconstruction parameters, so that reliable images of similar quality could be

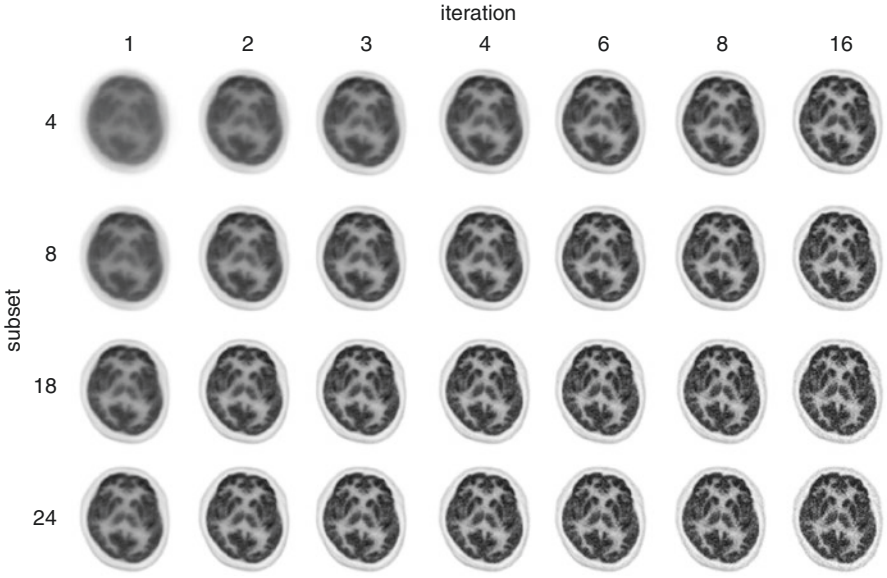

Fig. 16.2 Effect of reconstruction parameters (number of iterations and subsets in OSEM) applied to an identical data acquired with a Discovery-690 PET/CT camera upon the FDG-PET images of a normal subject

obtained across different imaging sites. This process is called "harmonization" between different PET cameras, and phantoms are used for this purpose. In a well quality-controlled multicenter clinical research, the PET QC manager (PET QC Core) selects the phantom(s) and examines each PET camera to test the performance and to determine the appropriate scanning conditions *before* the PET camera is used for subject scans of the project.

16.4 Essential Image Quality for Brain PET

16.4.1 Key Image Quality to FDG-PET

FDG, a marker of glucose metabolism, accumulates high in the cerebral cortex and low in the white matter, creating a clear contrast between gray and white, which provides structural information on the PET images and helps identification of lesion localization. The area of high FDG uptake on the surface of the brain presents itself as a ring on the axial tomogram and is called cortical rim. From the standpoint of histology, the cortical rim is actually a mixture of gray and white matter tissues interlacing each other. Because of partial volume effect, the apparent FDG uptake in the cortical rim reflects the fraction of gray matter tissue more than the FDG uptake per gray matter tissue volume. If pathological cortical atrophy occurs, the apparent FDG uptake in the cortical rim is decreased, sometimes making it difficult to distinguish pathological tissue hypometabolism from apparently decreased uptake due to atrophy.

Detection of localized hypometabolism is a key to interpretation of FDG-PET images in research and diagnosis on dementia, because AD and some other neurodegenerative disorders each present a characteristic pattern of hypometabolism [1]. Reduced FDG uptake in the temporoparietal cortex and in the posterior cingulate and precuneus area is called AD pattern, which is useful for early or differential diagnosis of AD. To detect mild hypometabolism, PET images should have sufficient resolution and contrast together with sufficiently low noise. Furthermore, uniformity is also important because regional FDG uptake is evaluated in comparison with other areas.

In addition to visual interpretation, so-called statistical image analysis such as 3D-SSP is often used, in which the subject's brain is spatially normalized to the standard coordinates system and the relative regional uptake is compared voxel by voxel with the normal database defined on the standard coordinates system to delineate areas of significant hypometabolism.

16.4.2 Key Image Quality to Amyloid-PET

In amyloid PET imaging, radioactivity uptake is observed in the cerebral cortex of subjects who have pathological deposition of amyloid beta plaque in corresponding areas. Positive scan is characterized by such abnormal uptake and is found in most AD

patients and in some cognitively normal old subjects, while negative scan is characterized by the absence of such abnormal cortical uptake [2].

There are a number of PET drugs used for amyloid PET imaging, but all of them, more or less, accumulate nonspecifically in the white matter. Therefore it is necessary to detect mild cortical uptake adjacent to the nonspecific uptake by the white matter, which may often be a challenge, especially in subjects with cortical atrophy. Therefore, PET images again should have sufficient resolution and contrast together with sufficiently low noise. The contrast between gray and white evaluated in the phantom image is especially important to detect mild cortical uptake on the subject images.

In the quantitative analysis of amyloid PET images, which is used as an adjunct to the visual interpretation as well as for evaluation of the effect of therapeutics, the ratio of cortex to cerebellum or pons as a reference region, called standardized uptake value ratio (SUVR), is used. Therefore, uniformity within the field of view is also essential in amyloid PET.

16.5 Phantom Test Criteria for FDG and Amyloid-PET

16.5.1 Phantom Tests in J-ADNI

A large-scale multicenter study named J-ADNI, followed by a similar study J-ADNI2, was launched in Japan, in which subjects with normal cognitive function, mild cognitive impairment (MCI), and mild AD were to be followed with various examinations including FDG and amyloid PET scans. To standardize the PET scanning protocol across the participating PET centers and to harmonize the PET image quality between different PET cameras, the J-ADNI PET QC Core determined the subject preparation condition, standard injection activity, and accumulation time and established the phantom test procedures and criteria, with which to determine the reconstruction parameters for each PET camera.

In the camera qualification and harmonization procedures, two types of phantoms, i.e., Hoffman 3D brain phantom (Data Spectrum Corporation) and uniform cylindrical phantom, are used to measure a total of four image quality parameters: (1) resolution, (2) gray-white contrast, (3) uniformity, and (4) image noise. These four parameters have been adopted because they are considered essential for qualification of PET cameras and for harmonization of the PET image quality between PET cameras in multicenter clinical research on dementia using FDG and amyloid-PET as discussed above.

These four parameters have also been adopted in the phantom test criteria by the Japanese Society of Nuclear Medicine (JSNM) and published in the JSNM guidelines [3].

16.5.2 JSNM Phantom Test Criteria

The JSNM phantom tests prompt measurement of the four physical parameters (resolution, gray-white contrast, uniformity, and image noise) on the phantom images as discussed above.

Table 16.1 Outline of JSNM standard protocol and phantom procedures for brain FDG and amyloid PET (January 2015)[a]

	Standard protocols			Phantom procedures	
	Standard injection activity (MBq), accumulation time[b] (min post injection), and scan time[c] (min)			Phantom scan time	
				Hoffman[d] (20 MBq)[e]	Uniform[f] (40 MBq)[e]
FDG	185 MBq	30 min p.i.	30 min	1800 s	860 s
Amyloid imaging					
^{11}C-PiB	555 MBq	50 min p.i.	20 min	130 s	65 s
^{18}F-florbetapir	370 MBq	50 min p.i.	20 min	705 s	345 s
^{8}F-flutemetamol	185 MBq	90 min p.i.	30 min	250 s	125 s
^{18}F-florbetaben	300 MBq	90 min p.i.	20 min	350 s	175 s

[a]May differ from standards issued by other organizations and subject to change based on future data and situations. For details, see JSNM web site [3]
[b]Interval between injection and start of emission data acquisition
[c]Duration of emission data acquisition
[d]Hoffman 3D brain phantom
[e]Phantom activity at start of scan
[f]Uniform cylindrical phantom (160 mm inner diameter, 300 mm inner length)

Table 16.2 Outline of JSNM phantom test criteria for brain FDG and amyloid PET (January 2015)[a]

Physical parameters	Phantom	Method of analysis	Reference values
Resolution	Hoffman 3D brain phantom	Comparison with filtered digital phantom	8 mm FWHM or better
Contrast	Hoffman 3D brain phantom	Ratio of predefined gray ROIs to white ROIs	%Contrast ≥55%
Uniformity	Uniform cylindrical phantom	Variability of 51 small ROIs (ROI mean)	SD of all ROIs ≤0.0249 (95% CI[b] within ±5%)
Noise	Uniform cylindrical phantom	Voxel values within a large circular ROI	SD/Mean ≤15%

[a]May differ from criteria issued by other organizations and subject to change based on future data and situations. For details, see JSNM web site [3]
[b]Confidence interval assuming Gaussian distribution

The phantom data acquisition methods have been determined based on the standard scanning protocol for each PET drug (FDG and four amyloid agents) and are summarized in Table 16.1. The phantoms are filled with specified radioactivity and scanned for the specified time that has been determined according to the standard injection activity, physical decay during the accumulation time, average brain uptake, and standard scan time for each PET drug. The four physical parameters of the phantom test criteria are summarized in Table 16.2, together with the reference values (cutoff values) for each physical parameter. The criteria are applied to brain FDG for research on AD and other neurodegenerative disorders and to amyloid imaging with ^{11}C–PiB, ^{18}F–florbetapir, ^{18}F–flutemetamol, or ^{18}F–florbetaben.

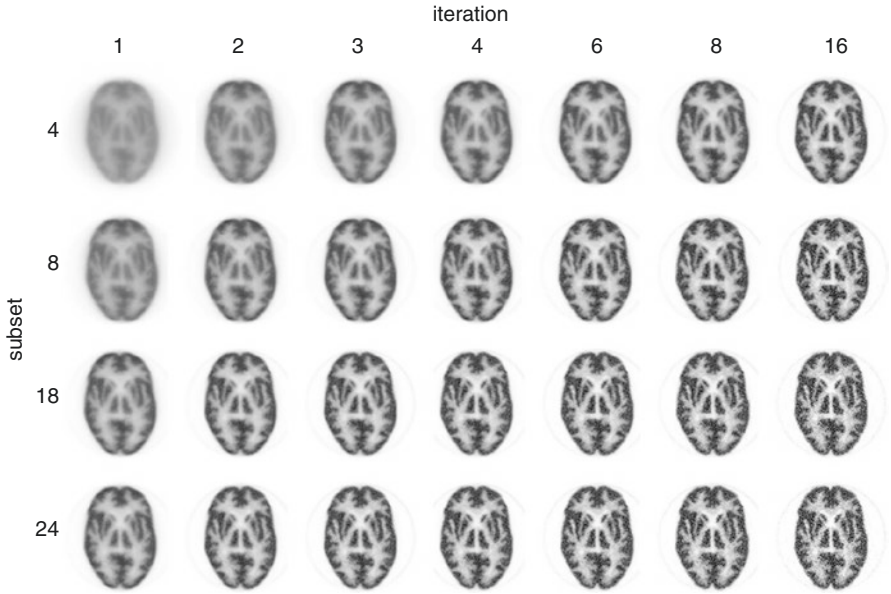

Fig. 16.3 Effect of reconstruction parameters (number of iterations and subsets in OSEM) applied to an identical data acquired with a Discovery-690 PET/CT camera upon the PET images of a Hoffman 3D brain phantom

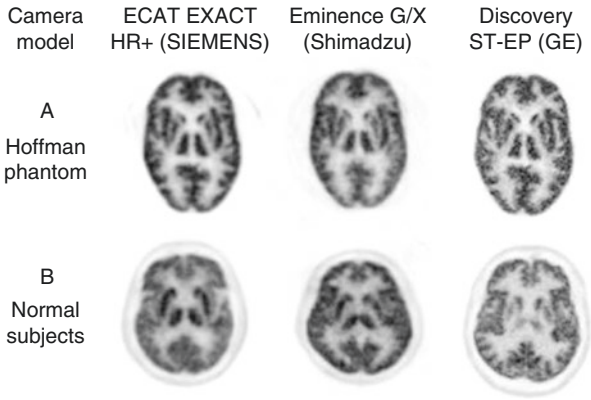

Fig. 16.4 Example of harmonization between three PET camera models. (**a**) PET image of a Hoffman 3D brain phantom reconstructed with appropriate parameters that generate images satisfying JSNM phantom test criteria for each PET camera. (**b**) FDG-PET image of a normal subject acquired and reconstructed with thus determined parameters for each PET camera. Subjects are different persons for the three PET cameras

To harmonize the PET image quality between PET centers and between PET cameras in a multicenter study, the investigator is supposed to find such appropriate reconstruction parameters that would generate phantom images satisfying the criteria (Figs. 16.3 and 16.4). The scan time (data acquisition time) may be adjusted

depending on the sensitivity of the PET camera so that sufficient gamma ray counts are collected. Due to a trade-off between image resolution and noise, a PET camera of poor intrinsic performance may have difficulty in finding the reconstruction parameters that would satisfy both resolution and noise described in Table 16.2. If no reconstruction parameters and scan time are found for a certain PET camera that could generate phantom images satisfying the criteria, then the investigator may decide not to use the PET camera for the multicenter project. It is, of course, up to the investigator whether to conform strictly to the criteria or to allow some deviations.

16.5.3 Basis for JSNM Phantom Criteria

It should be emphasized that no theoretically absolute reference values exist for those physical parameters of the phantom test. If the reference values are set at a high level, then the PET images acquired in the multicenter study will be of higher quality, which may possibly lead to a result demonstrating higher diagnostic capability of the PET imaging for the study population. However, only a few PET camera models will meet the criteria and can be used for the study project, which may reduce the number of participating PET centers and, accordingly, limit the number of study cases. If a new PET drug is approved by the regulatory authorities based on the multicenter study data, and if the phantom criteria become a requirement for the PET camera to be used, the PET scan may not be readily available to the public. On the other hand, if the reference values are set at a low level, then all PET camera models will meet the criteria, and all PET centers will be able to participate in the multicenter study from the viewpoint of PET camera performance. However, the quality of the PET images may not be high enough to demonstrate the efficacy of a new PET drug.

JSNM desires that most PET cameras currently used in Japan should be able to meet the phantom test criteria under appropriate scanning conditions so that most PET centers could participate in a multicenter study that adopts the JSNM criteria. JSNM also considers that the criteria should conform to the image quality level, at which clinical research has been performed to obtain the evidence of efficacy. Therefore, phantom experiments were carried out to obtain the parameter values on the PET camera models that were used in clinical research and clinical trials regarding brain FDG and amyloid imaging. Phantom experiments were also carried out on most PET cameras used in Japan to confirm that the criteria are achievable for most of them. Naturally, the reference values in the criteria might be changed in the future according to the development and advent of new PET cameras with higher physical performance.

16.6 Site and Camera Qualification

Unlike oncology FDG-PET, brain PET for dementia is not so popular in many countries including Japan as a routine clinical diagnostic scan. In a multicenter clinical research or clinical trial, the chief investigator and the sponsor first select clinical sites, in which subjects are to be recruited, registered, and clinically evaluated or

treated; then they search for PET centers for availability of the PET scan. Such PET centers are not necessarily used to brain PET imaging. Therefore, it is necessary to examine the experience of the PET centers and qualify each PET center and the PET camera for participating in the study. For qualification of the PET camera, phantom tests with the abovementioned phantom criteria may be used. In addition to the phantom tests, visiting the PET center and training the staff upon the purpose and scanning protocol of the study as well as data anonymization and transfer are valuable. It is also important to confirm the record of maintenance and calibration of the devices including PET camera, dose calibrator, and injector.

JSNM has launched a qualification program for PET imaging sites and cameras concerning brain FDG and amyloid PET scan. The program qualifies that the site is ready to acquire PET images of sufficient quality according to the JSNM standard protocol. The qualification process includes a site visit by designated auditors to examine the maintenance and calibration of the equipment as well as the organizational structure of the PET center. Phantom data are also acquired for qualification to confirm that the physical parameters of the phantom images meet the JSNM phantom test criteria. The reconstruction parameters may be determined in the course of qualification process by searching for appropriate parameters. A number of multicenter clinical research projects make the JSNM qualification a requirement for the PET center to participate in the project.

16.7 PET Quality Control in a Multicenter Study

Figure 16.5 depicts the entire view of the PET QC process in a multicenter study. It is PET QC Core that takes care of the quality of the PET data acquired in each participating PET center. In an industry-sponsored clinical trial, a professional organization called “imaging CRO” usually takes that role. It should be noted that the quality of PET drugs, not mentioned in Fig. 16.5, is also important in PET research, especially when the PET drug is unapproved or manufactured on site.

Based on the research protocol, the purpose of the PET is defined, and the PET methods are determined together with the PET manual describing the site qualification procedures and the PET scanning protocol. The PET imaging sites are selected, and questionnaires are sent to them inquiring about organization such as physician and technologist contact, experience of the kind of study, PET drug availability, equipment details including PET camera model name, PET scan slot availability, applicability of electronic system to anonymize and submit data, etc. A site visit and phantom tests then follow. The reconstruction parameters are determined based on the phantom tests as explained in detail in this chapter, and the site is qualified for the study.

Upon initiation of the multicenter study, PET QC Core should check the first PET scan from each PET imaging site before allowing the site to scan the second subject. After the project gets off the ground, each PET data from each PET center should be QC checked before being forwarded to image interpretation and data analysis. The QC check process confirms that the PET scan has been carried out and the images have been generated and transferred properly according to the protocol without errors and artifacts. The header of the image files is also checked, which

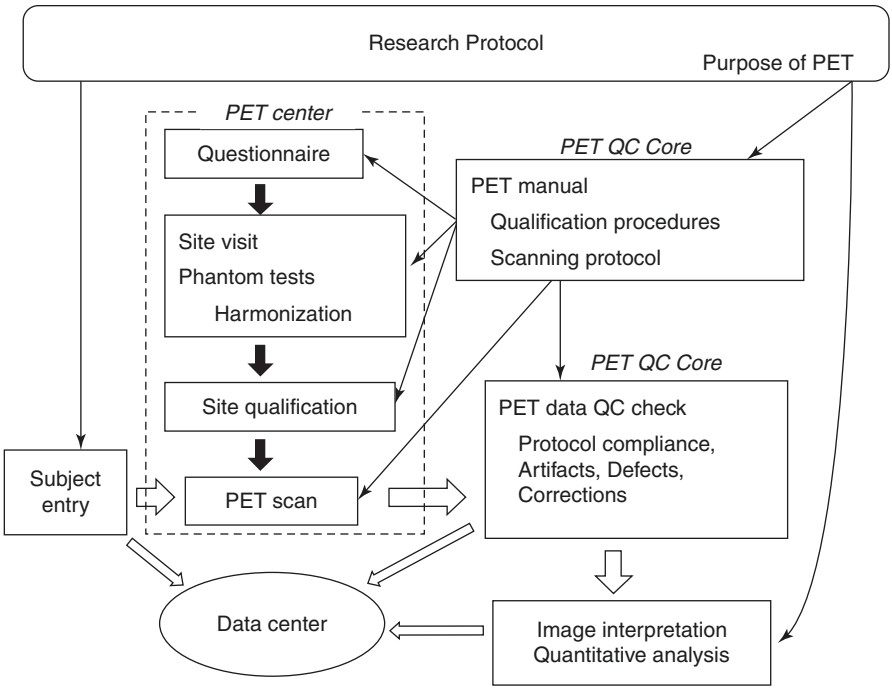

Fig. 16.5 Diagram of the PET quality control in a multicenter study

contains information associated with the scan such as date and time, scanning protocol, and reconstruction parameters.

PET images are then forwarded to image interpretation and analysis. The PET images are either interpreted visually or analyzed quantitatively based on regions of interest (ROI) or using automated software. In a multicenter study, this process is usually carried out by analysts who are bind to clinical information of the subjects [4, 5].

References

1. Silverman DH, Small GW, Chang CY, et al. Positron emission tomography in evaluation of dementia. Regional brain metabolism and long-term outcome. JAMA. 2001;286:2120–7.
2. Gelosa G, Brooks DJ. The prognostic value of amyloid imaging. Eur J Nucl Med Mol Imaging. 2012;39:1207–19.
3. http://www.jsnm.org/ (English information is limited).
4. Yamane T, Ikari Y, Nishio T, et al. Visual-statistical interpretation of ^{18}F-FDG-PET images for characteristic Alzheimer patterns in a multicenter study: inter-rater concordance and relationship to automated quantitative evaluation. Am J Neuroradiol. 2014;35:244–9.
5. Yamane T, Ishii K, Sakata M, et al. Inter-rater variability of visual interpretation and comparison with quantitative evaluation of ^{11}C-PiB PET amyloid images of the Japanese Alzheimer's Disease Neuroimaging Initiative (J-ADNI) multicenter study. Eur J Nucl Med Mol Imaging. 2017;44:850–857A.